UNIVERSIDADE DE LISBOA
INSTITUTO SUPERIOR TÉCNICO

Researches on Physical and Mathematical Models Applied to Continuum Electromechanics

Manuel José dos Santos Silva

Supervisor: Doctor Luiz Manuel Braga da Costa Campos
Co-Supervisor: Doctor Filipa Andreia de Matos Moleiro

Thesis approved in public session to obtain the PhD Degree in

Aerospace Engineering

Jury final classification: Pass with Distinction

2024

UNIVERSIDADE DE LISBOA
INSTITUTO SUPERIOR TÉCNICO

Researches on Physical and Mathematical Models Applied to Continuum Electromechanics

Manuel José dos Santos Silva

Supervisor: Doctor Luiz Manuel Braga da Costa Campos

Co-Supervisor: Doctor Filipa Andreia de Matos Moleiro

Thesis approved in public session to obtain the PhD Degree in

Aerospace Engineering

Jury final classification: Pass with Distinction

Jury

Chairperson: Doctor Paulo Jorge Coelho Ramalho Oliveira, Instituto Superior Técnico, Universidade de Lisboa

Members of the Committee:

Doctor Pedro Manuel Ponces Rodrigues de Castro Camanho, Faculdade de Engenharia, Universidade do Porto
Doctor Luiz Manuel Braga da Costa Campos, Instituto Superior Técnico, Universidade de Lisboa
Doctor Afzal Suleman, Instituto Superior Técnico, Universidade de Lisboa
Doctor Mário Rui Melício da Conceição, Escola de Ciências e Tecnologia, Universidade de Évora
Doctor Anna Guerman, Faculdade de Engenharia, Universidade da Beira Interior
Doctor Gustavo Alexandre Oliveira Rodrigues Dias, Escola de Engenharia, Universidade do Minho

Funding Institution

Fundação para a Ciência e a Tecnologia (FCT)

2024

Dear parents and sister,
thanks for everything . . .

Statement

"I declare that this document is an original work of my own authorship and that it fulfils all the requirements of the Code of Conduct and Good Practices of the Universidade de Lisboa."

Declaração

"Declaro que o presente documento é um trabalho original da minha autoria e que cumpre todos os requisitos do Código de Conduta e Boas Práticas da Universidade de Lisboa."

— Manuel José dos Santos Silva

March 2023

Acknowledgements

With the utmost pride and honour, I show you my doctoral thesis, which is the final result of four long, arduous, fatiguing, but rewarding years that I spent at Instituto Superior Técnico (IST) during my Ph.D. degree. Moreover, this thesis also represents the preceding years of my M.Sc. studies in Aerospace Engineering at the same university, during which I met wonderful people who helped me in the most challenging moments until these days, particularly during the development of this work, and made me a better person. Therefore I wrote this acknowledgement message to everyone who helped me in this challenging journey since its very beginning. It would be almost impossible to accomplish this project completely alone. That justifies this important message directed to all the people mentioned below who deserve this recognition.

First of all, a very great thanks to my supervisor of doctoral thesis, Professor Luiz Braga Campos, for inviting me to work on this Ph.D. project. Without a doubt I accepted the invitation because it happened at the final stage of my M.Sc. thesis with the same supervisor and I interpreted it as a recognition of my accomplishments. This honour to work with my supervisor is due to all his ideas and thoughts during this process, his persistent enthusiasm to make me a better researcher, and his endless insights and comments in all chapters of the thesis. I also want to express my gratitude to my supervisor for making a lot of his background research available to me and providing me with much assistance in this journey.

Secondly, I dedicate some words to my co-supervisor, Professor Filipa Moleiro, for her assistance in writing several papers and ensuring that I fulfilled all submission guidelines for each journal. Furthermore, this acknowledgement is not only for guiding me during the last academic years, but also for all her professionalism and patience whenever I needed help in this world of research.

I also wish to express my gratitude to all other co-authors of the papers produced during my Ph.D. degree, namely Professor Agostinho Fonseca and Professor João Oliveira, for their investigations and thoughts at the initial stages of some papers, and therefore for making my work a little bit easier. I also thank Fundação para a Ciência e Tecnologia for providing me with a Ph.D. scholarship, whose grant number is SFRH/BD/143828/2019.

The support and friendship of all my colleagues who have always motivated and pushed me were also the key to success in the last nine years since my enrolment at IST for the MSc degree. They were part of some wonderful moments in the master and doctoral degrees; hence it has been a pleasure to spend and share time with them. The university journey would be much more painful and difficult without these friends.

Last but not least, a special message for my family. To my parents for their endless love and support throughout my life, particularly during my academic path. To my sister for her tireless support and for trying to help me even though she did not understand what I had been doing in this thesis. And to my one-year-old niece/god-daughter, who gave me a new purpose to live and entirely changed my life.

Once more, with deep gratitude, I thank you all!

M. J. S. Silva
March 2023
IST, Portugal

To contact the author, use the following email addresses:
manuel.jose.dos.santos.silva@tecnico.ulisboa.pt
manuel.jose.s.silva@gmail.com

Resumo

O objectivo de estudar electromecânica dos meios contínuos é formular matematicamente problemas físicos que incluem deformação de matéria numa perspectiva macroscópica. Começa-se com a investigação dos efeitos de múltiplas propagações de ondas acústicas perto de um canto ou de um solo irregular. A onda acústica também é modificada pela atenuação atmosférica. Os efeitos dos três factores são estudados em duas dimensões para especificar o nível de pressão sonora do sinal total e o seu rácio pelo do sinal directo. Outro assunto, agora sobre propagação de ondas elásticas, é se as oscilações livres de um sistema contínuo podem ser atenuadas, ou pelo menos se a energia total é reduzida, devido à aplicação de forças externas, usando como exemplo oscilações transversais de uma corda elástica uniforme. Para oscilações amortecidas, um método efectivo em atenuá-las é aplicando uma força cuja amplitude decai exponencialmente com o tempo. Outro tema sobre ondas é que, após adicionar os campos magnético e gravítico ao gradiente de pressão, a propagação das ondas Alfvén num meio que as suporte ao longo das linhas do campo magnético de um dipolo é considerada usando coordenadas dipolares. A equação das ondas obtida é hipergeométrica gaussiana generalizada. Outro tema é verificar que ondas elásticas lineares são não-dispersivas em cristais ou matéria amorfa; neste último caso, as ondas longitudinais e transversais são isotrópicas, mas não a sobreposição delas. Sobre a mecânica estática dos sólidos, a teoria de vigas Euler-Bernoulli é analisada usando coordenadas Cartesianas na direcção da posição indeformada ou perpendicular à mesma, mas permitindo efeitos não-lineares para grandes declives de deformação. A forma não-linear da curva neutra é uma sobreposição de harmónicas lineares. Em relação à encurvadura não-linear de placas elásticas, as equações de Föppl-von Kármán são resolvidas usando expansões assimptóticas semelhantes para deslocamento transversal e função de tensão no plano, ambas com todas as ordens determinadas explicitamente.

Palavras-chave: Ondas acústicas; Supressão activa de vibrações; Fluxo de energia; Ondas Alfvén; Deformação de vigas e placas

Abstract

The purpose of studying continuum electromechanics is to formulate, mathematically and in a macroscopic perspective, physical problems that involve the deformation of matter. The thesis starts with an investigation about multipath effects of acoustic waves near a rough ground or near a corner. The atmospheric attenuation also modifies the acoustic wave. The effects of the three factors are studied in two dimensions to specify the acoustic pressure level of total signal and its ratio to the direct signal. Another issue, now about the propagation of elastic waves, is whether an external force can suppress the free oscillations of a continuous system, or at least reduce the total energy, using as example the transverse oscillations of a uniform elastic string. An effective method of countering the damped oscillations is applying a force with amplitude decaying exponentially in time. Another issue about waves is that, after adding the magnetic and gravitational fields to the pressure gradient, the propagation of Alfvén waves in a medium that can support them along dipole magnetic field lines is considered using dipolar coordinates. The waves equation obtained is an extended Gaussian hypergeometric equation. Another topic is to verify if the linear elastic waves are non-dispersive in crystals or amorphous matter; in this last case, the longitudinal and transversal waves are isotropic, but not their superposition. Related to the static mechanics of solids, the Euler-Bernoulli theory of beams is analysed using Cartesian coordinates along and normal to the undeflected position, but allowing the non-linear effects of a large slope of deformation. The non-linear shape of the neutral surface is a superposition of linear harmonics. About the non-linear bending of elastic plates, the Föppl-von Kármán equations are solved by a method of twin asymptotic expansions for the transverse displacement and in-plane stress function, both obtained explicitly to all orders.

Keywords: Acoustic waves; Active vibration suppression; Energy flux; Alfvén waves; Deformation of beams and plates

Extended abstract | List of published articles

THIS thesis deals with subjects of continuum electromechanics. It begins with the study of multipath effects that occur when receiving a wave near a corner, for example, the noise of some forms of urban air mobility near a building or even a telecommunications receiver antenna near an obstacle. The total signal received in a corner consists of four parts: (i) a direct signal from the source to the observer; (ii) a second signal reflected on the ground; (iii) a third signal reflected on the wall; (iv) a fourth signal reflected from both wall and ground. The problem is solved in two dimensions to specify the total signal, whose ratio to the direct signal specifies the multipath factor. Its amplitude and phase are plotted as functions of the frequency over the audible range for various relative positions of observer and source. They are also plotted for several combinations of the ground and wall reflection coefficients. The received signal consists of a double series of spectral bands. In other words: (i) the interference effects lead to spectral bands with peaks and zeros; (ii) the successive peaks also go through zeros and "peaks of the peaks". The noise received is also modified by atmospheric attenuation and reflections from the ground. All these effects must be considered concerning the path of the acoustic wave. Most of the literature about ground effects on noise considers a point source over flat ground, using the method of images, that does not extend readily to rough ground. The effect of this ground can be modelled by: (i) identification of reflection points; (ii) use of a complex reflection coefficient at each reflection point; (iii) adding all reflected waves within line-of-sight of the receiver that is not blocked by terrain (for a flat ground there is no blockage).

The thesis also addresses whether an applied external force suppresses the free oscillations of a continuous system, or at least reduces the total energy, for instance, in the linear transverse oscillations of a uniform elastic string. For undamped oscillations, the non-resonant forcing does not interact with the normal modes, whose energy is unchanged. It adds the energy of the forced oscillation, thus increasing the total energy, which is the opposite of the result sought. The resonant forcing leads to an amplitude growing linearly with time; hence, the energy grows quadratically with time, implying an increase in total energy after a sufficiently long time. A reduction in total energy is possible over a short time, say over the first period of oscillation, by optimising the forcing. In the case of a concentrated force, by optimising its magnitude and location, the total energy with forcing in the first period can be reduced by

a modest maximum of 2% relative to the free oscillation alone. In the case of a continuously distributed force, optimising the spatial distribution can reduce the energy of the total oscillation to one-fourth of that of the free oscillation over the first period of vibration. This optimisation shows that continuously distributed forces are more effective at vibration suppression than point forces. Regarding damped oscillations, active vibration suppression is considered again for the transverse oscillations of an elastic string. Assuming a finite elastic string fixed at both ends, the free oscillations are (i) sinusoidal modes in space-time with exponential decay in time due to damping. The non-resonant forced oscillations at an applied frequency distinct from a natural frequency are also (ii) sinusoidal in space-time, with a constant amplitude and a phase shift such that the work of the applied force balances the dissipation. For resonant forcing at an applied frequency equal to a natural frequency, the sinusoidal oscillations in space-time have (iii) a constant amplitude and a phase shift of $\pi/2$. In both cases, the (ii) non-resonant or (iii) resonant forcing dominates the decaying free oscillations after some time. Even after optimising the forcing to minimise the total energy of oscillation, it remains below the energy of the free oscillation alone, only for a short time, generally a fraction of the period. A more effective method of countering the damped free oscillations is to use a force with amplitude decaying exponentially in time; by suitable choice of the forcing decay relative to the free damping, the total energy of oscillation over all time can be reduced to no more than 3.6% of the energy of the free oscillation.

The energy balance equation, including the kinetic energy density, the deformation energy density and the power of external forces, identifies the energy flux as minus the product of the velocity by the stress tensor; this result does not depend on constitutive relations and applies to elastic or inelastic matter. The energy flux is also obtained for linear strains and, in the case of transverse vibrations of elastic strings, is extended to the non-linear case of unrestricted slope. In the linear case, the energy flux is obtained in elasticity for crystals and amorphous matter. By inspecting any linear wave equation in a steady homogeneous medium, it is possible to ascertain whether the waves are (a) isotropic and (b) dispersive, with no need for an explicit solution. Applying this result to linear elastic waves shows that: (i) they are non-dispersive in crystals or amorphous matter; (ii) for the latter material, the longitudinal and transversal waves are isotropic, but their sum is not. A consequence of (ii) is that the superposition of both waves: adds the two energy densities and powers of external forces; adds, to the two energy fluxes, a third cross-coupling energy flux that is proportional to the dilatation of the longitudinal wave multiplied by the velocity of the transverse wave.

After adding the magnetic and gravitational fields to the pressure gradient and considering a medium consisting of or surrounded by plasma, which can support Alfvén waves, the propagation of waves along dipole magnetic field lines is evaluated using a new coordinate system: dipolar coordinates. The application considered is to Alfvén waves propagating along a circle, that is a magnetic field line of a dipole, with transverse velocity and magnetic field perturbations; the various forms of the wave equation are linear second-order differential equations with variable coefficients. The coefficients are specified by a background magnetic field, which is force-free. The absence of a background magnetic force leads to a mean state of hydrostatic equilibrium, determined by the balance of gravity against the pressure gradient, for a perfect gas or incompressible liquid. The wave equation simplifies to a Gaussian hypergeometric type in the case of zero frequency; otherwise, for non-zero frequencies, an extended Gaussian hypergeometric equation is obtained. The solution of the last equation specifies the magnetic field perturbation spectrum and, via a polarisation relation, the velocity perturbation spectrum; both are plotted over half a circle for three values of the dimensionless frequency.

Another issue of continuum electromechanics is the deformation of beams and plates. The Euler-Bernoulli theory of beams is usually presented in two forms: (i) in the linear case of small slope using Cartesian coordinates along and normal to the straight undeflected position; and (ii) in the non-linear case of large slope using curvilinear coordinates along the deflected position specified by the arc length and angle of inclination. In this thesis, (iii) Cartesian coordinates along and normal to the undeflected position like (i) are used, but including exactly the non-linear effects of large slope like (ii). This third form of the equation of the elastica (neutral surface) shows that the exact non-linear shape is a superposition of linear harmonics; thus, the non-linear effects of a large slope are equivalent to the generation of harmonics of a linear solution for a small slope. In conclusion: (i) the critical buckling load is the same in the linear and non-linear cases because the fundamental mode determines it; (ii) the buckled shape of the elastica is different in the linear and non-linear cases because non-linearity adds harmonics to the fundamental mode. The non-linear shape of the elastica, when the square of the slope cannot be neglected, is illustrated for the first four buckling modes of cantilever, pinned, and clamped beams with different lengths and force amplitudes.

The Föppl-von Kármán equations for the non-linear bending of elastic plates are also solved by a novel method of twin asymptotic expansions for the transverse displacement and in-plane stress function. Unlike most asymptotic expansions, which can be derived explicitly only to the second or third order, in this thesis, both asymptotic expansions can be obtained explicitly to all orders. The perturbation relations form a causal chain of linear relations, with variable coefficients specified by the lower orders. Furthermore, this method applies to the axisymmetric case with external loading approximated by a polynomial of the radius. The method of perturbation expansions is illustrated explicitly up to second-order by applying to a clamped circular plate subject to a radial pressure and its weight.

List of published articles sorted by date

- L. M. B. C. Campos, F. Moleiro, M. J. S. Silva and J. Paquim (2018)[1]
  "On the regular integral solutions of a generalized Bessel differential equation",
  Advances in Mathematical Physics, 2018, ID 8919516,
  DOI: 10.1155/2018/8919516

[1] The article "On the regular integral solutions of a generalized Bessel differential equation" was done during the M.Sc. thesis.

- L. M. B. C. Campos, F. Moleiro and M. J. S. Silva (2019)[2]
  "On the fundamental equations of unsteady anisothermal viscoelastic piezoelectromagnetism",
  European Journal of Mechanics – A/Solids, 78, ID 103848,
  DOI: 10.1016/j.euromechsol.2019.103848

- L. M. B. C. Campos, M. J. S. Silva and F. Moleiro (2019)
  "On Alfvén wave propagation along a circle on dipolar coordinates",
  Journal of Plasma Physics, 85 (6), ID 905850608,
  DOI: 10.1017/S0022377819000837

- L. M. B. C. Campos, M. J. S. Silva and A. R. A. Fonseca (2021)
  "On the multipath effects due to wall reflections for wave reception in a corner",
  Noise Mapping, 8 (1), pp. 41–64,
  DOI: 10.1515/noise-2021-0004

- L. M. B. C. Campos and M. J. S. Silva (2021)
  "On the generation of harmonics by the non-linear buckling of an elastic beam",
  Applied Mechanics, 2 (2), pp. 383–418,
  DOI: 10.3390/applmech2020022

- L. M. B. C. Campos, M. J. S. Silva and J. M. G. S. Oliveira (2022)
  "On the effects of rough ground and atmospheric absorption on aircraft noise",
  Noise Mapping, 9 (1), pp. 23–47,
  DOI: 10.1515/noise-2022-0003

- L. M. B. C. Campos and M. J. S. Silva (2022)[3]
  "On a generalization of the Airy, hyperbolic and circular functions",
  Nonlinear Studies, 29 (2), pp. 529–545,
  URL: `www.nonlinearstudies.com/index.php/nonlinear/article/view/2137`

- L. M. B. C. Campos and M. J. S. Silva (2022)
  "On the countering of free vibrations by forcing: Part I – Non-resonant and resonant forcing with phase shifts",
  Applied Mechanics, 3 (4), pp. 1352–1384,
  DOI: 10.3390/applmech3040078

- L. M. B. C. Campos and M. J. S. Silva (2023)
  "On the countering of free vibrations by forcing: Part II – Damped oscillations and decaying forcing",
  Applied Mechanics, 4 (1), pp. 141–178,
  DOI: 10.3390/applmech4010009

[2] The article "On the fundamental equations of unsteady anisothermal viscoelastic piezoelectromagnetism" is not included in this Ph.D. thesis.
[3] The article "On a generalization of the Airy, hyperbolic and circular functions" is not included in this Ph.D. thesis.

Contents

List of tables

List of figures

List of symbols

Due to an extensive list of symbols used in this document, and since the chapters can be considered as independent of each other, the nomenclature is divided for each chapter. The following list does not contain the symbols from the appendices A to E since they are self-explanatory.

Chapter 2 – On the multipath effects due to wall reflections for wave reception near a corner

α Elevation angle for the observer's position O

β Elevation angle for the source's position S

$\Delta\mathrm{SPL}_{\mathrm{ground}}$, $\Delta\mathrm{SPL}_{\mathrm{wall}}$, $\Delta\mathrm{SPL}_{\mathrm{ground+wall}}$ Variation in the sound power level, in dB, due to a reflected wave on the ground, a reflected wave on the wall or three reflected waves simultaneously

λ, λ_{min} Wavelength and its minimum respectively

$\mathfrak{r}$, ϑ Polar coordinates

ϕ Phase change due to the reflection on the ground

θ Angles of incidence and reflection following the law of reflection

θ_1 Angles of incidence and reflection between the wave and normal to the ground at the point P_1

θ_2 Angles of incidence and reflection between the wave and normal to the wall at the point P_2

θ_{31} Angles of incidence and reflection between the wave and normal to the ground at the point P_{31}

θ_{32} Angles of incidence and reflection between the wave and normal to the wall at the point P_{32}

ε Average height of irregularities

A, B, C Functions of α and β that modify the factor F when the observer is at near-field and the source at far-field

c Sound speed

c_0 Speed of the light in vacuum

F Multipath factor ($= p_{\mathrm{tot}}/p_{\mathrm{dir}}$)

f Frequency of the wave

k Wavenumber

N Number of waves in phase received at the observer's position

O Order of the function

p_{dir} Acoustic pressure perturbation due to the direct wave

p_{tot} Total acoustic pressure perturbation

q Distance between the corner ($x = 0$ and $y = 0$) and the source's position S

r Distance between the positions O and S

R_1 Reflection factor at the point P_1

R_2 Reflection factor at the point P_2

R_{h} Reflection factor on the ground

R_{v} Reflection factor on the wall

r_{11} Distance between the positions S and P_1

r_{12} Distance between the positions P_1 and O

r_{21} Distance between the positions S and P_2

r_{22} Distance between the positions P_2 and O

R_{31} Reflection factor at the point P_{31}

r_{31} Distance between the positions S and P_{31}

R_{32} Reflection factor at the point P_{32}

r_{32} Distance between the positions P_{31} and P_{32}

r_{33} Distance between the positions P_{32} and O

s Distance between the corner ($x = 0$ and $y = 0$) and the observer's position O

x, y Cartesian coordinates

x_1 Coordinate x of the reflection point P_1 on the ground

x_{O}, y_{O} Observer's coordinates (position O)

x_{S}, y_{S} Acoustic source's coordinates (position S)

x_{31} Coordinate x of the reflection point P_{31} on the ground

y_2 Coordinate y of the reflection point P_2 on the wall

y_{32} Coordinate y of the reflection point P_{32} on the wall

Chapter 3 – Effects of rough ground and atmospheric absorption on aircraft noise

Δx Horizontal distance between the source and observer

δ, δ_{I}, δ_{II}, δ_{III} Atmospheric attenuation

κ, κ' Vertical wavenumbers of incidence and transmitted waves respectively

$\mathcal{R}_0$ Ratio of acoustic impedances to evaluate $\mathcal{R}$

$\mathcal{R}_j$ Reflection factor at the point R_j

$\mathfrak{r}$ Ratio between the distances of the direct and reflected waves

ω Temporal frequency of the wave

ϕ Angle between the arbitrary point P with x-axis in the source-observer coordinate system

Φ, Φ_{I}, Φ_{II}, Φ_{III} Variation in phase of the acoustic pressure perturbation due to reflected waves

ρ_0 Air density

ρ_1 Density of homogeneous ground

θ Angles of incidence and reflection following the law of reflection

θ' Angle of refraction following the Snell's law

θ_{max} Maximum slope of undulating ground

ε Uniform atmospheric attenuation per unit length

a Parameter in cosine argument

A, A_{I}, A_{II}, A_{III} Variation in sound power level, in dB, due to reflected waves

c_0, c_1 Sound speeds in air and ground respectively

d Horizontal coordinate of the position O ($= x_\mathrm{O}$)

E, E_I, E_II, E_III Complex magnitude of the multipath factor

F Multipath factor due to atmospheric attenuation

G, $\overline{G}$ Geometrical factors to evaluate F

H Height of rough ground

h Height of rough ground in a 2D plane passing through the source and observer

k Wavenumber

L Lengthscale of undulating ground

M Number of reflection points

p, p_I, p_II, p_III Total acoustic pressure perturbation

p_0 Acoustic pressure perturbation due to the direct wave

p_r Acoustic pressure perturbation due to the reflected wave on the flat ground

q Amplitude of undulating ground

r_1 Distance between the positions S and O

r_{2_j} Distance between the positions S and R_j

r_{3_j} Distance between the positions R_j and O

X, Y, Z Cartesian coordinates

x, z Cartesian coordinates in a 2D plane passing through the source and observer

X_O, Y_O, Z_O Observer's coordinates

x_O, z_O Observer's coordinates (position O) in a 2D plane passing through the source and observer

X_r, Z_r Coordinates of sinusoidally undulating ground

X_S, Y_S, Z_S Acoustic source's coordinates

x_S, z_S Acoustic source's coordinates (position S) in a 2D plane passing through the source and observer

x_{R_j}, z_{R_j} Coordinates of the reflection point R_j on the ground

Chapter 4 – On the countering of free vibrations by forcing: non-resonant or resonant forcing with phase shifts

α_m Phase of the resonant term of the vibration

α_n Phase related to the variables P_n and Q_n

β Phase shift of the forced oscillation

Δ Determinant of Hessian matrix

δ Dirac delta function

δ_{nr} Kronecker delta

λ_n Wavelength of the mode n

$\langle \ldots \rangle$ Time average over a period

ω Frequency of the applied force

ω_m Frequency of the resonant term of the vibration

ω_n Frequency of the mode n

$\overline{y}$ Amplitude of the forced vibration of an elastic string

ρ Mass density per unit length

τ Period of the function

τ_n Wave period of the mode n

θ Dimensionless time $(= \omega t)$

$\tilde{E}$, $\overline{E}$, E Energies equal to $4\tilde{e}/T$, $4\overline{e}/T$ and $4e/T$ respectively

$\tilde{e}$, $\overline{e}$, e Energy density per unit length of free, forced and total oscillations respectively

$\tilde{e}_{\mathrm{e}}$ Average elastic energy

$\tilde{e}_{\mathrm{k}}$ Average kinetic energy

$\tilde{y}$ Amplitude of the free vibration of an elastic string

ε Independent variable related to F and ξ $\left(= F \sin(k\xi) A^{-1} k^{-2} L^{-1}\right)$

ε_0 Constant $\left(= 3/8/\pi^2\right)$

ξ, ξ_m Localisation of the applied force with amplitude F and F_m respectively

ξ_+, ξ_- Critical localisations of the applied force to minimise resonant energy

A_n Amplitude related to the variables P_n and Q_n

a_n Amplitude of the mode n related to the sine series of δ

B Amplitude of the forced oscillation

B_n Terms of series defining B for continuously applied forces

b_n Amplitude of the mode n for each term of the series defining B in the case of a single concentrated force

c Wave speed

c_1, c_2, c_3 Coefficients of quadratic equation

E_* Energy per unit length associated to y_*

e_m Energy density per unit length of free plus forced resonant oscillations

f Continuously distributed force in space

F, F_m Amplitude of the applied force

F_+, F_- Critical forces to minimise resonant energy

f_n Amplitudes of Fourier series evaluating f

G Total resonant energy for the string

g Dimensionless parameter of total oscillation depending on θ and ε

G_* Total energy over the length of the string associated to E_*

G_+, G_- Critical resonant energies

h Indication of total energy $\left(= g^2\right)$

h, γ General function and parameter respectively

k Wavenumber of the applied force

k_m Wavenumber of the resonant term of the vibration

k_n Wavenumber of the mode n

L Length of the string

M Number of concentrated forces

P_n Constant of spatial mode n related to the initial deflection

Q_n Constant of spatial mode n related to the initial velocity

T Tangential tension

t Time

t' Temporal change $(= t - \alpha_n/\omega_n)$

x Position along the undeformed string

y Amplitude of the total vibration of an elastic string

y_* Free plus forced resonant forced oscillation for continuously distributed force

y_m Resonant term of the vibration

y_n Spatial mode n of the amplitude of the vibration

Chapter 5 – On the countering of free vibrations by forcing: damped oscillations and decaying forcing

α_n	Phase related to P_n and Q_n
β	Phase shift of the applied force
χ	Diffusivity
δ	Damping as the symmetric of the real part of complex roots v_n^+ and v_n^-
$\Delta\omega$	Half of the difference between free and applied frequencies
$\hat{\omega}$	Half of the sum between free and applied frequencies
$\hat{E}$	Energy density per unit length of the string associated to oscillation $\hat{y}$
$\hat{e}$	Average energy as function of time for oscillation $\hat{y}$
$\hat{G}$	Average energy as function of θ for oscillation $\hat{y}$
$\hat{H}$	Total energy over all time for oscillation $\hat{y}$
$\hat{y}$	Free plus forced oscillation with equal oscillation and applied frequencies and with opposing amplitudes
λ_n	Wavelength of the mode n
$\langle \ldots \rangle$	Time average over a period
$\rangle \ldots \langle$	Spatial average of the energy over the length of the string
μ	Damping proportional to the velocity
ω_n	Frequency of the mode n
$\overline{\omega}$	Frequency of the applied force
$\overline{y}$	Amplitude of the forced vibration of an elastic string
$\overline{y}_*$, $\overline{Y}_*$	Forced resonant oscillation
ϕ	Phase factor related to B
ψ	Ratio of damping ε to forcing decay δ
ψ_+, ψ_-	Critical values of ψ
ψ_e	Constant $(= 4/3)$
ρ	Mass density per unit length
τ	Period $(= 2\pi/\tilde{\omega})$
θ	Dimensionless time $(= \tilde{\omega}t - \alpha)$
θ_m	Value of θ to maximise g
$\tilde{\omega}_n$	Oscillation frequency as the symmetric of the real part of complex roots v_n^+ and v_n^-
$\tilde{E}$, E	Free and total energy density per unit length of the string respectively
$\tilde{e}$, e	Average energy as function of time for free and total oscillation respectively
$\tilde{E}_*$, E_*	Free and total resonant energy density per unit length of the string respectively
$\tilde{e}_*$, e_*	Free and total resonant average energy as function of time for total resonant oscillation
$\tilde{G}$	Average energy as function of θ for free oscillation
$\tilde{G}_*$, G_*	Average energy as function of θ for free and total resonant oscillation respectively
$\tilde{H}$, H_*	Total energy over all time for free and total resonant oscillation respectively
$\tilde{y}$, $\tilde{Y}$	Amplitude of the free vibration of an elastic string

$\tilde{y}_n$ Spatial eigenfunction n of the amplitude of free oscillations

ε Exponential decay of the applied force

A, α Amplitude and phase shift respectively of the free wave solution without damping

A_n Amplitude related to P_n and Q_n

B Amplitude of the forced oscillation

C Amplitude factor related to B

c Wave speed

D Amplitude of the damped forced resonant oscillation

F Amplitude of the applied force

g Time dependence of $\overline{Y}_*$

I Result of an integral that appears in the evaluation of H_*

J Ratio of total resonant energy H_* to the free energy $\tilde{H}$

k Wavenumber of the applied force

k_n Wavenumber of the mode n

L Length

O Order of the function

P_n, Q_n Constants determined by initial conditions in the solution of T_n

q Ratio of damping to oscillation frequency

R Ratio of total resonant energy $\hat{H}$ for oscillation $\hat{y}$ to the free energy $\tilde{H}$

R_+, R_- Critical values of R

T Tangential tension

t Time

t' Temporal change $(= t - \alpha_n/\tilde{\omega}_n)$

t_{m} Fraction of the period τ

T_n Temporal dependence of mode n of free oscillations

v_n Factor used in exponential function to evaluate T_n

v_n^+, v_n^- Roots of v_n satisfying quadratic equation

x Position along the undeformed string

X_n, Y_n Coefficients of the Fourier sine series that specify the initial displacement or velocity respectively

y, $\breve{y}$ Total oscillation

y_*, Y_* Total resonant oscillation

Chapter 6 – On the energy flux in elastic and inelastic bodies

α, β, ν General coefficients of differential equations

$\boldsymbol{\nabla}$ Gradient operator

$\bullet'_+$, $\bullet'_-$ Derivative with regard to the phase ϕ_+ and ϕ_- respectively

δ_{jr} Identity matrix

$\dot{W}$ Power or work per unit time

$\dot{W}^{\mathrm{s}}$, $\dot{W}^{\mathrm{l}}$ Transversal and longitudinal contributions respectively of the power of external applied forces

λ, μ Lamé elastic moduli

$\mathbf{b}$ Coefficient due to inhomogeneous media

$\mathbf{e}_{\mathrm{x}}$, $\mathbf{e}_{\mathrm{y}}$ Unit vectors along the x and y axes

$\mathbf{h}$ Contribution by rotational to the transversal displacement $\mathbf{u}^{\mathrm{s}}$

$\mathbf{w}^{\mathrm{l}}$ Longitudinal group velocity

$\mathbf{w}^{\mathrm{s}}$ Transversal group velocity

$\mathbf{w}_s$ Group velocity

ω Wave frequency

ω_s, $\omega_{s\pm}$ Roots of the frequency

∂_t Time derivative

∂_t^m Time derivative of order m

$\partial_{j_1 \ldots j_n}$ Spatial derivative with respect to $x_{j_1} \ldots x_{j_n}$

∂_j Spatial derivative with respect to x_j

$\partial^m_{tj_1 \ldots j_n}$ Time derivative of order m and spatial derivative with respect to $x_{j_1} \ldots x_{j_n}$

Φ Wave variable in time domain

ϕ_+, ϕ_- Phase of the plane wave solution

$\phi^{\mathrm{s}}_{\pm}$, $\phi^{\mathrm{l}}_{\pm}$ Phase of the transversal and longitudinal plane wave solutions respectively

Ψ Wave variable in temporal frequency domain

ψ Contribution by gradient to the transversal displacement $\mathbf{u}^{\mathrm{l}}$

ρ Mass density per unit volume

σ Poisson's ratio

ϑ Factor relating to longitudinal and transversal phase speeds ($= \lambda + \mu c_{\mathrm{l}}/c_{\mathrm{s}}$)

ζ Transverse displacement ($= u_{\mathrm{z}}$)

$A^m_{j_1 \ldots j_n}$ Coefficients of the wave equation

B Forcing term of the wave equation

c Phase speed

c_{s}, c_{l} Transversal and longitudinal phase speeds respectively

c_s Phase speed of wavefronts

D Flexural stiffness of the plate

E Total energy density per unit volume

E Young's modulus

E^{ks}, E^{kl} Kinetic energies of transversal and longitudinal waves respectively

E^{k} Kinetic energy

E^{s}, E^{l} Elastic plus kinetic energies of transversal and longitudinal waves respectively

E^{us}, E^{ul} Elastic energies of transversal and longitudinal waves respectively

E^{u} Deformation energy

F General function

f_+, f_- Waveform of the plane wave solution

$f_{\pm\mathrm{s}}$, $f_{\pm\mathrm{l}}$ Waveform of the transversal and longitudinal plane wave solutions respectively

F_r Energy flux

F_r^{sl} Cross-coupling energy flux

F_r^{s}, F_r^{l} Energy fluxes of transversal and longitudinal waves respectively

g_j Force density per unit volume

G_{jkmn} Stiffness double tensor

k Wavenumber

k_j Wave vector

n_j Wave normal

p Pressure

$P_{M,N}$ Characteristic polynomial of derivatives with regard to time of order M and regard to position of order N

s Arc length

S_{jr} Strain tensor

T	Tangential tension
t	Time
T_{ij}	Stress tensor
u_s, u_l	Transversal and longitudinal displacement along the wave normal and orthogonal to the wave normal respectively
u_x, u_y	Longitudinal displacements
u_j	Displacement vector
u_j^0	Amplitude of the plane wave solution
$u_j^{0\mathrm{s}}$, $u_j^{0\mathrm{l}}$	Amplitude of the transversal and longitudinal plane wave solutions respectively
v_z	Transverse velocity
v_j	Velocity vector
x, y, z	Cartesian coordinates normal to the transverse direction
x_j	Position vector

Chapter 7 – Alfvén wave propagation along a circle using dipolar coordinates

α, β	Conformal coordinates
$\boldsymbol{\nabla}$	Gradient operator
$\bullet'$	Derivative with respect to β
$\dot{\bullet}$	Time derivative
Γ	Gamma function
γ, δ, ε	Parameters of Gaussian differential equation
λ, κ	Wavelength and its wavenumber respectively
$\mathbf{B}$	Background magnetic field
$\mathbf{e}_\alpha$, $\mathbf{e}_\beta$, $\mathbf{e}_\mathrm{z}$	Unit vectors along the α, β and z axes
$\mathbf{g}$	Gravitational force
$\mathbf{V}$, $\mathbf{H}$	Total velocity and magnetic field respectively
$\mathbf{v}$, $\mathbf{h}$	Velocity and magnetic field perturbations respectively
μ	Magnetic permeability
ν	Alfvén index
Ω	Dimensionless frequency
ω	Frequency
$\overline{c}_1$, $\overline{c}_2$	Arbitrary constants of integration
$\overline{e}_n$, $\overline{f}_n$	Coefficients of the series defining W_1 and W_2 respectively
$\overline{h}_2$, $\overline{W}_2$	Dependent variables equal to $h_2\cos^2\theta$ and $W_2\cos\theta$ respectively
$\overline{J}$	Dependent variable $\left(= b^{-1}R^{-2}J\right)$
$\overline{J}_0$, $\overline{J}_{1/2}$	Particular solutions of the Frobenius-Fuchs series of $\overline{J}$
$\overline{Q}$	Dependent variable $\left(= b^{-1}R^{-2}Q\right)$
$\overline{Q}_0$, $\overline{Q}_1$	Particular solutions of the Frobenius-Fuchs series of $\overline{Q}$
ϕ	Angle between coordinate curve α with every radial lines
Ψ	Dependent variable $(= \Phi)$
ρ	Mass density
ρ_0	Constant mass density
σ	Arbitrary constant
$\tilde{h}$	Magnetic field perturbation spectrum depending on θ and Ω

$\tilde{h}_0'$ Derivative of the magnetic field perturbation spectrum with respect to θ at θ_0

$\tilde{h}_0$, $\tilde{h}_1$, $\tilde{h}_2$ Magnetic field perturbation spectrum with θ_0, θ_1 and θ_2 respectively

$\tilde{V}$, $\tilde{H}$ Fourier transform of v and h in time respectively

ϑ Polytropic index

ξ Independent variable $(= 1 - \zeta)$

ζ Independent variable $\left(= \cos^2 \theta\right)$

A Alfvén speed

a Alfvén speed at radius R

b Background magnetic field at radius R

C_1, C_2 Arbitrary constants of integration

$C_1^\star$, $C_2^\star$ Arbitrary constants of integration

c_n, χ Coefficients and index of the Frobenius-Fuchs series of $\overline{Q}$ respectively

D_1, D_2 Arbitrary constants of integration

d_n, ι Coefficients and index of the Frobenius-Fuchs series of $\overline{J}$ respectively

e_n, f_n Coefficients of the series defining h_1 and h_2 respectively

F Gaussian hypergeometric function

f General function

G, Φ Magnetic field perturbation spectrum

g_0 Magnitude of $\mathbf{g}$ at radius R

h_α, h_β Scale factor of dipolar coordinates α and β

h_m Magnetic field perturbation h depending on W_m

k, n Arbitrary real and integer numbers respectively

l Arc length

M Molar mass

O Order of the function

p Mean state pressure

p_0 Pressure at radius R

q Index of the series defining W_1 and W_2

Q, J Dependent variable $(= \Psi/\zeta^\sigma)$

R Inverse of coordinate α

r, θ Polar coordinates

R_g Constant of perfect gas

s Scale factor

T Temperature

T_0 Constant temperature

W, W_m Dimensionless velocity perturbation spectrum and its m-th solution

X Dependent variable $(= bV)$

x, y Cartesian coordinates

z, w Complex number and complex function respectively

Chapter 8 – On the generation of harmonics by the non-linear buckling of an elastic beam

$\bullet'$ Derivative with regard to x

$\bullet_1$, $\bullet_2$, $\bullet_3$ Variables related to clamped, pinned and cantilever beams respectively

$\bullet_\mathrm{max}$ Maximum possible value of $\bullet$

η Sine of the angle of inclination θ

$\overline{A}$, $\overline{B}$, $\overline{C}$, $\overline{D}$ Arbitrary constants of elastica equation defined by boundary conditions for linear buckling

Ψ Arbitrary variable to evaluate the integral $(= p\xi + pC)$

θ Angle of inclination of the elastica

ζ Elastica equation

ζ_n Harmonics of the deformation

$\zeta_{3,m}$ Coefficient of series defining ζ_3

A, B, C, D Arbitrary constants of elastica equation defined by boundary conditions for lowest-order non-linear buckling

a_m Coefficient of binomial series

A_n Coefficients of series defining ζ

b Amplitude of elastica for linear buckling

E Young's modulus

F Transverse force

f Transverse force per unit length

G Arbitrary constant $\left(= \sqrt{2 + B/p^2}\right)$

H Arbitrary constant $\left(= Ap^{-2}/2\right)$

I Second moment of inertia

k Curvature $(= \mathrm{d}\theta/\mathrm{d}s)$

L Length of the undeformed beam

M Bending moment

p Buckling parameter

$p_{1,n}$, $p_{2,n}$, $p_{3,n}$ Buckling load of order n for clamped, pinned and cantilever beams respectively

Q Amplitude of buckling harmonics

q Arbitrary constant $\left(= p/\sqrt{B + 2p^2}\right)$

s Arc length

T Tangential tension

T_x, T_y Horizontal and vertical components of tangential tension respectively

T_c Critical buckling load

$T_{1,n}$, $T_{2,n}$, $T_{3,n}$ Critical buckling load of order n for clamped, pinned and cantilever beams respectively

$T_{\mathrm{c},n}$ Critical loads

x, y Cartesian coordinates with x-axis along the undeformed beam

z Dependent variable $= \left(\eta - Ap^{-2}/2\right)$

Chapter 9 – On twin perturbation expansions for non-linear bending of plates

$\boldsymbol{\nabla}$ Gradient operator

$\bullet'$ Derivative with regard to r

δ, ∂ Variational and differential operator respectively

$\mathbf{e}_\mathrm{x}$, $\mathbf{e}_\mathrm{y}$, $\mathbf{e}_\mathrm{z}$ Unit vectors along Cartesian axes

$\mathcal{C}$, $\partial\mathcal{C}$ Domain and its contour of the domain of integration respectively

$\overline{E}$ Total elastic energy per unit area integrated over all directions

$\overline{E}_{n,m}$ Contribution of order (n, m) to the total energy $\overline{E}$

$\overline{N}_\mathrm{n}$, $\overline{N}_\mathrm{r}$ Augmented turning moment and its radial component respectively

$\overline{W}_n$, $\overline{\Theta}_n$ Contribution of order n to the work $\overline{W}$ and $\overline{\Theta}$ respectively

∂_α, d_α Partial and total derivative respectively with respect to r_α

$\partial_{\alpha\beta}$ Partial derivative of second order with respect to r_α and r_β

ϕ General solution that satisfies an unforced biharmonic equation

Ψ, $\overline{\Psi}$ Work of weight ρg in transversal displacement and its integration over all directions respectively

ρ Mass density

σ Poisson's ratio

Θ Airy's stress function

ε Perturbation parameter

$\wedge$ Numerical factor related to σ

ζ Transverse displacement

ζ_n, Θ_n, $u_{\mathrm{r},n}$, $S_{\alpha\beta,n}$, $T_{\alpha\beta,n}$ Contribution of order n to the perturbation expansions of ζ, Θ, u_r, $S_{\alpha\beta}$, $T_{\alpha\beta}$ respectively

a Radius of the circular plate

B Upper bound of ζ_n

$B_\bullet$, C, C_k Arbitrary constants

D Flexural rigidity

D_2, D_3 Area and volume changes respectively due to strains

E Young's modulus

E_1, W_1 Elastic energy per unit area due to bending and associated work W_1

E_2, W_2 Elastic energy per unit area due to transverse deflection and associated work W_2

E_3, W_3 Elastic energy per unit area due to in-plane deformation and associated work W_3

E_d Deformation energy per unit volume ($= E_2/h + E_3/h$)

E_T Total elastic energy per unit area

f Transverse force per unit area

f_α In-plane volume forces

F_n, G_n Forcing terms of order n in the perturbation expansions of ζ and Θ respectively

g Gravitational force

H Parameter ($= \rho g h/D/64$)

h Thickness of the plate

K Degree of polynomial of transverse force f

k_r, k_t Radial and tangential curvatures respectively

l, L Arc length in the undeflected and bent plane respectively

M_n, M_r Normal stress couple and its radial component respectively

N Order of the perturbation expansion

N_n, N_r Turning moment and its radial component respectively

p Axial pressure

p_4 Fourth-order polynomial of r

r, θ Polar coordinates

r_α, v_α In-plane position and velocity vector respectively

R_d Desired error of truncation at the N-th term of the series of ζ

R_N	Error of truncation at the N-th term of the series of ζ
S, s	Area and contour length of the domain of integration respectively
S_{ij}	Strain tensor
t	Time
$T_{\alpha\beta}$	In-plane stress tensor
U_α	Total displacement vector
u_α	In-plane displacement vector
W, $\overline{W}$	Work of pressure p in radial displacement and its integration over all directions respectively
x, y, z	Cartesian coordinates
X_1, X_2, X_3, X_4	Numerical factors

1 | Introduction

"A thought is an idea in transit."

— Pythagoras of Samos

Contents

ELECTROECHANICS aims to study the motion (or equilibrium) of matter and the forces or moments that cause such motion (or equilibrium). Electromechanics is based on the concepts of space, time, force, matter and energy. The knowledge of these concepts are fundamental for studying all branches of biology, chemistry, physics and engineering [1].

Some questions about these areas that affect our daily routine can be postulated. At home, how can a refrigerator keep the food fresh, maintaining a low temperature in the environment? Knowing that fridges and other household appliances need electrical work, how does the electricity from the street poles reach the outlets in our homes? How can the transmission lines carry electricity over long distances? Knowing that large towers hold the transmission lines, how are the trusses designed to sustain tensile or compressive forces? Now, suppose an aeroplane is flying above us. The wings must support loads and be under strain to keep the passengers, cargo and structures. How much strain are the wings subjected to? Have the wings sufficient strength? Many structural members, such as spars and ribs in the wings, are composed of bars or beams. How does one design such structural elements in order to not fracture at the same time that carry loads? When an aeroplane flies over us, how do we hear the sounds induced by the plane? Do we notice any difference in the sound during its flight? And about ourselves, how do we breathe? What changes take place in the lungs when we are breathing? Moreover, how does the blood pressure affect its movement and ultimately affect us? The blood circulation, starting from the heart, then going to every remote appendix of our body and finally coming back to the heart, is not a steady flow but has peaks of pressure and speed [1].

All these questions from different areas are concerned with some topics of electromechanics, for instance: force, work, motion, energy, flux, resistance, deformation, properties of materials or modification in materials. Constitutive equations characterise the properties of materials. Logically, many constitutive equations describe an almost infinite variety of materials. Nonetheless, idealised stress-strain relationships give a good description of the mechanical properties of many materials around us, namely, the non-viscous fluid and the perfectly elastic solid [1], which are considered in this thesis. These topics, with the postulates of continuum electromechanics, can be reduced to particular differential equations and boundary conditions. By solving such equations, as proposed in this thesis, precise quantitative information is achieved. In this work, considering fundamental principles that underlie these differential equations and boundary conditions is essential [1].

In the chapters 2 to 7, the motion produced in an elastic body or fluid by applied loadings is important. The action of a force or perturbation is not transmitted at once to all parts of the body or fluid respectively. For example, in the beginning, the remote portions of the body remain undisturbed, and deformations produced by force propagate through it in the form of elastic waves. Another example is the propagation of acoustic waves when the pressure perturbation is propagated with a finite velocity through the fluid. We have such problems in all the chapters except 8 and 9, and are explained in more detail in subsection 1.1. Otherwise, in the chapters 8 and 9, concerning the problems of elasticity which are explained in the subsection 1.2, the elastic body is at rest under the action of external loadings, and the resulting problems are problems of statics.

The continuum electromechanics has an important role in all branches of modern science because of its emphasis on basic concepts and fundamental principles. The subsection 1.3 will enunciate these principles. In other words, continuum electromechanics is the basis upon which several physics or engineering theories, such as fluid mechanics and elasticity in solids, are founded. This thesis is devoted to specific applications of continuum electromechanics, in particular, to subjects of ideal (non-viscous) incompressible or compressible fluids associated with the propagation of waves (subsection 1.1) and to linear theories of elasticity related to deformation or buckling (subsection 1.2). These theories are essential, not only because they apply to a majority of the problems in continuum electromechanics arising in practice, but because they form a solid base upon which one can readily construct more complex theories of material behaviour [2]. They aim to obtain solutions to particular problems which may be of practical importance.

1.1 Mechanical vibrations and propagation of waves

As mentioned before, the non-viscous fluids and the Hookean elastic solids are abstractions. Real materials may have more complex behaviours than these idealisations. No natural material behaves exactly as any of them, although some materials may follow one of these laws in certain situations accurately. For solids, most structural materials are, fortunately, Hookean in the useful range of stresses and strains, which will be assumed in this thesis [1]. For fluids, the action of shear stresses, no matter how small they may be, will cause the fluid to deform continuously as long as the stresses act. It follows, therefore, that a fluid at rest (or in a state of rigid body motion) is incapable of sustaining any shear stress whatsoever [3]. Air can be treated as non-viscous fluid in many problems. For example, in issues concerning the propagation of acoustic waves in air, excellent results can be obtained by ignoring the viscosity of the medium and treating it as a non-viscous fluid, which is assumed in this thesis.

A non-viscous fluid is a fluid for which the stress tensor is isotopic, $\sigma_{ij} = -p\delta_{ij}$, where δ_{ij} is the Kronecker delta and p is the static pressure. The presence of the pressure term p represents a fundamental difference between fluid mechanics and elasticity. To accommodate this new variable, there is an equation of state which relates the pressure p, the density ρ and the absolute temperature T. In the case of an ideal gas, the pressure p is related to the density ρ and temperature T by the equation of state $p = \rho RT$ where R is the gas constant. In an incompressible fluid, the equation of state is solely $\rho = \text{const}$ and the pressure p is left as an arbitrary variable (there is a mention for an incompressible fluid in chapter 7), which is determined merely by the equations of motion and the boundary conditions [1].

In the case of dynamic excitation, the natural frequencies and the corresponding mode shapes are important system characteristics. Once these are found by considering the homogeneous part of the governing differential equation, the response to a forcing function may be obtained as a particular solution. Also, these system characteristics, which can be determined without loadings, are helpful for classification. For example, structures are considered stiff or flexible based on natural frequencies [4]. Another characteristic, which is dependent only on the material properties, is the velocity at which an acoustic or elastic wave propagates through a medium or a body [4]. In dynamic response computations, damping, which represents energy dissipation, is also very important (considered, for instance, in chapter 5) [4].

1.2 Theory of elasticity in solids

The approximations generally used for determining the influence of applied forces or moments on elastic materials are the mechanics of materials and the theory of elasticity, each of considerable importance and each supplementing the other. Both must rely on the equilibrium conditions and use a constitutive equation between stress and strain associated with elastic bodies. The essential difference between these approximations lies in the extent to which the strain is described and in the types of simplifications assumed [5]. The mechanics of materials focuses mainly on basically approximate solutions to practical problems. This last approach uses an assumed deformation mode or strain distribution in the body as a whole and hence yields the average stress at a cut section under a given force or moment. Moreover, it usually treats separately each simple type of complex loading, for example, axial centric loading, torsion or bending (being valid the superposition principle). Although of practical importance, the formulas of the mechanics of materials are best suited for relatively slender members and are derived based on very restrictive conditions [5]. On the other hand, the theory of elasticity does not rely on an assumed deformation mode; it concerns with mathematical analysis to determine the "analytic" stress and strain distributions satisfying the general equations of equilibrium under any external loading system [5]. The theory of elasticity provides analytic solutions when the configurations of loading and boundary conditions are relatively simple, and it works as the basis of approximate solutions employing numerical methods. Thus, the theory of elasticity can verify the limitations of the solutions provided by the mechanics of materials. Several factors, including the influence of material anisotropy and the extent to which boundary conditions depart from reality, contribute to an error in this approach [5].

The theory of elasticity studies a set of equations uniquely describing the state of stress and strain at each point within an elastically deformable body. It contains equilibrium equations associating the stresses and loadings, kinematic equations associating the strains and displacements, constitutive equations associating the stresses and strains, and boundary conditions associating the physical domain and uniqueness constraints related to the validity of the solution [4]. When elasticity is selected as the approach for an engineering solution, a rigour is accepted that is distinct from the mechanics of materials basis which has its various specialised subjects such as the theories of bars, beams, plates and shells. The theory of elasticity is preferred when critical design constraints and high reliability imply a more exact solution, or when prior experiences are limited and intuition does not adequately supply the needed simplifications with any degree of accuracy. If properly applied, the theory of elasticity should yield solutions closer to the actual distribution of strain, stress, and displacement [5].

Solving the equations of elasticity analytically may be a challenging task (as in chapter 8); however, the inverse or semi-inverse method can solve them. The inverse method requires examining the assumed solutions and then verifying if they satisfy the governing equations and boundary conditions. The semi-inverse method requires the assumption of a partial solution formed by expressing stress, strain, displacement, or stress function in terms of known or undetermined coefficients (as in chapter 9) [5].

Many physical problems are simplified to two dimensions, which facilitates an eventual solution, for example, in the subjects of plate bending and beam buckling, both studied in this document in the chapters 8 and 9 [4]. In both chapters, the elasticity problems are reduced from three to two dimensions since there is no traction on one plane passing through the body, known as plane stress. Analytic solutions of some governing differential equations of beam and plate theories can only be obtained for particular boundary and load conditions. In most cases, nonetheless, the theory of elasticity may also be developed from energy methods (as in the chapter 9) yielding quite usable numeric solutions [4, 6].

All structural materials possess to a certain extent the property of elasticity, i.e. (*id est*), if external forces producing deformation of a structure do not exceed a certain limit, the deformation ceases with the removal of the forces. Throughout this thesis, the bodies subjected to the action of external forces are perfectly elastic, i.e., they return to their initial form after removing forces [7].

1.3 Principles of continuum electromechanics

Continuum electromechanics deals with physical quantities which are independent of any particular coordinate system that may be used to describe them. At the same time, those physical quantities are very often specified most conveniently by referring to an appropriate system of coordinates. Mathematically, tensors can represent such quantities. As a mathematical entity, a tensor is independent of any coordinate system. Yet it may be specified in a particular coordinate system by its components. If tensor equations are valid in one coordinate system, they are correct in any other coordinate system. Therefore, specifying the components of a tensor in one coordinate system determines the components in any other system

[1, 3]. Tensor equations can express the physical laws of continuum electromechanics; this thesis presents some of them (this fact is mentioned in subsection 1.5).

The atomic/molecular composition of matter is well established. On a small enough scale, for instance, a body of steel is a collection of discrete steel atoms stacked on one another in a particular repetitive lattice. On an even smaller scale, the atoms consist of a core of protons and neutrons around which electrons orbit. Although we may speak of a material body as "occupying" a region of physical space, it is evident that the body does not totally "fill" the space it occupies. Thus, the matter is not continuous. In numerous investigations of material behaviour, however, the individual molecule is of no concern and only the behaviour of the material as a whole is deemed necessary. There is a clear implication in such an approach that the minor element cut from the body possesses the same properties as the body. Random fluctuations in the properties of the material are thus of no consequence. In keeping with this continuum model, we assert that matter may be divided indefinitely into smaller and smaller portions, each of which retains all of the physical properties of the parent body. Accordingly, one can ascribe field quantities such as density and velocity to each point of the region of space that the body or medium occupies [3]. A similar consideration can be used to define several densities, such as the density of momentum and the density energy. A material continuum is a material for which the densities of mass, momentum, and energy exist in the mathematical sense [1]. This continuum concept of matter is the fundamental postulate of continuum electromechanics. Within the limitations for which the continuum assumption is valid, this concept provides a framework for studying the behaviour of solids, liquids and gases. Adopting the continuum viewpoint as the basis for the mathematical description of material behaviour means that field quantities such as stress and displacement are expressed as piecewise continuous functions of the space coordinates and time [5]. Moreover, the derivatives of such functions, if they enter into the theory, likewise will be continuous [3]. The time along with space is also a four-dimensional continuum.

There are two main topics which divide the continuum electromechanics. In the first, the emphasis is on the derivation of fundamental equations which are valid for all continuous media. These equations are based on universal laws of physics, such as the conservation of mass, the principles of energy or the conservation of momentum. In the second, the focus of attention is on the development of so-called constitutive equations characterizing the behaviour of specific idealised materials, the perfectly elastic solid and the non-viscous fluid being the best-known examples. These equations provide the focal points around which studies in elasticity and fluid mechanics proceed [3].

Mathematically, the fundamental equations of continuum electromechanics mentioned above may be developed in two separate but essentially equivalent formulations. One, the integral or global form, derives from a consideration of the basic principles being applied to a finite volume of the material. The other, a differential or field approach, leads to equations resulting from the basic principles being applied to a very small (infinitesimal) element of volume [3]. In this thesis, usually the second approach is chosen.

The axioms of physics are taken as the axioms of continuum electromechanics [1]. In particular, this thesis uses Newton's laws of motion and the laws of thermodynamics. There are additional axioms of continuum electromechanics. A material continuum remains a continuum under the action of forces. Another axiom of continuum electromechanics is that stress and strain can be defined everywhere in the body. Besides that, the stress at a point is related to the strain and its rate of change with respect to time at the same point. This axiom is a tremendous simplifying assumption: the stress at any point in the body depends only on the deformation in the immediate neighbourhood of that point [1].

The molecular structure of elastic bodies is not considered here. This work will assume that the matter of an elastic body is homogeneous and continuously distributed over its volume so that the smallest element cut from the body possesses the same physical properties as the body. To simplify the discussion, the body is isotropic whenever possible, i.e., that the elastic properties are the same in all directions [7]. Structural materials usually do not satisfy the above assumptions. For instance, the steel consists of crystals of various kinds and various orientations. The material is very far from being homogeneous. However, solutions of the theory of elasticity based on the assumptions of homogeneity and isotropy can be applied to steel structures with great accuracy. While the elastic properties of a single crystal of steel may be very different in distinct directions, the crystals are ordinarily distributed at random. The elastic properties of larger pieces of metal represent, therefore, averages of the properties of crystals. So long as the geometrical dimensions defining a body's form are large compared to the dimensions of a single crystal, the assumption of homogeneity can be used with great accuracy. If the crystals are orientated randomly, the material can be treated as isotropic [7].

From Newtonian mechanics, for analysing the statics or dynamics of a body, one force system may be replaced by another equivalent system whose force and moment resultants are identical. Although the force resultants, while equivalent, need not cause a similar strain distribution, Saint-Venant's principle permits using an equivalent loading to calculate stress and strain. This principle states that if an actual distribution of forces is replaced by a statically equivalent system, the stress and strain distribution throughout the body is altered only in the vicinity of the load application [5]. The contribution of Saint-Venant's principle to the solution of engineering problems is significant because the boundary conditions do not need to be prescribed very precisely. Furthermore, when a specific solution is predicated on a particular boundary loading, the solution can be valid for another type of statically equivalent boundary loading, even not quite the same as the first. When an analytical solution calls for a specific stress distribution on a boundary, the answer is not discarded when the boundary distribution is not quite the same as that required by the solution, consequently extending its usefulness [5].

1.4 Thesis outline and list of submitted articles

After the introductory topics on subsections 1.1 and 1.2, the reader may be conscious about the importance of the continuum electromechanics and, in particular, its applications in several areas such as elastic deformation of bodies or propagation of waves in fluids and solids. Since the list of applications of the continuum electromechanics is extensive and covers different areas, each chapter is related to one specific subject. Consequently, each chapter is written in a way that can be read and analysed by itself, without the necessity to read the preceding chapters. In the following list, the essence of each chapter is explained briefly, along with the key points. In summary, this thesis is divided as follows:

- **Chapter 1:** An introduction gives an overview of the continuum electromechanics, including its principles that are used in this document, and it also proposes the objectives set to be achieved with this thesis;

- **Chapter 2:** Near any corner, multipath effects occur due to the reflection of acoustic waves, for example, the noise of an helicopter or an aircraft or a drone or other forms of urban air mobility near a building, or even a telecommunications receiver antenna near an obstacle. Most of the literature about ground effects on aircraft noise considers a point source over a flat ground, using the method of images, that does not extend readily to rough ground. The total signal received in a corner consists of four parts: (i) a direct signal from source to observer; (ii) a second signal reflected on the ground; (iii) a third signal reflected on the wall; (iv) a fourth signal reflected on both wall and ground. The problem is solved in two-dimensions to specify the total signal, whose its ratio to the direct signal specifies the multipath factor. The amplitude and phase of the multipath factor are plotted as functions of the frequency over the audible range, for various relative positions of observer and source, and for several combinations of the reflection coefficients of the ground and wall. It is shown that the received signal consists of a double series of spectral bands, in other words: (i) the interference effects lead to spectral bands with peaks and zeros; (ii) the successive peaks also go through zeros and "peaks of the peaks". The results apply not only to sound, but also to other waves, for example electromagnetic waves using the corresponding frequency band and reflection factors.

- **Chapter 3:** The noise received from an aircraft or any other acoustic source is modified not only by reflections on ground, but also by atmospheric attenuation. The interference of direct and reflected waves is studied for a flat ground, with or without atmospheric attenuation, then multiple reflections that can occur for rough ground or mountainous surroundings are also analysed. The ground characteristics, like reflection and absorption factors or impedance, also affect the received sound. All these effects have to be considered with respect to the path of the acoustic wave. The effect of rough ground on aircraft noise can be modelled by: (i) identification of reflection points (there may be several points); (ii) use of a complex reflection coefficient (with amplitude and phase changes) at each reflection point; (iii) adding all reflected waves within line-of-sight of the receiver, that is not blocked by terrain. As in the chapter 2, the amplitude and phase of the multipath factor are plotted as functions of the frequency for the previous situations.

- **Chapter 4:** Continuing with the study of propagation of waves, in this case the linear transverse oscillations of a uniform elastic string, the question answered in this chapter is if the free oscillations can be attenuated, reducing the energy of propagation, due to external forcing. In this chapter, all the oscillations are undamped. When the frequency of the applied force is not equal to the natural frequency of the system, the total energy increases, that is the opposite of what is intended. When the applied frequency is equal to one of the natural frequencies, the amplitude of oscillation grows linearly with time, and hence the energy grows quadratically with time, implying an increase in total energy after a sufficiently long time. It is proved that a reduction in total energy is possible over a short time, specifically over the first period of oscillation, by optimizing the forcing, not only in the case of a concentrated force, but also for several concentrated forces. In the case of a continuously distributed force, by optimizing the spatial distribution, it is shown that reducing the energy of the total oscillation is also possible, at least, over the first period of vibration. It has also been proved that continuously distributed forces are more effective at vibration suppression than point forces.

- **Chapter 5:** Again for the transverse oscillations of an elastic string, but in this chapter with friction proportional to the velocity (typical of telegraph or wave-diffusion differential equation), in other words, for damped oscillations, the vibration suppression is investigated, due to external forces as in the chapter 4. As the damping is considered in this chapter, the free oscillations are sinusoidal modes in space-time and exponentially decay with time. When the applied frequency is equal to one of the natural frequencies, the sinusoidal oscillations have a constant amplitude and a phase shift of $\pi/2$. When the applied frequency is not equal to any of the natural frequencies, the sinusoidal oscillations have also a constant amplitude and a phase shift such that the work of the applied force balances the dissipation. In both cases, the resonant or non-resonant forcing dominates the decaying free oscillations after some time. This chapter proposes an optimisation of the forcing to minimise the total energy of oscillation, but after verifying that the energy remains below the energy of the free oscillation alone only for a short time, a more effective method of countering the damped free oscillations is proposed. It consists on use forcing with amplitude decaying exponentially in time and making a suitable choice of the forcing decay relative to the free damping, in such a way that the total energy of oscillation over all time can be reduced, in comparison to the energy of the free oscillation.

- **Chapter 6:** The energy balance equation, including the kinetic energy density, the deformation energy density and the power of external forces, identifies the energy flux as minus the product of the velocity by the stress tensor. It is shown that this result does not depend on constitutive relations, and therefore it is valid to elastic or inelastic matter. The energy flux is obtained for linear strains, and in the case of transverse vibrations of elastic strings and membranes it is generalised to the non-linear case of unrestricted slope. The energy flux is also obtained in elasticity for crystals and amorphous matter. By inspection of any linear wave equation in a steady homogeneous medium, it is possible to verify if the waves are (i) isotropic or not and (ii) dispersive or not, even if an explicit solution is not obtained. Regarding the linear elastic waves, it is shown that (i) they are non-dispersive in crystals or amorphous matter. In the latter case, the longitudinal and transversal waves are isotropic. However, the superposition of both waves induces an anisotropy. Consequently, the superposition adds, besides the two energy densities and powers of external forces, also a third cross-coupling energy flux, which is deduced in this chapter.

- **Chapter 7:** For the lowest order term, the multipolar representation of the magnetic field has a magnetic dipole that dominates the far-field. Thus, the far-field representation of the magnetic field of the Earth, Sun and other celestial bodies is a dipole. These bodies consist of or are surrounded by plasma, which can support Alfvén waves. This chapter introduces multipolar coordinates, which are an example of conformal coordinates. The conformal coordinates are orthogonal with equal scale factors, and can be extended from the plane to space, for instance as cylindrical or spherical dipolar coordinates. This new coordinate system is used to study the propagation of Alfvén waves along dipole magnetic field lines including, in particular, circle magnetic field lines, with transverse velocity and magnetic field perturbations. The various forms of the Alfvén wave equation are linear second-order differential equations, with variable coefficients, specified by a background magnetic field, which is force-free. The hydrostatic equilibrium, when the gravitational force balances the pressure gradient, for an incompressible fluid or perfect gas, is obtained when there is no background magnetic force. When the frequency of the Alfvén equation is zero, the wave equation is simplified to a Gaussian hypergeometric type, otherwise, for non-zero frequency, an extended Gaussian hypergeometric equation is obtained. The solution of the latter specifies the magnetic field perturbation spectrum, and also, via a polarisation relation, the velocity perturbation spectrum; both are plotted, over half-a-circle, for three values of the dimensionless frequency.

- **Chapter 8:** The study of the behaviour of an elastic beam under compression is made, where the Euler-Bernoulli theory is used, but taking into account the effect on non-linear terms in the curvature of the beam. The Euler–Bernoulli theory of beams is usually presented in two forms: (i) in the linear case of small slope using Cartesian coordinates along and normal to the straight undeflected position; (ii) in the non-linear case of large slope using curvilinear coordinates along the deflected position specified by the arc length and angle of inclination. This chapter starts with the exact equation in a third form, that is, (iii) using Cartesian coordinates along and normal to the undeflected position like (i), but including exactly the non-linear effects of large slope like (ii). This third form is analysed and it is proven that the exact non-linear shape of the neutral surface is a superposition of linear harmonics; thus, the non-linear effects of large slope are equivalent to the generation of harmonics of a linear solution for small slope. It is made a comparison of: (i) the critical buckling load in the linear and non-linear cases; (ii) the buckled shape of the neutral surface, again in the linear and non-linear cases. The non-linear shape of the neutral surface, for cases when the square of the slope cannot be neglected, is illustrated for the first four buckling modes of cantilever, pinned, and clamped beams with different lengths and amplitudes.

- **Chapter 9:** The Föppl-von Kármán equations for the non-linear bending of elastic plates are solved by a novel method of twin asymptotic expansions for the transverse displacement and in-plane stress function. Unlike most asymptotic expansions, that can be derived explicitly only to second or third order, exceptionally in this case both asymptotic expansions can be obtained explicitly to all orders. The perturbation relations form a causal chain of linear partial differential equations, with biharmonic operators and forcing specified by the lower orders. Furthermore, a method of exact analytical solutions applicable to all orders is presented for the axisymmetric case with loading represented by a polynomial or analytic function of the radius. In this case, the convergence of the parametric perturbation expansion is proved to any order and as an infinite series provided that the perturbation parameter is less than unity. The method of perturbation expansions is illustrated explicitly up to the lowest order by the application to a clamped circular plate subject to a radial pressure and its own weight. The scaling of the asymptotic expansion parameter on material and geometric properties indicates when coupling of bending to in-plane stresses is more significant.

Several articles were submitted to scientific journals and some of them were already published (in February 2023). The mathematical derivations are put in an elementary form. In some cases, necessary explanations and intermediate calculations are given so that the reader can follow all the derivations without difficulty. Furthermore, the thesis has the list of references to the papers or books in which the derivations can be found. This thesis is divided in such a way that each chapter contributes to one submitted paper. The following refereed papers arose from work related to this thesis:

- **Chapter 2:**
  L. M. B. C. Campos, M. J. S. Silva and A. R. A. Fonseca (2021) “On the multipath effects due to wall reflections for wave reception in a corner”, published in *Noise Mapping, De Gruyter*, 8(1), pp. 41–64, DOI: 10.1515/noise-2021-0004

- **Chapter 3:**
  L. M. B. C. Campos, M. J. S. Silva and J. M. G. S. Oliveira (2022) “On the effects of rough ground and atmospheric absorption on aircraft noise”, published in *Noise Mapping, De Gruyter*, 9(1), pp. 23–47, DOI: 10.1515/noise-2022-0003

- **Chapter 4:**
  L. M. B. C. Campos and M. J. S. Silva (2022) “On the countering of free vibrations by forcing: Part I – Non-resonant and resonant forcing with phase shifts”, published in *Applied Mechanics, MDPI*, 3(4), pp. 1352–1384, DOI: 10.3390/applmech3040078

- **Chapter 5:**
  L. M. B. C. Campos and M. J. S. Silva (2023) “On the countering of free vibrations by forcing: Part II – Damped oscillations and decaying forcing”, published in *Applied Mechanics, MDPI*, 4(1), pp. 141–178, DOI: 10.3390/applmech4010009

- **Chapter 6:**
  L. M. B. C. Campos and M. J. S. Silva (2023) “On the energy flux in elastic and inelastic bodies”, submitted in *Wave Motion, Elsevier* (Original version review)

- **Chapter 7:**
  L. M. B. C. Campos, M. J. S. Silva and F. Moleiro (2019) “On Alfvén wave propagation along a circle on dipolar coordinates”, published in *Journal of Plasma Physics, Cambridge University Press*, 85(6), ID 905850608, DOI: 10.1017/S0022377819000837

- **Chapter 8:**
  L. M. B. C. Campos and M. J. S. Silva (2021) “On the generation of harmonics by the non-linear buckling of an elastic beam”, published in *Applied Mechanics, MDPI*, 2(2), pp. 383–418,
  DOI: 10.3390/applmech2020022

- **Chapter 9:**
  L. M. B. C. Campos and M. J. S. Silva (2022) "On twin perturbation expansions for the non-linear bending of plates", submitted in *Quarterly Journal of Mechanics and Applied Mathematics, Oxford University Press* (Revised version review)

In parallel with the elaboration of the contents presented in this thesis, additional studies were conducted that are not directly related to continuum electromechanics, such as the generalisation of the Bessel differential equation or its related topics like Airy functions and hypergeometric functions. They have some applications, for instance, on acoustic-rotational waves in a uniform flow with rigid body swirl. The decision was not to include the contents of the following articles in this document and instead expose only the relevant works. All the subsequent research is being submitted in several articles, hereby cited:

- L. M. B. C. Campos and M. J. S. Silva (2022) "On generalized Hankel functions and a bifurcation of their asymptotic expansion", submitted in *Asymptotic Analysis, IOS Press*
  (Original version review)

- L. M. B. C. Campos and M. J. S. Silva (2022)[1] "On a generalization of the Airy, hyperbolic and circular functions", published in *Nonlinear Studies, Cambridge Scientific Publishers*, 29(2), pp. 529–545, URL: `www.nonlinearstudies.com/index.php/nonlinear/article/view/2137`

- L. M. B. C. Campos and M. J. S. Silva (2022) "On asymptotic expansions for generalized Airy, circular and hyperbolic functions", submitted in *Nonlinear Studies, Cambridge Scientific Publishers*
  (Original version review)

- L. M. B. C. Campos and M. J. S. Silva (2022) "On hyperspherical associated Legendre functions: the extension of spherical harmonics to N dimensions", submitted in *Nonlinear Studies, Cambridge Scientific Publishers* (Original version review)

1.5 Notation

Throughout this thesis, there are many mathematical variables that can be identified since they are always written in italic mode. If the letter or symbol is written in normal mode, it does not represent a mathematical variable. However, it means an abbreviation, or if it is written in a subscript or a superscript, it can be an identifier of what the mathematical variable represents. Therefore, these letters or symbols written in normal mode are useful to distinguish several variables. For instance, in chapter 9, E represents the Young's modulus of elasticity whereas E_{T} contains the subscript T that stands for total, which means that the variable E_{T} is the total elastic energy per unit volume of the plate during its deformation.

Some of those variables are tensors that can be of different orders and therefore they have distinct notations for each of them. The tensors with order zero are scalars and are represented by a variable

[1] The published article "On a generalization of the Airy, hyperbolic and circular functions" was done during the Ph.D. course, but it is not included in this document.

written in italic mode with no subscripts. For instance, A represents a scalar. The tensors with order one mean vectors (written also in italic), however they need one index (subscript) to represent them; that subscript follows the notation of multiplicities and is also written in italic. For instance, A_i represents a vector while i is its free index. In those cases, the vectors can be written also in bold mode, $\mathbf{A}$, instead of representing them with a subscript. Another example of a vector is $\boldsymbol{\nabla}$ that indicates the derivative operator (in all chapters of the thesis). The tensors with order two are also written in italic and they have two italic subscripts. For example, A_{ij} is a second-order tensor with i and j as free indices. In summary, to know which order the tensors are, the notation of multiplicities is used in this thesis to represent them, and the number of free indices is equal to the order of the tensor. Following that logic, A_{ijk} is a third order tensor and A_{ijkl} is a fourth order tensor. An important reminder is that all these indices can be Latin, Greek or other types of letters, but they must be written in italic mode[2]. Another note is that the bold symbols only represent vectors (first-order tensors) and not tensors of other orders.

There are also several variables with subscripts, but these subscripts cannot be regarded as usual indices of multiplicities. Whenever the subscripts are numbers or letters in not italic mode, they do not stand for multiplicities. For instance, as indicated in the first paragraph of this subsection 1.5, E_{T} is the energy of deformation, and the subscript T means that it is about the total energy; therefore, E_{T} is not a first-order tensor, but a scalar. Another example from the chapter 9 is the variable E_1 in which 1 stands for bending (it is not a free index); therefore, E_1 is a scalar and not a first-order tensor. Furthermore, in some sums or series (infinite sums) written throughout the thesis, there are variables with subscripts in some terms of the sums. These variables with subscripts do not represent tensors; although they have a subscript written in the italic mode because it is a mathematical variable, these indexed variables are coefficients representing each term of the sum and the subscript is the index of summation. For instance, $\sum_i^N a_i$ means a sum of the terms a_i and consequently a_i is not a first-order tensor, but a scalar term of the sum in which the subscript i is the index of summation, not an index that stands for a multiplicity. The indices of summation and the dummy variables of all sums are not indicated in the list of symbols.

The number of variables is large and the following chapters are almost independent of each other. For that reason, the list of symbols is separated by the various chapters to make the reader's search easier. Consequently, some variables are repeated in more than one chapter; for instance, x stands for x-axis in Cartesian coordinates and is present in the nomenclature not only in the chapter 2, but also in the chapter 3. Otherwise, some letters or symbols are used in more than one chapter, but represent different variables, depending on the chapter they are written in; for instance, the symbol μ means the Lamé second parameter in the chapter 6, however in the chapter 7 it represents the magnetic permeability.

Finally, there are some not italic letters (written in standard mode) that represent a mathematical variable. These variables are i as the imaginary number, d as the differential operator and e as the Napier's number. Other mathematical operators written in normal mode are Re that stands for the real part of a complex number, const that is when the mathematical symbol is a constant, $\log_{10}$ that is used to indicate logarithm with 10 as the basis and log that stands for a logarithm with e as the basis.

[2]There are exceptions in chapter 7 and appendix D: $\mathbf{e}_\alpha$, $\mathbf{e}_\beta$ and $\mathbf{e}_\phi$ are unit vectors in spherical dipolar referential since they are written in bold mode, although the subscripts α, β and ϕ are not free indices, but identifiers for each vector. The other example is h_α or h_β, which are scalar numbers (scale factors) and not vectors, although they have italic subscripts.

2 | On the multipath effects due to wall reflections for wave reception near a corner

"Reason we call that faculty innate in us of discovering laws and applying them with thought."

— Hermann von Helmholtz

Contents

Aircraft noise near airports can limit the use of runways at night and other times, leading to take-off weight limits that affect economics and, if not controlled, could become an obstacle to air traffic growth. Aircraft noise [8] is the subject of international certification standards, with some airports or local authorities applying lower limits. The efforts to reduce noise near airports lead to a balanced approach [9] combining low self-noise aircraft with low noise operations to minimise the number of people affected within given ground contours [10]. The certification and noise monitoring depend on measuring microphones that receive the direct sound wave from the aircraft. If the microphone is near the ground, a reflected wave is added to the direct wave; if the two waves are in-phase, the amplitude is doubled, corresponding to an increase of $10\log_{10} 2 \approx 3\,\mathrm{dB}$ for the amplitude and $20\log_{10} 2 \approx 6\,\mathrm{dB}$ for the power. If the microphone is in a corner, as sketched in figure 2.1, then there are three reflected waves: one from the ground, one from the wall and one reflected from both surfaces; together with the direct wave, there are four waves, and if all four are in-phase, the amplitude is multiplied by 4 leading to an increase of $10\log_{10} 4 \approx 6\,\mathrm{dB}$ for the amplitude and $20\log_{10} 4 \approx 12\,\mathrm{dB}$ for the power. Thus, the norms on noise measurement [11, 12] specify a 6 dB increase in power near the ground and 12 dB near the corner.

These noise corrections are extreme worst-case scenarios because: (i) if waves are out-of-phase, there is less amplification and there may be even cancellation; (ii) if the ground and wall are not perfectly

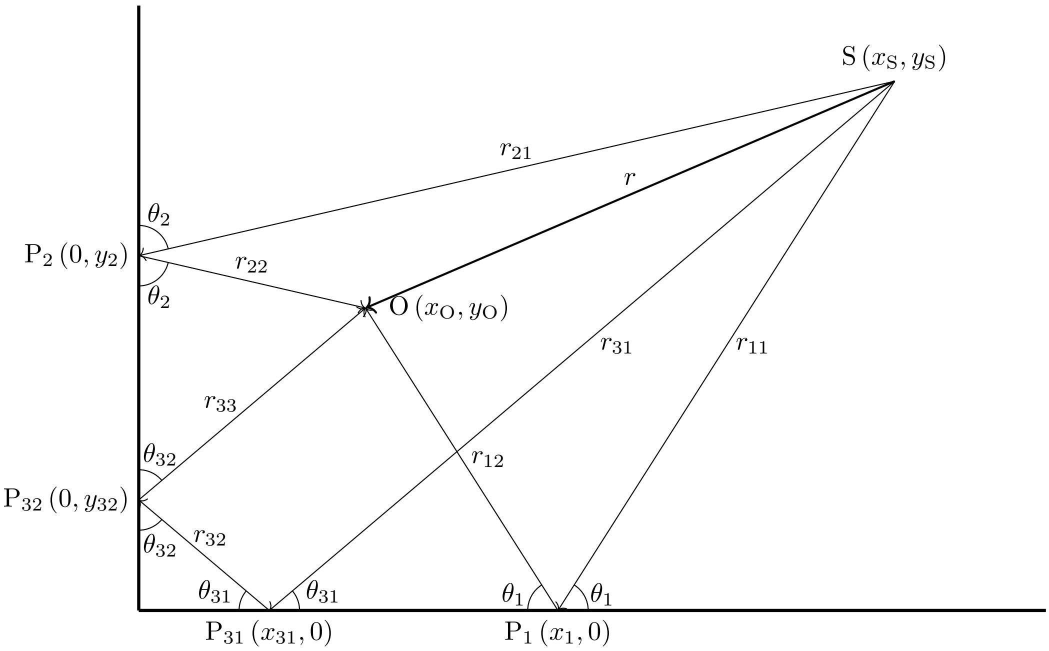

Figure 2.1: Observer O at (x_O, y_O) receiving from the source S at (x_S, y_S) four signals: (i) one direct from the source to observer at distance r; (ii) one with the reflection on the ground making the distance $r_{11}+r_{12}$; (iii) one with the reflection on the wall making the distance $r_{21}+r_{22}$; (iv) one with the reflection on the ground followed by the reflection on the wall making the distance $r_{31}+r_{32}+r_{33}$.

reflecting, then wave transmission or absorption reduces the amplitude. In addition, urban morphology [13–15] is not reduced to infinite plane and orthogonal corner reflectors. Further changes to the received sound field arise due to atmospheric wind and turbulence [16, 17]. More fundamentally, the effect of a reflector is to lead to interference between the direct and reflected waves, resulting in amplification, attenuation or even cancellation depending on the frequency (or wavelength) and position of the observer and source relative to the obstacle. In the case of an orthogonal corner, sketched in the figure 2.2, the position can be specified by Cartesian (x, y) or polar ($\mathfrak{r}$, ϑ) coordinates for the source and observer. The effect of reflections can be calculated for sound pulses [18] or for sinusoidal waves, which can form any spectrum by superposition. The present chapter considers a sound source and an observer/receiver at arbitrary positions relative to an orthogonal corner taking into account the interference between the direct and the three reflected waves for any frequency, allowing for different reflection coefficients from the ground and the wall.

In general, the problem of multipath propagation and interference applies to all waves, particularly acoustic [19–23] and electromagnetic waves [24–26]. The situation is illustrated in the two-dimensional case in figure 2.1, showing that the observer receives four signals: (i) one direct signal from the source; (ii) one signal reflected from the ground; (iii) one signal reflected from the wall; (iv) a fourth signal reflected from both wall and ground. The positions of the reflection points are determined by the condition of equal angles of incidence and reflection; once the positions of the reflection points are determined, the lengths of all the ray paths can be calculated. Together with the reflection coefficients, this specifies the total received signal; normalising with regard to the direct signal specifies the multipath factor accounting for the interference among the four waves. The multipath factor is generally complex, with the modulus setting the amplitude change and the argument specifying the phase change.

The problem is solved in two dimensions (figure 2.1) by determining the total received field (subsection 2.1.1), which consists of the direct plus three reflected waves. The waves reflected on the ground (subsection 2.1.2) and on the wall (subsection 2.1.3) are specified by the positions of the respective reflection points and by the lengths of the two resulting ray paths; for the fourth wave reflected on the ground and then on the wall (subsection 2.1.4), the positions of the two reflection points are coupled and specify the three lengths of ray paths. Concerning the fourth signal, there are three cases: (i) if the elevation angle of the observer is above that of the source ($\alpha > \beta$ in figure 2.2), then the first reflection is on the ground and the second on the wall (subsection 2.1.4); (ii) in the reverse case ($\beta > \alpha$ in figure A.1), the first reflection is on the wall and the second on the ground (appendices A.1.1 and A.1.2); (iii) in the intermediate case of observer and source on the same elevation angle ($\beta = \alpha$ in figure A.2), the double reflection on the corner is treated as the limit of the preceding cases (appendices A.1.2 and A.1.4). The total signal is the sum of all four signals taking into account the reflection coefficients (appendix A.3) on the ground and wall. The total signal is normalised to the direct signal to specify the multipath factor, whose amplitude and phase are plotted for: (subsection 2.2.1) two relative positions of source and observer (figures 2.3 and 2.4); (subsection 2.2.2) three combinations of the reflection factors on the ground and wall (figures 2.5 to 2.7). The results may be recast in terms of source distance and direction (subsection 2.2.3), and be simplified for a source in the far field. Thus, as an alternative to the preceding, for a fixed frequency, the amplitude and phase changes may be evaluated (subsection 2.2.4) as functions of source distance to the corner (figure 2.8) or as functions of the direction of arrival of the signal (figure 2.9). The contour maps for the amplitude (figures 2.10 and 2.12) and phase (figures 2.11 and 2.13) of the multipath factor apply not only to acoustic, but also to electromagnetic waves (section 2.3).

2.1 Direct, singly-reflected and doubly-reflected signals

The total signal received from a distant source by an observer in a corner (figure 2.1) consists of a direct signal (subsection 2.1.1), plus reflections on the ground (subsection 2.1.2) and on the wall (subsection 2.1.3) plus a double reflection on both surfaces (subsection 2.1.4).

2.1.1 Total signal as sum of four waves

Consider the two-dimensional problem (figure 2.1) of wave reception form a source S by an observer O near a corner between a horizontal ground $y = 0$ and a vertical wall $x = 0$ taken as axes of a Cartesian reference with origin at the corner. The observer,

$$\mathrm{O} \mapsto (x_\mathrm{O}, y_\mathrm{O}) = q\,(\cos\alpha, \sin\alpha)\,, \tag{2.1a}$$

and source,

$$\mathrm{S} \mapsto (x_\mathrm{S}, y_\mathrm{S}) = s\,(\cos\beta, \sin\beta)\,, \tag{2.1b}$$

are at the distance

$$r = \left[(x_\mathrm{S} - x_\mathrm{O})^2 + (y_\mathrm{S} - y_\mathrm{O})^2 \right]^{1/2} \tag{2.2}$$

where q is the distance between the corner and the observer, and s is the distance between the corner and the source. The distance r specifies the direct signal, to which are added reflected signals, illustrated in the figure 2.1, for source farther from the origin than the observer. The viscosity for the sound field in air at the most audible frequencies are negligible since the Reynolds number is very large, being of the order of 10^8. The sound is therefore considered as a weak motion of an inviscid fluid, in this case from an initial state of rest, and thermal conduction is also neglected. Since the sound wave induces small perturbations in the air, its presence can be assumed as a linear perturbation. Consequently, the product of two perturbations are neglected and the laws describing the movement are linear, using first-order approximations. Since there is no interaction between the sound waves, they can be added by superposition, to obtain the total sound field [27]. Four signals are received and the total acoustic pressure perturbation is given by

$$\begin{aligned} p_\mathrm{tot} = {} & \frac{1}{r}\exp(\mathrm{i}kr) + \frac{R_1}{r_{11}+r_{12}}\exp\left[\mathrm{i}k\left(r_{11}+r_{12}\right)\right] + \frac{R_2}{r_{21}+r_{22}}\exp\left[\mathrm{i}k\left(r_{21}+r_{22}\right)\right] \\ & + \frac{R_{31}R_{32}}{r_{31}+r_{32}+r_{33}}\exp\left[\mathrm{i}k\left(r_{31}+r_{32}+r_{33}\right)\right], \end{aligned} \tag{2.3}$$

corresponding to four contributions in (2.3), namely: (i) the first term, where k is the wavenumber, is due to the direct wave from source to observer, at distance r, and is taken with unit amplitude (the complex amplitude and the temporal part would drop out when normalizing the total signal to the direct signal); (ii) the second term involves the reflection factor R_1 of the horizontal wall at the reflection point P_1, whose coordinates $(x_1, 0)$ specify the distance from source to reflection point r_{11} and the distance from reflection point to observer r_{12}; (iii) the third term involves the reflection factor R_2 of the vertical wall at the reflection point P_2, whose coordinates $(0, y_2)$ specify the distance from source to reflection point r_{21} and the distance from reflection point to observer r_{22}; (iv) the last term involves the reflection factors of the two walls, R_{31} and R_{32}, respectively at the reflection points P_{31} and P_{32}, whose coordinates $(x_{31}, 0)$ and $(0, y_{32})$ specify the distances from source to first reflection point r_{31}, between reflection points r_{32}, and from the second reflection point to observer r_{33}, as sketched in figure 2.2. The angles in figure 2.1 follow the law of specular reflection stating that the angle between the normal to the surface and reflected wave is equal to the angle between the same normal and incident wave. The equation (2.3) is an harmonic solution of the linearised wave equation assuming that the pressure perturbation is radial (and unsteady) and represents a wave with outward spherical propagation centred at the source [27]. The physical solution can be given by the real part of (2.3). The reflection factors may be complex, involving amplitude and phase changes for an impedance ground and/or wall. If the reflection factor is uniform on the ground R_h and on the wall R_v, then (2.3) simplifies with

$$R_1 = R_{31} \equiv R_\mathrm{h}, \tag{2.4a}$$

$$R_2 = R_{32} \equiv R_\mathrm{v}. \tag{2.4b}$$

The reflection coefficients of the ground R_h and of the wall R_v may be different (for instance, grass and concrete) or equal (for instance, both concrete). A brief review about the reflection coefficients is described in the appendix A.1.3.

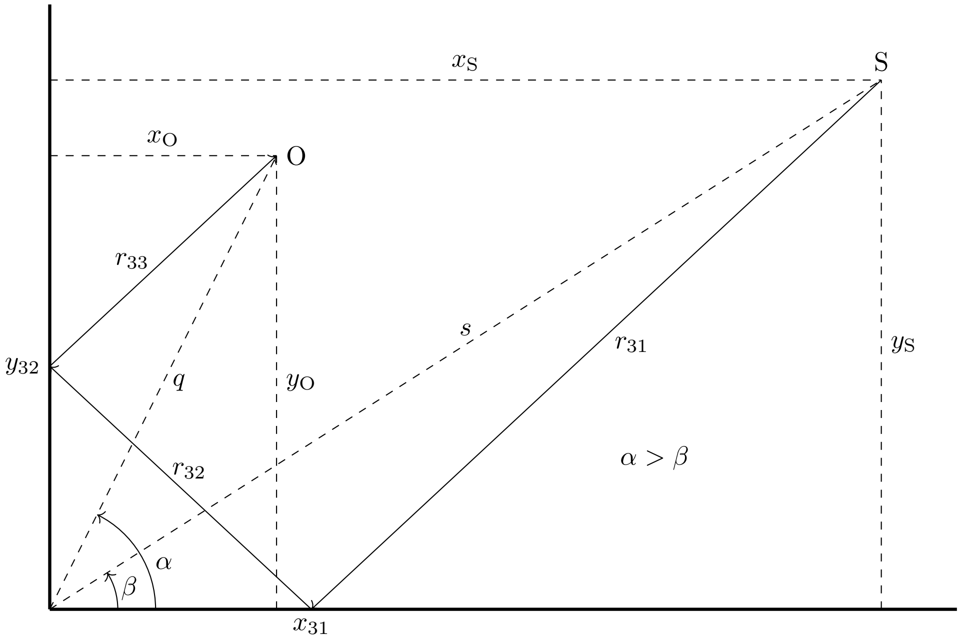

Figure 2.2: Sound source S and observer O near a corner, with elevation angle for the latter α larger than for the former β, that is, $\beta < \alpha$, showing only the reception path with two intermediate reflections.

2.1.2 Signal due to reflection on the ground

The equality of the angles θ_1 of incidence and reflection on the horizontal plane,

$$\frac{x_S - x_1}{y_S} = \cot\theta_1 = \frac{x_1 - x_O}{y_O}, \tag{2.5a}$$

specifies the position $(x_1, 0)$ at the reflection point P_1, that is,

$$x_1 = \frac{x_O y_S + y_O x_S}{y_S + y_O}. \tag{2.5b}$$

The latter determines the distance from the source to the reflection point,

$$r_{11} = \left[(x_S - x_1)^2 + y_S^2\right]^{1/2} = |y_S| \left[1 + \frac{(x_S - x_O)^2}{(y_S + y_O)^2}\right]^{1/2}, \tag{2.6a}$$

and the distance from the reflection point to the observer,

$$r_{12} = \left[(x_1 - x_O)^2 + y_O^2\right]^{1/2} = |y_O| \left[1 + \frac{(x_S - x_O)^2}{(y_S + y_O)^2}\right]^{1/2}, \tag{2.6b}$$

where (2.5b) was used. These two distances, in (2.6a) and (2.6b), determine the second term in (2.3) and specify the signal reflected on the horizontal ground.

2.1.3 Signal due to reflection on the wall

The equality of the angles θ_2 of incidence and reflection on the vertical plane,

$$\frac{y_S - y_2}{x_S} = \cot\theta_2 = \frac{y_2 - y_O}{x_O}, \tag{2.7a}$$

specifies the position $(0, y_2)$ at the reflection point P_2, that is,

$$y_2 = \frac{x_O y_S + y_O x_S}{x_S + x_O}. \tag{2.7b}$$

The latter determines the distance from the source to the reflection point,

$$r_{21} = \left[x_S^2 + (y_S - y_2)^2\right]^{1/2} = |x_S| \left[1 + \frac{(y_S - y_O)^2}{(x_S + x_O)^2}\right]^{1/2}, \tag{2.8a}$$

and the distance from the reflection point to the observer,

$$r_{22} = \left[x_O^2 + (y_2 - y_O)^2\right]^{1/2} = |x_O| \left[1 + \frac{(y_S - y_O)^2}{(x_S + x_O)^2}\right]^{1/2}, \tag{2.8b}$$

where (2.7b) was used. These two distances, in (2.8a) and (2.8b), determine the third term of (2.3), which specifies the signal reflected from the vertical wall.

2.1.4 Signal due to double reflection on the ground and on the wall

The angles of incidence or reflection on the horizontal, θ_{31}, and vertical, θ_{32}, planes couple the positions of the reflection point P_{31} on the ground $(x_{31}, 0)$,

$$\frac{x_S - x_{31}}{y_S} = \cot\theta_{31} = \frac{x_{31}}{y_{32}}, \tag{2.9a}$$

and the reflection point P_{32} on the wall $(0, y_{32})$,

$$\frac{y_{32}}{x_{31}} = \cot\theta_{32} = \frac{y_O - y_{32}}{x_O}. \tag{2.9b}$$

Solving the last two equations for y_{32} gives the equality

$$\frac{x_{31} y_S}{x_S - x_{31}} = y_{32} = \frac{x_{31} y_O}{x_O + x_{31}}, \tag{2.9c}$$

from which follows

$$(x_O + x_{31})\, y_S = y_O\, (x_S - x_{31}), \tag{2.9d}$$

which specifies the position of the first reflection point,

$$x_{31} = \frac{y_O x_S - x_O y_S}{y_S + y_O}. \tag{2.9e}$$

The position of the second reflection point,

$$y_{32} = \frac{y_\mathrm{O} x_\mathrm{S} - x_\mathrm{O} y_\mathrm{S}}{x_\mathrm{S} + x_\mathrm{O}}, \tag{2.9f}$$

follows substituting (2.9e) in (2.9a) or in any equality of (2.9c). The positions of both reflection points determine the distances: (i) from the source to the first reflection point on the ground,

$$r_{31} = \left[(x_\mathrm{S} - x_{31})^2 + y_\mathrm{S}^2\right]^{1/2} = |y_\mathrm{S}| \left[1 + \frac{(x_\mathrm{S} + x_\mathrm{O})^2}{(y_\mathrm{S} + y_\mathrm{O})^2}\right]^{1/2}; \tag{2.10a}$$

(ii) from the first reflection point on the ground to the second reflection point on the wall,

$$r_{32} = \left[(x_{31})^2 + (y_{32})^2\right]^{1/2} = |y_\mathrm{O} x_\mathrm{S} - x_\mathrm{O} y_\mathrm{S}| \left[\frac{1}{(x_\mathrm{S} + x_\mathrm{O})^2} + \frac{1}{(y_\mathrm{S} + y_\mathrm{O})^2}\right]^{1/2}; \tag{2.10b}$$

(iii) from the second reflection point on the wall to the observer,

$$r_{33} = \left[x_\mathrm{O}^2 + (y_\mathrm{O} - y_{32})^2\right]^{1/2} = |x_\mathrm{O}| \left[1 + \frac{(y_\mathrm{S} + y_\mathrm{O})^2}{(x_\mathrm{S} + x_\mathrm{O})^2}\right]^{1/2}. \tag{2.10c}$$

The last three equations are valid if $\beta \leq \alpha$. In the relations (2.10a) and (2.10b) was used (2.9e) and in the relations (2.10b) and (2.10c) was used (2.9f). The calculations from (2.9a) to (2.10c) assume that the first reflection is on the ground and the second is on the wall, as indicated in the figure 2.2. This is the case if the azimuth (or elevation angle) β of the source in (2.1b) is less than the azimuth α of the observer in (2.1a), $\beta \leq \alpha$. If the reverse was true, $\beta \geq \alpha$, then a similar calculation holds with reflection first on the wall and then on the ground. The third case of sound and observer on the same azimuth, $\beta = \alpha$, corresponds to reflection at the "corner", and can be treated as the boundary $\beta \to \alpha \pm 0$ between the two cases, $\beta \geq \alpha$ and $\beta \leq \alpha$. These differences affect only the doubly reflected wave, that is, the last term of (2.3).

2.2 Multipath effects on the amplitude and phase of the signal

The total signal normalised to the incident signal specifies the amplitude and phase changes (subsection 2.2.1). These changes are plotted over the whole audible range (subsection 2.2.2) for two relative positions of source and observer with three combinations of reflection factors of the ground and wall. For a distant source, the amplitude and phase changes may be simplified (subsection 2.2.3) and plotted in terms of direction of arrival β of the signal and for different source distances q in the plane (subsection 2.2.4).

2.2.1 Multipath factor due to ground and wall reflections

The multipath factor F is defined as the ratio to the pressure perturbation of the direct signal, assuming that is a spherical wave [27],

$$p_{\mathrm{dir}} \equiv \frac{1}{r} \exp\left(\mathrm{i}kr\right), \tag{2.11}$$

of the pressure perturbation of the total signal (2.3), that is,

$$F = \frac{p_{\mathrm{tot}}}{p_{\mathrm{dir}}} = p_{\mathrm{tot}} r \exp\left(-\mathrm{i}kr\right), \tag{2.12a}$$

leading to

$$\begin{aligned} F \equiv 1 &+ R_{\mathrm{h}} \frac{r}{r_{11} + r_{12}} \exp\left[\mathrm{i}k\left(r_{11} + r_{12} - r\right)\right] + R_{\mathrm{v}} \frac{r}{r_{21} + r_{22}} \exp\left[\mathrm{i}k\left(r_{21} + r_{22} - r\right)\right] \\ &+ R_{\mathrm{h}} R_{\mathrm{v}} \frac{r}{r_{31} + r_{32} + r_{33}} \exp\left[\mathrm{i}k\left(r_{31} + r_{32} + r_{33} - r\right)\right]. \end{aligned} \tag{2.12b}$$

The pressure perturbation of the direct signal (2.11) is an harmonic solution of the linearised outward spherical wave equation, centred from the source, where the physical solution can be given by its real part [27]. The multipath factor (2.12b) depends on the various distances, r, r_{11}, r_{12}, r_{21}, r_{22}, r_{31}, r_{32}, r_{33}, specified respectively by the relations determined in the section 2.1. The multipath factor is generally complex,

$$F = |F| \exp\left[\mathrm{i} \arg\left(F\right)\right], \tag{2.13}$$

and its amplitude and phase are plotted separately respectively at the top $|F|$ and bottom $\arg\left(F\right)$ of figures 2.3 to 2.7, versus frequency over the audible range, $20\,\mathrm{Hz} \leq f \leq 20\,\mathrm{kHz}$.

In all five figures, the source is far from the corner. It is assumed that the source is at the position $x_{\mathrm{S}} = 700\,\mathrm{m}$ and $y_{\mathrm{S}} = 30\,\mathrm{m}$. The observer position and the impedance of horizontal and vertical walls are indicated in the table 2.1.

Number of the figure	x_{O} [m]	y_{O} [m]	R_{h}	R_{v}
2.3	3	2	1	1
2.4	2	6	1	1
2.5	3	2	0.5	1
2.6	3	2	1	0.5
2.7	3	2	0.5	0.5

Table 2.1: Values of the observer position and reflection factors of the walls in figures 2.3 to 2.7.

The figure 2.3 is the baseline case with observer at the position $x_{\mathrm{O}} = 3\,\mathrm{m}$ and $y_{\mathrm{O}} = 2\,\mathrm{m}$. The horizontal and vertical walls have also uniform rigidity equal to one. When the reflection factors are equal to one, the wave is totally reflected because the acoustic pressure of both waves is the same. In figure 2.4 the observer position is changed, in figure 2.5 the observer position returns to the baseline position, but the ground has reflection coefficient one-half. Instead, in figure 2.6, the reflection coefficient is one-half on the wall. In figure 2.7, both surfaces have reflection coefficient one-half. Changing one set of parameters from the baseline shows separately the effect of observer position or the effect of halving the reflection coefficient not only of the ground, but also of the wall.

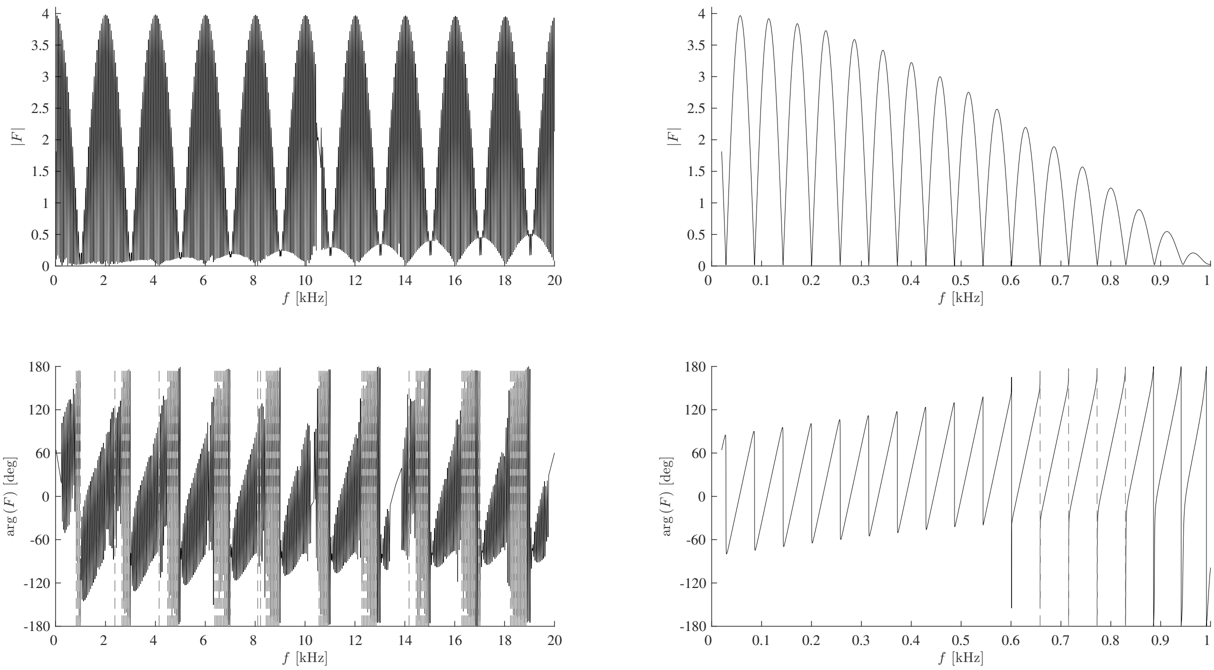

Figure 2.3: Modulus (top) and phase (bottom) of the multipath factor (2.12b) versus frequency in the audible range (left), $20 \leq f \leq 20000\,\mathrm{Hz}$, or in the sub-range (right), $20 \leq f \leq 1000\,\mathrm{Hz}$, for a fixed observer at the position $(x_\mathrm{O}, y_\mathrm{O}) = (3, 2)$ m and fixed source at the position $(x_\mathrm{S}, y_\mathrm{S}) = (700, 30)$ m. The ground and wall are completely rigid with $R_\mathrm{h} = R_\mathrm{v} = 1$.

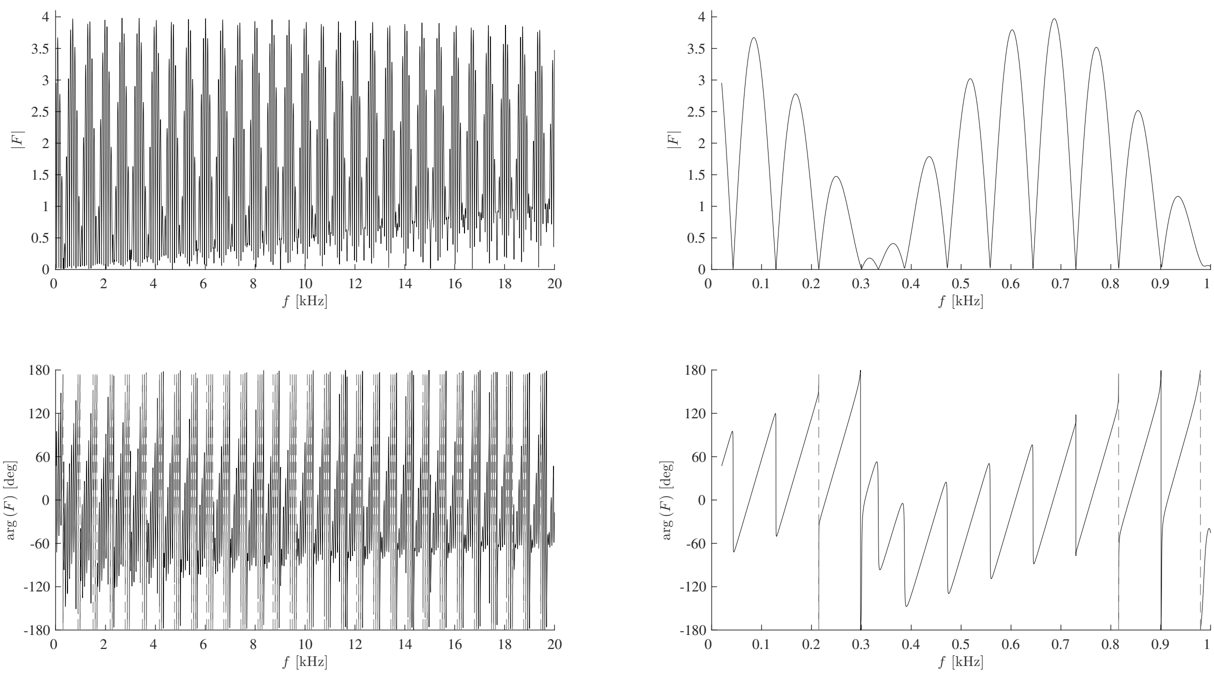

Figure 2.4: The same as figure 2.3, but for a modified observer at the position $(x_\mathrm{O}, y_\mathrm{O}) = (2, 6)$ m.

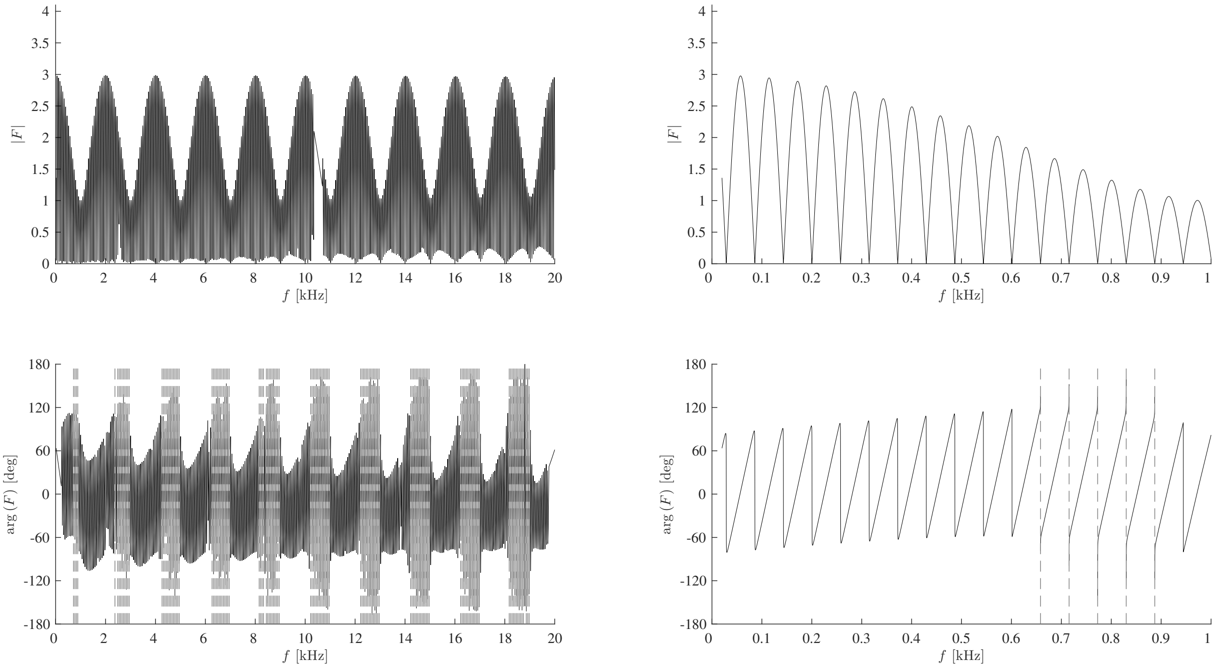

Figure 2.5: The same as figure 2.3, but for halved reflection factor on the ground, $R_\mathrm{h} = 0.5$.

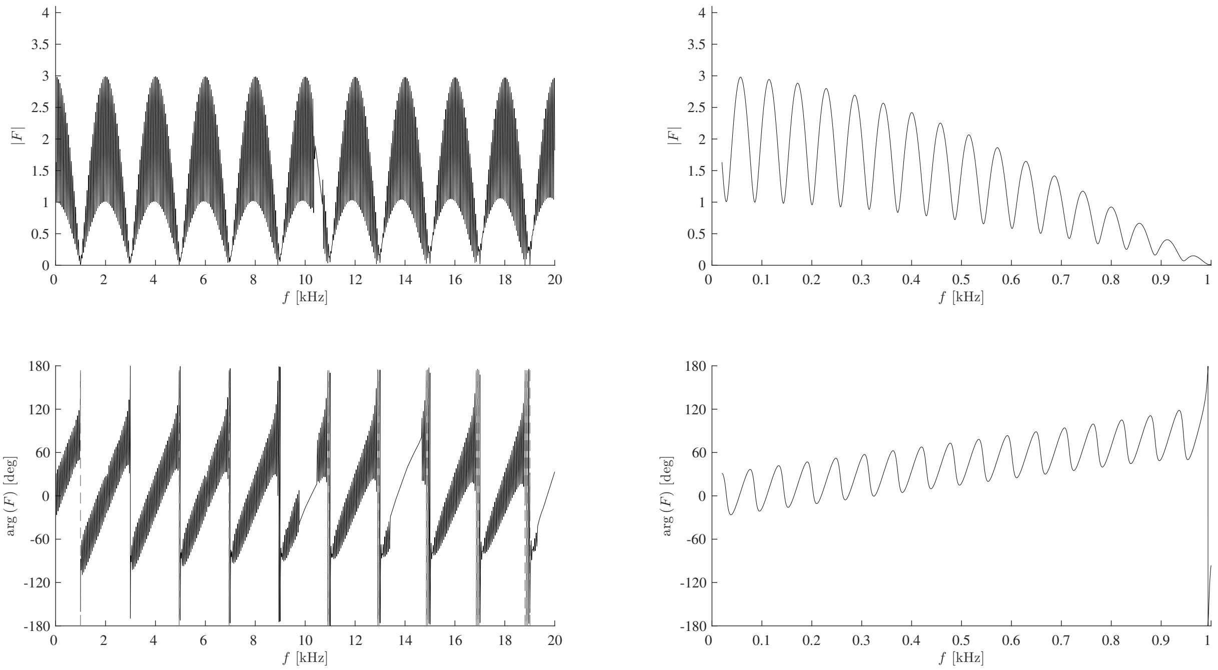

Figure 2.6: The same as figure 2.3, but for halved reflection factor on the wall, $R_\mathrm{v} = 0.5$.

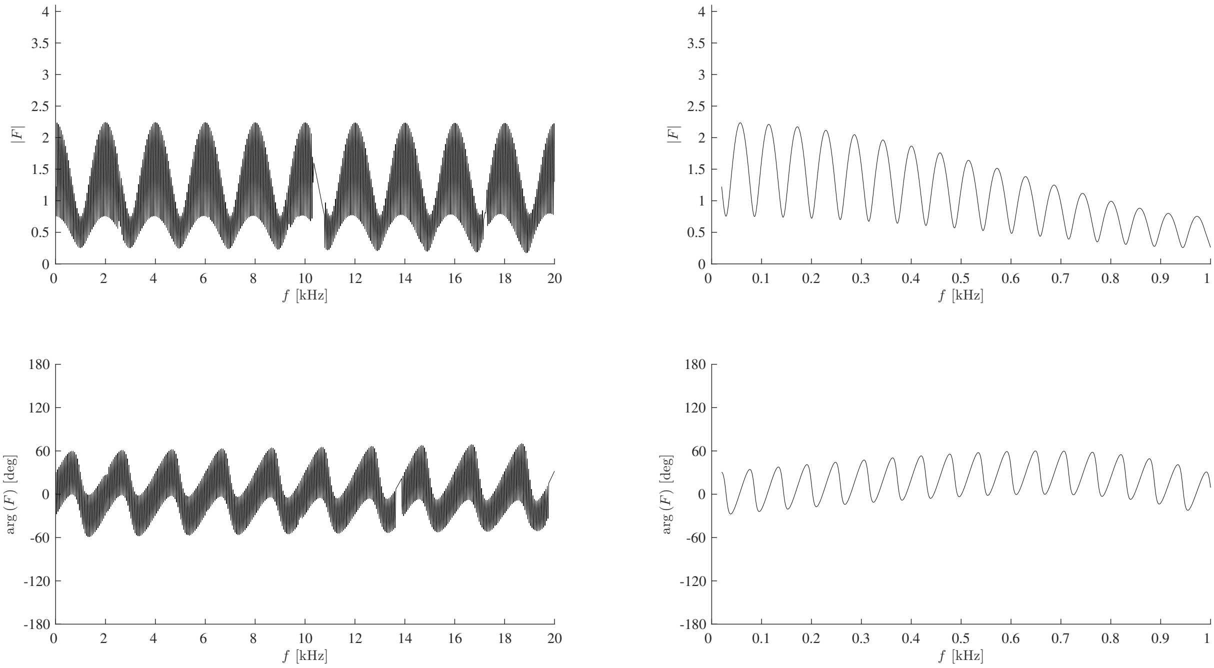

Figure 2.7: The same as figure 2.3, but for halved reflection factor on the the ground and on the wall, $R_\mathrm{h} = R_\mathrm{v} = 0.5$.

2.2.2 Effect of observer position and reflection coefficients of surfaces

The figures 2.3 to 2.7 have all the same format, with the modulus or amplitude of the multipath factor at the top and its argument or phase at the bottom; the spectrum is quite dense over the audible range, and in fact was drawn using symbolic expressions. Since the spikes which form the spectrum are very narrow, a part of the full spectrum at left is amplified at right, namely to the range $20 \leq f \leq 1000\,\mathrm{Hz}$. It is seen in figure 2.3 that the interference between direct and reflected signals leads to nulls and peaks; furthermore, the succession of peaks has itself peaks and nulls, like a phenomenon of beats; on the right-hand side, it can be seen clearly the individual peaks, and on the left-hand side only the "peaks of the peaks". The complex amplitude of F is a composition (square root, sum and squares of real and imaginary parts) of cosine and sine functions, all harmonic functions.

The figure 2.3 concerns an observer below the bisector of the corner and figure 2.4 an observer above. Changing the observer position does not influence significantly the maximum amplitude of $|F|$ and the extreme values of $\arg(F)$. It has a stronger effect on the frequency values which lead to the extreme values or zeros of $|F|$ and $\arg(F)$, since the multipath factor depends on the ray distances of all waves. In figure 2.5, the observer returns to the baseline position of figure 2.3, but the reflection coefficient of the ground is halved; the maximum amplitude of the multipath factor in figure 2.3 is almost 4, but when the reflection coefficient of the ground is halved, the maximum amplitude of the multipath factor reduces to almost 3, since that in this last case, the ground absorbs some of the acoustic energy of the propagating waves. Nonetheless, the frequency values which lead to maximum absolute value of multipath factor are the same because those frequency values depend only on the difference between ray distances of reflected waves and the ray distance of the direct wave (indeed, according to (2.12b), they depend on the exponential arguments). In figure 2.6, the reflection coefficient on the wall is halved instead of on the ground and the observations are the same to the last ones. In figure 2.7, the reflection coefficient is halved both on ground and on wall. Relative to this, the figure 2.7 shows a smaller maximum amplitude (almost 2.5) and a smaller maximum phase due to the attenuation effect of the absorbing surfaces.

2.2.3 Case of source in the far field and observer in the near field

The distances appearing in (2.12b) may be expressed in polar coordinates (2.1a) and (2.1b), and simplified for the observer in near field and the source in far field, for example: (i) the distance (2.2) from the source (2.1b) to the observer (2.1a) is

$$r = \left|s^2 + q^2 - 2sq\cos\left(\beta - \alpha\right)\right|^{1/2} = s - q\cos\left(\beta - \alpha\right) + O\left(\frac{q^2}{s}\right); \tag{2.14}$$

(ii) the distances from the source (2.6a) and observer (2.6b) to the reflection point on the ground are respectively

$$r_{11} = s - q\cot\beta\sin\left(\alpha + \beta\right) + O\left(\frac{q^2}{s}\right), \tag{2.15a}$$

$$r_{12} = q\sin\alpha\csc\beta + O\left(\frac{q^2}{s}\right) \tag{2.15b}$$

for single reflection; (iii) the distances from the source (2.8a) and observer (2.8b) to the reflection point on the wall are respectively

$$r_{21} = s - q\tan\beta\sin\left(\alpha + \beta\right) + O\left(\frac{q^2}{s}\right), \tag{2.16a}$$

$$r_{22} = q\cos\alpha\sec\beta + O\left(\frac{q^2}{s}\right) \tag{2.16b}$$

for single reflection; (iv) in the case of double reflection, the distance from the source to the reflection point on the ground (2.10a) is

$$r_{31} = s - q\cot\beta\sin\left(\alpha - \beta\right) + O\left(\frac{q^2}{s}\right), \tag{2.17a}$$

from this last point to the reflection point on the wall (2.10b) is

$$r_{32} = q\sec\beta\csc\beta\sin\left(\alpha - \beta\right) + O\left(\frac{q^2}{s}\right) \tag{2.17b}$$

and from the wall to the observer (2.10c) is

$$r_{33} = q\cos\alpha\sec\beta + O\left(\frac{q^2}{s}\right). \tag{2.17c}$$

The last three relations are valid if $\beta \leq \alpha$.

Note that the far field approximation requires that all distances can be approximated to $O\left(q\right)$, implying that: (i) if the leading term is $O\left(s\right)$, then the next approximation $O\left(q\right)$ is needed, for instance to specify the $O(q)$ terms in (2.14), (2.15a), (2.16a) and (2.17a); (ii) if the leading term is $O(q)$, as in (2.15b), (2.16b), (2.17b) and (2.17c) the next term would be $O\left(q^2/s\right)$ and can be omitted. The last three results hold if $\alpha \geq \beta$, and the opposite case is considered in appendix A.1.3. Substituting the simplified distances, the multipath factor (2.12b) can be written explicitly as

$$\begin{aligned} F = 1 &+ R_\mathrm{h}\left[1 - \frac{q}{s}A(\alpha,\beta)\right]\exp\left[ikq\,A(\alpha,\beta)\right] + R_\mathrm{v}\left[1 - \frac{q}{s}B(\alpha,\beta)\right]\exp\left[ikq\,B(\alpha,\beta)\right] \\ &+ R_\mathrm{h}R_\mathrm{v}\left[1 - \frac{q}{s}C(\alpha,\beta)\right]\exp\left[ikq\,C(\alpha,\beta)\right] \end{aligned} \tag{2.18a}$$

where

$$A(\alpha,\beta) = \cos(\alpha-\beta) + \sin\alpha\csc\beta - \cot\beta\sin(\alpha+\beta), \tag{2.18b}$$

$$B(\alpha,\beta) = \cos(\alpha-\beta) + \cos\alpha\sec\beta - \tan\beta\sin(\alpha+\beta), \tag{2.18c}$$

$$C(\alpha,\beta) = \cos(\alpha-\beta) + \cos\alpha\sec\beta - \sin(\alpha-\beta)\csc\beta\,(\cos\beta - \sec\beta) \tag{2.18d}$$

and noting that the last expression is valid if $\alpha \geq \beta$. The relation (2.18a) assumes the approximation $q^2 \ll s^2$. For a source in the far field at lower elevation angle than the observer in the near field, $\alpha \geq \beta$, the direct wave has amplitude and phase corrections for single reflections on the ground and on the wall, and double reflection on both.

2.2.4 Effect of direction of arrival of the signal and source position

The amplitude and phase changes are indicated in the figures 2.8 and 2.9 for the baseline observer position and rigid walls (first line of table 2.1), but for a fixed frequency $f = 1\,\mathrm{kHz}$ corresponding at the sound speed $c \approx 343.21\,\mathrm{m\,s^{-1}}$ to the wavenumber $k = 2\pi f/c \approx 18.31\,\mathrm{m^{-1}}$. In the table 2.2 and figure 2.8, the source is kept in the same grazing direction,

$$\beta = \arctan\left(\frac{y_\mathrm{S}}{x_\mathrm{S}}\right) = \arctan\left(\frac{30}{700}\right) \approx 2.45°, \tag{2.19a}$$

but the source position

$$(x_\mathrm{S}, y_\mathrm{S}) = s\,(\cos\beta, \sin\beta) \approx s\,(0.9991, 0.0428)\ \mathrm{m} \tag{2.19b}$$

varies with the distance, $4\,\mathrm{m} < s < 200\,\mathrm{m}$, and so varies the Helmholtz number for the frequency $f = 1\,\mathrm{kHz}$, specifically $73.2285 \leq ks \leq 3661.42$; higher and lower frequencies, $f = 10\,\mathrm{kHz}$ and $f = 100\,\mathrm{Hz}$ respectively, are also considered in the table 2.2 and figure 2.8. In the figure 2.9, the source distance is kept at

$$s = \left(x_\mathrm{S}^2 + y_\mathrm{S}^2\right)^{1/2} = \left(700^2 + 30^2\right)^{1/2} \approx 700.64\,\mathrm{m} \tag{2.20a}$$

corresponding to a Helmholtz number $ks \approx 12826.7$ for the frequency $f = 1\,\mathrm{kHz}$, and the direction changes over the whole corner, $0 \leq \beta \leq \pi/2\,\mathrm{rad}$, so that the source position is

$$(x_\mathrm{S}, y_\mathrm{S}) \approx 700.64\,(\cos\beta, \sin\beta)\ \mathrm{m}. \tag{2.20b}$$

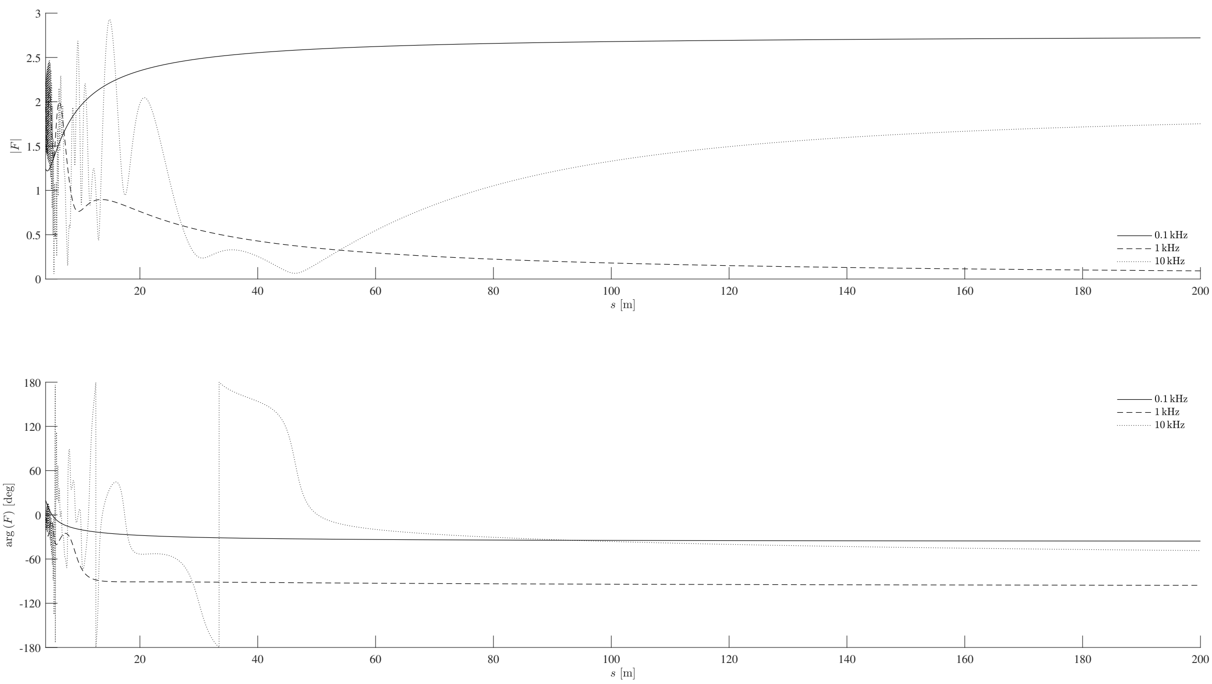

Figure 2.8: Modulus (top) and phase (bottom) of the multipath factor (2.12b) versus source distance, $4\,\text{m} < s < 200\,\text{m}$, in a fixed direction, $\beta \approx 2.45°$, with rigid ground and wall, $R_\text{h} = R_\text{v} = 1$, and observer position at $(x_\text{O}, y_\text{O}) = (3, 2)$ m, adding to the frequency $f = 1000\,\text{Hz}$ other two frequencies, one with larger order of magnitude, $f = 10000\,\text{Hz}$, and one with smaller order of magnitude, $f = 100\,\text{Hz}$.

Frequency [Hz]	**Absolute value** $\lvert F\rvert$	**Argument** $\arg(F)$ [deg]
100	2.7531	−36.3838
500	1.8857	−2.9399
1000	0.0233	−99.5285
5000	0.1054	−138.6572
10000	1.9056	−59.1402

Table 2.2: Mean value of the modulus (middle column) and phase (right column) of the multipath factor (2.12b) versus source distance, $400\,\text{m} < s < 1400\,\text{m}$, in a fixed direction, $\beta \approx 2.45°$, with rigid ground and wall, $R_\text{h} = R_\text{v} = 1$, and observer position at $(x_\text{O}, y_\text{O}) = (3, 2)$ m, adding to the frequency $f = 1000\,\text{Hz}$ other four frequencies, two with larger order of magnitude and two with smaller order of magnitude.

The table 2.2 shows only the mean values because the changing of the distance s of the far away source between the values 400 and 1400 meters has little effect, for any fixed frequency f, independently of its value. Although the amplitude and phase of the multipath effect are almost independent of source distance s, they are quite sensitive to frequency, as it can be seen in table 2.2. The amplitude of the multipath factor (second column of table 2.2) slightly increases with source distance for $f = 100\,\text{Hz}$, $f = 500\,\text{Hz}$ and $f = 10000\,\text{Hz}$, but slightly decreases for $f = 1000\,\text{Hz}$ and $f = 5000\,\text{Hz}$ showing that the behaviour of the multipath factor is strongly dependent on the frequency, in contrast to the source distance. Regarding the phase (third column of 2.2), for all the values of the frequency, the source distance does not significantly influence the phase. The table 2.2 shows that the phase is negative for the five values of the frequency. However, that is not always the true because there are some frequencies for which the phase is positive as it can be seen in the appendix A.2, specifically in the figure A.4 (in that

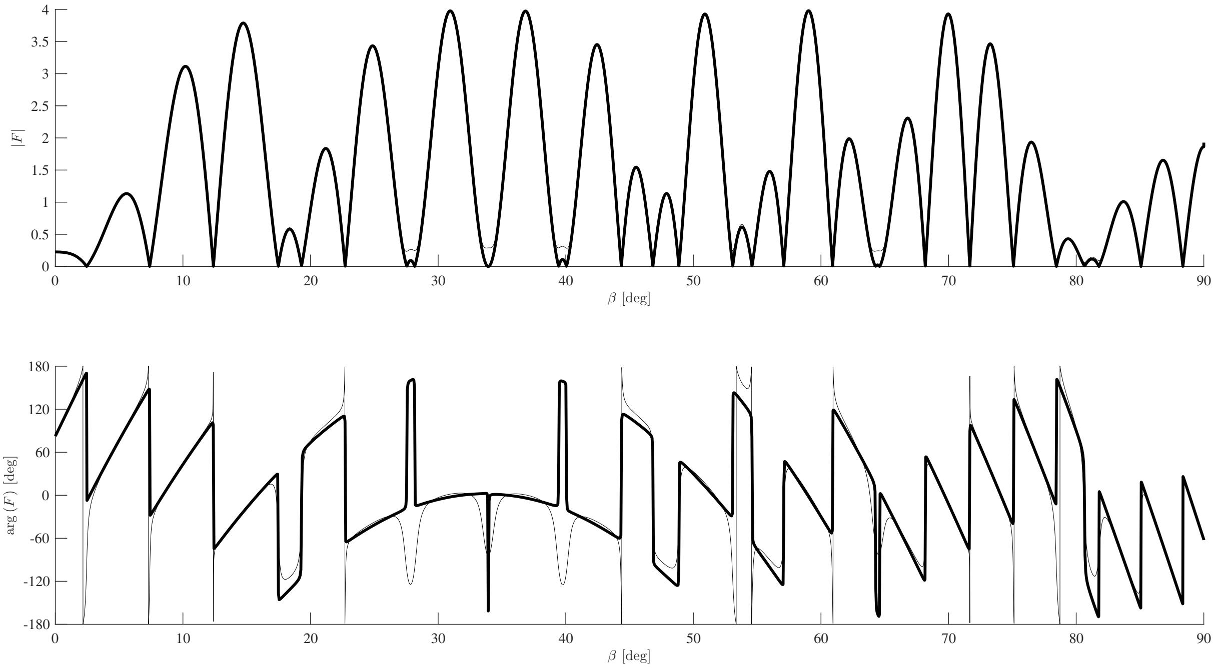

Figure 2.9: The same as figure 2.8 with the source at fixed distance, $s \approx 700.64\,\mathrm{m}$, and variable elevation, $0 \leq \beta \leq \pi/2\,\mathrm{rad}$, for the fixed frequency, $f = 1000\,\mathrm{Hz}$, showing the result of: (i) the exact multipath factor (2.12b) as thin line; (ii) the far field approximation (2.18a) as thick line.

figure, the source distance is fixed). That means that the frequency also strongly influences the phase of the multipath factor, in contrast with the source distance.

The conclusion that the multipath factor varies only slightly with the source distance does not hold for all the values, as shown in figure 2.8. When the source is close to the observer, the effects of varying the source distance are significant not only for the absolute value but also for the phase value of F, especially for higher frequencies, and the effects become negligible for frequencies above a given value.

The multipath factor can be calculated from (2.18a) using the equations (2.18b) to (2.18d) which: (i) holds for amplitude and phase specifically when the source is far away from the observer, that is, when $q^2 \lll s$; (ii) is valid for any value of the frequency and any value of the reflection coefficients of both surfaces; (iii) may fail at grazing incidences close to $\vartheta = 0$ and $\vartheta = \pi/2$ when some of the approximations, from (2.15a) to (2.17c), may cease to hold. Thus, the asymptotic approximation (2.18a) is more accurate for amplitude than for phase and should be used at intermediate elevations. As an alternative, substituting (2.1a) and (2.1b) in the exact expression (2.12b) specifies the multipath factor, correct to all orders of q and s, and valid in all directions, $0 \leq \vartheta \leq \pi/2$, including grazing directions. The figure 2.9 shows that both the amplitude (top) and phase (bottom) of the multipath factor are strongly affected by source direction, in contrast with source distance, which has little effect.

The figure 2.9 also shows the exact multipath factor (thin line) in comparison with the far field approximation (thick line). The far field approximation (2.18a) is extremely accurate for the amplitude (figure 2.9, top) since the thick line overlaps the thin line of the exact expression (2.12b) of the multipath factor. Concerning the phase (figure 2.9, bottom), the far field approximation (thick line) follows closely the exact theory (thin line) except for local peaks. The amplitude and phase of the multipath factor are shown for fixed frequency $f = 1\,\text{kHz}$ for all source directions in figure 2.9, and conversely over the audible range, $20 \leq f \leq 20000\,\text{Hz}$, for four source directions in figures A.3 to A.6 in the appendix A.2.

2.3 Main conclusions of the chapter 2

The amplification of amplitude of the signal is given by $10\log|F|$, which depends on the absolute value of the multipath factor $|F|$, whereas the amplification of power is equal to $10\log|F|^2$, dependent on the square of the absolute value $|F|^2$. The maximum amplification of a signal due to reflections from surfaces near the receiver is shown in the table 2.3 for N waves in phase, both for amplitude, $\text{dB} = 10\log N$, and for power, $\text{dB} = 20\log N$. The reception near an infinite plane (studied in more detail in chapter 3) consists of one direct and one reflected wave; if the two waves are in phase, the amplitude is doubled, $10\log 2 \approx 3\,\text{dB}$, and the power multiplied by four, $10\log 4 \approx 6\,\text{dB}$. In the case of an orthogonal corner formed by two infinite planes, the reception consists of: (i) a direct wave; (ii) two waves, each one reflected once on each plane; (iii) one wave reflected twice, once on each plane. There is a total of four waves, and if they are all in phase, the maximum amplitude is multiplied by four, $10\log 4 \approx 6\,\text{dB}$, and the power is multiplied by sixteen, $10\log 16 \approx 12\,\text{dB}$. This applies both in: (i) the two-dimensional case considered here with all waves in a plane perpendicular to the corner; (ii) the three-dimensional case with the incident and reflected waves in a plane oblique to the two-dimensional corner. In the case of a three-dimensional corner consisting of three orthogonal planes, the reception includes: (i) one direct wave; (ii) three waves, each one reflected once at one plane; (iii) three waves, each one reflected twice on a pair of planes; (iv) one wave reflected three times, that is, once on each plane. If all eight waves are in phase, the maximum amplitude is multiplied by eight, $10\log 8 \approx 9\,\text{dB}$, and the power is multiplied by sixty-four, $20\log 8 \approx 18\,\text{dB}$.

Receiver near a:	**plane**	**2-D corner**	**3-D corner**
Direct wave	1	1	1
Reflected once	1	2	3
Reflected twice	0	1	3
Reflected three times	0	0	1
Total number of waves N	2	4	8
Maximum amplification:			
– for amplitude: $\text{dB} = 10\log N$	3.01 dB	6.02 dB	9.03 dB
– for power: $\text{dB} = 20\log N$	6.02 dB	12.04 dB	18.06 dB

Table 2.3: Maximum amplification from wall reflections.

Suppose the ground is the only surface considered, without any other surfaces. In that case, the multipath factor is given by only the first two terms of (2.12b), while the addition of a vertical wall induces the sum of the last two terms of (2.12b) to the multipath factor. The figures 2.3 to 2.7 show five particular cases whose greatest and lowest changes in decibels are indicated in table 2.4. The decibels are $10\log_{10}|F|$ for the sound pressure level in figures 2.3 to 2.7 and $10\log_{10}|F|^2 = 20\log_{10}|F|$ for the sound power level (SPL). In table 2.4, ΔSPL is the difference of the SPL at the observer position between the cases of only direct wave received and direct wave plus reflected waves received by the observer. $\Delta\mathrm{SPL}_{\mathrm{ground}}$ is the change, in decibels, due to a wave reflected on the ground, $\Delta\mathrm{SPL}_{\mathrm{wall}}$ is the change, in decibels, due to a wave reflected on the wall and $\Delta\mathrm{SPL}_{\mathrm{ground+wall}}$ is the change, in decibels, due to the three reflected waves, as depicted in the figure 2.1. The maximum increase occurs when the ground and wall are both considered because, in that case, there are three "new" waves due to reflections on surfaces travelling to the observer position, besides the direct wave. The increase can reach approximately 12.04 dB if the two surfaces (ground plus wall) totally reflect the wave and if the observer is near the corner, but if it is considered only one surface, again one that totally reflects the wave, the increase can be, at maximum, 6.02 dB, justifying, therefore, the norms on noise measurement [11, 12].

					Maximum | Minimum		
Figure	x_{O} [m]	y_{O} [m]	R_{h}	R_{v}	$\Delta\mathrm{SPL}_{\mathrm{ground}}$ [dB]	$\Delta\mathrm{SPL}_{\mathrm{wall}}$ [dB]	$\Delta\mathrm{SPL}_{\mathrm{ground+wall}}$ [dB]
2.3	3	2	1	1	6.0195 | −72.1629	5.9835 | −41.3899	12.0023 | −86.1743
2.4	2	6	1	1	6.0174 | −62.6480	5.9958 | −44.8957	11.9992 | −69.3974
2.5	3	2	0.5	1	3.5211 | −6.0185	5.9835 | −41.3899	9.5039 | −96.2305
2.6	3	2	1	0.5	6.0195 | −72.1629	3.4971 | −5.9469	9.5159 | −57.3175
2.7	3	2	0.5	0.5	3.5211 | −6.0185	3.4971 | −5.9469	7.0175 | −15.2550

Table 2.4: Maximum increase or decrease of the sound power level (SPL), for a certain frequency, due to reflections on the ground and wall of the wave originated from the source at $(x_{\mathrm{S}}, y_{\mathrm{S}}) = (700, 30)$ m, for the cases of figures 2.3 to 2.7.

These maximum increases of power in decibels can occur for several frequencies. However, the figures 2.3 to 2.7 show that, for some frequencies, $|F|$ is less than 1 (for some frequencies, almost equal to 0) because of the destructive interference from the superposition of the waves, resulting in a decrease of decibels. The pressure reflection coefficient on the ground for spherical waves is $R_{\mathrm{h}} = |R_{\mathrm{h}}| \exp(\mathrm{i}\phi)$, where ϕ represents the phase change on reflection. In the cases of figures 2.3 to 2.7, ϕ is equal to 0, usually set for an acoustically hard boundary [28] (the same was used for the reflection coefficient of the vertical wall). Consequently, the phase difference between a direct wave and a reflected wave is caused only by the path length difference of the waves, that have the same frequency. Since the path difference always exists (except for the case $\alpha = \beta$), there is always some destructive interference. Therefore it is not possible to reach the maximum theoretical value of SPL when adding two or more waves (the worst case scenario when adding two waves with the same frequency would be if they also have the same phase). The increase or decrease of power in decibels depends on the reflection coefficients and the observer position, despite being more influenced by the former. The results of the table 2.4 are valid for one single wave originating from the source with one frequency. The sound spectrum can consist of a superposition of several harmonics of distinct frequencies, leading, therefore, to a more significant increase of power in decibels at the same observer position.

A three-dimensional plot for each of the modulus $|F|$ and phase $\arg(F)$ of the multipath factor as a function of the observer coordinates x_{O} and y_{O} would be difficult to visualise due to a large number of closely spaced peaks and nulls and to the wide range of values. A better way to visualise the modulus and phase of the multipath factor is to plot the isolines of $|F|$ and $\arg(F)$, that are closed curves where the function has a constant value, knowing at first the values of 1000×1000 different coordinates uniformly spaced in the 2D region. The figure 2.10 shows the isolines for four different values of the modulus of F: 0, 4, 8 and 11 decibels (there are also regions with 12 decibels, however it would be hard to visualise them). The walls are rigid, $R_\mathrm{h} = R_\mathrm{v} = 1$, the source point is at the coordinates $(700, 30)$ m, that is, at the upper right corner in each plot, and the selected frequency is $f \approx 2003.9\,\mathrm{Hz}$, equal to the frequency of the first line in table 2.4, corresponding therefore to the worst case scenario when the observer is at the coordinates $(3, 2)$ m with the same remaining conditions. In figure 2.10, the axis x and y stand for the distances to the vertical and horizontal walls, respectively, and not to the source position. There are many more points (for example, more 337410 points forming more 5540 isolines between the first and last plots in figure 2.10) where the presence of walls does not change the modulus of F (resulting in isolines of $0\,\mathrm{dB}$) than the points where there is an increase of $11\,\mathrm{dB}$. The isolines of $0\,\mathrm{dB}$ are plotted in the whole 2D region, however the isolines of $11\,\mathrm{dB}$ exist only in the area near the vertical wall, specifically near the corner. Near the corner, both the reflected wave on the wall and the reflected wave on the ground travel approximately the same distance as the direct wave, mathematically, $r_{11} + r_{12} \approx r$ and $r_{21} + r_{22} \approx r$ (moreover, near the corner, the reflected distances r_{12} and r_{22} are much smaller than the distances r_{11} and r_{21}, with the reflected distances being almost 0). Furthermore, the distance travelled by the wave that impinges on both surfaces is also almost equal to the distance travelled by the direct wave, $r_{31} + r_{32} + r_{33} \approx r$. Since the ray distances of the three waves are almost equal to each other (that do not happen far away from the corner), the three waves, which have the same frequency, are almost in phase, leading to an almost total constructive interference. Consequently, near the corner, the total acoustic pressure is almost four times the acoustic pressure due only to the direct wave and the multipath factor is almost four leading to an increase slightly less than $12\,\mathrm{dB}$. The same applies to the phase of the multipath factor, as depicted in the figure 2.11, where the points for lower phase values are much more numerous (for example, more 252361 points forming more 10475 isolines between the cases of 40 and 160 degrees in figure 2.11) than the points for greater phase values. The isolines for large phase values, for instance, 160 degrees, are plotted not only near the corner, as it happens with the modulus (fourth plot of figure 2.10), but also for regions far away from the corner. This means that being near a corner influences more the modulus of the multipath factor than its phase. The figures 2.12 and 2.13 show the isolines of the modulus and the phase respectively of the multipath factor F, but for lower values of the reflection coefficients of both walls, specifically $R_\mathrm{h} = R_\mathrm{v} = 0.5$. The frequency is the same, $f \approx 2003.9\,\mathrm{Hz}$, because that value also corresponds to the fifth line of table 2.4, leading to the worst-case scenario when the observer is at the position $(3, 2)$ m. The remarks are the same; the only difference is that in this case, the maximum values of the modulus and phase of F are not as much increased as for the maximum values when the reflection coefficients of both walls are equal to unity, as depicted in the figures 2.10 and 2.11. The plots of the phase in figures 2.11 and 2.13 show the isolines only for positive values; the plots would be practically the same if the isolines were drawn for the negative phases.

The present theory assumes perfectly flat walls. Real walls are rough, and if the average height of irregularities is ε, the walls may be considered smooth if the wavelength λ is much larger, $\lambda \gg \varepsilon$.

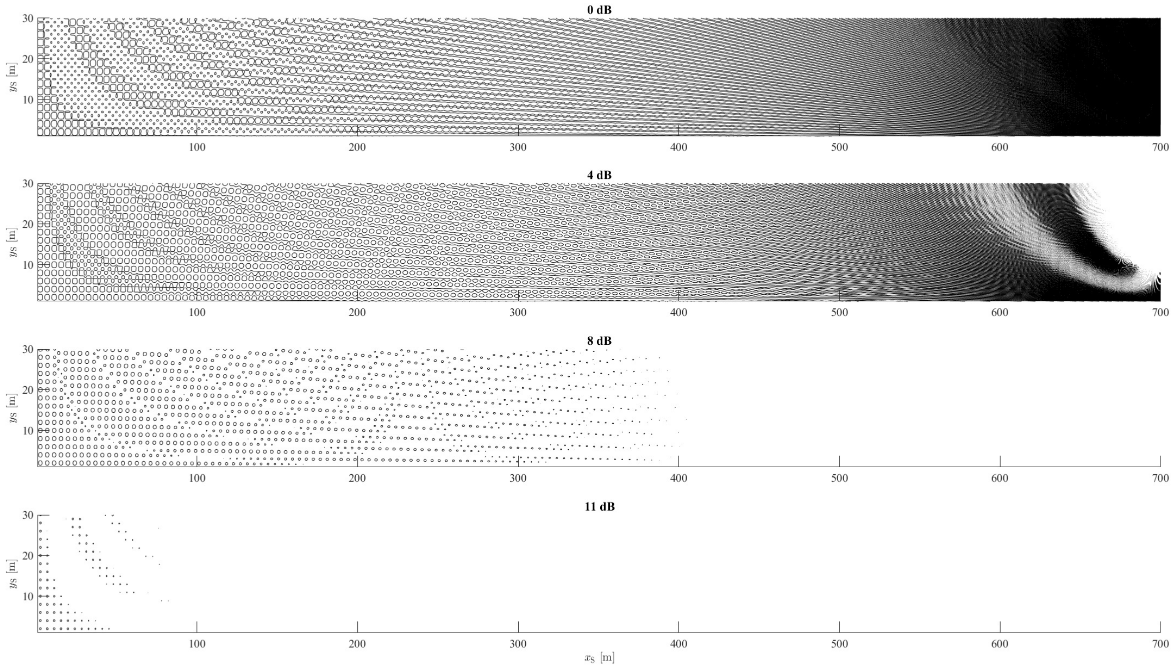

Figure 2.10: Map of the modulus of the multipath factor F as a function of observer position in the plane for a fixed source position at the upper right corner in each plot, for rigid walls, $R_\mathrm{h} = R_\mathrm{v} = 1$ and for the frequency $f \approx 2003.9\,\mathrm{Hz}$. The variables x and y in the axis labels stand for the distances to the vertical and horizontal walls respectively.

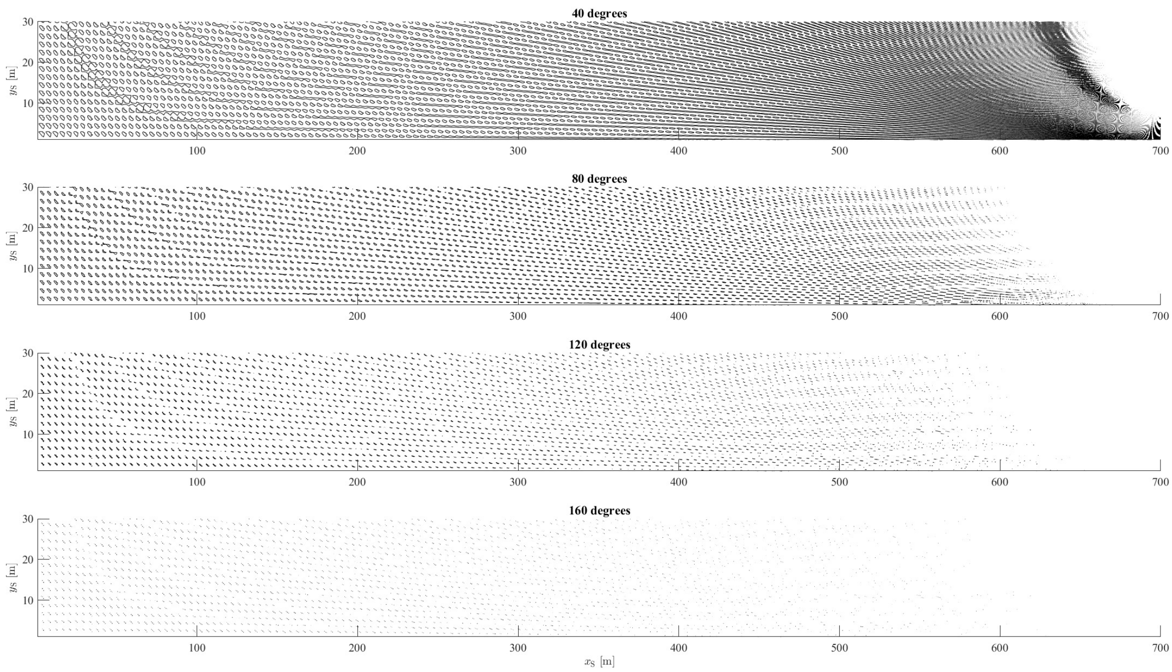

Figure 2.11: Map of the phase of the multipath factor F as a function of observer position for the same conditions as in the figure 2.10.

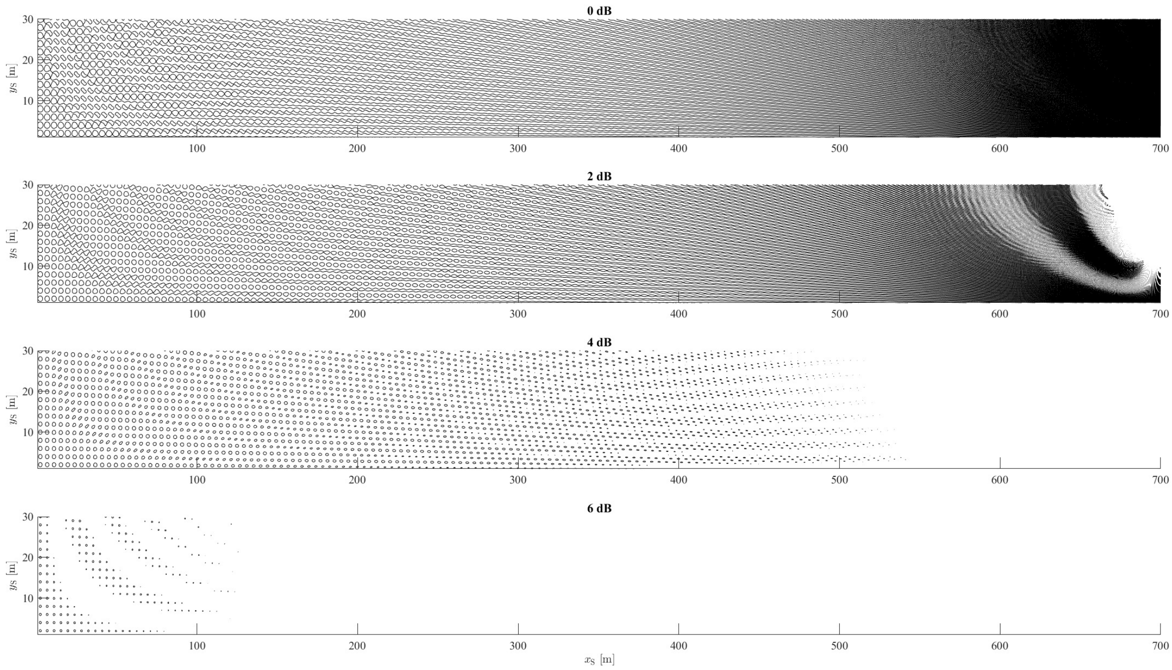

Figure 2.12: The same as figure 2.10, but for semi-rigid walls, $R_{\mathrm{h}} = R_{\mathrm{v}} = 0.5$.

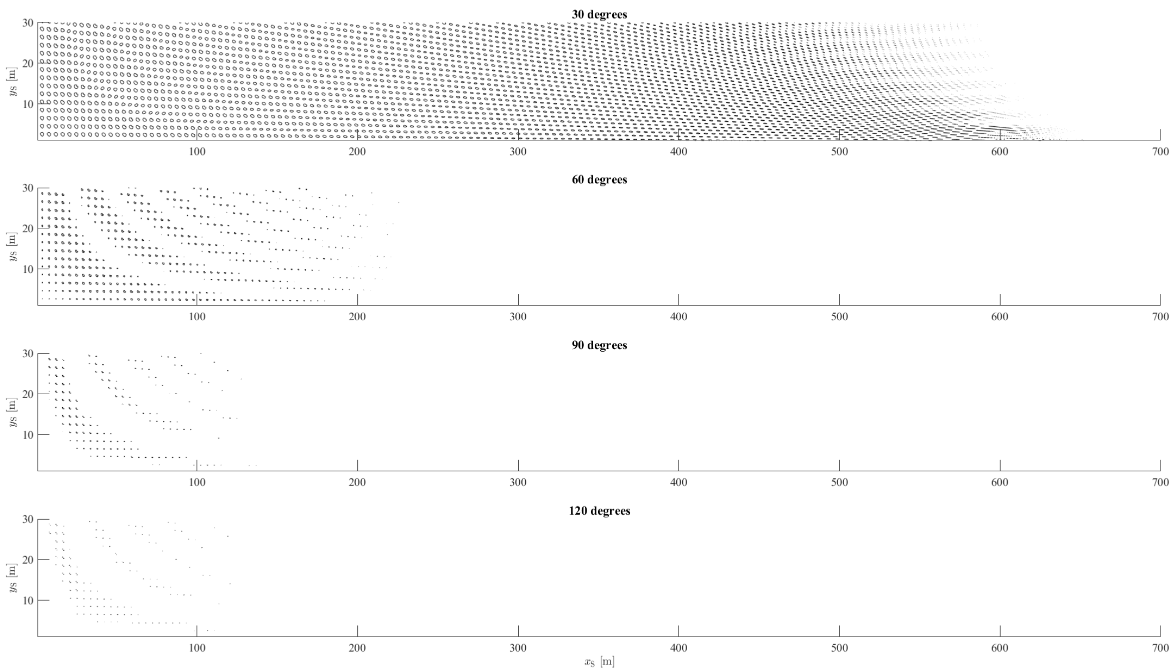

Figure 2.13: The same as figure 2.11, but for semi-rigid walls, $R_{\mathrm{h}} = R_{\mathrm{v}} = 0.5$.

Considering audible frequency range from 20 Hz to 20 kHz,

$$f = 2 \times 10\,\mathrm{s}^{-1} - 2 \times 10^4\,\mathrm{s}^{-1}, \tag{2.21a}$$

for sound propagation in the atmosphere at sea level with the sound speed $c \approx 340\,\mathrm{ms}^{-1}$, the wavelength is

$$\varepsilon \ll \lambda = \frac{c}{f} \approx 1.7 \times 10^{-2}\,\mathrm{m} - 17\,\mathrm{m} \tag{2.21b}$$

and the wall may be considered smooth if the average roughness ε is much smaller than the smallest wavelength $\lambda_{\min} \approx 1.7\,\mathrm{cm}$, say $\varepsilon < 2\,\mathrm{mm}$. The theory applies to acoustic and other waves, for example electromagnetic waves, always in terms of wavelength, not frequency. The same range of wavelengths,

$$1.7 \times 10^{-2}\,\mathrm{m} < \lambda < 1.7\,\mathrm{m}, \tag{2.22a}$$

for electromagnetic waves propagating at the speed of light $c_0 \approx 3 \times 10^8\,\mathrm{ms}^{-1}$, that is much higher than the sound speed $c \approx 340\,\mathrm{ms}^{-1}$, leads to much higher frequencies,

$$f = \frac{c_0}{\lambda} \approx 1.76 \times 10^8\,\mathrm{Hz} - 1.76 \times 10^{11}\,\mathrm{Hz} = 17.6\,\mathrm{Mhz} - 17.6\,\mathrm{GHz}. \tag{2.22b}$$

Thus, for the same average surface roughness $\varepsilon = 2\,\mathrm{mm}$, the present theory applies to electromagnetic waves in the range of frequencies (2.22b) spanning the high frequencies indicated in the table 2.5. The theory also applies to lower bands of electromagnetic waves with longer wavelengths, spanning the medium and low frequencies, also indicated in the table 2.5. The theory could not apply, unless the roughness was smaller, to higher frequencies and shorter wavelengths, for instance, to the frequencies indicated in the table 2.6.

Name	**Initials**	**Frequency band**
Super High Frequencies	SHF	3 GHz – 30 GHz
Ultra High Frequencies	UHF	300 MHz – 3 GHz
Very High Frequencies	VHF	30 MHz – 300 MHz
High Frequencies	HF	3 MHz – 30 MHz
Medium Frequencies	MF	300 kHz – 3 MHz
Low Frequencies	LF	30 kHz – 300 kHz
Very Low Frequencies	VLF	3 kHz – 30 kHz
Ultra Low Frequencies	ULF	300 Hz – 3 kHz
Super Low Frequencies	SLF	30 Hz – 300 Hz
Extremely Low Frequencies	ELF	3 Hz – 30 Hz

Table 2.5: Ranges of frequencies in which the theory in this chapter can be applied.

The contour plots in figures 2.10 to 2.13 assume a frequency $f \approx 2003.9\,\mathrm{Hz}$ corresponding to sound waves with wavelength $\lambda \approx 340/2003.9\,\mathrm{m} \approx 0.170\,\mathrm{m}$. They also apply to other waves with the same wavelength, for example, electromagnetic waves with frequency $f \approx 3 \times 10^8/1.7\,\mathrm{Hz} \approx 17.6\,\mathrm{MHz}$ in

Name	Initials	Frequency band
Extremely High Frequencies	EHF	30 GHz – 300 GHz
Far Infra-Red	FIR	300 GHz – 3 THz
Mid Infra-Red	MIR	3 THz – 30 THz
Near Infra-Red	NIR	30 THz – 300 THz
Visible and Ultraviolet	UV	300 THz – 30 PHz
Soft X-rays	SX	30 PHz – 3 EHz
Hard X-rays	HX	3 EHz – 30 EHz
Gamma rays	γ	30 EHz – 300 EHz

Table 2.6: Ranges of frequencies in which the theory in this chapter cannot be applied.

the HF band. Although the theory applies equally well to electromagnetic waves [24–26], this chapter concentrates on the acoustic literature for brevity. The theory is directly applicable to noise mapping in urban environments [8–15] due to surface transport and aircraft. In the latter case of aircraft, the effects of atmospheric propagation have to be considered [16, 17]. A spherical wave incident on a plane gives rise to a reflected wave considered here, and a surface lateral wave [20, 28–32], that has been neglected here as a smaller second-order effect away from the wall. Here, the simplest approach was chosen based on the superposition of spherical waves in general acoustics [19–23, 27]. The present approach demonstrates that the interference of reflected spherical waves together with the direct wave can lead to amplitudes much smaller than the maximum and complex interference patterns. The results are presented for the whole audible range of monochromatic frequencies and can be superimposed via a Fourier integral to any spectrum of the incident signal. The walls may be considered smooth for wavelengths much larger than the surface roughness. For example, suppose the surface roughness does not exceed a few millimetres. In that case, the theory applies to the whole audible acoustic spectrum and to electromagnetic waves in the ultra-high frequency (UHF) band and below.

The theory in the general forum presented allows for different reflection factors from each wall. The calculation of reflection factors is a significant subject in its own right, briefly reviewed in appendix A.3.

3 | Effects of rough ground and atmospheric absorption on aircraft noise

"There are only two kinds of certain knowledge: awareness of our own existence and the truths of mathematics."

— Jean le Rond d'Alembert

Contents

The aircraft noise is a significant environmental issue for residents near airports. It has been a major topic in the literature from the last century [33] to the present [34]. The aircraft noise can lead to: (i) curfews, limiting the operating hours of airports, such as forbidding night flights; (ii) local noise limits, which may be more restrictive than the ICAO certification rules, and thus limiting the take-off weight and hence payload-range with an adverse effect on operating economics. The helicopter noise is the main limitation in their use over urban and populated areas, affecting medical emergencies, law enforcement, city centre business travel and other services. The emerging market for UAM (Urban Air Mobility) using e-VTOL (electric powered Vertical Take-Off and Landing) aircraft is subject to noise limitations similar to helicopters. The decreasing tolerance of local communities to aircraft and helicopter noise stands in contrast to the long-term growth of long range and local air transport.

The two main aspects of aircraft noise are: (i) atmospheric propagation [17, 35–37] including the effects of stratification leading to not only non-uniform sound speed, but also convection and refraction by wind and turbulence; (ii) ground effects considered in most of the literature [16, 20, 29–32, 38] by a source and its image on a flat impedance ground, including the lateral wave. Ground effects on sound can be more complex: (i) the presence of obstacles like buildings and other constructions leads to corner reflections [39] with three reflected waves instead of one from flat ground, in addition to the direct wave from the sound source, as explained in chapter 2; (ii) the current methods of calculation of noise contours around airports [40, 41] are based on models of sound propagation over flat ground [42–44], and do not account for the variable elevations of rough ground that may surround the airport. The main aim of the present chapter is to consider sound reflection over a rough ground using a wave reflection method distinct from the image source method, as shown in the figure 3.1. These two differences from the usual approach in the literature are discussed briefly next and in more detail in the section 3.6.

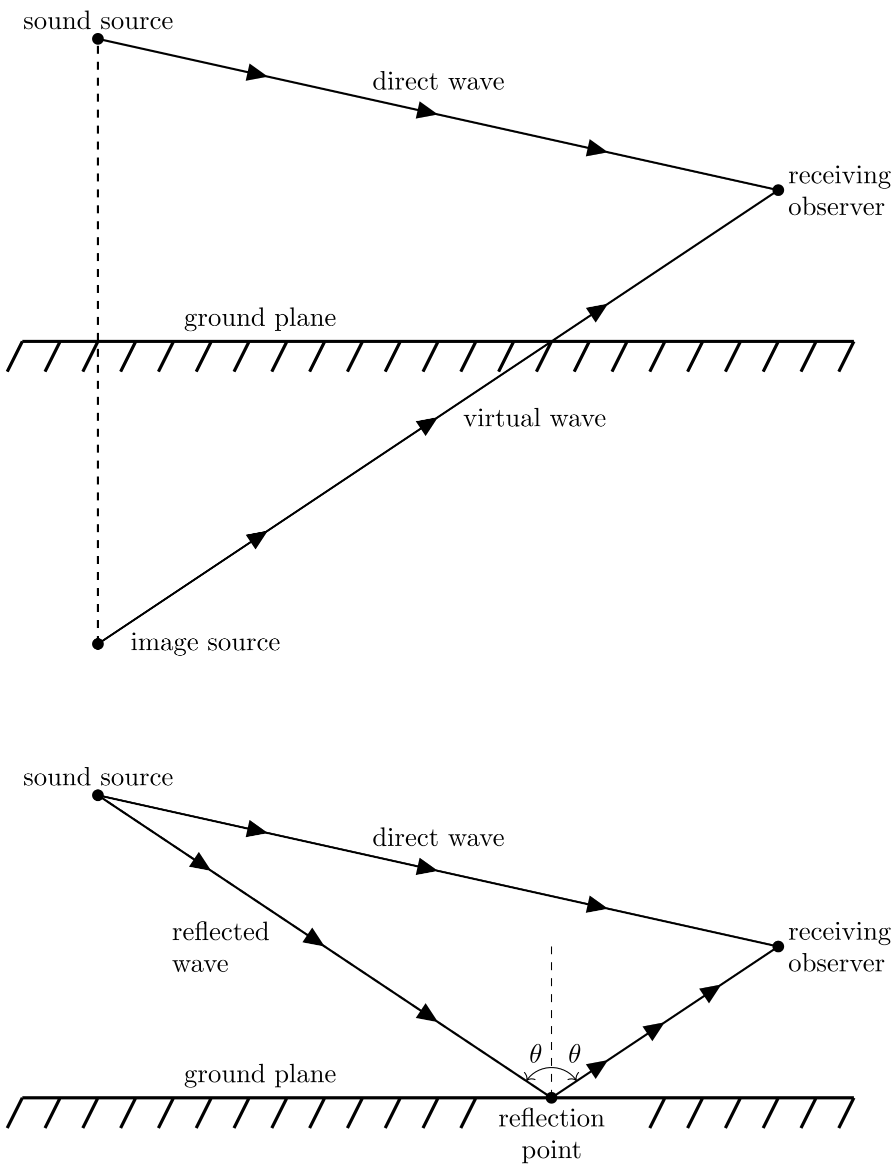

Figure 3.1: Comparison of (I) the method of image (top) and (II) the method of reflection (bottom) for a point sound source above a plane. In both cases, there is a direct wave from the sound source to the receiving observer, as in free space. The ground effect is represented: (I) in the image method by adding a virtual wave from the image source to the receiving observer so as to satisfy the acoustic boundary condition on the ground plane; (II) in the reflection method by adding a reflected wave making an equal angle θ of incidence and reflection relative to the normal at the reflection point, with a complex reflection coefficient accounting for amplitude and phase changes.

The effect of flat ground on the sound emitted by a real sound source can be represented by a virtual image source emitting a virtual wave to the observer. The sum of the direct and virtual waves satisfies the boundary condition on the ground. Instead of a virtual source and closer to physical reality, the ground effect is equivalent to adding to the direct wave from the source to the observer another wave reflected from the ground. This method is simple and quite general since the reflection coefficient on the ground can be complex, introducing both amplitude and phase changes in the reflected wave. This method has been applied to sound reflection near a corner in chapter 2 involving three reflected waves. An alternative would have been to use three images [39] in the corner. The method of images does not extend easily to reflection by a rough ground since it could require several images and the determination of their strength and location. The method of reflection extends readily from flat to rough ground by: (i) determining geometrically all reflection points; (ii) applying the complex reflection coefficient, including amplitude and phase, at each point; (iii) adding all waves that are not blocked by the terrain and that can be radiated towards the observer. The latter effect of wave blockage by terrain elevation is not present for flat ground.

In addition to sound reflection from rough ground, the effect of atmospheric absorption is also considered. Concerning ground reflection, starting with the most straightforward cases for reference is convenient as more effects are added. In the case of a point sound source over flat ground, there is: (i) a direct wave from the source to the observer; (ii) a wave with an intermediate reflection on the ground. Since the original and reflected waves travel in the same medium, and consequently the frequency of both waves is the same, the resultant sound pressure level depends on the phase difference between the two sound waves. Thus, the worst-case scenario happens when they are in phase, duplicating the total amplitude and increasing $20\log_{10} 2 \approx 6.02\,\mathrm{dB}$ for the power. If the waves are out-of-phase, there is less amplification and they can even cancel each other out when they have exactly opposite phases. Furthermore, if the ground does not perfectly reflect the wave, then the existence of a reflected wave reduces the total amplitude perceived by the observer. The present chapter studies, in two-dimensional cases, the interference between the direct and reflected waves, resulting in the amplification, attenuation or cancellation. The interference depends on the frequency and positions of the source and receiver, specifically addressing the effects on the aircraft noise that result from the sound reflection on the irregular ground and from the atmospheric absorption.

The baseline model I, as sketched in the figure 3.2, uses a single reflection point over flat ground and relies on the following assumptions, as in chapter 2: (i) isotropic, point source of sound emitting spherical waves (valid if the distance of observer is large relative to the helicopter or aircraft size); (ii) static source (neglects Doppler effects for aircraft speed small relative to the sound speed); (iii) flat, horizontal ground (excludes mountainous ground and obstacles, hence there are no multipath effects with multiple reflections or multiple scattering); (iv) homogeneous atmosphere (neglects density and temperature variations, or sound speed stratification, hence no refraction effects); (v) atmosphere at rest (no wind or mean flow convection or turbulence effects on sound); (vi) uniform ground impedance (same ground composition everywhere all the time, excluding different soils, humidity, changes during the day, etc.).

This simplest baseline model I serves as a reference for two extensions that relax some of its restrictions to include: (i) non-flat ground considering multiple paths in the model II; (ii) atmospheric absorption in the case of flat ground extending the model I to the model III. The application of all three models depends on the calculation of reflection points, which is done for: (i) reflection from a flat ground, applicable to the models I and III; (ii) reflection from a two-dimensional slice of ground, applicable to the model II. For each of these models, formulas for the sound power level (SPL) variation and the phase shift of acoustic pressure are presented.

As examples of the applications from this set of three models, two cases are considered: (i) flat impedance ground using the model I or the model III; (ii) rigid undulating ground using the model II. The general theory for the three models and two applications substantiate some conclusions.

3.1 Baseline model I of reflection by flat ground

The baseline model I relies on the assumption indicated in the introduction of this chapter. The figure 3.2 shows the source-observer coordinate system: (i) the x-axis is horizontal and the z-axis is vertical in the vertical plane passing through the source S and observer O; (ii) the y-axis forms a right-handed triad and the origin is any point on the intersection of the vertical plane with the ground. For definiteness, the origin may be taken on the ground, for instance in the vertical through the observer, in the case where $x_{\mathrm{O}} = 0$ (the general case is shown in the figure 3.2). The section 3.5 will prove that only the horizontal distance between the observer and source matters and not the explicit values of both horizontal coordinates.

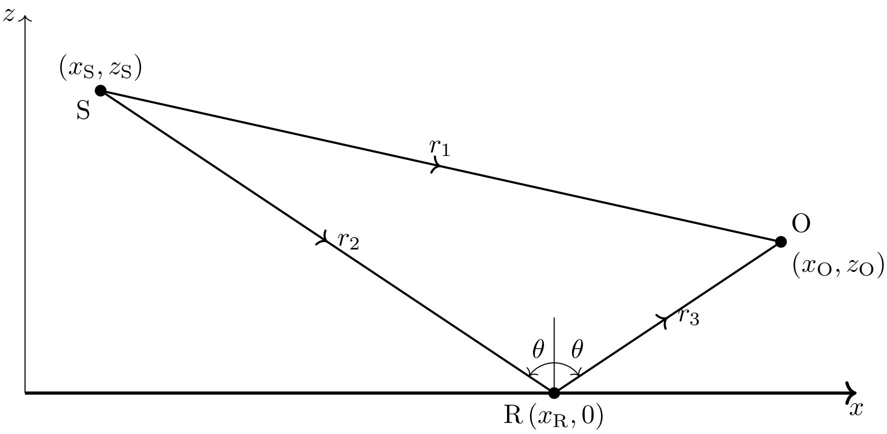

Figure 3.2: Direct and reflected sound paths for source S and observer O at arbitrary positions over a flat ground.

The problem of several paths of propagation and interferences can be applied to all waves, in this chapter particularly to acoustic waves. The figure 3.2 illustrates the two-dimensional case of propagation of acoustic waves, where it is shown that the observer (or monitoring device) receives two signals: (i) one direct signal from the source; (ii) one signal reflected from the ground. Following a purely geometric methodology, it is necessary to determine the position of the reflection point to calculate the length of all the ray paths, making use of the Snell's law of specular reflection: the angle between the normal to the surface and incident wave must be equal to the angle between the same normal and reflected wave.

Finally, knowing the value of the reflection coefficient at the reflection point, the total received signal can be specified and then it can be normalised with the direct wave, specifying the modification factors, generally complex numbers, due to multipath effects.

Using the vertical plane through the source and observer, in other words the line-of-sight plane, the focus is on the two-dimensional problem of wave propagation from a source S to an observer O near a horizontal ground $z = 0$ taken as an axis of a Cartesian reference with the origin at some point on the ground and in such a way that the coordinates of the observer are $(x_\mathrm{O}, z_\mathrm{O})$ and the coordinates of the source are $(x_\mathrm{S}, z_\mathrm{S})$. The direct received acoustic pressure is

$$p_0 = \frac{\mathrm{e}^{\mathrm{i}kr_1}}{r_1} \tag{3.1}$$

where a complex constant amplitude and a frequency factor $\exp(\mathrm{i}\omega t)$ are omitted, whereas r_1 is the distance from the observer to the source:

$$r_1 = \left[(x_\mathrm{O} - x_\mathrm{S})^2 + (z_\mathrm{O} - z_\mathrm{S})^2 \right]^{1/2}. \tag{3.2}$$

The equation (3.1) is an harmonic solution of the linearised wave equation assuming that the pressure perturbation is radial and propagates spherically outward from the source. The wave equation assumes that the sound is a weak motion of an inviscid fluid since the viscosity for the sound field in air at the most audible frequencies is negligible, neglecting thermal conduction and noting that the air before perturbed by acoustic waves is at rest. Because the acoustic waves induce small perturbations in the medium, the wave equation can be linearised. The physical meaning can be given by the real part of (3.1).

The line-of-sight reflection occurs at the reflection point R with coordinates $(x_\mathrm{R}, 0)$, such that the angles of incidence and reflection θ are the same,

$$\frac{x_\mathrm{O} - x_\mathrm{R}}{z_\mathrm{O}} = \tan\theta = \frac{x_\mathrm{R} - x_\mathrm{S}}{z_\mathrm{S}}. \tag{3.3a}$$

This can be solved for x_R,

$$x_\mathrm{R} = \frac{x_\mathrm{O} z_\mathrm{S} + x_\mathrm{S} z_\mathrm{O}}{z_\mathrm{O} + z_\mathrm{S}}, \tag{3.3b}$$

to specify the position of the point-of-reflection. The sound field reflected in line-of-sight,

$$p_\mathrm{r} = \mathcal{R}\frac{\mathrm{e}^{\mathrm{i}k(r_2+r_3)}}{r_2 + r_3}, \tag{3.4}$$

consists of: (i) a spherical wave travelling from the sound source to the reflection point at a distance

$$r_2 = \left[(x_\mathrm{S} - x_\mathrm{R})^2 + z_\mathrm{S}^2 \right]^{1/2} \tag{3.5}$$

and from the reflection point to the observer at a distance

$$r_3 = \left[(x_\mathrm{O} - x_\mathrm{R})^2 + z_\mathrm{O}^2 \right]^{1/2}; \tag{3.6}$$

(ii) a complex reflection coefficient of the ground, which can have a modulus $|\mathcal{R}| \leq 1$ and a phase angle $\arg(\mathcal{R})$, and depends on ground properties. Again, (3.4) is an harmonic solution of the linearised wave equation where the physical solution can be given by its real part. This solution is modified by the complex reflection factor $\mathcal{R}$ at the reflection point. The lateral wave resulting from the reflection of a spherical wave with a flat ground [20, 29–32] is neglected, since it is a surface wave that decays away from the ground.

As the presence of an acoustic wave is a small perturbation, the product of two perturbations are neglected and the laws describing the propagation are linear. Consequently, the interaction between the reflected and direct waves is negligible and the total acoustic field is a result of superposition method, summing the results of both waves. Hence, the total acoustic pressure perturbation,

$$p_{\mathrm{I}} = p_0 + p_{\mathrm{r}} = \frac{\mathrm{e}^{\mathrm{i}kr_1}}{r_1} + \mathcal{R}\frac{\mathrm{e}^{\mathrm{i}k(r_2+r_3)}}{r_2+r_3}, \tag{3.7}$$

is the sum of the direct (3.1) and reflected (3.4) acoustic pressure perturbations. The last expression can be compared with the equation (2.3) of total acoustic pressure perturbation in the case of propagation near a corner, and observing that the equation (3.7) corresponds to the first two terms of the equation (2.3) since they are related to the propagation of the direct wave and the reflected wave on the ground.

The total signal (3.7) normalised to the direct signal (3.1) is called the multipath factor since it specifies the amplitude and phase changes due to the presence of a reflected wave. Since it is defined as the ratio between two complex acoustic pressure perturbations, assuming that they are harmonic solutions of the linearised outward spherical wave equation, centred from the source, the multipath factor is also generally complex; the modulus and phase of the multipath factor specify respectively the amplitude and phase changes of the received signal that can be analysed separately. The SPL change in the equation (3.8c) and the phase change in the equation (3.9b) of the acoustic pressure perturbation are valid for arbitrary reflection factor $\mathcal{R}$, which may involve an amplitude $|\mathcal{R}|$ and a phase $\arg(\mathcal{R})$. The effect of the ground reflection on the acoustic energy of the free acoustic field corresponds to the complex magnitude of the multipath factor,

$$E_{\mathrm{I}} \equiv \left|\frac{p_{\mathrm{I}}}{p_0}\right|^2 = \left|1 + \frac{p_{\mathrm{r}}}{p_0}\right|^2, \tag{3.8a}$$

and in the present case is

$$E_{\mathrm{I}} = \left|1 + \frac{r_1}{r_2+r_3}\mathcal{R}\mathrm{e}^{\mathrm{i}k(r_2+r_3-r_1)}\right|^2. \tag{3.8b}$$

This corresponds to a change in SPL for power in a decibel (dB) scale

$$A_{\mathrm{I}} \equiv 10\log E_{\mathrm{I}} = 10\log\left\{1 + \left(\frac{r_1}{r_2+r_3}\right)^2 |\mathcal{R}|^2 + \frac{2r_1|\mathcal{R}|}{r_2+r_3}\cos\left[k\left(r_2+r_3-r_1\right) + \arg(\mathcal{R})\right]\right\}. \tag{3.8c}$$

The amplitude change depends on all the three ray distances and on the reflection coefficient (not only its modulus, but also its phase). It is also dependent on the frequency of the acoustic waves. In the particular case when the receiver is near the ground, that is when the points O and R nearly coincide, the distance travelled by the reflected wave is the same as the distance travelled by the direct wave, $r_1 = r_2 + r_3$. In that case, $p_r = \mathcal{R} p_0$ or equivalently $p_I = (1+\mathcal{R})\, p_0$. The reflected wave changes the acoustic pressure perturbation by the factor $1+\mathcal{R}$ and changes the SPL in decibels by $10 \log \left\{ 1 + |\mathcal{R}|^2 + 2\, |\mathcal{R}| \cos\left[\arg(\mathcal{R})\right] \right\}$. If both waves travel the same distance, the multipath factor does not depend on the frequency. If the phase of the wave does not change when it impinges on the ground, $\arg(\mathcal{R}) = 0$, usually set for an acoustically hard boundary, the change of SPL reduces to $20 \log \{1 + |\mathcal{R}|\}$, and moreover if the boundary totally reflects the wave, $|\mathcal{R}| = 1$, the total acoustic pressure perturbation is doubled leading to the increase of 6.02 dB. Indeed, in that particularly case, when the ground does not change neither the phase wave nor the modulus of the wave and the distance travelled by both waves is the same, the observer receives two waves with the same frequency, the same amplitude and the same phase. The phase of the acoustic pressure perturbation has a variation

$$\Phi_I \equiv \arg(p_I) - \arg(p_0) = \arg\left(\frac{p_I}{p_0}\right) = \operatorname{arccot}\left[\frac{\operatorname{Re}(p_I/p_0)}{\operatorname{Im}(p_I/p_0)}\right] \tag{3.9a}$$

and is given in the case (3.8c) by

$$\Phi_I = \operatorname{arccot}\left\{ \cot\left[k(r_2+r_3-r_1) + \arg(\mathcal{R})\right] + \left(\frac{r_2+r_3}{r_1\, |\mathcal{R}|}\right) \csc\left[k(r_2+r_3-r_1) + \arg(\mathcal{R})\right] \right\}. \tag{3.9b}$$

The phase change also depends on all the three distances, on the modulus and argument of the reflection factor, and on the frequency of the waves. In the particular case of the receiver near the ground, when $r_1 \approx r_2 + r_3$, and moreover when the ground does not change the phase of the wave, $\arg(\mathcal{R}) \approx 0$, there is not any phase change due to the presence of the reflected wave, $\Phi_I \approx 0$.

3.2 Model II for multiple paths in mountainous terrain

The extension to non-flat ground (figure 3.3) requires knowledge of the terrain profile $z = h(x)$ in the plane of the line-of-sight.

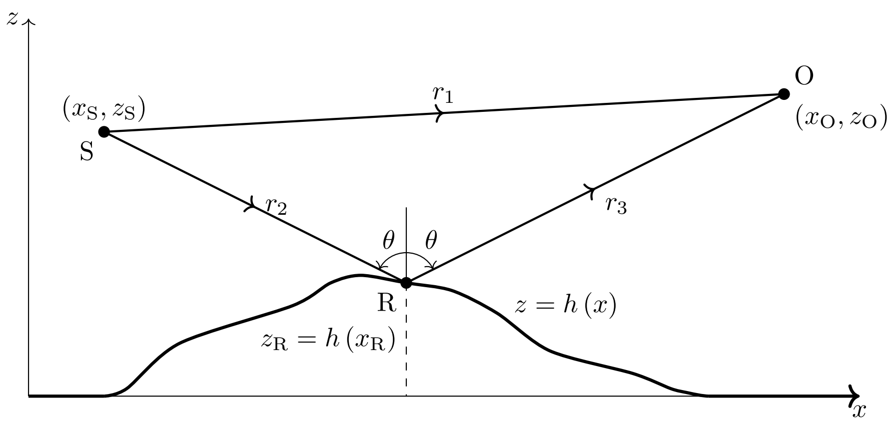

Figure 3.3: As in figure 3.2 over rough ground with a given altitude profile in two dimensions.

Regarding one wave which reflect on the ground and reaches the observer's position, the formulas for reflected (3.4) and hence for total (3.7) acoustic pressure, due to one wave originated from the source, can also be used in the model II. In this model, the pressure perturbation represents again a wave with outward spherical propagation centred at the source and depends only on the radial distance and the frequency. Therefore, the harmonic solutions (3.4) and (3.7), using the principle of superposition, remain valid as solutions of the linearised wave equation, deduced from the same assumptions, and do not depend on terrain profile.

Although the distance r_1 remains valid in the model II, the ray distances r_2 and r_3 that also appear in the previously mentioned equations cannot be calculated in the same way than in the model I because those expressions consider the terrain profile depicted in the figure 3.2, valid only if the ground is flat. To calculate the two ray distances (3.5) and (3.6), the coordinates of the reflection point are necessary. The difference from the case of flat ground is that the location of the reflection point is no longer given by the equations (3.3a) or (3.3b), because the reflection point is no longer at zero height:

$$R \mapsto [x_\mathrm{R}, h(x_\mathrm{R})]. \tag{3.10}$$

Thus, the condition (3.3a) is replaced (figure 3.3) by

$$\frac{z_\mathrm{O} - h(x_\mathrm{R})}{x_\mathrm{O} - x_\mathrm{R}} = \cot\theta = \frac{z_\mathrm{S} - h(x_\mathrm{R})}{x_\mathrm{R} - x_\mathrm{S}} \tag{3.11a}$$

that states again the equality of angles of incidence and reflection asserted by the Snell's law of specular reflection. In (3.11a), the terms dependent on the reflection point x_R are separated on right-hand side:

$$\frac{x_\mathrm{O} z_\mathrm{S} + x_\mathrm{S} z_\mathrm{O}}{z_\mathrm{O} + z_\mathrm{S}} = x_\mathrm{R} + \frac{x_\mathrm{O} + x_\mathrm{S} - 2x_\mathrm{R}}{z_\mathrm{O} + z_\mathrm{S}} h(x_\mathrm{R}). \tag{3.11b}$$

Given the source S at coordinates $(x_\mathrm{S}, z_\mathrm{S})$ and observer O at coordinates $(x_\mathrm{O}, z_\mathrm{O})$, the solutions of the equation (3.11b) for x_R give the reflection point(s) in the plane of line-of-sight. For flat ground, $h(x_\mathrm{R}) = 0$, there is only one solution, given explicitly by (3.3b). For rough ground there may be several x_{R_j} reflection points R_j, with $j = 1, \ldots, M$, depending on the terrain profile $z = h(x)$. Then, by knowing the coordinates of the reflection point(s), the ray distances r_{2_j} from source S to reflection point R_j and r_{3_j} from reflection point R_j to observer O can be calculated for each reflection point in the same way than in the equations (3.5) and (3.6), but substituting z_S and z_O respectively by $z_\mathrm{S} - h\left(x_{\mathrm{R}_j}\right)$ and $z_\mathrm{O} - h\left(x_{\mathrm{R}_j}\right)$ because in this model the coordinates of the reflection points are now given by (3.10). However, the equation (3.11b) is not the most accurate to determine the coordinates of reflection points in such a way that the wave, after the reflection on the ground, reaches the observer's position. The equality of the angles in (3.11a) was made regarding the geometric characteristics of the figure 3.3 and with the application of Snell's law, asserting that the angles of incidence and reflection have the same value in which they are measured from the correspondent wave to the normal of ground; however, as highlighted in the figure 3.3, it is assumed in (3.11b) that the normal to the surface lies in vertical (in the z direction), and the latter may not be exactly perpendicular to the ground. This simplification that will be retained in the remainder of this chapter under the assumption that the slope of the terrain is neglected,

$$\left(\frac{\mathrm{d}h}{\mathrm{d}x}\right)^2 \ll 1, \tag{3.12}$$

yields that the angles of incidence and reflection are still measured from a vertical normal direction.

The total sound field,

$$p_{\mathrm{II}} = \frac{\mathrm{e}^{\mathrm{i}kr_1}}{r_1} + \sum_{j=1}^{M} \mathcal{R}_j \frac{\mathrm{e}^{\mathrm{i}k\left(r_{2_j}+r_{3_j}\right)}}{r_{2_j}+r_{3_j}}, \tag{3.13}$$

is similar to the equation (3.7) with a sum over all the reflection points, where the reflection factor $\mathcal{R}_j$ may vary with the reflection point, whereas r_{2_j} and r_{3_j} are the distances from the source and observer, respectively, to the j-th reflection point. The effect on the acoustic energy is obtained substituting (3.13) in the equation (3.8a),

$$E_{\mathrm{II}} \equiv \left|\frac{p_{\mathrm{II}}}{p_0}\right|^2 = \left|1 + \sum_{j=1}^{M} \mathcal{R}_j \frac{r_1}{r_{2_j}+r_{3_j}} \mathrm{e}^{\mathrm{i}k\left(r_{2_j}+r_{3_j}-r_1\right)}\right|^2, \tag{3.14a}$$

or the change of SPL on a decibel scale,

$$\begin{aligned} A_{\mathrm{II}} \equiv 10\log E_{\mathrm{II}} = 10\log & \left\{ 1 + \sum_{j=1}^{M} \left(\frac{r_1}{r_{2_j}+r_{3_j}}\right)^2 |\mathcal{R}_j|^2 \right. \\ & + 2\sum_{j=1}^{M} \frac{r_1 |\mathcal{R}_j|}{r_{2_j}+r_{3_j}} \cos\left[k\left(r_{2_j}+r_{3_j}-r_1\right) + \arg\left(\mathcal{R}_j\right)\right] \\ & \left. + 2\sum_{j=2}^{M}\sum_{l=1}^{j-1} \frac{r_1}{r_{2_j}+r_{3_j}} \frac{r_1}{r_{2_l}+r_{3_l}} |\mathcal{R}_j| |\mathcal{R}_l| \cos\left[k\left(r_{2_j}+r_{3_j}-r_{2_l}-r_{3_l}\right) + \arg\left(\mathcal{R}_j\right) - \arg\left(\mathcal{R}_l\right)\right] \right\}. \end{aligned} \tag{3.14b}$$

If there is only one reflection point, $M = 1$, the last sum inside the curly brackets of (3.14b) is zero. Since the last summation varies from $l = 1$ to $j - 1$, then when $j = 1$ the last term yields zero leading back to equation (3.8c). The change of phase of the acoustic pressure perturbation,

$$\Phi_{\mathrm{II}} \equiv \arg\left(p_{\mathrm{II}}\right) - \arg\left(p_0\right) = \operatorname{arccot}\left[\frac{\operatorname{Re}\left(p_{\mathrm{II}}/p_0\right)}{\operatorname{Im}\left(p_{\mathrm{II}}/p_0\right)}\right], \tag{3.15a}$$

is given by

$$\begin{aligned} \Phi_{\mathrm{II}} = \operatorname{arccot} & \left\{ \left(1 + \sum_{j=1}^{M} |\mathcal{R}_j| \frac{r_1}{r_{2_j}+r_{3_j}} \cos\left[k\left(r_{2_j}+r_{3_j}-r_1\right) + \arg\left(\mathcal{R}_j\right)\right]\right) \right. \\ & \left. \times \left(\sum_{j=1}^{M} |\mathcal{R}_j| \frac{r_1}{r_{2_j}+r_{3_j}} \sin\left[k\left(r_{2_j}+r_{3_j}-r_1\right) + \arg\left(\mathcal{R}_j\right)\right]\right)^{-1} \right\}. \end{aligned} \tag{3.15b}$$

With one reflection point, $M = 1$, the equations (3.14b) (3.15b) simplify respectively to the equations of model I (3.8c) and (3.9b). In this model, there can be more than one reflected wave reaching the observer's position and all these waves influence the multipath factor, that is, it is a result of the combination of all these waves (superposition principle). The amplitude and phase of the acoustic pressure perturbation induced by the reflected waves when they reach the final position depend on how far they travel, on their frequencies (although the frequency of all reflected waves is the same) and on the reflection coefficient at each reflection point; fundamentally, they depend on the coordinates of each reflection point. Since these coordinates are functions of the ground profile, in order to predict a final result from the superposition of all reflected waves besides the direct wave, the ground profile must be known accurately. In an hypothetical situation when the ray distance of all the reflected waves is equal to the ray distance of the direct wave (the real situation is $r_2 + r_3 > r_1$), the change in SPL or in phase do not depend on the frequency of waves and if moreover the reflection coefficient is unit throughout the ground, then $A_{\mathrm{II}} = 10\log(1+M)^2 = 20\log(1+M)$ (when $M = 1$, there is one reflected wave and the increase of SPL would be 6.02 dB). It follows from the equation (3.14a), and considering a constant reflection coefficient, that the reflected waves which have a greater influence on the multipath factor are the waves that propagate a shorter distance $r_2 + r_3$. Hence, if there is a reflected wave that propagates a much smaller distance than the others, the problem of several reflected waves can be simplified to the case of model I: besides the direct wave, the existence of the reflected wave that propagates the smallest distance.

3.3 Model III for the effects of atmospheric attenuation

It is assumed that the atmosphere is homogeneous and at rest, so that the attenuation $\delta(r)$ depends only on the distance of propagation, *videlicet* (*viz.*) equation (3.7) is replaced by

$$p_{\mathrm{III}} = \frac{\mathrm{e}^{\mathrm{i}kr_1-\delta_1}}{r_1} + \mathcal{R}\frac{\mathrm{e}^{\mathrm{i}k(r_2+r_3)-\delta_2-\delta_3}}{r_2+r_3} \tag{3.16}$$

and in the case of uniform atmospheric absorption per unit length, $\varepsilon = \text{const}$, the attenuations are

$$\{\delta_1, \delta_2, \delta_3\} = \varepsilon\{r_1, r_2, r_3\}. \tag{3.17}$$

The effect of ground reflection,

$$p_{\mathrm{III}} = \frac{\mathrm{e}^{\mathrm{i}kr_1-\delta_1}}{r_1}F, \tag{3.18}$$

is equivalent to the multiplication by a factor $F \equiv 1 + \mathcal{R}G$, that differs from unity on account: (i) of the geometrical factor $G \equiv r_1(r_2+r_3)^{-1}\exp[\mathrm{i}k(r_2+r_3-r_1)+\delta_1-\delta_2-\delta_3]$, that depends only on observer and source positions; (ii) of the reflection factor $\mathcal{R}$, that depends on ground properties.

The effect on acoustic energy (3.8a) is now

$$E_{\mathrm{III}} \equiv \left|\frac{p_{\mathrm{III}}}{p_0\mathrm{e}^{-\delta_1}}\right|^2 = |1+\mathcal{R}G|^2 = \left|1+\mathcal{R}\left(\frac{r_1}{r_2+r_3}\right)\mathrm{e}^{\mathrm{i}k(r_2+r_3-r_1)+\delta_1-\delta_2-\delta_3}\right|^2, \tag{3.19a}$$

i.e. the change in SPL is

$$\begin{aligned} A_{\mathrm{III}} \equiv 10\log E_{\mathrm{III}} = 10\log\Bigg\{1 &+ \left(\frac{r_1}{r_2+r_3}\right)^2|\mathcal{R}|^2\mathrm{e}^{2\delta_1-2\delta_2-2\delta_3} \\ &+ 2\frac{r_1}{r_2+r_3}|\mathcal{R}|\mathrm{e}^{\delta_1-\delta_2-\delta_3}\cos[k(r_2+r_3-r_1)+\arg(\mathcal{R})]\Bigg\}. \end{aligned} \tag{3.19b}$$

As in the model I, the amplitude change depends on all the three ray distances, on the frequency of the waves and on the reflection coefficient. However, in this model, it also depends on the three attenuations. With a uniform atmospheric absorption per unit length, being valid the equation (3.17), the particular case of receiver near the ground, O $\approx$ R, when the distances travelled by the reflected and direct waves are approximately the same, $r_1 \approx r_2 + r_3$, leads to a similar result to model I, since $G = 1$, and with a correction for attenuation $\overline{G} \equiv \exp(-\delta_1)$, that is $p_{\mathrm{r}} = \mathcal{R}\overline{G}p_0$; the same correction applies to the direct wave, $p_0 \to p_0\overline{G}$, implying for the total wave $p_{\mathrm{III}} = (1+\mathcal{R})\,\overline{G}p_0$. At this point, two definitions for the change in SPL (or in phase) can be used: assuming or not, for the evaluation of multipath factor, that the atmosphere attenuates the acoustic pressure of the direct wave; mathematically, if, for example, $E_{\mathrm{III}} = |p_{\mathrm{III}}/p_0|^2$ as in model I (also being valid in model III) or $E_{\mathrm{III}} = \left|p_{\mathrm{III}}/\left(p_0\overline{G}\right)\right|^2$ which can only be used in model III. If the definition for case I is used where the atmospheric attenuation is not considered in the direct wave, $E_{\mathrm{III}} = |p_{\mathrm{III}}/p_0|^2$, consequently the SPL in decibels changes by $10\log\left\{1+|\mathcal{R}|^2\overline{G}^2+2|\mathcal{R}|\overline{G}\cos[\arg(\mathcal{R})]\right\}$. Therefore, if both waves travel the same distance, the multipath factor does not depend on the frequency, except possibly through the attenuation factor that generally increases with frequency. In the case $\arg(\mathcal{R}) = 0$, the change of SPL reduces to $20\log\left\{1+|\mathcal{R}|\overline{G}\right\}$ and if the boundary totally reflects the wave, $|\mathcal{R}| = 1$, the total acoustic pressure perturbation changes by $20\log\left(1+\overline{G}\right)$; moreover, in the presence of atmospheric attenuation $\overline{G} < 1$, this is less than $20\log 2 \approx 6.02\,\mathrm{dB}$. That attenuation does not alter the fact that the observer receives two waves of the same frequency, amplitude and phase (doubling the incident wave) when the ground does not change none of the characteristics of the wave and the distance travelled by both waves is the same. If one considers the last definition, then the SPL in decibels changes by $10\log\left\{1+|\mathcal{R}|^2+2|\mathcal{R}|\cos[\arg(\mathcal{R})]\right\}$ and the maximum change is $20\log 2 \approx 6.02\,\mathrm{dB}$ when the ray distances are equal and the surface does not modify the acoustic wave, in other words, when $\arg(\mathcal{R}) = 0$ and $|\mathcal{R}| = 1$. Therefore, if the most appropriate definition of changes in SPL for the case III is used, $E_{\mathrm{III}} = \left|p_{\mathrm{III}}/\left(p_0\overline{G}\right)\right|^2$, then the total acoustic pressure perturbation changes at most by $20\log 2 \approx 6.02\,\mathrm{dB}$ when the boundary totally reflects the wave, $\mathcal{R} = 1$, and when the ray distances are the same.

The change in phase of the acoustic pressure perturbation is

$$\begin{aligned}\Phi_{\mathrm{III}} &\equiv \arg\left(\frac{p_{\mathrm{III}}}{p_0\mathrm{e}^{-\delta_1}}\right)\\ &= \operatorname{arccot}\left\{\cot\left[k\left(r_2+r_3-r_1\right)+\arg(\mathcal{R})\right]+\frac{r_2+r_3}{r_1|\mathcal{R}|}\mathrm{e}^{\delta_2+\delta_3-\delta_1}\csc\left[k\left(r_2+r_3-r_1\right)+\arg(\mathcal{R})\right]\right\}.\end{aligned} \tag{3.20}$$

It also depends on all the three ray distances, on the modulus and argument of the reflection factor, on the frequency of the waves and, in this model, on all the three attenuations. As in the first model, in the particular case when $r_1 = r_2 + r_3$ and the ground does not change the phase of the wave, $\arg(\mathcal{R}) = 0$, there is not any phase change due to the presence of the reflected wave.

In the absence of atmospheric attenuation, $\delta_1 = \delta_2 = \delta_3 = 0$, then the equations (3.19b) and (3.20) reduce respectively to the equations (3.8c) and (3.9b).

The simplest form of the reflection coefficient $\mathcal{R}$ [37] is

$$\mathcal{R} = \frac{1 - \mathcal{R}_0}{1 + \mathcal{R}_0}, \tag{3.21a}$$

for a homogeneous ground of density ρ_1, generally much higher than the air density ρ_0,

$$\mathcal{R}_0 = \frac{\rho_0 \kappa'}{\rho_1 \kappa}, \tag{3.21b}$$

where: (i) the vertical wavenumbers of incidence κ and transmission κ' [27] are given respectively by $\kappa = (\omega/c_0)\cos\theta$ and $\kappa' = (\omega/c_1)\cos\theta'$ (ii) c_0 and c_1 are the sound speeds in air and ground respectively; (iii) the angles of incidence θ and transmission θ' are related by Snell's law [27],

$$\frac{\sin\theta}{c_0} = \frac{\sin\theta'}{c_1}, \tag{3.21c}$$

stating the continuity of the transverse wavenumber. Substituting the equation (3.21c) in the equations of κ and κ', and then into (3.21b) leads to

$$\mathcal{R}_0 = \frac{\rho_0 c_0}{\rho_1 c_1}\sqrt{\sec^2\theta - \left(\frac{c_1}{c_0}\right)^2 \tan^2\theta}, \tag{3.21d}$$

which specifies the reflection factor (3.21a) in terms of the angle θ that can be evaluated from the relations (3.3a) and (3.11a). In (3.21d) appears the ratio of plane wave impedances of air $\rho_0 c_0$ and ground $\rho_1 c_1$.

3.4 Determination of the coordinates of reflection points

The study of the effects caused by ground reflection and atmospheric absorption on aircraft noise depends on the location of the reflection point(s). The latter affects the length of the ray paths and hence, since the multipath factor depends on all the distances, it also affects the amplitude and phase of the pressure perturbation due to the atmosphere and ground profile. The location of the reflection point(s) is calculated in the cases of: (i) flat ground; (ii) two-dimensional slice of rough ground.

3.4.1 Reflection from flat ground

Each of the three ground reflection and atmosphere models mentioned in the beginning of this chapter, analysed in the sections 3.1 to 3.3, leads to a formula for the effects of ground reflection and atmospheric absorption on the total acoustic pressure perturbation p, that specifies: (i) the difference in acoustic energy or difference in SPL in dB,

$$A \equiv 10\log_{10}|E| \equiv 20\log_{10}\left|\frac{p}{p_0}\right|; \tag{3.22}$$

(ii) the phase shift of the acoustic pressure

$$\Phi \equiv \arg\left(\frac{p}{p_0}\right) = \arg(p) - \arg(p_0). \tag{3.23}$$

Since the pressure perturbations are harmonic solutions that are functions of the ray distances, these outputs depend on the calculation of the reflection point(s). Before proceeding in the sequel to reflections on rough ground, first the simplest case of flat ground is considered, that applies to the models I and III, for which there is a single reflection point. The figure 3.4 shows a three-dimensional situation for both models.

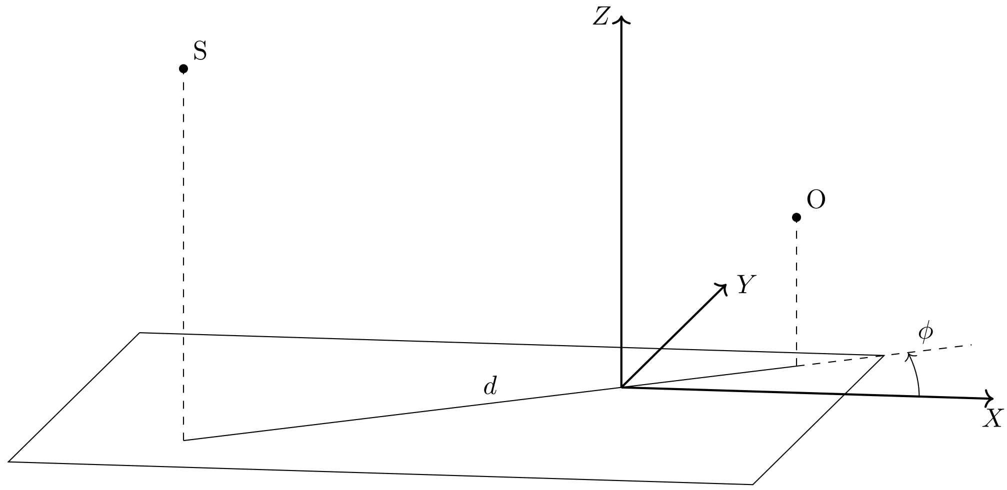

Figure 3.4: Relative positions of source and observer over a flat ground as in figure 3.2.

The source $S \mapsto (X_S, Y_S, Z_S)$ and observer $O \mapsto (X_O, Y_O, Z_O)$ positions are given in figure 3.4. Their horizontal projections are at distance d; the line joining the horizontal projections makes an angle ϕ with the X-axis. If the ground is flat, the only single reflection point is on a vertical plane that contains the source and observer points, between both positions. That means the only reflected wave that arrives at the observer position travels only on that plane. All other waves (moving out of the vertical plane) will not reach the observer position. Therefore, in this case, we can reduce the problem to two dimensions. Making a section by a vertical plane passing through the source and observer positions (figure 3.5), while choosing Cartesian coordinates with Ox-axis on the ground and Oz-axis passing through the source leads to the coordinates in the source-observer reference system:

$$x_S = 0, \quad z_S = Z_S, \tag{3.24}$$

for the source and

$$z_O = Z_O, \quad x_O = d \equiv \left[(X_S - X_O)^2 + (Y_S - Y_O)^2\right]^{1/2} \tag{3.25}$$

for the observer (in the last relation it was assumed that $x_O > 0$). The orientation of x-axis can be defined so that x_O is positive. The location of the reflection point and the effects on acoustic energy follow as in (3.3b) for the model I and for its extension to include atmospheric absorption in the model III.

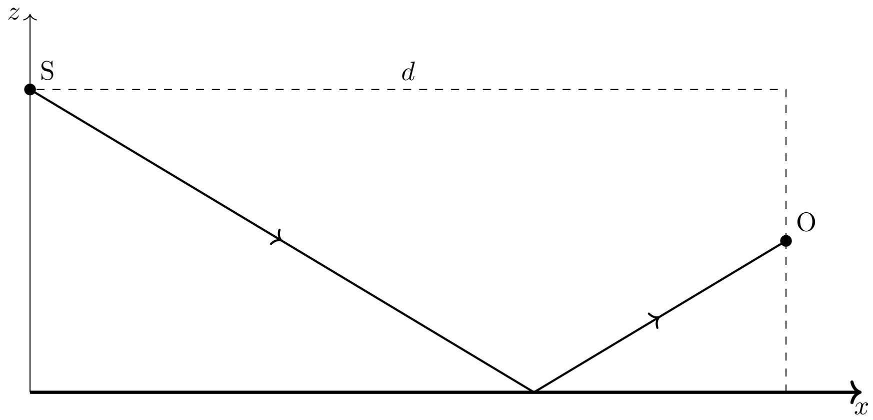

Figure 3.5: Two-dimensional slice in the vertical plane through source and observer in the case of flat ground.

3.4.2 Two-dimensional slice of rough ground

Let the height of the rough ground be given by $Z = H(X, Y)$. The two-dimensional slice (figure 3.5) made as before leads for an arbitrary point P at coordinates (X, Y, Z) to an x-coordinate in the source-observer coordinate system,

$$x = \left[(X - X_\mathrm{S})^2 + (Y - Y_\mathrm{S})^2 \right]^{1/2}, \tag{3.26}$$

and the angle ϕ with the x-axis,

$$\tan\phi = \frac{Y - Y_\mathrm{S}}{X - X_\mathrm{S}}. \tag{3.27}$$

This last definition implies that the x-coordinate is positive. Also, the point P must belong to the vertical plane which pass through the source and observer positions. Using the transformation

$$X = X_\mathrm{S} + x\cos\phi, \tag{3.28a}$$

$$Y = Y_\mathrm{S} + x\sin\phi, \tag{3.28b}$$

the two-dimensional slice through the rough ground is specified in the source-observer coordinate system by

$$h(x) = H(X_\mathrm{S} + x\cos\phi, Y_\mathrm{S} + x\sin\phi). \tag{3.29}$$

This specifies the terrain profile function $h(x)$ used in the model II.

3.5 Application of the three models due to ground and atmospheric effects

The method of application is similar for all the preceding three models presented in this chapter, allowing for rough, irregular or mountainous ground with a given profile and including or not atmospheric absorption. The simplest ground profiles are: (i) flat ground, *exempli gratia* (e.g.) a horizontal ground with arbitrary impedance; (ii) undulating ground, e.g. a sinusoid with given height and wavelength.

3.5.1 General method to determine the multipath factor

The steps in the solution procedure, valid for any of the three preceding models, are as follows:

1. input the source and observer positions;
2. in the case of flat ground, use the equations (3.24) and (3.25) to locate the reflection point (3.3b), or in the case of uneven ground, $Z = H(X, Y)$, construct the two-dimensional slice by a vertical plane (3.29) using the equations (3.26) to (3.28b), then determine the reflection points as solutions of (3.11b);
3. from each reflection point, calculate the distances to source (3.5) and observer (3.6);
4. calculate the reflection factor from (3.21a) and (3.21d) for hard ground, or take from the literature relevant to the particular type of ground being considered;
5. the expression of the total acoustic pressure perturbation is different in the three models, knowing however that the pressure induced by the direct wave, $p_0 = \exp(\mathrm{i}kr_1 - \delta_1)/r_1$, is the same:
    (a) the effect of reflection at one point on a flat ground is then given by (3.7) in the model I;
    (b) taking a constant atmospheric absorption per unit length ε leads to an extension to (3.16) in the model III;
    (c) in the case of reflection at a discrete set of points over mountainous terrain, the effect of all reflections is considered in (3.13) by the model II, where the correction for the atmospheric absorption can be included as before in (3.16);
6. all the previous three forms of E lead to amplitude (3.22) and phase changes (3.23) combining all effects of ground reflection and atmospheric absorption, knowing that the total acoustic pressure perturbation p is equal to p_{I}, p_{II} or p_{III} respectively for the models I, II or III.

As an application to the preceding theories including the calculation of reflection points, the case of static source and observer in fixed positions over flat ground, applying the model I, is considered, and then extended to sinusoidally undulating ground, applying the model II, or extended to include atmospheric absorption, applying the model III. The standard case is the sound source in a fixed position at the altitude of 30 m *viz.* $Z_{\mathrm{S}} = 30\,\mathrm{m}$, while the observer, for instance a human being, is at 2 m above a flat ground, $Z_{\mathrm{O}} = 2\,\mathrm{m}$. The comparison is made with sinusoidally undulating ground,

$$Z_{\mathrm{r}} = h(X_{\mathrm{r}}) = q \sin\left(\frac{2\pi X_{\mathrm{r}}}{L}\right), \tag{3.30}$$

with amplitude $q = 3\,\mathrm{m}$ and lengthscale L:

$$L = \{20, 40, 60, \infty\}\,\mathrm{m}. \tag{3.31a}$$

The case $L = \infty$ is flat ground, and the other cases lead to a maximum slope

$$\theta_{\max} = \arctan\left(\frac{2\pi q}{L}\right). \tag{3.31b}$$

In addition, three levels of atmospheric absorption,

$$\varepsilon = \left\{10^{-2}, 5\times 10^{-2}, 10^{-1}\right\} \mathrm{m}^{-1}, \tag{3.32}$$

are considered to apply the model III. The levels of atmospheric absorption in (3.32) vary widely, in order to make the effects visible. The case of undulating ground is preceded by comparison with flat ground.

3.5.2 Acoustic waves over flat impedance ground

The preceding methods are illustrated by applying the models I and III to fixed sound sources over a flat impedance ground. The model I is illustrated in figure 3.6 for sound source, $S \mapsto (x_\mathrm{S}, z_\mathrm{S})$, and observer, $O \mapsto (x_\mathrm{O}, z_\mathrm{O})$, at positions $Z_\mathrm{S} = 30\,\mathrm{m}$ and $Z_\mathrm{O} = 2\,\mathrm{m}$ over a flat ground. The sound attenuation (that is, the SPL variation) and the phase shift of acoustic pressure perturbation are shown for a rigid ground $\mathcal{R} = 1$ or for a ground with reflection coefficient $\mathcal{R} = 0.5 + 0.5\mathrm{i}$, for a horizontal distance between the source and observer $\Delta x = x_\mathrm{O} - x_\mathrm{S} = 50\,\mathrm{m}$, for a source at height of $z_\mathrm{S} = 30\,\mathrm{m}$, and for an observer at height of $z_\mathrm{O} = 2\,\mathrm{m}$. Because the ground remains flat, the multipath factor does not depend on the particular values of horizontal coordinates of observer and source, x_S and x_O, but only on their difference $\Delta x = x_\mathrm{O} - x_\mathrm{S}$. Thus, the coordinates x_O and x_S appear only through Δx. Together with the vertical coordinates of source z_S and observer z_O, the difference Δx specifies the lengths of the ray paths $r_1 = \left[\Delta x^2 + (z_\mathrm{O} - z_\mathrm{S})^2\right]^{1/2}$, $r_2 = z_\mathrm{S}\left[1 + \Delta x^2/\left(z_\mathrm{O} + z_\mathrm{S}\right)^2\right]^{1/2}$ and $r_3 = z_\mathrm{O}\left[1 + \Delta x^2/\left(z_\mathrm{O} + z_\mathrm{S}\right)^2\right]^{1/2}$. These last three expressions were deduced with the equation (3.3b) that is valid only for flat ground. In the example of figure 3.6 (for $\mathcal{R} = 1$, top), the distances are almost equal, $r_1 \approx 57.31\,\mathrm{m}$ whereas $r_2 + r_3 \approx 59.36\,\mathrm{m}$, and therefore the successive peaks in the upper left plot correspond to 5.86 dB, very close to 6.02 dB. In summary, when the waves with the same frequency are in phase, a condition that depends on both ray paths and the wavenumber k, the total amplitude reaches a maximum (constructive interference). Besides that, the value of that maximum amplitude depends on the factor $r_1/\left(r_2 + r_3\right)$ and only in the particular situation when $r_1 = r_2 + r_3$ it reaches the highest possible value: twice the amplitude of the direct wave, leading to $A_\mathrm{I} \approx 6.02\,\mathrm{dB}$. On the other hand, the successive minimum values on the plot correspond to waves that are in opposite phases, and in the specific example of figure 3.6 (upper left figure), these minimums have the value $-29.21\,\mathrm{dB}$. The lowest possible value occurs if the waves are in the opposite phase (that depends on both ray distances and wavenumber k) and if $r_1 = r_2 + r_3$, where there is a total cancellation of them, $p_\mathrm{I} = 0$, leading to a theoretical value of $A_\mathrm{I} \to -\infty\,\mathrm{dB}$. All the ray paths are even functions with respect to Δx and their values don't change if one permutes the z_O and z_S values. Consequently, the multipath factor and subsequent plots will be the same if one switches the positions of observer and source.

The perfect interference of direct and reflected waves for rigid ground (figure 3.6, top left) leads to

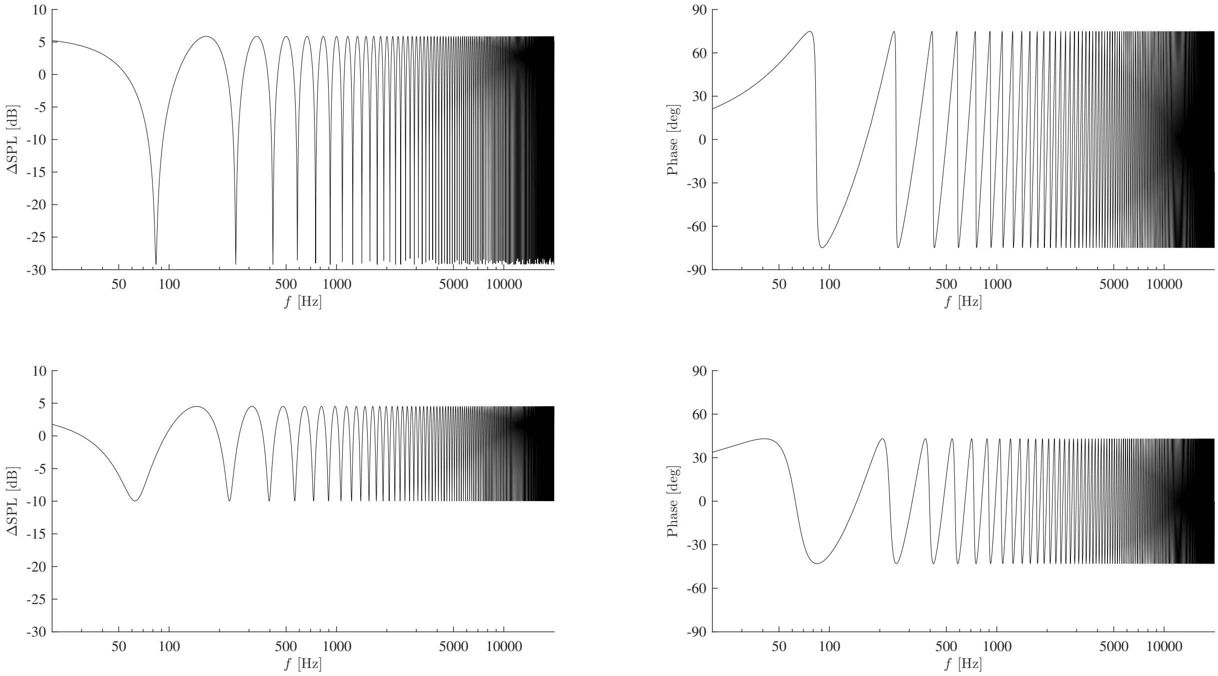

Figure 3.6: Sound attenuation A_{I} and phase shift Φ_{I} of the acoustic pressure for a ground reflection $\mathcal{R} = 1$ (top) or $\mathcal{R} = 0.5 + 0.5\mathrm{i}$ (bottom), a horizontal distance between source and observer $\Delta x = x_{\mathrm{O}} - x_{\mathrm{S}} = 50\,\mathrm{m}$, a source at a height of $z_{\mathrm{S}} = 30\,\mathrm{m}$, and an observer at a height of $z_{\mathrm{O}} = 2\,\mathrm{m}$, as functions of sound frequency.

maxima of almost double amplitude and minima of almost zero amplitude. When two waves superpose, it can form a total wave of greater, lower or same amplitude. Suppose that the two waves (direct and reflected on the ground) have the same amplitude and frequency along their ray paths, and reach the observer's position. To simplify, consider first the case of $\mathcal{R} = 1$ (figure 3.6, top) when the phase and the complex amplitude of the wave are not changed when it impinges on the surface. One extreme case is the constructive interference when at the observer's point the phase difference between the two waves is an even multiple of π $(\ldots, -2\pi, 0, 2\pi, \ldots)$ or, equivalently, when the difference between the ray distances of both waves is an integer multiple of the wavelength. Consequently, $k\,(r_2 + r_3 - r_1) = 2\pi n$ (n is an integer) and A_{I} is maximum. Note that when the distances travelled by both waves are exactly the same, $r_2 + r_3 - r_1 = 0$, the conditions are satisfied too. One can check the validity of these observations in (3.8c) because when that happens, the cosine function in the equation is equal to one and the value of A_{I} is maximum. Respecting these conditions, the two waves are in phase but it doesn't mean that the amplitude of the sum of both waves is twice the amplitude of the direct wave. Consider, for instance, $k\,(r_2 + r_3 - r_1) = 0$, but the ray distances are different, $r_1 < r_2 + r_3$ (for geometric reasons, it is impossible to have $r_1 > r_2 + r_3$). As explained before, in that case the waves are in phase, hence the value of A_{I} is maximum. Nevertheless, because the waves are spherical, the complex amplitude of the acoustic pressure perturbation is directly proportional to $1/r$ where r is the distance travelled by the wave. Therefore, since $r_1 < r_2 + r_3$, the complex amplitude of p_{r} is lower than p_0, or the complex amplitude of $p_{\mathrm{I}} = p_{\mathrm{r}} + p_0$ is lower than $2p_0$, and consequently A_{I} is lower than $20 \log 2 \approx 6.02\,\mathrm{dB}$ (we are summing two waves with same frequency, in phase, but of different amplitudes). One can have the same conclusion through the equation (3.8c) with $\mathcal{R} = 1$, $r_1 < r_2 + r_3$ and $k\,(r_2 + r_3 - 1) = 2\pi n$ and noting that

$A_{\mathrm{I}} < 10 \log 4 \approx 6.02\,\mathrm{dB}$. The other extreme case is the destructive interference when at the observer's point the phase difference between the two waves is an odd multiple of π $(\ldots, -3\pi, -\pi, \pi, 3\pi, \ldots)$ or, equivalently, when the difference between the ray distances of both waves is an integer plus one-half multiple of the wavelength. In that case, $k\,(r_2 - r_3 - r_1) = (\pi + 2\pi n)$, the cosine function in (3.8c) is -1 and A_{I} is minimum. Additionally, if the two waves have the same amplitude, A_{I} tends to $-\infty\,\mathrm{dB}$, however that only happens if the sum of both waves is zero and that is only possible, due to their spherical propagations, if $r_1 = r_2 + r_3$ (when the waves have the same complex amplitudes). In this study, we always have $r_2 + r_3 > r_1$, therefore the complex amplitudes are different and then, even when they are in opposite phases, the sum is not zero, but it can be almost zero (resulting in negative minimums of A_{I}).

The bottom left plot of the figure 3.6 shows the effect of varying the value $\mathcal{R}$ on the SPL values, keeping constant the positions of observer and source. According to (3.8c), there are two independent effects of changing $\mathcal{R}$ on SPL plots, one caused by changing its complex magnitude and another by its phase: its phase influences the positions of maximum and minimum values, in other words, keeping constant the positions of observer and source, it determines the values of frequency in which the two waves are in phase or in opposite phase, for instance, if $\arg(\mathcal{R}) > 0$ the extreme values occur at lower frequencies in comparison when $\arg(\mathcal{R}) = 0$; the complex magnitude of $\mathcal{R}$ changes only the values of maxima and minima of A_{I}. Then, when $\mathcal{R}$ changes from 1 to $0.5 + 0.5\mathrm{i}$, the extreme values of A_{I} will be lower in modulus and will occur at lower frequencies.

The extremes presented in the upper left plot of figure 3.6 correspond to zeros of the function in the upper right one. When a crest of a wave meets a crest of another wave of the same frequency at the same point (constructive interference) or when a crest of one wave meets a trough of another wave (destructive interference), the phase of total wave will be equal to the phase of direct wave, therefore $\Phi_{\mathrm{I}} = 0$ in (3.9a). Considering the first equality of (3.7), and the condition that the incident waves are in phase, $\arg(p_{\mathrm{r}}) = \arg(p_0) + 2\pi n$, then

$$|p_{\mathrm{I}}|\,\mathrm{e}^{\mathrm{i}\arg(p_{\mathrm{I}})} = (|p_0| + |p_{\mathrm{r}}|)\,\mathrm{e}^{\mathrm{i}\arg(p_0)} \tag{3.33}$$

implying that the phase of total wave remains the same while its complex magnitude is the sum of magnitudes of both incident waves. If the waves are in opposite phases, $\arg(p_{\mathrm{r}}) = \arg(p_0) + \pi + 2\pi n$, the phase of the total wave would be also equal to the phase of the direct wave because

$$|p_{\mathrm{I}}|\,\mathrm{e}^{\mathrm{i}\arg(p_{\mathrm{I}})} = |p_0|\,\mathrm{e}^{\mathrm{i}\arg(p_0)} + |p_{\mathrm{r}}|\,\mathrm{e}^{\mathrm{i}\arg(p_{\mathrm{r}})} = (|p_0| - |p_{\mathrm{r}}|)\,\mathrm{e}^{\mathrm{i}\arg(p_0)}, \tag{3.34}$$

taking into account that $|p_{\mathrm{r}}| = |\mathcal{R}| / (r_2 + r_3) < |p_0| = 1/(r_1)$ and therefore the expression in curved parentheses is equivalent to $|p_{\mathrm{I}}|$ while $\arg(p_0) = \arg(p_{\mathrm{I}})$. The equation (3.9b) leads to the same conclusion: when the phase of the waves differ by a multiple of π, $k\,(r_2 + r_3 - r_1) + \arg(\mathcal{R}) = n\pi$, then $\cot(n\pi)$ and $\csc(n\pi)$ are (both positive or negative) infinities and consequently (with the sum of positive or negative infinities being equal to positive or negative infinity respectively) the arccotangent function approaches to zero (in either cases). In summary, the constructive or destructive interferences of the two waves correspond to zeros of the plots of phase change. The bottom right plot of figure 3.6 shows the effect of varying the value of $\mathcal{R}$ in the phase of multipath factor. As in the plots of the complex magnitude, there are also two independent effects: the phase of $\mathcal{R}$ determines the frequencies that correspond to zeros (relating to constructive and destructive interferences), maxima and minima of phase Φ_I, for instance, increasing the phase of $\mathcal{R}$, like from 1 to $0.5+0.5\mathrm{i}$, in figure 3.6, reduces the frequencies of zeros and extreme values of Φ_I as one can compare in the right plots; the complex magnitude of $\mathcal{R}$ influences the range of phase values of Φ_I, for instance, the effect of decreasing $|\mathcal{R}|$ is to reduce the extreme values of phase of the multipath factor and the right plots of figure 3.6 show that changing the value of $\mathcal{R}$ from 1 to $0.5 + 0.5\mathrm{i}$ (hence reducing the complex magnitude of $\mathcal{R}$) shrinks the range of phase values of the multipath factor. One can infers the same conclusions analysing mathematically the equation (3.9b).

As shown in figure 3.6, the maximum and minimum extremes are more closely spaced for higher frequencies, both for amplitude (left plots) and phase (right plots), but it happens only because the independent axis is in a logarithmic scale. Actually, the extremes remain equally spaced for higher frequencies. The ground with complex reflection coefficient (figure 3.6, bottom) smooths out the maxima and minima, leading to a smaller range of amplitudes (bottom left) and phases (bottom right). Although the figure 3.6 shows the SPL and phase changes for a certain reflection coefficient and for certain positions of receptor and source, the plots would be similar (a succession of equally spaced crests and troughs) for other values of the aforementioned parameters, and with the maximum theoretical change of SPL also being equal to 6.02 dB. The differences would be in the range of the SPL and phase values, and also in the frequencies corresponding to crests or troughs because the positions of constructive or destructive interference would be shifted.

The frequency as independent variable in figure 3.6 is replaced by observer height z_O, source height z_S and observer-source distance Δx respectively in figures 3.8, 3.9 and 3.10. The plots of figure 3.6 show that the modulus (left plots) and phase (right plots) oscillations have extreme amplitudes with the same value independently of frequency (changing the frequency only leads to different positions where extreme amplitudes take place), therefore the subsequent plots are set for one frequency, $f = 1\,\mathrm{kHz}$. However, the values of extreme amplitudes of the multipath factor depend on the other three parameters: (i) increasing the observer height (figure 3.8) decreases the extreme amplitudes of intensity (top) and phase (bottom) oscillations; (ii) increasing the source height (figure 3.9) does not affect the extreme amplitude but increases the spacing of extrema of intensity (top) and phase (bottom) oscillations; (iii) increasing the observer-source distance (figure 3.10) affects both the spacing and extreme amplitudes of intensity (top) and phase (bottom) oscillations. For all the plots from figures 3.8 to 3.10, two geometrical parameters are fundamental to analyse them: the difference of ray lengths, $r_2+r_3-r_1$ and also their ratio, $r_1/\left(r_2+r_3\right)$. The plots of these two parameters are shown in figure 3.7 to help understanding the multipath factor effects.

Considering z_O as independent variable, the maxima and minima of SPL changes (figure 3.8, top) are related to constructive and destructive interferences respectively and, regarding (3.8c), the cosine function must be equal to one in modulus. To simplify, consider $\mathcal{R} = 1$. In the case of constructive interference, setting the cosine function to one (when the cosine function is one, we are analysing the maximum values of A_I), although the three ray distances depend on z_O, the factor $\mathfrak{r} = r_1/\left(r_2+r_3\right)$ is

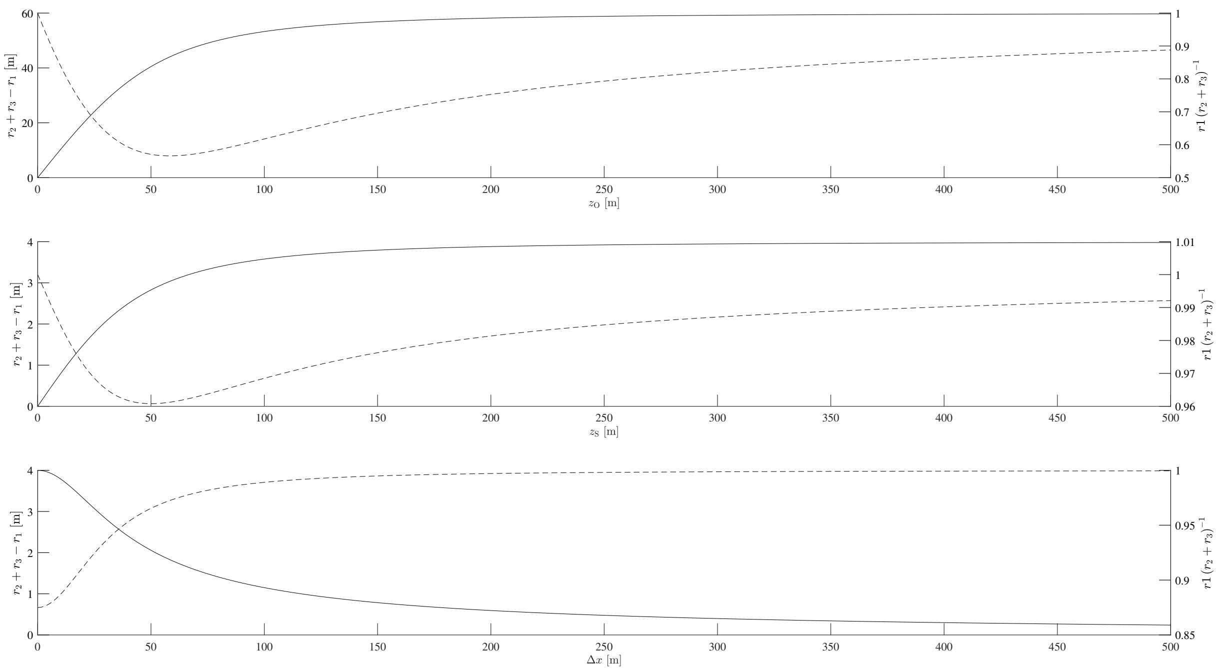

Figure 3.7: Geometrical parameters $r_2 + r_3 - r_1$ (continuous line) and $r_1/\left(r_2 + r_3\right)$ (dashed line) plotted for $z_\mathrm{O} = 2\,\mathrm{m}$, $z_\mathrm{S} = 30\,\mathrm{m}$ and $\Delta x = 50\,\mathrm{m}$ case, but where each one of them is assumed as independent variable.

a monotonic decreasing function until 10 meters at least (this fact is demonstrated in the top plot of figure 3.7) and consequently the term in bracket parentheses of (3.8c), equal to $(1+\mathfrak{r})^2$, decreases with z_O. Hence, the successive peaks of A_I slightly monotonically decrease with z_O. On the other hand, in the case of destructive interference, when the cosine function is equal to minus one (hence analysing the minimum values of A_I), the term in bracket parentheses reduces to $(1-\mathfrak{r})^2$, that increases with z_O (because the variable $\mathfrak{r}$ is decreasing), and consequently the successive minimum values of A_I also increase, as shown in the top plot of figure 3.8. Actually, the effect of varying z_O is more noticeable in the increasing of minima than in decreasing of maxima of A_I. The reason is because of the logarithm effect in (3.8c) where the logarithm function changes quicker near the abscissa 0 (when the term in bracket parentheses is almost 0, a phenomenon of destructive interference) than in abscissa greater than 1 (when the term in bracket parentheses is almost 4, a phenomenon of constructive interference). These interpretations also explain the behaviour of extremes in the bottom plot of figure 3.8 because, as indicated in (3.9b), the parameter $r_1/\left(r_2 + r_3\right)$ also appears in the equation and is useful to understand that plot. The phase space between maxima, minima or zeros of both plots in figure 3.8 is almost constant because $r_2 + r_3 - r_1$ behaves approximately like z_O for small values of z_O (note the almost proportional behaviour between z_O and $r_2 + r_3 - r_1$ in the top plot of figure 3.7 for $z_\mathrm{O} < 25\,\mathrm{m}$), then the cosine function can be simplified to $\cos\left(kz_\mathrm{O}\right)$ in (3.8c) and the same thing for the phase plot in (3.9b) when the argument of the trigonometric functions is also reduced to kz_O.

The same reasoning can be applied to figures 3.9 and 3.10. Assuming z_S as independent variable in figure 3.9, the middle plot in figure 3.7 is important in this case. When $z_\mathrm{S} < 25\,\mathrm{m}$, according to the plot, one can approximate the difference of ray paths $r_2 + r_3 - r_1$ as $0.08 z_\mathrm{S}$ and because of the cosine function presented in (3.8c), the space between the extrema is much larger in figure 3.9 than in

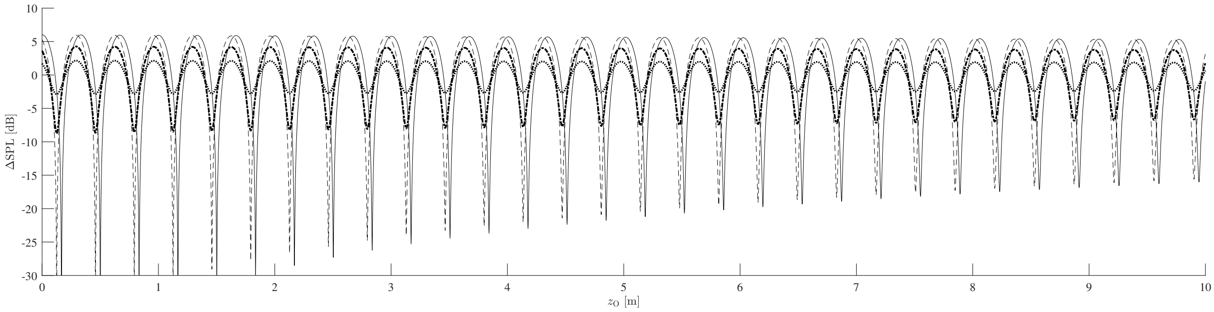

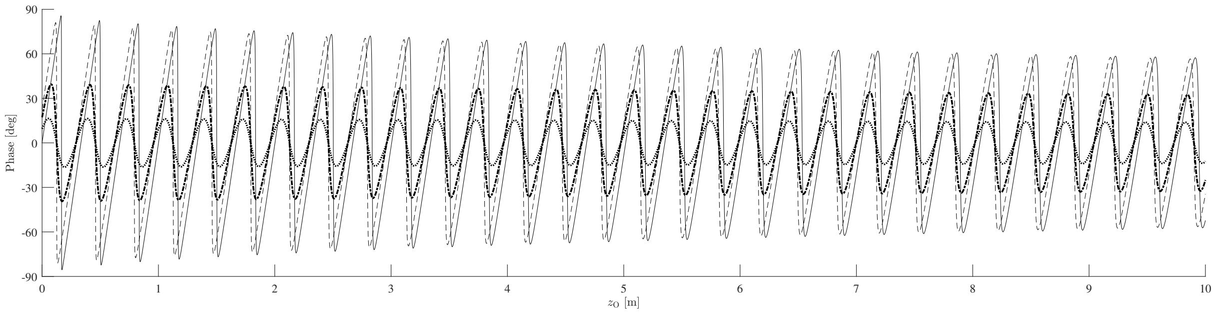

Figure 3.8: Sound attenuation A_I and phase shift Φ_I as functions of observer height z_O, for flat hard ground with $\mathcal{R} = 1$ (solid line) or for semi-flat grounds with $\mathcal{R} = 0.7 + 0.7\mathrm{i}$ (dashed line), $\mathcal{R} = 0.45 + 0.45\mathrm{i}$ (dash-dotted line) and $\mathcal{R} = 0.2 + 0.2\mathrm{i}$ (dotted line). The sound frequency is $f = 1\,\mathrm{kHz}$, the observer is at a horizontal distance $\Delta x = 50\,\mathrm{m}$ from the source, and the source is at a height $z_\mathrm{S} = 30\,\mathrm{m}$.

3.8. Furthermore, that space in figure 3.9 is increasing with z_S, specifically for $z_\mathrm{S} > 25\,\mathrm{m}$, because the derivative of $r_2 + r_3 - r_1$ with respect to z_S is lowering and consequently the cosine function behaves like $\cos(kaz_\mathrm{S})$ with $a < 0.08$, hence the space between the extrema starts to increase in comparison with the space for $z_\mathrm{S} < 25\,\mathrm{m}$ (and as a consequence, also the space between the zeros of the function Φ_I in figure 3.9). On the other hand, the values of the maxima and minima of the functions A_I and Φ_I, mainly the former one, remain approximately constant because the ratio between ray paths, $r_1 (r_2 + r_3)^{-1}$, also remains approximately constant with z_S as one can observe from the middle dashed plot in figure 3.7. In the case of bottom plot of figure 3.7, for $\Delta x < 50\,\mathrm{m}$, the derivative of the continuous line starts to decrease, reaches a constant negative value and then begins to increase, therefore the space between the extrema points in top and bottom plots and the space between the zeros in bottom plot, both of figure 3.10, follow the same pattern as the change of the derivative aforementioned (the space starts to decrease until a certain point, then remains constant and finally the space increases). Moreover, for $\Delta x < 50\,\mathrm{m}$, the dashed line in the bottom plot of figure 3.7 monotonically increases (instead of the dashed lines of other plots in figure 3.7), hence the maximum values increase while the minimum values decrease with Δx (because of the logarithm function, the effect is more noticeable in the minimum values). Note that the increasing/decreasing the values of extrema points is more visible in the figure 3.8 than in figures 3.9 and 3.10 due to a wider range of values of the parameter $r_1 (r_2 + r_3)^{-1}$, as one can observe from a comparison between the ranges of the dashed lines in the figure 3.7.

The figures 3.7 to 3.10 show the plots for certain positions of observer and source and for a certain frequency. However, independently of that values, the SPL and phase changes depend always on the parameters $r_2 + r_3 - r_1$ and $r_1 (r_2 + r_3)^{-1}$. If one changes the positions of the observer and source, the

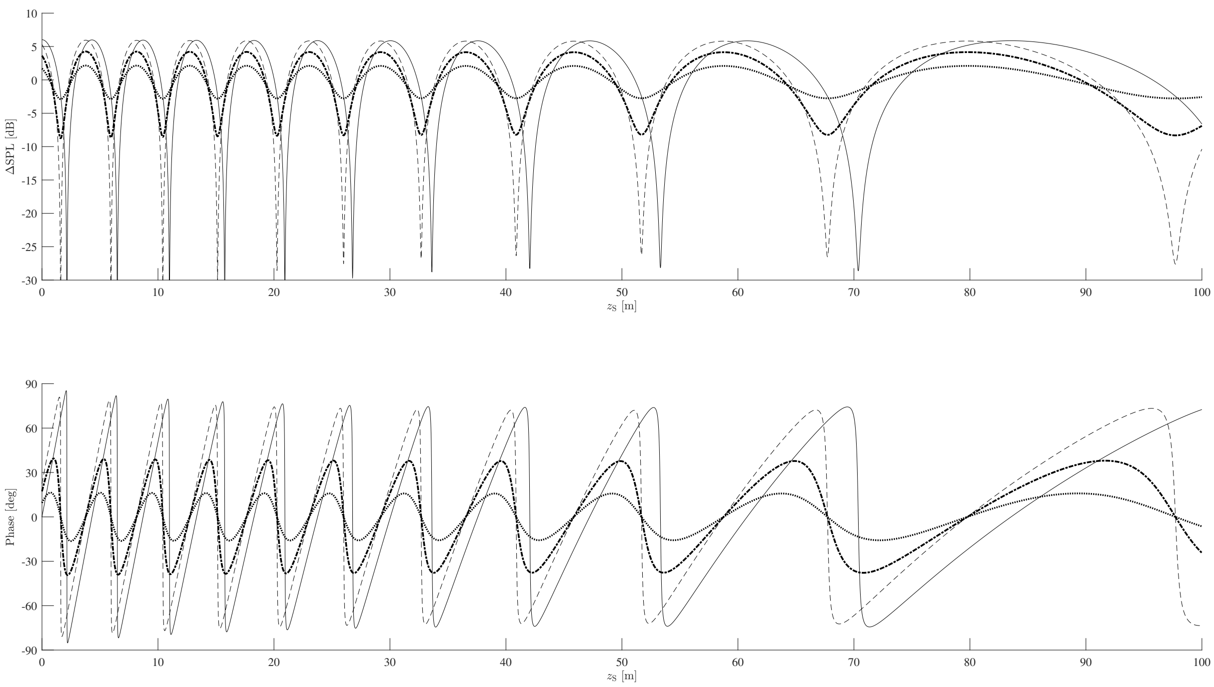

Figure 3.9: Sound attenuation A_{I} and phase shift Φ_{I} as functions of source height z_{S}, for flat hard ground with $\mathcal{R} = 1$ (solid line) or for semi-flat grounds with $\mathcal{R} = 0.7 + 0.7\mathrm{i}$ (dashed line), $\mathcal{R} = 0.45 + 0.45\mathrm{i}$ (dash-dot line) and $\mathcal{R} = 0.2 + 0.2\mathrm{i}$ (dotted line). The sound frequency is $f = 1\,\mathrm{kHz}$, and the observer is at a horizontal distance $\Delta x = 50\,\mathrm{m}$ from the source and at a height $z_{\mathrm{O}} = 2\,\mathrm{m}$.

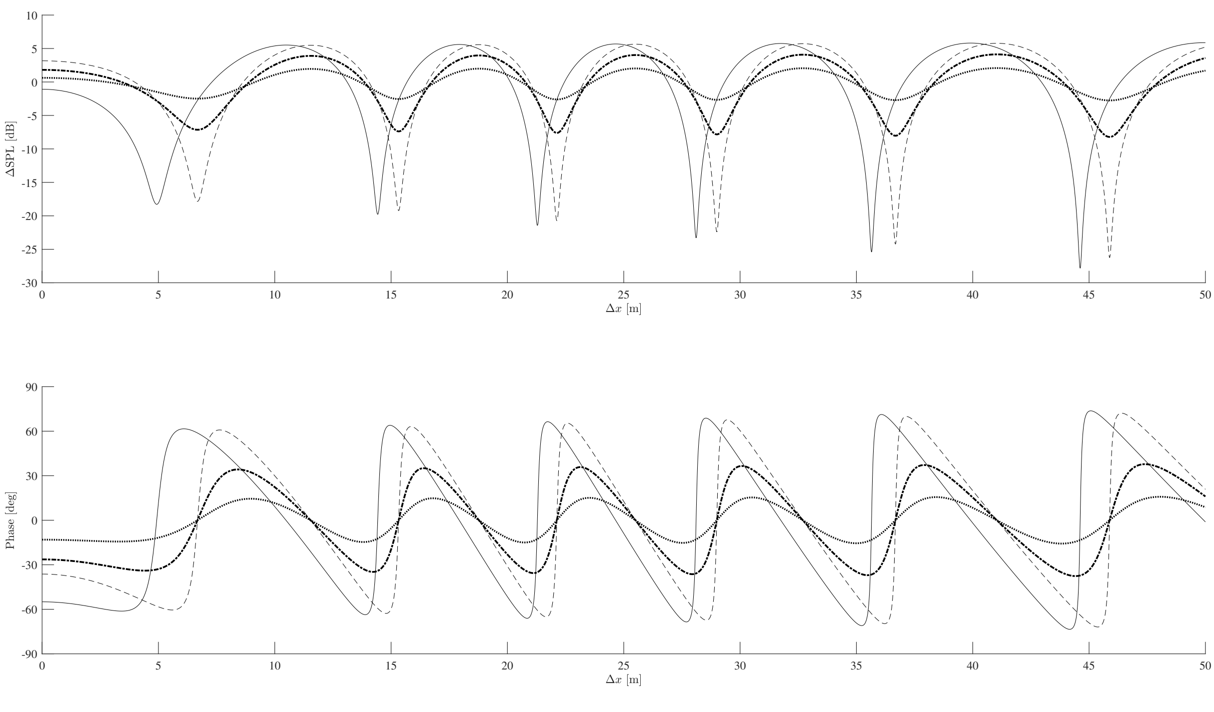

Figure 3.10: Sound attenuation A_{I} and phase shift Φ_{I} as functions of observer-source distance Δx, for flat hard ground with $\mathcal{R} = 1$ (solid line) or for semi-flat grounds with $\mathcal{R} = 0.7 + 0.7\mathrm{i}$ (dashed line), $\mathcal{R} = 0.45 + 0.45\mathrm{i}$ (dash-dot line) and $\mathcal{R} = 0.2 + 0.2\mathrm{i}$ (dotted line). The sound frequency is $f = 1\,\mathrm{kHz}$, the observer is at a height $z_{\mathrm{O}} = 2\,\mathrm{m}$, and the source is at a height $z_{\mathrm{S}} = 30\,\mathrm{m}$.

shapes of the curves shown in the figure 3.7 would be similar. For instance, in the top plot of the figure 3.7, the parameter $r_2 + r_3 - r_1$ would continue to monotonically increase while the parameter $r_1\,(r_2 + r_3)^{-1}$ would continue to form an U-shaped curve (however, the minimum of the value would shift its abscissa).

The differences would be in the range of the values of both parameters. For instance, keeping $\Delta x = 50\,\mathrm{m}$, if $z_{\mathrm{O}} = 50\,\mathrm{m}$, the parameter $r_2+r_3-r_1$ increases from 0 to 100 meters while the parameter $r_1\,(r_2+r_3)^{-1}$ is between 0.4 and 1; otherwise, if $z_{\mathrm{O}} = 95\,\mathrm{m}$, the parameter $r_2+r_3-r_1$ increases up to 190 meters while the parameter $r_1\,(r_2+r_3)^{-1}$ is between 0.25 and 1. Moreover, keeping constant the value $z_{\mathrm{S}} = 30\,\mathrm{m}$, if $\Delta x = 5\,\mathrm{m}$, the parameter $r_1\,(r_2+r_3)^{-1}$ varies between 0.08 and 1, but if $\Delta x = 95\,\mathrm{m}$, the parameter $r_1\,(r_2+r_3)^{-1}$ varies between 0.73 and 1; however, if Δx changes while the heights of the source z_{S} and receptor z_{O} are constant, the parameter $r_2+r_3-r_1$ has the same range of values. In all these cases, the shapes of the curves of both parameters remain the same; consequently, the plots of the figure 3.8 would have the same shape, with a succession of crests and troughs, with the parameter $r_2+r_3-r_1$ controlling the spacing between the “waves” of the plots and with the parameter $r_1\,(r_2+r_3)^{-1}$ controlling the amplitude of that “waves”. Besides, in most of the cases, the maximum increase of SPL is between 5 and 6 decibels. Regarding the middle plots of the figure 3.7, changing the value of Δx or z_{O}, the range of values of the parameters $r_2+r_3-r_1$ and $r_1\,(r_2+r_3)^{-1}$ would also change. The only exception is the parameter $r_2+r_3-r_1$ remaining constant when one changes the horizontal distance Δx, keeping constant the other values. Nevertheless, the shape of both curves in the middle plot of the figure 3.7 is the same: the parameter $r_2+r_3-r_1$ monotonically increases while the parameter $r_1\,(r_2+r_3)^{-1}$ forms an U-shaped curve (but the minimum of the curve changes its abscissa). Therefore, the conclusions about the figure 3.9 hold for different coordinates of the observer and source, and even for a different frequency (but can have different amplitudes and different spacing between the “waves”). All previous observations are the same for the bottom plot of the figure 3.7. Changing the heights of the receptor z_{O} and source z_{S} will change the values of both aforementioned parameters (however, when only the height of the source z_{S} or only the height of the observer z_{O} changes, keeping constant the other values, not only the range but also the format of the curve of the parameter $r_2+r_3-r_1$ remain the same, provided that the condition $z_{\mathrm{S}} \geq z_{\mathrm{O}}$ is checked), but in the other side the format of both curves will be kept (a S-curved shape for $r_1\,(r_2+r_3)^{-1}$ and an inverted S-curved shape for $r_2+r_3-r_1$). Consequently, the spacing of the “waves” and their amplitudes in the figure 3.10 will show the same trends while Δx increases for different values of the other parameters.

All the plots from the figures 3.8 to 3.10 show also the effects of $\mathcal{R}$ on the multipath factor. The interpretation mentioned to explain the figure 3.6 can be used to explain the figures 3.8 to 3.10. Comparing the continuous with dashed lines in figures 3.8 to 3.10, one can observe the effect of changing the phase of $\mathcal{R}$ because the complex magnitudes of $\mathcal{R}$ for both lines are almost the same: 1 and 0.99. Since $\arg(\mathcal{R})$ only appears in the arguments of trigonometric functions in the equations (3.8c) and (3.9b) respectively for the modulus and phase plots, increasing the phase of $\mathcal{R}$ only shifts the extreme points and zeros to the left or right and the plots do not move vertically, while increasing its complex magnitude also increases the values of the extreme points. Comparing the dashed line with the dash-dotted and dotted lines in figures 3.8 to 3.10 shows the effects of varying only the value $|\mathcal{R}|$ because the phase of $\mathcal{R}$ is exactly the same between the three lines. Looking at the ΔSPL plots, resulting from the equation (3.8c), one can conclude that the decrease in the value of $|\mathcal{R}|$ leads only to a vertical shrink of the values in that plots, therefore the extremes values decrease in modulus, but do not translate them horizontally, consequently the zeros and extrema points remain at the same abscissas; increasing the complex magnitude of $\mathcal{R}$ leads to the opposite effect since it only extends vertically the plots. The effect of translating vertically the plots due to a change in $|\mathcal{R}|$ is also visible in the bottom plots of figures 3.8 to 3.10, but it is not the only one. Decreasing the complex magnitude also shifts right or left the plots of Φ_{I} (bottom plots) because $|\mathcal{R}|$ appears in the arccotangent function, but doesn't shift horizontally the plots of A_{I} (top plots). Therefore, since the extrema points of A_{I} have the same abscissas when one changes only the complex magnitude of $\mathcal{R}$ (because that plots do not not move horizontally), the zeros of Φ_{I} (in bottom plots) remain at the same coordinates because that points and the extrema points of A_{I} have always the same abscissas.

Knowing the effects of all coordinates $(z_{\mathrm{S}}, z_{\mathrm{O}}, \Delta x)$ and reflection coefficient $\mathcal{R}$ on the multipath factor, the atmospheric attenuation can now be discussed to understand how it also influences the multipath factor. Considering in this chapter the simplest case, when the atmospheric attenuation has spherical symmetry and depends only on the distance of propagation, as stated in the assumption (3.17), the only important parameter to consider is the difference of ray distances between the direct and reflected waves, $r_2 + r_3 - r_1$. In the formulas of the multipath factor for the model III, (3.19b) and (3.20) for its complex magnitude and phase respectively, the three attenuations $(\delta_1, \delta_2, \delta_3)$ appear in the equations merely in the form $\exp\left[-\varepsilon\left(r_2 + r_3 - r_1\right)\right]$ with $\varepsilon \geq 0$. Starting from $\varepsilon = 0$, the exponential function reduces to 1 and therefore the multipath factor will be equal to that of model I, with no attenuation. If one increases the value of ε, or in other words increasing the strength of atmospheric attenuation, and plots the data as a function of some distance, like it was done in the figures 3.8 to 3.10, the results would be very similar to the plots shown in that figures and it would be observed that increasing ε leads to a smaller range (a vertical shrink of the plots) of SPL and phase values, similar to the effect of decreasing $|\mathcal{R}|$ that is visible in the previously mentioned figures. Indeed, increasing ε or decreasing $|\mathcal{R}|$ weakens the strength of the signal received at the observer position, the first due to an atmospheric absorption and the last due to a creation of a transmitted wave from the surface with $|\mathcal{R}| < 1$ when the incident wave impinges on it. Note that to effectively shrink the plots of the multipath factor, in the last case, a sufficient condition is the ground not being acoustically hard, $|\mathcal{R}| < 1$; however, in the former case, it is not sufficient to have some atmospheric attenuation because to shrink the plots, the reflected wave must be more attenuated than the direct wave, that is, $\delta_2 + \delta_3 > \delta_1$ (in the simplified case of uniform attenuation, this is always verified since $r_2 + r_3 > r_1$). One additional remark has to be considered: when $r_2 + r_3 = r_1$, since both waves travel the same distance and consequently suffer the same "amount" of uniform atmospheric attenuation, the multipath factor is not modified when that attenuation is considered. Indeed, the atmospheric effect is less visible when both ray distances tend to be very similar because in that particular circumstance the direct and reflected waves are almost equally attenuated due to the atmosphere and therefore the SPL and phase changes tend to be equal to the changes with no atmospheric attenuation. Mathematically, when $r_2 + r_3 \to r_1$, then the change of SPL approaches the result of the model I (with no atmospheric attenuation), $A_{\mathrm{III}} \to A_{\mathrm{I}}$, and the same consequence to the phase change, $\Phi_{\mathrm{III}} \to \Phi_{\mathrm{I}}$. These consequences are valid for any reflection factor and positions of observer and source. Therefore, one can know when the difference of ray paths is approximately zero by following the continuous lines of figure 3.7 and consequently, for that combination of values of Δx, z_{S} and z_{O} (to determine the difference $r_2 + r_3 - r_1$), one can predict that the atmospheric attenuation (mainly to small values of ε) changes only slightly the multipath factor. Moreover, the constructive and destructive interferences do not depend on the atmospheric attenuation, that is, the extreme points of the complex magnitude (and consequently the zeros of the phase) of the multipath factor remain at the same abscissas because the attenuations only influence the amplitudes of waves and not their phases of propagation. Indeed, according to (3.19b), the attenuation parameter does not appear in the cosine argument which is the responsible term for the location of the extreme points of the SPL plots (and zeros of the phase plots).

The effect of atmospheric absorption (figure 3.11) is equally noticeable for the intensity (top) as for the phase (bottom) of the multipath factor. The lines are plotted for the next case: the ground is acoustically hard, $\mathcal{R} = 1$, the heights of the observer and source are respectively 2 and 30 meters, while they are 50 meters apart, and the frequency of the waves is 1 kHz. However, each line represents a variation of one single value from the default case, which is represented by the black solid line. The line colour specifies which variable (except the frequency) has its value changed from the default set, and for the same colour, each line style has a different value of the variable concerned. All these changes are pointed out in the table 3.1 to clarify the meaning of each line in the figures 3.11 and 3.12. Independently of the geometrical parameters, reflection coefficient of the ground and frequency of the waves, when the atmospheric attenuation is very small, that is, when is negligible, the SPL and phase changes are almost equals to the changes if the attenuation is not included in the calculus; when $\varepsilon \to 0$, then $A_{\mathrm{III}} \to A_{\mathrm{I}}$ and $\Phi_{\mathrm{III}} \to \Phi_{\mathrm{I}}$. By looking at the plots in figure 3.11, the attenuation effect becomes important when $\varepsilon > 0.02\,\mathrm{m}^{-1}$. However, the importance of atmospheric attenuation is influenced not only by the value of ε, but also by the difference of ray paths, $r_2 + r_3 - r_1$. As the uniform atmospheric attenuation is considered, if that difference is small, both waves are attenuated with the same intensity and the only difference between these waves and the waves with no attenuation is that the former ones reach the observer's position with lower amplitudes, but at the same ratio between the direct and reflected waves; that is, mathematically when $r_2 + r_3 - r_1 \to 0$, then $|p|_{\mathrm{dir.I}} \,/\, |p|_{\mathrm{refl.I}} = |p|_{\mathrm{dir.III}} \,/\, |p|_{\mathrm{refl.III}}$ with $|p|_{\mathrm{dir.III}} < |p|_{\mathrm{dir.I}}$ and $|p|_{\mathrm{refl.III}} < |p|_{\mathrm{refl.I}}$, where dir. and refl. stand for direct and reflected waves respectively, while I and III stand for the models I (without attenuation) and III (with attenuation). Consequently, in that situation, the results approach also the ones of the model I. To summarise, the fundamental parameter that influences the multipath factor is $\varepsilon\,(r_2 + r_3 - r_1)$ and the effects of atmosphere become negligible for small values of that parameter. On the other hand, when the atmospheric absorption increases, the SPL and phase changes tend to be almost zero, independent of the difference of ray paths. That happens because for large atmospheric absorptions, in the general case of $r_2 + r_3 > r_1$, the reflected wave is much more attenuated (because it travels a greater distance) than the direct wave, and hence the total wave received at the observer's position is reduced to the direct wave only, $p_{\mathrm{III}} \approx p_0 \exp(-\delta_1)$; mathematically, for bigger ε, then $\exp\left[-\varepsilon\,(r_2 + r_3 - r_1)\right] \to 0$, consequently $A_{\mathrm{III}} \to 0$ and $\Phi_{\mathrm{III}} \to \operatorname{arccot}\left\{\cot\left[k\,(r_2 + r_3 - r_1) + \arg(\mathcal{R})\right]\right\}$.

The difference in intensity with and without atmospheric attenuation (figure 3.12) increases sharply as the latter exceeds about $0.02\,\mathrm{m}^{-1}$, at least, for all cases mentioned in the table 3.1. The figure reinforces the interpretation that in these cases, for $\varepsilon < 0.02\,\mathrm{m}^{-1}$, the difference is insignificant, since the SPL

Line colour		**Line style**	
	Solid	Dashed	Dotted
Black	$z_\mathrm{O} = 2\,\mathrm{m}$	$z_\mathrm{O} = 12\,\mathrm{m}$	$z_\mathrm{O} = 22\,\mathrm{m}$
Red	$z_\mathrm{S} = 15\,\mathrm{m}$	$z_\mathrm{S} = 45\,\mathrm{m}$	$z_\mathrm{S} = 60\,\mathrm{m}$
Blue	$\Delta x = 10\,\mathrm{m}$	$\Delta x = 30\,\mathrm{m}$	$\Delta x = 70\,\mathrm{m}$
Green	$\mathcal{R} = 0.7 + 0.7\mathrm{i}$	$\mathcal{R} = 0.45 + 0.45\mathrm{i}$	$\mathcal{R} = 0.2 + 0.2\mathrm{i}$

Table 3.1: List of the cases for each line in both plots of figures 3.11 and 3.12. The default case is the next set of values: $\{z_\mathrm{O}, z_\mathrm{S}, \Delta x, \mathcal{R}\} = \{2, 30, 50, 1\}$ corresponding to the black solid line.

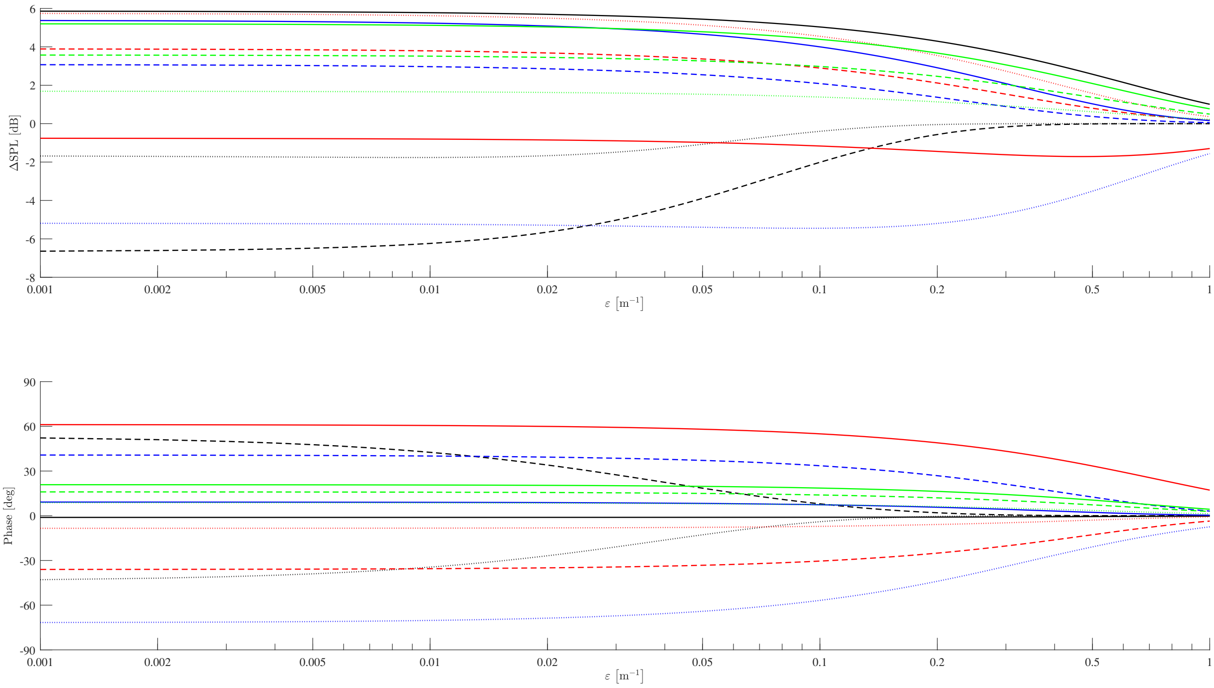

Figure 3.11: Sound attenuation A_III and phase shift Φ_III due to ground effect as functions of atmospheric absorption per unit length ε, where the default case (black solid line) is for hard ground $\mathcal{R} = 1$, the sound frequency $f = 1\,\mathrm{kHz}$, the observer at a height $z_\mathrm{O} = 2\,\mathrm{m}$, the source at a height $z_\mathrm{S} = 30\,\mathrm{m}$ and at a distance of $\Delta x = 50\,\mathrm{m}$ from the observer. Each line represents a variation of one single value aforementioned and it is indicated in table 3.1.

changes of the models I and III (with and without atmospheric attenuation) are almost equal. The difference starts to increase when $\varepsilon > 0.02\,\mathrm{m}^{-1}$. That difference can be positive or negative, depending on the geometrical parameters, the reflection coefficient and the frequency of waves. When $\varepsilon \sim 1\,\mathrm{m}^{-1}$, the waves are strongly attenuated by the atmosphere, with the reflected wave much more attenuated than the direct wave, since $r_2 + r_3$ is greater than r_1, and usually $A_\mathrm{III} \sim 0\,\mathrm{dB}$, (for instance, in all the cases of table 3.1 we have $-1.56\,\mathrm{dB} < A_\mathrm{III} < 1.01\,\mathrm{dB}$). Consequently, the difference can be simplified to merely $-A_\mathrm{I}$ and therefore can be predicted by the results of model I. In figure 3.12, there are three cases of positive differences when $\varepsilon > 0.02\,\mathrm{m}^{-1}$, $A_\mathrm{III} - A_\mathrm{I} \approx -A_\mathrm{I} > 0$, because A_I is negative in all those situations; in other cases, the difference is negative because A_I is positive in that situations (except for the red solid line where A_III is “more” negative than A_I; the attenuation shrinks vertically the ΔSPL plots, but the intersection between the plots with $\varepsilon = 0$ and $\varepsilon = 1$ do not occur when ΔSPL is 0 dB). To predict the signal of the values of A_I, the reader can analyse the top plots of figures 3.8 to 3.10 to observe when A_{I} is positive or negative and read the discussion about model I.

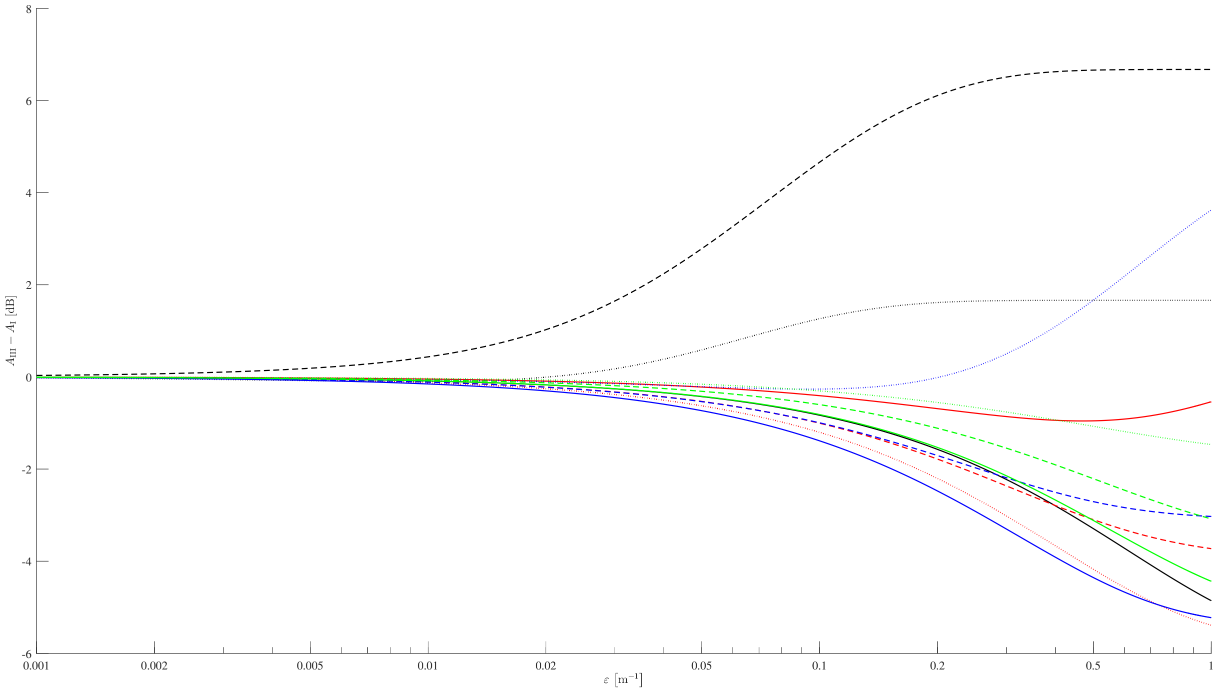

Figure 3.12: Difference between sound attenuation due to ground effect with and without atmospheric absorption, $A_{\mathrm{III}} - A_{\mathrm{I}}$, as a function of atmospheric absorption per unit length ε, where the default case (solid thinner line) is for hard ground $\mathcal{R} = 1$, sound frequency $f = 1\,\mathrm{kHz}$, observer at a height $z_{\mathrm{O}} = 2\,\mathrm{m}$, source at a height $z_{\mathrm{S}} = 30\,\mathrm{m}$ and at a distance of $\Delta x = 50\,\mathrm{m}$ from the observer. Each line represents a variation of one single value aforementioned, in the same way as in the figure 3.11, and that variation is indicated in table 3.1.

The conclusions about the figures 3.11 and 3.12 hold for other values of the parameters, including not only the coordinates of the observer and source, but also the frequency. Nevertheless, the effect of atmospheric attenuation, or equivalently the difference between the change of SPL with and without atmospheric absorption, $A_{\mathrm{III}} - A_{\mathrm{I}}$, can be significant from a value of ε less than $0.02\,\mathrm{m}^{-1}$.

Understanding the influence of ε and its related parameters on the ΔSPL and phase shift plots, one can now analyse the plots of difference in intensity with and without atmospheric absorption as a function of some geometrical parameters (as it was done in the figures 3.8 to 3.10), for instance, of the observer distance (figure 3.13). The plots show peaks at the locations of destructive interference, because the latter is less effective in the presence of attenuation. As discussed before, since the positions of destructive interference are not influenced by the presence of atmospheric attenuation nor its value (they are influenced mainly by the difference of ray paths and frequency of the waves), the peaks of the figure 3.13 occur at the same values of Δx, independent of the value of ε. In the figure 3.13, one can observe that, for $\varepsilon = 0.1\,\mathrm{m}^{-1}$, the presence of attenuation can lead to an increase of 16 dB. However, that is not a problem for the noise monitoring because those maximum increases occur always at the positions of total destructive interferences, where A_{I} is, at least, lower than -15 dB (see the top plot of figure 3.10), and consequently A_{III}, that considers the atmospheric attenuation, never reaches a positive value at the positions of peaks shown in the figure 3.13. On the other hand, the minimum values of the figure 3.13 occur at the positions of constructive interferences. In those positions, both A_{I} and A_{III} are positive values, but A_{III} is lower than A_{I}, hence resulting in negative differences shown in the figure 3.13. Indeed, as mentioned before in this section 3.5, the presence of ε shrinks the plots of SPL changes and therefore the maximum values of ΔSPL with atmospheric attenuation are lower than the maximum values without attenuation and, on the other hand, the minimum values of ΔSPL with attenuation are higher than the minimums without attenuation (equivalently, A_{III} is lower than A_{I} in modulus). The graphs in figure 3.13 are plotted assuming Δx as the independent variable, however the graphs and the discussion would be similar if one assumes z_{S} or z_{O} as independent variable rather than Δx, because the atmospheric attenuation always shrinks the plots of SPL changes. These conclusions hold not only for other values of the coordinates of observer and source, but also for other values of the frequency. However, it is possible that in a specific case the minimum value of the plot reach a value less than -1 decibel as shown in the figure 3.13 (for instance, increasing the observer's height z_{O} to 80 meters, the minimum value of the plot reaches less than -4 decibels; the lowest theoretical minimum would be -6.02 decibels when the atmospheric attenuation is high enough to attenuate totally the reflected wave, A_{III} is equal to 0, and consequently the difference $A_{\mathrm{III}} - A_{\mathrm{I}}$ is equal to $-A_{\mathrm{I}} \approx -6.02\,\mathrm{dB}$ in the positions of total constructive interference).

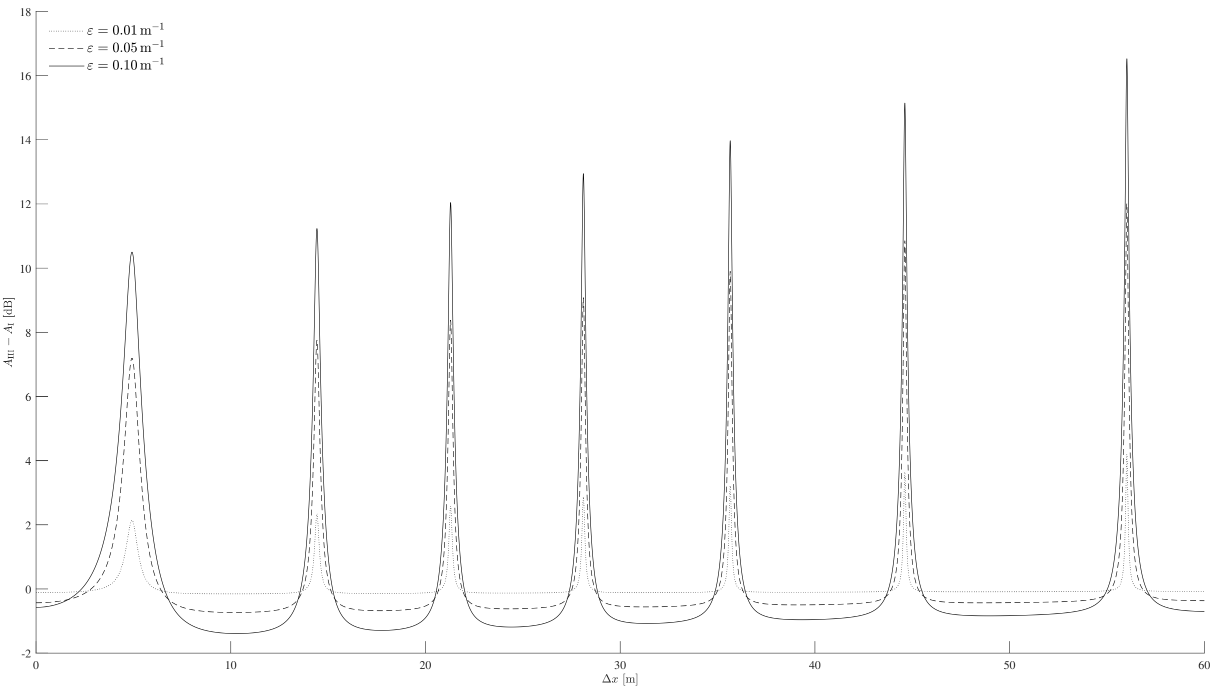

Figure 3.13: Difference between sound attenuation due to ground effect with and without atmospheric absorption, $A_{\mathrm{III}} - A_{\mathrm{I}}$, for three values of ε and for hard ground $\mathcal{R} = 1$, as a function of the distance between source and observer. The sound frequency is $f = 1\,\mathrm{kHz}$, the observer is at a height $z_{\mathrm{O}} = 2\,\mathrm{m}$, and the source is at a height $z_{\mathrm{S}} = 30\,\mathrm{m}$.

3.5.3 Effect of undulating ground compared with flat ground

To study the effects of undulating ground on the multipath factor, the model II is illustrated for a terrain profile specified by a continuous function with a continuous derivative, of which the sine function is a good example to represent an undulating ground,

$$z = q \sin\left(\frac{2\pi x}{L}\right). \tag{3.35}$$

Note that the maximum and minimum amplitudes of the ground are $\pm q$ while L is its period. The coordinates of reflection points, required to calculate the multipath factor, are determined by the equation (3.11b). If the ground is flat, $h(x_\mathrm{R}) = 0$ and then (3.11b) reduces to (3.3b). Therefore, the horizontal positions of the observer x_O and source x_S affect the attenuation and phase only through their difference $\Delta x = x_\mathrm{O} - x_\mathrm{S}$ in the case of flat ground (the only parameter that influences the result is merely Δx and not x_O and x_S themselves), with the results represented in figures 3.6 to 3.13. However, in the case of an undulated ground, represented in figures 3.14 to 3.17, the positions of the source x_O and observer x_S relative to the undulations affect the variation in SPL and phase shift. In this case, as the ground is a periodic function, if the horizontal coordinates of observer and source are changed, while keeping the same distance Δx between them and their vertical coordinates z_S and z_O, the SPL and phase changes would be periodic with x_O (or with $x_\mathrm{S} = x_\mathrm{O} - \Delta x$).

The figures 3.14 to 3.16, similar to the figures 3.8 to 3.10 respectively, continue to show the SPL variations (left) and phase shifts (right) for a sound wave of one frequency $f = 1\,\mathrm{kHz}$. The ground is acoustically hard, $\mathcal{R} = 1$, because it corresponds to the worst-case scenario of noise monitoring. The amplitude of the ground is always $q = 3\,\mathrm{m}$, but its period varies: $L = 20\,\mathrm{m}$ (top plots), $L = 40\,\mathrm{m}$ (middle plots) or $L = 60\,\mathrm{m}$ (bottom plots). The figures 3.8 to 3.10 for flat ground correspond to $L = \infty$ and all these plots are very similar, consisting on several peaks and troughs, and they have the same range values: approximately -30 to 6 decibels in change of SPL and -90 to 90 degrees in phase shift. All these plots are derived from the same physical assumptions and indeed the plots for flat ground can be done by assuming that L is very large (ideally, tending to infinity). The table 3.2 summarises the positions of source and observer for the plots in the figures 3.14 and 3.15 (in the plots of figure 3.17, the independent variable is the horizontal distance Δx between the observer and source).

Line style	**Position**		
	Observer x_O [m]	Source x_S [m]	Difference $x_\mathrm{O} - x_\mathrm{S}$ [m]
Solid	10	0	10
Dashed	35	0	35
Dotted	60	0	60

Table 3.2: Parameters for the figures 3.14 and 3.15.

The figures 3.8 and 3.14 show the dependence of the intensity (left) and phase (right) changes on the observer height, respectively, for flat and undulating grounds. As the height of the observer over ground increases, the amplitude and phase oscillations decrease for flat ground (figure 3.8); the same happens to undulating ground. These peaks and troughs decrease in modulus with z_O because as the observer stays in a higher position, the ray path of reflected wave usually became longer (it is possible to consider another ground to became shorter but this it is not the case), decreasing therefore the ratio $r_1/(r_2 + r_3)$, and because of the proportional decaying of the acoustic amplitude with the propagation distance (due to the characteristic of a spherical wave), the reflected wave is losing its “strength”. This is the same reasoning to explain the decreasing of peaks and troughs in modulus for the flat ground in figure 3.8 and can be applied independently of the horizontal coordinate of observer and the characteristics of the ground, as one can conclude from the figure 3.14. Note however that it is possible to consider another ground in such a way that, as the height of observer increases, the total ray distance of the reflected wave shortens because the shortening of the distance r_2 due to the new location of the reflection point is more considerable than the increment of the distance r_3, leading consequently to opposite conclusions. The undulation of the ground leads to two new features. In the middle plot, for $L = 40\,\mathrm{m}$, the solid line is invisible for $z_\mathrm{O} < 3\,\mathrm{m}$ (middle plots of figure 3.14) because in that case the observer is under the line of sight and only when its height is higher than 3 m, the observer is able to receive acoustic waves. When the direct wave cannot reach the observer’s position, the ΔSPL and phase of the multipath factor are not plotted. The other feature occurs, for instance, when $L = 20\,\mathrm{m}$ and $x_\mathrm{O} = 60\,\mathrm{m}$, corresponding to the dotted lines of top plots in figure 3.14. The signal interruptions that are visible in the top plots occur for the shortest undulation $L = 20\,\mathrm{m}$ of the same height $q = 3\,\mathrm{m}$, that have a larger slope and can block the line of sight from the source to the observer, more frequent in the grazing directions. With the specific values of figure 3.14, the ΔSPL and phase values are always zero, independent of z_O, because there is no reflected wave that can reach the observer’s position. These two new features are also visible in the subsequent figures.

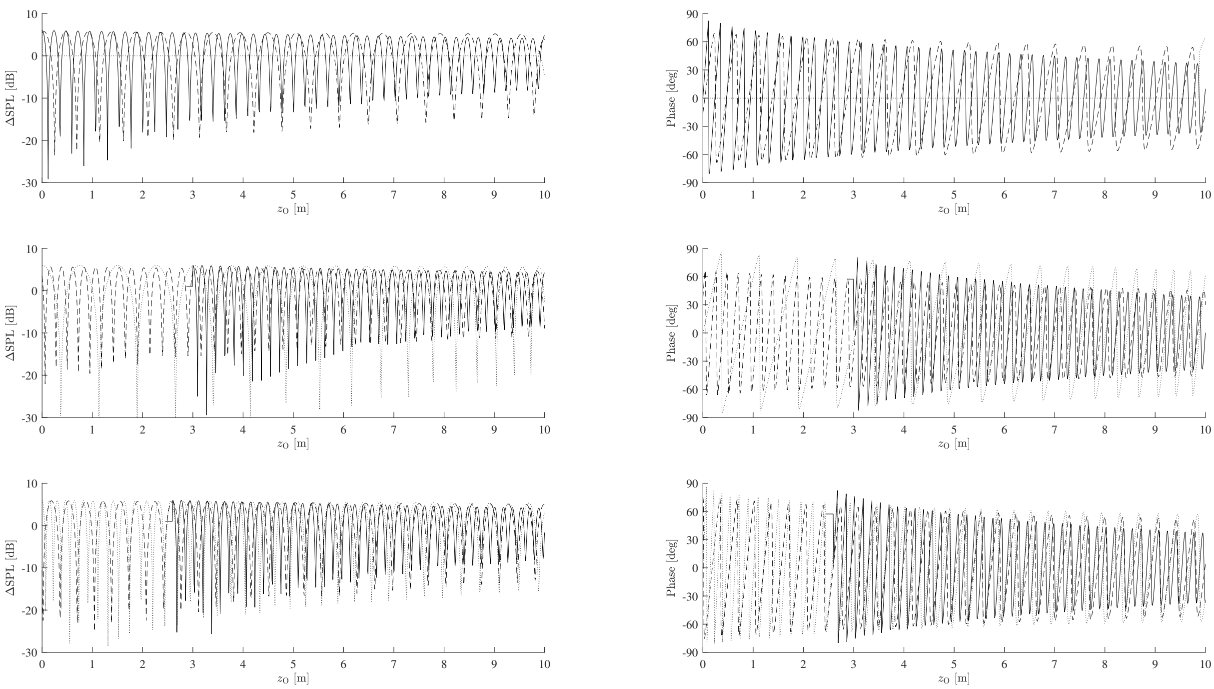

Figure 3.14: Sound attenuation A_II and phase shift Φ_II as functions of observer height z_O, for hard ground $\mathcal{R} = 1$ and undulating ground (3.35) with $q = 3\,\mathrm{m}$ and for $L = 20\,\mathrm{m}$ (top), $L = 40\,\mathrm{m}$ (middle) and $L = 60\,\mathrm{m}$ (bottom). The sound frequency is $f = 1\,\mathrm{kHz}$, the source is at a height $z_\mathrm{S} = 30\,\mathrm{m}$ and at a horizontal position $x_\mathrm{S} = 0\,\mathrm{m}$, while the observer has different distances from the source, $x_\mathrm{O} = \{10, 35, 60\}$ m for solid, dashed and dotted lines, as indicated in the table 3.2.

The figures 3.9 and 3.15 show the dependence of intensity (left) and phase (right) oscillations on source height, respectively for flat and undulating grounds. In this figure, the observer is always 2 meters above the ground. Increasing the source height leads to a greater spacing of oscillations for flat (figure 3.9 and undulating grounds (figure 3.15). The reasons are the same for both types of ground. The parameter that explains the spacing of oscillations is the difference of ray paths, $r_2 + r_3 - r_1$, and if the ratio of that difference with z_{S} is lowering, the space between oscillations starts to increase; on the other hand, if that ratio is increasing, the space starts to narrow. The same conclusion can be reached by observing at the cosine and sine arguments in the equations (3.14b) and (3.15b). The variation with z_{S} influences more the parameter $r_2 + r_3 - r_1$ than the parameter $r_1/(r_2 + r_3)$, which is approximately constant with z_{S} and therefore the amplitude of extreme points remains constant. Shorter undulations do not affect much the spacing of oscillations, but introduce a blocking of the line-of-sight and signal cut-off visible not only for steeper undulations, $L = 20\,\mathrm{m}$ (top) or even $L = 40\,\mathrm{m}$ (middle), but also for shallower undulations, $L = 60\,\mathrm{m}$ (bottom); otherwise the blocking does not exist for the extreme case of flat ground (figure 3.9). Since the height of undulations is fixed ($q = 3\,\mathrm{m}$) in figures 3.14 and 3.15, the shorter undulations have steeper slope q/L and lead to the blocking of the line-of-sight from the source to the observer in the grazing directions (not forgetting that the block of signals is also very influenced by the position of observer and source).

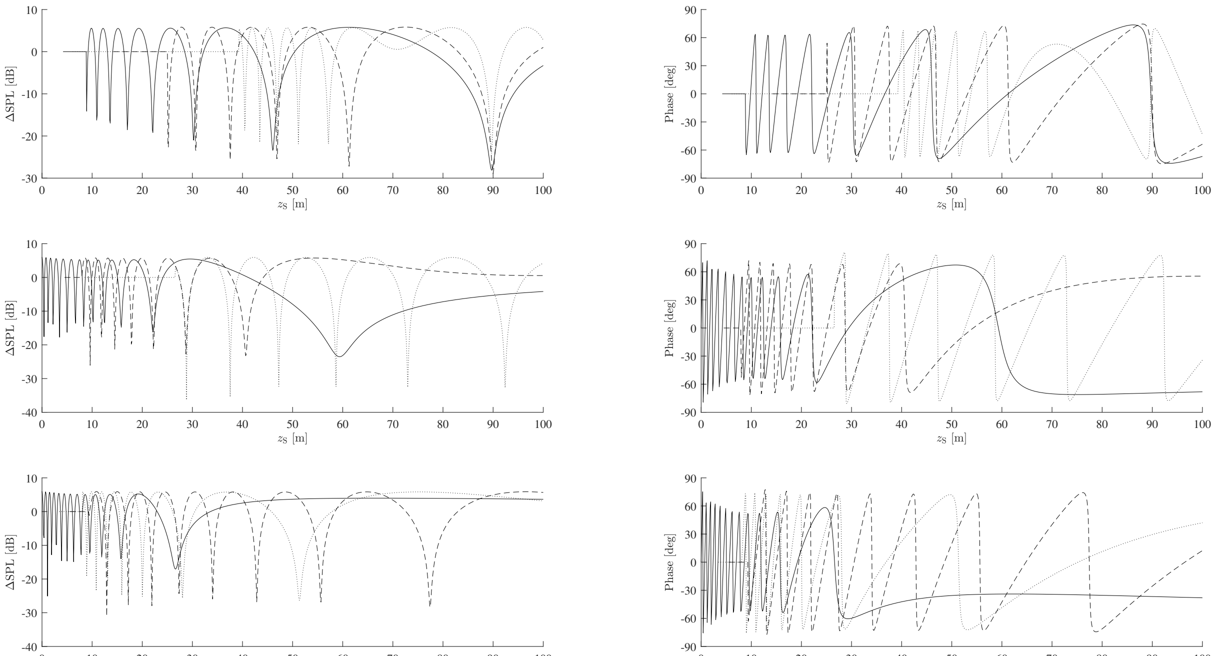

Figure 3.15: Sound attenuation A_{II} and phase shift Φ_{II} as functions of source height z_{S}, for hard ground $\mathcal{R} = 1$ and undulating ground (3.35) with $q = 3\,\mathrm{m}$ and for $L = 20\,\mathrm{m}$ (top), $L = 40\,\mathrm{m}$ (middle) and $L = 60\,\mathrm{m}$ (bottom). The sound frequency is $f = 1\,\mathrm{kHz}$, the source is at a horizontal position $x_{\mathrm{S}} = 0\,\mathrm{m}$ while the observer is always 2 meters above the ground, $z_{\mathrm{O}} = h(x) + 2\,\mathrm{m}$, but with different distances from the source, $x_{\mathrm{O}} = \{10, 35, 60\}$ m for solid, dashed and dotted lines, as indicated in the table 3.2.

The figures 3.10 and 3.16 concern the effect of horizontal distance between source and observer respectively for flat and undulating grounds. In this figure, the observer is again 2 meters above the ground, but the source positions is different for each type of line: $x_{\mathrm{S}} = 0\,\mathrm{m}$ for solid, $x_{\mathrm{S}} = 10\,\mathrm{m}$ for dashed and

$x_S = 20\,\text{m}$ for dotted line. The intensity (left) and phase (right) oscillations are affected both in magnitude and spacing (although the effect is more noticeable in the spacing), not only for flat (figure 3.10) but also for undulating grounds (figure 3.16). The signal interruptions again occur for shorter or steeper undulations and grazing directions associated with larger distances from the source to the observer (for instance, the dashed line, with $x_S = 10\,\text{m}$, of top plots with $L = 20\,\text{m}$). Note that the dotted line of top plots follows exactly the solid one because both lines represent the same situation since the ground is periodic with $L = 20\,\text{m}$.

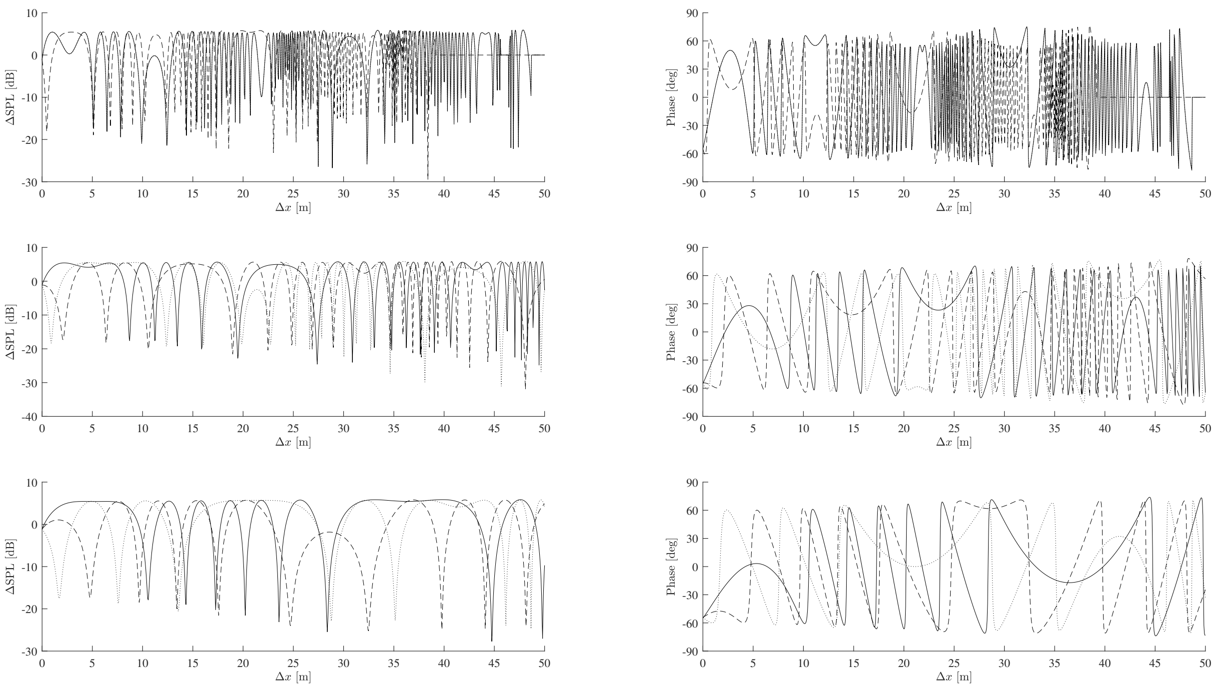

Figure 3.16: Sound attenuation A_{II} and phase shift Φ_{II} as a function of observer-source distance Δx, for hard ground $\mathcal{R} = 1$ and undulating ground (3.35) with $q = 3\,\text{m}$ and for $L = 20\,\text{m}$ (top), $L = 40\,\text{m}$ (middle) and $L = 60\,\text{m}$ (bottom). The sound frequency is $f = 1\,\text{kHz}$. The source is at a height $z_S = 30\,\text{m}$ and at the horizontal position $x_S = \{0, 10, 20\}$ m for solid, dashed and dotted lines. The observer is always 2 meters above the ground, $z_O = h(x) + 2\,\text{m}$, but with its distance from the source varying continuously since $x_O = \Delta x + x_S$.

Whereas the figures 3.10 to 3.16 keep the height of undulations and vary their length, the reverse applies in the final figure 3.17. The sound intensity depends on the length L of undulations for non-flat ground and in the figure 3.17 the plots are shown for $q = \{1, 2, 3, 4\}\,\text{m}$. In all these plots, the source is at the height $z_S = 30\,\text{m}$ while the observer is 2 meters above the ground. The horizontal coordinates of observer and source are indicated in the table 3.3. They are in the same vertical plane as crests or troughs of the different ground profiles. That remark is also indicated in the table 3.3. The sound level goes always through several minima and maxima, corresponding respectively to destructive and constructive interferences, that occur for smaller and more numerous values of the length of undulations L if the horizontal distance between the observer and source Δx increases. There is no great difference in the results when the amplitude of the ground q changes. The effect on the multipath factor is more noticeable when the length of undulations is modified. However, keeping the ground undulating like a sine function does not alter the range of SPL changes: approximately -30 to 6 decibels.

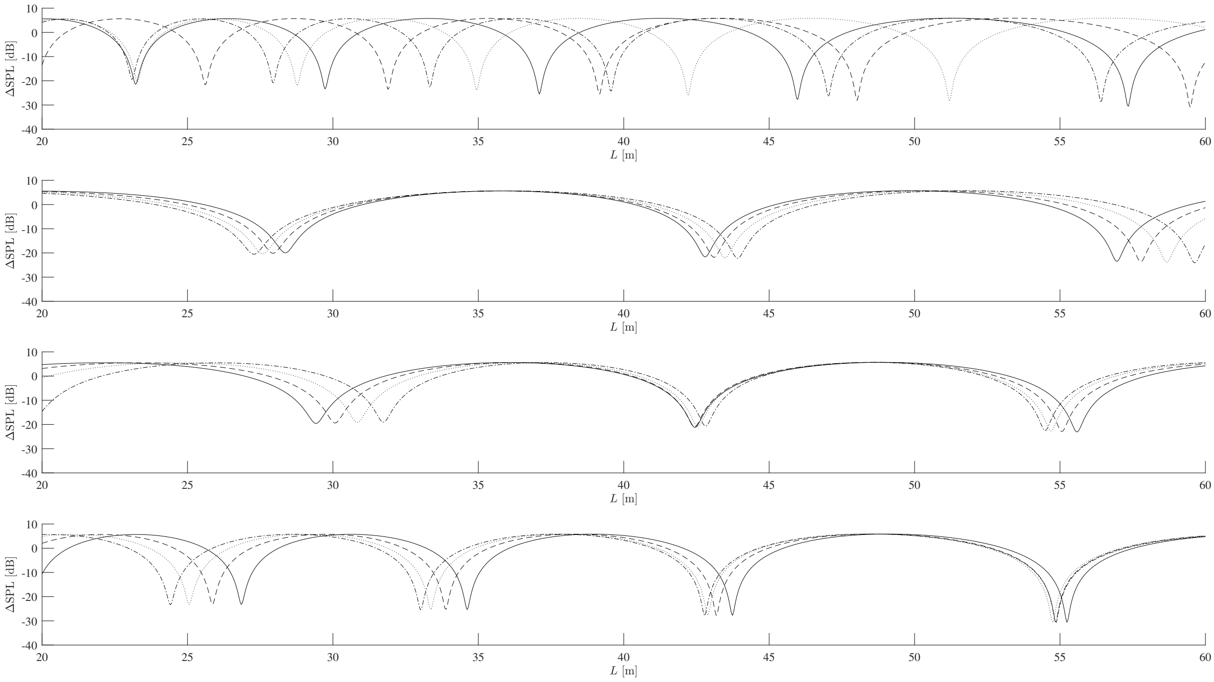

Figure 3.17: Sound attenuation A_{II} as a function of L for hard $\mathcal{R} = 1$ and undulating ground with $q = 1$ (solid line), $q = 2$ (dashed line), $q = 3$ (dotted line), or $q = 4$ (dash-dotted line). The sound frequency is $f = 1\,\text{kHz}$, the observer is 2 meters above the ground with $z_{\text{O}} = h\,(x) + 2\,\text{m}$, the source is at a height $z_{\text{S}} = 30\,\text{m}$. The horizontal distances of observer and source are indicated in table 3.3.

The range of ΔSPL aforementioned is valid for all the plots of figures 3.14 to 3.17. This is a consequence that is very rare to have more than one reflected wave that can reach the observer's position. Almost in all situations of the undulating ground, there is only one solution of the equation (3.11b), indicating that there is only one reflection point and consequently two waves reach the observer: one direct from the source plus one reflected from the ground. For the ground profile (3.35), the model II can be analysed *a priori* by the results of the model I that studies the situation of flat ground where the same number of waves reaches the observer. However, this model II does not take into account multiple reflections on the ground and that explains why in almost every cases there is only one reflected wave. If one considers waves that can imping on the ground several times and then reach the observer, hence there will be more reflected waves with the main difference being the maximum theoretical value of the SPL changes: instead of 6.02 decibels, with 2 reflected waves it can be at maximum 9.53 decibels, or with 3 reflected waves the maximum value can be 12.04 decibels. The case of multiple reflections before reaching the observer should occur only for very particular directions of propagation.

3.6 Main conclusions of the chapter 3

Aircraft noise [33, 34] contours at airports [40, 41] are currently predicted using the model of a point source of sound at the aircraft with the effect of flat ground represented by an image source [16, 20, 29–32, 38, 42–44]. The real environment around airports may involve non-flat ground, such as buildings that act as corner reflectors (chapter 2) or uneven and mountainous terrain that can cause reflections from several points. In the case of flat ground, an alternative to the (I) method of images is the (II) method

Sub-figure	Horizontal coordinate		
	Observer x_{O} [m]	Source x_{S} [m]	Difference $x_{\mathrm{O}} - x_{\mathrm{S}}$ [m]
First	$5L/4$ (crest)	$L/4$ (crest)	L
Second	$3L/4$ (trough)	$L/4$ (crest)	$L/2$
Third	$5L/4$ (crest)	$3L/4$ (trough)	$L/2$
Fourth	$7L/4$ (trough)	$3L/4$ (trough)	L

Table 3.3: Horizontal coordinates of the observer and source for the figure 3.17.

of reflected waves. To the direct wave from the real sound source to the observer, the method I adds a virtual sound wave from the image source that is replaced in the method II by a wave reflected from the ground. In both methods I and II, the acoustic boundary condition on the ground must be met. In the case of method II of reflection, this leads to a complex reflection coefficient, including both amplitude and phase changes. In the case of method I, the amplitude and phase are specified by the position and strength of the image source.

Both methods of (I) images and (II) reflections apply to building effects on sound, like a corner reflector. Using the method I of images, there are three images [39]: on the ground, on the wall and in the apex. Using the method II of reflected waves (mentioned in chapter 2), there are also three reflected waves: on the ground, on the wall and on both. The applicability of the two methods differs in the case of rough ground: (i) the method of images does not extend readily to rough ground, as it is necessary to find the location and strength of possibly several image sources; (ii) the method of reflections extends to the rough ground by identifying all reflection points, applying the corresponding reflection coefficients and adding all waves in line-of-sight of the observer. After the method II of reflection points is applied to rough ground, it would be possible to identify a set of equivalent image sources for the method I of images, but this would be redundant. Most of the acoustic measurements and experiments compare with theories of sound reflection from flat ground and do not record the terrain profile. Comparing the present approach of sound reflection by rough ground with experiments would require both the acoustic signal and terrain profile.

The problem of ground effect and atmospheric attenuation on aircraft noise can be addressed by a sequence of three progressively more sophisticated models. The models evolve from (i) a single reflection from flat ground to (ii) multiple reflections from the rough ground; the atmospheric absorption can be included with (i) uniform or (ii) non-uniform attenuation. The ground may be (i) rigid or have (ii) a uniform impedance or (iii) a reflection coefficient with specified amplitude and phase. Some of these many possibilities were illustrated, namely the influence of source and observer heights, relative horizontal distance and frequency on sound intensity and phase, for: (i) flat ground, either rigid or with complex reflection coefficients; (ii) non-flat ground with sinusoidal shape allowing a choice of two parameters, namely height and length of undulations. The rough ground models allow for arbitrary terrain profiles and are by no means restricted to the simple sinusoidal shape used.

4 | On the countering of free vibrations by forcing: non-resonant or resonant forcing with phase shifts

"All truths are easy to understand once they are discovered; the point is to discover them."

— Galileo Galilei

Contents

The research in the present chapter relates to the active suppression of (a) acoustic oscillations and (b) vibrations of beams. Concerning the first topic (a) of acoustic oscillations, the simplest one-dimensional case is the classical problem of sound propagation in ducts [21, 22, 45–48], including active noise reduction [49, 50]. The extensions include the duct acoustics of generally varying cross-section that is studied most simply for quasi-one-dimensional propagation [51, 52], when the wavelength is larger than the transverse dimensions of the duct; in this case, the classical wave equation is replaced by the horn wave equation, for which a variety of solutions exist [53–60]. An extension including mean flow is the quasi-one-dimensional propagation of sound in a duct of varying cross-section [61–64]. A different extension, without flow, is the acoustics of curved [65–73] or twisted [74] tubes. The applications of duct acoustics include the noise of jet engines and air conditioning systems.

The topic (b) of vibration of beams is based on the classic Bernoulli [75] and Euler [76] theory that is a standard introductory subject in textbooks on elasticity [77–81] and leads to the phenomenon of buckling

[82], which has been considered in several conditions: (i) geometric and material non-linearities [83], as in the chapter 8; (ii) in combination with shear [84, 85] that is more significant for thin-walled beams [86–90]; (iii) constraints [91–93], such as hyper or non-local elasticity [94, 95]; (iv) vibrations [96, 97] that can be excited by unsteady applied forces [98–101], leading to control problems [102]; (v) steady mechanical [103] or thermal [104–106] effects; and (vi) vibrations of tapered beams [107–116], with multiple applications like airplane wings, flexible aircraft and helicopters [117–122]. The applications include active vibration suppression [123–125].

There are generic topics applicable to active vibration suppression [126] independent of the specific application. The active suppression of (a) noise is based on (A) boundary or radiation conditions introducing sound waves with opposite phases. The active suppression of (b) vibration of beams is based on (B) forcing by applied forces and moments either concentrated or continuously distributed or a superposition of both. The contrast between the two approaches suggests a hybrid case concerning the active suppression of transverse oscillations of an elastic string instead of (A) superimposing oscillations with opposite phases through the boundary using (B) forcing by concentrated or distributed forces. The hybrid case is investigated by considering whether the energy of free transverse oscillations of an elastic string can be reduced by forcing. The (α) undamped and (β) damped cases are described by different equations, namely the (α) classical wave equation and (β) the wave-diffusion or telegraph equation. This suggests considering (α) the undamped case first in the present chapter to assess the interaction of free and forced oscillations, including non-resonant and resonant cases; the additional effects of damping (β) are considered in a follow-on chapter.

In this introduction, different problems have been identified by distinct symbols: (i) acoustic oscillations (a) and vibration of beams (b); (ii) active partial or total suppression introducing opposite oscillations from sources or through the boundaries (A) or by forcing with applied forces and moments (B); (iii) models without (α) and with (β) damping; (iv) cases of non-resonant (I) or resonant (II) forcing. An additional criterion (v) would be forcing by point or continuous forces. With this classification, this chapter concerns the transverse oscillations of an elastic string (a), without damping (α), whereas the damping (β) is deferred in the next chapter. The applications are undamped systems described by the classical wave equation (chapter 4) and damped systems described by the wave-diffusion or telegraph equation (chapter 5). The wave equation applies to acoustic, elastic and electromagnetic waves, and damping effects can be thermal conduction or radiation, viscosity, electrical resistance and mass diffusion. The theory of oscillations applies not only to continuous systems, but also to discrete systems such as: (i) mechanical oscillators consisting of masses, springs, dampers and forcing actuators; (ii) electrical circuits consisting of inductors, capacitors and resistors powered by batteries; (iii) analogous circuits in acoustics, hydraulics and other fields.

Thus, the transverse oscillations of an elastic string are used as a sample case on the use of forcing for active suppression of material vibration. There are two cases to be considered [127], depending on whether the forcing is (II) or not (I) at a natural frequency of the undamped system. Assuming the free oscillation of the system at its natural frequency (or frequencies), the forcing at any other non-resonant frequency (case I) will increase the total energy because the energy of the forced vibration adds to that of the free vibration. Thus, no vibration suppression will occur, unless forcing is applied at the natural frequency, leading to the resonant case (case II). Concerning the remaining second case (case II), with resonance: (i) the free oscillations are sinusoidal, with constant amplitude; (ii) the forced resonant oscillation is sinusoidal with amplitude increasing linearly with time; (iii) the total, free plus forced, oscillation, has amplitude varying with time. It is clear that the oscillation cannot be totally suppressed, and the total energy will eventually increase. Thus, the question can be modified: how long can the energy of oscillation of an undamped system be prevented from increasing by optimising the resonant forcing relative to the free oscillation? This is the fundamental question addressed in the present chapter.

The question of vibration suppression is answered by an exact, analytical solution for the "simplest" vibrating system and forcing: (i) the transverse vibrations of an elastic string fixed at both ends; (ii) resonant forcing by a single or several concentrated forces or a distributed force; (iii) minimisation of the energy over the first period of oscillation. After outlining the problem in this chapter, the method of solution is presented as follows: calculation of the free oscillations, as a superposition of natural modes, and of the response to a concentrated force, in non-resonant cases (section 4.1); calculation of the total (kinetic plus elastic) energy density, averaged over a period, for free, forced and combined oscillations (section 4.2), showing that the energy adds in the non-resonant case, but not in the resonant case; thus, the energy integrated over the length of the string can be minimised with regard to the magnitude of the force, to the position where it is applied or both simultaneously (section 4.3). In this way, the total energy can be reduced marginally (by less than 2%), by optimum forcing, over the first period, but not much longer, as shown (section 4.4) by plotting the total oscillation and its energy over a period for optimal and non-optimal forcing conditions (figures 4.7 to 4.10). The case of several concentrated forces at different locations is equivalent to a single overall force and location (section 4.5), leading to the same result. In the case of a continuously distributed force (section 4.6), it is shown that it is possible to reduce the total energy of the oscillation over the first period by, at best, one-fourth of the energy of the free oscillation. This requires an optimal choice of the forcing, as concerns spatial distribution and amplitude relative to the free oscillation, and shows (section 4.7) that continuously distributed forces are more effective vibration suppressors than point forces.

This kind of analysis could be applied to more general vibrating systems [21, 22, 45–48, 128, 129].

4.1 Free oscillations and forcing by concentrated force

Consider the linear free vibrations $\tilde{y}$ of an elastic string that are described by the classical wave equation [1, 4, 7, 45]

$$\frac{\partial^2 \tilde{y}}{\partial x^2} - \frac{1}{c^2}\frac{\partial^2 \tilde{y}}{\partial t^2} = 0, \tag{4.1a}$$

with wave speed c specified by [45]

$$c \equiv \sqrt{\frac{T}{\rho}}, \tag{4.1b}$$

where ρ is the mass density per unit length and T is the tangential tension, both assumed to be constant. The string is fixed at the two ends at $x = 0$ and $x = L$:

$$\tilde{y}\left(0, t\right) = 0 = \tilde{y}\left(L, t\right). \tag{4.2}$$

The transverse displacement is given by a superposition of normal spatial modes [45],

$$y_n\left(x\right) = \sin\left(\frac{n\pi x}{L}\right), \tag{4.3a}$$

with sinusoidal oscillations in time:

$$\tilde{y}\left(x, t\right) = \sum_{n=1}^{\infty} y_n\left(x\right)\left[P_n \cos\left(\frac{n\pi ct}{L}\right) + Q_n \sin\left(\frac{n\pi ct}{L}\right)\right]. \tag{4.3b}$$

The last solution is obtained with the method of separation of variables t and x. The amplitudes are determined by the initial deflection,

$$\tilde{y}\left(x, 0\right) = \sum_{n=1}^{\infty} P_n \sin\left(\frac{n\pi x}{L}\right), \tag{4.4a}$$

and the initial velocity,

$$\frac{\partial\tilde{y}}{\partial t}\left(x, 0\right) = \frac{\pi c}{L}\sum_{n=1}^{\infty} nQ_n \sin\left(\frac{n\pi x}{L}\right), \tag{4.4b}$$

of the string at time $t = 0$. From the sine series (4.4a) and (4.4b) follows that the coefficients P_n and Q_n are specified respectively by the initial displacement,

$$P_n = \frac{2}{L}\int_0^L \tilde{y}\left(x, 0\right)\sin\left(k_n x\right)\,\mathrm{d}x, \tag{4.5a}$$

and the initial velocity,

$$Q_n = \frac{2}{\pi cn}\int_0^L \frac{\partial\tilde{y}}{\partial t}\left(x, 0\right)\sin\left(k_n x\right)\,\mathrm{d}x, \tag{4.5b}$$

where k_n denotes the wavenumber of the mode n:

$$k_n \equiv \frac{n\pi}{L}. \tag{4.6a}$$

The corresponding wavelength is $\lambda_n \equiv 2\pi/k_n = 2L/n$. The wave period is

$$\tau_n \equiv \frac{\lambda_n}{c} = \frac{2L}{nc} \tag{4.6b}$$

and the frequency is

$$\omega_n \equiv \frac{2\pi}{\tau_n} = \frac{n\pi c}{L} = k_n c. \tag{4.6c}$$

The partial amplitudes (P_n, Q_n) may be replaced by the amplitude A_n and phase α_n,

$$P_n \equiv A_n \cos(\alpha_n), \tag{4.7a}$$

$$Q_n \equiv A_n \sin(\alpha_n), \tag{4.7b}$$

with inverses given by

$$A_n = \left(P_n^2 + Q_n^2\right)^{1/2}, \tag{4.7c}$$

$$\tan\alpha_n = \frac{Q_n}{P_n}. \tag{4.7d}$$

In particular, if the string has no deformation at the initial time, $\tilde{y}(x,0) = 0$, then $P_n = 0$ or equivalently $\alpha_n = \pi/2$. In contrast, if the string is released without velocity, $\partial\tilde{y}/\partial t\,(x,0) = 0$, then $Q_n = 0$ and therefore $\alpha_n = 0$. Substituting the partial amplitudes P_n and Q_n in (4.3b), the total oscillation is given by

$$\tilde{y}(x,t) = \sum_{n=1}^{\infty} A_n \sin(k_n x)\cos(\omega_n t - \alpha_n). \tag{4.8}$$

The phase α_n of each mode may be eliminated by changing time to

$$t' \equiv t - \frac{\alpha_n}{\omega_n}, \tag{4.9a}$$

so that

$$\cos(\omega_n t - \alpha_n) = \cos(\omega_n t'). \tag{4.9b}$$

Therefore there is no loss of generality in the following figures to set $\alpha_n = 0$, since this is equivalent to a time shift.

The figure 4.1 shows the values of the dimensionless transverse displacement, $\tilde{y}/A_n$, of the free oscillations for the first three natural frequencies, $n = \{1,2,3\}$. The plots show the oscillations along the string as a function of the dimensionless coordinate, x/L. In the case of figure 4.1, the string is released without velocity, therefore $Q_n = 0 = \alpha_n$ and $A_n = P_n$. Otherwise, if the string is released with some velocity, then $\alpha_n \neq 0$ and that case is equivalent to a time shift (4.9a), implying (4.9b), of the plots in the figure 4.1. According to (4.8), once the value of time shift α_n is defined, the shape of the string is dependent on the dimensionless parameter x/L and for each natural frequency the shape is plotted at six different times:

$$t = \{0.0, 0.4, 0.8, 1.2, 1.6, 2.0\}\, L/c. \tag{4.10}$$

The total deformation of the string is the sum of all the contributions of each natural mode of shape (for each value of n). The deformation is dominated by the natural modes with larger values of A_n. That influence depends only on the initial deflection, that is, on the shape of the string at the initial time, when it is released without velocity; otherwise, that influence depends only on the initial velocity, that is, the velocity of the string at the initial time, when it has no deformation initially; if the string has some deformation and is released with some velocity initially, the factor A_n depends on both factors.

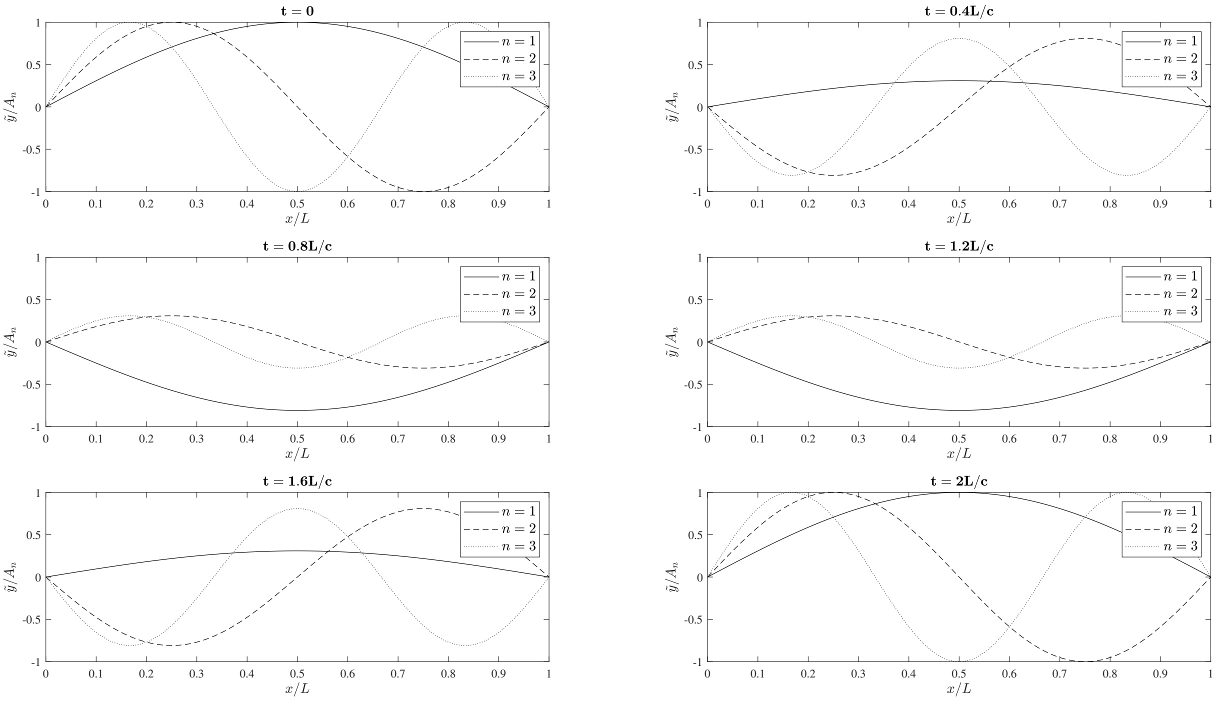

Figure 4.1: Dimensionless transverse displacement of the free oscillation of a string fixed at the two ends and released without velocity, with $\alpha_n = 0$, for the first three natural frequencies, $n = \{1, 2, 3\}$. The plots are shown for six distinct dimensionless times.

The figure 4.1 illustrates the shape of the string at six equally spaced times between $t = 0$ and $t = 2L/c$. Each term of $\tilde{y}$ is proportional to $\cos(\omega_n t)$ that is a periodic function. Its period is given by (4.6b). Consequently, the first mode of deformation has period equal to $2L/c$. Considering the second mode, the lowest period is $2L/(2c) = L/c$, implying that $2L/c$ is also a period of the second mode. Generally, each mode of deformation of frequency ω_n has the lowest period equal to $2L/(nc)$ (increasing the mode of deformation n, the period decreases) and therefore, multiplying it by n, $2L/c$ is also the period of each mode. That is the reason why the figure 4.1 illustrates the deformation from the initial time $t = 0$ until the instant $t = 2L/c$ because it is the period of each mode of deformation (note that the plots are the same for the two instants). In particular, for $n = 2$ the string made two complete oscillations, and for $n = 3$ the string made three complete oscillations, at the final instant $t = 2L/c$. The figure 4.1 shows that the string is always fixed at the two ends for any mode of deformation all the time. Furthermore, for each mode n, the string has n peaks and $n - 1$ nodes (not counting both ends of the string). These nodes and peaks remain at the same positions all the time due to the separation of variables t and x in the solution. According to the figure 4.1, the plots are the same for the instants $t = 0.4L/c$ and $t = 1.6L/c$. The temporal dependence of the oscillation $\tilde{y}$ is $\cos(\omega_n t)$ and because $\cos(t_1) = \cos(2L/c - t_1)$ for any instant t_1, the free oscillation has the property $\tilde{y}(x, t) = \tilde{y}(x, 2L/c - t)$. The plots are also the same when $t = 0.8L/c$ and $t = 1.2L/c$ for the same reasons. However, the direction of the movement of the oscillation, that is determined by $\partial\tilde{y}/\partial t$, is not the same. For example, at the instant $t = 0.4L/c$, the string of the first natural mode oscillation ($n = 1$) is moving downwards while the same string at the instant $t = 1.6L/c$ is moving upwards.

Consider next $\overline{y}$ the vibrations caused by a force , of frequency ω and amplitude F, concentrated at the point $x = \xi$,

$$\frac{\partial^2 \overline{y}}{\partial x^2} - \frac{1}{c^2}\frac{\partial^2 \overline{y}}{\partial t^2} = F\delta\left(x-\xi\right)\cos\left(\omega t + \beta\right), \tag{4.11}$$

where δ is the Dirac delta function [130, 131], that can be used to represent a concentrated force. The time dependence of the concentrated force is sinusoidal with applied frequency ω; this is one term of the representation by a Fourier series of any function of time with bounded fluctuation [39]. In (4.11) was introduced a phase shift β of the forced oscillation generally distinct from the phase shift α_n of the free oscillations (4.8), that is determined through the equation (4.7d) by the initial conditions (4.5a) and (4.5b). The response will have the same frequency and the same phase shift as the applied force,

$$\overline{y}\left(x,t\right) = B\left(x\right)\cos\left(\omega t + \beta\right), \tag{4.12a}$$

leading to the differential equation

$$\frac{\mathrm{d}^2 B}{\mathrm{d}x^2} + \left(\frac{\omega}{c}\right)^2 B\left(x\right) = F\delta\left(x-\xi\right), \tag{4.12b}$$

that can be solved by expanding the Dirac delta function in sine series in the interval $(0, L)$:

$$\delta\left(x-\xi\right) = \sum_{n=1}^{\infty} a_n \sin\left(\frac{n\pi x}{L}\right). \tag{4.13a}$$

This assumes that mathematically F is repeated at all $\xi + mL$ positions with $m = 1, 2, 3, \ldots$, and with reversed sign $-F$ at $-\xi - mL$ with $m = 0, 1, 2, \ldots$, so that it specifies an odd function of x, represented by the sine series (4.13a) with coefficients

$$a_n = \frac{2}{L}\int_0^L \delta\left(x-\xi\right)\sin\left(\frac{n\pi x}{L}\right)\mathrm{d}x = \frac{2}{L}\sin\left(\frac{n\pi\xi}{L}\right). \tag{4.13b}$$

Substituting (4.13b) in (4.13a) follows that the Dirac delta function is represented by the Fourier sine series. Then, substituting the function $\delta\left(x-\xi\right)$ in (4.12b), with $k \equiv \omega/c$, leads to

$$\frac{\mathrm{d}^2 B}{\mathrm{d}x^2} + k^2 B = \frac{2F}{L}\sum_{n=1}^{\infty}\sin\left(k_n x\right)\sin\left(k_n \xi\right), \tag{4.14}$$

and suggests the solution

$$B\left(x\right) = \sum_{n=1}^{\infty} b_n \sin\left(k_n x\right), \tag{4.15a}$$

leading to the condition

$$\left(k^2 - k_n^2\right) b_n = \frac{2F}{L}\sin\left(k_n \xi\right). \tag{4.15b}$$

Substituting (4.15b) in (4.15a) and then in (4.12a), the forced oscillations are given by

$$\overline{y}\left(x,t\right) = \frac{2F}{L}\cos\left(\omega t + \beta\right)\sum_{n=1}^{\infty}\frac{1}{k^2 - k_n^2}\sin\left(k_n \xi\right)\sin\left(k_n x\right), \tag{4.16}$$

for a wavenumber k outside of resonance, $k \neq k_n$, and including all modes of oscillation with $n = 1, \ldots, \infty$.

In the resonant case, $k = k_m$ for some integer m, hence the m-th term of (4.16) would appear to be infinite. This is physically absurd, because the oscillation cannot have infinite amplitude or energy. It is the result of mathematical error, namely dividing (4.15b) by zero, $k^2 - k_m^2 = 0$, when $k = k_m$. Thus, the m-th term of (4.16) is invalid as a solution of (4.14) if $k = k_m$ or $\omega = \omega_m$. To find a valid solution in this case [127, 132], the equation (4.15b) is rewritten with the time dependence:

$$\left(\omega^2 - \omega_m^2\right) b_m \cos\left(\omega t + \beta\right) = \frac{2Fc^2}{L} \sin\left(k_m \xi\right) \cos\left(\omega t + \beta\right). \tag{4.17}$$

Differentiating with regard to ω in both sides of (4.17) leads to

$$-\left(\omega^2 - \omega_m^2\right) b_m t \sin\left(\omega t + \beta\right) + 2\omega b_m \cos\left(\omega t + \beta\right) = -\frac{2Fc^2}{L} \sin\left(k_m \xi\right) t \sin\left(\omega t + \beta\right), \tag{4.18}$$

and letting ω tending to ω_m yields

$$b_m \cos\left(\omega_m t + \beta\right) = -\frac{Fc^2}{\omega_m L} \sin\left(k_m \xi\right) t \sin\left(\omega_m t + \beta\right). \tag{4.19}$$

Using the last equality (4.19) in the m-th term of (4.15a) and (4.15b), while the remaining terms $n \neq m$ are unchanged, leads to the forced response

$$\begin{aligned} \overline{y}\left(x, t\right) = &-\frac{F}{k_m^2 L} \sin\left(k_m \xi\right) \sin\left(k_m x\right) \omega_m t \sin\left(\omega_m t + \beta\right) \\ &+ \frac{2F}{L} \sum_{\substack{n=1 \\ n \neq m}}^{\infty} \left(k_m^2 - k_n^2\right)^{-1} \sin\left(k_n \xi\right) \sin\left(k_n x\right) \cos\left(\omega_m t + \beta\right), \end{aligned} \tag{4.20}$$

consisting of oscillations of constant maximum amplitude (when the cosine function is equal to 1) at all wavenumbers $k_n \neq k_m$, except k_m, for which the amplitude increases linearly with time.

The figure 4.2 shows the dimensionless forced displacements $\overline{y}/\left(FL\right)$ of the forced oscillations for the first three natural frequencies, $n = \{1, 2, 3\}$. As in the figure 4.1, the plots shown the oscillations along the string as a function of the dimensionless coordinate, x/L. According to (4.20), and bearing in mind (4.6a), the position x appears always divided by L, in the dimensionless coordinate x/L. The total deformation of the string due to the external force is the sum of all the contributions of each natural mode of shape (for each value of n). The first three contributions are plotted in the figure 4.2. In contrast with the free oscillation, the force F contributes equally to each deformation plotted in the figure 4.2 for each value of n (and to the contributions not depicted in figure 4.2 for $n \geq 4$) because forcing by an impulse in (4.13a) is equivalent to "white noise". The total forced deformation is obtained summing each deformation and then multiplying it by F/L. Also, in contrast to the free oscillations, the forced oscillations do not depend on boundary conditions, that is, on the coefficients P_n and Q_n. In the figure 4.2, it is assumed that the point force applied at $\xi = 0.25L$. Consequently, the term $\sin\left(k_n \xi\right)$ that appears in the solution is equal to $\sin\left(n\pi/4\right)$. The forced frequency of the excitation is equal to the first natural mode of free oscillation, that is, the figure is obtained with $\omega_m = \omega_1 = \pi c/2L$ $(m = 1)$. Consequently, at the initial time ($t = 0$), the string remains horizontal ($\overline{y} = 0$) for the first mode of deformation ($n = 1$) because, according to (4.20), the resonant term is proportional to the time. Moreover, the figure 4.2 is obtained with $\beta = 0$, which corresponds to a maximum amplitude of the oscillatory applied force at the initial time, according to the right-hand side of (4.11). The plots would be similar with $\beta \neq 0$, since β only introduces a phase shift to the results. Therefore, the plots of the figure 4.2 can be obtained with $\beta \neq 0$, but for times distinct than those indicated above each plot of the figure. The exception is the resonant term because it also depends on the term $\omega_m t$.

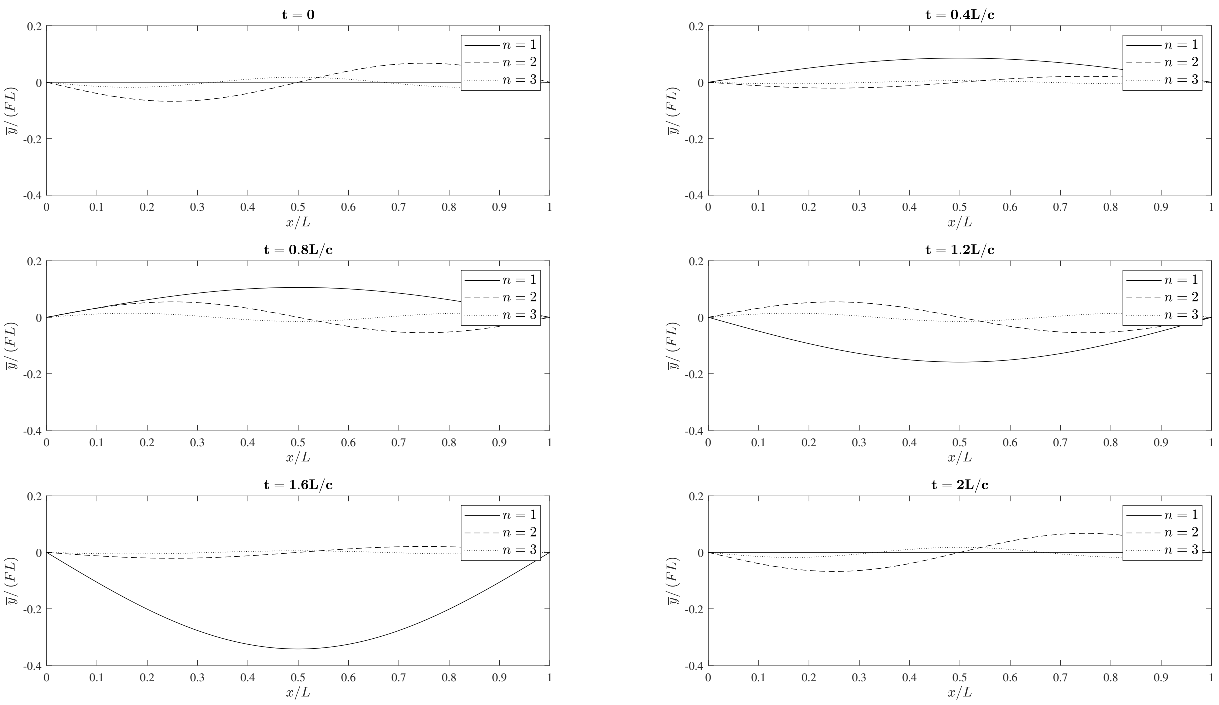

Figure 4.2: Forced displacements of the forced oscillations of a string fixed at the two ends, with $\beta = 0$, for the first three natural frequencies, $n = \{1, 2, 3\}$. The point oscillatory force is applied at 25% of the length of the string, measured from its beginning. The frequency of the force ω is equal to the first natural frequency $\omega_1 = \pi c/L$ of the oscillation of the string. The plots are shown for the same six distinct dimensionless times as in the figure 4.1.

The figure 4.2 shows the string at six times between $t = 0$ and $t = 2L/c$, the same as in the figure 4.1. Each non-resonant term of $\overline{y}$ is proportional to $\cos(\omega t)$ that is a periodic function. Its period is $2\pi/\omega$ and in the particular case of figure 4.2 is equal to $2\pi/\omega_1 = 2L/c$. For that reason, the figure 4.2 illustrates the deformation from the initial time $t = 0$ until the instant $t = 2L/c$ because it is the period of all non-resonant modes of deformation (note that the plots are the same for the two instants, although the deformation of the resonant mode, $n = 1$, is not periodic because it is proportional to $\omega_m t$.). As opposed to the free oscillations, the period of each mode of oscillation is the same and it depends only on the frequency ω of the force. This was already imposed by the solution in (4.12a). However, in the resonant mode, when the frequency of the force is equal to one of the natural frequencies of the free oscillation, the resonant term is not periodic because the oscillation grows linearly with $\omega_m t$.

As in the free oscillations, the figure 4.2 shows that the string is always fixed at the two ends for any mode of forced deformation all the time. Furthermore, for each mode n, the string has n peaks and $n - 1$ nodes (not counting both ends of the string). These nodes and peaks remain at the same positions all the time due to the separation of variables t and x in the solution. Moreover, the nodes and peaks of the forced oscillations are at the same position as those of free oscillations. Therefore, all the terms of forced oscillations have the same properties as the free oscillations (the only difference is the period of the oscillations as explained before). The only exception is in the resonant term where the amplitude of oscillation increase with time due to the term $\omega_m t$. Another property in common with free oscillations is that the plots of the non-resonant forced oscillations are the same for the instants $t = 0.4L/c$ and $t = 1.6L/c$. The temporal dependence of the non-resonant oscillation $\overline{y}$ is again $\cos(\omega t + \beta)$ and therefore theses oscillations have the property $\overline{y}(x,t) = \overline{y}(x, 2\pi/\omega - t)$, or in particular case of the figure 4.2, $\overline{y}(x,t) = \overline{y}(x, 2L/c - t)$. However, as in the free oscillations, the direction of the movement of the oscillation, that is determined by $\partial\overline{y}/\partial t$, is not the same. The plots of the non-resonant oscillations are also the same when $t = 0.8L/c$ and $t = 1.2L/c$ for the same reasons. This property does not hold with the resonant term due to the term $\omega_m t$ (in the figure 4.2, the resonant oscillation is the plot of $n = 1$). It should also be noted that the resonant and non-resonant oscillations have phases in quadrature, hence when the non-resonant oscillation has maximum amplitude in modulus, the resonant oscillation has zero deformation, and vice-versa. This property is true for any value of phase β and for any mode of resonant oscillation m.

The total oscillation, that is free plus forced oscillation, $y(x,t) = \tilde{y}(x,t) + \overline{y}(x,t)$, is given, for $\omega \neq \omega_n$, by

$$y(x,t) = \sum_{n=1}^{\infty} \sin(k_n x) \left\{ A_n \cos(\omega_n t - \alpha_n) + \frac{2F}{L} \left(k^2 - k_n^2\right)^{-1} \sin(k_n \xi) \cos(\omega t + \beta) \right\} \tag{4.21a}$$

in the absence of resonance, and, for $\omega = \omega_m$, by

$$\begin{aligned} y(x,t) = &\sum_{\substack{n=1 \\ n\neq m}}^{\infty} \sin(k_n x) \left\{ A_n \cos(\omega_n t - \alpha_n) + \frac{2F}{L} \left(k_m^2 - k_n^2\right)^{-1} \sin(k_n \xi) \cos(\omega_m t + \beta) \right\} \\ &+ \sin(k_m x) \left\{ A_m \cos(\omega_m t - \alpha_m) - \frac{F}{k_m^2 L} \sin(k_m \xi)\, \omega_m t \sin(\omega_m t + \beta) \right\} \end{aligned} \tag{4.21b}$$

in the presence of resonance. Note that even in the case of zero phase shift, $\alpha_n = 0 = \beta$, in neither case the forced oscillation can exactly cancel the free oscillation, because: (i) in the non-resonant case (4.21a) the frequencies $\omega \neq \omega_n$ are different; (ii) in the resonant case (4.21b) the frequency is the same ($\omega = \omega_m$ in the last term), but the amplitudes are different, since it is constant for the free oscillation, but is increasing linearly with time for the forced oscillation.

The upper left plot of the figure 4.3 shows the maximum amplitude (in modulus) of the free oscillations over time for the first three natural modes of oscillation, $n \leq 3$. The other three plots of the figure 4.3 show the maximum amplitude (in modulus) of the forced oscillations, each one for a different location of the applied force. In all three plots, the frequency of the force is equal to the first natural mode of the free oscillation, that is, $\omega = \omega_1 = \pi c/L$. Therefore, the plots for $n = 1$ represent the maximum amplitude of the resonant term. The figure 4.3 shows the results for the instants between $t = 0$ and $t = 2L/c$ because $2L/c$ is the period of all free oscillations. Since $2L/c$ is also the period of the applied force, then the forced oscillations have the same period. Note that in these plots, there is no phase shift of the free oscillations and applied force, $\alpha_n = 0 = \beta$. If $\alpha_n \neq 0$, there is a phase shift on the result of n mode of oscillation, visualised in the upper left plot of the figure 4.3. Setting $\beta \neq 0$ introduces a phase shift on all n non-resonant modes of forced oscillations, while on the m resonant mode, the plot is also modified, but not with a phase shift due to the term $\omega_m t$.

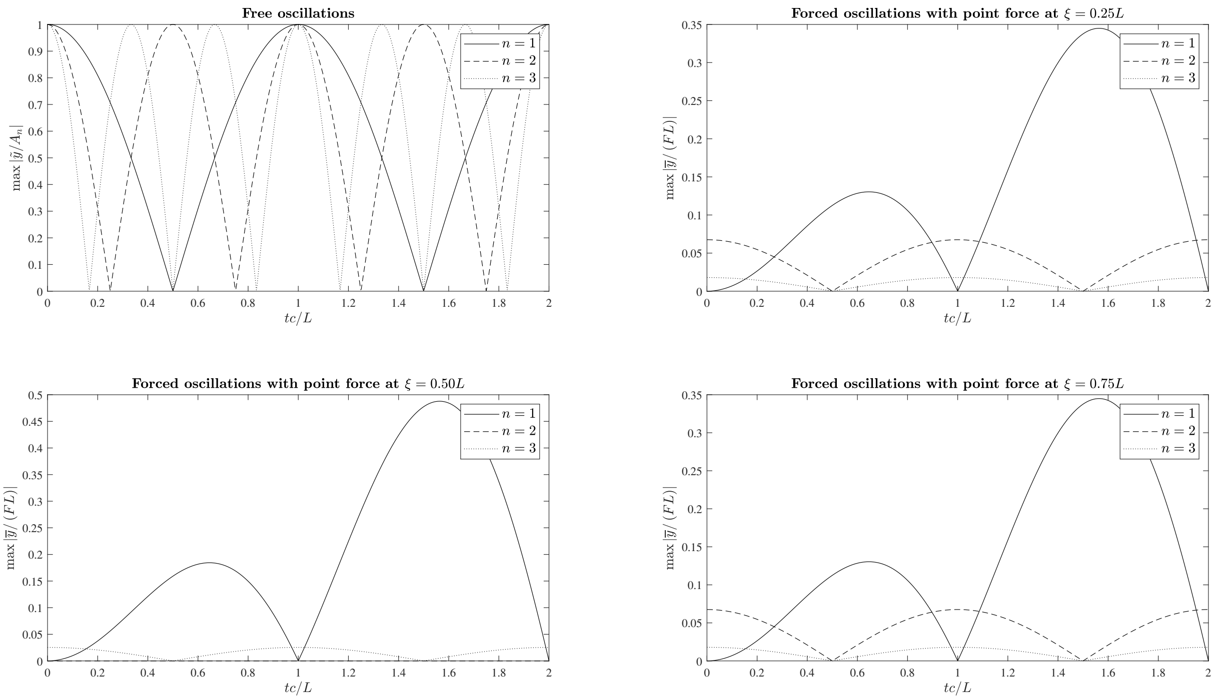

Figure 4.3: Maximum amplitude of the free or forced oscillations over time of a string fixed at the two ends and released without velocity, $\alpha_n = 0$. There is no phase shift of the applied force, $\beta = 0$. The frequency of the point force ω is equal to the first natural frequency of the free oscillation $\omega_1 = \pi c/L$.

The maximum amplitude of the free oscillations over time has also an oscillatory behaviour. Indeed, the maximum amplitudes over time can be deduced from (4.8), knowing the parameters α_n and A_n, and assuming the maximum value for $|\sin(k_n x)|$, equal to 1. Consequently, the maximum amplitude of free oscillations, for each mode of vibration n, is proportional to $\cos(\omega_n t - \alpha_n)$. Therefore, the maximum amplitude can reach the value A_n when $t = Lp/(nc) + L\alpha_n/(nc\pi)$ with p being a natural number. The number of times the maximum amplitude of the free oscillations occurs is greater when the value of n increases because the period of the oscillations is lower. These conclusions are similar when $\alpha_n \neq 0$.

The oscillatory behaviour is also present in the forced oscillations over time. The times at which the maximum amplitude occurs depend on the frequency of the applied force, not on its location, as shown in the figure 4.3 for $\beta = 0$. In this situation, all the non-resonant terms have maximum amplitude when $t = p\pi/\omega$ (in this case, when $t = Lp/c$) with p being a natural number. The maximum amplitudes occur when the applied oscillatory force is also maximum. Indeed, this result can be deduced from (4.21a) assuming $\cos(\omega t) = \pm 1$. For the non-resonant oscillations, the maximum amplitude is greater when k_n approaches the value k from the applied force (in the case of figure 4.3, the greatest amplitudes of non-resonant forced oscillations are for $n = 2$ because it is the mode of oscillation that is closest to the frequency of the applied force $n = 1$). However, this property is not always true due to the value

$\sin(k_n\xi)$. For instance, when the force is applied at the middle of the beam, $\xi = 0.5L$, the non-resonant oscillation for $n = 2$ is null (therefore, the oscillation for $n = 3$ is greater). This exception results from (4.21b) for the second term ($n = 2$), knowing that $\sin(k_2\xi) = 0$. The figure 4.3 also shows that the maximum amplitudes of the resonant term (in this case for $n = 1$) increases over time because of the term $\omega_m t$ in (4.21b). Also, the maximum amplitudes of the non-resonant oscillations happen when the resonant oscillation is zero, because when $\cos(\omega t) = \pm 1$, then $\sin(\omega t) = 0$. The maximum amplitudes of the resonant oscillation occur when $\sin(\omega t) + \omega t \cos(\omega t) = 0$. These conclusions are similar when $\beta \neq 0$.

Next it is investigated to what extent the forced oscillation can be used to reduce the energy of the free oscillation.

4.2 Minimisation of total (kinetic plus elastic) energy

The time average over a period τ is defined by [127]

$$\langle h(\omega t)\rangle \equiv \frac{1}{\tau}\int_0^\tau h(\omega t)\, \mathrm{d}t, \tag{4.22a}$$

and can be reduced to an integration along a unit circular arc, assuming the period τ as $2\pi/\omega$, specified by:

$$0 \le t < \tau = 2\pi/\omega \Leftrightarrow 0 \le \theta \equiv \omega t < \omega\tau = 2\pi. \tag{4.22b}$$

The total energy density per unit length averaged over a period,

$$\tilde{e}(x) = \frac{\rho}{2}\left\langle \left|\frac{\partial \tilde{y}(x,t)}{\partial t}\right|^2 \right\rangle + \frac{T}{2}\left\langle \left|\frac{\partial \tilde{y}(x,t)}{\partial x}\right|^2 \right\rangle, \tag{4.23}$$

is the sum of the kinetic energy [127] that involves the mass density per unit length ρ and of the elastic energy [129] that involves the tangential tension T. For a free oscillation with displacement (4.8), each mode n of vibration has period equal to $\tau = 2\pi/\omega_n$, as in (4.6c). The velocity has a mean square over a period given by

$$\left\langle \left|\frac{\partial \tilde{y}(x,t)}{\partial t}\right|^2 \right\rangle = \sum_{n=1}^{\infty}\sum_{r=1}^{\infty} A_n A_r \omega_n \omega_r \sin(k_n x)\sin(k_r x)\left\langle \sin(\omega_n t - \alpha_n)\sin(\omega_r t - \alpha_r)\right\rangle \tag{4.24a}$$

and the strain has a mean square over a period given by

$$\left\langle \left|\frac{\partial \tilde{y}(x,t)}{\partial x}\right|^2 \right\rangle = \sum_{n=1}^{\infty}\sum_{r=1}^{\infty} A_n A_r k_n k_r \cos(k_n x)\cos(k_r x)\left\langle \cos(\omega_n t - \alpha_n)\cos(\omega_r t - \alpha_r)\right\rangle. \tag{4.24b}$$

The average over a period of the product of sines and cosines with different phases is given by (B.1) and (B.2) in the appendix B, repeated here for convenience,

$$\left\langle \sin(\omega_n t - \alpha_n)\sin(\omega_r t - \alpha_r)\right\rangle = \frac{1}{2}\delta_{nr} = \left\langle \cos(\omega_n t - \alpha_n)\cos(\omega_r t - \alpha_r)\right\rangle \tag{4.25}$$

where δ_{nr} is the identity matrix. Hence the average kinetic energy is given by

$$\tilde{e}_{\mathrm{k}} \equiv \frac{\rho}{2}\left\langle\left|\frac{\partial \tilde{y}(x,t)}{\partial t}\right|^2\right\rangle = \frac{\rho}{4}\sum_{n=1}^{\infty}(\omega_n A_n)^2 \sin^2(k_n x), \tag{4.26a}$$

and the average elastic energy is equal to

$$\tilde{e}_{\mathrm{e}} \equiv \frac{T}{2}\left\langle\left|\frac{\partial \tilde{y}(x,t)}{\partial x}\right|^2\right\rangle = \frac{T}{4}\sum_{n=1}^{\infty}(k_n A_n)^2 \cos^2(k_n x). \tag{4.26b}$$

Using the wave speed (4.1a) in $\rho(\omega_n)^2 = \rho(k_n c)^2 = T k_n^2$, the total energy per unit length of string, which is the sum of average kinetic and elastic energies, is constant and equal to

$$\tilde{E} \equiv \frac{4\tilde{e}(x)}{T} = \frac{4\tilde{e}_{\mathrm{k}}(x) + 4\tilde{e}_{\mathrm{e}}(x)}{T} = \sum_{n=1}^{\infty}(A_n k_n)^2 > 0 \tag{4.27}$$

for the free oscillation.

The table 4.1 shows the total dimensionless energy density of the free oscillations along the string averaged over one period, for the first four modes of the vibration n. In this case, the total energy is constant along the string, not depending on explicit values of position x. The results of the table 4.1 are obtained from (4.27) which follows from the mean square velocity (4.26a) and the mean square strain (4.26b). To obtain the mean squares, the values of $\langle\sin(\omega_n t - \alpha_n)\sin(\omega_r t - \alpha_r)\rangle$ and $\langle\cos(\omega_n t - \alpha_n)\cos(\omega_r t - \alpha_r)\rangle$ were needed. The time averages of the product of sines and cosines are calculated over a period in appendix B; the period of both functions for the time average, $\sin(\omega_n t - \alpha_n)\sin(\omega_r t - \alpha_r)$ and $\cos(\omega_n t - \alpha_n)\cos(\omega_r t - \alpha_r)$, is $2L/c$ for any combination of the values n and r (although in some cases the lowest period is L/c or even lower). The phase shifts α_n and α_r do not change the period of both functions. Therefore, in the table 4.1, the first period is from $t = 0$ until $t = 2L/c$, the second period is from $t = 2L/c$ to $t = 4L/c$, and so on.

Order of vibration n	**First period**	**Second period**	**Third period**	**Fourth period**
$n = 1$	2.467	2.467	2.467	2.467
$n = 2$	9.870	9.870	9.870	9.870
$n = 3$	22.207	22.207	22.207	22.207
$n = 4$	39.478	39.478	39.478	39.478

Table 4.1: Total dimensionless energy density per unit length of the free oscillations averaged over some period. The first period is from $t = 0$ to $t = 2L/c$, the second period is from $t = 2L/c$ to $t = 4L/c$, and so on. The numerical results correspond to the dimensionless parameter $\tilde{e}L^2/\left(TA_n^2\right)$.

As indicated by the equation (4.27), the energy density is constant along the string for each mode of free oscillation n. The energy density increases with n^2 because k_n appears to the square in (4.27). Also modes with larger A_n (noting that A_n is always positive) contribute more to the energy. For the same value of A_n, modes of higher order n contribute more to the energy because k_n increases with n in the respective energy density. Another property is that the contribution of each mode of oscillation n

to the energy density is independent of the other modes of oscillation. Therefore, it is possible to show in a tabular form the contribution to the energy for each mode of oscillation separately, as outlined in the table 4.1. The energy remains unchanged when the oscillations advance one period, because the time averages have the same values, so the results in the table 4.1 are the same for different periods. Hence, the period used to perform the time average is irrelevant in the evaluation of the energy density of free oscillations.

The total energy averaged over a period for the forced oscillation is given by

$$\overline{e}(x) = \frac{1}{2}\rho \left\langle \left| \frac{\partial \overline{y}(x,t)}{\partial t} \right|^2 \right\rangle + \frac{1}{2} T \left\langle \left| \frac{\partial \overline{y}(x,t)}{\partial x} \right|^2 \right\rangle, \tag{4.28a}$$

leading by (4.12a) to

$$\overline{e}(x) = \frac{1}{4}\rho\omega^2 |B(x)|^2 + \frac{1}{4} T \left| \frac{\mathrm{d}B(x)}{\mathrm{d}x} \right|^2. \tag{4.28b}$$

To obtain the last result, one of the intermediate steps is to evaluate the time averages of $\sin^2(\omega t + \beta)$ and $\cos^2(\omega t + \beta)$ because, according to (4.12a), the forced oscillation is proportional to $\cos(\omega t + \beta)$. The period of both functions is $2\pi/\omega$ (although the lowest period is π/ω), noting that the phase shift of the applied force β does not change the period. Both time averages are equal to $1/2$, as shown in appendix B. Using (4.15a) in (4.28b), it follows that the energy of forced oscillations is

$$\overline{E} \equiv \frac{4\overline{e}(x)}{T} = k^2 \left[\sum_{n=1}^{\infty} b_n \sin(k_n x) \right]^2 + \left[\sum_{n=1}^{\infty} k_n b_n \cos(k_n x) \right]^2. \tag{4.29}$$

In the non-resonant case, where the frequency of the force ω is not equal to any of the natural frequencies of the free oscillation ω_n, the equation (4.15b), for which $k \neq k_n$, leads to

$$\overline{E} = k^2 \left[\frac{2F}{L} \sum_{n=1}^{\infty} \frac{1}{k^2 - k_n^2} \sin(k_n \xi) \sin(k_n x) \right]^2 + \left[\frac{2F}{L} \sum_{n=1}^{\infty} \frac{k_n}{k^2 - k_n^2} \sin(k_n \xi) \cos(k_n x) \right]^2 > 0, \tag{4.30}$$

showing that the total energy density of the forced oscillation (4.30) is not constant along the string, unlike for the free oscillation (4.27), although both are positive. Moreover, the external force supplies energy to all forced n modes of oscillation, in contrast with the free oscillations, where in some n modes the contribution to the energy is zero when $A_n = 0$.

The figure 4.4 shows the dimensionless energy density of the forced oscillations along the string averaged over some period, for the first tree modes of the vibration n. The results are obtained from (4.30). Contrary to the free oscillations, the energy of forced oscillations for a certain mode n is coupled to the energy of all other modes of oscillation, as shown in (4.30). It is not possible to plot the energy for a single mode of oscillation, in contrast to the table 4.1 in which the energy values are indicated for each mode separately. Therefore, in the figure 4.4: the solid line represents the contribution of the first mode of oscillation, $n = 1$; the dashed line corresponds to the first two modes of oscillation, $n = 1$ and $n = 2$ combined, as if the two series in (4.30) were truncated after the second term; the dotted line is obtained with the same two series truncated after the third term, $n = 1$ to $n = 3$. As explained before, the period

τ in which the time averages were performed is $2\pi/\omega$. Hence, in the figure 4.4, specifically in the upper plots, the period 1 is from $t = 0$ until $t = 2\pi/\omega$ and the period 2 is from $t = 2\pi/\omega$ until $t = 4\pi/\omega$.

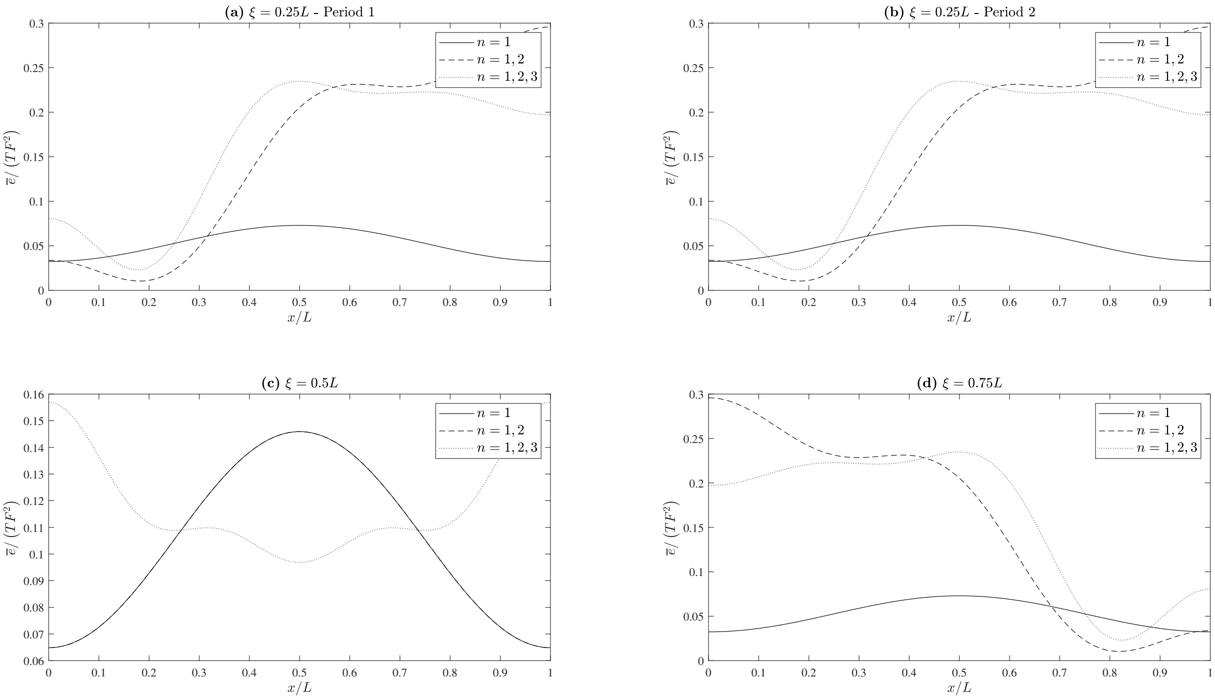

Figure 4.4: Total dimensionless energy density per unit length of the forced oscillations averaged over some period. The period 1 is from $t = 0$ to $t = 2\pi/\omega$, the period 2 is from $t = 2\pi/\omega$ to $t = 4\pi/\omega$, and so on. The force is applied at $x = 0.25L$, $x = 0.5L$ or $x = 0.75L$. In this figure, ω is equal to $1.5\pi c/L$, hence not being equal to any of the natural frequencies ω_n of the free oscillations.

As indicated by the equation (4.30), the energy density is not constant along the string and exhibits an almost oscillatory behaviour. The plots also show that using only the first three terms in the series of (4.30) is not accurate to represent the energy density and therefore more terms of the series should be used. The contribution of each mode of oscillation n to the forced energy density is coupled to all the other modes. Similar to the free oscillations, the energy remains unchanged when the forced oscillations advance one period, hence the upper plots of the figure 4.4 are the same for different periods. Consequently, the period used to perform the time average is also irrelevant in the evaluation of the energy density of forced oscillations (that is the reason why in the bottom plots the period number is not stated because they are equal whatever the period). This property holds for any location ξ and frequency ω of the applied force.

Concerning the total energy of the total or combined (free plus forced) oscillation,

$$e(x) = \frac{1}{2}\rho \left\langle \left| \frac{\partial y(x,t)}{\partial t} \right|^2 \right\rangle + \frac{1}{2} T \left\langle \left| \frac{\partial y(x,t)}{\partial x} \right|^2 \right\rangle, \tag{4.31}$$

since in the outside resonance the frequencies are different with $\omega \neq \omega_n$, the cross-products of sines and cosines have zero average over a period if the ratio of ω to some natural frequency ω_n is equal to a rational number. Recalling the equations (B.3) to (B.5) in the appendix B, repeated here for convenience,

$$\langle \cos(\omega_n t - \alpha_n) \cos(\omega t + \beta) \rangle = 0 = \langle \sin(\omega_n t - \alpha_n) \sin(\omega t + \beta) \rangle, \tag{4.32}$$

the energy is the sum of the parts due to the free and forced oscillations,

$$e(x) = \tilde{e}(x) + \overline{e}(x), \tag{4.33a}$$

with

$$E = \frac{4e(x)}{T} = \tilde{E} + \overline{E} > \tilde{E}. \tag{4.33b}$$

If the frequency of the force ω is not equal to some rational number times the natural frequency ω_n, the functions $\cos(\omega_n t - \alpha_n)\cos(\omega t + \beta)$ and $\sin(\omega_n t - \alpha_n)\sin(\omega t + \beta)$ may not be periodic and consequently their time averages to evaluate the integral in (4.22a) may result in a non-zero value. In that case, an additional term appear on the right-hand side of (4.33a) that represents the coupling between free and forced oscillations. Anyway, if starting with a free vibration consisting of normal modes, forcing at any other frequency will only serve to increase the energy. Thus, if the energy of the free oscillation can be reduced at all, it must be through forcing at a natural frequency, which then leads to resonance. It is investigated next whether it is feasible or not to prevent energy growth at an undamped resonance condition, and for how long.

Concerning forcing at a natural frequency with $\omega = \omega_m$, the functions $\cos(\omega_n t - \alpha_n)\cos(\omega_m t - \alpha_m)$ and $\sin(\omega_n t - \alpha_n)\sin(\omega_m t - \alpha_m)$, for all terms $n \neq m$, are always periodic (appendix B) with $\tau = 2L/c$ (it may not be the lowest period). Hence, the result (4.32) holds when $\omega = \omega_m$ for certain m. Then, forcing at a natural frequency, for all terms $n \neq m$, leads to the same result (4.33b) as before; the energies of the free and non-resonant forced oscillations add up to (4.33b), however there are also additional terms due to the coupling between free and forced resonant oscillations that are not considered in the final expression of the total energy. If A_m is much greater than any other amplitude A_n, it can be singled out for further analysis only the resonant term, specifically the second term on the right-hand side of (4.21b):

$$y_m(x,t) = \sin(k_m x)\left\{A_m \cos(\omega_m t - \alpha_m) - \frac{F}{k_m^2 L}\sin(k_m \xi)\,\omega_m t \sin(\omega_m t + \beta)\right\}. \tag{4.34}$$

The subscript m can be omitted in the sequel, corresponding to the change of notation $\{k_m, \omega_m, A_m, \alpha_m\}$ to $\{k, \omega, A, \alpha\}$, which cannot cause any confusion henceforth.

The total energy (kinetic plus elastic) of the total (free plus forced) resonant oscillation, for the resonant mode $n = m$, written explicitly in (4.34), is

$$\frac{2e_m}{\rho} = \left\langle \left|\frac{\partial y_m(x,t)}{\partial t}\right|^2 \right\rangle + c^2 \left\langle \left|\frac{\partial y_m(x,t)}{\partial x}\right|^2 \right\rangle. \tag{4.35}$$

It involves two terms: the first term, evaluated for the first period, is

$$\begin{aligned}\left\langle \left|\frac{\partial y_m(x,t)}{\partial x}\right|^2 \right\rangle = k^2 \cos^2(kx)\Bigg\{ & A^2 \left\langle \cos^2(\omega t - \alpha)\right\rangle + \left(\frac{F}{k^2 L}\right)^2 \sin^2(k\xi)\left\langle (\omega t)^2 \sin^2(\omega t + \beta)\right\rangle \\ & - 2\left(\frac{AF}{k^2 L}\right)\sin(k\xi)\left\langle (\omega t)\cos(\omega t - \alpha)\sin(\omega t + \beta)\right\rangle \Bigg\}\end{aligned} \tag{4.36a}$$

and the second term, also evaluated for the first period, is

$$\left\langle \left| \frac{\partial y_m(x,t)}{\partial t} \right|^2 \right\rangle = \omega^2 \sin^2(kx) \left\{ A^2 \left\langle \sin^2(\omega t - \alpha) \right\rangle \right.$$
$$+ \left(\frac{F}{k^2 L} \right)^2 \sin^2(k\xi) \left\langle \left[\sin(\omega t + \beta) + (\omega t) \cos(\omega t + \beta) \right]^2 \right\rangle$$
$$\left. + 2 \left(\frac{AF}{k^2 L} \right) \sin(k\xi) \left\langle \sin(\omega t - \alpha) \left[\sin(\omega t + \beta) + (\omega t) \cos(\omega t + \beta) \right] \right\rangle \right\} . \quad (4.36b)$$

In the last two equations appear the following averages over a period $2\pi/\omega = 2L/(mc)$, evaluated in appendix B as (B.6) to (B.11b). The first result,

$$\left\langle \cos^2(\omega t - \alpha) \right\rangle = \frac{1}{2} = \left\langle \sin^2(\omega t - \alpha) \right\rangle , \quad (4.37a)$$

is independent of the period (for instance, if the integral in (4.22a) is evaluated from $t = 2L/(mc)$ to $t = 4L/(mc)$, the last result would be equal). Since the last result is independent of the period, the last time average can be evaluated from $t = 0$ to $t = 2\pi/\omega$ because $\tau = 2\pi/\omega$ is always a period of the function, regardless the value of α. In the calculation of the energy of forced resonant oscillations, the following averages over a period are also needed:

$$\left\langle \omega t \cos(\omega t - \alpha) \sin(\omega t + \beta) \right\rangle = \frac{\pi}{2} \sin(\alpha + \beta) - \frac{1}{4} \cos(\beta - \alpha) , \quad (4.37b)$$

$$\left\langle (\omega t)^2 \sin^2(\omega t + \beta) \right\rangle = \frac{2\pi^2}{3} - \frac{\pi}{2} \sin(2\beta) - \frac{1}{4} \cos(2\beta) , \quad (4.37c)$$

$$\left\langle \left[\sin(\omega t + \beta) + \omega t \cos(\omega t + \beta) \right]^2 \right\rangle = \frac{1}{2} + \frac{2\pi^2}{3} + \frac{\pi}{2} \sin(2\beta) - \frac{1}{4} \cos(2\beta) , \quad (4.37d)$$

$$\left\langle \sin(\omega t - \alpha) \left[\sin(\omega t + \beta) + \omega t \cos(\omega t + \beta) \right] \right\rangle = \frac{\cos(\alpha + \beta)}{2} - \frac{\cos(\beta - \alpha)}{4} - \frac{\pi}{2} \sin(\alpha + \beta) . \quad (4.37e)$$

These last results are only valid for the first "period", that is, when the integral (4.22a) is evaluated from $t = 0$ to $t = 2\pi/\omega$. Indeed, none of the last functions to do the time average are periodic functions, due to the term ωt. However, the results are deduced assuming $\tau = 2\pi/\omega$. Substitution of (4.37a) to (4.37e) in the total resonant energy equation (4.35) shows that the total energy in the resonant case, averaged over the first period, depends on phase values and on position of the applied force:

$$\frac{2e_m(x)}{\rho\omega^2} = \frac{A^2}{2} + \left(\frac{F}{k^2 L} \right)^2 \sin^2(k\xi) \left[\frac{2\pi^2}{3} + \frac{1}{2} \sin^2(kx) \right]$$
$$+ \left(\frac{AF}{2k^2 L} \right) \sin(k\xi) \left[\cos(\beta - \alpha) \cos(2kx) + 2\cos(\alpha + \beta) \sin^2(kx) - 2\pi \sin(\alpha + \beta) \right]$$
$$- \left(\frac{F}{2k^2 L} \right)^2 \sin^2(k\xi) \left[\cos(2\beta) + 2\pi \sin(2\beta) \cos(2kx) \right] . \quad (4.38)$$

The phase α of the free oscillation can be set to zero by suitable choice of initial time. The total energy of the free plus forced resonant oscillation has four terms on the right-hand side of (4.38): (i) the first is the energy of the free oscillation; (ii) the second term, being non-negative, adds to the total energy, and is independent of the phases α and β; (iii) in the third term, when $\alpha = 0$, the factor in square brackets is simplified to $\cos\beta - 2\pi\sin\beta$, and hence this term does not have a fixed sign, but reduces the total energy most for the forcing phase shift $\beta = 2\arctan\left[\left(1+\sqrt{1+4\pi^2}\right)(2\pi)^{-1}\right]$, when the factor in square brackets is $-\left(1+4\pi^2\right)\left(1+\sqrt{1+4\pi^2}\right)\left(1+4\pi^2+\sqrt{1+4\pi^2}\right)^{-1} \approx -6.362$; (iv) the fourth term does not depend on the phase of free oscillations, does not have a fixed sign and the reduction of the total energy due to that term depends not only on the phase β, but also on the value kx. For instance, choosing the phases $\alpha = 0$ and $\beta = 0$, the total energy is simplified to

$$\frac{2e_m(x)}{\rho\omega^2} = \frac{A^2}{2} + \left(\frac{F}{2k^2L}\right)^2 \sin^2(k\xi)\left[\frac{8\pi^2}{3} - \cos(2kx)\right] + \left(\frac{AF}{2k^2L}\right)\sin(k\xi). \tag{4.39}$$

The figure 4.5 shows the dimensionless energy density of the total resonant oscillation (4.34) along the string averaged over one period, for the resonant mode of oscillation $n = m$. For the first period, the upper left plots of the figure 4.5 are obtained from (4.39). The only difference to the other periods are the results of the time averages in (4.37b) to (4.37e). Independently of the period, the energy of the resonant oscillation e_m has always three terms (as in (4.39) for the first period).

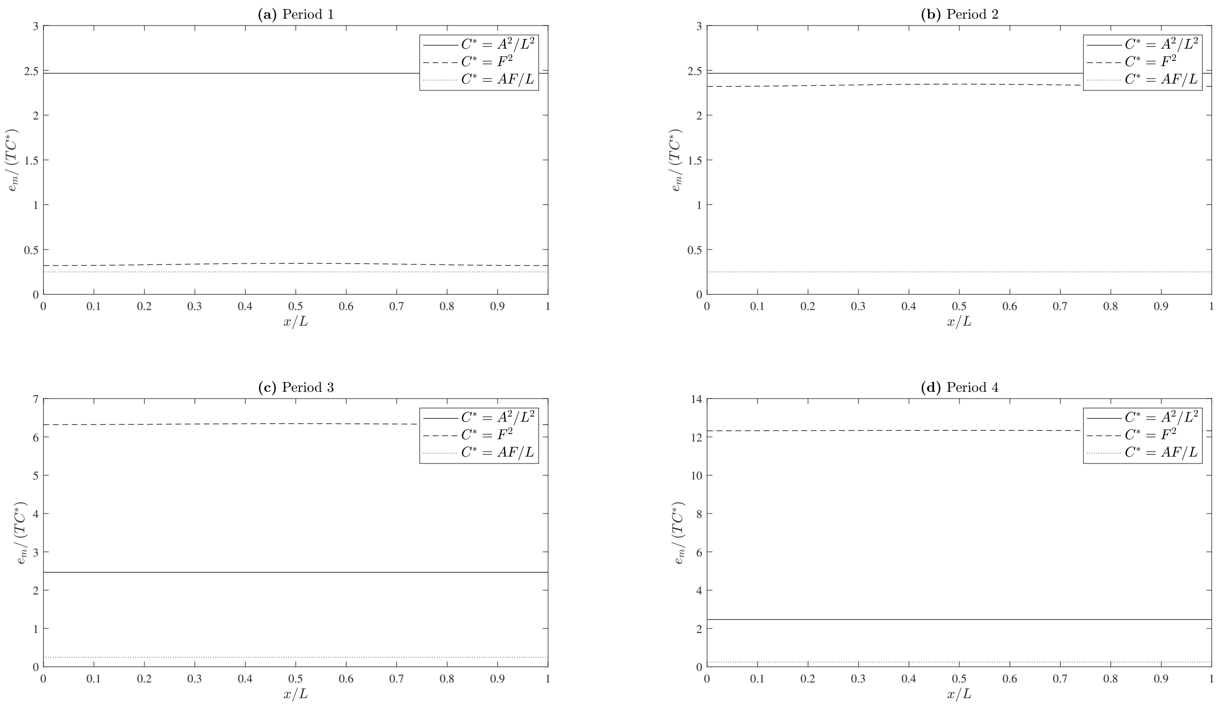

Figure 4.5: Total dimensionless energy density per unit length of the free plus forced resonant oscillations averaged over one period. The frequency of the force ω is equal to $\pi c/L$, that is, equal to the first natural frequency ω_1. The period 1 is from $t = 0$ to $t = 2L/c$, the period 2 is from $t = 2L/c$ to $t = 4L/c$, and so on. The force is applied at $x = 0.5L$. The solid line represents the term of the resonant energy e_m proportional to A^2/L^2, the dashed line represents the term proportional to F^2 and the dotted line corresponds to the term proportional to AF/L. The plots are obtained with $\alpha = 0 = \beta$.

One term is proportional to A^2/L^2 and represents the free oscillation for the resonant mode of oscillation $n = m$. It is represented by the solid lines in the figure 4.5. As usual with free oscillations, it is constant along the string and does not change with the period. A second term is proportional to F^2 and is due to the forced oscillation in the resonant mode. It corresponds to the dashed lines. As usual with forced oscillations, it is not constant along the string and has an oscillatory term, not dominant because $\cos(2kx) \leq 1 \ll 8\pi^2/3 \approx 26.32$ in (4.39). It also changes with the period because of the time averages (4.37b) to (4.37e) that appear in this contribution. The last term is proportional to AF/L and corresponds to the dotted lines. This term represents the coupling between free and forced oscillations in the resonant energy. It is constant along the string and does not change with the period when $\alpha = 0 = \beta$ as in the figure 4.5 (nevertheless, when any of the phase shits is not zero, the term can be not constant along the string). The second and third terms can be negative, useful to reduce the energy e_m, if one chooses other values for α and β. Furthermore, the second term is proportional to $1/k^4$ while the third term is proportional to $1/k^2$; therefore, both terms are dependent on the square of the frequency of the force ω^2. Therefore, for different frequencies of the force, the numeric values would be different, but the shape of the plots (constant for the solid and dotted lines; oscillatory for the dashed line) are unchanged.

Bearing in mind that (4.39) is the resonant energy density, or energy per unit length, for $\alpha = 0 = \beta$, the total resonant energy for the string of length L (with the next definition, the dimensions are m^2),

$$G(F,\xi) \equiv \frac{2}{\rho\omega^2 L}\int_0^L e_m(x)\,\mathrm{d}x, \tag{4.40a}$$

is given by

$$G = \frac{1}{2}A^2 + \left(\frac{F}{k^2 L}\right)^2 \sin^2(k\xi) + \left(\frac{AF}{2k^2 L}\right)\sin(k\xi). \tag{4.40b}$$

The term “total” energy has been used with three distinct meanings: (i) kinetic plus elastic energies; (ii) energy of the total or combined oscillation, that is free plus forced oscillation; (iii) energy of the string, that is energy density integrated over its length. The function (4.40b), to be optimised, is the “total” energy in all of these three senses, that is the kinetic plus elastic energy density, averaged over one period, for the free plus forced resonant oscillation, integrated along the length of the string. This total energy should be minimised, by optimising the magnitude F and location ξ of the force; the aim is to check whether, due to the presence of resonant forcing, the total resonant energy over the first period (4.40b), can be made smaller than the energy $A^2/2$ of the free oscillation in the first term.

4.3 Optimisation of strength and location of forcing effect

Consider first the dependence of the total energy (4.40b), with respect to the magnitude F of the applied force. The latter $F = F_+$ is chosen in order to minimise the energy, accomplishing the conditions $\partial G/(\partial F_+) = 0$ and $\partial^2 G/\left(\partial F_+^2\right) > 0$. From (4.40b) it follows that the energy does have a minimum with respect to the magnitude of the force,

$$\frac{\partial^2 G}{\partial F^2} = \frac{4\pi^2}{3k^4 L^2}\sin^2(k\xi) > 0. \tag{4.41}$$

when $\sin(k\xi) \neq 0$. Equating to zero the first derivative of the total energy,

$$\frac{\partial G}{\partial F} = \sin(k\xi)\left[\frac{4\pi^2 F}{3k^4 L^2}\sin(k\xi) + \frac{A}{2k^2 L}\right], \tag{4.42a}$$

specifies the magnitude of the optimal force,

$$F_+ = -\frac{3}{8\pi^2} k^2 L A \csc(k\xi), \tag{4.42b}$$

which minimises the total energy:

$$G_+ \equiv G(F_+, \xi) = \frac{1}{2} A^2 \left(1 - \frac{3}{16\pi^2}\right). \tag{4.42c}$$

This optimal result does not depend on the point of application of the force. Compared with the energy of the free oscillation,

$$G_0 = \frac{1}{2} A^2, \tag{4.43a}$$

optimal forcing at resonance provides a very small reduction of energy,

$$\frac{G_+}{G_0} = 1 - \frac{3}{16\pi^2} = 0.981, \tag{4.43b}$$

of less than 2%, over the first period. Since resonant forcing causes an oscillation of amplitude increasing with time, it is clear that even with optimal forcing, the total energy will exceed that of the free vibration, for a time span slightly longer than a period. Thus, active suppression of a normal mode by a resonant point force can be achieved very marginally, for a time span of at most one period.

It is shown next that the total energy has a maximum with respect to the point of application ξ of the concentrated force, following the conditions $\partial G / (\partial \xi_\pm) = 0$ and $\partial^2 G / \left(\partial \xi_\pm^2\right) < 0$. Substituting (4.40b) in the first condition of optimisation leads to

$$0 = \frac{\partial G}{\partial \xi} = \frac{F}{kL} \cos(k\xi) \left[\frac{A}{2} + \frac{4\pi^2}{3} \left(\frac{F}{k^2 L}\right) \sin(k\xi)\right]. \tag{4.44}$$

There are two sets of stationary values: one coincident with (4.42b),

$$\sin(k\xi_+) = -\frac{3}{8\pi^2} \frac{A k^2 L}{F_+}, \tag{4.45a}$$

and one different,

$$\cos(k\xi_-) = 0. \tag{4.45b}$$

Since the minimisation with regard to F did not depend on ξ in (4.42c), it may be expected that the second set (4.45b) is not a minimum. Indeed, from (4.40b) or (4.44), it follows that

$$\frac{\partial^2 G}{\partial \xi^2} = -\frac{AF}{2L} \sin(k\xi) + \frac{4\pi^2}{3} \left(\frac{F}{kL}\right)^2 \left[1 - 2\sin^2(k\xi)\right]. \tag{4.46}$$

In particular for the second set of roots (4.45b), it implies $\sin(k\xi_-) = \pm 1$, and the second condition of optimisation leads to

$$\left.\frac{\partial^2 G}{\partial \xi^2}\right|_{\xi = \xi_-} = \frac{F}{2L} \left[\mp A - \frac{8\pi^2}{3} \left(\frac{F}{k^2 L}\right)\right]; \tag{4.47a}$$

where the last expression must be positive; however the last expression is negative with $-$ sign in A for a positive force $F > 0$ or when $F < -3Ak^2L/\left(8\pi^2\right)$ and the last expression with $+$ sign is also negative for a negative force $F < 0$ or when $F > 3Ak^2L/\left(8\pi^2\right)$, so the second condition of optimisation is not always met. For the first set of roots (4.45a),

$$\left.\frac{\partial^2 G}{\partial \xi^2}\right|_{\xi=\xi_+} = \frac{1}{3}\left(\frac{2\pi F}{kL}\right)^2 - 3\left(\frac{kA}{4\pi}\right)^2 = \frac{4\pi^2}{3k^2L^2}\left[F^2 - \left(\frac{3k^2LA}{8\pi^2}\right)^2\right] < 0, \tag{4.47b}$$

so the second condition of optimisation is met for $|F| < 3Ak^2L/\left(8\pi^2\right)$. Thus, the case $F = F_+$ is a minimum at constant ξ, but $\xi = \xi_+$ can be a maximum at constant F. The critical point $\xi = \xi_-$ at constant F in (4.45b) would correspond in (4.42b) to

$$F_- = -\frac{3k^2LA}{8\pi^2}\csc\left(k\xi_-\right) = \mp\frac{3k^2LA}{8\pi^2}. \tag{4.48}$$

The minimum for F in (4.42b) with ξ fixed, and the critical point for ξ in (4.45a) and (4.45b) with F fixed, are particular cases of the general case when both F and ξ can vary.

The most general approach is to regard the total energy (4.40b) as a joint function of magnitude F and location ξ of the applied force, so that the conditions of stationarity are $\partial G/\left(\partial F\right) = 0$ and $\partial G/\left(\partial \xi\right) = 0$. The condition related to being a maximum or minimum is related to the second-order differential equal to

$$\mathrm{d}^2 G = \left(\frac{\partial^2 G}{\partial F^2}\right)\mathrm{d}F^2 + \left(\frac{\partial^2 G}{\partial \xi^2}\right)\mathrm{d}\xi^2 + 2\left(\frac{\partial^2 G}{\partial F \partial \xi}\right)\mathrm{d}F\mathrm{d}\xi. \tag{4.49}$$

The second-order differential specifies (i) a local minimum if it is positive, (ii) a maximum if it is negative, and (iii) an inflexion or higher-order extremum if it is zero. Since G is (a) maximum or minimum with regard to ξ at fixed F and (b) minimum with regard to F at fixed ξ, this suggests the case (iii) of inflexion or higher-order extremum, with the condition

$$\Delta \equiv \begin{vmatrix} \partial^2 G/\partial F^2 & \partial^2 G/\partial F \partial \xi \\ \partial^2 G/\partial F \partial \xi & \partial^2 G/\partial \xi^2 \end{vmatrix} = 0. \tag{4.50}$$

The condition (4.50) involves a cross-derivate which can be evaluated from (4.42a) leading to

$$\frac{\partial^2 G}{\partial F \partial \xi} = \cos\left(k\xi\right)\left[\frac{8\pi^2 F}{3k^3L^2}\sin\left(k\xi\right) - \frac{A}{2kL}\right]. \tag{4.51}$$

The second order derivatives of (4.40b) in (4.41), (4.46) and (4.51) are given, for the case (4.42b) equivalent to (4.45a), which includes (4.48), by:

$$\left.\frac{\partial^2 G}{\partial F^2}\right|_{\xi=\xi_+} = 3\left(\frac{A}{4\pi F}\right)^2, \tag{4.52a}$$

$$\left.\frac{\partial^2 G}{\partial \xi^2}\right|_{\xi=\xi_+} = \frac{1}{3}\left(\frac{2\pi F}{kL}\right)^2 - 3\left(\frac{kA}{4\pi}\right)^2, \tag{4.52b}$$

$$\left.\frac{\partial^2 G}{\partial F \partial \xi}\right|_{\xi=\xi_+} = \mp \frac{A}{2kL}\left[1 - \left(\frac{3k^2 LA}{8\pi^2 F}\right)^2\right]^{1/2}. \tag{4.52c}$$

It can be checked that the determinant is zero, independent of the value of F,

$$\Delta = \frac{\partial^2 G}{\partial F^2}\frac{\partial^2 G}{\partial \xi^2} - \left(\frac{\partial^2 G}{\partial F \partial \xi}\right)^2 = 0, \tag{4.53}$$

confirming (4.50).

The figure 4.6 provides an overview of the total resonant energy, given by (4.40b), in the plane of the parameters F/L and ξ/L, the last one between 0 and 1. The values of the contour lines result from the difference between the total resonant energy and the free oscillation energy, that is, $G - A^2/2$, for the first period. It means that the value 0 of the contour plot happens when the sum of forced and coupled resonant energy is zero, in other words, when the total resonant energy equals only the free oscillation energy, $G = A^2/2$. The values of the contour plots depend also on the explicit value of A, because of the third term of (4.40b). In this case, the figure 4.6 is obtained setting $A = 1$. Each plot corresponds to a different resonant frequency. For example, the upper left plot of the figure 4.6 corresponds to the frequency of the applied force ω equal to the first natural frequency of the free oscillation, ω_1. The thick red line highlights the combination of the values of the parameters F/L and ξ/L for a minimum possible resonant energy G.

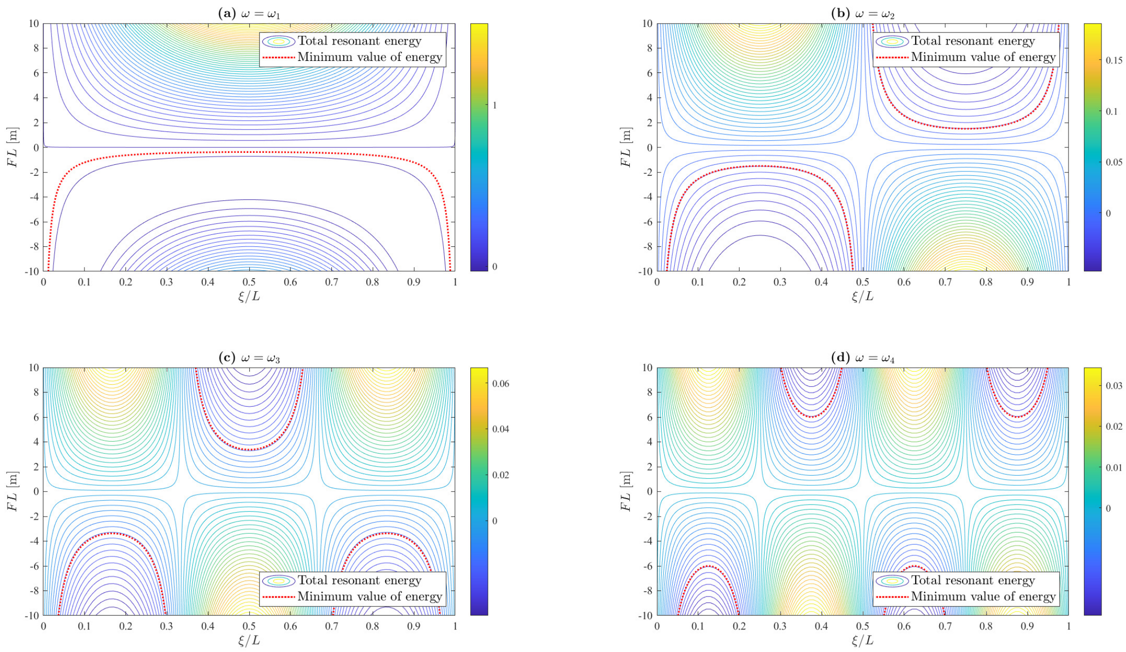

Figure 4.6: Difference between the total resonant energy G, given by (4.40b), and the free oscillation energy $A^2/2$, in m^2, for a given pair of the parameters $(\xi/L, F/L)$. The thick red line represents the combination of the values of ξ/L and F/L to obtain the minimum possible resonant energy G. Each plot corresponds to a different resonant frequency. The plots are obtained for $A = L$.

Although the resonant energy depends on the two parameters F and ξ simultaneously, according to (4.40b), the parameters are combined only in the form $F \sin(k\xi)$. The resonant energy can be interpreted as a quadratic equation of the combined parameter $F\sin(k\xi)$, that is, $G = c_1\left[F\sin(k\xi)\right]^2 + c_2\left[F\sin(k\xi)\right] + c_3$ with $c_1 > 0$. Consequently, the minimum of the value of the resonant energy G is given by $F\sin(k\xi) = -c_2/(2c_1)$ which corresponds to the equation (4.42b) and to the thick red lines presented in the figure 4.6. The figure shows therefore that the minimum value of the resonant energy can be obtained with a force applied at any position of the string, except at the points where $\sin(kx) = 0$. In those positions, regardless the value of the applied force F, the resonant energy equals the free oscillation energy, $G = A^2/2$, the same effect as if there is no applied force, $F = 0$. The contour values, as mentioned before, depend on the value of A; the minimum value of G, according to (4.42c), also depends on the value of A. Furthermore, due to the thick red lines of the figure 4.6, there are infinite combinations of the values of both parameters to get the minimum possible resonant energy. Observing the red lines, to reduce the resonant energy, the point force must be applied at a position where $\cos(kx) = 0$ if it is intended that the force has the lowest possible value. For instance, when $\omega = \omega_1$, the best position to apply a force is at the middle of the string. The worst locations to apply a force are in the vicinity of the positions where $\sin(kx) = 0$ that are the ends of the string. The number of these best or worst locations to apply a force increases with the resonant frequency. Moreover, when the frequency ω increases, looking at the red dashed lines in the figure 4.6, the value of the force $|F|$ to minimise G also increases. This observation agrees with the equation (4.42b) since F increases for a greater value of k or ω.

4.4 Oscillation and energy for optimal and non-optimal forcing

The free vibrations of an elastic string consist of a superposition of normal modes. The question addressed in this chapter is whether forcing can be used to suppress totally normal modes, or in a case of failing that, at least reduce the energy of the total free plus forced oscillation relative to the energy of the free oscillation alone. Clearly, forcing at a frequency distinct from all natural frequencies will not do: it does not couple to the free motion and just increases the total energy. Forcing at a natural frequency will cause resonance, that is an amplitude increasing linearly with time, for the forced vibration,

$$\overline{y}(x,t) = -\frac{F}{k^2 L}\sin(k\xi)\sin(kx)\,\omega t\sin(\omega t)\,, \tag{4.54a}$$

compared to the free vibration

$$\tilde{y}(x,t) = A\sin(kx)\cos(\omega t)\,. \tag{4.54b}$$

The phases are zero in the last two relations. The total energy over the first period can be marginally reduced regarding (4.42b) if

$$F = -\varepsilon_0 A k^2 L\csc(k\xi)\,, \tag{4.55a}$$

with

$$\varepsilon_0 \equiv \frac{3}{8\pi^2} \approx 0.038, \tag{4.55b}$$

but for longer time spans it will be increased by any choice of the magnitude of the forcing. The preceding result holds optimising the magnitude F of the forcing at a fixed location.

The total or combined oscillation is given by

$$y(x,t) = \tilde{y}(x,t) + \overline{y}(x,t) = \sin(kx)\left[A\cos(\omega t) - \frac{F}{k^2 L}\sin(k\xi)\,\omega t \sin(\omega t)\right], \tag{4.56}$$

which can be written in the form

$$y(x,t) = A\sin(kx)\,g(\theta,\varepsilon) \tag{4.57a}$$

with the independent variable θ defined by $\theta \equiv \omega t$ in (4.22b) and the other independent variable ε as

$$\varepsilon \equiv F/\left(Ak^2 L\right)\sin(k\xi), \tag{4.57b}$$

leading to

$$g(\theta,\varepsilon) \equiv \cos\theta + \varepsilon\theta\sin\theta, \tag{4.57c}$$

where all the time dependence appears in (4.57c). The equation $h(\theta,\varepsilon) \equiv [g(\theta,\varepsilon)]^2$ gives an indication of the energy. The functions g and h are plotted respectively in figures 4.7 and 4.8 for small values of ε around ε_0 in (4.55b):

$$\varepsilon = \{0.00, 0.01, 0.02, 0.03, \varepsilon_0, 0.04, 0.05, 0.06, 0.07, 0.08, 0.09, 0.10\}; \tag{4.58}$$

the thick line corresponds to ε_0 and leads to the oscillation (in figure 4.7) with the smallest energy or area below the curve in figure 4.8. For larger values of ε (except $\varepsilon = 0.0$), specifically

$$\varepsilon = \{0.0, 0.1, 0.2, 0.3, 0.4, 0.5, 0.6, 0.7, 0.8, 0.9, 1.0\}, \tag{4.59}$$

the resonance dominates the total oscillation even in the first period, leading to large amplitude (in figure 4.9) and energy (in figure 4.10).

The conclusion that the energy of the combined oscillation cannot be kept below the energy of the free oscillation, for much longer than a period, applies to a single concentrated force. Use of several concentrated forces or a distributed force would be possible also, and is investigated next.

4.5 Forcing by multiple concentrated forces

In the case of M forces F_m concentrated at the points $x = \xi_m$ with $m = 1, \ldots, M$, the undamped resonant response (4.54a) would be replaced by

$$\overline{y}(x,t) = -\frac{1}{k^2 L}\sin(kx)\,\omega t\sin(\omega t)\sum_{m=1}^{M} F_m \sin(k\xi_m). \tag{4.60}$$

This is equivalent by (4.54a) to a single force F concentrated at ξ, such that

$$F\sin(k\xi) = \sum_{m=1}^{M} F_m \sin(k\xi_m). \tag{4.61}$$

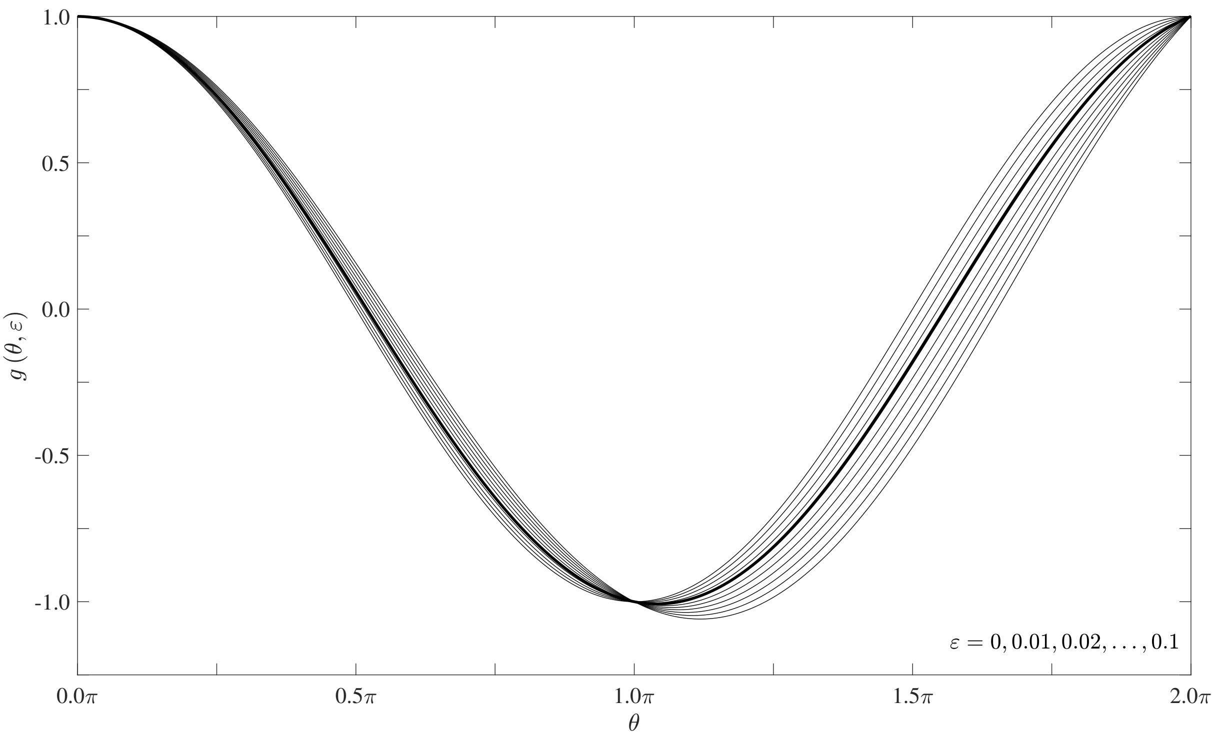

Figure 4.7: Peak spatial amplitude of the oscillation of the string, normalised to free oscillation amplitude, as a function of dimensionless time $\theta \equiv \omega t = 2\pi t/\tau$ over one period $0 \leq t \leq \tau$ or $0 \leq \theta \leq 2\pi$. The magnitude of forcing relative to the amplitude of free oscillation is given with values around the optimum for minimum total energy (thick line).

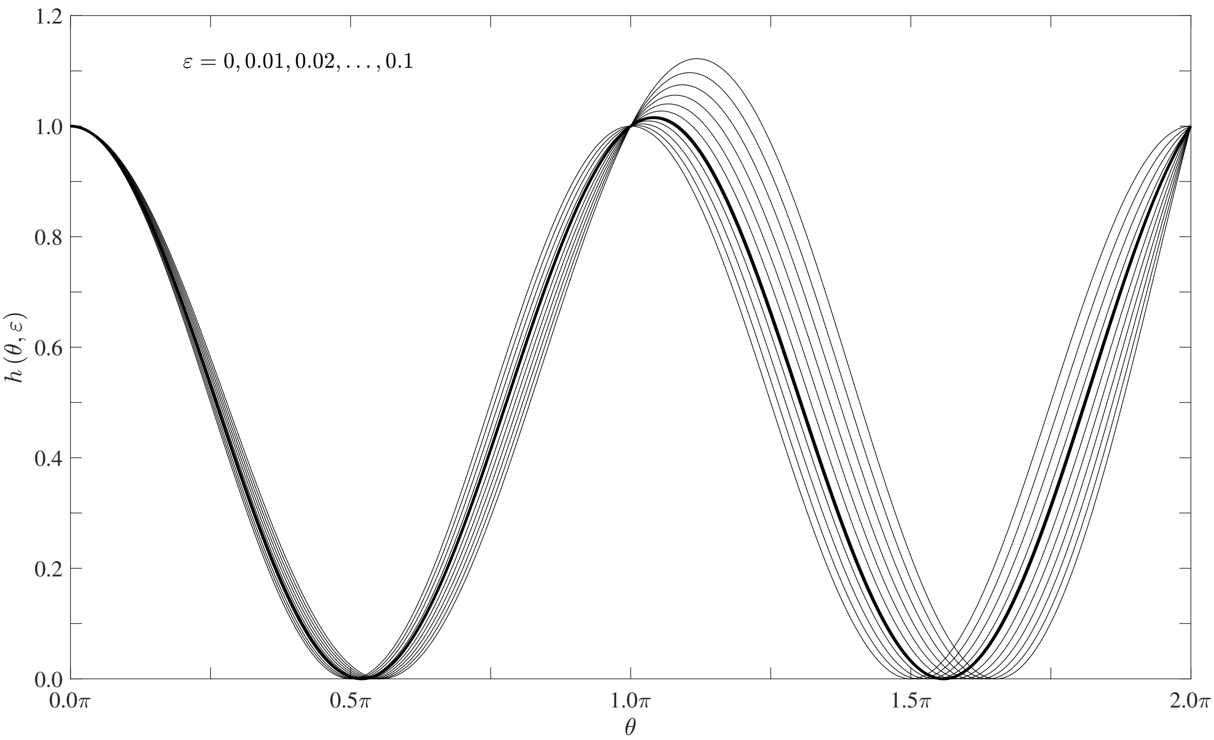

Figure 4.8: As in figure 4.7 for the square of peak spatial amplitude of the oscillation of the string, normalised to free oscillation amplitude, representing dimensionless energy.

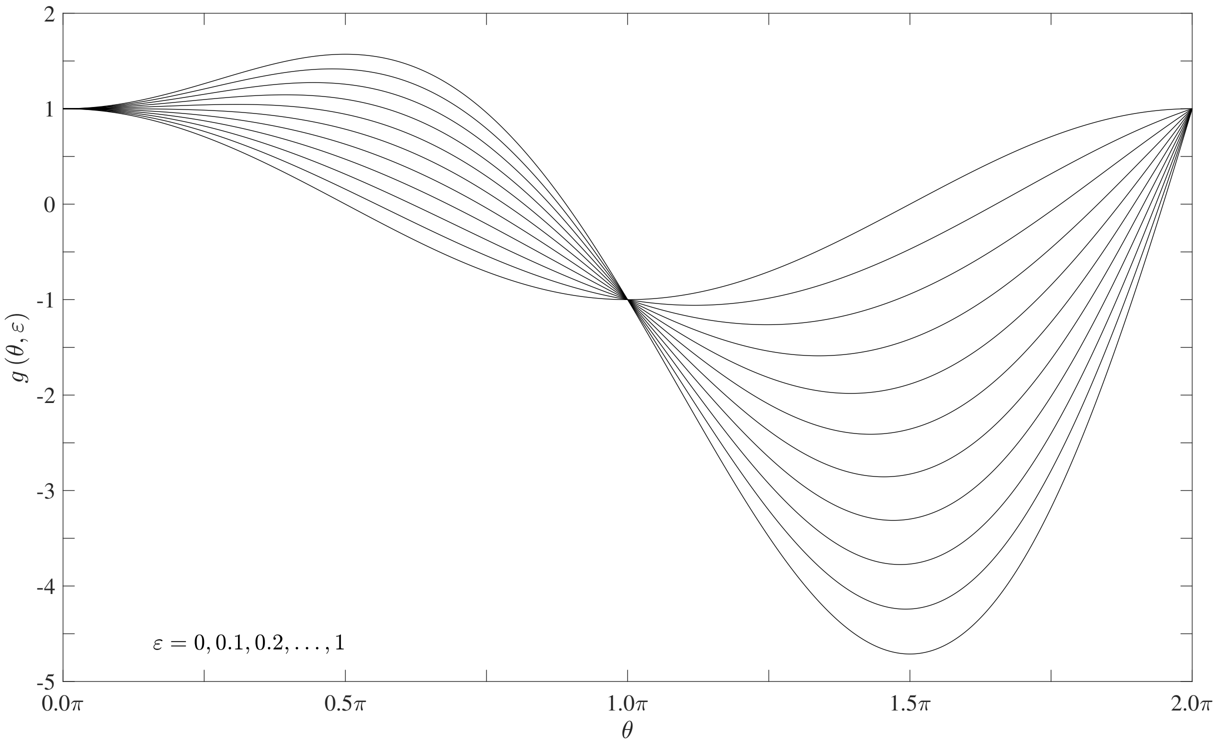

Figure 4.9: Amplitude as in figure 4.7 for larger values of the forcing parameter.

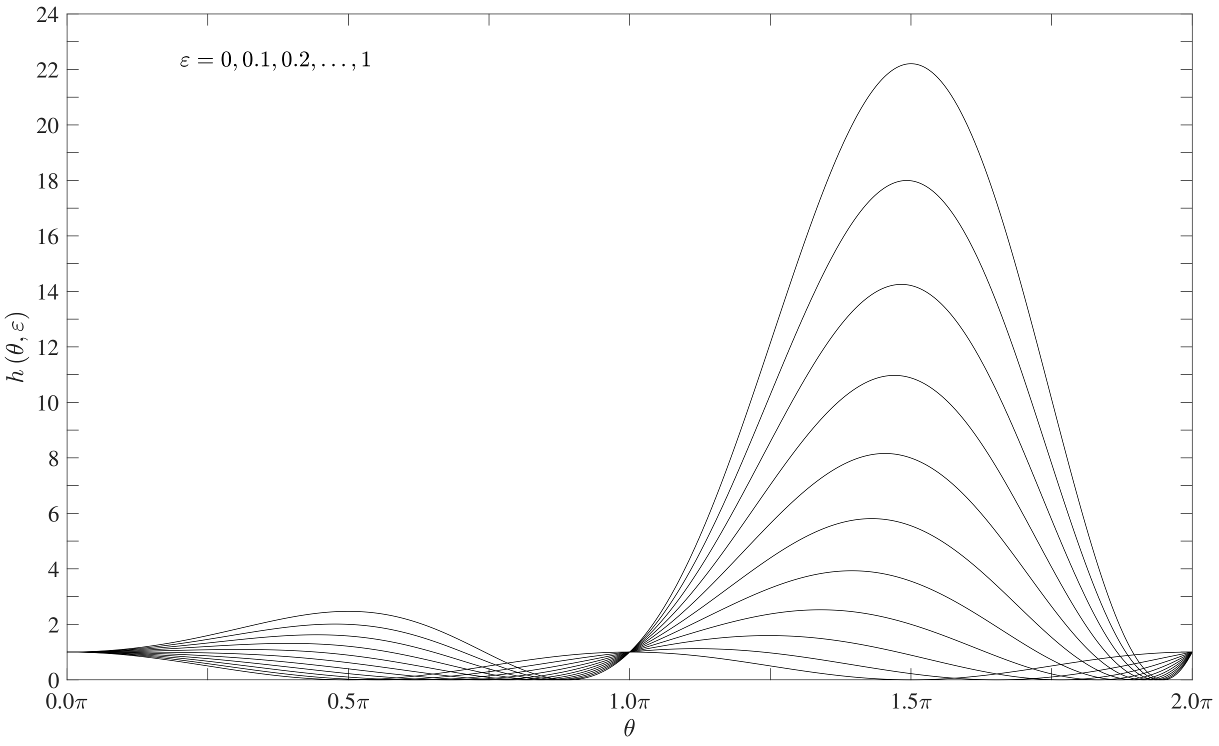

Figure 4.10: Energy as in figure 4.8, for the same values of forcing parameter as in figure 4.9.

Thus, the conclusions are the same; for instance, regarding (4.55a), the energy over the first wave period can be marginally reduced if

$$\sum_{m=1}^{M} F_m \sin(k\xi_m) = -\varepsilon_0 A k^2 L, \tag{4.62}$$

where A is the amplitude of the free oscillation (4.54b) and ε_0 is the constant (4.55b). The difference between (4.62) and (4.55a) is that there is a greater choice of pairs (F_m, ξ_m). A further case deserves investigation, namely that of continuously distributed forces.

4.6 Optimisation of continuously distributed forces

In the case of an applied force, which is harmonic in time, with frequency ω and continuously distributed in space, the forced wave equation (4.11) is replaced by

$$\frac{\partial^2 \overline{y}}{\partial x^2} - \frac{1}{c^2}\frac{\partial^2 \overline{y}}{\partial t^2} = f(x)\cos(\omega t) \tag{4.63}$$

which has a solution (4.12a), where $B(x)$ satisfies

$$\frac{\mathrm{d}^2 B}{\mathrm{d}x^2} + k^2 B = f(x). \tag{4.64}$$

If the spatial force distribution $f(x)$ is a function of bounded fluctuation in $0 \leq x \leq L$, it has [133] a Fourier series representation:

$$f(x) = f_0 + \sum_{n=1}^{\infty}\left[f_n \cos(k_n x) + f_{-n}\sin(k_n x)\right]. \tag{4.65}$$

A solution of (4.64) may be sought as a series,

$$B(x) = \sum_{n=-\infty}^{\infty} B_n(x), \tag{4.66}$$

in which the terms satisfy

$$\frac{\mathrm{d}^2 B_0}{\mathrm{d}x^2} + k^2 B_0 = f_0, \tag{4.67a}$$

$$\frac{\mathrm{d}^2 B_n}{\mathrm{d}x^2} + k^2 B_n = f_n \cos(k_n x), \tag{4.67b}$$

$$\frac{\mathrm{d}^2 B_{-n}}{\mathrm{d}x^2} + k^2 B_{-n} = f_{-n}\sin(k_n x), \tag{4.67c}$$

with given f_n, k and k_n.

In the non-resonant case $k \neq k_n$, the solution of (4.67a) to (4.67c) is a sinusoidal oscillation with constant amplitude for all terms with $n \neq 0$,

$$B_n(x) = \frac{f_n}{k^2 - k_n^2}\cos(k_n x), \tag{4.68a}$$

$$B_{-n}(x) = \frac{f_{-n}}{k^2 - k_n^2}\sin(k_n x), \tag{4.68b}$$

except for the term $n = 0$ that is constant, $B_0 = f_0/k^2$. In the case of resonance, $k = k_m$ for some m and the solution may be obtained as in (4.17) to (4.20), that is differentiating the numerator and denominator with regard to k_n, leading to

$$B_m(x) = \frac{f_m}{2k_m} x \sin(k_m x), \tag{4.69a}$$

$$B_{-m}(x) = -\frac{f_{-m}}{2k_m} x \cos(k_m x). \tag{4.69b}$$

The first boundary condition of (4.2) is not satisfied by (4.68a), and the second boundary condition is not satisfied by (4.69b) in general, implying

$$f_{-m} = f_0 = f_1 = \ldots = f_{m-1} = f_{m+1} = f_{m+2} = \ldots = 0, \tag{4.70a}$$

as restrictions on the applied force (4.65), that simplifies to

$$f(x) = f_m \cos(k_m x) + \sum_{\substack{n=1 \\ n \neq m}}^{\infty} f_{-n} \sin(k_n x). \tag{4.70b}$$

The forced response of the string is

$$B(x) = \frac{f_m}{2k_m} x \sin(k_m x) + \sum_{\substack{n=1 \\ n \neq m}}^{\infty} \frac{f_{-n}}{k^2 - k_n^2} \sin(k_n x). \tag{4.71}$$

Taking a free oscillation of the form (4.54b), it cannot be suppressed for the same reasons as before: (i) if $n \neq m$, the last terms on the right-hand side of (4.71) have a different wavenumber; (ii) if the wavenumber coincides, $k = k_m$, the first term on the right-hand side of (4.71) shows that the undamped resonance has a growing amplitude which cannot be matched to the remaining term of (4.71), that is the total, free (4.54b) plus forced (first term on the right-hand side of (4.71)) oscillation is

$$y_*(x,t) = \left(A + \frac{f}{2k} x\right) \sin(kx) \cos(\omega t), \tag{4.72}$$

where the index m is again suppressed for brevity, substituting $\{f_m, k_m, \omega_m\}$ by $\{f, k, \omega\}$.

As in (4.33a) and (4.35), the energy of the total oscillation per unit length of string is given by

$$\frac{2E_*(x)}{\rho} \equiv \left\langle \left| \frac{\partial y_*}{\partial t} \right|^2 \right\rangle + c^2 \left\langle \left| \frac{\partial y_*}{\partial x} \right|^2 \right\rangle \tag{4.73}$$

where the time averages (4.22a) are evaluated readily, by (B.6) and (B.7), after substituting (4.72) into (4.73), leading to

$$\frac{2E_*(x)}{\rho} = \frac{\omega^2}{2} \left(A + \frac{f}{2k} x\right)^2 \sin^2(kx) + \frac{k^2 c^2}{2} \left[\left(A + \frac{f}{2k} x\right) \cos(kx) + \frac{f}{2k^2} \sin(kx)\right]^2, \tag{4.74a}$$

which can be simplified to

$$\frac{2E_*(x)}{\rho} = \frac{\omega^2}{2} \left[\left(A + \frac{f}{2k} x\right)^2 + \left(\frac{f}{2k^2}\right)^2 \sin^2(kx) + \frac{f}{2k^2} \left(A + \frac{f}{2k} x\right) \sin(2kx)\right]. \tag{4.74b}$$

The total energy over the length of the string is defined as in (4.40a), namely

$$G_*(x) \equiv \frac{2}{\rho\omega^2 L}\int_0^L E_*(x)\ \mathrm{d}x, \tag{4.75}$$

and substitution of (4.74b) in (4.75) leads to two integrals: (i) the first integral uses $kL = 2\pi$,

$$\frac{f^2}{8k^4 L}\int_0^L \sin^2(kx)\ \mathrm{d}x = \frac{f^2}{16k^4}; \tag{4.76a}$$

(ii) the second integral uses $\gamma = kx$,

$$\frac{1}{2L}\int_0^L \frac{f}{2k}x\frac{f}{2k^2}\sin(2kx)\ \mathrm{d}x = \frac{f^2}{8k^5 L}\int_0^{2\pi}\beta\sin(2\gamma)\ \mathrm{d}\gamma = -\frac{\pi f^2}{8k^5 L} = -\frac{f^2}{16k^4}. \tag{4.76b}$$

Since (4.76a) and (4.76b) add to zero, the total energy over the length of the string (4.75) follows

$$G_*(f) = \frac{A^2}{2} + \frac{AfL}{4k} + \frac{f^2L^2}{24k^2}. \tag{4.77}$$

The total energy has a minimum, since the second-order derivative of G_* is positive. That minimum corresponds to $dG_*/df = 0$ leading to the applied force

$$f_* = -\frac{3kA}{L}, \tag{4.78a}$$

or in dimensionless form $f_*L^2/A = -3kL = -6\pi$. The minimum energy is

$$G_*(f_*) = \frac{A^2}{8} = \frac{1}{4}G_0, \tag{4.78b}$$

25% of the energy of oscillation, that is a 75% reduction. Thus, choosing the continuously distributed force (4.78a) leads, by (4.72), to a resonant oscillation:

$$\overline{y}(x,t) = \frac{f_*}{2k}x\sin(kx)\cos(\omega t) = -\frac{3}{2}A\frac{x}{L}\sin(kx)\cos(\omega t); \tag{4.78c}$$

the latter adds to the free oscillation, to produce a combined oscillation,

$$y(x,t) = A\left(1 - \frac{3}{2}\frac{x}{L}\right)\sin(kx)\cos(\omega t), \tag{4.78d}$$

which reduces the energy by a factor 0.25 in (4.78b), which is the lowest (because the second derivative is negative) attainable value. This value is lower than the obtainable (4.43b) with single force, specified by (4.42b), or multiple point forces, specified by (4.62).

4.7 Main conclusions of the chapter 4

The question addressed in the present chapter is whether the linear undamped free vibrations of an elastic string can be suppressed, or at least their total energy reduced, by using applied external forces concentrated or distributed along its length. The linear undamped free vibrations of an elastic string consist of the superposition of a fundamental mode and harmonics, and two cases are considered, namely the applied frequency of the external forces: (case I) does not coincide with any natural frequency, for non-resonant forcing; (case II) coincides with one of the natural frequencies for resonant forcing. The two cases are quite distinct because: (I) the non-resonant forcing has constant amplitude and energy; (II) the resonant forcing has amplitude increasing linearly with time, and hence energy increases quadratically with time until non-linear effects come into play.

Starting with (I) non-resonant forcing at an applied frequency distinct from all natural frequencies: (i) the energy, that is the sum of kinetic and elastic energies, is constant both for the (a) linear undamped free oscillation and for the (b) linear forced non-resonant oscillation; (ii) the applied frequency being distinct from all natural frequencies, there is no interaction with the free oscillations, whose energy remains the same; (iii) the forced non-resonant oscillation adds a constant energy, so the total energy of free plus forced oscillation is larger than the energy of the free oscillation alone; (iv) this is the reverse of the result sought, and thus non-resonant forcing cannot decrease and instead increases the total energy when superimposed on free oscillations. Thus, if it is possible at all to reduce the energy of free oscillations, it can only be through (II) resonant forcing using either (IIa) concentrated or (IIb) distributed forces, that can be optimised to minimise the total energy.

The reduction of the total energy of oscillation by resonant forcing is possible with two limitations: (i) it applies only to the free oscillation whose natural frequency coincides with the applied frequency and has no effect on all the other modes; (ii) since the energy of the resonant forced oscillation increases quadratically with time, it will ultimately dominate the total energy over a sufficiently long time, so that total energy reduction is possible only over a short initial time, say the first period of oscillation. Thus, the question being addressed can be rephrased: can the resonant forcing reduce the total energy over the first period of oscillation? Although the answer is "yes" in both cases, the result is quite different for (IIa) concentrated and (IIb) distributed applied forces, using optimisation in each case.

In the case (IIa) of single or multiple point forces, the total energy over the first period of oscillation, relative to the free oscillation, can be reduced by a maximum of no more than 2% by resonant forcing at an applied frequency equal to the natural frequency. The less than 2% reduction is a minimum of the total energy obtained by optimising the magnitude of the applied concentrated force at a fixed location. Since the energy of the forced resonant oscillation increases quadratically with time, this slight reduction is quickly overwhelmed beyond the first period of oscillation. The case (IIb) is somewhat more favourable since by optimising the magnitude and spatial variation of the continuously distributed force applied along the length of the string, the resonant forcing reduces the total energy over the first period of oscillation by 75% relative to the free oscillation alone. Since the energy of the forced oscillation increases quadratically with time, it becomes dominant for times moderately beyond one period. These results exclude the effects of damping, which is present in many practical situations, and is considered in the follow-on chapter.

5 | On the countering of free vibrations by forcing: damped oscillations and decaying forcing

"Mathematics compares the most diverse phenomena and discovers the secret analogies that unite them."

— Joseph Fourier

Contents

THE active suppression of oscillations is considered: (i) in acoustics [21, 22, 45–48] by considering anti-noise sources that generate sound with opposite phase [49, 50]; (ii) in solid mechanics [77–81, 129, 133] using forces and moments to oppose the vibrations [82, 107, 109–112, 114, 116, 122]. In the chapter 4 that has an extensive bibliography was considered a hybrid approach using forced oscillations superimposed on the free oscillations of an elastic string, in the simplest case of constant tangential tension and with constant mass density per unit length, in the absence of damping. The countering of free vibrations by forcing without damping was considered in chapter 4 for non-resonant forcing by point and distributed forces, allowing for different phases of the free oscillation and the forcing. After considering some possible cases without damping, it was found that suppression of oscillations or reduction of their energy was of limited effectiveness and for short periods. These not-so-promising results motivate the extension in the present chapter to include damping, which causes amplitude decay and introduces a third phase. Again, non-resonant and resonant forcing is considered, and the inclusion of damping still does not lead to effective vibration suppression for constant damping amplitude. The countering of vibrations or partial vibration suppression is quite effective for forcing decaying exponentially with time with a suitably chosen decay rate. Therefore the main difference between chapters 4 and 5 is the inclusion of damping and allowing for forcing decaying exponentially in time. This implies replacing the classical wave equation for the transverse displacement of the elastic string with the wave-diffusion or telegraph equation.

The background literature addresses two distinct problems: (i) the transverse vibrations of an elastic string, corresponding to one-dimensional acoustics (references [21, 22, 45–74, 134–148], also cited in the first paragraph of chapter 4), for which active sound cancellation corresponds to superposition of a wave with the same amplitude and opposite phase; (ii) transverse vibrations of elastic bars for which active vibration suppression is done by applied forces or moments (references [75–107, 109–125, 149, 150], also cited in the second paragraph of chapter 4). The present problem is a hybrid since it considers (i) transverse vibrations of an elastic string and (ii) attempts suppression by applied forces. There are four combinations of the superposition of free and forced oscillations: (a) absence or presence of damping; (b) non-resonant or resonant forcing. The cases of superposition of resonant and non-resonant forcing with free oscillations were considered without damping in chapter 4, as a baseline to add damping effects in the present chapter. The distinction starts with the fundamental equation, namely the classical wave equation in chapter 4 is extended to the wave-diffusion or telegraph equation to include damping in the present chapter.

The free or unforced solutions are (section 5.1) sinusoidal waves in space-time with amplitude decaying exponentially in time due to dissipation; the wavenumbers and frequencies are determined by boundary conditions fixing the string at the two ends (subsection 5.1.1) and the amplitude and phase are specified by the initial displacement and velocity (subsection 5.1.2). The sinusoidal forcing of the damped space-time oscillation with applied frequency and phase leads (section 5.2) to two cases: (i) non-resonant case if the applied frequency is distinct from the natural frequency leading (subsection 5.2.1) to forced space-time oscillations with constant amplitude and a phase shift such that the work of the applied force balances the dissipation; (ii) resonant case if the applied frequency equals the natural frequency and (subsection 5.2.2) the space-time oscillations have a constant amplitude with a phase shift of $\pi/2$. In both cases, the decaying free oscillation is dominated (subsection 5.2.3) for a long time by the forced (i) non-resonant or (ii) resonant oscillation with constant amplitude.

The total energy (section 5.3) is the sum of (i) kinetic energy associated to the transverse velocity and mass density with (ii) elastic energy associated to the slope and tangential tension. The total energy decays for the damped free oscillation, but not when the forced oscillation is superimposed either in the (i) non-resonant (subsection 5.3.1) or (ii) resonant (subsection 5.3.2) cases, because forcing leads to constant amplitude. Thus, an energy of the total, free plus forced, oscillation less than for the free oscillation is possible only: (i) by selecting the forcing to oppose the free oscillation; (ii) matching the applied phase to the phase of free oscillation and phase shift due to damping; (iii) for a sufficiently short time.

Total cancellation of the free oscillation by forcing is not possible because: (i) the amplitudes vary differently in time, namely exponential decay for the free oscillation and constant amplitude for the forced non-resonant or resonant oscillation; (ii) the phases are different for the free and forced oscillations, with the frequency being the same for the forced resonant oscillation or with the frequency being also different for the forced non-resonant oscillation. In conclusion, even optimizing the forcing, the total energy of the free plus forced oscillation can be less than the energy of the free oscillation only for a short time, usually a small fraction of the first period of oscillation.

It follows that the objective of substantial suppression of free oscillations over several periods is not attainable by the four standard strategies I-IV of superimposing: (I) non-resonant undamped, (II) resonant undamped, (III) non-resonant damped and (IV) resonant damped oscillations.

This is the motivation to consider two novel strategies, namely (V) resonant and (VI) non-resonant forcing with exponential time decay. The forcing with exponential time decay (section 5.4) can be considered with: (i) opposite free and forcing amplitudes; (ii) matched free, applied and damping phases; (iii) applied frequency equal to the oscillation frequency. This leads to resonance (subsection 5.4.2) if the forcing decay equals damping, but no resonance otherwise (subsection 5.4.1).

Considering the energy of the total free plus forced oscillation in the strategy V of forcing decay equal to damping (section 5.5), the forced oscillation has amplitude initially increasing linearly with time until dominated by exponential time decay at a later time. The build-up of energy of the forced oscillation (subsection 5.5.1) may be too slow to compensate the damping of the free oscillation with little or no benefit of overall energy reduction (subsection 5.5.2).

The final most effective strategy VI is to avoid resonance by having a forcing decay distinct from damping (section 5.6), which is compatible with: (i) applied frequency equal to oscillation frequency; (ii) opposite free and forcing amplitudes; (iii) matched free, damping and applied phases. In this case, both the free and forced oscillations decay exponentially with time (subsection 5.6.1) at different damping and decay rates, both leading to finite energy over all time. Their ratio can be adjusted to achieve a reduction of the energy over all time of the total oscillation of more than 96% relative to the free oscillation (subsection 5.6.2). In conclusion (section 5.9), the strategy VI is the most effective at partial suppression of free oscillations (section 5.7). It also suggests a redefinition of the concept of resonance for more general types of forcing than constant amplitude (section 5.8).

5.1 Free damped modes with dissipation

The free damped waves are described by the unforced wave diffusion equation with boundary conditions, specifying the wavenumbers and frequencies (subsection 5.1.1), and with the initial conditions, specifying the amplitudes and phases (subsection 5.1.2).

5.1.1 Wavenumbers and frequencies from wave-diffusion equation

The classical wave equation applies to the linear transverse vibration $\tilde{y}$ of an elastic string with constant tangential tension T and mass density per unit length ρ. In the presence of damping μ proportional to the velocity, the wave equation is extended to

$$\rho \frac{\partial^2 \tilde{y}}{\partial t^2} + \mu \frac{\partial \tilde{y}}{\partial t} - T \frac{\partial^2 \tilde{y}}{\partial x^2} = 0, \tag{5.1a}$$

that can be written in the form of a wave-diffusion equation,

$$\frac{\partial^2 \tilde{y}}{\partial x^2} - \frac{1}{\chi} \frac{\partial \tilde{y}}{\partial t} - \frac{1}{c^2} \frac{\partial^2 \tilde{y}}{\partial t^2} = 0, \tag{5.1b}$$

involving, besides the wave speed $c \equiv \sqrt{T/\rho}$, also the diffusivity $\chi \equiv T/\mu$. In the absence of damping, $\mu = 0$, the diffusivity is infinite, $\chi = \infty$, and the wave-diffusion equation (5.1b) reduces to the classical wave equation:

$$\frac{\partial^2 \tilde{y}}{\partial t^2} - c^2 \frac{\partial^2 \tilde{y}}{\partial x^2} = 0. \tag{5.2}$$

Considering an elastic string of length L held at the two ends, $\tilde{y}(0,t) = 0 = \tilde{y}(L,t)$, the spatial eigenfunctions [45] are

$$\tilde{y}_n(x) = \sin(k_n x) \tag{5.3}$$

with wavenumbers $k_n = n\pi/L$. The solution of the wave-diffusion equation is sought by separation of variables [45] in the form

$$\tilde{y}(x,t) = \sum_{n=1}^{\infty} T_n(t)\, \tilde{y}_n(x), \tag{5.4a}$$

leading to

$$\frac{\mathrm{d}^2 T_n}{\mathrm{d}t^2} + \frac{c^2}{\chi} \frac{\mathrm{d}T_n}{\mathrm{d}t} + (k_n c)^2 T_n = 0. \tag{5.4b}$$

There is a solution exponential in time, $T_n(t) = \exp(v_n t)$, with v_n satisfying

$$v_n^2 + \frac{c^2}{\chi} v_n + (k_n c)^2 = 0, \tag{5.4c}$$

whose roots are

$$v_n^{\pm} = -\frac{c^2}{2\chi} \pm \sqrt{\left(\frac{c^2}{2\chi}\right)^2 - (k_n c)^2}, \tag{5.4d}$$

and thus

$$T_n(t) = P_n \exp\left(v_n^+ t\right) + Q_n \exp\left(v_n^- t\right) \tag{5.4e}$$

where P_n and Q_n are constants determined by initial conditions.

5.1.2 Amplitudes and phases from initial displacement and velocity

In the case of high diffusivity or sub-critical damping, $k_n > c/(2\chi)$, the roots (5.4d) are $v_n^{\pm} = -\delta \pm \mathrm{i}\tilde{\omega}_n$ where

$$\delta = \frac{c^2}{2\chi} \tag{5.5}$$

plays the role of damping and

$$\tilde{\omega}_n = \sqrt{(k_n c)^2 - \left(\frac{c^2}{2\chi}\right)^2} = \sqrt{(k_n c)^2 - \delta^2} \tag{5.6}$$

plays the role of oscillation frequency. Knowing that $v_n^{\pm}$ are the two complex roots of the characteristic equation (5.4d), then the equation can have solutions proportional to $\mathrm{e}^{-\delta t}\cos(\tilde{\omega}_n t)$ and $\mathrm{e}^{-\delta t}\sin(\tilde{\omega}_n t)$ which are linear combinations of the solutions $\mathrm{e}^{v_n^+ t} = \mathrm{e}^{(-\delta + \mathrm{i}\tilde{\omega}_n)t}$ and $\mathrm{e}^{v_n^- t} = \mathrm{e}^{(-\delta - \mathrm{i}\tilde{\omega}_n)t}$ as written in (5.4e). In this way, the two solutions only take real values when the time t is a real number. The exponential solution in time can therefore be written as

$$T_n(t) = \mathrm{e}^{-t\delta}\left[P_n \cos(\tilde{\omega}_n t) + Q_n \sin(\tilde{\omega}_n t)\right]. \tag{5.7}$$

Choosing the amplitude A_n and phase α_n by

$$P_n = A_n \cos(\alpha_n), \tag{5.8a}$$

$$Q_n = A_n \sin(\alpha_n), \tag{5.8b}$$

as in the case of undamped oscillations in subsection 4.1 with inverses equal to (4.7c) and (4.7c), leads to the real solution

$$T_n(t) = \mathrm{e}^{-t\delta} A_n \cos(\tilde{\omega}_n t - \alpha_n). \tag{5.9}$$

Substitution of (5.9) in (5.4a) specifies the free vibrations of the string,

$$\tilde{y}(x,t) = \mathrm{e}^{-t\delta} \sum_{n=1}^{\infty} A_n \sin(k_n x)\cos(\tilde{\omega}_n t - \alpha_n), \tag{5.10}$$

that consist of a superposition of modes: (i) all with the same damping (5.5); (ii) with wavenumbers $k_n = n\pi/L$ related to the wavelength λ_n by $\lambda_n \equiv 2\pi/k_n = 2L/n$; (iii) with oscillation frequencies (5.6) given by

$$\tilde{\omega}_n = c\sqrt{k_n^2 - \left(\frac{c}{2\chi}\right)^2}; \tag{5.11}$$

(iv) with amplitudes A_n and phases α_n determined by the initial displacement,

$$\tilde{y}(x,0) = \sum_{n=1}^{\infty} A_n \sin(k_n x)\cos\alpha_n, \tag{5.12a}$$

and initial velocity,

$$\frac{\partial \tilde{y}}{\partial t}(x,0) = -\sum_{n=1}^{\infty} A_n(\delta\cos\alpha_n - \omega_n \sin\alpha_n)\sin(k_n x). \tag{5.12b}$$

The Fourier sine series (5.12a) and (5.12b) may be inverted to specify the coefficients:

$$X_n \equiv A_n \cos\alpha_n = \frac{1}{L}\int_0^L \tilde{y}(x,0)\sin(k_n x)\,\mathrm{d}x, \tag{5.13a}$$

$$Y_n \equiv A_n \sin\alpha_n - \frac{\delta}{\omega_n} A_n \cos\alpha_n = \frac{1}{\omega_n L} \int_0^L \frac{\partial \tilde{y}}{\partial t}(x,0) \sin(k_n x)\, \mathrm{d}x. \tag{5.13b}$$

Rewriting (5.13b) in the form

$$A_n \sin\alpha_n = \frac{\delta}{\omega_n} X_n + Y_n, \tag{5.13c}$$

it follows that the amplitudes and phases are given by

$$A_n = \left[X_n^2 + \left(Y_n + \frac{\delta}{\omega_n} X_n \right)^2 \right]^{1/2}, \tag{5.14a}$$

$$\tan\alpha_n = \frac{Y_n}{X_n} + \frac{\delta}{\omega_n}. \tag{5.14b}$$

In the non-dissipative case, $\delta = 0$, the shape of the string is given by

$$\tilde{y}(x,t) = \sum_{n=1}^{\infty} A_n \sin(k_n x) \cos(\omega_n t - \alpha_n), \tag{5.15}$$

with $\omega_n = k_n c$ in agreement with the equation (4.6c) or with the equation (5.6) when $\delta = 0$.

The figure 5.1 shows the dimensionless displacements, $\tilde{y}/A$, of the free oscillations (for instance, of a string), without forcing, versus dimensionless axial coordinate x/L. All the oscillations shown in the figure result from the equation (5.10). Each line corresponds to one term of the series in (5.10), depending on the mode of oscillation n (or depending on the row of the figure). The total deformation of the string is the sum of all the contributions of each natural mode n of oscillation. The deformation is dominated by the natural modes with greater values of A_n (these constants are always positive) which depend on the boundary conditions. The blue solid lines correspond to oscillations without damping, $\delta = 0$, whereas the red dashed lines are for oscillations with damping, $\delta = 0.5c/L$. The figure 5.1 shows three distinct situations regarding the values of the mode of oscillation n and consequently the values of wavenumber k_n. The upper plots are obtained for $\{n, k_n\} = \{1, \pi/L\}$, the plots at the middle row are for $\{n, k_n\} = \{2, 2\pi/L\}$ and the bottom plots correspond to $\{n, k_n\} = \{3, 3\pi/L\}$. The oscillation frequencies $\tilde{\omega}_n$ are obtained from (5.6). In all the three cases, the oscillations are shown for three distinct times: $t = \{0, 0.5, 1\}\, L/c$. The plots are obtained with no phase shift, $\alpha_n = 0$. There is no loss of generality in the next figure to set $\alpha_n = 0$ because the phase α_n of each mode may be eliminated by changing the time t to $t' \equiv t - \alpha_n/\tilde{\omega}_n$. In all the plots, the vibration is always fixed with $\tilde{y} = 0$ at the two ends of the string because that was imposed as the boundary conditions.

By comparing the lines of the figure 5.1, the effect of changing the mode of oscillation n, which corresponds to one term of the series in (5.10), can be observed. The mode of oscillation n has direct effects on the values of spatial wavenumber k_n and consequently on the temporal frequency ω_n. The two effects can be studied separately because the solution of the differential equation (5.1b) was deduced by separation of the temporal and spatial variables, t and x respectively. The first effect, specifically the changing of the value of spatial wavenumber k_n, can be noticed by comparing the plots of the figure 5.1 for the same time, for instance, at times $t = 0$ and $t = 1L/c$. The bottom plots are obtained for a higher value of n, therefore for a higher value of wavenumber k_n, compared to the top plots. Increasing

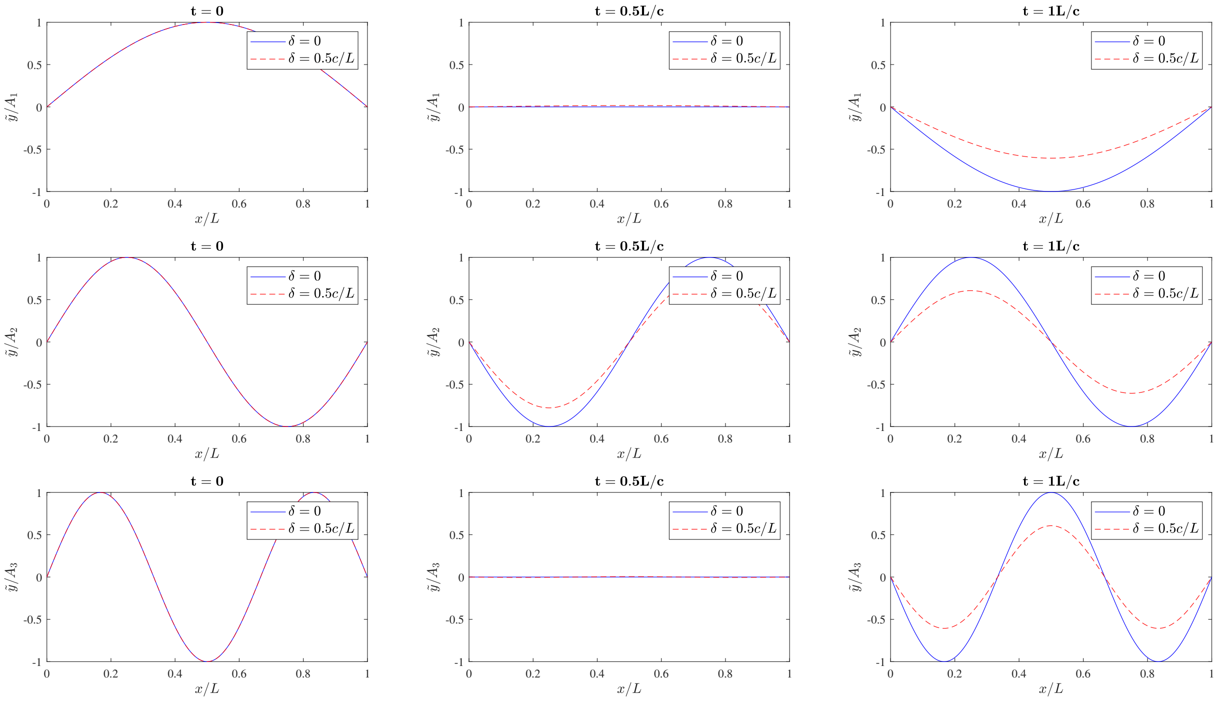

Figure 5.1: Free damped oscillations (for instance, of a string) at three distinct times. The blue solid lines are shown for no damping and the red dashed lines represent the oscillations with damping, $\delta = 0.5c/L$. Each row corresponds to a distinct set of values of the mode of free oscillation n and consequently on the value of wavenumber k_n: the upper row is for $\{n, k_n\} = \{1, \pi/L\}$, the middle row is for $\{n, k_n\} = \{2, 2\pi/L\}$ and the bottom row is for $\{n, k_n\} = \{3, 3\pi/L\}$. The plots are obtained for $\alpha_n = 0$.

the wavenumber means reducing the wavelength of the vibration, according to the relation $\lambda_n \equiv 2\pi/k_n$. Therefore, the bottom plots show a vibration with a higher number of crests, troughs and nodes, since the vibration is spatially more "compact". For each mode n, the string has n peaks and $n-1$ nodes (not counting the both ends of the string). These peaks and nodes remain at the same positions all the time due to the separation of the variables x and t in the solution. For a higher mode of oscillation n, the temporal frequency $\tilde{\omega}_n$ also increases and consequently the movement of the vibration is faster (the period of oscillations is lower), that is, it increases the velocity of the wave for the same velocity of propagation c and decay rate δ; this property is verified in (5.6). For instance, in the case of the figure 5.1, in the upper plots where the frequency is lower (the period is greater), the stage of vibration at $t = 1L/c$ is the same as at $t = 0.5L/c$ in the intermediate plots where the frequency is greater (the period is lower). The stage of vibration at $t = 1L/c$ of the intermediate row is only reached by the vibration of the upper row at $t = 2L/c$ (these equivalences of stages of vibration neglect the effect of damping). Another difference is related to the direction of the movement of the oscillation. For instance, although the upper and lower plots of the figure 5.1 are identical at the time $t = 0.5L/c$, the direction of the movement is not the same: in the upper plot the string is moving downwards whereas in the lower plot the string is moving upwards. The figure 5.1 also shows the effect of the value of decay rate δ. At the initial time, there is no difference between the plots with and without damping. When $\delta = 0$, as in the blue solid lines of the plots, there is no damping and the maximum amplitudes (in modulus) of the vibration remain constant over time. When $\delta \neq 0$, the vibrations are damped and the amplitudes of the vibrations are decreasing over time (the vibrations cease to exist when $t \to \infty$). The greater the damping value, the faster the oscillations are damped. Also, the presence of damping changes the temporal frequency $\tilde{\omega}_n$, according to (5.6). With damping, the temporal frequency decreases and consequently the period of the oscillation is greater.

The damped oscillations are considered both free (section 5.1) and with forcing (section 5.2).

5.2 Forced oscillations with applied frequency and phase

Next is considered forcing of the wave diffusion equation (section 5.1) with constant amplitude, and an arbitrary frequency and phase shift (subsection 5.2.1). The cases of applied frequency distinct from or equal to the natural frequency lead respectively to non-resonant or resonant forcing (subsection 5.2.2). This allows a comparison of total, free plus forced, oscillations in the non-resonant and resonant cases (subsection 5.2.3).

5.2.1 Damped non-resonant forced oscillations with phase shift

Next is considered the forced oscillations $\overline{y}$ with damping δ and forcing F (the unit of F is per meter m^{-1}) of the dissipative wave-diffusion equation (5.1b), with the same wavenumber $k_n \equiv k$ as one mode of natural oscillation, applied frequency $\overline{\omega}$ and phase shift β in

$$\frac{\partial^2 \overline{y}}{\partial x^2} - \frac{1}{\chi}\frac{\partial \overline{y}}{\partial t} - \frac{1}{c^2}\frac{\partial^2 \overline{y}}{\partial t^2} = F \sin(kx) \exp(-\mathrm{i}\overline{\omega} t - \mathrm{i}\beta), \tag{5.16}$$

knowing that the phase shift β can be distinct from the free oscillation (5.10) when each mode n has a phase shift α_n. The solution of (5.16) is sought as a plane wave with the same wavenumber $k_n \equiv k$, applied frequency $\overline{\omega}$ and phase shift β:

$$\overline{y}(x,t) = B \sin(kx) \exp(-\mathrm{i}\overline{\omega} t - \mathrm{i}\beta). \tag{5.17}$$

Substitution of (5.17) in (5.16) and omission of common space-time dependence leads to

$$c^2 \frac{F}{B} = \overline{\omega}^2 + \frac{\mathrm{i}\overline{\omega} c^2}{\chi} - k^2 c^2. \tag{5.18a}$$

The substitution of the damping (5.6) gives

$$c^2 \frac{F}{B} = \overline{\omega}^2 - k^2 c^2 + 2\mathrm{i}\overline{\omega}\delta \equiv C \mathrm{e}^{\mathrm{i}\phi}, \tag{5.18b}$$

corresponding to: (i) the amplitude factor

$$C = \left| \left(\overline{\omega}^2 - k^2 c^2\right)^2 + 4\overline{\omega}^2 \delta^2 \right|^{1/2}; \tag{5.19a}$$

(ii) the phase factor

$$\tan\phi = \frac{2\overline{\omega}\delta}{\overline{\omega}^2 - k^2 c^2}. \tag{5.19b}$$

Using the oscillation frequency (5.6) in (5.18b) leads to the alternative results,

$$c^2 \frac{F}{B} = \overline{\omega}^2 - \tilde{\omega}^2 - \delta^2 + 2\mathrm{i}\overline{\omega}\delta = C\mathrm{e}^{\mathrm{i}\phi}, \tag{5.20}$$

and hence to the amplitude factor

$$C = \left| \left(\overline{\omega}^2 - \tilde{\omega}^2 - \delta^2\right)^2 + 4\overline{\omega}^2\delta^2 \right|^{1/2} \tag{5.21a}$$

and phase factor

$$\tan\phi = \frac{2\overline{\omega}\delta}{\overline{\omega}^2 - \tilde{\omega}^2 - \delta^2}. \tag{5.21b}$$

In the non-resonant case of distinct applied and natural frequencies, $\overline{\omega} \neq kc$, then the equation (5.18b) can be solved for B, and substitution in (5.17) specifies the forced damped oscillation:

$$\overline{y}(x,t) = \frac{c^2 F}{C} \sin(kx) \exp\left[-\mathrm{i}\left(\overline{\omega}t + \beta + \phi\right)\right]. \tag{5.22}$$

Taking real parts, the forced wave diffusion equation (5.16),

$$\frac{\partial^2 \overline{y}}{\partial x^2} - \frac{1}{\chi}\frac{\partial \overline{y}}{\partial t} - \frac{1}{c^2}\frac{\partial^2 \overline{y}}{\partial t^2} = F\sin(kx)\cos(\overline{\omega}t + \beta), \tag{5.23}$$

leads to the forced oscillations

$$\overline{y}(x,t) = \frac{c^2 F}{C}\sin(kx)\cos(\overline{\omega}t + \beta + \phi) = c^2 F \left| \left(\overline{\omega}^2 - k^2c^2\right)^2 + 4\overline{\omega}^2\delta^2 \right|^{-1/2} \sin(kx)\cos(\overline{\omega}t + \beta + \phi). \tag{5.24}$$

The figure 5.2 shows the dimensionless displacements, $\overline{y}/\left(FL^2\right)$, of the forced oscillations at three distinct times: $t = \{0, 0.5, 1\}\, L/c$. All the oscillations shown in the figure result from the equation (5.24). The blue solid lines correspond to oscillations without damping, $\delta = 0$, whereas the red dashed lines are for oscillations with damping, $\delta = 0.5c/L$. The figure 5.2 shows three distinct situations regarding the values of the mode of oscillation n (or as a consequence in the wavenumber $k = n\pi/L$) and forced $\overline{\omega}$ frequency. The upper plots are obtained for $\{n, \overline{\omega}\} = \{1, 4\pi c/L\}$, the plots at the middle row are for $\{n, \overline{\omega}\} = \{2, 4\pi c/L\}$ and the bottom plots correspond to $\{n, \overline{\omega}\} = \{1, 3\pi c/L\}$. In all the three cases, $\overline{\omega} \neq kc$ which means that the oscillations are not resonant.

The values of the mode of oscillation n and forced frequency $\overline{\omega}$ influence the amplitude and phase of the oscillation. The presence of damping attenuates the amplitude of oscillations. Indeed, the equation (5.19a) shows that when the value of damping δ increases, the amplitude factor C is greater and consequently the amplitude of oscillation decreases. The other effect of damping that can be visualised in figure 5.2 is that it delays the stage of oscillation. This property can be confirmed by the equation (5.19b) with the existence of damping δ. As opposed to the free oscillations, the maximum and minimum amplitudes of the forced oscillations remain constant over time. The maximum amplitude of the oscillation does not depend on time.

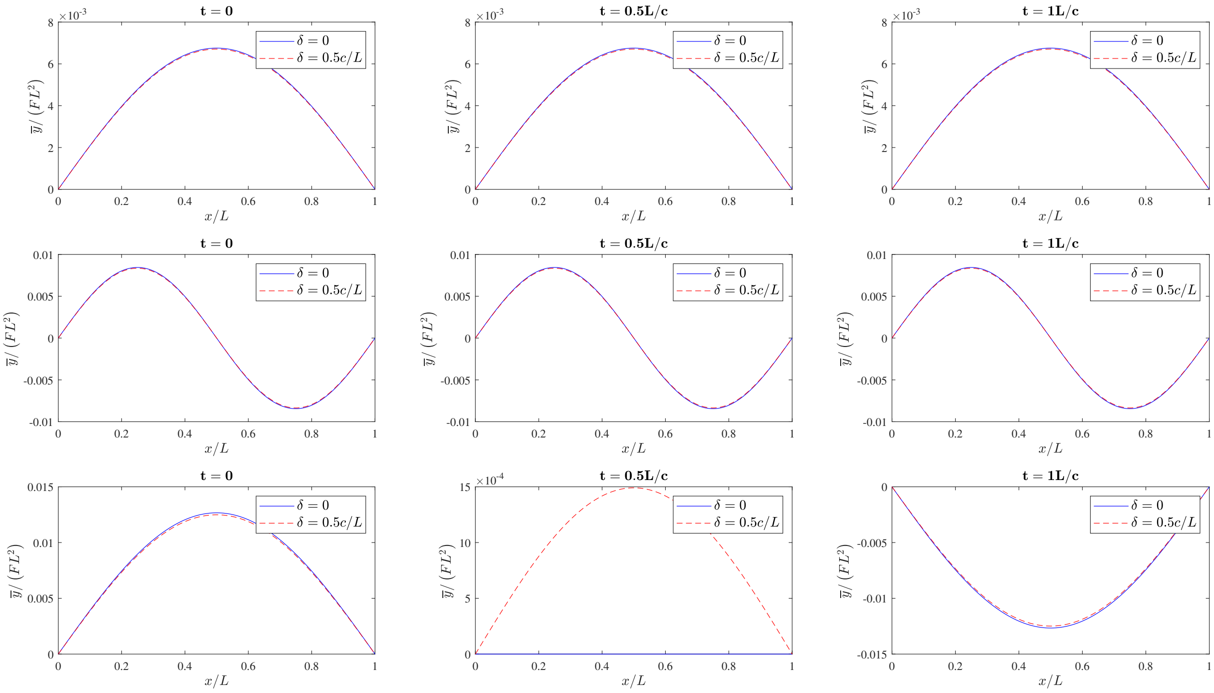

Figure 5.2: Forced non-resonant oscillations at three distinct times. The blue solid lines correspond to no damping, $\delta = 0$, whereas the red dashed lines correspond to oscillations with damping, $\delta = 0.5c/L$. Each row corresponds to a distinct set of values of the mode of oscillation n (which influences the value of spatial wavenumber k) and $\overline{\omega}$: the upper row is for $\{n, \overline{\omega}\} = \{1, 4\pi c/L\}$, the middle row is for $\{n, \overline{\omega}\} = \{2, 4\pi c/L\}$ and the bottom row is for $\{n, \overline{\omega}\} = \{1, 3\pi c/L\}$. In all the cases, the wavenumber is related to n by $k_n = n\pi/L$. The plots are obtained for $\beta = 0$.

The free oscillation is considered for the mode n with the simplified notation $\{k_n, \tilde{\omega}_n, A_n, \alpha_n\}$ replaced by $\{k, \tilde{\omega}, A, \alpha\}$ in

$$\tilde{y}(x,t) = A \exp(-t\delta) \sin(kx) \cos(\tilde{\omega}t - \alpha), \tag{5.25}$$

and adds to the forced oscillation (5.24) in the total oscillation,

$$y(x,t) = \tilde{y}(x,t) + \overline{y}(x,t) = \sin(kx) \left[A e^{-t\delta} \cos(\tilde{\omega}t - \alpha) + \frac{c^2 F}{C} \cos(\overline{\omega}t + \beta + \phi) \right], \tag{5.26}$$

showing that the cancellation for all time is not possible because: (i) the applied $\overline{\omega}$ and oscillation $\tilde{\omega}$ (5.6) frequencies are generally distinct,

$$\overline{\omega} \neq \tilde{\omega} = \sqrt{k^2 c^2 - \delta^2}; \tag{5.27}$$

(ii) the free damped oscillations decay exponentially with time,

$$\lim_{t\to\infty} \tilde{y}(x,t) = 0; \tag{5.28}$$

(iii) the forced oscillations have constant amplitude and dominate for a long-time,

$$\lim_{t\to\infty} y(x,t) = \overline{y}(x,t) = \frac{c^2 F}{C} \sin(kx) \cos(\overline{\omega}t + \beta + \phi). \tag{5.29}$$

Choosing the forcing amplitude

$$F = -\frac{CA}{c^2} = -\frac{A}{c^2} \left| \left(\overline{\omega}^2 - k^2 c^2 \right)^2 + 4\overline{\omega}^2 \delta^2 \right|^{-1/2} \tag{5.30a}$$

still does not cancel the total oscillation at any time,

$$y\left(x,t\right) = A\sin\left(kx\right)\left[\mathrm{e}^{-t\delta}\cos\left(\tilde{\omega}t - \alpha\right) - \cos\left(\overline{\omega}t + \beta + \phi\right)\right], \tag{5.30b}$$

because $y\left(x,t\right) = 0$ would require the real part of $\exp\left(\mathrm{i}\tilde{\omega}t - \mathrm{i}\alpha - t\delta\right)$ being equal to the real part of $\exp\left(\mathrm{i}\overline{\omega}t + \mathrm{i}\beta + \mathrm{i}\phi\right)$; that equality is equivalent to $\mathrm{i}\tilde{\omega}t - \mathrm{i}\alpha - t\delta = \mathrm{i}\overline{\omega}t + \mathrm{i}\beta + \mathrm{i}\phi + \mathrm{i}2\pi p$, where p is an integer; solving the last relation leads to a complex time

$$t = \frac{\alpha + \beta + \phi + 2\pi p}{\tilde{\omega} - \overline{\omega} + \mathrm{i}\delta}, \tag{5.31}$$

and thus the total oscillation (5.30b) cannot vanish for real time.

The figure 5.3 shows the dimensionless displacements, y/A, of the total (free plus forced) oscillations at three distinct times: $t = \{0, 0.5, 1\}\, L/c$, and equating the unknown constants of both oscillations, $A = FL^2$. All the oscillations shown in the figure result from the equation (5.26), by defining the values of $\overline{\omega}$, k (or mode of oscillation n) and δ, as in the figures 5.1 and 5.2. The phase shifts are equal to zero,

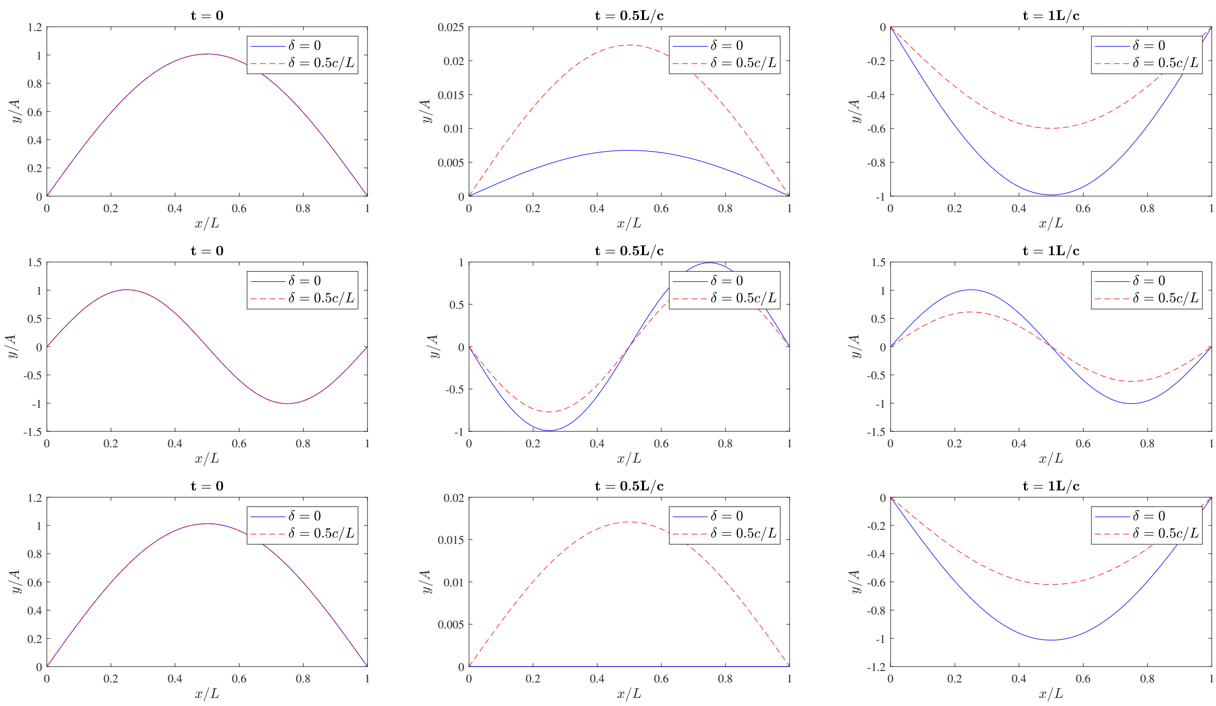

Figure 5.3: Total, free plus forced, non-resonant oscillations at three distinct times. The blue solid lines correspond to no damping, $\delta = 0$, whereas the red dashed lines correspond to oscillations with damping, $\delta = 0.5c/L$. Each row corresponds to a distinct set of values of the mode of oscillation n (which influences the value of spatial wavenumber k) and $\overline{\omega}$: the upper row is for $\{n, \overline{\omega}\} = \{1, 4\pi c/L\}$, the middle row is for $\{n, \overline{\omega}\} = \{2, 4\pi c/L\}$ and the bottom row is for $\{n, \overline{\omega}\} = \{1, 3\pi c/L\}$. In all the cases, the wavenumber is related to n by $k = n\pi/L$. The plots are obtained for $\alpha = 0 = \beta$. The plots are also obtained by setting $A = FL^2$.

$\alpha = 0 = \beta$. The blue solid lines correspond to oscillations without damping, $\delta = 0$, whereas the red dashed lines are for oscillations with damping, $\delta = 0.5c/L$. The figure 5.3 shows three distinct situations, one for each line. The three situations, regarding the values of mode of oscillation n and forced frequency $\overline{\omega}$, are the same as in the figure 5.2. In all the three cases, the wavenumber is related to the mode of oscillation by $k = n\pi/L$. Consequently, in all the cases, $\overline{\omega} \neq kc$ meaning non-resonant oscillations.

In this particular set of values of forced frequency, wavenumber and damping ratio, the amplitudes of forced oscillations are much smaller than the amplitudes of free oscillations. Therefore, the total oscillation is almost reduced to only free oscillations, unless the value of the force F is much greater than the value of the constant A. Ultimately for sufficiently long time, the forced oscillation with constant amplitude will always dominate the exponentially decaying free oscillation, as stated in (5.29).

5.2.2 Resonant forced oscillation with dissipation and phase shift

The resonant case corresponds to applied frequency $\overline{\omega}$ equal to the natural frequency,

$$\overline{\omega} = kc, \tag{5.32}$$

implying that (5.18b) simplifies to

$$c^2 \frac{F}{B} = \mathrm{i}2\overline{\omega}\delta = \mathrm{i}2kc\delta = C\mathrm{e}^{\mathrm{i}\phi}, \tag{5.33}$$

corresponding to the amplitude factor $C = 2\overline{\omega}\delta = 2kc\delta$ and phase shift of 90 degrees, $\phi = \pi/2$. From (5.33) follows $B = -\mathrm{i}cF/(2k\delta)$, implying by (5.17) the resonant forced oscillation:

$$\overline{y}_* (x,t) = -\frac{cF}{2k\delta} \sin(kx) \sin(kct + \beta). \tag{5.34}$$

The non-resonant case, $\overline{\omega} \neq kc$, is valid for zero damping, $\delta = 0$, when the amplitude factor (5.19a) simplifies to $C = \overline{\omega}^2 - k^2c^2$ and the phase (5.19b) reduces to zero, $\phi = 0$, leading by (5.24) to the undamped non-resonant forced oscillation:

$$\overline{y}(x,t) = \frac{F}{\overline{\omega}^2/c^2 - k^2} \sin(kx) \cos(\overline{\omega}t + \beta). \tag{5.35}$$

In the case of resonant forcing (5.32), the limit of zero damping $\delta \to 0$ is not valid, because it involves a division by zero in (5.34); the correct solution, as explained in chapter 4, involves a linear increase of amplitude with time. Henceforth only the case with damping will be considered comparing (subsection 5.2.3) non-resonant (subsection 5.2.1) with resonant (subsection 5.2.2) forcing.

5.2.3 Comparison of total free damped oscillation plus resonant or non-resonant forcing

The comparison of non-resonant forcing (5.24) with $\overline{\omega} \neq kc$ and resonant forcing (5.34) with $\overline{\omega} = kc$ shows that: (i) the amplitude is constant both for non-resonant forcing (5.24) and for resonant forcing

(5.34); (ii) the resonant amplitude factor $C = 2kc\delta$ coincides with the second term in the non-resonant factor (5.19a), excluding the first term, $\overline{\omega} = \pm kc$, that would be zero for resonance; (iii) the non-resonant phase shift (5.19b) reduces to the resonant phase shift $\phi = \pi/2$ for coincident applied and natural frequencies, $\overline{\omega} = \pm kc$ since $\tan\phi = \infty$ implies $\phi = \pm\pi/2$, meaning that (iv) the resonant case (5.34) has a phase shift of $\pi/2$ relative to the forcing (5.23) because $\sin(kct + \beta) = \cos(kct + \beta - \pi/2)$. In the resonant case, the total free (5.25) plus forced (5.34) oscillation,

$$y_*(x,t) = \tilde{y}(x,t) + \overline{y}_*(x,t) = \sin(kx)\left[A\mathrm{e}^{-t\delta}\cos(\tilde{\omega}t - \alpha) - \frac{cF}{2k\delta}\sin(kct + \beta)\right], \tag{5.36}$$

cannot be zero, even though the applied and natural frequencies coincide, $\overline{\omega} = \tilde{\omega} = kc$, because: (i) the free oscillation decays exponentially with time as in (5.28) while the forced oscillation has constant amplitude and thus dominates for long time,

$$\lim_{t\to\infty} y_*(x,t) = \overline{y}_*(x,t) = \frac{cF}{2k\delta}\sin(kx)\sin(kct + \beta); \tag{5.37}$$

(ii) even if the amplitudes are opposite,

$$F = \frac{2k\delta}{c}A, \tag{5.38a}$$

there is still a phase shift of $\pi/2$,

$$y_*(x,t) = A\sin(kx)\left[\mathrm{e}^{-t\delta}\cos(\tilde{\omega}t - \alpha) - \cos\left(kct + \beta - \frac{\pi}{2}\right)\right], \tag{5.38b}$$

besides the phase shifts of $-\alpha$ for the free oscillation and β for the forced oscillation. Choosing for the forced oscillation a phase shift

$$\beta = \frac{\pi}{2} - \alpha, \tag{5.39a}$$

the total cancellation of (5.38b),

$$y_*(x,t) = A\sin(kx)\left[\mathrm{e}^{-t\delta}\cos(\tilde{\omega}t - \alpha) - \cos(kct - \alpha)\right], \tag{5.39b}$$

would be zero at time zero: $y_*(x,0) = 0$. The oscillation would not be zero at other times because: (i) the free oscillation decays exponentially and the forced oscillation has constant amplitude; (ii) the free oscillation frequency (5.27) coincides with the natural frequency (5.32) only for weak damping, $\delta^2 \ll k^2c^2$ with

$$\tilde{\omega} = \sqrt{k^2c^2 - \delta^2} \sim kc. \tag{5.40a}$$

In the latter case of weak damping (5.40a) and forcing out-of-phase to the free oscillation (5.39a), the total oscillation,

$$y_*(x,t) = A\sin(kx)\cos(kct - \alpha)\left(\mathrm{e}^{-t\delta} - 1\right), \tag{5.40b}$$

does not vanish due to the damping effect alone.

The figure 5.4 shows the dimensionless amplitudes, y_*/A, of the total (free plus forced) resonant oscillations at three distinct times: $t = \{0, 0.5, 1\}\, L/c$. In this case, the applied frequency and wavenumber are related by (5.32). All the oscillations shown in the figure are from the equation (5.39b), which are deduced assuming that the amplitudes of the free and forced oscillations are opposite, as in (5.38a). Furthermore, there is a phase shift difference of $\pi/2$ between α and β, according to (5.39a). The value of α is set as zero. The blue solid lines correspond to oscillations without damping, $\delta = 0$, whereas the red dashed lines are for oscillations with damping, $\delta = 0.5c/L$. The figure 5.4 shows three distinct situations, one for each line, depending on the values of the mode of oscillation n and consequently on the wavenumber k given by $k \equiv k_n = n\pi/L$. The first row is considered as the default case, when $\{n, k_n\} = \{1, \pi/L\}$; in the second row, the value of n is greater, in which $\{n, k_n\} = \{2, 2\pi/L\}$; in the last row, the value of n is even greater compared to the second row, because $\{n, k_n\} = \{3, 3\pi/L\}$. In all the cases, $\overline{\omega} = kc$ implying resonant oscillations.

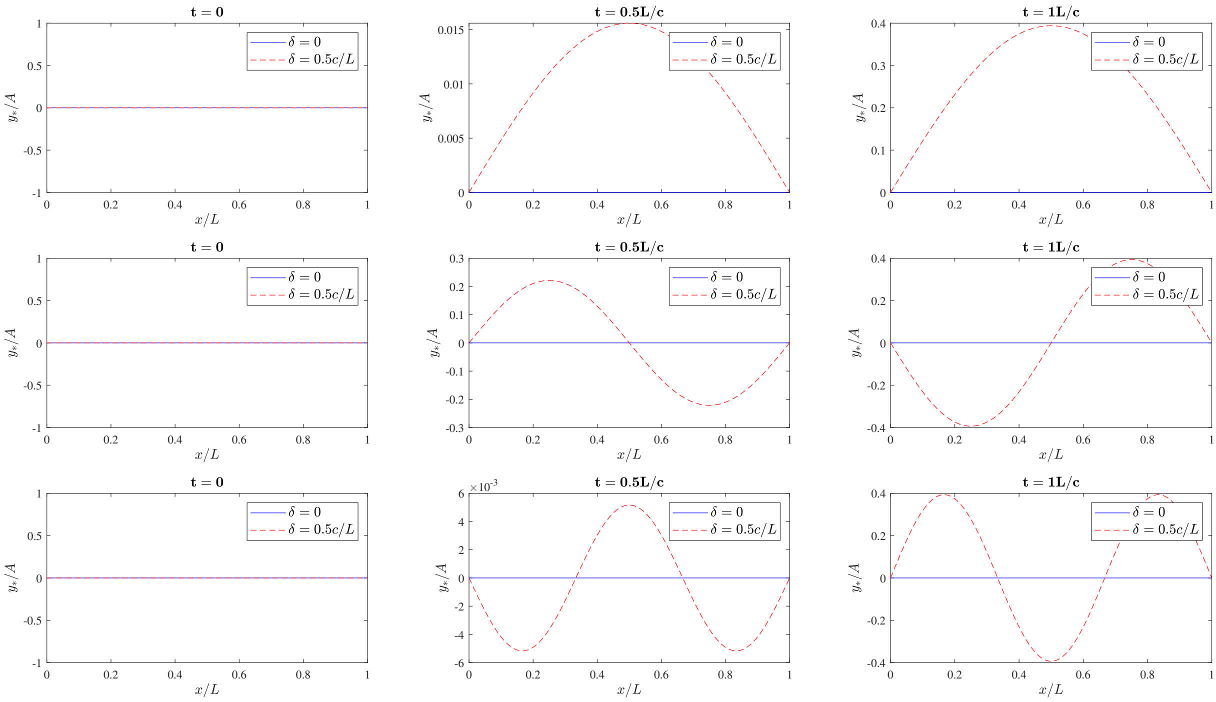

Figure 5.4: Total, that is free plus forced, resonant oscillations with opposing amplitudes at three distinct times. The blue solid lines correspond to no damping, $\delta = 0$, whereas the red dashed lines correspond to oscillations with damping, $\delta = 0.5c/L$. In all the cases, the wavenumber is related to n by $k = n\pi/L$. Each row corresponds to a distinct set of values of the mode of free oscillation n and consequently on the value of wavenumber k_n: the upper row is for $\{n, k\} = \{1, \pi/L\}$, the middle row is for $\{n, k\} = \{2, 2\pi/L\}$ and the bottom row is for $\{n, k\} = \{3, 3\pi/L\}$. The forced frequency is given by $\overline{\omega} = kc$. The plots are obtained for $\alpha = 0$ and $\beta = \pi/2 - \alpha$.

Comparing the rows of the figure 5.4, the effect of changing the mode of oscillation n can be observed. The second row shows the oscillations for a greater value of the mode of oscillation n than in the first row and the third row shows the oscillation for an even greater value of n. With a greater value of n, the free and forced frequencies increase and therefore the period of oscillations is lower, which means that the velocity of oscillations is slower. Moreover, the effect of changing the value of mode of oscillation n is also present in the value of spatial wavenumber k. For a greater value of n, the wavenumber k also increases. Increasing the wavenumber means reducing the wavelength of the vibration. Therefore, the bottom plots show a vibration with a higher number of crests, troughs and nodes, similar to the figure 5.1. The figure 5.4 also shows the effect of the damping δ. When $\delta = 0$, as in the blue solid lines of the plots, there is no damping and the maximum amplitudes (in modulus) of the vibration remain constant over time. In this particular case, the forced and free frequencies coincide and because the amplitudes of the free and forced oscillations are opposite, according to (5.38a), there is no oscillation when there is no damping. When $\delta \neq 0$, the free and forced oscillations are different and hence the free oscillation is not opposite to the forced oscillation; consequently the difference between them does not result in a zero deformation. Even with the presence of damping, the total oscillation is zero only at the initial time. With some attenuation, the vibrations are also damped and the amplitudes of the vibrations are decreasing over time. There will be an instant when the damping significantly attenuates the free oscillations, meaning that the total oscillation will be reduced to a forced oscillation (with maximum amplitude in modulus equal to A). The greater the damping value, the faster the oscillations decay.

The decay of the free oscillation and dominance of the forced oscillation for long time, both in non-resonant (5.26) and resonant (5.36) cases, imply that the reduction of total energy is possible only for a limited time (section 5.6), because the free oscillation decays due to dissipation, whereas the forced oscillation remains for a constant applied force.

5.3 Total energy of free plus forced oscillations

The superposition of free oscillations (section 5.1) with forced oscillations (section 5.2) can lead to partial suppression of the total oscillation that can be assessed considering the energy (section 5.3). The total energy consists of kinetic and elastic energies. It is compared between (i) the free oscillation and (ii) the total free plus forced oscillation. The comparison is made in the cases of non-resonant (subsection 5.3.1) and resonant (subsection 5.3.2) forcing.

5.3.1 Energy of total oscillations in non-resonant case

The total energy density per unit length of the string is the sum of kinetic [127] and elastic [129] energies:

$$E = \frac{1}{2}\rho\left|\frac{\partial y}{\partial t}\right|^2 + \frac{1}{2}T\left|\frac{\partial y}{\partial x}\right|^2. \tag{5.41}$$

The resonant forced oscillation (5.34) is the particular case, according to (5.32), of the non-resonant forced oscillation (5.24), so only the latter needs to be considered in the total, free plus forced, oscillation (5.26). Choosing the forcing (5.30a) leads to the total oscillation (5.30b) that can be zero at time zero, but not at other times.

The figure 5.5 shows the dimensionless amplitudes, y/A, of the total (free plus forced) non-resonant oscillations at three distinct times: $t = \{0, 0.5, 1\}\,L/c$. The constants of free and forced oscillations follow the relation (5.30a), given by $F = -CA/c^2$, remembered here for convenience. All the oscillations shown in the figure result from the equation (5.30b), similar to the figure 5.3 which is obtained from the equation (5.26), but with the relation between F and A according to (5.30a). The blue solid lines correspond to oscillations without damping, $\delta = 0$, whereas the red dashed lines are for oscillations with damping, $\delta = 0.5c/L$. The figure 5.5 shows three distinct situations, one for each line. The three situations, regarding the values of frequencies, are the same as in the figures 5.2 and 5.3. In all the three cases, the wavenumber is given by $n\pi/L$. Consequently, regardless the case, $\overline{\omega} \neq kc$ meaning non-resonant oscillations. The plots are obtained with no phase shifts, $\alpha = 0 = \beta$.

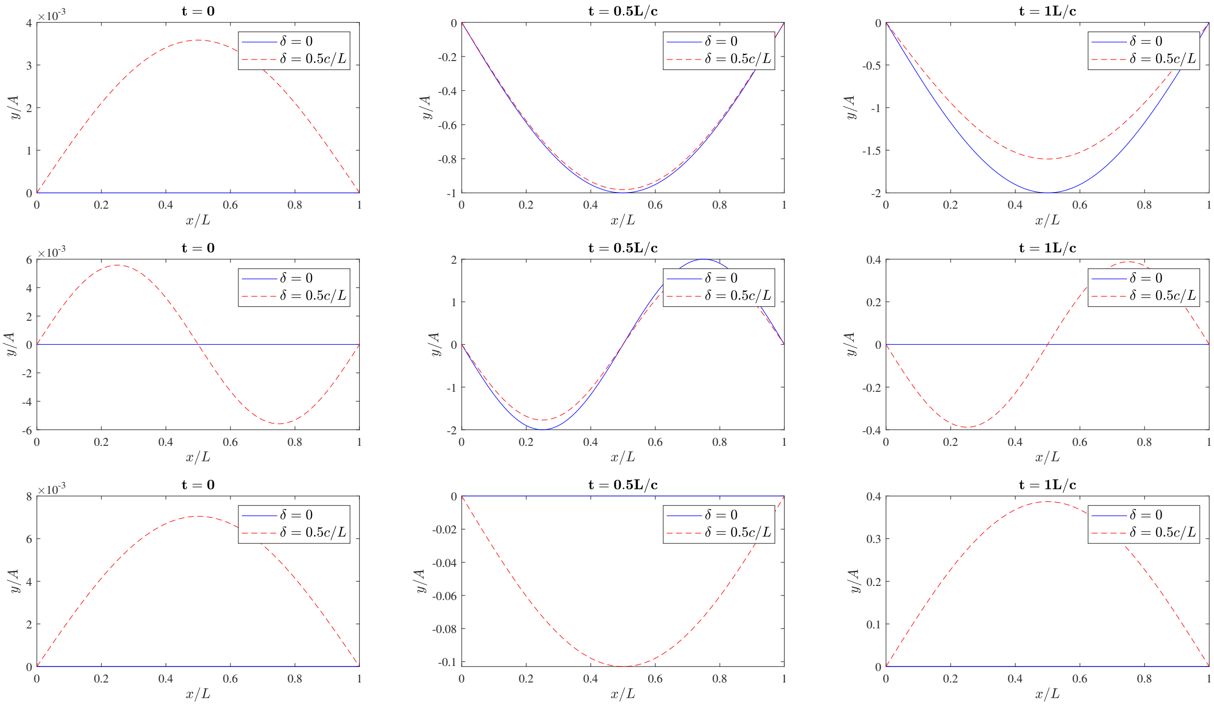

Figure 5.5: Total non-resonant oscillations, at three distinct times, with forcing cancelling the initial free oscillation at time zero. The blue solid lines correspond to no damping, $\delta = 0$, whereas the red dashed lines correspond to oscillations with damping, $\delta = 0.5c/L$. Each row corresponds to a distinct set of values of the mode of oscillation n (which influences the values of spatial wavenumber k and free oscillation $\tilde{\omega}$) and $\overline{\omega}$: the upper row is for $\{n, \overline{\omega}\} = \{1, 4\pi c/L\}$, the middle row is for $\{n, \overline{\omega}\} = \{2, 4\pi c/L\}$ and the bottom row is for $\{n, \overline{\omega}\} = \{1, 3\pi c/L\}$. In all the cases, the wavenumber is related to n by $k = n\pi/L$. The plots are obtained for $\alpha = 0 = \beta$.

The parameters of the oscillations, such as the applied frequency, the damping factor, the oscillation frequency and wavenumber (with the last two defined by the mode of oscillation n), are the same in the figure 5.5 and figure 5.3. The only difference is in the value of F. In the figure 5.5, the force F is opposite to the amplitude A, following the relation (5.30a) whereas in the figure 5.3 the relation is $A = FL^2$. The figure 5.5 shows that, even with this relation, the total oscillation is not cancelled at all time. Indeed, only at time zero the oscillation is totally cancelled when there is no damping. Otherwise, with damping, the total oscillation is not cancelled at any time, including the initial instant. This property can be verified using the equation (5.30b) at time zero,

$$y(x, 0) = A \sin(kx) [\cos\alpha - \cos(\beta + \phi)] \neq 0, \tag{5.42}$$

unless $\beta + \phi = \alpha$; in the figures, $\beta = 0 = \alpha$ and $\phi \neq 0$ so this last condition is not met. This would be zero only if ϕ is zero which corresponds to no damping. In this last case, with no damping (with

$\delta = \phi = 0$), when the phase shifts are related by $\alpha = -\beta$, as in the blue solid lines of figure 5.5, there is no oscillation if the natural $\tilde{\omega} = kc$ and applied $\overline{\omega}$ frequencies coincide. However, in that lines of figure 5.5, the two frequencies do not coincide and they show zero oscillation only at instants when $\tilde{\omega}t = \overline{\omega}t + 2\pi p$ or $\tilde{\omega}t = -\overline{\omega}t + 2\pi p$ with p being an integer number.

In the case (5.30a) of forcing F and natural amplitude A having opposite signs, the total oscillation (5.30b) does not vanish at all time and leads to the energy

$$\begin{aligned} 2\frac{E(x,t)}{A^2} &= Tk^2\cos^2(kx)\left[\mathrm{e}^{-t\delta}\cos(\tilde{\omega}t-\alpha) - \cos(\overline{\omega}t+\beta+\phi)\right]^2 \\ &\quad + \rho\sin^2(kx)\left\{\overline{\omega}\sin(\overline{\omega}t+\beta+\phi) - \mathrm{e}^{-t\delta}\left[\tilde{\omega}\sin(\tilde{\omega}t-\alpha)+\delta\cos(\tilde{\omega}t-\alpha)\right]\right\}^2. \end{aligned} \tag{5.43}$$

When averaging the energy (5.43) over the length of the string denoted by the symbol $\rangle\ldots\langle$, appear the factors

$$\rangle\cos^2(kx), \sin^2(kx)\langle \equiv \frac{1}{L}\int_0^L \left[\frac{1}{2} \pm \frac{1}{2}\cos(2kx)\right]\mathrm{d}x = \frac{1}{2} \pm \frac{1}{2L}\left[\frac{1}{2k}\sin(2kx)\right]_0^L = \frac{1}{2}, \tag{5.44}$$

and thus the average energy as a function of time is given by

$$\begin{aligned} \frac{4e(t)}{A^2} &= \frac{4}{A^2}\rangle E(x,t)\langle = Tk^2\cos^2(\overline{\omega}t+\beta+\phi) + \rho\overline{\omega}^2\sin^2(\overline{\omega}t+\beta+\phi) \\ &- 2\mathrm{e}^{-t\delta}\left\{Tk^2\cos(\overline{\omega}t+\beta+\phi)\cos(\tilde{\omega}t-\alpha)\right. \\ &+ \left.\rho\overline{\omega}\sin(\overline{\omega}t+\beta+\phi)\left[\tilde{\omega}\sin(\tilde{\omega}t-\alpha)+\delta\cos(\tilde{\omega}t-\alpha)\right]\right\} \\ &+ \mathrm{e}^{-2t\delta}\left[Tk^2\cos^2(\tilde{\omega}t-\alpha) + \rho\tilde{\omega}^2\sin^2(\tilde{\omega}t-\alpha) + 2\rho\tilde{\omega}\delta\sin(\tilde{\omega}t-\alpha)\cos(\tilde{\omega}t-\alpha)\right], \end{aligned} \tag{5.45a}$$

where was used the assumption of weak damping (5.40a) implying $\rho\tilde{\omega}^2 = \rho k^2c^2 = k^2T$ and leading to

$$\begin{aligned} \frac{4e(t)}{A^2} &= Tk^2\cos^2(\overline{\omega}t+\beta+\phi) + \rho\overline{\omega}^2\sin^2(\overline{\omega}t+\beta+\phi) - 2\mathrm{e}^{-t\delta}\left\{Tk^2\cos(\overline{\omega}t+\beta+\phi)\cos(kct-\alpha)\right. \\ &+ \left.\rho\overline{\omega}\sin(\overline{\omega}t+\beta+\phi)\left[kc\sin(kct-\alpha)+\delta\cos(kct-\alpha)\right]\right\} + \mathrm{e}^{-2t\delta}\left[Tk^2 + \rho kc\delta\sin(2kct-2\alpha)\right]. \end{aligned} \tag{5.45b}$$

The total energy simplifies further in the case of resonant forcing.

5.3.2 Energy of total oscillations in resonant case

The resonant forcing is the particular case (5.32) of non-resonant forcing, simplifying the forced non-resonant oscillation (5.24) to the forced resonant oscillation (5.34). Choosing the forcing amplitude to oppose the free oscillation (5.38a) leads to the total oscillation (5.38b). The total energy is (5.45b) with

(5.32) leading to

$$\frac{4e_*(t)}{Tk^2A^2} = 1 - 2\mathrm{e}^{-t\delta}\left\{\cos(kct+\beta+\phi)\cos(kct-\alpha)\right.$$
$$\left. + \sin(kct+\beta+\phi)\left[\sin(kct-\alpha) + \frac{\delta}{kc}\cos(kct-\alpha)\right]\right\} + \mathrm{e}^{-2t\delta}\left[1+\frac{\delta}{kc}\sin(2kct-2\alpha)\right], \tag{5.46a}$$

or equivalently

$$\frac{4e_*(t)}{Tk^2A^2} = 1 - 2\mathrm{e}^{-t\delta}\cos(\alpha+\beta+\phi) + \mathrm{e}^{-2t\delta}$$
$$+ \mathrm{e}^{-t\delta}\frac{\delta}{kc}\left[-2\sin(kct+\beta+\phi)\cos(kct-\alpha) + \mathrm{e}^{-t\delta}\sin(2kct-2\alpha)\right]. \tag{5.46b}$$

Choosing the phase $\beta+\phi = \pi/2-\alpha$, the energy (5.46b) simplifies further to

$$\frac{4e_*(t)}{Tk^2A^2} = 1 + \mathrm{e}^{-2t\delta} + \mathrm{e}^{-t\delta}\frac{\delta}{kc}\left[-2\cos^2(kct-\alpha) + \mathrm{e}^{-t\delta}\sin(2kct-2\alpha)\right]. \tag{5.47}$$

Taking the average over a period, denoted by $\langle\ldots\rangle$, the time average $\left\langle\cos^2(kct-\alpha)\right\rangle$ equal to $1/2$ and the time average $\langle\sin(2kct-2\alpha)\rangle$ equal to 0 can be used to evaluate the average total energy that becomes

$$\frac{4}{Tk^2A^2}\langle e_*(t)\rangle \equiv G_* = 1 + \mathrm{e}^{-2t\delta} - \frac{\delta}{kc}\mathrm{e}^{-t\delta}. \tag{5.48}$$

The free oscillation has energy corresponding to the terms in (5.43) with factor $\exp(-t\delta)$:

$$\frac{2\tilde{E}_*(x,t)}{A^2}\mathrm{e}^{2t\delta} = Tk^2\cos^2(kx)\cos^2(\tilde{\omega}t-\alpha) + \rho\sin^2(kx)\left[\tilde{\omega}\sin(\tilde{\omega}t-\alpha)+\delta\cos(\tilde{\omega}t-\alpha)\right]^2. \tag{5.49}$$

Using (5.44) in (5.49) simplifies the energy of the free oscillation,

$$\frac{4\tilde{e}_*(t)}{A^2} = \frac{4}{A^2}\rangle E_*(x,t)\langle = \mathrm{e}^{-2t\delta}\left[Tk^2\cos^2(\tilde{\omega}t-\alpha) + \rho\tilde{\omega}^2\sin^2(\tilde{\omega}t-\alpha) + \rho\tilde{\omega}\delta\sin(2\tilde{\omega}t-2\alpha)\right]; \tag{5.50}$$

with the weak damping approximation (5.40a) and regarding $\rho\tilde{\omega}^2 = k^2T$, it simplifies to

$$\frac{4\tilde{e}_*(t)}{Tk^2A^2} = \mathrm{e}^{-2t\delta}\left[1+\frac{\delta}{kc}\sin(2kct-2\alpha)\right]. \tag{5.51}$$

Using again the result $\langle\sin(2kct-2\alpha)\rangle = 0$, the average over a period for the free oscillation (5.51) is

$$\frac{4}{Tk^2A^2}\langle\tilde{e}_*\rangle \equiv \tilde{G}_* = \mathrm{e}^{-2t\delta}. \tag{5.52}$$

Consequently the ratio of energies of the total oscillation to the free oscillation is

$$\frac{G_*}{\tilde{G}_*} = 1 - \frac{\delta}{kc}\mathrm{e}^{t\delta} + \mathrm{e}^{2t\delta} > 1, \tag{5.53}$$

showing that there is an increase, because the forced oscillation has constant amplitude and dominates the damped free oscillation.

The figure 5.6 shows the ratio of energies of forced oscillation G_* to free oscillation $\tilde{G}_*$ as function of dimensionless time. The plots are based on the equation (5.53). Therefore the plots follow that equation which is a composition of exponential functions and so the ratio of energies increases over time. That ratio increases faster for a greater value of damping $\delta L/c$ because as damping increases the free oscillation decays faster and has less energy compared with the forced oscillation that has constant amplitude. Although it seems that the plots in the subfigures of figure 5.6 are the same for different values of k, in fact the values of the graphs are slightly different. Changing the value of k only has effect on the second term on the right-hand side of (5.53). In all the cases, the value of $\delta/(kc)$ is almost zero and therefore this term is negligible with respect to the plots of figure 5.6. For weak damping (5.40a) from $\mathrm{e}^{t\delta} > 1 > \delta/(kc)$ follows $G_*(t)/\tilde{G}_*(t) > 1$, that the total energy of the free plus forced oscillation will exceed the energy of the free oscillation. Thus, forcing with constant amplitude is not an effective method of suppressing damped free oscillations. This suggests the consideration of forcing with amplitude decaying exponentially with time (sections 5.4 and 5.5).

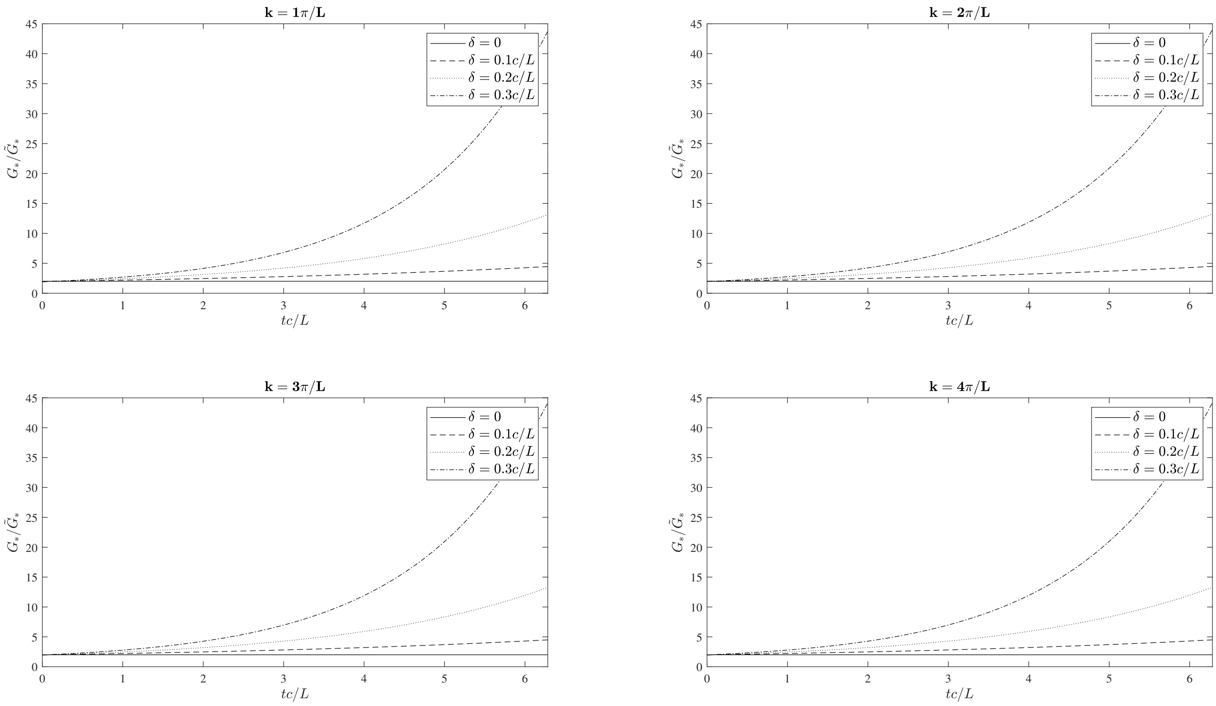

Figure 5.6: Energy of total oscillation G_* divided by the energy of free oscillation $\tilde{G}_*$ as a function of dimensionless time tc/L. The plots are shown as functions of k and $\delta L/c$ whereas in all cases $k = n\pi/L$.

5.4 Forcing with applied frequency, phase and decay

Next, the forcing is reconsidered still with arbitrary applied frequency and phase, replacing constant magnitude (section 5.2) by magnitude decaying exponentially with time (section 5.4), with a decay rate that does not need to coincide with the damping. The applied frequency may be distinct or coincident with the natural frequency respectively in non-resonant (subsection 5.4.1) and resonant (subsection 5.4.2) cases. The forced oscillation is considered with: (i) amplitude opposing the free oscillation; (ii) exponential decay in time of the forcing equal to the damping of the free oscillation; (iii) matching of the applied and free phases due to damping.

5.4.1 Non-resonant forcing with exponential time decay

Next, the wave-diffusion equation (5.1b) is forced not only with applied frequency $\overline{\omega}$, but also with exponential decay ε in time,

$$\frac{\partial^2 \overline{y}}{\partial x^2} - \frac{1}{\chi}\frac{\partial \overline{y}}{\partial t} - \frac{1}{c^2}\frac{\partial^2 \overline{y}}{\partial t^2} = F \sin(kx) \exp(-\varepsilon t) \exp(-\mathrm{i}\overline{\omega} t - \mathrm{i}\beta), \tag{5.54}$$

retaining the phase shift β relative to $-\alpha$ for the free oscillation. The forced oscillation is sought in a similar form,

$$\overline{y}(x,t) = B \sin(kx) \exp(-\varepsilon t) \exp(-\mathrm{i}\overline{\omega} t - \mathrm{i}\beta), \tag{5.55}$$

and substitution of (5.55) in (5.54) gives

$$c^2 \frac{F}{B} = -(\mathrm{i}\overline{\omega} + \varepsilon)^2 + \frac{(\mathrm{i}\overline{\omega} + \varepsilon) c^2}{\chi} - k^2 c^2 = \overline{\omega}^2 + \mathrm{i}\overline{\omega}\left(\frac{c^2}{\chi} - 2\varepsilon\right) - k^2 c^2 + \frac{c^2 \varepsilon}{\chi} - \varepsilon^2, \tag{5.56a}$$

that simplifies to (5.18a) for $\varepsilon = 0$. Introducing the damping (5.5) and oscillation frequency (5.27) in (5.56a) leads to

$$c^2 \frac{F}{B} = \overline{\omega}^2 - k^2 c^2 - \varepsilon^2 + 2\varepsilon\delta + 2\mathrm{i}\overline{\omega}(\delta - \varepsilon) = \overline{\omega}^2 - \tilde{\omega}^2 - (\delta - \varepsilon)^2 + 2\mathrm{i}\overline{\omega}(\delta - \varepsilon) \equiv C \mathrm{e}^{\mathrm{i}\phi}, \tag{5.56b}$$

with amplitude

$$C = \left| \left[\overline{\omega}^2 - \tilde{\omega}^2 - (\delta - \varepsilon)^2\right]^2 + 4\overline{\omega}^2 (\delta - \varepsilon)^2 \right|^{1/2} \tag{5.57a}$$

and phase

$$\tan\phi = \frac{2\overline{\omega}(\delta - \varepsilon)}{\overline{\omega}^2 - \tilde{\omega}^2 - (\delta - \varepsilon)^2}. \tag{5.57b}$$

Setting $\varepsilon = 0$ in (5.57a) and (5.57b) leads back respectively to (5.21a) and (5.21b). Substituting (5.56b) in (5.55) and taking the real part, the forced oscillation with applied frequency $\overline{\omega}$, phase β and decay ε is given by

$$\overline{y}(x,t) = c^2 \frac{F}{C} \sin(kx)\, \mathrm{e}^{-\varepsilon t} \cos(\overline{\omega} t + \beta + \phi), \tag{5.58}$$

as the solution of the real part of the differential equation (5.54),

$$\frac{\partial^2 \overline{y}}{\partial x^2} - \frac{1}{\chi}\frac{\partial \overline{y}}{\partial t} - \frac{1}{c^2}\frac{\partial^2 \overline{y}}{\partial t^2} = F \sin(kx)\, \mathrm{e}^{-\varepsilon t} \cos(\overline{\omega} t + \beta), \tag{5.59}$$

that is the wave diffusion equation with sinusoidal forcing with applied frequency $\overline{\omega}$, phase shift β and amplitude F decaying exponentially with time at rate ε.

Adding to the forced oscillation (5.58) the free oscillation (5.10) still leads to the next oscillation,

$$y\left(x,t\right) = \tilde{y}\left(x,t\right) + \overline{y}\left(x,t\right) = \sin\left(kx\right)\left[A\mathrm{e}^{-t\delta}\cos\left(\tilde{\omega}t-\alpha\right) + c^2\frac{F}{C}\mathrm{e}^{-\varepsilon t}\cos\left(\overline{\omega}t+\beta+\phi\right)\right], \tag{5.60}$$

where: (i) both oscillations have the same spatial dependence (5.3); (ii) the amplitudes are different, and choosing opposite values,

$$F = -\frac{CA}{c^2} = -A\left|\left[\frac{\overline{\omega}^2-\tilde{\omega}^2}{c^2} - \frac{\left(\delta-\varepsilon\right)^2}{c^2}\right]^2 + 4\overline{\omega}^2\frac{\left(\delta-\varepsilon\right)^2}{c^4}\right|^{1/2}, \tag{5.61a}$$

leads to

$$y\left(x,t\right) = A\sin\left(kx\right)\left[\mathrm{e}^{-t\delta}\cos\left(\tilde{\omega}t-\alpha\right) - \mathrm{e}^{-\varepsilon t}\cos\left(\overline{\omega}t+\beta+\phi\right)\right]; \tag{5.61b}$$

(iii) the damping δ (5.5) of the free oscillation is generally distinct from the decay ε of the forced oscillation, and if they coincide,

$$\varepsilon = \delta = \frac{c^2}{2\chi}, \tag{5.62a}$$

then the forcing amplitude F, opposite to A, is related to the free wave amplitude A by

$$F = -\frac{A}{c^2}\left(\overline{\omega}^2 - \tilde{\omega}^2\right), \tag{5.62b}$$

and the forced oscillation simplifies to

$$y\left(x,t\right) = \frac{Fc^2}{\tilde{\omega}^2-\overline{\omega}^2}\sin\left(kx\right)\mathrm{e}^{-t\delta}\left[\cos\left(\tilde{\omega}t-\alpha\right) - \cos\left(\overline{\omega}t+\beta+\phi\right)\right]. \tag{5.62c}$$

Choosing an applied phase shift

$$\beta = -\phi - \alpha \tag{5.63a}$$

simplifies further the total oscillation to

$$y\left(x,t\right) = \frac{Fc^2}{\tilde{\omega}^2-\overline{\omega}^2}\sin\left(kx\right)\mathrm{e}^{-t\delta}\left[\cos\left(\tilde{\omega}t-\alpha\right) - \cos\left(\overline{\omega}t-\alpha\right)\right]. \tag{5.63b}$$

Choosing an applied frequency equal to the oscillation frequency (5.6),

$$\overline{\omega} = \tilde{\omega} = \sqrt{k^2c^2-\delta^2}, \tag{5.64}$$

leads to resonance, that is considered next.

5.4.2 Resonant forcing with exponential time decay

Next is considered the resonant forcing, with: (i) applied frequency equal to the oscillation frequency (5.64), that reduces to the natural frequency (5.32) in the absence of damping; (ii) exponential temporal decay of the forcing (5.62a) equal to the damping of the free oscillation (5.5); (iii) applied phase (5.63a) matched to the phase of free oscillation (5.14b) and phase shift due to damping (5.19b). This corresponds to the limit $\overline{\omega} \to \tilde{\omega}$ in (5.63b), for which both the numerator and denominator vanish. Applying L'Hôpital's rule [39], the 0/0 indeterminacy is solved differentiating with regard to $\overline{\omega}$ the numerator,

$$\frac{\partial}{\partial \overline{\omega}} \left[\cos\left(\tilde{\omega} t - \alpha\right) - \cos\left(\overline{\omega} t - \alpha\right)\right] = t \sin\left(\overline{\omega} t - \alpha\right), \tag{5.65a}$$

and denominator,

$$\frac{\partial}{\partial \overline{\omega}} \left(\tilde{\omega}^2 - \overline{\omega}^2\right) = -2\overline{\omega}; \tag{5.65b}$$

then, taking the limit $\overline{\omega} \to \tilde{\omega}$ leads to a finite solution:

$$\overline{y}_* \left(x, t\right) = \lim_{\overline{\omega} \to \tilde{\omega}} y\left(x, t\right) = -\frac{Fc^2 t}{2\tilde{\omega}} \sin\left(kx\right) \mathrm{e}^{-t\delta} \sin\left(\tilde{\omega} t - \alpha\right). \tag{5.65c}$$

Note that the linear amplitude growth in time typical of resonance is ultimately dominated by the exponential time decay of the forcing.

An alternative method to obtain the result (5.65c) is to reconsider (5.63b) when the natural frequency $\tilde{\omega}$ and applied frequency $\overline{\omega}$ are close, in other words, when the frequency difference $2\Delta\omega$ is small compared with the average frequency $\hat{\omega}$:

$$2\Delta\omega \equiv \overline{\omega} - \tilde{\omega} \ll \hat{\omega} \equiv \frac{\tilde{\omega} + \overline{\omega}}{2}. \tag{5.66a}$$

That is equivalent to assume

$$\overline{\omega} = \hat{\omega} + \Delta\omega \tag{5.66b}$$

and

$$\tilde{\omega} = \hat{\omega} - \Delta\omega. \tag{5.66c}$$

Noting also the property $\overline{\omega}^2 - \tilde{\omega}^2 = \left(\overline{\omega} - \tilde{\omega}\right)\left(\overline{\omega} + \tilde{\omega}\right) = 2\hat{\omega}\Delta\omega$ and substituting these last relations in (5.63b) gives

$$\begin{aligned} y\left(x, t\right) &= -\frac{Fc^2}{2\hat{\omega}} \sin\left(kx\right) \mathrm{e}^{-t\delta} \left\{\cos\left[\left(\hat{\omega} + \Delta\omega\right) t - \alpha\right] - \cos\left[\left(\hat{\omega} - \Delta\omega\right) t - \alpha\right]\right\} \\ &= -\frac{Fc^2}{2\hat{\omega}\Delta\omega} \sin\left(kx\right) \mathrm{e}^{-t\delta} \sin\left(\hat{\omega} t - \alpha\right) \sin\left(t\Delta\omega\right), \end{aligned} \tag{5.66d}$$

demonstrating the phenomenon of "beats", that is sinusoidal oscillation at the average frequency $\hat{\omega}$ with a slow $\Delta\omega \ll \hat{\omega}$ sinusoidal amplitude modulation. The limit $\overline{\omega} \to \tilde{\omega}$ corresponds to $\Delta\omega \to 0$ and using

$$\lim_{\Delta\omega \to 0} \frac{\sin\left(t\Delta\omega\right)}{\Delta\omega} = t \tag{5.67a}$$

in (5.66d) leads to the resonant solution

$$\overline{y}_* \left(x, t\right) = \lim_{\Delta\omega \to 0} y\left(x, t\right) = -\lim_{\hat{\omega} \to \tilde{\omega}} \frac{Fc^2 t}{2\hat{\omega}} \sin\left(kx\right) \mathrm{e}^{-t\delta} \sin\left(\hat{\omega} t - \alpha\right) = -\frac{Fc^2 t}{2\tilde{\omega}} \sin\left(kx\right) \mathrm{e}^{-t\delta} \sin\left(\tilde{\omega} t - \alpha\right), \tag{5.67b}$$

which coincides with (5.65c).

The forced resonant oscillation is considered: (i) for zero phase $\alpha = 0$ choosing initial time suitably, $t \to t + \alpha/\tilde{\omega}$; (ii) introducing the dimensionless time,

$$\theta \equiv \tilde{\omega} t - \alpha, \tag{5.68}$$

in the resonant oscillation (5.65c)

$$\overline{Y}_* \left(x, \theta\right) = \overline{y}_* \left(x, t\right) = D \sin\left(kx\right) g\left(\theta\right), \tag{5.69}$$

where the time dependence appears in

$$g\left(\theta\right) \equiv \left(\tilde{\omega} t + \alpha\right) \mathrm{e}^{-t\delta} \sin\left(\tilde{\omega} t\right) = \left(\theta + \alpha\right) \mathrm{e}^{-q\theta} \sin\theta \tag{5.70a}$$

with q denoting the ratio of damping (5.5) to oscillation frequency (5.6),

$$q \equiv \frac{\delta}{\tilde{\omega}} = \frac{\delta}{\sqrt{k^2 c^2 - \delta^2}} = \left|\frac{k^2 c^2}{\delta^2} - 1\right|^{-1/2} = \left|\left(\frac{2k\chi}{c}\right)^2 - 1\right|^{-1/2}, \tag{5.70b}$$

and with amplitude

$$D \equiv -\frac{F c^2}{2\tilde{\omega}^2} \exp\left(-\frac{\alpha\delta}{\tilde{\omega}}\right). \tag{5.71}$$

The time dependence (5.70a) is illustrated in figure 5.7 for several values of the parameter:

$$q = \left\{0.05, 0.10, 0.15, 0.20, 0.25, 0.30\right\}. \tag{5.72}$$

The initial linear growth in θ is ultimately dominated by the exponential, with maximum at the root of

$$0 = \frac{\mathrm{d}g}{\mathrm{d}\theta} = \mathrm{e}^{-q\theta} \left[\sin\theta + \left(\theta + \alpha\right)\left(\cos\theta - q\sin\theta\right)\right]. \tag{5.73a}$$

Thus, the maximum is at

$$\frac{1}{\theta_\mathrm{m} + \alpha} = \frac{q\sin\theta_\mathrm{m} - \cos\theta_\mathrm{m}}{\sin\theta_\mathrm{m}} = q - \cot\theta_\mathrm{m}. \tag{5.73b}$$

The table 5.1 indicates for each value of (5.72) the values of θ_m, corresponding to the time t_m as fraction of the period: $t_\mathrm{m}/\tau = \tilde{\omega} t_\mathrm{m}/\left(2\pi\right) = \theta_\mathrm{m}/\left(2\pi\right)$. The peak amplitude at the time t_m is

$$g\left(\theta_\mathrm{m}\right) = \left(\theta_\mathrm{m} + \alpha\right) \exp\left(-q\theta_\mathrm{m}\right) \sin\theta_\mathrm{m}. \tag{5.73c}$$

The oscillation has a lower peak earlier as q increases, implying a reduction in the energy of oscillation.

The figure 5.7 illustrates the temporal dependence of the forced resonant oscillations (5.70a) as a function of dimensionless time (5.68) for different ratios (5.70b) of damping to oscillation frequency. Resonance requires three conditions: (i) applied frequency equal to oscillation frequency (5.64); (ii) decay of the forcing equal to the damping (5.62a); (iii) matching (5.63a) of the phases of forcing β, damping ϕ and free oscillations α. The amplitude is given by (5.71). The oscillations with amplitude initially growing linearly with time are ultimately dominated by the exponential decay, sooner for larger decay.

q	θ_{m} (rad)	θ_{m} (°)	t_{m}/τ	$g(\theta_{\mathrm{m}})$
0.05	1.9949	114.3	0.3175	1.6456
0.10	1.9600	112.3	0.3119	1.4906
0.15	1.9251	11.03	0.3064	1.3527
0.20	1.9650	108.0	0.3000	1.2297
0.25	1.8535	106.2	0.2950	1.1198
0.30	1.8169	104.1	0.2892	1.0217

Table 5.1: Resonant forcing with exponential time decay. The results are obtained for $\alpha = 0$.

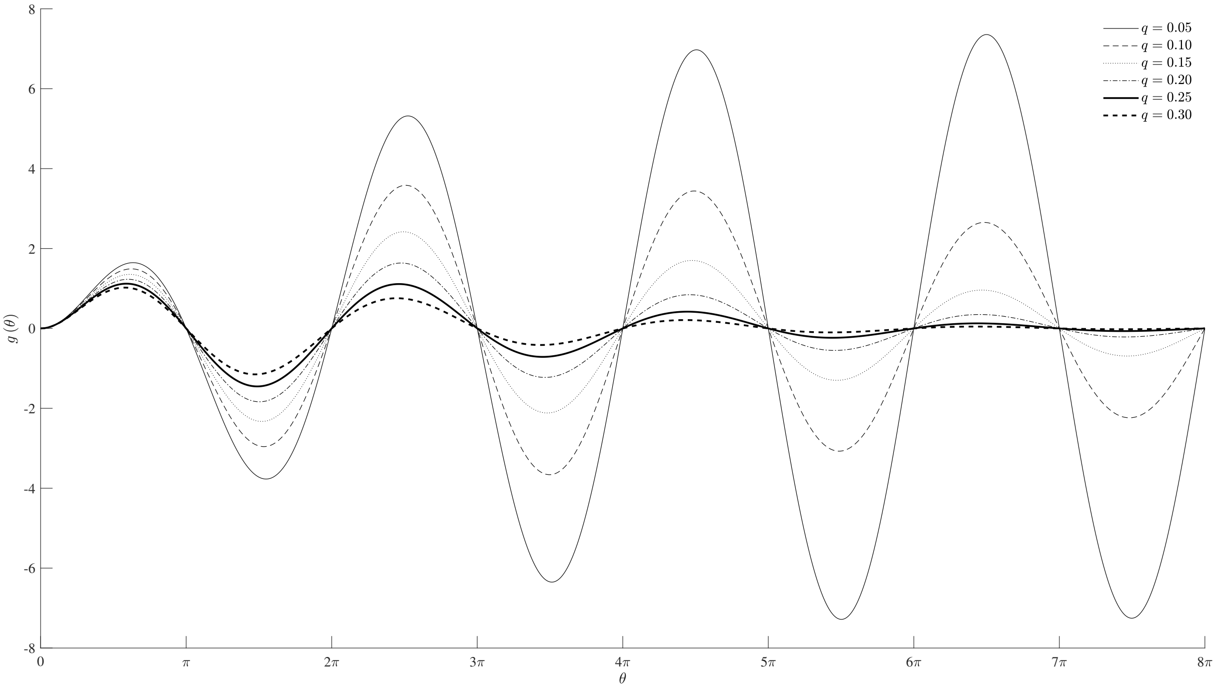

Figure 5.7: Temporal dependence of the forced resonant oscillations g of a linear damped oscillator as a function of dimensionless time $\theta \equiv \tilde{\omega} t$ where the applied frequency $\overline{\omega}$ is equal to the oscillation frequency $\tilde{\omega}$, that is, $\overline{\omega} = \tilde{\omega}$. The plots are obtained for $\alpha = 0$. The forcing decays exponentially with time at the same rate as the free wave damping. The phases are matched to lead to oscillations initially increasing with time, ultimately decaying to damping, sooner for stronger damping.

5.5 Comparison of the energies of total and free oscillations

The total energy density (5.41) is the sum of kinetic and elastic energies. It may be averaged (5.44) over the length of the string. The time average over a period may be taken not including a slowly decaying exponential term. The latter ensures a finite oscillation energy over all time (subsection 5.5.1) that is compared between (i) the free damped oscillation and (ii) the resonant forced oscillation with the same decay (subsection 5.5.2).

5.5.1 Energy averaged over period and length of string

The energy density (5.41) is given in terms of the dimensionless time (5.68) by

$$2E\left(x,\theta\right)=\rho\tilde{\omega}^{2}\left|\frac{\partial Y}{\partial\theta}\right|^{2}+T\left|\frac{\partial Y}{\partial x}\right|^{2}. \tag{5.74}$$

The free oscillation corresponds to the first term in (5.61b),

$$\tilde{Y}\left(x,\theta\right)=A\sin\left(kx\right)\mathrm{e}^{-q\theta}\cos\theta, \tag{5.75}$$

and the corresponding energy is

$$\frac{2\tilde{E}\left(x,\theta\right)}{A^{2}}=\mathrm{e}^{-2q\theta}\left[k^{2}T\cos^{2}\left(kx\right)\cos^{2}\theta+\rho\tilde{\omega}^{2}\sin^{2}\left(kx\right)\left(\sin\theta+q\cos\theta\right)^{2}\right]. \tag{5.76}$$

The spatial average (5.44) leads to

$$\frac{2}{A^{2}}\left\rangle\tilde{E}\left(x,\theta\right)\right\langle=\frac{\mathrm{e}^{-2q\theta}}{2}\left\{\rho c^{2}k^{2}\left[\cos^{2}\theta+\left(\sin\theta+q\cos\theta\right)^{2}\right]-\rho\delta^{2}\left(\sin\theta+q\cos\theta\right)^{2}\right\}, \tag{5.77}$$

that simplifies for weak damping $\delta^{2}\ll\tilde{\omega}^{2}\sim k^{2}c^{2}$ or $q^{2}\ll1$ to

$$\tilde{e}\left(\theta\right)\equiv\frac{4\left\rangle\tilde{E}\left(x,\theta\right)\right\langle}{\rho c^{2}k^{2}A^{2}}=\mathrm{e}^{-2q\theta}\left[1+q\sin\left(2\theta\right)\right]. \tag{5.78}$$

Knowing the result $\left\langle\sin\left(2\theta\right)\right\rangle=0$, evaluated in the appendix B.1, the average over a period leads to $\tilde{G}\left(\theta\right)\equiv\left\langle\tilde{e}\left(\theta\right)\right\rangle=\exp\left(-2q\theta\right)$. The total energy over all time of the damped oscillation is finite,

$$\tilde{H}\equiv\int_{0}^{\infty}\tilde{G}\left(\theta\right)\,\mathrm{d}\theta=\int_{0}^{\infty}\mathrm{e}^{-2q\theta}\,\mathrm{d}\theta=\frac{1}{2q}=\frac{\tilde{\omega}}{2\delta}, \tag{5.79}$$

and larger for higher oscillation frequency and smaller damping. If there is no damping, $\delta\rightarrow0$, the amplitude is constant and the energy is infinite over infinite time.

For the total oscillation, the forced oscillation (5.69) and (5.70a) is added to the free oscillation (5.75):

$$Y_{*}\left(x,\theta\right)=\tilde{Y}\left(x,\theta\right)+\overline{Y}_{*}\left(x,\theta\right)=\mathrm{e}^{-q\theta}\left[A\cos\theta+D\left(\theta+\alpha\right)\sin\theta\right]\sin\left(kx\right). \tag{5.80}$$

Choosing opposite amplitudes, $D=-A$, and setting $\alpha=0$ lead to

$$Y_{*}\left(x,\theta\right)=A\sin\left(kx\right)\mathrm{e}^{-q\theta}\left(\cos\theta-\theta\sin\theta\right). \tag{5.81}$$

The corresponding energy density is given by

$$\begin{aligned}2\frac{E_{*}\left(x,\theta\right)}{A^{2}}=\mathrm{e}^{-2q\theta}&\left\{Tk^{2}\cos^{2}\left(kx\right)\left(\cos\theta-\theta\sin\theta\right)^{2}\right.\\&\left.+\rho\tilde{\omega}^{2}\sin^{2}\left(kx\right)\left[\left(\theta\cos\theta+2\sin\theta\right)-q\left(\cos\theta-\theta\sin\theta\right)\right]^{2}\right\}.\end{aligned} \tag{5.82a}$$

The weak damping approximation (5.40a) implies $q^2 \ll 1$ in (5.70b) and simplifies the last equation to

$$\begin{aligned}
2\frac{E_*\left(x,\theta\right)}{\rho c^2 k^2 A^2} &= \mathrm{e}^{-2q\theta}\left\{\cos^2\left(kx\right)\left(\cos\theta-\theta\sin\theta\right)^2\right.\\
&\left.+\sin^2\left(kx\right)\left[\left(\theta\cos\theta+2\sin\theta\right)^2-2q\left(\theta\cos\theta+2\sin\theta\right)\left(\cos\theta-\theta\sin\theta\right)\right]\right\}.
\end{aligned}\tag{5.82b}$$

The spatial average (5.44) leads to

$$\begin{aligned}
\mathrm{e}^{2q\theta}\mathrm{e}_*\left(\theta\right) \equiv 4\frac{\rangle E_*\left(x,\theta\right)\langle}{\rho c^2 k^2 A^2}\mathrm{e}^{2q\theta} &= \theta^2+\cos^2\theta+4\sin^2\theta+\theta\sin\left(2\theta\right)\\
&-2q\left[\theta\cos^2\theta-2\theta\sin^2\theta+\sin\left(2\theta\right)-\frac{\theta^2}{2}\sin\left(2\theta\right)\right].
\end{aligned}\tag{5.83}$$

The averages over a period are calculated in the appendix B.1 and are repeated here for convenience:

$$\left\langle\cos^2\theta\right\rangle = \frac{1}{2} = \left\langle\sin^2\theta\right\rangle, \tag{5.84a}$$

$$\left\langle\sin\left(2\theta\right)\right\rangle = 0, \tag{5.84b}$$

$$\left\langle\theta\sin\left(2\theta\right)\right\rangle = -\frac{1}{2}, \tag{5.84c}$$

$$\left\langle\theta\cos^2\theta\right\rangle = \frac{\pi}{2} = \left\langle\theta\sin^2\theta\right\rangle, \tag{5.84d}$$

$$\left\langle\theta^2\sin\left(2\theta\right)\right\rangle = -\pi. \tag{5.84e}$$

Thus, the average energy of the total oscillation is

$$G_*\left(\theta\right) = \left\langle e_*\left(\theta\right)\right\rangle = \mathrm{e}^{-2q\theta}\left(\theta^2+2\right). \tag{5.85}$$

The total energy over all time is given by

$$H_* \equiv \int_0^\infty G_*\left(\theta\right)\,\mathrm{d}\theta = I+\frac{1}{q}, \tag{5.86a}$$

where

$$I \equiv \int_0^\infty \theta^2\mathrm{e}^{-2q\theta}\,\mathrm{d}\theta \tag{5.86b}$$

is evaluated next to compare with the total energy of the free oscillation.

5.5.2 Total energy of total oscillation over all time

Noting the property

$$\frac{\partial}{\partial q}\left(\mathrm{e}^{-2q\theta}\right) = -2\theta\mathrm{e}^{-2q\theta}, \tag{5.87a}$$

the integral (5.86b) is evaluated by

$$I = \left(-\frac{1}{2}\frac{\partial}{\partial q}\right)^2\int_0^\infty \mathrm{e}^{-2q\theta}\,\mathrm{d}\theta = \frac{1}{4}\frac{\partial^2}{\partial q^2}\left(\frac{1}{2q}\right) = \frac{1}{4q^3}. \tag{5.87b}$$

Therefore the energy of the total oscillation (5.86a) is

$$H_* = \frac{1}{4q^3} + \frac{1}{q}. \tag{5.87c}$$

The ratio to the energy of the free oscillation (5.79) is

$$J \equiv \frac{H_*}{\tilde{H}} = \frac{1}{2q^2} + 2 = \frac{\tilde{\omega}^2}{2\delta^2} + 2 = \frac{k^2c^2}{2\delta^2} + 2 = \frac{2k^2\chi^2}{c^2} + 2 \tag{5.88}$$

where were used (5.70b), (5.64) and (5.5) in the weak damping approximation $\tilde{\omega} \sim kc$. The figure 5.8 shows as a function of $0.05 < q < 0.3 \ll 1$ the energy over all time of the free oscillation (5.79), total oscillation (5.87c) and their ratio (5.88).

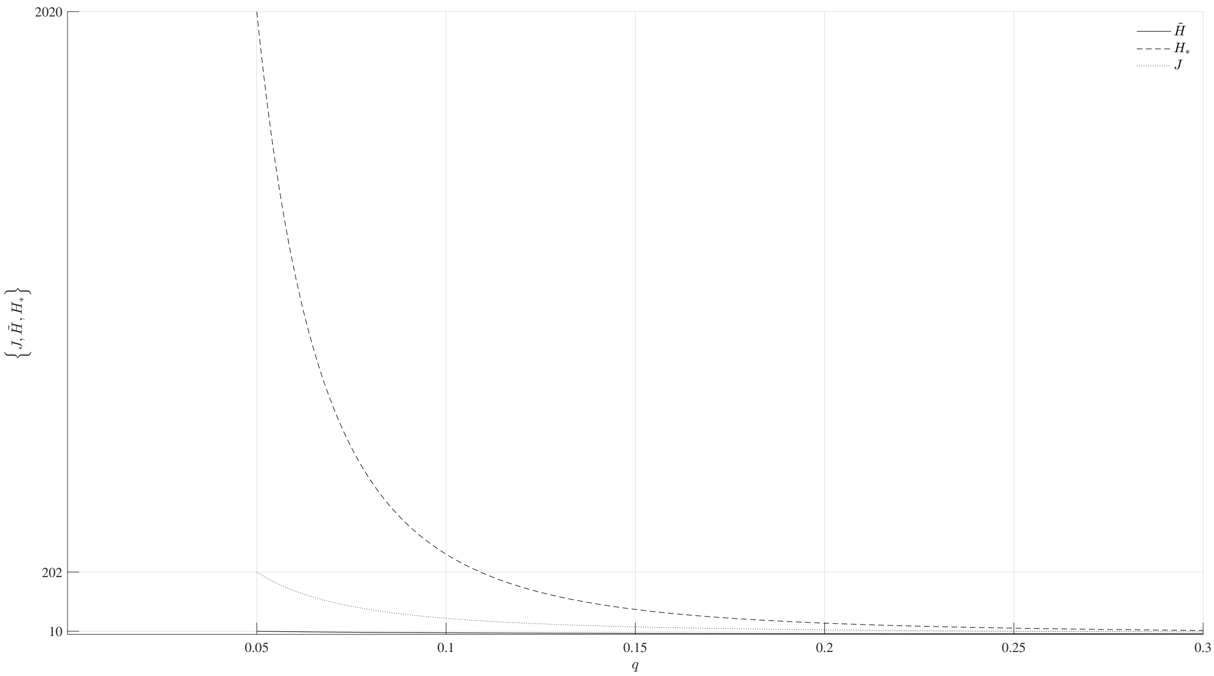

Figure 5.8: Total energy over all time of the total oscillation H_*, total energy over all time of the free oscillation $\tilde{H}$ and the ratio $J \equiv H_*/\tilde{H}$, plotted as functions of the ratio of damping to oscillation frequency, $q \equiv \delta/\tilde{\omega}$.

The weak damping approximation (5.40a) implies $q^2 \ll 1$ that is satisfied by $q < 0.3$. A positive value $J > 0$ in (5.88) requires $1/\left(2q^2\right) + 2 > 0$ that is met by all positive values of q and thus the results are consistent with the weak damping approximation. The suppression of damped free oscillations by resonant forcing at the same frequency (5.64) with opposite amplitude (5.62b), matched phase (5.63a) and decay equal to damping (5.62a), is limited because: (i) the forced oscillations have amplitude initially increasing with time; (ii) the time decay is slow to limit the amplitude growth for weak decay equal to weak damping; (iii) the forced oscillation, in spite of starting at zero, may at intermediate times overwhelm the free oscillation, although both ultimately decay to zero; (iv) the final outcome may be that the energy over all time of the total oscillation may not be smaller, or indeed exceed the energy of the free oscillation for all time. This suggests the consideration of decaying forcing without resonance.

5.6 Non-resonant and resonant forcing with time decay

The forcing of damped oscillations with the applied frequency equal to the oscillation frequency (5.64) leads to resonance (sections 5.4 and 5.5) if the decay rate of forcing equals the damping (5.62a). Making the latter distinct avoids resonance (subsection 5.6.1) and the initially growing amplitude. This allows a comparison of the energy over all time of the total compared with the free oscillation for all ratios of forcing decay to damping (subsection 5.6.2).

5.6.1 Matched oscillations with unequal damping and forcing decay

The total oscillation (5.60) consists of the superposition of free oscillations with amplitude A, damping δ, oscillation frequency $\tilde{\omega}$ and phase α, with the forced oscillations with amplitude c^2F/C, decay ε, applied frequency $\overline{\omega}$ and phase $\beta - \phi$. If the oscillation $\tilde{\omega}$ and applied $\overline{\omega}$ frequencies are distinct, the energies of the free and forced oscillations add together, which is the opposite of the countering of vibrations sought. Hence the oscillation and applied frequencies are assumed to be equal (5.64), and choosing also opposing amplitudes (5.61a), the total oscillation (5.60) simplifies to

$$\hat{y}\left(x,t\right) = A\sin\left(kx\right)\left[\mathrm{e}^{-t\delta}\cos\left(\tilde{\omega}t - \alpha\right) - \mathrm{e}^{-\varepsilon t}\cos\left(\tilde{\omega}t + \beta + \phi\right)\right]. \tag{5.89a}$$

Matching also the phase (5.63a) leads to

$$\hat{y}\left(x,t\right) = A\sin\left(kx\right)\left(\mathrm{e}^{-t\delta} - \mathrm{e}^{-\varepsilon t}\right)\cos\left(\tilde{\omega}t - \alpha\right). \tag{5.89b}$$

The magnitude of the forcing (5.61a) is given by

$$F = -A\frac{\delta - \varepsilon}{c^2}\left|\left(\delta - \varepsilon\right)^2 + 4\overline{\omega}^2\right|^{1/2}, \tag{5.90a}$$

and for weak damping, $\left\{\delta^2, \varepsilon^2, \varepsilon\delta\right\} \ll \tilde{\omega}^2 \sim k^2c^2$, the forcing simplifies to

$$F = -\frac{2A\overline{\omega}}{c^2}\left(\delta - \varepsilon\right) = -\frac{2Ak}{c}\left(\delta - \varepsilon\right). \tag{5.90b}$$

The case of resonance (sections 5.4 and 5.5) is excluded from (5.89b) to (5.90b) by having a forcing decay $\varepsilon \neq \delta$ distinct from the damping.

The total, kinetic plus elastic, energy density (5.41) of the oscillation (5.89b) is

$$\begin{aligned}\frac{2}{A^2}\hat{E}\left(x,t\right) = {}& Tk^2\cos^2\left(kx\right)\left(\mathrm{e}^{-t\delta} - \mathrm{e}^{-\varepsilon t}\right)^2\cos^2\left(\tilde{\omega}t - \alpha\right) \\ &+ \rho\sin^2\left(kx\right)\left[\tilde{\omega}\left(\mathrm{e}^{-t\delta} - \mathrm{e}^{-\varepsilon t}\right)\sin\left(\tilde{\omega}t - \alpha\right) + \left(\delta\mathrm{e}^{-t\delta} - \varepsilon\mathrm{e}^{-\varepsilon t}\right)\cos\left(\tilde{\omega}t - \alpha\right)\right]^2.\end{aligned} \tag{5.91}$$

Averaging over the length of the string (5.44) leads in the weak damping and decay approximation

$\left\{\delta^2, \varepsilon^2, \varepsilon\delta\right\} \ll \tilde{\omega}^2 \sim k^2c^2$ to

$$\frac{4}{\rho c^2 k^2 A^2} \rangle \hat{E}(x,t) \langle = \hat{e}(t) = \left(\mathrm{e}^{-t\delta} - \mathrm{e}^{-\varepsilon t}\right)^2 \\ + 2\left(\mathrm{e}^{-t\delta} - \mathrm{e}^{-\varepsilon t}\right)\left(\delta\mathrm{e}^{-t\delta} - \varepsilon\mathrm{e}^{-\varepsilon t}\right)\cos\left(\tilde{\omega}t - \alpha\right)\sin\left(\tilde{\omega}t - \alpha\right). \tag{5.92}$$

Averaging over a period, and using the results in the appendix B.1, the second term on the right-hand side of (5.92) vanishes leading to

$$\hat{G}(t) \equiv \langle \hat{e}(t) \rangle = \left(\mathrm{e}^{-t\delta} - \mathrm{e}^{-\varepsilon t}\right)^2 = \mathrm{e}^{-2t\delta} + \mathrm{e}^{-2\varepsilon t} - 2\mathrm{e}^{-(\varepsilon+\delta)t}. \tag{5.93}$$

5.6.2 Comparison of free and total energies over all time

The energy of the total oscillation over all time is

$$\hat{H} \equiv \int_0^\infty \hat{G}(t)\;\mathrm{d}t = \frac{1}{2\delta} + \frac{1}{2\varepsilon} - \frac{2}{\varepsilon+\delta}; \tag{5.94a}$$

comparing to the energy of the free oscillation,

$$\tilde{H} = \int_0^\infty \mathrm{e}^{-2t\delta}\,\mathrm{d}t = \frac{1}{2\delta}, \tag{5.94b}$$

the ratio is

$$\frac{\hat{H}}{\tilde{H}} = 1 + \frac{\delta}{\varepsilon} - \frac{4\delta}{\varepsilon+\delta} = 1 - \frac{\delta}{\varepsilon}\frac{3\varepsilon-\delta}{\varepsilon+\delta}. \tag{5.94c}$$

Therefore the energy of the total oscillation is less than the energy of the free oscillation, $\hat{H} < \tilde{H}$, if the forcing decay exceeds one third of the damping, $\varepsilon > \delta/3$. The ratio of energy for all time of the total to the free oscillation depends only on the ratio of damping to forcing decay, $\psi \equiv \varepsilon/\delta$:

$$R(\psi) \equiv \frac{\hat{H}}{\tilde{H}} = 1 - \frac{1}{\psi}\frac{3\psi-1}{\psi+1}. \tag{5.95}$$

The ratio of energies must be positive, $R > 0$, requiring $3\psi - 1 < \psi(\psi+1)$. This last condition is always met for positive values of ψ, except $\psi = 1$, since

$$0 \leq \psi^2 - 2\psi + 1 = (\psi-1)^2. \tag{5.96}$$

The extrema of the energy of total oscillation corresponds to ψ as a root of

$$0 = \frac{\mathrm{d}R}{\mathrm{d}\psi} = \frac{(2\psi+1)(3\psi-1) - 3\psi(\psi+1)}{\psi^2(\psi+1)^2}, \tag{5.97a}$$

implying

$$0 = 3\psi^2 - 2\psi - 1 = (\psi - \psi_+)(\psi - \psi_-). \tag{5.97b}$$

The two roots are

$$\psi_{\pm} = \frac{1 \pm 2}{3} = \left\{ -\frac{1}{3}, 1 \right\}. \tag{5.97c}$$

Consequently: (i) the negative root is unphysical since the ratio of decays ψ must be positive, $\psi > 0$, in (5.95) and the negative root would lead to $R(\psi_-) = -8 < 0$; (ii) the positive root marginally meets the condition $R \geq 0$ and leads to $R(\psi_+) = 0$ that would be a minimum with zero energy, but is actually invalid because it is the resonant case $\varepsilon = \delta$ when (5.89b) does not apply. Thus, the forcing decay should not be too close to the damping. Moderate deviations lead to values of ψ with energy reduction as seen in the plot of $R(\psi)$ in figure 5.9 and confirmed by the nine particular values indicated in the table 5.2.

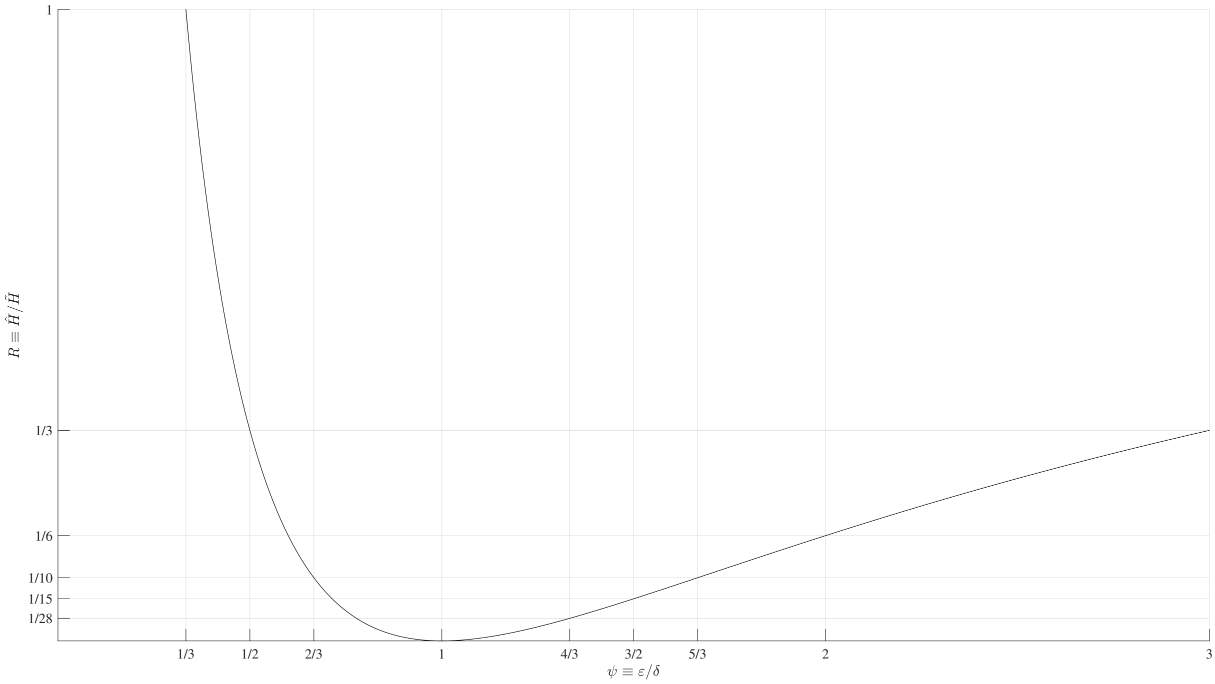

Figure 5.9: Ratio of the total to the free energy of oscillations as a function of the ratio of forcing decay ε to free damping δ showing a minimum at $\psi = 1$ in agreement with table 5.2.

Formulas	**Values**								
ψ	1/3	1/2	2/3	1	4/3	3/2	5/3	2	3
$R(\psi)$	1	1/3	1/10	0	1/28	1/15	1/10	1/6	1/3
$R(\psi)$	1	0.330	0.100	0	0.036	0.067	0.100	0.167	0.333

Table 5.2: Several values of the ratio ψ of forcing decay to free damping and the corresponding total energy of oscillation as a fraction R of the energy of the free oscillation, showing large reductions, which means strong vibration suppression.

The case $\varepsilon = \delta$ corresponds to resonance (sections 5.4 and 5.5) so the value $R = 0$ of zero total energy for $\psi_+ = 1$ in (5.97c) is excluded. The resonance has similarities and differences to "beats", according to (5.67b), when the applied frequency ϖ is close to the oscillation frequency $\tilde{\omega}$, leading to the total oscillation (5.66d). When the forcing decay is close to the damping, the factor in curved brackets in (5.89b) becomes

$$e^{-t\delta} - e^{-\varepsilon t} = (\varepsilon - \delta)\, t + O\left[\left(\varepsilon^2 - \delta^2\right) t^2\right], \tag{5.98a}$$

and to the leading order there is, using (5.90b), an amplitude growth linear on time,

$$\overline{y}\,(x,t) = A\,(\varepsilon - \delta)\, t \sin{(kx)} \cos{(\tilde{\omega} t - \alpha)} = \frac{Fc}{2k} t \sin{(kx)} \cos{(\tilde{\omega} t - \alpha)}\,, \tag{5.98b}$$

that is typical of resonance. Values of ε not too close to δ are valid in (5.89b) and lead to the results indicated in table 5.2. The figure 5.9 shows the ratio R of the energy of the total oscillation to the energy of the free oscillation as a function of the ratio ψ of the forcing decay ε to the damping δ. For example, a forcing decay equal to 4/3 of the damping reduces the total energy over all time to 3.6% of the energy of the free oscillation:

$$\psi_{\rm e} \equiv \frac{\varepsilon}{\delta} = \frac{4}{3} \Rightarrow R\,(\psi_{\rm e}) = 0.036. \tag{5.99a}$$

These values of the forcing decay ε and damping δ in (5.99a) are sufficiently different,

$$\varepsilon - \delta = (\psi_{\rm e} - 1)\,\delta = \frac{\delta}{3} = \left(1 - \frac{1}{\psi_{\rm e}}\right)\varepsilon = \frac{\varepsilon}{4}, \tag{5.99b}$$

to be far from resonance $\varepsilon = \delta$. The figure 5.10 shows that the oscillation is nearly suppressed by the forced oscillation for all time, including the first few periods when damping and forcing decay have not significantly reduced the oscillation.

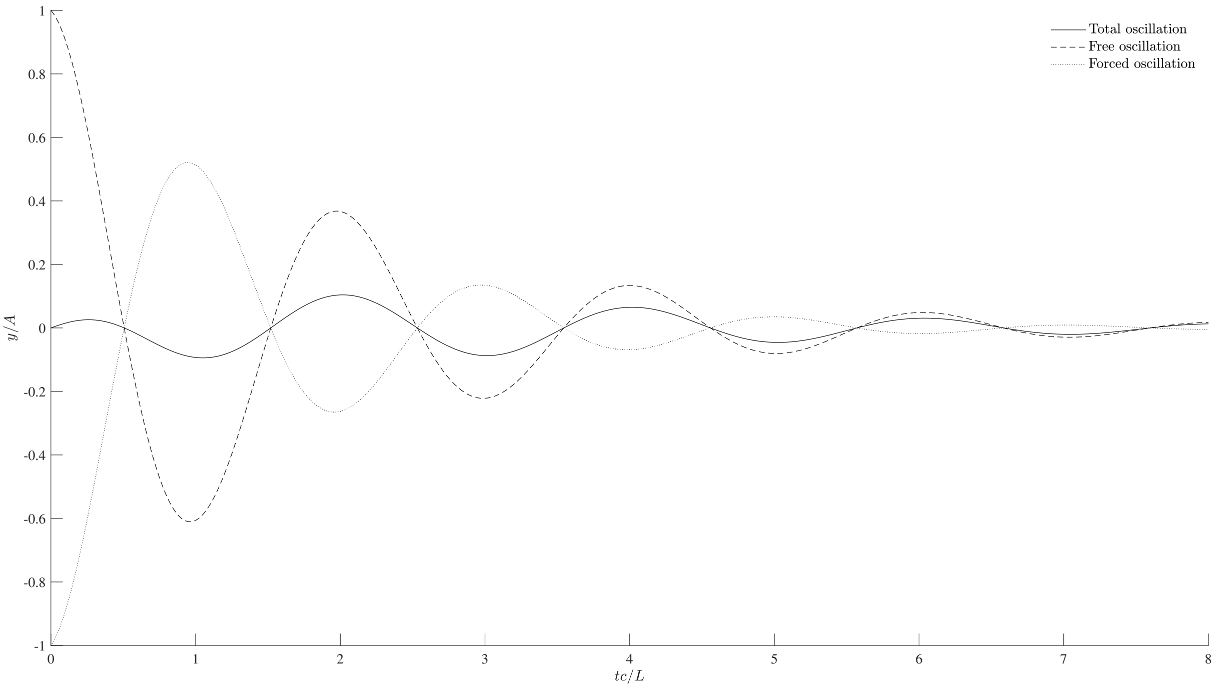

Figure 5.10: Free oscillation for the first mode of oscillation leading to $k = k_1 = \pi/L$, with damping $\delta = 0.5c/L$, no phase shift, $\alpha = 0$, and at the middle of the string, $x = L/2$ (dashed line); forced oscillation, also for the first mode of oscillation, $k = k_1 = \pi/L$, with opposing amplitude to the free oscillation, $F = -CA/c^2$, with applied phase shift, $\beta = -\phi - \alpha$, and with damping $\varepsilon = 4\delta/3 \approx 0.667c/L$, representing the case VI (dotted line); total oscillation as the sum of free and forced oscillations, in these conditions given by (5.89b) (solid line). The three oscillations are represented as functions of dimensionless time tc/L.

The substantial reduction of the energy of oscillation, corresponding to a significant partial suppression of the free oscillation for an intermediate decay of forcing can be explained as follows: (i) if the decay of forcing is much smaller than the damping, $\varepsilon < \psi_e \delta$, the forced oscillation decays slowly, and dominates the faster damped free oscillation; (ii) if the decay of the forcing is much larger than the damping, $\varepsilon > \psi_e \delta$, the forced oscillation decays too quickly to counter the energy of the free oscillation; (iii) the effective forcing decay $\varepsilon = \psi_e \delta$ is such that it extracts most energy from the free damped oscillation by decaying neither too slow (adds energy) or too fast (small effect). Thus, of the six strategies for suppression of free oscillations (table 5.4), the most effective, with over 96% reduction, for $\psi_e = \varepsilon/\delta = 4/3$ or $\varepsilon = 4\delta/3$ in table 5.2, is forcing: (i) at applied equal to oscillation frequency (5.64); (ii) applied phase (5.63a) equal to the sum of free oscillation phase (5.14b), and damping phase (5.19b); (iii) forcing with exponential time decay the fraction 4/3 of the damping; (iv) amplitude of the forcing F related to the amplitude of the free oscillation A by (5.90b),

$$-\frac{F}{A} = 2k(\delta - \varepsilon) = 2k\delta(1 - \psi_e) = \frac{kc^2}{\chi}\left(1 - \frac{4}{3}\right) = -\frac{kc^2}{3\chi}. \tag{5.100}$$

Values of the forcing decay closer to the damping (table 5.3) would lead to greater reductions of the total energy relative to the energy of free oscillation, at the risk of triggering resonance, which would render the result invalid. In order to avoid excessive proximity to resonance, the choice of effective forcing decay 4/3 of the damping, regarding the equations (5.99a) to (5.100), may be a safe compromise. A closer proximity to resonance may be possible depending on (i) the accuracy of the determination of the damping and (ii) the precision of application of the forcing decay, bearing in mind that the margins of error in both (i) and (ii) should not lead to overlap.

Formulas	**Values**							
ψ	4/3	5/4	6/5	7/6	8/7	9/8	10/9	11/10
$R(\psi)$	1/28	1/45	1/66	1/91	1/120	1/153	1/171	1/210
$R(\psi)$	0.0357	0.0222	0.0152	0.0110	0.0083	0.0065	0.0058	0.0048

Table 5.3: As the forcing decay comes closer to the damping, the reduction of total relative to free oscillation energy is more significant at the risk of coming too close to resonance which could invalidate the result.

This sixth most effective strategy of countering free oscillations is compared next (section 5.7) with the five preceding strategies (table 5.5).

5.7 Strategies for partial vibration suppression

The usual method of active vibration suppression is to add to the oscillation (5.15) another out-of-phase by half a period,

$$\begin{aligned}\breve{y}(x,t) &= A\exp(-t\delta)\exp\left\{\mathrm{i}\left[kx \mp \omega\left(t + \frac{\tau}{2}\right) - \alpha\right]\right\} = A\exp(-t\delta)\exp\left[\mathrm{i}(kx \mp \omega t) \mp \mathrm{i}\pi - \mathrm{i}\alpha\right] \\ &= -A\exp(-t\delta)\exp\left[\mathrm{i}(kx \mp \omega t - \alpha)\right] = -\tilde{y}(x,t),\end{aligned} \tag{5.101}$$

so that the sum is zero. This is best done by inserting through the boundary the opposite oscillation (5.101) to cancel (5.15). The opposite oscillation has: (i) the same wavenumber k; (ii) the same frequency ω; (iii) the same amplitude A; (iv) the opposite phase. The question of whether the "opposite" oscillation can be generated by forcing can be posed in the non-dissipative (chapter 4) and dissipative (present chapter) cases, where it is shown that perfect cancellation is not possible. The question can be relaxed to question whether the addition of a forced oscillation can lead to a total energy less than that of the free oscillation and the answer is that this can be achieved with constraints that are mentioned next. Six cases I to VI of partial vibration suppression, using forced oscillations to counter free oscillations have been considered and evaluated comparing (table 5.4) the energy of the total oscillation with that of the free oscillation.

Oscillations	**Free**	**Forced**
Amplitude	A	$F = -CA/c^2$
Frequency	$\tilde{\omega} = \sqrt{k^2c^2 - \delta^2}$	$\overline{\omega}$
Phase	$-\alpha$	β
Exponential decay in time	$\delta = c^2/(2\chi)$	ε

Table 5.4: Comparison of free and forced oscillations.

The six strategies to counter free oscillations are listed in the table 5.5. The first four strategies I-IV are standard combinations of undamped or damped free oscillations with non-resonant and resonant forcing, and lead at best to 75% reduction in energy. Two novel strategies V-VI are resonant and non-resonant forcing with magnitude decaying in time, and can lead to energy reduction, of over 96%. These six strategies I-VI are discussed briefly as a conclusion.

Number	**Case**	**Main phenomenon**	**Energy**
I	Non-resonant forcing	Distinct frequency adds energy	Increases
II	Resonant forcing	Applied frequency equal to natural frequency	Up to 75% reduction in first period
III	Non-resonant without decay	Forcing with constant amplitude dominates	Small reduction in first period
IV	Resonant without decay	Forcing with constant amplitude dominates	Small reduction over fraction of first period
V	Resonant with decay	Damping slow to dominate resonant growth	Reduction only for strong damping
VI	Non-resonant with decay	Decay of total oscillation	Reduction up to over 96% in energy over all time

Table 5.5: Six cases to counter free oscillations (I-II: undamped; III-VI: with damping) and forcing with constant (III-IV) or decaying (V-VI) amplitude. Both non-resonant (I, III, VI) and resonant (II, IV, V) cases are considered.

Starting with the non-dissipative case, the free oscillations are sinusoidal with constant amplitude.

In the absence of damping, the (case I) non-resonant forced oscillations have a constant amplitude and different frequency from free oscillation and do not interact; thus, the energies of the free and forced oscillations add, that is the opposite of what was intended. The (case II) resonant forced oscillations have the same frequency as the free oscillations, but their amplitude increases linearly with time, thus eventually increasing the energy of the total oscillation. Considering a limited time span, say the first period of oscillation, it is possible to optimise the forcing to bring the total energy below that of the free oscillation by at most 75%.

Turning to the dissipative case, the free oscillations are sinusoidal in space-time with amplitude decaying exponentially with time due to damping. The (case III) dissipative non-resonant forcing involves a different frequency, a constant amplitude and a phase shift, which prevent perfect cancellation. The (case IV) dissipative resonant forcing involves the same frequency, and a constant amplitude, and there is a phase shift of $\pi/2$, again not allowing perfect cancellation. Furthermore, the decaying free oscillation is eventually dominated by the forced oscillation with constant amplitude both in the non-resonant and resonant cases, so the total energy increases in both cases of forcing for a sufficiently long time. In the resonant case, the forced oscillation is 90 degrees out-of-phase to the free oscillation which tends to increase the total energy, but may be countered by a forcing phase.

In summary, there are four standard cases for the evolution of total energy as a function of time:

– Undamped non-resonant forcing (case I): the free and forced oscillations have constant amplitude and different frequencies, so the energies are constant and added; the total energy increases and is independent of time;

– Undamped resonant forcing (case II): the free oscillation has constant amplitude and is ultimately dominated by the forced oscillation that is out-of-phase and has amplitude increasing linearly with time; optimised forcing may reduce the total energy over the first period (concentrated forces) or somewhat longer (distributed forces) before being overwhelmed by the energy of the forced oscillation growing like the square of time; the highest possible energy reduction is 75% over the first period using distributed forcing optimised along the string; this favourable result is lost for times exceeding significantly one period, because for the forced resonant oscillation the amplitude increases linearly with time and the energy like the square;

– Damped non-resonant forcing (case III): the free oscillation decays exponentially due to damping and is dominated by the forced oscillation with constant amplitude; since the natural and applied frequencies are different, the energies of the free and forced oscillation add, with the former decaying relative to the latter; thus, the decay of the free oscillation is overwhelmed by the non-decaying forced oscillation, that is counter productive;

– Damped resonant forcing (case IV): although the natural and applied frequencies coincide, there is again the contrast between the free oscillations decaying exponentially in time and the forced oscillations out-of-phase and with constant amplitude; even optimizing the forcing to counter the free oscillation, the total energy is ultimately dominated by the forced oscillation, which is counter productive as in case III.

Since none of the standard cases I-IV is very effective at countering free oscillations over time for several periods, two novel cases V-VI are introduced. They apply to damped free oscillations and use forcing that decays in time. It is possible to consider: (i) opposing amplitudes of the free and forced oscillations; (ii) matched phases; (iii) equal oscillation and applied frequencies. The case of forcing decay equal to damping (case V) leads to resonance with the forcing causing an amplitude growing linearly with time, but ultimately dominated by the exponential time decay. This is less favourable than having distinct forcing decay and damping (case VI) for which both the energy of the free and forced oscillation are finite when integrated over all time. Tuning the decay of the forcing to a suitable fraction of the damping, $\psi_{\mathrm{e}} = \varepsilon/\delta = 4/3$, the total energy can be reduced, $R\left(\psi_{\mathrm{e}}\right) = 0.036$, by more than 96%. This case is represented by the figure 5.10, that provides a graphic display of how the forced oscillation counters the free oscillation in an effective way, leading to substantial reduction or almost suppression, in the first few periods of oscillation, before the ultimate damping and decay for long time.

The consideration of forcing with non-constant amplitude suggests a generalised definition of resonance (section 5.8).

5.8 A generalised definition of resonance

The usual concept of resonance in its simplest terms can be considered for the classical wave equation (5.2) with free wave solution (5.10) without damping $\delta = 0$ for one mode,

$$\tilde{y}\left(x,t\right) = A\sin\left(kx\right)\cos\left(kct-\alpha\right), \tag{5.102}$$

with amplitude A, wavenumber k, frequency $\tilde{\omega} = kc$ and phase shift $-\alpha$. The forcing with a generally distinct applied frequency $\overline{\omega}$, but with a same phase shift $-\alpha$, and with a certain amplitude F spatially distributed with the same wavenumber k,

$$\frac{\partial^2\overline{y}}{\partial t^2} - c^2\frac{\partial^2\overline{y}}{\partial x^2} = F\sin\left(kx\right)\cos\left(\overline{\omega}t-\alpha\right), \tag{5.103}$$

leads to distinct solutions in two cases. The non-resonant case of applied frequency $\overline{\omega}$ distinct from the natural frequency $\tilde{\omega} = kc$ has the constant amplitude and the same phase,

$$\overline{y}\left(x,t\right) = \frac{F}{c^2k^2-\overline{\omega}^2}\sin\left(kx\right)\cos\left(\overline{\omega}t-\alpha\right), \tag{5.104}$$

but does not hold for $\overline{\omega} = \pm kc$. The latter is the resonant case,

$$\frac{\partial^2\overline{y}_*}{\partial t^2} - c^2\frac{\partial^2\overline{y}_*}{\partial x^2} = F\sin\left(kx\right)\cos\left(kct-\alpha\right), \tag{5.105}$$

leading to oscillations with amplitude increasing linearly with time,

$$\overline{y}_*\left(x,t\right) = \frac{F}{2kc}t\sin\left(kx\right)\sin\left(kct-\alpha\right), \tag{5.106}$$

and with a phase shift of $\pi/2$. This suggests two definitions of "resonance": (A) the usual "physical" definition of applied frequency $\overline{\omega}$ equal to natural frequency; (B) the equivalent "mathematical" definition that the amplitude grows linearly with time. It is shown next that (B) is the more general definition, by considering a more general case.

Consider: (i) instead of the classical wave equation (5.2), the wave-diffusion or telegraph equation (5.1b); (ii) instead of forcing (5.103) with same wavenumber k and applied frequency $\overline{\omega}$, a forcing (5.54) with also a generally distinct phase shift β and an amplitude F decaying exponentially with time at a decay rate ε. Now there are four forcing parameters (table 5.4) and the resonance, in the sense of amplitude of forced oscillation initially growing linearly with time (5.65c), requires three conditions: (i) applied frequency equal (5.64) to the oscillation frequency (5.6), that is the natural frequency kc modified by damping; (ii) matching (5.63a) of the phases of the forcing β in (5.54), of the free oscillation $-\alpha$ in (4.7d) and of the damping ϕ in (5.19b); (iii) exponential decay ε of the forcing in (5.54) equal (5.62a) to the damping (5.5); (iv) matching of free A and forced F amplitudes (5.61a). Clearly the definition A of equal oscillation and applied frequencies, corresponding to one condition (i), is not sufficient to have oscillation with amplitude initially growing with time, because other conditions are needed as well.

This suggests the following definition of resonance: resonant forcing leads to oscillations with amplitude initially increasing with time, and requires matching of all parameters of forcing with those of the free oscillation, namely (table 5.4): (i) the applied frequency must equal the free oscillation frequency; (ii) the forcing phase plus the damping phase must equal the phase of the free oscillation; (iii) the damping of the free oscillation must be matched by the exponential decay in time of the forcing. The linear growth with time of the forced oscillations for short time may be ultimately dominated by damping. To prevent resonance, it is sufficient to break one of the three conditions (i) to (iii) above. The most effective strategy VI for the suppression of free damped oscillation is: (α) to keep (i) applied equal to natural frequency and (ii) match applied, damping and free phases; (β) avoid resonance by a forcing decay different from damping, being selected to substantially decrease the total energy (table 5.2 and figure 5.9); (γ) choose opposite amplitudes for the forced and free oscillations. Choosing (β) a forcing decay ε related to damping δ by $\psi_{\mathrm{e}} = \varepsilon/\delta = 4/3$ in table 5.2 reduces the total energy of oscillation over all time to 3.6% of the energy of the free oscillation, (5.99a) and (5.99b), and nearly suppresses the free oscillation (figure 5.10) in the critical first periods before damping and decay take over.

5.9 Main conclusions of the chapter 5

The present chapter has considered forcing as a physical mechanism to reduce the energy of free transverse oscillations of an elastic string with two contrasting results: (chapter 4) limited effectiveness in all cases for undamped oscillations, which is a "negative" but genuine result, indicating the limitations arising from laws of physics; (present chapter) good effectiveness for damped oscillations using decaying forcing, that is a "desirable" result compatible with the laws of physics. The implementation of the most effective forcing is a follow-on problem, not addressed here, for which the results of the present chapter provide the objective. Implementing forcing decaying exponentially in time should be simple and well within the capabilities of control systems using actuators, sensors and processing.

The main difference between this chapter and the previous chapter is that chapter 4 deals with undamped and this chapter with damped oscillations, hence the two chapters 4 and 5 deal with different equations, namely wave equation in chapter 4 and wave-diffusion equation in chapter 5. The present chapter considers only continuously distributed forces, whereas the chapter 4 considers also forcing at a single point and forcing at multiple points. Both chapters 4 and 5 comprehensively cover non-resonant and resonant forcing with constant amplitude, with significant differences between the two undamped cases in chapter 4 and the four damped cases in this chapter. Since forcing with constant amplitude is of limited effectiveness in partial vibration suppression, the present chapter considers forcing with amplitude decaying exponentially in time. The assessment of effectiveness of partial vibration suppression is assessed by comparing the energy of the free vibration with the energy of the total, free plus forced, oscillation; this is done for all cases of undamped (chapter 4) and damped (present chapter) oscillations resulting in somewhat extensive calculations.

The calculations in the present chapter are extensive because there are five cases to consider: (i) damped free oscillations (section 5.1); (ii-iii) oscillations forced with constant amplitude without and with resonance (sections 5.2 and 5.3) including associated energies (section 5.5); (iv-v) oscillations forced with amplitude decaying exponentially with time in resonant and non-resonant cases (sections 5.5 and 5.6), including associated energies that are relevant to a comparison of strategies for partial vibration suppression (section 5.7). This leads to a generalised definition of resonance (section 5.8) before the conclusion (section 5.9). The innovation in the chapter 5 is outlined in its introduction.

The four key elements for effective vibration suppression are the following: (i) the applied frequency equals the natural frequency so that the forced oscillation can be kept at all times in opposition to the free oscillation; (ii) the free and forced oscillations will be in opposition for all time if the phases of the free oscillation and forcing are matched at initial time taking into account the phase associated with damping; (iii) the amplitude of the forced oscillation equals that of the free oscillation with opposite sign or phase at initial time; (iv) the forcing decays exponentially in time at a rate "close to but not equal to" the damping, because: (iv-a) if the forcing decay equals the damping, there is resonance, and the amplitude grows initially in time linearly, adding energy that is eventually dissipated, and failing to suppress oscillations in the near term; (iv-b) if the forcing decay is very different from the damping, one of the free and forced oscillations decays much faster than the other, preventing effective vibration suppression; (iv-c) a forcing decay "not equal to" the damping avoids resonance (iv-a), and being "close to" the damping allows a comparable decay in time (iv-b), so that partial vibration suppression (i-iii) is effective over time until both the free and forced oscillations become negligible.

In conclusion, free damped oscillations have finite energy E_0 over infinite time due to damping. Due to decay, the forced oscillation with exponential decay in time also has finite energy E_* over all time. Partial vibration suppression reduces the total energy to $E_0 - E_*$ by keeping the free and forced oscillations out-of-phase. This requires (i) equal free and applied frequencies, (ii) matching of free, forced and damping phases, and (iii) equal initial amplitudes with opposite signs or phases. The forcing decay and damping should not be equal to avoid resonance, but may be close enough to suppress more than 90% of the energy of vibration. The verification of this theoretical prediction of the most effective strategy for partial vibration suppression can be subject to experimental demonstration that is beyond the scope of the present thesis.

The applications of the present theory of partial vibration suppression are undamped systems described by the classical wave equation (chapter 4) and damped systems described by the wave-diffusion or telegraph equation (presented chapter). The wave equation applies to acoustic, elastic and electromagnetic waves, and damping effects can be thermal conduction or radiation, viscosity, electrical resistance and mass diffusion. The most effective method of reduction of vibration energy by more than 90% is forcing at the natural frequency with amplitude decaying exponentially with time. It applies not only to continuous systems, but also to discrete systems such as: (i) mechanical oscillators consisting of masses, springs, dampers and forcing actuators; (ii) electrical circuits consisting of inductors, capacitors and resistors powered by batteries; (iii) analogous circuits in acoustics, hydraulics and other fields.

6 | On the energy density and energy flux in elastic bodies

"If I have seen further than others, it is by standing upon the shoulders of giants."

— Isaac Newton

Contents

The vast literature on theory of elasticity [7, 77, 78, 80, 81, 151–153] and solid mechanics [154–168] considers in detail the energy density, but gives less emphasis to the energy flux and associated energy equation in the unsteady case involving motion and dynamics. The purpose of the present chapter is to consider the energy flux, in general, in inelastic and elastic solids and some of its implications in the particular case of elastic waves.

The total energy density per unit volume in a solid consists of: (i) the kinetic energy involving the mass density and velocity, with the latter equal to the time derivative of the displacement vector; (ii) the deformation energy involving the stress and strain tensors, with the latter specified by spatial derivatives of the displacement vector. Using the balance of forces and stresses, the rate of change in time of the total energy leads to an energy conservation equation (section 6.1) involving: (i) the power or work per unit time of the external forces; (ii) the divergence of the energy flux. This shows that the energy flux equals (subsection 6.1.1) minus the product of the velocity vector by the stress tensor, for general matter without assumptions on constitutive properties. The simplest particular case is isotropic stresses, for which the energy flux equals the product of pressure by velocity, as for sound waves in a fluid. The energy flux is given for: (i) linear and non-linear transverse waves in elastic strings and membranes (subsection 6.1.2); (iii) linear elastic waves in three-dimensional elasticity of crystals and amorphous or isotropic matter (subsection 6.1.3).

Before applying the energy flux (section 6.1) to longitudinal and transversal waves in an isotropic elastic medium (section 6.3), some general properties of waves are considered (section 6.2). The waves may be classified into: (a) isotropic if the wave speed is equal in all directions, which is independent of wave normal direction, and anisotropic otherwise; (b) non-dispersive if the wave speed is independent of wavenumber, when a "wave packet" propagates in a permanent waveform, and dispersive otherwise, if the components with different wavenumbers of a wave packet spread out as they propagate. It is possible to determine if the waves are (a) isotropic or non-isotropic and (b) non-dispersive or dispersive, by inspecting the wave equation with no need to solve it, as follows: (a) if all spatial derivatives appear in Laplacians, the waves are isotropic, otherwise if there are other spatial derivatives, the waves are anisotropic (subsection 6.2.1); (b) if all space, time and combined derivatives are of the same order, the waves are non-dispersive, otherwise if there are derivatives of different orders, the waves are dispersive (subsection 6.2.2). It follows that isotropic non-dispersive waves are specified by the classical wave equation (subsection 6.2.3) for which the energy or group velocity equals the wave speed in the wave normal direction. Thus, in this case, the energy flux lies in the direction of propagation.

Applying the general wave theory (section 6.2) to the energy flux of elastic waves in isotropic media (section 6.1), follow several conclusions (sections 6.3 and 6.4): (i) longitudinal (subsection 6.3.1) and transversal (subsection 6.3.2) elastic waves are isotropic non-dispersive, thus both satisfy separately the classical wave equation and both have energy fluxes in the direction of propagation, with different longitudinal and transverse wave speeds (subsection 6.3.3); (ii) the superposition of the longitudinal and transversal elastic waves (section 6.4) satisfies a second-order wave equation that does not coincide with the classical wave equation, and thus the waves are non-dispersive and anisotropic (subsection 6.4.1), implying that the energy flux has a component transverse to the direction of propagation (subsection 6.4.2); (iii) although the total energy of elastic waves is the sum of the energies of longitudinal and transversal waves, the energy flux has three terms, with a cross-flux between longitudinal and transversal waves that is transverse to the direction of propagation and has zero divergence (subsection 6.4.3).

The discussion (section 6.5) highlights the two main conclusions: (i) the general expression for the energy flux in elastic and inelastic solids, including one-dimensional (strings and bars), two-dimensional (membranes and plates) and three-dimensional crystalline and amorphous elastic media; (ii) the implication that the superposition of longitudinal and transversal elastic waves in isotropic uniform media, while adding the energy densities, concerning the energy flux, leads to a cross-term namely a cross-coupled longitudinal-transversal wave energy flux that has zero divergence and is transverse to the direction of propagation.

6.1 Energy density, flux and power

The energy equation (subsection 6.1.1) balances the power of external forces versus the sum of: (i) the rate-of-change in time of the total energy density per unit volume, consisting of kinetic and deformation energies; (ii) the divergence of energy flux that crosses the unit area in unit time, and is shown to equal minus the velocity vector multiplied by the stress tensor. The energy flux is considered in the one and two-dimensional cases of an elastic string and membrane respectively, with non-linear or large transverse vibrations (subsection 6.1.2). Also, the energy flux is considered for three-dimensional linear elastic waves (subsection 6.1.3) in anisotropic and isotropic media like crystals and amorphous matter respectively.

6.1.1 Balance of forces, stresses and energies

The deformation of the medium is represented by the displacement vector $u_j\left(x_k, t\right)$ as a function of position vector x_k and time t. The time derivative is the velocity v_j, that multiplied by the mass density per unit volume ρ specifies the linear momentum ρv_j [3]. Its time derivative is the inertia force,

$$\frac{\partial}{\partial t}\left(\rho \frac{\partial u_j}{\partial t}\right) = g_j + \frac{\partial T_{jr}}{\partial x_r}, \tag{6.1}$$

that balances the force density per unit volume g_j and the divergence of the stress tensor T_{jr}. The work per unit time of the inertia force in an infinitesimal displacement $\mathrm{d}u_j$ is the rate of change with time of the kinetic energy E^{k} [3]:

$$\frac{\partial E^{\mathrm{k}}}{\partial t} \equiv \frac{\partial u_j}{\partial t}\frac{\partial}{\partial t}\left(\rho \frac{\partial u_j}{\partial t}\right). \tag{6.2}$$

If the mass density is independent of time, $\partial \rho / \left(\partial t\right) = 0$, the kinetic energy is one half of the product of mass density by the square of the modulus of velocity [3]:

$$E^{\mathrm{k}} = \frac{1}{2}\rho\left(\frac{\partial u_j}{\partial t}\right)^2. \tag{6.3}$$

It is possible to do the reverse: the kinetic energy is defined by (6.3), and then the independence of mass density with respect to time implies (6.2).

The differential of the deformation energy is the product of the stress tensor by the differential of the strain tensor [3]:

$$\mathrm{d}E^{\mathrm{u}} \equiv T_{jr}\mathrm{d}S_{jr}. \tag{6.4}$$

For linear or small deformations, the strain tensor consists of symmetric spatial derivatives of the displacement vector [79]:

$$2S_{jr} \equiv \frac{\partial u_j}{\partial x_r} + \frac{\partial u_r}{\partial x_j} = 2S_{rj}. \tag{6.5}$$

The balance of moments of forces implies that the stress tensor is symmetric, $T_{jr} = T_{rj}$ [79]. Substituting (6.5) in (6.4) and using the symmetry of the stress tensor lead to

$$\mathrm{d}E^{\mathrm{u}} = T_{jr}\,\mathrm{d}\left(\frac{\partial u_j}{\partial x_r}\right) \tag{6.6}$$

for the differential of the energy of deformation.

The total energy density per unit volume is the sum of kinetic and deformation energies, $E \equiv E^{\mathrm{k}} + E^{\mathrm{u}}$, and from (6.2) and (6.6) follows its rate of change in time:

$$\frac{\partial E}{\partial t} = \frac{\partial E^{\mathrm{k}}}{\partial t} + \frac{\partial E^{\mathrm{u}}}{\partial t} = \frac{\partial u_j}{\partial t}\frac{\partial}{\partial t}\left(\rho\frac{\partial u_j}{\partial t}\right) + T_{jr}\frac{\partial^2 u_j}{\partial t \partial x_r}. \tag{6.7}$$

Substituting the force balance (6.1) in the first term on the right-hand side of (6.7) gives

$$\frac{\partial E}{\partial t} = g_j \frac{\partial u_j}{\partial t} + \frac{\partial u_j}{\partial t} \frac{\partial T_{jr}}{\partial x_r} + T_{jr} \frac{\partial^2 u_j}{\partial t \partial x_r}. \tag{6.8a}$$

The first term on the right-hand side of (6.8a) is the power or work per unit time of the volume forces:

$$\dot{W} \equiv g_j \frac{\partial u_j}{\partial t}. \tag{6.8b}$$

Therefore the relation (6.8a) can be rewritten as

$$\frac{\partial E}{\partial t} - \frac{\partial}{\partial x_r} \left(T_{jr} \frac{\partial u_j}{\partial t} \right) = \dot{W}, \tag{6.8c}$$

that takes the form of an energy conservation equation,

$$\frac{\partial E}{\partial t} + \frac{\partial F_r}{\partial x_r} = \dot{W}, \tag{6.8d}$$

with energy flux

$$F_r \equiv -T_{jr} \frac{\partial u_j}{\partial t}, \tag{6.8e}$$

equal to minus the product of the velocity vector by the stress tensor. The simplest particular case is isotropic stresses corresponding to a pressure p in $T_{jr} = -p\delta_{jr}$, for which the energy flux (6.8e) equals the product of pressure by velocity, $F_r = p\partial u_r / (\partial t)$, as for sound waves in a perfect fluid. The general expression of the energy flux (6.8e) for linear strains (6.5) is valid for arbitrary matter, since no constitutive relation, elastic or otherwise, was used in the derivation of the energy equation from (6.1) to (6.8d). The energy flux is considered next in particular for: (a) non-linear transverse vibrations of elastic strings and membranes (subsection 6.1.2); (b) three-dimensional linear elastic waves in crystals and isotropic matter (subsection 6.1.3).

6.1.2 Non-linear vibrations of strings and membranes

The shape of an elastic string is given in Cartesian coordinates by the transverse displacement, $u_{\mathrm{z}} \equiv \zeta(x,t)$, as a function of longitudinal coordinate x and time t. The transverse velocity is given by

$$v_{\mathrm{z}} = \frac{\partial \zeta}{\partial t} \tag{6.9}$$

and the tangential tension T specifies the shear stress [130],

$$T_{\mathrm{xz}} = T \frac{\mathrm{d}\zeta}{ds}, \tag{6.10}$$

involving the arc-length, $(\mathrm{d}s)^2 = (dx)^2 + (d\zeta)^2$. Substituting the expression of arc-length in (6.10) gives

$$T_{\mathrm{xz}} = T \left(\frac{\partial \zeta}{\partial x} \right) \left[1 + \left(\frac{\partial \zeta}{\partial x} \right)^2 \right]^{-1/2} \tag{6.11}$$

for the shear stress.

The energy flux (6.8e) is given by $F_\mathrm{x} = -v_\mathrm{z} T_\mathrm{xz}$, implying from (6.9) and (6.11) the expression

$$F_\mathrm{x} = -T \frac{\partial \zeta}{\partial t} \frac{\partial \zeta}{\partial x} \left[1 + \left(\frac{\partial \zeta}{\partial x} \right)^2 \right]^{-1/2} \tag{6.12}$$

for non-linear transverse vibration of the elastic string with large slope. In the linear case of small slope, $\left[\partial \zeta / (\partial x) \right]^2 \ll 1$, the energy flux simplifies to

$$F_\mathrm{x} = -T \frac{\partial \zeta}{\partial t} \frac{\partial \zeta}{\partial x}. \tag{6.13}$$

The energy flux (6.12) for the general non-linear vibrations and the energy flux (6.13) for the particular case of linear vibrations can be obtained directly from an energy balance (6.8d) for elastic strings using methods (subsection 6.1.1) similar to the equations (6.1) to (6.8c).

The shape of an elastic membrane is given in Cartesian coordinates by the transverse displacement, $u_\mathrm{z} \equiv \zeta(x, y, t)$, as a function of in-plane Cartesian coordinates (x, y) and time t. The transverse velocity is given by (6.9) and the spatial derivatives for the string, $\partial \zeta / \partial x$, are replaced by the gradient for the membrane [130]:

$$\boldsymbol{\nabla} \zeta = \mathbf{e}_\mathrm{x} \frac{\partial \zeta}{\partial x} + \mathbf{e}_\mathrm{y} \frac{\partial \zeta}{\partial y}. \tag{6.14}$$

It follows that the energy flux for non-linear transverse vibrations of an elastic string (6.12) is obtained replacing $\partial \zeta / \partial x$ by (6.14) for an elastic membrane with isotropic tangential tension T leading to

$$\mathbf{F} = -T \frac{\partial \zeta}{\partial t} \boldsymbol{\nabla} \zeta \left[1 + \boldsymbol{\nabla} \zeta \cdot \boldsymbol{\nabla} \zeta \right]^{-1/2}, \tag{6.15a}$$

with Cartesian components

$$\{F_\mathrm{x}, F_\mathrm{y}\} = -T \frac{\partial \zeta}{\partial t} \left[1 + \left(\frac{\partial \zeta}{\partial x} \right)^2 + \left(\frac{\partial \zeta}{\partial y} \right)^2 \right]^{-1/2} \left\{ \frac{\partial \zeta}{\partial x}, \frac{\partial \zeta}{\partial y} \right\}. \tag{6.15b}$$

In the case of linear vibrations with small slope,

$$1 \gg |\boldsymbol{\nabla} \zeta|^2 = \left(\frac{\partial \zeta}{\partial x} \right)^2 + \left(\frac{\partial \zeta}{\partial y} \right)^2, \tag{6.16a}$$

the energy flux is given by

$$\mathbf{F} = -T \frac{\partial \zeta}{\partial t} \boldsymbol{\nabla} \zeta \tag{6.16b}$$

with Cartesian components

$$\{F_\mathrm{x}, F_\mathrm{y}\} = -T \frac{\partial \zeta}{\partial t} \left\{ \frac{\partial \zeta}{\partial x}, \frac{\partial \zeta}{\partial y} \right\}. \tag{6.16c}$$

After the one and two dimensional examples (subsection 6.1.2) of energy flux (subsection 6.1.1) for elastic strings and membranes respectively, are given three-dimensional examples (subsection 6.1.3) for anisotropic and isotropic media like crystals and amorphous matter respectively.

6.1.3 Elastic waves in crystals and isotropic matter

The differentials of the stress T_{jk} and strain S_{mn} tensors are related linearly by the stiffness double tensor G_{jkmn} for general matter [79],

$$\mathrm{d}T_{jr} = G_{jrpq}\mathrm{d}S_{pq}, \tag{6.17a}$$

that equals the derivatives of the stress tensor with regard to the strain tensor:

$$G_{jrpq} \equiv \frac{\partial T_{jr}}{\partial S_{pq}}. \tag{6.17b}$$

The first-order derivatives of the elastic energy (6.4) with regard to the strain tensor specify the stress tensor [4, 79],

$$T_{jr} = \frac{\partial E^{\mathrm{u}}}{\partial S_{jr}}, \tag{6.18}$$

and from (6.17b) the second-order derivatives specify the stiffness double tensor:

$$G_{jrpq} = \frac{\partial^2 E^{\mathrm{u}}}{\partial S_{jr}\partial S_{pq}}. \tag{6.19}$$

The stiffness double tensor has symmetries, $G_{jrpq} = G_{rjpq} = G_{jrqp} = G_{pqjr}$ [4], following the first equality from the symmetry of stress tensor, the second equality from the strain tensor (6.5) and the third equality from the elastic energy (6.19).

In an elastic medium, the stiffness double tensor does not depend on the strain tensor, that is, $\partial G_{jrpq}/\left(\partial S_{mn}\right) = 0$. In a steady medium, it does not depend on time, $\partial G_{jrpq}/\left(\partial t\right) = 0$, and in a homogeneous medium it does not depend on position, $\partial G_{jrpq}/\left(\partial x_m\right) = 0$. If all these conditions are met, the stiffness double tensor is constant, $G_{jrpq} = \mathrm{const}$, and thus: (i) the stress-strain constitutive relation (6.17a) is linear, omitting residual stresses [3, 4], in

$$T_{jr} = G_{jrpq}S_{pq}; \tag{6.20}$$

(ii) the deformation energy density (6.4) is simplified [79] to

$$E^{\mathrm{u}} = \frac{1}{2}G_{jrpq}S_{jr}S_{pq} = \frac{1}{2}T_{jr}S_{jr}; \tag{6.21}$$

(iii) the energy flux (6.8e) is given by

$$F_r = -\frac{\partial u_j}{\partial t}G_{jrpq}S_{pq} = -G_{jrpq}\frac{\partial u_j}{\partial t}\frac{\partial u_p}{\partial x_q}, \tag{6.22}$$

where were used the symmetries (6.5) and the symmetries of the stiffness double tensor.

The preceding relations from (6.20) to (6.22), valid for an elastic crystal, simplify for isotropic media, like amorphous matter, when the stiffness double tensor is specified by the Lamé elastic moduli (λ, μ)

multiplied by identity matrices [1, 3]:

$$G_{jrpq} = \mu\delta_{jp}\delta_{rq} + \mu\delta_{jq}\delta_{rp} + \lambda\delta_{jr}\delta_{pq}. \tag{6.23a}$$

The last expression follows all the symmetries of the stiffness double tensor. The Lamé moduli of elasticity may be replaced by the Young modulus E and Poisson ratio σ [1, 3]:

$$2\mu \equiv \frac{E}{1+\sigma}, \tag{6.23b}$$

$$\lambda \equiv \frac{2\mu\sigma}{1-2\sigma}. \tag{6.23c}$$

For isotropic matter (6.23a), follows: (i) regarding (6.20) the stress-strain relation [79]

$$T_{jr} = 2\mu S_{jr} + \lambda S_{pp}\delta_{jr} = \mu\left(\frac{\partial u_j}{\partial x_r} + \frac{\partial u_r}{\partial x_j}\right) + \lambda\left(\boldsymbol{\nabla}\cdot\mathbf{u}\right)\delta_{jr}; \tag{6.24}$$

(ii) according to (6.21) the deformation energy density [79]

$$2E^{\mathrm{u}} = 2\mu S_{jr}S_{jr} + \lambda\left(S_{pp}\right)^2 = \frac{\mu}{2}\left(\frac{\partial u_j}{\partial x_r} + \frac{\partial u_r}{\partial x_j}\right)^2 + \lambda\left(\boldsymbol{\nabla}\cdot\mathbf{u}\right)^2; \tag{6.25}$$

(iii) from (6.22) the energy flux

$$F_r = -\frac{\partial u_j}{\partial t}\left[2\mu S_{jr} + \lambda S_{pp}\delta_{jr}\right] = -\mu\frac{\partial u_j}{\partial t}\left(\frac{\partial u_j}{\partial x_r} + \frac{\partial u_r}{\partial x_j}\right) - \lambda\left(\boldsymbol{\nabla}\cdot\mathbf{u}\right)\frac{\partial u_r}{\partial t}. \tag{6.26}$$

The consideration of the energy balance (section 6.1) for elastic waves (sections 6.3 and 6.4) is preceded by some general properties of isotropic/anisotropic and dispersive/non-dispersive waves (section 6.2).

6.2 Isotropic/anisotropic and dispersive/non-dispersive waves

By inspection of the linear wave equation in steady, homogeneous media (subsection 6.2.1), without actually obtaining a solution, it is possible to ascertain whether: (a) the waves are isotropic when they propagate equally in all directions, or are anisotropic and propagate differently in some directions (subsection 6.2.2); (b) the waves are non-dispersive when the velocity of propagation is independent of wavelength and a “packet” of waves with different wavelengths propagates together in a “permanent” waveform, whereas for dispersive waves the “packet” spreads out as waves of different lengths travel at distinct velocities.

6.2.1 Linear waves in steady, homogeneous media

The wave variable Φ is a scalar or a component of a vector or a component of a tensor, and is the dependent variable $\Phi\left(x_j, t\right)$ depending on position vector x_j and time t. The dependent variable Φ has: (i) time derivatives of the first order, denoted by $\partial_t\Phi \equiv \partial\Phi/\left(\partial t\right)$, up to the M-th order, $\partial_t^m\Phi \equiv \partial^m\Phi/\left(\partial t^m\right)$, for $m = \{1, \ldots, M\}$; (ii) spatial derivatives of the first order, denoted by $\partial_j\Phi \equiv \partial\Phi/\left(\partial x_j\right)$, up to the N-th order, $\partial_{j_1 \dots j_n}\Phi \equiv \partial^n\Phi / (\partial x_{j_1} \dots \partial x_{j_n})$, for $n = \{1, \dots, N\}$, where each index j_n spans the dimension of space,

$$j_1 = \{1, \dots, P\}, \quad j_2 = \{1, \dots, P\}, \quad \dots, \quad j_n = \{1, \dots, P\}, \tag{6.27}$$

with $P = \{1, 2, 3\}$; for strings or bars $P = 1$, for membranes or plates $P = 2$, or for three-dimensional bodies $P = 3$; (iii) mixed temporal and spatial derivatives, $\partial^m_{tj_1 \dots j_n}\Phi \equiv \partial^{m+n}\Phi / (\partial t^m \partial x_{j_1} \dots \partial x_{j_n})$. A wave equation is a relation among the wave variable Φ, time, position vector and derivatives of the variable Φ with regard to the time up to order M or regard to the position up to order N:

$$F\left(\Phi; t, x_j; \partial_t\Phi, \partial_{j_1}\Phi, \partial_t^2\Phi, \partial_{tj_1}\Phi, \partial_{j_1 j_2}\Phi, \dots, \partial_t^M\Phi, \partial_{j_1 \dots j_N}\Phi, \partial^M_{tj_1 \dots j_N}\Phi\right) = 0. \tag{6.28}$$

It corresponds to a partial differential equation of order M in time and order N in position.

For linear waves with small amplitude and/or space-time derivatives, there are no powers or cross-products and the linear wave equation is

$$B(\mathbf{x}, t) = \sum_{m=0}^{M} \sum_{n=0}^{N} A^m_{j_1 \dots j_n}(\mathbf{x}, t) \frac{\partial^{m+n}\Phi}{\partial t^m \partial x_{j_1} \dots \partial x_{j_n}} \tag{6.29}$$

where: (i) the repeated indices $(j_1, \dots, j_n)$ are summed over their range (6.27)[1]; (ii) the forcing term is zero, $B = 0$, for free waves; (iii) the coefficients $A^m_{j_1 \dots j_n}$ may depend on position for inhomogeneous media or may depend on time for unsteady media. The variable m in the coefficients $A^m_{j_1 \dots j_n}$ is merely a superscript; it does not mean a mathematical power of an exponentiation. For homogeneous media, the coefficients do not depend on position, $\partial_j A^m_{j_1 \dots j_n} = 0$, and for steady media, the coefficients do not depend on time, $\partial_t A^m_{j_1 \dots j_n} = 0$. If and only if the last two conditions are met, the coefficients are constant, $A^m_{j_1 \dots j_n} = \text{const}$. Thus, linear free waves in a steady homogeneous medium are specified by a wave variable Φ in space-time $(\mathbf{x}, t)$, satisfying a linear unforced partial differential equation with constant coefficients,

$$\left\{P_{M,N}\left(\frac{\partial}{\partial t}, \frac{\partial}{\partial x_j}\right)\right\}\Phi(\mathbf{x}, t) = 0, \tag{6.30a}$$

which is the wave operator, with a characteristic polynomial

$$P_{M,N}\left(\frac{\partial}{\partial t}, \frac{\partial}{\partial x_j}\right) = \sum_{m=0}^{M} \sum_{n=0}^{N} A^m_{j_1 \dots j_n} \frac{\partial^{m+n}}{\partial t^n \partial x_{j_1} \dots \partial x_{j_n}} \tag{6.30b}$$

of derivatives with regard to time and position of degree M and N respectively.

The solution exists as a superposition of plane waves (for example sinusoidal plane waves) with frequency ω, wave vector $\mathbf{k}$ and amplitude Ψ represented by the Fourier transform in space-time:

$$\Phi(\mathbf{x}, t) = \int_{-\infty}^{+\infty} \mathrm{d}\omega \int_{-\infty}^{+\infty} \mathrm{d}^3\mathbf{k}\, \Psi(\mathbf{k}, \omega) \exp\left[\mathrm{i}\left(\mathbf{k} \cdot \mathbf{x} - \omega t\right)\right]. \tag{6.31}$$

[1] In (6.29) it occurs an abuse of notation since the equation omits n sums, so the more correct expression is

$$B(\mathbf{x}, t) = \sum_{m=0}^{M}\left[A^m \frac{\partial^m\Phi}{\partial t^m} + \sum_{n=1}^{N} \sum_{j_1=1}^{P} \dots \sum_{j_n=1}^{P} A^m_{j_1 \dots j_n}(\mathbf{x}, t) \frac{\partial^{m+n}\Phi}{\partial t^m \partial x_{j_1} \dots \partial x_{j_n}}\right].$$

Since temporal or spatial derivatives of the wave variable are equivalent to multiplying the Fourier spectrum Ψ by $-\mathrm{i}$ times the frequency or by $+\mathrm{i}$ times the wave vector,

$$\{\partial_t \Phi, \partial_j \Phi\} \longleftrightarrow \int_{-\infty}^{+\infty} \mathrm{d}\omega \int_{-\infty}^{+\infty} \mathrm{d}^3\mathbf{k}\ \{-\mathrm{i}\omega, \mathrm{i}k_j\}\, \Psi(\mathbf{k},\omega) \exp\left[\mathrm{i}\left(\mathbf{k}\cdot\mathbf{x} - \omega t\right)\right], \tag{6.32}$$

the wave equation (6.30a) leads to $P_{M,N}(-\mathrm{i}\omega, \mathrm{i}k_j)\,\Psi(\mathbf{k},\omega) = 0$. A non-trivial solution, $\Psi(\mathbf{k},\omega) \neq 0$, implies the dispersion relation

$$0 = P_{M,N}(-\mathrm{i}\omega, \mathrm{i}\mathbf{k}) \equiv D_{M,N}(\omega, \mathbf{k}), \tag{6.33a}$$

that is, by (6.30b), a polynomial of degree M and N in frequency and wave vector respectively,

$$D_{M,N}(\omega,\mathbf{k}) = \sum_{m=0}^{M}\sum_{n=0}^{N} (-1)^m\, \mathrm{i}^{n+m} \omega^m A^m_{j_1\ldots j_n} k_{j_1}\ldots k_{j_n}, \tag{6.33b}$$

with M roots,

$$D_{M,N}(\omega,\mathbf{k}) = (-\mathrm{i})^M \sum_{n=0}^{N} \mathrm{i}^n A^M_{j_1\ldots j_n} k_{j_1}\ldots k_{j_n} \prod_{s=1}^{M}\left[\omega - \omega_s(\mathbf{k})\right]. \tag{6.33c}$$

The variable s in the root ω_s is merely a subscript and it does not mean an index of a multiplicity[2]. These roots or temporal modes specify the frequency as a function of wave vector:

$$\omega = \omega_s(\mathbf{k}) = \omega_s(k, \mathbf{n}), \tag{6.34a}$$

The wavevector consists on a wavenumber, $k \equiv |\mathbf{k}|$, and a wave normal,

$$\mathbf{n} = \frac{\mathbf{k}}{k}. \tag{6.34b}$$

The wavefronts travel at phase speed $c_s \equiv \omega_s/k$ and the energy at group velocity

$$\mathbf{w}_s \equiv \frac{\partial \omega_s}{\partial \mathbf{k}}. \tag{6.34c}$$

The waves are isotropic (subsection 6.2.2) or non-dispersive (subsection 6.2.3) if and only if the phase speed depends only on wavenumber or wave normal respectively.

6.2.2 Laplacian and isotropic/anisotropic waves

The waves are isotropic if and only if they propagate equally in all directions, thus when the frequency (6.34a) cannot depend on the wave normal (6.34b) and depends only on wavenumber k,

$$\omega = \omega_s(k), \tag{6.35a}$$

[2]Not only in the variable ω_s, but also in the variables $\mathbf{w}_s$ and c_s, all present in this chapter 6, the subscript s does not mean an index of a multiplicity since these variables are scalars and not vectors. The subscript s is written in italic because it represents a term of the sum in (6.33c).

as well as the phase speed,

$$c_s(k) = \frac{\omega_s(k)}{k}; \tag{6.35b}$$

From (6.34b) follows

$$\frac{\partial \mathbf{k}}{\partial k} = \mathbf{n} = \frac{\partial k}{\partial \mathbf{k}} \tag{6.36a}$$

and

$$\mathbf{w}_s = \frac{\partial \omega_s}{\partial \mathbf{k}} = \frac{\partial \omega_s}{\partial k}\frac{\partial k}{\partial \mathbf{k}} = \mathbf{n}\frac{\partial \omega_s}{\partial k}, \tag{6.36b}$$

implying that the group velocity (6.34c) lies in the wave normal direction (6.36b) for isotropic waves.

From (6.32) follows that the square of the wavenumber corresponds to minus the Laplacian:

$$k^2 = \mathbf{k}\cdot\mathbf{k} \longleftrightarrow -\mathrm{i}\frac{\partial}{\partial x_j}\left(-\mathrm{i}\frac{\partial}{\partial x_j}\right) = -\frac{\partial^2}{\partial x_j \partial x_j} = -\boldsymbol{\nabla}^2. \tag{6.37a}$$

Therefore the waves are isotropic if and only if in the wave equation (6.29) all spatial derivatives appear as Laplacians:

$$B(\mathbf{x},t) = \sum_{m=0}^{M}\sum_{n=0}^{N} A_n^m \frac{\partial^m}{\partial t^m}\left(\boldsymbol{\nabla}^{2n}\Phi\right). \tag{6.37b}$$

In this case, for free waves $B(\mathbf{x},t) = 0$ and from (6.32) follows the dispersion relation,

$$0 = \sum_{m=0}^{M}\sum_{n=0}^{N} (-1)^{n+m}\, \mathrm{i}^m A_n^m \omega^m k^{2n} = D_{M,N}(\omega,k), \tag{6.38a}$$

whose roots

$$0 = D_{M,N}(\omega,k) = (-\mathrm{i})^M \sum_{n=0}^{N} (-1)^n A_n^M k^{2n} \prod_{s=1}^{M} [\omega - \omega_s(k)] \tag{6.38b}$$

specify isotropic waves as stated from (6.35a) to (6.36b).

In other words, if the wave equation (6.29) contains any spatial derivatives that are not part of Laplacians, the waves are anisotropic. For example, the vibration in an infinite elastic medium is generally anisotropic since the Lamé equation in z-direction, which governs the transversal displacement ζ, when the inertial forces correspond to the acceleration, is [1, 4]

$$B(\mathbf{x},t) = \mu\left(\frac{\partial^2\zeta}{\partial x^2} + \frac{\partial^2\zeta}{\partial y^2} + \frac{\partial^2\zeta}{\partial z^2}\right) + (\lambda+\mu)\left(\frac{\partial^2 u_{\mathrm{x}}}{\partial x \partial z} + \frac{\partial^2 u_{\mathrm{y}}}{\partial y \partial z} + \frac{\partial^2\zeta}{\partial z^2}\right) - \rho\frac{\partial^2\zeta}{\partial t^2}, \tag{6.39}$$

however, in particular the shear waves which produce transverse motion (say in the z-direction) while cause no volume change and no extensional deformation, therefore setting $\partial u_i / (\partial x_i) = 0$ in the previous equation [4], lead to a Laplacian in

$$B(\mathbf{x},t) = \mu\left(\frac{\partial^2\zeta}{\partial x^2} + \frac{\partial^2\zeta}{\partial y^2} + \frac{\partial^2\zeta}{\partial z^2}\right) - \rho\frac{\partial^2\zeta}{\partial t^2} = \mu\boldsymbol{\nabla}^2\zeta - \rho\frac{\partial^2\zeta}{\partial t^2}. \tag{6.40}$$

and induce isotropy. Another example of isotropy is related to the transverse vibrations of a stiff elastic plate [6], governed by

$$\rho\frac{\partial^2\zeta}{\partial t^2} = D\left(\frac{\partial^4\zeta}{\partial x^4} + \frac{\partial^4\zeta}{\partial y^4} + 2\frac{\partial^4\zeta}{\partial x^2 \partial y^2}\right) = D\boldsymbol{\nabla}^4\zeta, \tag{6.41}$$

where D is the flexural stiffness of the plate, and the vibrations are isotropic because the spatial derivatives appear in a biharmonic operator, that is a double Laplacian. If instead of depending on wavenumber for isotropic waves (subsection 6.2.1) the phase speed depends only on wave normal, the waves are non-dispersive.

6.2.3 Conditions for non-dispersive/dispersive waves

The waves are non-dispersive if a wave packet consisting of waves of different lengths propagates together preserving a permanent wave form. Thus, the phase speed cannot depend on wavenumber and only on wave normal, implying that the frequency is a linear function of wave vector,

$$\omega_s = c_s(\mathbf{n})\, k = \mathbf{w}_s \cdot \mathbf{k}, \tag{6.42}$$

whose constant coefficient is the group velocity (6.34c) since (6.42) implies $\partial \omega_s / \partial \mathbf{k} = \mathbf{w}_s$ in agreement with (6.34c). In this case, the dispersion relation must be of the form

$$0 = D_{M,N}(\omega, \mathbf{k}) = (-\mathrm{i})^M A^M \prod_{s=1}^{M} (\omega - \mathbf{w}_s \cdot \mathbf{k}), \tag{6.43}$$

that is a polynomial of $(\omega, \mathbf{k})$ with all powers equal to M. In the term A^M, the variable M is a superscript and not a power of an exponentiation.

Thus, the waves are non-dispersive if and only if in the wave equation (6.29) all derivatives are of the same order M:

$$B(\mathbf{x}, t) = \sum_{n=0}^{M} A^{M-n}_{j_1 \cdots j_n} \frac{\partial^M \Phi}{\partial t^{M-n} \partial x_{j_1} \ldots \partial x_{j_n}}. \tag{6.44}$$

For free waves $B(\mathbf{x}, t) = 0$ and this leads to the dispersion relation

$$0 = \sum_{n=0}^{M} (-\mathrm{i})^{M-n}\, \mathrm{i}^n A^{M-n}_{j_1 \cdots j_n} \omega^{M-n} k_{j_1} \ldots k_{j_n}, \tag{6.45}$$

that is a homogeneous polynomial of degree M, whose roots are a linear relation between frequency and wave vector.

Thus, if a wave equation has derivatives of different orders, the waves are dispersive. For example, the waves where the term $\mathbf{b} \cdot \boldsymbol{\nabla}$ is typical of inhomogeneous media [130] (α, β and ν are general parameters),

$$\alpha \frac{\partial^2 \Phi}{\partial t^2} = \nu \boldsymbol{\nabla}^2 \Phi + (\mathbf{b} \cdot \boldsymbol{\nabla}) \frac{\partial \Phi}{\partial t}, \tag{6.46}$$

are non-dispersive, because all derivatives are of second-order, and are anisotropic because of the spatial derivative $\mathbf{b} \cdot \boldsymbol{\nabla}$ that is not a Laplacian. Some wave equations have the form

$$\alpha \frac{\partial^2 \Phi}{\partial t^2} + \beta \frac{\partial \Phi}{\partial t} = \nu \boldsymbol{\nabla}^2 \Phi \tag{6.47}$$

and represent dispersive waves due to the first-order derivative with regard to time corresponding to damping. The wave equation [130]

$$\rho \frac{\partial^2 \Phi}{\partial t} = T \nabla^2 \Phi + \mathbf{b} \cdot \nabla \Phi \tag{6.48}$$

is anisotropic and dispersive because the term $\mathbf{b} \cdot \nabla \Phi$ contains first-order spatial derivatives that are not Laplacians.

The most general second-order isotropic non-dispersive wave equation is the classical wave equation with Laplacian and second-order time derivatives [2]:

$$B(\mathbf{x}, t) = \rho \frac{\partial^2 \Phi}{\partial t^2} - T \nabla^2 \Phi. \tag{6.49}$$

The next isotropic non-dispersive wave equation is of fourth-order,

$$B(\mathbf{x}, t) = \rho \frac{\partial^4 \Phi}{\partial t^4} - T \nabla^4 \Phi + \nu \frac{\partial^2}{\partial t^2} \left(\nabla^2 \Phi \right), \tag{6.50}$$

with double Laplacian, fourth-order time derivative and a cross-term with Laplacian and second-order time derivative. The general wave theory (section 6.2) is applied to the energy flux (section 6.1) of elastic waves in isotropic (section 6.3) and anisotropic (section 6.4) cases.

6.3 Elastic waves in crystals and amorphous matter

The elastic waves in a steady homogeneous medium are non-dispersive, with up to three modes in the case of anisotropic matter (subsection 6.3.1) like crystals. For amorphous matter, there are two modes, longitudinal/transversal waves, that are isotropic if considered separately (subsections 6.3.2 and 6.3.3) and become anisotropic if superimposed (section 6.4).

6.3.1 Three elastic modes in crystals

The force balance equation (6.1) in the absence of external forces, $g_i = 0$, for an elastic material with stress-strain constitutive relation (6.20) becomes

$$\frac{\partial}{\partial t} \left(\rho \frac{\partial u_j}{\partial t} \right) = \frac{1}{2} \frac{\partial}{\partial x_r} \left[G_{jrpq} \left(\frac{\partial u_p}{\partial x_q} + \frac{\partial u_q}{\partial x_p} \right) \right], \tag{6.51a}$$

that can be rewritten as

$$\rho \frac{\partial^2 u_j}{\partial t^2} - \frac{1}{2} G_{jrpq} \left(\frac{\partial^2 u_p}{\partial x_r \partial x_q} + \frac{\partial^2 u_q}{\partial x_r \partial x_p} \right) = \frac{1}{2} \left(\frac{\partial u_p}{\partial x_q} + \frac{\partial u_q}{\partial x_p} \right) \frac{\partial G_{jrpq}}{\partial x_r} - \frac{\partial \rho}{\partial t} \frac{\partial u_j}{\partial t}. \tag{6.51b}$$

If the mass density depends on time or the stiffness double tensor depends on position, then the equation (6.51b) has derivatives of different orders and the elastic waves are dispersive. If the mass density is independent of time, $\partial \rho / (\partial t) = 0$, and the stiffness double tensor independent of position in divergence form, $\partial G_{jrpq} / (\partial x_r) = 0$, the equation (6.51b) reduces to the left-hand side with all derivatives of the same second-order:

$$\rho \frac{\partial^2 u_j}{\partial t^2} = \frac{1}{2} G_{jrpq} \left(\frac{\partial^2 u_p}{\partial x_r \partial x_q} + \frac{\partial^2 u_q}{\partial x_r \partial x_p} \right). \tag{6.52}$$

Therefore, the elastic waves are non-dispersive.

For constant mass density, $\rho = \text{const}$, and constant stiffness double tensor, $G_{jrpq} = \text{const}$, the anisotropic elastic wave equation (6.52) has plane wave solutions,

$$u_j(\mathbf{x}, t) = u_j^0 f_\pm (\mathbf{n} \cdot \mathbf{x} \mp ct), \tag{6.53}$$

in which: (i) the amplitude is constant, $u_j^0 = \text{const}$; (ii) the waveform is a twice differentiable function, $f(\phi_\pm) \in \mathcal{D}^2(\mathbb{R})$, where the space-time dependence appears only through the phase,

$$\phi_\pm(\mathbf{x}, t) \equiv \mathbf{n} \cdot \mathbf{x} \mp ct. \tag{6.54}$$

The phase (6.54) is a linear function of position vector through the wave normal, $\mathbf{n} = \mathbf{k}/k$, and a linear function of time through the minus the phase speed, $c = \omega/k$, so that constant phase, $\phi_\pm(\mathbf{x}, t) = \text{const}$, implies propagation at phase speed c along $+\mathbf{n}$ or opposite $-\mathbf{n}$ to the wave normal:

$$\mathbf{n} \cdot \frac{\mathrm{d}\mathbf{x}}{\mathrm{d}t} = \pm c, \tag{6.55}$$

A sinusoidal plane wave (6.31),

$$u_j(\mathbf{x}, t) = u_j^0 \exp\left[\mathrm{i}(\mathbf{k} \cdot \mathbf{x} \mp \omega t)\right], \tag{6.56a}$$

is a particular case of (6.53) with a sinusoidal function,

$$f_\pm(\phi_\pm) = \exp(\mathrm{i}k\phi_\pm), \tag{6.56b}$$

of the phase (6.54) with wavenumber k. Since the waves are non-dispersive, the propagation is independent of wavenumber and the sinusoidal plane wave (6.56a) can be replaced by a plane wave (6.53) with arbitrary twice differentiable waveform, $f(\phi_\pm) \in \mathcal{D}^2(\mathbb{R})$.

Denoting by prime the total derivative with regard to the phase, $f'_\pm \equiv \mathrm{d}f_\pm/(\mathrm{d}\phi_\pm)$, it follows that the gradient equals the product by the wave normal,

$$\frac{\partial u_j}{\partial x_r} = u_j^0 f'_\pm n_r, \tag{6.57a}$$

and the partial time derivative equals the product by the minus or plus the phase speed,

$$\frac{\partial u_j}{\partial t} = \mp c u_j^0 f'_\pm. \tag{6.57b}$$

Substituting the plane wave solution (6.53) in the wave equation (6.52), while using the partial derivatives

(6.57a) and (6.57b), leads to

$$f''_{\pm}\left[\rho c^2 u_j^0 - \frac{1}{2} G_{jrpq} n_r \left(n_q u_p^0 + n_p u_q^0\right)\right] = 0 \tag{6.58a}$$

and that is equivalent to

$$f''_{\pm} u_p^0 \left[\rho c^2 \delta_{jp} - \frac{1}{2} n_r n_q \left(G_{jrpq} + G_{jrqp}\right)\right] = 0, \tag{6.58b}$$

using the identity matrix δ_{jp}. A non-trivial solution, $\rho f''_{\pm} \mathbf{u}^0 \neq \mathbf{0}$, of the homogeneous linear system (6.58b) requires the determinant to be zero:

$$\det\left[c^2 \delta_{jp} - \frac{n_r n_q}{2\rho}\left(G_{jrpq} + G_{jrqp}\right)\right] = 0; \tag{6.59a}$$

thus, the last dispersion relation is a cubic polynomial on the square of the phase speed,

$$\prod_{s=1}^{3}\left\{c^2 - \left[c_s(\mathbf{n})\right]^2\right\} = 0, \tag{6.59b}$$

whose roots are three anisotropic phase speeds, $c = \pm c_s(\mathbf{n})$, corresponding to the frequencies

$$\omega_{\mathrm{s}\pm} = \pm k\, c_s(\mathbf{n}) \tag{6.60a}$$

and group velocities

$$\mathbf{w}_{s\pm} = \frac{\partial \omega_{s\pm}}{\partial \mathbf{k}} = \pm c_s(\mathbf{n})\, \mathbf{n} \pm \frac{\partial c_s(\mathbf{n})}{\partial \mathbf{n}} \mp n_j \frac{\partial c_s(\mathbf{n})}{\partial n_j} \mathbf{n}. \tag{6.60b}$$

Therefore, the group velocity also lies in the wave normal direction, as in the case of isotropic waves. The anisotropic elastic waves in a crystal (subsection 6.3.1) reduce, as particular case for isotropic or amorphous matter, to two modes, namely longitudinal and transversal elastic waves (subsection 6.3.2).

6.3.2 Longitudinal and transversal elastic waves

Substituting in the dispersion relation (6.59a) the stiffness double tensor (6.23a) for isotropic elasticity leads to

$$\begin{aligned} 0 &= \det\left[c^2 \delta_{jp} - \frac{n_r n_q}{\rho}\left(\mu \delta_{jp} \delta_{rq} + \mu \delta_{jq} \delta_{rp} + \lambda \delta_{jr} \delta_{pq}\right)\right] = \det\left(c^2 \delta_{jp} - \frac{\mu}{\rho} \delta_{jp} n_r n_r - \frac{\mu + \lambda}{\rho} n_j n_p\right) \\ &= \det\left[\left(c^2 - \frac{\mu}{\rho}\right)\delta_{jp} - \frac{\mu + \lambda}{\rho} n_j n_p\right]. \end{aligned} \tag{6.61}$$

The x-axis is chosen along the wave normal, $\mathbf{n} = \mathbf{e}_{\mathrm{x}}$, and the y-axis in such a way that that the displacement vector $\mathbf{u}$ lies in the (x, y)-plane, $\mathbf{u} = \mathbf{e}_{\mathrm{x}} u_{\mathrm{l}} + \mathbf{e}_{\mathrm{y}} u_{\mathrm{s}}$, so that u_{l} is the longitudinal displacement along the wave normal and u_{s} is the transversal displacement orthogonal to the wave normal. Substitution of $\mathbf{n}$ and $\mathbf{u}$ in (6.61) leads to

$$\begin{vmatrix} c^2 - \frac{2\mu+\lambda}{\rho} & 0 \\ 0 & c^2 - \frac{\mu}{\rho} \end{vmatrix} = 0, \tag{6.62a}$$

showing that there are two elastic waves,

$$\left(c^2 - \frac{2\mu + \lambda}{\rho}\right)\left(c^2 - \frac{\mu}{\rho}\right) = \left[c^2 - (c_\mathrm{l})^2\right]\left[c^2 - (c_\mathrm{s})^2\right] = 0, \tag{6.62b}$$

with longitudinal

$$c_\mathrm{l} \equiv \sqrt{\frac{2\mu + \lambda}{\rho}} = \sqrt{\frac{E/\rho}{1+\sigma}\frac{1-\sigma}{1-2\sigma}} \tag{6.62c}$$

and transversal

$$c_\mathrm{s} \equiv \sqrt{\frac{\mu}{\rho}} = \sqrt{\frac{E/(2\rho)}{1+\sigma}} \tag{6.62d}$$

phase speeds in terms of Lamé moduli or equivalently, by (6.23b) and (6.23c), in terms of Young modulus E and Poisson ratio σ, as denoted in the two last equations. The longitudinal phase speed is greater than the transversal phase speed, $c_\mathrm{l} > c_\mathrm{s}$.

Instead of obtaining the longitudinal (6.62c) and transversal (6.62d) wave speeds as particular cases of the determinant evaluated in (6.61) to (6.62b), knowing the equations (6.52) to (6.60a) of elastic waves in crystals, they can be obtained directly from the force balance equation (6.52) with isotropic double stiffness tensor (6.23a) leading to

$$\rho\frac{\partial^2 u_j}{\partial t^2} = \mu\frac{\partial}{\partial x_r}\left(\frac{\partial u_j}{\partial x_r} + \frac{\partial u_r}{\partial x_j}\right) + \lambda\frac{\partial}{\partial x_j}\left(\frac{\partial u_r}{\partial x_r}\right) = \mu\frac{\partial^2 u_j}{\partial x_r \partial x_r} + (\lambda + \mu)\frac{\partial^2 u_r}{\partial x_j \partial x_r}, \tag{6.63a}$$

that can be written in vector notation:

$$\rho\frac{\partial^2 \mathbf{u}}{\partial t^2} - \mu\boldsymbol{\nabla}^2\mathbf{u} - (\lambda + \mu)\boldsymbol{\nabla}(\boldsymbol{\nabla}\cdot\mathbf{u}) = \mathbf{0}. \tag{6.63b}$$

A vector field can be represented by

$$\mathbf{u} = \boldsymbol{\nabla}\psi + \boldsymbol{\nabla}\wedge\mathbf{h} = \mathbf{u}^\mathrm{l} + \mathbf{u}^\mathrm{s} \tag{6.64}$$

where: (i) the first term represents a longitudinal displacement, $\mathbf{u}^\mathrm{l} \equiv \boldsymbol{\nabla}\psi$, without rotation,

$$\boldsymbol{\nabla}\wedge\mathbf{u}^\mathrm{l} = \mathbf{0}, \tag{6.65a}$$

that accounts for the dilatation,

$$\boldsymbol{\nabla}\cdot\mathbf{u}^\mathrm{l} = \boldsymbol{\nabla}\cdot\mathbf{u}; \tag{6.65b}$$

(ii) the second term represents a transversal displacement, $\mathbf{u}^\mathrm{s} \equiv \boldsymbol{\nabla}\wedge\mathbf{h}$, without dilatation,

$$\boldsymbol{\nabla}\cdot\mathbf{u}^\mathrm{s} = 0, \tag{6.66a}$$

that accounts for the rotation,

$$\boldsymbol{\nabla}\wedge\mathbf{u}^\mathrm{s} = \boldsymbol{\nabla}\wedge\mathbf{u}. \tag{6.66b}$$

The longitudinal, $\mathbf{u}^\mathrm{l}$, and transversal, $\mathbf{u}^\mathrm{s}$, displacements lead to separate wave equations as shown next.

Using the identity $\nabla^2 \mathbf{u} = \nabla (\nabla \cdot \mathbf{u}) - \nabla \wedge (\nabla \wedge \mathbf{u})$, the force balance (6.63b) is rewritten as

$$\rho \frac{\partial^2 \mathbf{u}}{\partial t^2} - (2\mu + \lambda) \nabla (\nabla \cdot \mathbf{u}) + \mu \nabla \wedge (\nabla \wedge \mathbf{u}) = \mathbf{0}. \tag{6.67}$$

Substituting (6.64), while using the properties (6.65a) and (6.66a), lead to

$$\frac{\partial^2 \mathbf{u}^\mathrm{l}}{\partial t^2} - \frac{2\mu + \lambda}{\rho} \nabla \left(\nabla \cdot \mathbf{u}^\mathrm{l}\right) = -\frac{\mu}{\rho} \nabla \wedge (\nabla \wedge \mathbf{u}^\mathrm{s}) - \frac{\partial^2 \mathbf{u}^\mathrm{s}}{\partial t^2} = \mathbf{0}. \tag{6.68a}$$

Since the right-hand and left-hand sides of (6.68a) are vectors that are orthogonal to each other, the equality is possible only if both sides vanish, as stated in the last equality. This leads to the longitudinal,

$$\frac{\partial^2 \mathbf{u}^\mathrm{l}}{\partial t^2} = \frac{2\mu + \lambda}{\rho} \nabla \left(\nabla \cdot \mathbf{u}^\mathrm{l}\right) = \frac{2\mu + \lambda}{\rho} \nabla^2 \mathbf{u}^\mathrm{l} = (c_\mathrm{l})^2 \, \nabla^2 \mathbf{u}^\mathrm{l}, \tag{6.68b}$$

and transversal,

$$\frac{\partial^2 \mathbf{u}^\mathrm{s}}{\partial t^2} = -\frac{\mu}{\rho} \nabla \wedge (\nabla \wedge \mathbf{u}^\mathrm{s}) = \frac{\mu}{\rho} \nabla^2 \mathbf{u}^\mathrm{s} = (c_\mathrm{s})^2 \, \nabla^2 \mathbf{u}^\mathrm{s}, \tag{6.68c}$$

wave equations that are classical wave equations with the longitudinal (6.62c) and transversal (6.62d) phase speeds respectively. The longitudinal and transversal elastic waves considered separately are isotropic non-dispersive (subsection 6.3.3), but their superposition, while remaining non-dispersive is anisotropic (section 6.4) because the differential equation (6.67) is not a classical wave equation.

6.3.3 Energy balance for longitudinal and transversal waves

Both the longitudinal (6.68b) and transversal (6.68c) elastic wave equations have, by (6.53), plane wave solutions in a steady homogeneous medium, $\{\rho, \lambda, \mu\} = \mathrm{const}$, respectively given by

$$\mathbf{u}^\mathrm{l}(\mathbf{x}, t) = \mathbf{u}^{0\mathrm{l}} f_{\pm \mathrm{l}} (\mathbf{n} \cdot \mathbf{x} \mp c_\mathrm{l} t), \tag{6.69a}$$

$$\mathbf{u}^\mathrm{s}(\mathbf{x}, t) = \mathbf{u}^{0\mathrm{s}} f_{\pm \mathrm{s}} (\mathbf{n} \cdot \mathbf{x} \mp c_\mathrm{s} t), \tag{6.69b}$$

with: (i) constant amplitude since $\mathbf{u}^{0\mathrm{l}} = \mathrm{const}$ and $\mathbf{u}^{0\mathrm{s}} = \mathrm{const}$; (ii) waveform as a twice differentiable function, then $f_{\pm \mathrm{l}}\left(\phi^\mathrm{l}_\pm\right) \in \mathcal{D}^2(\mathbb{R})$ and $f_{\pm \mathrm{s}}\left(\phi^\mathrm{s}_\pm\right) \in \mathcal{D}^2(\mathbb{R})$; (iii) phase differing only on the phase speed, that is,

$$\phi^\mathrm{l}_\pm(\mathbf{x}, t) = \mathbf{n} \cdot \mathbf{x} \mp c_\mathrm{l} t, \tag{6.70a}$$

$$\phi^\mathrm{s}_\pm(\mathbf{x}, t) = \mathbf{n} \cdot \mathbf{x} \mp c_\mathrm{s} t, \tag{6.70b}$$

and with the same unit wave normal vector, $\mathbf{n} \cdot \mathbf{n} = 1$, which is parallel to the longitudinal displacement for the longitudinal waves,

$$\mathbf{n} \cdot \mathbf{u}^\mathrm{l} = u^\mathrm{l}, \tag{6.71a}$$

whose its amplitude satisfies $\mathbf{n}\cdot\mathbf{u}^{0\mathrm{l}} = u^{0\mathrm{l}}$, and orthogonal to the transversal displacement for the transversal waves,

$$\mathbf{n}\cdot\mathbf{u}^{\mathrm{s}} = 0, \tag{6.71b}$$

whose its amplitude satisfies $\mathbf{n}\cdot\mathbf{u}^{0\mathrm{s}} = 0$.

The kinetic energy (6.3) is given for longitudinal waves, regarding (6.69a) and (6.62c), by

$$2E^{\mathrm{kl}} = \rho\left(\frac{\partial\mathbf{u}^{\mathrm{l}}}{\partial t}\cdot\frac{\partial\mathbf{u}^{\mathrm{l}}}{\partial t}\right) = \rho\left(u^{0\mathrm{l}}f'_{\pm\mathrm{l}}c_{\mathrm{l}}\right)^2 = (2\mu+\lambda)\left(u^{0\mathrm{l}}f'_{\pm\mathrm{l}}\right)^2. \tag{6.72}$$

For transversal waves, considering (6.69b) and (6.62d), it is equal to

$$2E^{\mathrm{ks}} = \rho\left(\frac{\partial\mathbf{u}^{\mathrm{s}}}{\partial t}\cdot\frac{\partial\mathbf{u}^{\mathrm{s}}}{\partial t}\right) = \rho\left(u^{0\mathrm{s}}f'_{\pm\mathrm{s}}c_{\mathrm{s}}\right)^2 = \mu\left(u^{0\mathrm{s}}f'_{\pm\mathrm{s}}\right)^2. \tag{6.73}$$

For transversal waves, knowing (6.66a), the elastic energy in (6.25) involves only the first term on the right-hand side of the last equality,

$$\begin{aligned}2E^{\mathrm{us}} &= \frac{\mu}{2}\left(\frac{\partial u^{\mathrm{s}}_j}{\partial x_r}+\frac{\partial u^{\mathrm{s}}_r}{\partial x_j}\right)^2 = \frac{\mu}{2}\left(f'_{\pm\mathrm{s}}\right)^2\left(u^{0\mathrm{s}}_j n_r + u^{0\mathrm{s}}_r n_j\right)^2 = \frac{\mu}{2}\left(f'_{\pm\mathrm{s}}\right)^2\left(u^{0\mathrm{s}}_j n_r + u^{0\mathrm{s}}_r n_j\right)\left(u^{0\mathrm{s}}_j n_r + u^{0\mathrm{s}}_r n_j\right)\\ &= \mu\left(f'_{\pm\mathrm{s}}\right)^2\left(u^{0\mathrm{s}}_j u^{0\mathrm{s}}_j n_r n_r + u^{0\mathrm{s}}_j n_j u^{0\mathrm{s}}_r n_r\right) = \mu\left(u^{0\mathrm{s}}f'_{\pm\mathrm{s}}\right)^2 = 2E^{\mathrm{ks}},\end{aligned} \tag{6.74}$$

and equals the kinetic energy (6.73) of transversal waves. For the elastic energy of longitudinal waves, the first term on the right-hand side in the last equality of (6.25) is evaluated as in the previous relations and the second term added,

$$\begin{aligned}2E^{\mathrm{ul}} &= \frac{\mu}{2}\left(\frac{\partial u^{\mathrm{l}}_j}{\partial x_r}+\frac{\partial u^{\mathrm{l}}_r}{\partial x_j}\right)^2 + \lambda\left(\frac{\partial u^{\mathrm{l}}_j}{\partial x_j}\right)^2 = \left(f'_{\pm\mathrm{l}}\right)^2\left[\mu\left(u^{0\mathrm{l}}_j u^{0\mathrm{l}}_j n_r n_r + u^{0\mathrm{l}}_j n_j u^{0\mathrm{l}}_r n_r\right) + \lambda\left(u^{0\mathrm{l}}_j n_j\right)^2\right]\\ &= (2\mu+\lambda)\left(u^{0\mathrm{l}}f'_{\pm\mathrm{l}}\right)^2 = 2E^{\mathrm{kl}},\end{aligned} \tag{6.75}$$

with the result being equal to the kinetic energy (6.72) of longitudinal waves.

The energy flux for transversal waves (6.69b) is specified by the first term on the right-hand side of the second equality in (6.26):

$$F^{\mathrm{s}}_r = -\mu\frac{\partial u^{\mathrm{s}}_j}{\partial t}\left(\frac{\partial u^{\mathrm{s}}_j}{\partial x_r}+\frac{\partial u^{\mathrm{s}}_r}{\partial x_j}\right) = \pm\mu c_{\mathrm{s}}\left(f'_{\pm\mathrm{s}}\right)^2\left(u^{0\mathrm{s}}_j n_r + u^{0\mathrm{s}}_r n_j\right)u^{0\mathrm{s}}_j = \pm\mu c_{\mathrm{s}}\left(u^{0\mathrm{s}}f'_{\pm\mathrm{s}}\right)^2 n_r. \tag{6.76}$$

The energy flux for longitudinal waves (6.69a) adds the second term on the right-hand side of the second equality in (6.26):

$$\begin{aligned}F^{\mathrm{l}}_r &= -\mu\frac{\partial u^{\mathrm{l}}_j}{\partial t}\left(\frac{\partial u^{\mathrm{l}}_j}{\partial x_r}+\frac{\partial u^{\mathrm{l}}_r}{\partial x_j}\right) - \lambda\frac{\partial u^{\mathrm{l}}_r}{\partial t}\frac{\partial u^{\mathrm{l}}_j}{\partial x_j}\\ &= \pm\left(f'_{\pm\mathrm{l}}\right)^2 c_{\mathrm{l}}\left[\lambda u^{0\mathrm{l}}_r u^{0\mathrm{l}}_j n_j + \mu u^{0\mathrm{l}}_j\left(u^{0\mathrm{l}}_j n_r + u^{0\mathrm{l}}_r n_j\right)\right] = \pm(\lambda+2\mu)\,c_{\mathrm{l}}\left(u^{0\mathrm{l}}f'_{\pm\mathrm{l}}\right)^2 n_r.\end{aligned} \tag{6.77}$$

For longitudinal waves, the elastic energy (6.75) equals the kinetic energy (6.72) and thus the total energy, that is their sum, equals twice either of them leading to

$$E^{\mathrm{l}} = E^{\mathrm{kl}} + E^{\mathrm{ul}} = 2E^{\mathrm{kl}} = 2E^{\mathrm{ul}} = (2\mu + \lambda)\left(u^{0\mathrm{l}} f'_{\pm\mathrm{l}}\right)^2 . \tag{6.78}$$

The energy flux for longitudinal waves (6.77) equals the energy density (6.78) multiplied by longitudinal phase speed (6.62c) along or opposite to the wave normal,

$$\mathbf{F}^{\mathrm{l}} = \pm c_{\mathrm{l}} E^{\mathrm{l}} \mathbf{n} = \pm E^{\mathrm{l}} \mathbf{w}^{\mathrm{l}}, \tag{6.79}$$

corresponding to the longitudinal group velocity, $\mathbf{w}^{\mathrm{l}} = c_{\mathrm{l}} \mathbf{n}$.

For transversal waves, the elastic energy (6.74) also equals the kinetic energy (6.73) and the total energy, that is their sum, is twice either of them being equal to

$$E^{\mathrm{s}} = E^{\mathrm{ks}} + E^{\mathrm{us}} = 2E^{\mathrm{ks}} = 2E^{\mathrm{us}} = \mu\left(u^{0\mathrm{s}} f'_{\pm\mathrm{s}}\right)^2 . \tag{6.80}$$

The energy flux of transversal waves (6.76) equals the energy density (6.80) multiplied by the transversal phase speed (6.62d) along or opposite to the wave normal,

$$\mathbf{F}^{\mathrm{s}} = \pm E^{\mathrm{s}} c_{\mathrm{s}} \mathbf{n} = \pm E^{\mathrm{s}} \mathbf{w}^{\mathrm{s}}, \tag{6.81}$$

corresponding to the transversal group velocity, $\mathbf{w}^{\mathrm{s}} = c_{\mathrm{s}} \mathbf{n}$.

The longitudinal total energy density (6.78) and energy flux (6.79) satisfy, through (6.8d), the energy conservation equation,

$$\frac{\partial E^{\mathrm{l}}}{\partial t} + \boldsymbol{\nabla} \cdot \mathbf{F}^{\mathrm{l}} = \dot{W}^{\mathrm{l}}, \tag{6.82a}$$

while the transversal total energy density (6.80) and energy flux (6.81) satisfy, also through (6.8d), the energy conservation equation,

$$\frac{\partial E^{\mathrm{s}}}{\partial t} + \boldsymbol{\nabla} \cdot \mathbf{F}^{\mathrm{s}} = \dot{W}^{\mathrm{s}}, \tag{6.82b}$$

both splitting the power (6.8b) of external applied forces,

$$\dot{W} = \mathbf{g} \cdot \left(\frac{\partial \mathbf{u}^{\mathrm{l}}}{\partial t} + \frac{\partial \mathbf{u}^{\mathrm{s}}}{\partial t}\right) = \dot{W}^{\mathrm{l}} + \dot{W}^{\mathrm{s}}, \tag{6.83a}$$

into longitudinal and transversal contributions, respectively

$$\left\{\dot{W}^{\mathrm{l}}, \dot{W}^{\mathrm{s}}\right\} = \left\{\mathbf{g} \cdot \frac{\partial \mathbf{u}^{\mathrm{l}}}{\partial t}, \mathbf{g} \cdot \frac{\partial \mathbf{u}^{\mathrm{s}}}{\partial t}\right\}. \tag{6.83b}$$

In the absence of external force, $\mathbf{g} = \mathbf{0}$, as assumed for free or unforced waves in (6.51a), the right-hand sides of (6.82a) and (6.82b) are zero, $\dot{W}^{\mathrm{l}} = 0 = \dot{W}^{\mathrm{s}}$. The energy balance for separate longitudinal waves, given by (6.82a), (6.78) and (6.79), and transversal waves, given by (6.82b), (6.80) and (6.81), must be reconsidered for their superposition (section 6.4) that leads to anisotropic waves, because the classical wave equation, given respectively by (6.68b) and (6.68c), is replaced by (6.63b) or equivalently (6.67).

6.4 Superposition of longitudinal and transversal waves

The superposition of longitudinal and transversal waves adds: (i) the kinetic and elastic energies (subsection 6.4.1) and hence the total energies; (ii) the power of external forces (subsection 6.4.2). However, the total energy flux does not lie along the wave normal because the superposition of longitudinal and transversal waves, with different phase speeds, is anisotropic. Since longitudinal and transversal waves separately are isotropic and have an energy flux along the wave normal, their superposition leads to the appearance of a coupling energy flux (subsection 6.4.3) transverse to the wave normal, and hence with zero divergence, that does not affect the total energy balance (subsection 6.4.3).

6.4.1 Kinetic and elastic energy densities

Since the longitudinal displacement is parallel to the wave normal as stated in (6.71a) and the transverse displacement is orthogonal to the wave normal as stated in (6.71b), the two displacements are orthogonal to each other, $\mathbf{u}^{\mathrm{l}} \cdot \mathbf{u}^{\mathrm{s}} = 0 = \mathbf{u}^{0\mathrm{l}} \cdot \mathbf{u}^{0\mathrm{s}}$, and the total kinetic energy (6.3) is the sum of the longitudinal (6.72) and transversal (6.73) kinetic energies:

$$\begin{aligned} E^{\mathrm{k}} &= \frac{\rho}{2}\left(\frac{\partial \mathbf{u}}{\partial t} \cdot \frac{\partial \mathbf{u}}{\partial t}\right) = \frac{\rho}{2}\left(\frac{\partial \mathbf{u}^{\mathrm{l}}}{\partial t} + \frac{\partial \mathbf{u}^{\mathrm{s}}}{\partial t}\right) \cdot \left(\frac{\partial \mathbf{u}^{\mathrm{l}}}{\partial t} + \frac{\partial \mathbf{u}^{\mathrm{s}}}{\partial t}\right) = \frac{\rho}{2}\left|\mp c_{\mathrm{l}} \mathbf{u}^{0\mathrm{l}} f'_{\pm\mathrm{l}} \mp c_{\mathrm{s}} \mathbf{u}^{0\mathrm{s}} f'_{\pm\mathrm{s}}\right|^2 \\ &= \frac{\rho}{2}\left(c_{\mathrm{l}} u^{0\mathrm{l}} f'_{\pm\mathrm{l}}\right)^2 + \left(c_{\mathrm{s}} u^{0\mathrm{s}} f'_{\pm\mathrm{s}}\right)^2 + \rho c_{\mathrm{l}} c_{\mathrm{s}} f'_{\pm\mathrm{l}} f'_{\pm\mathrm{s}} \left(\mathbf{u}^{0\mathrm{l}} \cdot \mathbf{u}^{0\mathrm{s}}\right) = E^{\mathrm{kl}} + E^{\mathrm{ks}}. \end{aligned} \tag{6.84}$$

Concerning the elastic energy (6.4) for an isotropic elastic medium (6.25), the second term on the right-hand side, knowing the property (6.65b), involves only the longitudinal displacement,

$$\lambda\left(\boldsymbol{\nabla} \cdot \mathbf{u}\right)^2 = \lambda\left(\boldsymbol{\nabla} \cdot \mathbf{u}^{\mathrm{l}}\right)^2 = \lambda\left(n_j u_j^{0\mathrm{l}} f'_{\pm\mathrm{l}}\right)^2 = \lambda\left(u^{0\mathrm{l}} f'_{\pm\mathrm{l}}\right)^2, \tag{6.85}$$

and the first term involves both longitudinal and transversal displacements. The expression

$$\frac{\partial u_j}{\partial x_r} + \frac{\partial u_r}{\partial x_j} = \frac{\partial u_j^{\mathrm{l}}}{\partial x_r} + \frac{\partial u_r^{\mathrm{l}}}{\partial x_j} + \frac{\partial u_j^{\mathrm{s}}}{\partial x_r} + \frac{\partial u_r^{\mathrm{s}}}{\partial x_j} = f'_{\pm\mathrm{l}}\left(u_j^{0\mathrm{l}} n_r + u_r^{0\mathrm{l}} n_j\right) + f'_{\pm\mathrm{s}}\left(u_j^{0\mathrm{s}} n_r + u_r^{0\mathrm{s}} n_j\right) \tag{6.86a}$$

appears to the square in the first term on the right-hand side of the second equality in the elastic energy, presented in the equation (6.25):

$$\begin{aligned} \left(\frac{\partial u_j}{\partial x_r} + \frac{\partial u_r}{\partial x_j}\right)^2 &= \left(f'_{\pm\mathrm{l}}\right)^2\left(u_j^{0\mathrm{l}} n_r + u_r^{0\mathrm{l}} n_j\right)^2 + \left(f'_{\pm\mathrm{s}}\right)^2\left(u_j^{0\mathrm{s}} n_r + u_r^{0\mathrm{s}} n_j\right)^2 \\ &\quad + 2 f'_{\pm\mathrm{l}} f'_{\pm\mathrm{s}}\left[\left(u_j^{0\mathrm{l}} n_r + u_r^{0\mathrm{l}} n_j\right)\left(u_j^{0\mathrm{s}} n_r + u_r^{0\mathrm{s}} n_j\right)\right]. \end{aligned} \tag{6.86b}$$

The cross-term between longitudinal and transversal displacements in square brackets on the right-hand side of (6.86b) is zero:

$$u_j^{0\mathrm{l}} n_r u_j^{0\mathrm{s}} n_r + u_j^{0\mathrm{l}} u_r^{0\mathrm{s}} n_r n_j + u_r^{0\mathrm{l}} u_j^{0\mathrm{s}} n_j n_r + u_r^{0\mathrm{l}} u_r^{0\mathrm{s}} n_j n_j = 2\left(\mathbf{u}^{0\mathrm{l}} \cdot \mathbf{u}^{0\mathrm{s}}\right) + 2\left(\mathbf{u}^{0\mathrm{l}} \cdot \mathbf{n}\right)\left(\mathbf{u}^{0\mathrm{s}} \cdot \mathbf{n}\right) = 0, \tag{6.86c}$$

and thus on the right-hand side of (6.86b) only remain the separate terms for the longitudinal and transversal waves. To evaluate the terms of longitudinal waves, the equation (6.86c) is used with the substitution s $\rightarrow$ l in all the terms; to evaluate the terms of transversal waves, the equation (6.86c) is used again, but making the substitution l $\rightarrow$ s. With this calculations, the equation (6.86b) reduces further to

$$\left(\frac{\partial u_j}{\partial x_r} + \frac{\partial u_r}{\partial x_j}\right)^2 = 4\left(u^{0\mathrm{l}} f'_{\pm\mathrm{l}}\right)^2 + 2\left(u^{0\mathrm{s}} f'_{\pm\mathrm{s}}\right)^2. \tag{6.86d}$$

Substituting (6.86d) in the first term on the right-hand side of the second equality in (6.25) and using (6.85) in the second term specify the total elastic energy as the sum of the elastic energies of the longitudinal (6.75) and transversal (6.74) waves:

$$E^{\mathrm{u}} = \left(\mu + \frac{\lambda}{2}\right)\left(u^{0\mathrm{l}} f'_{\pm\mathrm{l}}\right)^2 + \frac{\mu}{2}\left(u^{0\mathrm{s}} f'_{\pm\mathrm{s}}\right)^2 = E^{\mathrm{ul}} + E^{\mathrm{us}}. \tag{6.87}$$

Thus, the total kinetic plus elastic energy (6.7) is the sum, regarding (6.84) and (6.87), of the total kinetic and elastic energies,

$$E = E^{\mathrm{k}} + E^{\mathrm{u}} = E^{\mathrm{kl}} + E^{\mathrm{ks}} + E^{\mathrm{ul}} + E^{\mathrm{us}} = E^{\mathrm{l}} + E^{\mathrm{s}}, \tag{6.88}$$

or of the total longitudinal (6.78) and transversal (6.80) waves. The power of external applied forces (6.83a) is also the sum of the contributions of longitudinal and transversal waves. The comparison of the total energy balance (subsection 6.4.2) with the energy balances for longitudinal (subsection 6.3.2) and transversal (subsection 6.3.3) waves shows that the total energy flux is not the sum of the energy fluxes for longitudinal and transversal waves because there is a coupling cross-flux term when both are present.

6.4.2 Longitudinal, transversal and total energy balances

In the total energy balance (6.8d),

$$\frac{\partial E}{\partial t} - \dot{W} = -\boldsymbol{\nabla} \cdot \mathbf{F}, \tag{6.89a}$$

the energy density (6.88) and power of external forces (6.83a) are the sum of contributions of longitudinal and transversal waves without cross-terms:

$$\frac{\partial E^{\mathrm{l}}}{\partial t} - \dot{W}^{\mathrm{l}} + \frac{\partial E^{\mathrm{s}}}{\partial t} - \dot{W}^{\mathrm{s}} = -\boldsymbol{\nabla} \cdot \mathbf{F}. \tag{6.89b}$$

Substituting the energy balances for longitudinal (6.82a) and transversal (6.82b) waves leads to $0 = \boldsymbol{\nabla} \cdot \left(\mathbf{F} - \mathbf{F}^{\mathrm{l}} - \mathbf{F}^{\mathrm{s}}\right) = \boldsymbol{\nabla} \cdot \mathbf{F}^{\mathrm{sl}}$, showing that the difference between the total energy flux of superimposed longitudinal with transversal waves and the energy flux of separate longitudinal with transversal waves must have zero divergence. This implies that the cross-coupling energy flux must be transversal to the wave normal, $\mathbf{n} \cdot \mathbf{F}^{\mathrm{sl}} = 0$.

Since both the longitudinal (6.68b) and transversal (6.68c) waves satisfy the classical wave equation

(6.48), the waves are isotropic non-dispersive and their energy fluxes, given respectively by (6.77) and (6.76), lie along the wave normal:

$$\mathbf{F}^{\mathrm{l}} \wedge \mathbf{n} = \mathbf{0} = \mathbf{F}^{\mathrm{s}} \wedge \mathbf{n}. \tag{6.90}$$

The superposition of longitudinal and transversal waves satisfies a wave equation (6.63b) or (6.67) that: (i) has all space-time derivatives of the same second-order, so the waves are not dispersive; (ii) not all spatial derivatives appear in the Laplacian, and thus the superposition of longitudinal and transversal waves is anisotropic because they propagate at different phase speeds, given by (6.62c) and (6.62d). Thus, the total energy flux does not lie along the wave normal:

$$\mathbf{F} \wedge \mathbf{n} \neq \mathbf{0}. \tag{6.91}$$

From (6.90) and (6.91), it follows that a cross-coupling energy flux between longitudinal and transversal waves must exist,

$$\mathbf{0} \neq \mathbf{n} \wedge \left(\mathbf{F} - \mathbf{F}^{\mathrm{l}} - \mathbf{F}^{\mathrm{s}}\right) = \mathbf{n} \wedge \mathbf{F}^{\mathrm{sl}}, \tag{6.92}$$

and it is transverse to the wave normal.

The total energy flux consists of the energy fluxes of longitudinal (6.79) plus transversal (6.81) plus cross-coupling terms:

$$\mathbf{F} = \mathbf{F}^{\mathrm{l}} + \mathbf{F}^{\mathrm{s}} + \mathbf{F}^{\mathrm{sl}}. \tag{6.93a}$$

The total group velocity is obtained dividing the energy flux (6.93a) by the energy density (6.88):

$$\mathbf{w} = \frac{\mathbf{F}}{E} = \frac{\mathbf{F}^{\mathrm{l}} + \mathbf{F}^{\mathrm{s}} + \mathbf{F}^{\mathrm{sl}}}{E^{\mathrm{l}} + E^{\mathrm{s}}}. \tag{6.93b}$$

Considering longitudinal and transversal waves propagating in the same direction, both along $+\mathbf{n}$ or opposite $-\mathbf{n}$ to the wave normal, the group velocity is given by:

$$\mathbf{w} = \pm\mathbf{n}\frac{c_{\mathrm{l}}E^{\mathrm{l}} + c_{\mathrm{s}}E^{\mathrm{s}}}{E^{\mathrm{l}} + E^{\mathrm{s}}} + \frac{\mathbf{F}^{\mathrm{sl}}}{E^{\mathrm{l}} + E^{\mathrm{s}}}. \tag{6.93c}$$

In order to specify completely the group or energy velocity (6.93c), the cross-coupling energy flux between longitudinal and transversal waves is calculated explicitly (subsection 6.4.3), confirming that it is transversal to the direction of propagation (6.92) and hence has zero divergence.

6.4.3 Cross-coupling longitudinal-transversal energy flux

The total energy flux is given for an isotropic elastic material by (6.26) and the second-term on the right-hand side is

$$-\lambda\left(\boldsymbol{\nabla}\cdot\mathbf{u}\right)\frac{\partial u_r}{\partial t} = -\lambda\left(\boldsymbol{\nabla}\cdot\mathbf{u}^{\mathrm{l}}\right)\left(\frac{\partial u_r^{\mathrm{l}}}{\partial t} + \frac{\partial u_r^{\mathrm{s}}}{\partial t}\right) = \pm\lambda u^{0\mathrm{l}} f'_{\pm\mathrm{l}}\left(c_{\mathrm{l}} u_r^{0\mathrm{l}} f'_{\pm\mathrm{l}} + c_{\mathrm{s}} u_r^{0\mathrm{s}} f'_{\pm\mathrm{s}}\right) \tag{6.94}$$

where: (i) the first term on the last equality of (6.94) appears in the longitudinal energy flux (6.77); (ii) the second term is a cross-coupling of longitudinal and transversal waves. The remaining term of the total energy flux (6.26) is

$$-\mu\frac{\partial u_j}{\partial t}\left(\frac{\partial u_j}{\partial x_r}+\frac{\partial u_r}{\partial x_j}\right)=\pm\mu\left(c_{\mathrm{l}}u_j^{0\mathrm{l}}f'_{\pm\mathrm{l}}+c_{\mathrm{s}}u_j^{0\mathrm{s}}f'_{\pm\mathrm{s}}\right)\left[f'_{\pm\mathrm{l}}\left(u_j^{0\mathrm{l}}n_r+u_r^{0\mathrm{l}}n_j\right)+f'_{\pm\mathrm{s}}\left(u_j^{0\mathrm{s}}n_r+u_r^{0\mathrm{s}}n_j\right)\right], \quad (6.95)$$

that consists of three terms. The term for longitudinal waves,

$$\pm\mu c_{\mathrm{l}}\left(f'_{\pm\mathrm{l}}\right)^2\left(u_j^{0\mathrm{l}}u_j^{0\mathrm{l}}n_r+u_r^{0\mathrm{l}}u_j^{0\mathrm{l}}n_j\right)=\pm2\mu c_{\mathrm{l}}\left(u^{0\mathrm{l}}f'_{\pm\mathrm{l}}\right)^2n_r, \quad (6.96)$$

appears in the last equality of (6.77); thus, the sum of (6.96) and the first term on the right-hand side of the last equality in (6.94) accounts for the energy flux of longitudinal waves. The second term on the right-hand side of (6.95) corresponding to transversal waves,

$$\pm\mu c_{\mathrm{s}}\left(f'_{\pm\mathrm{s}}\right)^2u_j^{0\mathrm{s}}\left(u_j^{0\mathrm{s}}n_r+u_r^{0\mathrm{s}}n_j\right)=\pm\mu c_{\mathrm{s}}\left(u^{0\mathrm{s}}f'_{\pm\mathrm{s}}\right)^2n_r, \quad (6.97)$$

is the energy flux of transversal waves (6.76). The remaining third cross-term on the right-hand side of (6.95) simplifies to

$$\begin{aligned}&\pm\mu f'_{\pm\mathrm{l}}f'_{\pm\mathrm{s}}\left[c_{\mathrm{l}}u_j^{0\mathrm{l}}\left(u_j^{0\mathrm{s}}n_r+u_r^{0\mathrm{s}}n_j\right)+c_{\mathrm{s}}u_j^{0\mathrm{s}}\left(u_j^{0\mathrm{l}}n_r+u_r^{0\mathrm{l}}n_j\right)\right]\\&=\pm\mu f'_{\pm\mathrm{l}}f'_{\pm\mathrm{s}}\left[\left(c_{\mathrm{l}}+c_{\mathrm{s}}\right)\left(\mathbf{u}^{0\mathrm{l}}\cdot\mathbf{u}^{0\mathrm{s}}\right)n_r+c_{\mathrm{l}}u_r^{0\mathrm{s}}\left(\mathbf{u}^{0\mathrm{l}}\cdot\mathbf{n}\right)+c_{\mathrm{s}}u_r^{0\mathrm{l}}\left(\mathbf{u}^{0\mathrm{s}}\cdot\mathbf{n}\right)\right]=\pm\mu f'_{\pm\mathrm{l}}f'_{\pm\mathrm{s}}c_{\mathrm{l}}u^{0\mathrm{l}}u_r^{0\mathrm{s}}. \quad (6.98)\end{aligned}$$

Thus, the cross-coupling flux between the longitudinal and transversal waves is given by the sum of (6.98) with the second term on the right-hand side of (6.94):

$$F_r^{\mathrm{sl}}=\pm\left(c_{\mathrm{s}}\lambda+c_{\mathrm{l}}\mu\right)f'_{\pm\mathrm{l}}f'_{\pm\mathrm{s}}u^{0\mathrm{l}}u_r^{0\mathrm{s}}. \quad (6.99)$$

Using the formulas

$$\frac{\partial\mathbf{u}^{\mathrm{s}}}{\partial t}=\mp c_{\mathrm{s}}f'_{\pm\mathrm{s}}\mathbf{u}^{0\mathrm{s}}, \quad (6.100a)$$

$$\boldsymbol{\nabla}\cdot\mathbf{u}^{\mathrm{l}}=n_rf'_{\pm\mathrm{l}}u_r^{0\mathrm{l}}=f'_{\pm\mathrm{l}}\mathbf{u}^{0\mathrm{l}}\cdot\mathbf{n}=f'_{\pm\mathrm{l}}u^{0\mathrm{l}} \quad (6.100b)$$

in (6.99) leads to the cross-coupling energy flux between longitudinal and transversal waves that can be written in vector notation,

$$\mathbf{F}^{\mathrm{sl}}=-\left(\lambda+\frac{c_{\mathrm{l}}}{c_{\mathrm{s}}}\mu\right)\left(\boldsymbol{\nabla}\cdot\mathbf{u}^{\mathrm{l}}\right)\frac{\partial\mathbf{u}^{\mathrm{s}}}{\partial t}, \quad (6.101a)$$

as the product of: (i) the dilatation that is non-zero if and only if longitudinal waves are present; (ii) the velocity of transverse waves, that confirms that the cross-flux is transversal since

$$\mathbf{F}^{\mathrm{sl}}\cdot\mathbf{n}=-\left(\lambda+\frac{c_{\mathrm{l}}}{c_{\mathrm{s}}}\mu\right)\left(\boldsymbol{\nabla}\cdot\mathbf{u}^{\mathrm{l}}\right)\frac{\partial}{\partial t}\left(\mathbf{u}^{\mathrm{s}}\cdot\mathbf{n}\right)=0, \quad (6.101b)$$

in agreement with the orthogonality between energy flux and wave normal; (iii) the factor

$$-\vartheta \equiv -\left(\lambda + \frac{c_\mathrm{l}}{c_\mathrm{s}}\mu\right) = -\lambda - \mu\sqrt{2 + \frac{\lambda}{\mu}} = -\rho\left(c_\mathrm{l}^2 + c_\mathrm{l}c_\mathrm{s} - 2c_\mathrm{s}^2\right), \tag{6.101c}$$

relating to the longitudinal (6.62c) and transversal (6.62d) phase speeds. The divergence of the cross-flux (6.101a) is zero,

$$\boldsymbol{\nabla}\cdot\mathbf{F}^\mathrm{sl} = -\vartheta\left[\left(\boldsymbol{\nabla}\cdot\mathbf{u}^\mathrm{l}\right)\frac{\partial}{\partial t}\left(\boldsymbol{\nabla}\cdot\mathbf{u}^\mathrm{s}\right) + \left(\frac{\partial\mathbf{u}^\mathrm{s}}{\partial t}\cdot\boldsymbol{\nabla}\right)\left(\boldsymbol{\nabla}\cdot\mathbf{u}^\mathrm{l}\right)\right] = 0, \tag{6.102}$$

confirming that the divergence is zero. Substitution of (6.77), (6.76) and (6.99) in (6.93a) specifies the total energy flux of longitudinal plus transversal waves in an isotropic elastic medium in terms of Lamé moduli and wave speeds,

$$\mathbf{F} = \mathbf{F}^\mathrm{l} + \mathbf{F}^\mathrm{s} + \mathbf{F}^\mathrm{sl} = \pm\left[(\lambda + 2\mu)\,c_\mathrm{l}\left(u^{0\mathrm{l}}f'_{\pm\mathrm{l}}\right)^2 + \mu c_\mathrm{s}\left(u^{0\mathrm{s}}f'_{\pm\mathrm{s}}\right)^2\right]\mathbf{n} \pm \left(c_\mathrm{s}\lambda + c_\mathrm{l}\mu\right)f'_{\pm\mathrm{l}}f'_{\pm\mathrm{s}}u^{0\mathrm{l}}\mathbf{u}^{0\mathrm{s}}, \tag{6.103a}$$

or using (6.62c) and (6.62d) in terms of only wave speeds and mass density,

$$\mathbf{F} = \pm\rho\left[c_\mathrm{l}^3\left(u^{0\mathrm{l}}f'_{\pm\mathrm{l}}\right)^2 + c_\mathrm{s}^3\left(u^{0\mathrm{s}}f'_{\pm\mathrm{s}}\right)^2\right]\mathbf{n} \pm \rho c_\mathrm{s}\left[c_\mathrm{l}\left(c_\mathrm{l} + c_\mathrm{s}\right) - 2c_\mathrm{s}^2\right]f'_{\pm\mathrm{l}}f'_{\pm\mathrm{s}}u^{0\mathrm{l}}\mathbf{u}^{0\mathrm{s}}. \tag{6.103b}$$

In the case of sinusoidal waves (6.56b), the derivative of the wave forms with regard to the phase is specified by the wavenumber, that is, $f'_{\pm\mathrm{l}} = \mathrm{i}kf_{\pm\mathrm{l}}$ and $f'_{\pm\mathrm{s}} = \mathrm{i}kf_{\pm\mathrm{s}}$, implying $\left(f'_{\pm\mathrm{l}}\right)^2 = -k^2 f_{\pm\mathrm{l}}^2 = -k^2\exp\left(2\mathrm{i}k\phi_\pm^\mathrm{l}\right)$ and $\left(f'_{\pm\mathrm{s}}\right)^2 = -k^2 f_{\pm\mathrm{s}}^2 = -k^2\exp\left(2\mathrm{i}k\phi_\pm^\mathrm{s}\right)$. The energy flux, considering the equations (6.103a) and (6.103b), is given by

$$\begin{aligned}\mathbf{F} &= \mp\rho k^2\left\{\left[(\lambda + 2\mu)\,c_\mathrm{l}\left(u^{0\mathrm{l}}\right)^2\exp\left(2\mathrm{i}k\phi_\pm^\mathrm{l}\right) + \mu c_\mathrm{s}\left(u^{0\mathrm{s}}\right)^2\exp\left(2\mathrm{i}k\phi_\pm^\mathrm{l}\right)\right]\mathbf{n}\right.\\ &\quad\left. + \left(c_\mathrm{s}\lambda + c_\mathrm{l}\mu\right)u^{0\mathrm{l}}\exp\left[\mathrm{i}k\left(\phi_\pm^\mathrm{l} + \phi_\pm^\mathrm{s}\right)\right]\mathbf{u}^{0\mathrm{s}}\right\}\\ &= \mp\rho k^2\left\{\left[c_\mathrm{l}^3\left(u^{0\mathrm{l}}\right)^2\exp\left(2\mathrm{i}k\phi_\pm^\mathrm{l}\right) + c_\mathrm{s}^3\left(u^{0\mathrm{s}}\right)^2\exp\left(2\mathrm{i}k\phi_\pm^\mathrm{s}\right)\right]\mathbf{n}\right.\\ &\quad\left. + c_\mathrm{s}\left[c_\mathrm{l}\left(c_\mathrm{l} + c_\mathrm{s}\right) - 2c_\mathrm{s}^2\right]u^{0\mathrm{l}}\exp\left[\mathrm{i}k\left(\phi_\pm^\mathrm{l} + \phi_\pm^\mathrm{s}\right)\right]\mathbf{u}^{0\mathrm{s}}\right\}.\end{aligned} \tag{6.104}$$

Among its multiple possible applications in elastodynamics, the conclusion (section 6.5) mentions impact damage associated with wave generation and propagation.

6.5 Main conclusions of the chapter 6

The energy flux is a fundamental concept in elastodynamics as it specifies the energy transport across an elastic (or inelastic) body. As a simple example, consider a parallel-sided plate subject to the impact of a projectile or a similar type of impact that generates waves. In the case of elastic waves propagating perpendicular to the plate: (i) the longitudinal waves can cause “spalling” or deformation of material on the side opposite to the impact; (ii) the transversal waves cause shear between the two sides and may lead to cracks that can open further under fatigue loads; (iii) if the longitudinal and transversal waves coexist, and even if they propagate normal to the sides of the plate, there is a cross energy flux parallel to the sides of the plates implying a lateral spread of strains and stresses. The preceding example is just a simple particular case of the energy flux associated with any unsteady deformation of an elastic or inelastic material.

In general, the energy flux appears in the energy balance (6.8d), together with the power (6.8b) of external forces (6.1) and the energy density (6.7). The energy density consists of the sum of kinetic (6.2) and deformation (6.4) energies. The energy flux (6.8e) equals the contracted product of minus the velocity by the stress tensor, with the assumption of linear strains (6.5). The energy flux for the transverse vibrations of an elastic string (6.13) or membrane (6.16b) in the linear case, respectively $[\partial\zeta/(\partial x)]^2 \ll 1$ and (6.16a), can be extended to the non-linear case of unrestricted slope, by (6.12) and (6.15b) respectively. The energy flux in elasticity (6.22) is related to the spatial and temporal derivatives of the displacement vector through the stiffness double-tensor for anisotropic matter (6.17b), leading to three types of elastic waves (6.56a) in crystals, given in the relations from (6.59a) to (6.60b). In the case of isotropic elasticity, (6.23a) to (6.23c), there are longitudinal (6.68b) and transversal (6.68c) waves that can be superimposed (6.64) to (6.66b), equivalently in (6.63b) or (6.67).

Concerning the general properties of linear waves in steady homogeneous media that are described by linear partial differential equations with constant coefficients (6.30a) and (6.30b), they represent: (i) isotropic waves, propagating equally in all directions, if and only if all spatial derivatives appear as Laplacians (6.37b); (ii) non-dispersive waves, propagating at the same speed for all wavelengths, thus retaining the permanent waveform of a wave packet, if and only if all derivatives are of the same order (6.44). It follows that: (i) if there are spatial derivatives outside Laplacians, the waves are anisotropic; (ii) if there are derivatives of different orders, the waves are dispersive. Thus, it is possible by inspection of the wave equation, with no need to solve it, to ascertain if the waves are (i) isotropic or anisotropic and (ii) dispersive or not. Concerning the elastic wave equation in a homogeneous steady medium, all space and time derivatives are of second order (6.52). Therefore elastic waves are anisotropic and non-dispersive, both in crystals and amorphous matter. In the case of inhomogeneous or unsteady media, the elastic waves (6.51b) are dispersive and anisotropic.

In isotropic elasticity, the wave equation for: (i) separate longitudinal (6.68b) and transversal (6.68c) waves involves only Laplacians, and hence the waves are isotropic; (ii) the superposition of longitudinal and transversal waves (6.63b) involves spatial derivatives other than Laplacians, and hence the waves are anisotropic. The anisotropy is a consequence of longitudinal waves travelling faster than transversal waves in any direction. The anisotropy of the superposition of longitudinal and transversal waves: (i) does not prevent the power (6.83a) and (6.83b) and the energy density (6.88) from adding together; (ii) implies that the sum of energy fluxes, that lie in the wave normal direction for isotropic waves, cannot equal the total energy flux, that does not lie in the wave normal direction for anisotropic waves. Thus, the total energy flux of the superposition of longitudinal and transversal waves (6.103a) consists of: (i-ii) the sum of the energy fluxes of separate longitudinal (6.79) and transversal waves (6.81) that lie in the wave normal direction; (iii) plus a cross-coupling flux (6.99) involving the product of the dilatation of longitudinal waves by the velocity of transversal waves (6.101a).

7 | Alfvén wave propagation along a circle using dipolar coordinates

"It is with logic that one proves; it is with intuition that one invents."

— Henri Poincaré

Contents

A general magnetic field due to an arbitrary steady distribution of electric charges [24] leads to a vector Poisson equation, whose solution is a multipolar expansion [169, 170]. The multipolar expansion extends to electromagnetic waves due to unsteady electric charges and currents as a solution of the forced wave equation [25]. Since the multipolar expansion is considered only for the background magnetic field, the steady case [130] is reconsidered briefly (see appendix C), showing that the higher-order terms are important in the near field. In contrast, the far field is dominated by the lowest-order term, which decays more slowly, like a dipole [39]. For this reason, the simplest far-field model of the magnetic field of the Earth, Sun and other celestial bodies is a magnetic dipole. The monopole that exists for an irrotational field cannot exist for solenoidal fields because it does not meet the conservation of magnetic flux across a closed surface unless a split monopole is used. The dipolar magnetic far field of most celestial bodies permeates a plasma, like the ionosphere of the Earth or the atmosphere of the Sun and other stars. A plasma can support Alfvén waves [128, 171–175] that are transverse hydromagnetic motions propagating along magnetic field lines. This motivates the study of Alfvén waves propagating along the field lines of a magnetic dipole, using a new orthogonal curvilinear coordinate system: dipolar coordinates. Conformal coordinates are specified by the real and imaginary parts of a complex analytic function; it follows immediately that they are a plane orthogonal coordinate system with equal scale factors along the two (generally curvilinear) coordinate axes. It can be readily shown that the common scale factor is the modulus of the inverse of the derivative of the function. Among the conformal coordinates, only four allow separation of variables in the two-dimensional Laplace operator, namely [19]: Cartesian, polar, parabolic and confocal. Besides these four best known plane orthogonal coordinate systems, there are many others, e.g. every analytic function specifies one. An example is spiral coordinates [176], and in the present chapter, another example is considered, *viz.* multipolar coordinates (see section 7.1.1).

A particular case is dipolar coordinates (see section 7.1.2) for which the two sets of coordinate curves (figure 7.1) are circles with the centre on one coordinate axis and tangent to the other. These coordinate systems are particularly convenient for problems for which quantities vary only along one of the coordinate curves, e.g. Alfvén waves propagating along a spiral [176], as relevant to the magnetic field in the solar wind, or along a circle (see section 7.2.1), as appropriate to the Earth's dipolar magnetic field (see section 7.1.3), in the present chapter. The exact analytical solution of the Alfvén wave equation in conformal coordinates depends on the scale factor and is distinct for different coordinate systems; for example, the propagation along a logarithmic spiral is specified by Bessel functions, whereas in the present case of propagation along a circle an extended form of the Gaussian hypergeometric function is needed (see section 7.2.2). The original Gaussian hypergeometric differential equation has three regular singularities [132]; however, in the present case, an extended form appears for which one of the singularities is irregular. The extended Gaussian hypergeometric differential equation has series solutions, whose recurrence formulas for the coefficients are less straightforward than the original; using these solutions, the velocity and magnetic field perturbations spectra of the Alfvén waves (see section 7.3.1) are computed and plotted (figures 7.3 to 7.6) for several values of the dimensionless frequency (see section 7.4) which is the only parameter in the problem.

In terms of mathematical complexity, Alfvén waves propagating along a circle are one echelon above the cases solvable using (I) elementary functions, (II) Bessel functions and (III) Gaussian hypergeometric functions. The first class (I) of problems, solvable in terms of elementary functions, concerns non-dissipative [172, 177, 178] and dissipative [171, 173, 174, 179] Alfvén waves in homogeneous media, for which the wave speed and diffusivities are constant. The second class (II) of problems, solvable in terms of Bessel functions, includes Alfvén waves in an isothermal atmosphere, under a uniform background magnetic field [128, 175, 180–182], as well as extensions to include displacement [183] and Hall [184] currents; other cases include Alfvén waves in a linear temperature gradient [185], and spherical Alfvén waves [186]. The third class (III) of problems, solvable using Gaussian hypergeometric functions, concerns Alfvén waves with a critical layer, *viz.* due to the Hall effect [187], and viscous and resistive dissipation [188–190]. Other methods have been used to study Alfvén waves in a non-uniform background magnetic field [191, 192], in moving media [193–195] and in the presence of viscous and resistive dissipation [196, 197].

The theoretical developments of Alfvén waves can be fundamental to understanding some features taking place in the Earth's magnetosphere. Plasma turbulence exists in space and astrophysical plasmas under some conditions [198]. Therefore the study of magnetic field fluctuations is important because they influence the dynamics of the Earth's magnetosphere, the energy and mass inflows from the solar wind to the magnetosphere and, at the atomic scale, the heating and acceleration of particles. The solar wind influences the plasma processes within the magnetosheath and this research topic is significant to

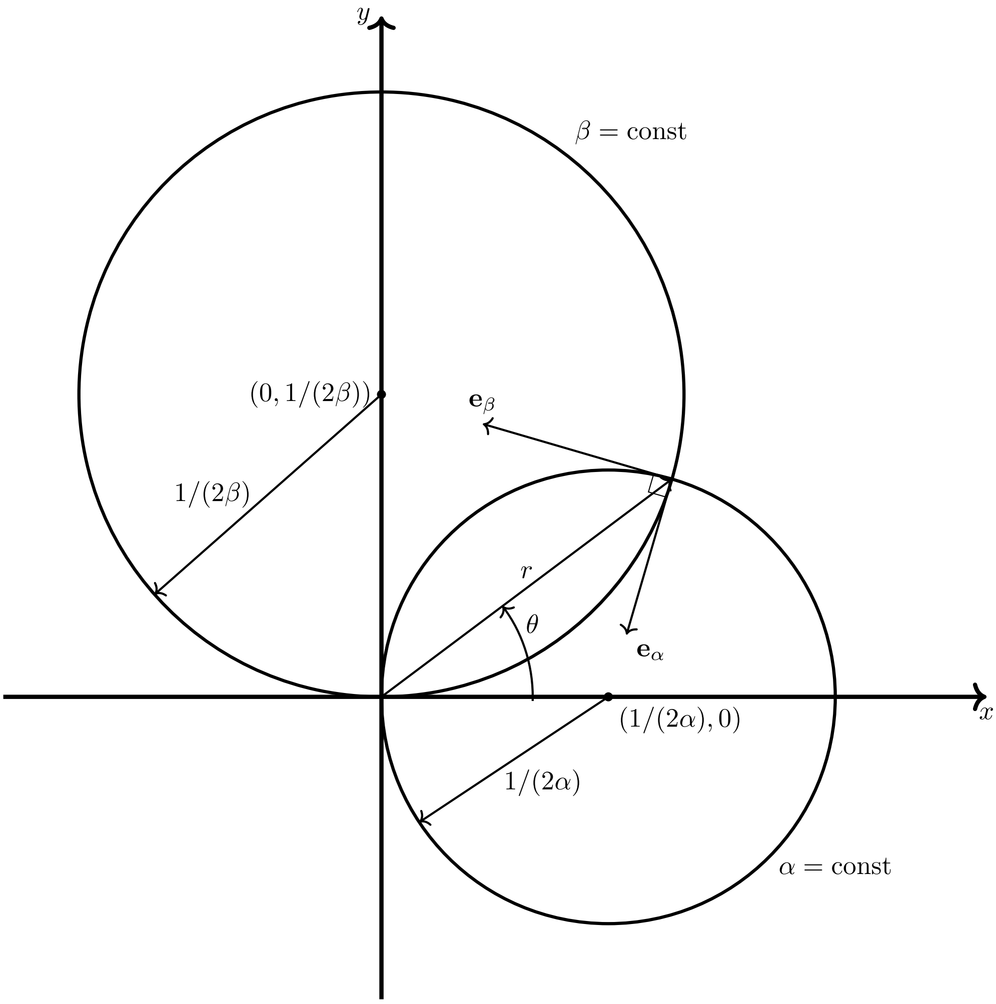

Figure 7.1: The dipolar coordinates in the plane have, for coordinate curves, circles with centres in one axis tangent to the other axis forming two families of orthogonal curves with the same conformal scale factor.

understanding the plasma turbulence close to the Earth. Several researchers undertook a comparison between experimental results and simulations. For instance, in work by [199], the measurement of magnetic field turbulence spectra in the magnetosheath region of the Earth, obtained by the Cluster-1 magnetometer [200] and the Cluster Ion Spectroscopy experiment [201], are compared with the numerical results obtained by the two-fluid model and the dynamical equations of kinetic Alfvén waves to research the turbulent dynamics of the magnetosheath plasma using spectral analysis of magnetic field fluctuations. Otherwise, the nonlinear kinetic Alfvén waves can describe the nature of small-scale turbulence. The processes of particles acceleration at the Earth's bow shock and Alfvén wave generation by accelerated particles are also investigated in several research articles [202, 203], by comparing calculated spectra of accelerated ions with the experimentally observed spectra of accelerated ions [204]. These processes are accompanied by a significant increase in the level of turbulence induced by Alfvén waves. Therefore a consistent description must include the generation of these waves by accelerated ions. For instance, the paper by [205] shows that using a refined growth rate of the Alfvén waves excited by accelerated particles based on results from [206] yields that, while the equilibrium state is approached, the amplitude of Alfvén waves increases monotonically. The comparison between the calculated accelerated ions and Alfvénic turbulence spectra with the measurements shows that the theory agrees well with the main features observed in experiments.

There is conjointly an enormous quantity of research devoted to studying the problem of determining a relationship between the field of Alfvén waves and electromagnetic oscillations on the Earth's ground. A theoretical treatment of the penetration of the Alfvén wave field from the magnetosphere to the ground through the ionosphere and atmosphere is formed in several articles [207, 208]. The ionospheric effects in the Alfvén wave penetration method are also explained briefly in these papers since they act to drive currents within the ionospheric layer which are associated with magnet sound waves inducing the pulsations on the ground. These effects act differently depending on the frequency of the waves. Particularly, in work by [209], the boundary conditions on the ionosphere for standing Alfvén waves and the analytical expressions to describe the field of electromagnetic oscillations induced on the terrestrial surface by the same waves in the magnetosphere have been obtained. It was also concluded that the process of penetration to the ground of the poloidal part of the electromagnetic field originated from the magnetospheric Alfvén oscillations is induced mainly by the Pedersen conductivity of the ionosphere. A numerical model, used by [210], of the magnetospheric Alfvén wave interaction with the ionosphere and penetration to the ground based on the solution of multi-fluid magnetohydrodynamic full-wave equations in a realistic ionosphere was developed. This model predicts that the upper part of the Pc1 spectrum (approximately 0.2 to 5 Hz) is severely absorbed upon wave transmission through the daytime ionosphere to the ground. At night time, the transmission coefficient of Alfvén waves has an oscillatory dependence on frequency. Moreover, modelling the ground signatures of waves externally generated in the outer magnetosphere, such as Pc1 oscillations, is complicated because the electromagnetic skin depth [211] is comparable to the ionospheric thickness and, consequently, resolving the vertical structure of the ionosphere is necessary. Furthermore, the Hall conductivity and shear Alfvén waves in the ionosphere are coupled to compressional mode waves that can propagate across field lines. In the model developed by [212], the interactions of Alfvén waves can be described in the 1 Hz frequency band with the ionosphere. These interactions can determine the ground observations of Pc1 oscillations not only on the field lines on which they are generated but also as they propagate horizontally through the ionospheric waveguide. A strong point in that model is the ability to determine the ground magnetic field produced by a model run and compare these fields with those produced on the ground. Some well-known results, such as the "Hughes rotation" of the magnetic field, the production of 1 Hz waves by the inhomogeneity of the ionosphere and the ducting of compressional waves through an ionospheric waveguide, have been reproduced by the model.

These works prove, therefore, that developing mathematical models that can describe the propagation of the Alfvén waves can be useful to prove some experimental results provided by observations on the ground and this chapter, therefore, intends to construct a model that describes the Alfvén waves propagating along a dipolar magnetic field.

7.1 Conformal coordinates and atmospheric equilibrium

Among the conformal coordinates (see section 7.1.1), the dipolar coordinates are chosen (see section 7.1.2). The atmospheric equilibrium is also adopted (see section 7.1.3) as a preliminary to the consideration of Alfvén wave propagation.

7.1.1 Conformal coordinates and equal scale factors

Conformal coordinates (α, β) are specified by the real and the imaginary conjugate parts of a complex function w,

$$\alpha - \mathrm{i}\beta \equiv w = f(z), \tag{7.1}$$

which specifies its relation with Cartesian (x, y) or polar (r, θ) coordinates,

$$z = x + \mathrm{i}y = r\mathrm{e}^{\mathrm{i}\theta}. \tag{7.2}$$

If the function is analytic, $\mathrm{d}w = \mathrm{d}f\,(\mathrm{d}z)^{-1}\,\mathrm{d}z$, then the arclength $(\mathrm{d}l)^2 = |\mathrm{d}z|^2 = |\mathrm{d}f/\,(\mathrm{d}z)|^{-2}\,|\mathrm{d}w|^2$ is given by

$$(\mathrm{d}l)^2 = s^2\left[(\mathrm{d}\alpha)^2 + (\mathrm{d}\beta)^2\right] \tag{7.3}$$

which shows that the conformal coordinate system is orthogonal (no $\mathrm{d}\alpha\mathrm{d}\beta$ term) and the scale factor s is the same along both coordinate axes,

$$s \equiv \left|\frac{\mathrm{d}f}{\mathrm{d}z}\right|^{-1} = \left|\frac{\mathrm{d}w}{\mathrm{d}z}\right|^{-1}, \tag{7.4}$$

and equal to the modulus of the inverse of the function's derivative.

As an example, reconsider spiral coordinates [176] which can be specified by the complex function

$$w = (1 + \mathrm{i}k)\log z \tag{7.5}$$

where k is a constant. It follows from $\alpha = \log r - k\theta$ and $-\beta = k\log r + \theta$ that coordinate curves of α and β are logarithmic spirals,

$$\frac{1}{r}\left(\frac{\mathrm{d}r}{\mathrm{d}\theta}\right)_\alpha = k \equiv \cot\phi, \tag{7.6a}$$

$$\frac{1}{r}\left(\frac{\mathrm{d}r}{\mathrm{d}\theta}\right)_\beta = -\frac{1}{k} = -\tan\phi = \cot\left(\phi + \frac{\pi}{2}\right), \tag{7.6b}$$

making a constant angle, respectively $\phi \equiv \arctan(1/k)$ and $\pi/2 + \phi$, with every radial line. The scale factor is given by (7.4) and (7.5), *viz.*

$$s = \left|\frac{z}{1 + \mathrm{i}k}\right| = \frac{r}{\sqrt{1 + k^2}}, \tag{7.7}$$

or using the inverse coordinate transformation,

$$r = \exp\left(\frac{\alpha - k\beta}{1+k^2}\right), \tag{7.8a}$$

$$\theta = -\frac{\beta + k\alpha}{1+k^2}, \tag{7.8b}$$

the scale factor is given by

$$s = \left|1+k^2\right|^{-1/2} \exp\left(\frac{\alpha - k\beta}{1+k^2}\right). \tag{7.9}$$

This result could have been obtained by substituting the expressions of r and θ in the arclength in polar coordinates,

$$(\mathrm{d}l)^2 = (\mathrm{d}r)^2 + r^2(\mathrm{d}\theta)^2, \tag{7.10}$$

and then showing it takes the form (7.3) with s given by (7.9).

As another example, consider multipolar coordinates, which are specified by $w = z^{-n}$, with n an integer. They relate (7.1) and (7.2) to polar coordinates by

$$\alpha = r^{-n}\cos(n\theta), \tag{7.11a}$$

$$\beta = r^{-n}\sin(n\theta), \tag{7.11b}$$

whose inverse is

$$r = \left(\alpha^2 + \beta^2\right)^{-1/(2n)}, \tag{7.12a}$$

$$\theta = \frac{1}{n}\arctan\left(\frac{\beta}{\alpha}\right). \tag{7.12b}$$

The scale factor is $s = \left|-nz^{-n-1}\right|^{-1} = n^{-1}r^{n+1}$ or, using (7.12a),

$$s = \frac{1}{n}\left(\alpha^2 + \beta^2\right)^{-1/2-1/(2n)}. \tag{7.13}$$

This result could also be obtained by substituting both equations of (7.12) in (7.10), and writing it in the form (7.3) to show that the scale factors are given by (7.13).

7.1.2 Plane dipolar coordinates

Further consideration is given to the particular case $n = 1$ of multipolar coordinates, $w = z^{-1}$. Using (7.1) and (7.2), the transformation from polar (r, θ) to dipolar (α, β) coordinates is

$$\alpha = \frac{1}{r}\cos\theta, \tag{7.14a}$$

$$\beta = \frac{1}{r}\sin\theta \tag{7.14b}$$

and the inverse transformation from dipolar to polar coordinates is

$$r = \frac{1}{|\alpha^2 + \beta^2|^{1/2}}, \tag{7.16a}$$

$$\theta = \arctan\left(\frac{\beta}{\alpha}\right). \tag{7.16b}$$

The scale factor is

$$s = \left|\frac{\mathrm{d}(1/z)}{\mathrm{d}z}\right|^{-1} = \left|z^2\right| = r^2 \tag{7.17a}$$

in polar coordinates and

$$s = \frac{1}{\alpha^2 + \beta^2} \tag{7.17b}$$

in dipolar coordinates, leading to

$$(\mathrm{d}l)^2 = \frac{(\mathrm{d}\alpha)^2 + (\mathrm{d}\beta)^2}{\left(\alpha^2 + \beta^2\right)^2} \tag{7.18}$$

as the dipolar arc element, according to (7.3).

The α coordinate curve $\alpha = r^{-1}\cos\theta = \text{const}$ is a circle (figure 7.1) with centre on the OX axis at $(1/(2\alpha), 0)$ and radius $R/2 = 1/(2\alpha)$ such that it is tangent to the OY axis at the origin, *id est* (i.e.) the diameter is given by $R \equiv 1/\alpha$. The coordinate curve $\beta = \text{const}$ is an orthogonal circle, with centre on the OY axis at $(0, 1/(2\beta))$ and radius $1/(2\beta)$ such that it is tangent to the OX axis at the origin.

Considering the wave propagation along the α circle of diameter R, regarding the α coordinate curve and the expression of diameter, $r = \cos\theta/\alpha = R\cos\theta$ along which the coordinate β varies according to $\beta = \sin\theta/r = \tan\theta/R$. The scale factor is now given by

$$s = r^2 = R^2\cos^2\theta \tag{7.19}$$

and derivatives with regard to β can be transformed according to

$$\frac{\mathrm{d}}{\mathrm{d}\beta} = R\cos^2\theta\frac{\mathrm{d}}{\mathrm{d}\theta} \tag{7.20}$$

into derivatives with regard to θ. The scale factors of the plane dipolar coordinates $(\alpha,\ \beta)$ are the same and equal to $h_\alpha = \left(\alpha^2 + \beta^2\right)^{-1} = h_\beta = s$.

The plane dipolar coordinates can be extended by translation or rotation to respectively cylindrical and spherical dipolar coordinates in space. These systems of coordinates are detailed in the appendix D.

7.1.3 Magnetic field and atmospheric equilibrium

The background magnetic field is assumed to be dipolar and to lie along the circle $\alpha = \text{const}$. The transverse, unsteady velocity $\boldsymbol{v}$ and magnetic field perturbations $\boldsymbol{h}$ are assumed to be parallel and tangent to the coordinate curves $\beta = \text{const}$ (according to figure 7.2),

$$\boldsymbol{V} = v(\beta, t)\boldsymbol{e}_\alpha, \tag{7.21a}$$

$$\boldsymbol{H} = B(\beta)\boldsymbol{e}_\beta + h(\beta, t)\boldsymbol{e}_\alpha, \tag{7.21b}$$

and all quantities depend on β, which varies along the curve $\alpha = \text{const}$. Note that the motion is not incompressible,

$$\boldsymbol{\nabla} \cdot \boldsymbol{V} = \frac{1}{s^2}\frac{\partial(sv)}{\partial\alpha} = \frac{v}{s^2}\frac{\partial s}{\partial\alpha}, \tag{7.22a}$$

where, from (7.17b),

$$\frac{\partial s}{\partial\alpha} = -\frac{2\alpha}{\left(\alpha^2 + \beta^2\right)^2} = -2\alpha s^2 \tag{7.22b}$$

and consequently the equation (7.22a) shows that the dilatation is non-zero,

$$\boldsymbol{\nabla} \cdot \boldsymbol{V} = -2\alpha v = -2\frac{v}{R}; \tag{7.22c}$$

thus, there is near incompressibility only for large R or small α, i.e. a circle of large radius.

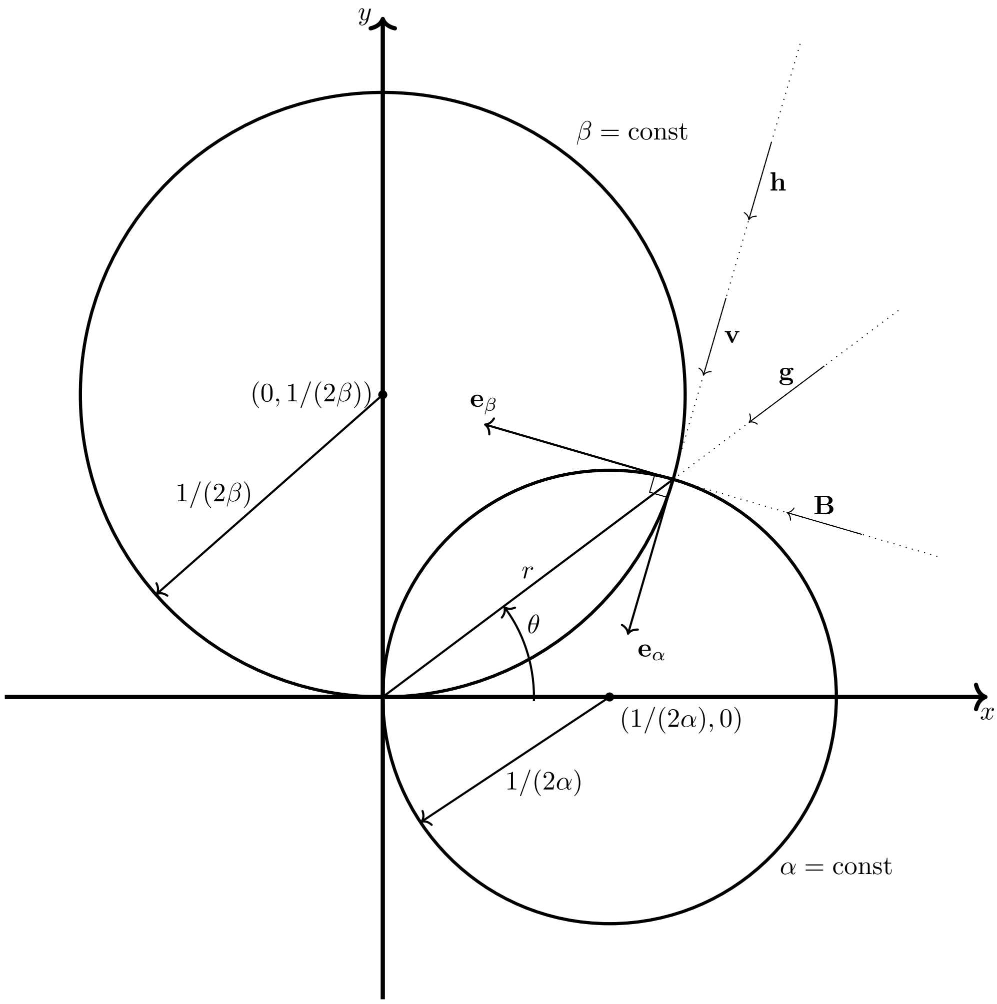

Figure 7.2: Alfvén wave propagating along a circle with transverse perturbations.

The background magnetic field is divergence free,

$$0 = \boldsymbol{\nabla} \cdot (B(\beta)\boldsymbol{e}_\beta) = \frac{1}{s^2}\frac{\partial(sB)}{\partial\beta}, \tag{7.23}$$

if it varies like the inverse of the scale factor, $Bs = \text{const}$, *viz.*

$$B(r) = \frac{bR^2}{s} = \frac{bR^2}{r^2} = b\sec^2\theta \tag{7.24}$$

where b is the magnetic field strength at radius R, $b \equiv B(R)$. The background magnetic field is, to the level of approximation $O(1/R)$, current free, $\boldsymbol{\nabla} \times (B(\beta)\,\boldsymbol{e}_\beta) = 0$, and hence force free, so that the hydrostatic equilibrium, $\boldsymbol{\nabla} p = \rho \boldsymbol{g}$, applies to the mean state pressure p, mass density ρ and gravity $\boldsymbol{g}$, the latter with polar symmetry,

$$\boldsymbol{g} = -g_0\frac{R}{r}\boldsymbol{e}_r, \tag{7.25}$$

where g_0 is the magnitude of the gravity field at radius R, that is, $g_0 \equiv |\boldsymbol{g}(R)|$. Although a uniform magnetic field, $\boldsymbol{B} = \text{const}$, would be exactly current free, it would not be divergence free and thus it is excluded from the present analysis.

In the case of an incompressible fluid, the density is constant (it does not vary with the radius) and therefore we assume $\rho = \text{const} \equiv \rho_0$. In this case, the hydrostatic equilibrium implies $\mathrm{d}p/(\mathrm{d}r) = -\rho_0 g_0 R/r$. The pressure profile is then given by

$$p(r) = p_0 - \rho_0 g_0 R \log\left(\frac{r}{R}\right), \tag{7.26}$$

where p_0 is the pressure at radius $r = R$, that is, $p_0 \equiv p(R)$. The Alfvén speed, defined as

$$A \equiv B\sqrt{\frac{1}{\mu\rho}} \tag{7.27}$$

using the International System (SI) of units convention, where μ is the magnetic permeability and ρ is the mass density, is given, according to (7.24), by

$$A(r) = \frac{aR^2}{s} = \frac{aR^2}{r^2} = a\sec^2\theta \tag{7.28}$$

where a is the Alfvén speed at radius $r = R$ and therefore $a \equiv b\sqrt{1/(\mu\rho_0)} = A(R)$.

In the case of a perfect gas of constant R_g, at temperature T, with molar mass M, the equation of state

$$p = \frac{\rho R_\mathrm{g} T}{M} \tag{7.29}$$

may be substituted in the condition of hydrostatic equilibrium with

$$\boldsymbol{\nabla}(\log p) = \frac{\rho\boldsymbol{g}}{p} = \frac{M\boldsymbol{g}}{R_\mathrm{g}T} \tag{7.30}$$

and in isothermal conditions, $T = \text{const} \equiv T_0$, with

$$\frac{\mathrm{d}\,(\log p)}{\mathrm{d}r} = -\frac{M g_0}{R_\mathrm{g} T_0}\frac{R}{r}, \tag{7.31a}$$

the pressure profile is a polytropic,

$$\frac{\rho(r)}{\rho_0} = \frac{p(r)}{p_0} = \left(\frac{r}{R}\right)^{-\vartheta}, \tag{7.31b}$$

whose index ϑ is given by $\vartheta \equiv g_0 M R/\left(R_\mathrm{g} T_0\right)$ where the subscript 0 refers to quantities at radius $r = R$. In this case, ρ_0 is the density only at $r = R$ (the density depends on the radius) while p_0 continues to be the value at the same location. Using $R_\mathrm{g} = 8.31\,\mathrm{J\,K^{-1}\,mol^{-1}}$ for the ideal gas constant, the polytropic index can be calculated for the atmosphere of Earth and the end of the solar corona, whose values are indicated in table 7.1. The values of the temperature and the radius for solar corona are established for the location where the solar wind emerges, in other words, where a stream of particles starts to travel outward to form the heliosphere [figure 1 of 175, 213]. The solar corona is constituted of ionised hydrogen and therefore its molar mass is $1.0 \times 10^{-3}\,\mathrm{kg\,mol^{-1}}$. As the values correspond to the height approximately equal to 2% of the solar radius, the value of the gravitational acceleration is almost the same as at the solar surface. The exponent ν applies to the Alfvén speed (7.27), then substituting (7.24) and (7.31b) leads to

$$A = a\left(\frac{r}{R}\right)^{-\nu} = a\sec^\nu\theta = a\left(\frac{R^2}{s}\right)^{\nu/2} \tag{7.32}$$

with $\nu \equiv 2 - \vartheta/2$. Comparing (7.32) with (7.28) it follows that $\nu = 2$ for an incompressible fluid.

Quantity	**Symbol**	**Earth's atmosphere**	**Solar corona**	**Unit**
Acceleration of gravity	g_0	9.8	2.7×10^2	$\mathrm{m\ s^{-2}}$
Radius	R	6.4×10^6	7.1×10^8	m
Temperature	T_0	288	1.6×10^6	K
Molar mass	M	2.9×10^{-2}	1.0×10^{-3}	$\mathrm{kg\ mol^{-1}}$
Polytropic index	ϑ	7.6×10^2	1.4×10^1	–
Alfvén index	ν	-3.8×10^2	-5.2	–

Table 7.1: Values of several quantities for the atmosphere of Earth and the solar corona [175, 213].

7.2 Alfvén wave equation and extended hypergeometric function

The Alfvén wave equation for propagation along a dipolar magnetic field (see section 7.2.1) can be solved in terms of Gaussian hypergeometric functions in the limit of zero frequency (see section 7.2.2) and otherwise requires the solution of an extended Gaussian hypergeometric differential equation (see section 7.2.3).

The case of zero frequency is considered because it leads to a closed form solution in terms of Gaussian hypergeometric functions. This serves as the stepping stone to the more general case of non-zero frequency that leads to the extended Gaussian hypergeometric differential equation and also has power series solutions with a less simple three-term recurrence formula for the coefficients.

7.2.1 Alfvén wave equation and polarisation relation

The equations of magnetohydrodynamics, in conformal coordinates, for the case (7.21) read [see 176, §4]

$$s\dot{h} = (Bv)', \tag{7.33a}$$

$$s^2\dot{v} = \frac{B}{\mu\rho}(sh)', \tag{7.33b}$$

where the terms for the acceleration which are quadratic in the velocity have been neglected. The dot and prime denote derivatives with respect to respectively time t and dipolar coordinate β, that is, $\dot{f} \equiv \partial f/\partial t$ and $f' \equiv \partial f/\partial\beta$. The definition of Alfvén speed (7.27) is introduced in (7.33b) leading to

$$s^2\dot{v} = \frac{A^2}{B}(sh)'. \tag{7.34}$$

It is possible to eliminate between (7.33a) and (7.34) either for the velocity (7.35a) or for the magnetic field perturbations (7.35b),

$$s^2\ddot{v} = \frac{A^2}{B}(Bv)'', \tag{7.35a}$$

$$s\ddot{h} = \left[\left(\frac{A}{s}\right)^2 (sh)'\right]'. \tag{7.35b}$$

Since the mean state is steady, it is convenient to use a Fourier transform in time, *viz.*

$$v(\beta;t) \equiv \int_{-\infty}^{+\infty} \tilde{V}(\beta;\omega)\mathrm{e}^{-\mathrm{i}\omega t}\,\mathrm{d}\omega, \tag{7.36a}$$

$$h(\beta;t) \equiv \int_{-\infty}^{+\infty} \tilde{H}(\beta;\omega)\mathrm{e}^{-\mathrm{i}\omega t}\,\mathrm{d}\omega, \tag{7.36b}$$

where $\tilde{V}$ and $\tilde{H}$ denote respectively the velocity and magnetic field perturbations spectra, for a wave of frequency ω, at position β. Substituting (7.36a) and (7.36b) in the Alfvén wave equations for the velocity (7.35a) and magnetic field perturbations (7.35b) respectively lead to

$$\tilde{V}'' + 2\left(\frac{B'}{B}\right)\tilde{V}' + \left[\left(\frac{\omega s}{A}\right)^2 + \frac{B''}{B}\right]\tilde{V} = 0, \tag{7.37a}$$

$$\tilde{H}'' + 2\left(\frac{A'}{A}\right)\tilde{H}' + \left[\left(\frac{\omega s}{A}\right)^2 + \frac{s}{A^2}\left(\frac{A^2 s'}{s^2}\right)'\right]\tilde{H} = 0, \tag{7.37b}$$

hence ordinary instead of partial differential equations.

It is sufficient to solve one of the previous wave equations, e.g. the simplest, because once one of $\tilde{V}$ or $\tilde{H}$ is known, the other can be determined from the polarisation relations,

$$\tilde{H} = \frac{\mathrm{i}}{\omega s} \left(B\tilde{V} \right)', \tag{7.38a}$$

$$\tilde{V} = \frac{\mathrm{i}A^2}{\omega s^2 B} \left(s\tilde{H} \right)', \tag{7.38b}$$

which follow from substitution of (7.36a) and (7.36b) in (7.33a) and (7.34). Rather than start from the two Alfvén wave equations, in (7.37), it is simpler to introduce a magnetic field perturbation spectrum modified by a scale factor,

$$G(\beta;\omega) \equiv s(\beta)\tilde{H}(\beta;\omega), \tag{7.39}$$

which satisfies a simpler wave equation, starting from (7.35b),

$$0 = \omega^2 G + \left[\left(\frac{A}{s} \right)^2 G' \right]', \tag{7.40a}$$

and that may be re-written in the following form:

$$G'' + 2\left[\log\left(\frac{A}{s} \right) \right]' G' + \left(\frac{\omega s}{A} \right)^2 G = 0. \tag{7.40b}$$

This equation has only one coefficient with derivative, in contrast with the two equations (7.37), that have several coefficients with derivatives. This coefficient is evaluated from (7.19) and (7.32),

$$\frac{A}{s} = aR^{\nu} s^{-1-\nu/2} = \frac{a}{R^2} \cos^{-\nu-2}\theta, \tag{7.41}$$

and the derivative with regard to β is replaced, using (7.20), by a derivative with regard to θ,

$$\left[\log\left(\frac{A}{s} \right) \right]' = R\cos^2\theta \frac{\mathrm{d}}{\mathrm{d}\theta} \left[(-\nu-2)\log\left(\cos\theta\right) \right] = R\left(\nu+2\right)\cos\theta\sin\theta. \tag{7.42}$$

After substituting the last two equations in (7.40b), *viz.*

$$G'' + 2R(\nu+2)\cos\theta\sin\theta G' + \left(\frac{\omega R^2}{a} \right)^2 \cos^{2\nu+4}\theta G = 0, \tag{7.43}$$

it is appropriate to replace the derivatives with regard to β, e.g. $G'' \equiv \partial^2 G/\partial\beta^2$, by derivatives with regard to θ, e.g. $\partial^2\Phi/\partial\theta^2 \equiv \Phi''$, noting that $\Phi\left(\theta;\Omega\right) \equiv G\left(\beta;\omega\right)$, and using (7.20), *viz.*

$$\cos^2\theta\,\Phi'' + 2\left(\nu+1\right)\cos\theta\sin\theta\,\Phi' + \Omega^2\cos^{2\nu+2}\theta\,\Phi = 0; \tag{7.44}$$

the Alfvén wave equation (7.44) involves only one parameter, namely, the dimensionless frequency $\Omega \equiv \omega R/a$.

The Alfvén wave equation (7.44) has coefficients which are trigonometric functions of θ in the range

$0 \leq \theta \leq 2\pi$, and these can be transformed to polynomial coefficients, via the change of independent variable,

$$\zeta = \cos^2\theta, \tag{7.45a}$$

$$\Psi(\zeta;\Omega) = \Phi(\theta;\Omega), \tag{7.45b}$$

where $0 \leq \zeta \leq 1$,

$$4\zeta^2(1-\zeta)\Psi'' - 2\zeta[1+2\nu(1-\zeta)]\Psi' + \Omega^2\zeta^{\nu+1}\Psi = 0. \tag{7.46}$$

The degree of the polynomial coefficients of the highest derivative Ψ'', *viz.* three in (7.46), can be depressed to two via the change of dependent variable,

$$\Psi(\zeta;\Omega) = \zeta^\sigma Q(\zeta;\Omega), \tag{7.47}$$

where the constant σ can be chosen at will, e.g. so that

$$4(1-\zeta)\zeta^2 Q'' - 2[1-2(2\sigma-\nu)(1-\zeta)]\zeta Q' + \left[\Omega^2\zeta^{1+\nu} - 4\sigma\zeta(\sigma-1-\nu) + 2\sigma(2\sigma-3-2\nu)\right]Q = 0 \tag{7.48}$$

can be divided through by ζ. This is the case if the term in the last curved brackets vanishes,

$$\sigma = \frac{3}{2} + \nu, \tag{7.49a}$$

$$\Psi(\zeta;\Omega) = \zeta^{\nu+3/2}Q(\zeta;\Omega), \tag{7.49b}$$

in which case the wave equation simplifies to

$$4(1-\zeta)\zeta Q'' - 2[1-2(3+\nu)(1-\zeta)]Q' + \left(\Omega^2\zeta^\nu - 3 - 2\nu\right)Q = 0. \tag{7.50}$$

A dipolar magnetic field is an approximate first-order representation of the Earth's field, remembering that ν is given by $\nu \equiv 2 - \vartheta/2$, with $\vartheta \equiv g_0 MR/(R_{\mathrm{g}}T_0)$, in the case of Alfvén waves in the ionosphere, which is gaseous, or $\nu = 2$ in (7.28) for Alfvén waves in the molten core, which is incompressible. This application is limited by our consideration of a planar rather than spherical problem, and neglect of rotation, a non-central symmetry. In the case of an incompressible fluid, e.g. a liquid, the Alfvén wave equation (7.50) simplifies, with $\nu = 2$, to

$$4(1-\zeta)\zeta Q'' + 2(9-10\zeta)Q' + \left(\Omega^2\zeta^2 - 7\right)Q = 0. \tag{7.51}$$

The differential equation (7.51) reduces to the Gaussian hypergeometric type, leading to an analytic closed form solution, in the limit of zero frequency, corresponding to the steady magnetic field (see section 7.2.2) in contrast with the case of the unsteady magnetic field for Alfvén waves when a power series solution also exists (see section 7.2.3) with a three-term instead of a two-term recurrence formula for the coefficients.

7.2.2 Limit of zero frequency and hypergeometric functions

In the limiting case of zero frequency, i.e. quasi-steady field, the differential equation for an incompressible fluid (7.51) simplifies, with $\Omega = 0$, to

$$(1-\zeta)\,\zeta Q'' + \left(\frac{9}{2} - 5\zeta\right) Q' - \frac{7}{4} Q = 0 \tag{7.52}$$

which is of the Gaussian hypergeometric type,

$$(1-\zeta)\,\zeta Q'' + \left[\gamma - (\alpha + \epsilon + 1)\,\zeta\right] Q' - \alpha\epsilon Q = 0, \tag{7.53}$$

with parameters satisfying $\gamma = 9/2$, $\delta + \epsilon = 4$ and $\delta\epsilon = 7/4$, leading to $\delta = 1/2$ and $\epsilon = 7/2$. The general integral of the Gaussian hypergeometric differential equation (7.52) is

$$Q\,(\zeta;0) = \bar{c}_1 F\,(\delta,\epsilon;\gamma;\zeta) + \bar{c}_2 \zeta^{1-\gamma} F\,(1+\delta-\gamma, 1+\epsilon-\gamma; 2-\gamma;\zeta) \tag{7.54}$$

where γ is not an integer while $\bar{c}_1$ and $\bar{c}_2$ are arbitrary constants of integration. In this case, it is

$$Q\,(\zeta;0) = \bar{c}_1 F\left(\frac{1}{2},\frac{7}{2};\frac{9}{2};\zeta\right) + \bar{c}_2 \zeta^{-7/2} F\left(-3, 0; -\frac{5}{2};\zeta\right). \tag{7.55}$$

Recalling the expressions (7.19), (7.39), the definition of Φ, (7.45) and (7.49) the magnetic field perturbation is

$$\tilde{H}\,(\beta;\omega) = \frac{G\,(\beta;\omega)}{s} = \frac{\Phi\,(\theta;\Omega)}{R^2\cos^2\theta} = \frac{\Psi\left(\cos^2\theta;\Omega\right)}{R^2\cos^2\theta} = \frac{\cos^{2\nu+1}\theta\, Q\left(\cos^2\theta;\Omega\right)}{R^2}. \tag{7.56}$$

If the magnetic field decays like $O\,(1/R)$ the magnetic flux across a sphere of radius R is not conserved, unless the angular dependence leads to a zero integral over the surface of the sphere. All the solutions for the magnetic field in this chapter decay like $O\left(1/R^2\right)$ implying that the magnetic flux crossing a sphere of radius R is constant for any angular dependence, and thus the Gauss's law for magnetism is met.

Defining a magnetic field perturbation spectrum $\tilde{h}\,(\theta;\Omega)$ that does not depend on the radius R of the circle and depends only on the angle θ along the circle; in the case $\nu = 2$ and $\Omega = 0$, it simplifies to

$$\tilde{h}(\theta;0) \equiv b^{-1}\tilde{H}\,(\theta;0) = C_1\cos^5\theta F\left(\frac{1}{2},\frac{7}{2};\frac{9}{2};\cos^2\theta\right) + C_2\sec^2\theta F\left(-3,0;-\frac{5}{2};\cos^2\theta\right) \tag{7.57}$$

where in the second equality the constants b^{-1} and R^{-2} were incorporated in the constants of integration, that is, $C_1 \equiv b^{-1}R^{-2}\bar{c}_1$ and $C_2 \equiv b^{-1}R^{-2}\bar{c}_2$. The second hypergeometric function on the right-hand side of (7.57), knowing that

$$\begin{aligned} F\,(\delta,\epsilon;\gamma;\zeta) = 1 &+ \frac{\delta\epsilon}{1!\gamma}\zeta^1 + \frac{\delta\,(\delta+1)\,\epsilon\,(\epsilon+1)}{2!\gamma(\gamma+1)}\zeta^2 + \ldots \\ &+ \frac{\delta\,(\delta+1)\ldots(\delta+n-1)\,\epsilon\,(\epsilon+1)\ldots(\epsilon+n-1)}{n!\gamma\,(\gamma+1)\ldots(\gamma+n-1)}\zeta^n + \ldots, \end{aligned} \tag{7.58}$$

reduces to unity because ϵ is zero,

$$F\left(-3, 0; -\frac{5}{2}; \cos^2\theta\right) = 1, \tag{7.59}$$

implying that $\zeta^{-7/2}$ is a solution of (7.52), as can be checked directly. It can be noted in passing that, since a solution $\zeta^{-7/2}$ is known, another solution can be obtained [132], *viz.*

$$\zeta^{-7/2}\int (1-\zeta)^{-1/2}\zeta^{5/2}\,\mathrm{d}\zeta, \tag{7.60}$$

which must be a linear combination of the two in (7.55). These two algebraic solutions would avoid the use of hypergeometric functions, whereas the latter are more closely linked to the case of non-zero frequency and Alfvén waves. However, the factor $\sec^2\theta$ is singular for $\theta = \pm\pi/2$ and a finite magnetic field requires $C_2 = 0$, simplifying (7.57) to

$$\tilde{h}(\theta; 0) = C_1 \cos^5\theta F\left(\frac{1}{2}, \frac{7}{2}; \frac{9}{2}; \cos^2\theta\right) \tag{7.61}$$

that vanishes for $\theta = \pm\pi/2$. The hypergeometric series in the first term is finite for $|\cos\theta| < 1$. Since $\gamma - \delta - \epsilon = 1/2$ the hypergeometric series converges [214, 215] on its radius of convergence $|\cos\theta| = 1$ or $\theta = 0, \pi$. Using the property

$$F(\delta, \epsilon; \gamma; 1) = \frac{\Gamma(\gamma)\,\Gamma(\gamma-\delta-\epsilon)}{\Gamma(\gamma-\delta)\,\Gamma(\gamma-\epsilon)} \tag{7.62}$$

where Γ is the gamma function [216] specifies the constant of integration C_1 from the magnetic field at $\theta = 0$,

$$\tilde{h}(0; 0) = C_1 F\left(\frac{1}{2}, \frac{7}{2}; \frac{9}{2}; 1\right) = C_1 \frac{\Gamma(9/2)\,\Gamma(1/2)}{\Gamma(4)\,\Gamma(1)} = C_1 \frac{\frac{7}{2}\frac{5}{2}\frac{3}{2}\left[\Gamma\left(\frac{1}{2}\right)\right]^2}{3!} = \frac{35\pi}{16} C_1, \tag{7.63}$$

using in the last equality $\Gamma(1/2) = \sqrt{\pi}$ [217, 218]. Thus, the magnetic field in the incompressible case $\nu = 2$, for zero frequency $\Omega = 0$, simplifies from (7.57) to (7.61) to be bounded for all $0 \leq \theta \leq 2\pi$ with the constant C_1 determined by the value (7.63) at $\theta = 0$, so that

$$\tilde{h}(\theta; 0) = \tilde{h}(0; 0)\,\frac{16}{35\pi}\cos^5\theta F\left(\frac{1}{2}, \frac{7}{2}; \frac{9}{2}; \cos^2\theta\right). \tag{7.64}$$

This closed form solution shares the angular dependence of the leading term $\cos^5\theta$ with the more interesting case of non-zero frequency, leading to an extension of the Gaussian hypergeometric differential equation.

7.2.3 Non-zero frequency and extended hypergeometric equations

In the more interesting case of non-zero frequency, the wave equation (7.51) is of the extended Gaussian hypergeometric type, so-called because: (i) $\zeta = 0, 1$ are regular singularities, as for the original Gaussian hypergeometric equation (7.52); (ii) the point-at-infinity $\zeta = \infty$ is a regular singularity for the latter, and an irregular singularity for the former, in this case of degree two. Since $\zeta = 0$ is a regular singularity, solutions exist, with radius of convergence unity, $|\zeta| < 1$, limited by the nearest singularity, in terms of a

Frobenius-Fuchs series,

$$\overline{Q}\,(\zeta;\Omega) \equiv b^{-1}R^{-2}Q\,(\zeta;\Omega) = \sum_{n=0}^{\infty} c_n\,(\chi)\,\zeta^{n+\chi}, \tag{7.65}$$

with index χ and the recurrence formula for the coefficients $c_n\,(\chi)$ to be determined. Substitution of (7.65) in (7.51) leads to the recurrence formula for the coefficients

$$(n+\chi+1)\left(n+\chi+\frac{9}{2}\right)c_{n+1}\,(\chi) = \left[(n+\chi)\,(n+\chi+4)+\frac{7}{4}\right]c_n\,(\chi) - \left(\frac{\Omega}{2}\right)^2 c_{n-2}\,(\chi)\,. \tag{7.66}$$

In the case of zero frequency, $\Omega = 0$, this would reduce to the simple recurrence formula for Gaussian hypergeometric functions

$$c_{n+1}\,(\chi) = \left[\frac{(n+\chi)\,(n+\chi+4)+7/4}{(n+\chi+1)\,(n+\chi+9/2)}\right]c_n\,(\chi) = c_0\,(\chi)\prod_{m=0}^{n}\left[\frac{(m+\chi+1/2)\,(m+\chi+7/2)}{(m+\chi+1)\,(m+\chi+9/2)}\right] \tag{7.67}$$

in agreement with the values of γ, δ and ϵ for zero frequency; otherwise, for non-zero frequency $\Omega \neq 0$, the recurrence relation (7.66) has three terms. Setting $n = -1$ yields in both cases the indicial equation

$$\chi\left(\chi+\frac{7}{2}\right) = 0 \tag{7.68}$$

whose roots $\chi = 0$ and $\chi = -7/2$ specify two linearly independent particular integrals, respectively

$$\overline{Q}_0\,(\zeta;\Omega) \equiv \sum_{n=0}^{\infty} c_n(0)\zeta^n, \tag{7.69a}$$

$$\overline{Q}_1\,(\zeta;\Omega) \equiv \sum_{n=0}^{\infty} c_n\left(-\frac{7}{2}\right)\zeta^{n-7/2}, \tag{7.69b}$$

whose linear combination, for $0 < \zeta < 1$, is the general integral

$$\tilde{h}\,(\zeta;\Omega) = \cos^5\theta\,\overline{Q}_0\,(\zeta;\Omega) + \cos^5\theta\,\overline{Q}_1\,(\zeta;\Omega)\,. \tag{7.70}$$

Substituting in (7.56) leads, for $0 < \theta < \pi$, to the magnetic field perturbation spectrum

$$\tilde{h}\,(\theta;\Omega) = \cos^5\theta\sum_{n=0}^{\infty} c_n\,(0)\cos^{2n}\theta + \sec^2\theta\sum_{n=0}^{\infty} c_n\left(-\frac{7}{2}\right)\cos^{2n}\theta \tag{7.71}$$

where the role of arbitrary constants, to be consistent with the zero frequency case, is played by $C_1 \equiv c_0\,(0)$ and $C_2 \equiv c_0\,(-7/2)$. The second term of the wavefield (7.71) is singular at $\theta = \pm\pi/2$; thus, a finite solution over the whole circle $0 \leq \theta \leq \pi$ requires $C_2 = 0$.

The first term corresponds to the series (7.69a) which converges for $|\zeta| < 1$ or $\cos^2\theta < 1$ or $0 < \theta < \pi$, so that the wavefield is finite in this range. The points $\theta = 0, \pi$ correspond to the boundary of convergence. In order to find out whether the wavefield is finite at $\theta = 0, \pi$ in the case $\Omega \neq 0$, as for $\Omega = 0$, it is necessary to determine $\tilde{h}\,(0;\Omega)$. Since generalisations of the relations (7.62) are not available for extended hypergeometric functions, it is necessary to go back to the differential equation (7.51) and perform the change of variable

$$\xi \equiv 1 - \zeta = \sin^2\theta, \tag{7.72a}$$

$$J(\xi;\Omega) = Q(\zeta;\Omega); \tag{7.72b}$$

this transforms the wave equation (7.51) to

$$4\xi(1-\xi)J'' + 2(1-10\xi)J' + \left(\Omega^2\xi^2 - 2\Omega^2\xi + \Omega^2 - 7\right)J = 0. \tag{7.73}$$

Since $\zeta = 1$ is a regular singularity of (7.51), $\xi = 0$ is a regular singularity of (7.73), and a solution as a Frobenius-Fuchs series exists:

$$\overline{J}(\xi;\Omega) \equiv b^{-1}R^{-2}J(\xi;\Omega) = \sum_{n=0}^{\infty} d_n(\iota)\,\xi^{n+\iota}. \tag{7.74}$$

The recurrence formula for the coefficients

$$\begin{aligned}(n+\iota+1)\left(n+\iota+\frac{1}{2}\right)d_{n+1}(\iota) = &\left[(n+\iota)(n+\iota+4) + \frac{7}{4} - \frac{\Omega^2}{4}\right]d_n(\iota)\\ &+ \frac{\Omega^2}{2}d_{n-1}(\iota) - \left(\frac{\Omega}{2}\right)^2 d_{n-2}(\iota)\end{aligned} \tag{7.75}$$

leads to the indicial equation

$$\iota\left(\iota - \frac{1}{2}\right) = 0 \tag{7.76}$$

with the roots $\iota = \{0, 1/2\}$. It is clear that the wavefield will be finite $\overline{J}_0(\xi) \sim O(1)$ or vanish $\overline{J}_{1/2}(\xi) \sim O\left(\sqrt{\xi}\right)$ at $\xi = 0$, i.e. for $\theta = 0$ and $\theta = \pi$; therefore both of (7.69a) and (7.69b), which are linear combinations of $\overline{J}_0$ and $\overline{J}_{1/2}$, must be finite at $\theta = 0$ and $\theta = \pi$. As before, the general integral may be written as

$$\tilde{h}(\theta;\Omega) = \cos^5\theta\left[\sum_{n=0}^{\infty} d_n(0)\sin^{2n}\theta + \sin\theta\sum_{n=0}^{\infty} d_n\left(\frac{1}{2}\right)\sin^{2n}\theta\right] \tag{7.77}$$

where the arbitrary constants of integration, again to be consistent with the zero frequency case, are now $D_1 \equiv d_0(0)$ and $D_2 \equiv d_0(1/2)$. This formula shows that at $\theta = \{0, \pi\}$ the wavefield is finite because $\tilde{h}(0;\Omega) = d_0(0) = D_1 = -\tilde{h}(\pi,\Omega)$.

7.3 Velocity and magnetic field perturbations

The solution of the Alfvén wave equation (see section 7.2) leads to series expansions for the velocity and magnetic field perturbations (see section 7.3.1) which converge rapidly (see section 7.3.2) and allow plotting of the wavefields.

7.3.1 Boundary conditions and wave perturbations

The pairs of arbitrary constants C_1 and C_2 are determined by two non-trivial, independent and compatible boundary conditions, e.g. specifying the magnetic field perturbation at two points,

$$\tilde{h}\left(\theta_1;\Omega\right) \equiv \tilde{h}_1\left(\Omega\right), \tag{7.78a}$$

$$\tilde{h}\left(\theta_2;\Omega\right) \equiv \tilde{h}_2\left(\Omega\right), \tag{7.78b}$$

or the magnetic field perturbation and its derivative at one point,

$$\tilde{h}\left(\theta_0;\Omega\right) \equiv \tilde{h}_0\left(\Omega\right), \tag{7.79a}$$

$$\left.\frac{\mathrm{d}\tilde{h}}{\mathrm{d}\theta}\right|_{\theta=\theta_0} \equiv \tilde{h}_0'\left(\Omega\right). \tag{7.79b}$$

Note that the polarisation relation (7.38b) implies that the derivative of the magnetic field perturbation spectrum is related to the velocity perturbation spectrum (7.36) by

$$\tilde{V}(\beta;\omega) = \mathrm{i}\frac{a^2R^2}{\omega b}s^{-3}\frac{\mathrm{d}[s\tilde{H}(\beta;\omega)]}{\mathrm{d}\beta} \tag{7.80}$$

where (7.24) and (7.28) were used, followed by (7.19) and (7.20) leading to

$$X(\theta;\Omega) \equiv b\tilde{V}(\beta;\omega) = \mathrm{i}\frac{a^2}{\omega R}\sec^4\theta\frac{\mathrm{d}}{\mathrm{d}\theta}\left[\cos^2\theta\tilde{H}(\theta;\Omega)\right]. \tag{7.81}$$

The two components of the magnetic field perturbation, according to (7.71), are given by

$$e_0 \equiv 1: \quad h_1\left(\theta;\Omega\right) = \sum_{n=0}^{\infty} e_n\cos^{2n+5}\theta, \tag{7.82a}$$

$$f_0 \equiv 1: \quad h_2\left(\theta;\Omega\right) = \sum_{n=0}^{\infty} f_n\cos^{2n-2}\theta, \tag{7.82b}$$

where the coefficients $e_n \equiv c_n\left(0\right)$ and $f_n \equiv c_n\left(-7/2\right)$, beginning from (7.66), satisfy the recurrence formulas respectively

$$n\left(n+\frac{7}{2}\right)e_n = \left[\left(n-1\right)\left(n+3\right)+\frac{7}{4}\right]e_{n-1} - \left(\frac{\Omega}{2}\right)^2 e_{n-3}, \tag{7.83a}$$

$$n\left(n-\frac{7}{2}\right)f_n = \left[\left(n-\frac{1}{2}\right)\left(n-\frac{9}{2}\right)+\frac{7}{4}\right]f_{n-1} - \left(\frac{\Omega}{2}\right)^2 f_{n-3}. \tag{7.83b}$$

Introducing a dimensionless velocity perturbation spectrum

$$W\left(\theta;\Omega\right) \equiv \frac{\mathrm{i}\omega R}{ba^2}X\left(\theta;\Omega\right) \tag{7.84}$$

leads, using (7.81), to

$$W_m\left(\theta;\Omega\right) = -\sec^4\theta\frac{\mathrm{d}}{\mathrm{d}\theta}\left[\cos^2\theta h_m\left(\theta;\Omega\right)\right] \tag{7.85}$$

where was used $H_m = bh_m$. The velocity perturbations corresponding to the magnetic field perturbations (7.82a) and (7.82b) are thus given respectively by

$$W_1(\theta;\Omega) = \sin\theta \sum_{n=0}^{\infty} e_n (2n+7) \cos^{2n+2}\theta, \tag{7.86a}$$

$$W_2(\theta;\Omega) = \sin\theta \sum_{n=0}^{\infty} f_n (2n) \cos^{2n-5}\theta. \tag{7.86b}$$

Since the magnetic field perturbations (7.82a) and (7.82b) are symmetric functions of θ and the velocity perturbations (7.86a) and (7.86b) are skew-symmetric, it is sufficient to plot them over half a circle. The figures that are indicated in table 7.2 correspond to the plots of the magnetic field and velocity perturbations.

Wave perturbation	**Magnetic field $\tilde{H}$**	**Velocity $\tilde{V}$**
First component	Figure 7.3	Figure 7.5
Second component	Figure 7.4	Figure 7.6

Table 7.2: Figures that represent both components of magnetic field and velocity perturbations.

7.3.2 Polarisation relation and improvement of convergence

The series for the magnetic field perturbation spectrum (7.82a) and (7.82b) have a unit radius of convergence, and thus the coefficients (7.83a) and (7.83b) may be expected to be $O(1)$ as $n \to \infty$; in this case the series obtained by differentiation (7.86a) and (7.86b) would diverge because the coefficients would be $O(n)$ as $n \to \infty$, *viz.* it is well known that differentiation worsens the convergence of trigonometric series. The convergence would be improved, i.e. the coefficients would become $O(1/n)$ as $n \to \infty$, by integration of (7.82a) and (7.82b), and to do this it is necessary to start from the polarisation relation (7.38a), instead of (7.38b), *viz.*

$$\tilde{H}(\beta;\omega) = \frac{\mathrm{i}}{\omega s}\left(B\tilde{V}\right)' = \frac{\mathrm{i}bR^2}{\omega s}\frac{\mathrm{d}\left(\tilde{V}/s\right)}{\mathrm{d}\beta} \tag{7.87}$$

where (7.24) was used. From the equations (7.19) and (7.20), it follows that

$$\tilde{h}(\theta;\Omega) = \frac{\mathrm{i}}{\omega R}\frac{\mathrm{d}}{\mathrm{d}\theta}\left[\sec^2\theta\tilde{V}(\beta;\omega)\right] \tag{7.88}$$

which, regarding the definition of the velocity perturbation spectrum, corresponds to

$$h_m(\theta;\Omega) = \left(\frac{a}{\omega R}\right)^2 \frac{\mathrm{d}}{\mathrm{d}\theta}\left[\sec^2\theta W_m(\theta;\Omega)\right] \tag{7.89}$$

and has to be integrated for W_m, with (7.82a) and (7.82b) known. In the case $m = 1$, the integration of

$$h_1(\theta; \Omega) = \sum_{n=0}^{\infty} e_n \cos^{2n+5}\theta = \left(\frac{a}{\omega R}\right)^2 \frac{\mathrm{d}}{\mathrm{d}\theta}\left[\sec^2\theta\, W_1(\theta; \Omega)\right] \tag{7.90}$$

can be made via the substitution

$$\left(\frac{a}{\omega R}\right)^2 W_1(\theta; \Omega) = \sin\theta \sum_{n=0}^{\infty} \overline{e}_n \cos^{2n+q}\theta \tag{7.91}$$

with $\overline{e}_n$ and q to be chosen, *viz.*

$$\sum_{n=0}^{\infty} e_n \cos^{2n+5}\theta = \sum_{n=0}^{\infty} \overline{e}_n \left[(2n+q-1)\cos^{2n+q-1}\theta - (2n+q-2)\cos^{2n+q-3}\theta\right] \tag{7.92}$$

which is satisfied for $q = 6$, with

$$\sum_{n=0}^{\infty} \cos^{2n+5}\theta \left[e_n - (2n+5)\,\overline{e}_n + (2n+6)\,\overline{e}_{n+1}\right] = 0. \tag{7.93}$$

Thus, the velocity perturbation spectra corresponding to (7.82a) and (7.82b) are respectively

$$\left(\frac{a}{\omega R}\right)^2 W_1(\theta; \Omega) = \sin\theta \sum_{n=1}^{\infty} \overline{e}_n \cos^{2n+6}\theta, \tag{7.94a}$$

$$\left(\frac{a}{\omega R}\right)^2 W_2(\theta; \Omega) = \sin\theta \sum_{n=1}^{\infty} \overline{f}_n \cos^{2n-1}\theta, \tag{7.94b}$$

with coefficients given by

$$e_n = (2n+5)\,\overline{e}_n - (2n+6)\,\overline{e}_{n+1}, \tag{7.95a}$$

$$f_n = (2n-2)\,\overline{f}_n - (2n-1)\,\overline{f}_{n+1}. \tag{7.95b}$$

where $q = 6$ for (7.95a) and $q = -1$ for (7.95b). Note that the pairs of formulas (7.82a) and (7.82b), (7.94a) and (7.94b), (7.95a) and (7.95b) are similar replacing $2n+5$ by $2n-2$. Also, setting $n = -1$ in (7.95a) and (7.95b) yields $\overline{e}_0 = \overline{f}_0 = 0$, so the series (7.94a) and (7.94b) start with $n = 1$; besides, setting $n = 0$ in (7.95a) and (7.95b), the starting values of $\overline{e}_1$ and $\overline{f}_1$ are obtained, $\overline{e}_1 = -e_0/6 = -1/6$ and $\overline{f}_1 = f_0 = 1$, where the relations (7.82a) and (7.82b) were used. The successive coefficients $\overline{e}_{n+1}$ and $\overline{f}_{n+1}$ can be calculated from the preceding $\overline{e}_n$ and $\overline{f}_n$, and from (7.83a) and (7.83b), that is, for $n = 1, 2, \ldots$, we have

$$\overline{e}_{n+1} = \frac{(2n+5)\,\overline{e}_n - e_n}{2n+6}, \tag{7.96a}$$

$$\overline{f}_{n+1} = \frac{(2n-2)\,\overline{f}_n - f_n}{2n-1}. \tag{7.96b}$$

Thus, all coefficients in the magnetic field and velocity perturbations spectra are specified.

7.4 Main conclusions of the chapter 7

The incompressibility condition $\nabla \cdot \boldsymbol{V} = 0$ is met by these waves to $O(1/R)$, according to (7.22c); similarly, using (7.22b) the force-free condition

$$\nabla \times (B(\beta)\, \boldsymbol{e}_\beta) = 2\boldsymbol{e}_z s^{-2} \frac{\partial (Bs)}{\partial \alpha} = 2\boldsymbol{e}_z B s^{-2} \frac{\partial s}{\partial \alpha} = -4\alpha B \boldsymbol{e}_z = -4\frac{B}{R}\boldsymbol{e}_z \tag{7.97}$$

is met only to $O(1/R)$. The Gauss's law for magnetism $\nabla \cdot \boldsymbol{h} = 0$ is also met to $O(1/R)$ since $\nabla \cdot \boldsymbol{h} = -2h/R$ as in (7.22c). Note that all these results arise because the scale factor $s = s(\alpha, \beta)$ depends on both dipolar coordinates, according to (7.17b). The criterion for the Gauss's law for magnetism $\nabla \cdot \boldsymbol{h} = 0$ to be approximately satisfied may be chosen by $|\nabla \cdot \boldsymbol{h}| \ll |\nabla \times \boldsymbol{h}|$, where $\nabla \times \boldsymbol{h} = \mu \boldsymbol{j}$ specifies the electric current associated with the Alfvén wave. Noting that $|\nabla \times \boldsymbol{h}| \sim h\overline{k} = 2\pi h/\lambda$ where $\overline{k}$ is the wavenumber, and λ the wavelength, and $\nabla \cdot \boldsymbol{h} \sim h/R$, it follows that $|\nabla \cdot \boldsymbol{h}| \ll |\nabla \times \boldsymbol{h}|$ implies $1/R \ll 2\pi/\lambda$. Thus, the Maxwell equation $|\nabla \cdot \boldsymbol{h}| = 0$ is approximately satisfied; also, the pair of laws $\nabla \cdot \boldsymbol{v} = 0$ and $\nabla \times \boldsymbol{B} = \boldsymbol{0}$ is satisfied as well, if $1 \ll 2\pi R/\lambda = \omega R/a = \Omega$ in terms of the dimensionless parameter Ω.

A typical application of the present problem of Alfvén wave propagation in a dipolar magnetic field concerns planetary fields. In the case of the Earth, Alfvén waves in the ionosphere correspond to a gaseous background, and in the molten core, to an incompressible liquid medium. Taking for the ionospheric magnetic field $B_0 = 5.0 \times 10^{-9}\,\mathrm{T}$ at approximately the Earth's radius $R_0 = 6.4 \times 10^6\,\mathrm{m}$, in the core at one-tenth of the radius $R_1 = 0.1R_0 = 6.4 \times 10^5\,\mathrm{m}$ a dipolar magnetic field, which scales like the inverse cube of distance $\sim 1/R^3$, is one thousand times bigger $B_1 = 10^3 B_0 = 5.0 \times 10^{-6}\,\mathrm{T}$. For a mass density $\rho = 5.5 \times 10^3\,\mathrm{kg\,m^{-3}}$ and the value of magnetic permeability equal to the permeability of the free space, this leads to a low Alfvén speed $a_1 = B_1/\sqrt{\mu\rho} = 6.0 \times 10^{-5}\,\mathrm{m\,s^{-1}}$. Taking the period of one day, $\tau = 24 \times 3600\,\mathrm{s} = 8.64 \times 10^4\,\mathrm{s}$, or frequency $\omega = 2\pi/\tau = 7.3 \times 10^{-5}\,\mathrm{s^{-1}}$, leads to the value $\Omega_1 = \omega R_1/a_1 = 7.7 \times 10^5 \gg 1$, which meets the conditions stated in the preceding paragraph. As a second example, deeper in the core, at one-hundredth of the Earth's radius $R_2 = 10^{-2} R_0 = 6.4 \times 10^4\,\mathrm{m}$, the magnetic field $B_2 = 10^6 B_0 = 5.0 \times 10^{-3}\,\mathrm{T}$ leads to an Alfvén speed $a_2 = B_2/\sqrt{\mu\rho} = 6.0 \times 10^{-2}\,\mathrm{m\,s^{-2}}$. The corresponding value of the parameter $\Omega_2 = \omega R_2/a_2 = 7.8 \times 10^1$ still meets the condition $\Omega \gg 1$.

For the purpose of illustration of the velocity and magnetic field perturbations, the parameter is given by the values $\Omega = \{10, 20, 50\}$ which satisfy $\Omega \gg 1$, and also given the symmetries of the fields over the full circle $0 \leq \theta \leq 2\pi$, only one half is plotted, $0 \leq \theta \leq \pi$. Since $\theta = \pi/2$ corresponds to the magnetic north pole, the range for plotting $0 \leq \theta \leq \pi$ corresponds to the upper hemisphere. Starting with the magnetic field perturbation and the component (7.82a), which is finite over the whole circle $0 \leq \theta \leq 2\pi$, it is a symmetric function of θ. Hence, the plot over the northern hemisphere (figure 7.3) can be repeated on the lower hemisphere by symmetry on the equator. The field vanishes at the magnetic poles $h_1(\pm\pi/2; \Omega) = 0$, and is skew-symmetric relative to the polar axis because $h_1(\pi/2 - \theta; \Omega) = -h_1(\pi/2 + \theta; \Omega)$. Away from the poles $\theta = \pm\pi/2$, i.e., towards the equator $\theta = 0$ or $\theta = \pi$, the magnetic field perturbation oscillates with smaller amplitude, and shorter wavelength, for larger Ω.

The component (7.82b) of the magnetic field perturbation is unbounded at the poles $\theta = \pm\pi/2$. Thus,

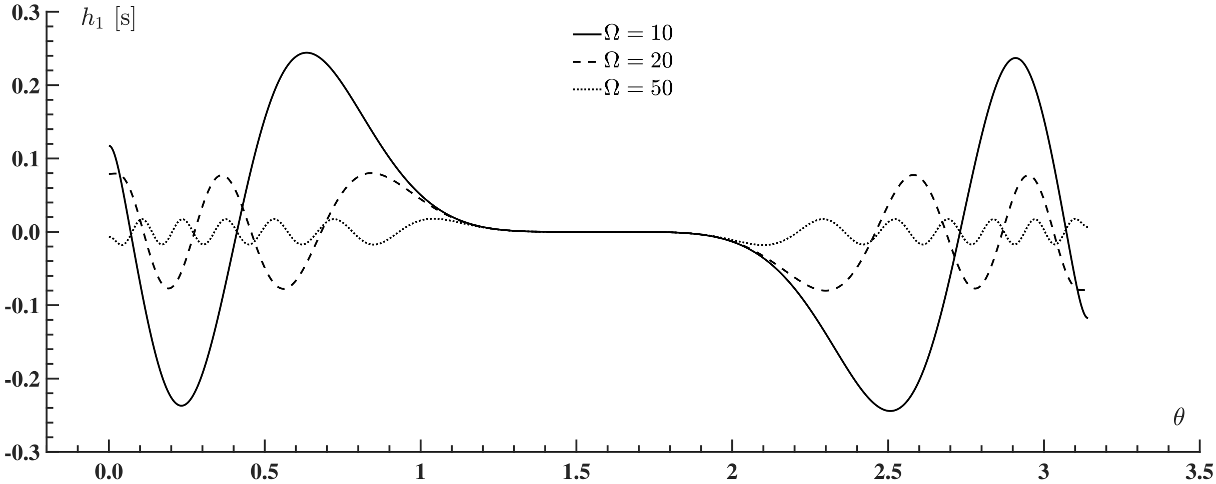

Figure 7.3: Component of magnetic field perturbation spectrum (7.82a), which is finite over the whole circle, versus radial angle along a half-circle, for three values of the dimensionless frequency Ω.

the general wavefield

$$\tilde{h}(\theta;\Omega) = C_1^\star h_1(\theta;\Omega) + C_2^\star h_2(\theta;\Omega) \tag{7.98}$$

is finite over the whole circle only if $C_2^\star = 0$ is met, in which case the remaining constant of integration $C_1^\star$ can be determined using

$$\tilde{h}(0;\Omega) = C_1^\star \sum_{n=0}^{\infty} e_n \tag{7.99}$$

and knowing the magnetic field perturbation spectrum $\tilde{h}(0;\Omega)$ at $\theta = 0$. It follows that the dimensionless magnetic field perturbation is a constant multiple $C_1^\star$ of $h_1(\theta;\Omega)$ plotted in figure 7.3. In order to plot $h_2(\theta;\Omega)$ it is convenient to remove the singularity at $\theta = \pm\pi/2$, by inserting the factor $\cos^2\theta$, *viz.*

$$\overline{h}_2(\theta;\Omega) \equiv \cos^2\theta h_2(\theta;\Omega) = \sum_{n=0}^{\infty} f_n \cos^{2n}\theta. \tag{7.100}$$

The magnetic field perturbation is symmetric on the southern and northern hemispheres. It vanishes at the poles, $\overline{h}_2(\pm\pi/2;\Omega) = 0$, is symmetric relative to the polar axis, $\overline{h}_2(\pi/2-\theta;\Omega) = \overline{h}_2(\pi/2+\theta;\Omega)$, and oscillates with larger amplitude and shorter wavelength for larger Ω (figure 7.4). The range of values of $\overline{h}_2$ in figure 7.4 is more than one order of magnitude larger than the range of values of h_1 in figure 7.3, so the latter is plotted separately to aid visibility. Comparing h_1 and $\overline{h}_2$ as Ω increases, there are more nodes for both; also, as Ω increases the amplitude decreases for h_1 and increases for $\overline{h}_2$.

Concerning the component of the velocity perturbation (7.86a), which is finite over the whole circle $0 \leq \theta \leq 2\pi$, it is skew-symmetric, $W_1(\theta;\Omega) = -W_1(-\theta;\Omega)$, so that in the lower hemisphere it has the opposite sign to the upper hemisphere (figure 7.5). It vanishes at the magnetic poles and equator $\theta = \pm\pi/2, 0, \pi$, and is symmetric relative to the polar axis because $W_1(\pi/2+\theta;\Omega) = W_1(\pi/2-\theta;\Omega)$. For $\Omega = 10$, there is a single large extremum, and on increasing Ω, the number of local extrema increases and their magnitude decreases. The other component of the velocity perturbation spectrum (7.86b) is

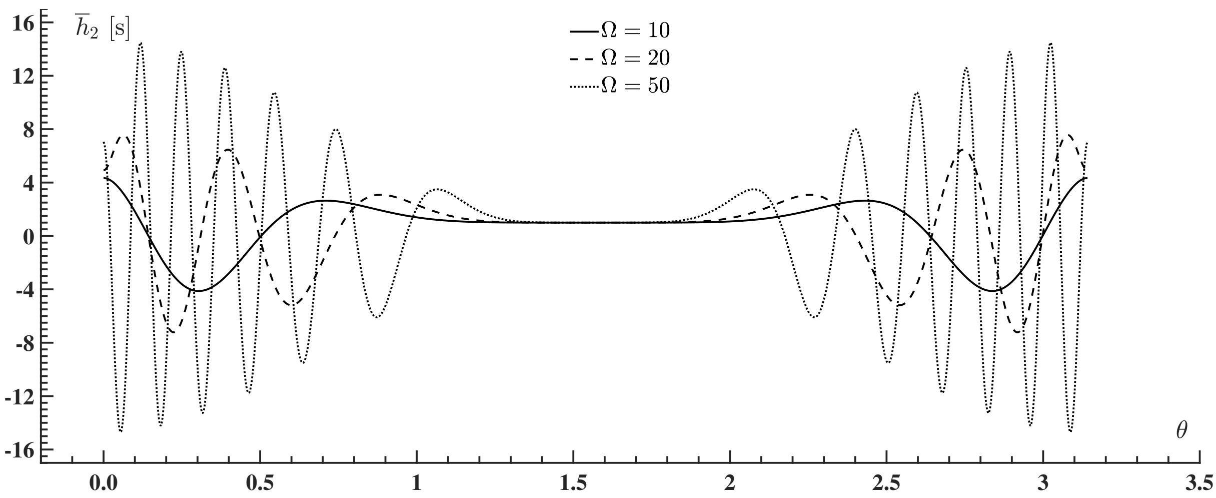

Figure 7.4: Component of magnetic field perturbation spectrum (7.82b), which is singular, versus radial angle along a half-circle, with singularity removed (7.100), for three values of the dimensionless frequency Ω.

singular at the magnetic poles $\theta = \pm\pi/2$. The singularity is suppressed by inserting a suitable factor:

$$\left(\frac{a}{\omega R}\right)^2 \overline{W}_2\left(\theta;\Omega\right) \equiv \left(\frac{a}{\omega R}\right)^2 \cos\theta\, W_2\left(\theta;\Omega\right) = \sin\theta \sum_{n=0}^{\infty} \overline{f}_n \cos^{2n}\theta. \tag{7.101}$$

The velocity perturbation is a skew-symmetric function of θ, i.e. has opposite signs in the upper and lower hemispheres. It vanishes at the magnetic poles and equator, and it is symmetric relative to the polar axis (figures 7.5 and 7.6). For increasing Ω, the wavelength is larger and the amplitude of oscillations also larger. Comparing W_1 and $\overline{W}_2$, it is clear that there are more oscillations for both as Ω increases; for increasing Ω, the amplitude is smaller for W_1 and larger for $\overline{W}_2$. Also, $\overline{W}_2$ has an oscillatory sign, i.e. is alternatively positive and negative, whereas W_1 is always negative.

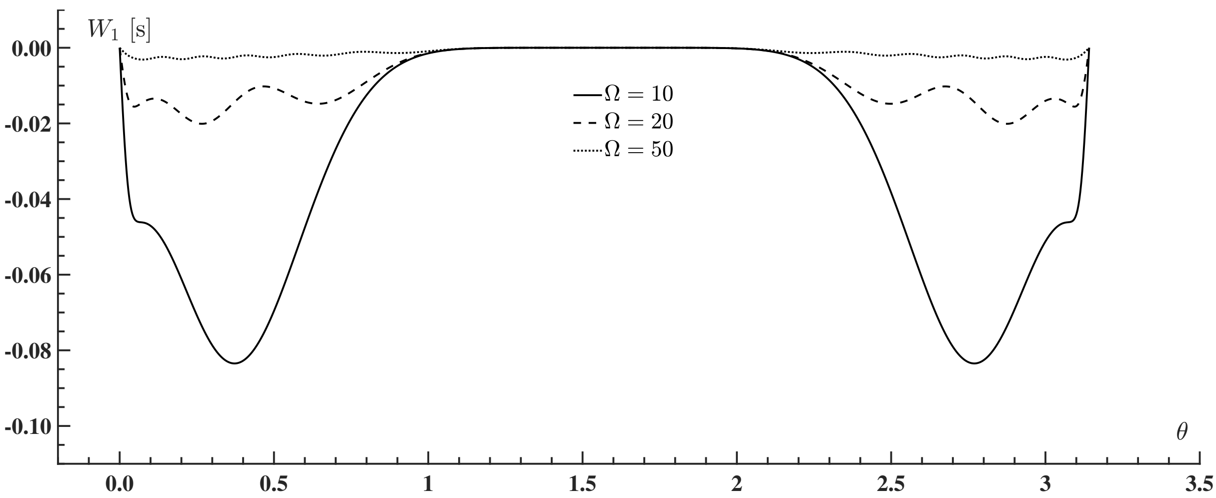

Figure 7.5: Component of velocity perturbation spectrum (7.94a), which is finite over the whole circle, versus radial angle along a half-circle, for three values of the dimensionless frequency Ω.

In figures 7.3 to 7.6 , the circular magnetic field lines are described from $\theta = 0$ to $\theta = \pi$. If the field lines (and magnetic poles) do not follow the geographical positioning, that is, if the field lines were

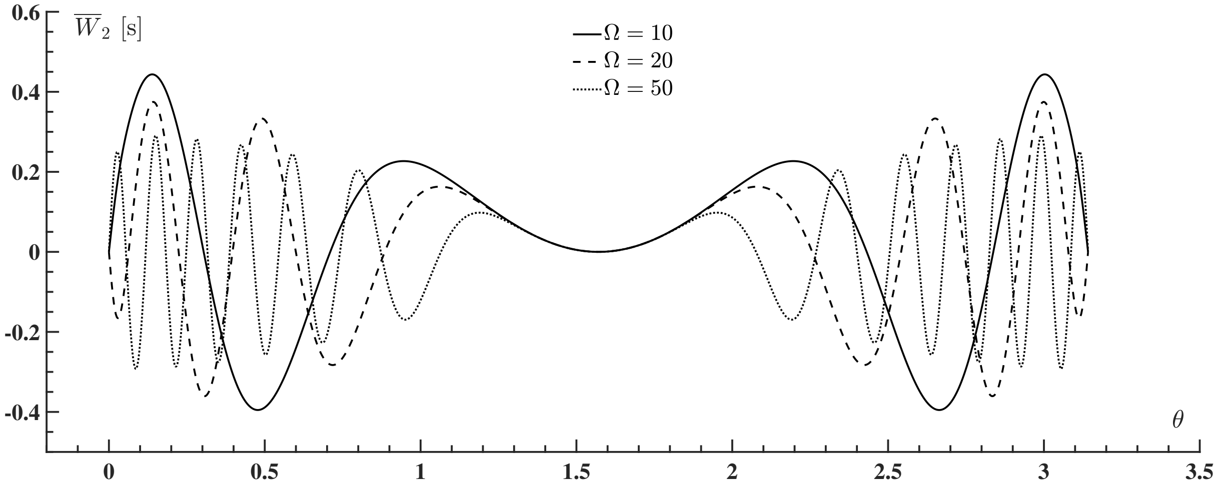

Figure 7.6: Component of velocity perturbation spectrum (7.94b), which is singular, versus radial angle along a half-circle, with singularity removed (7.101), for three values of the dimensionless frequency Ω.

not measured between 0 and π, the effect on the propagation of Alfvén waves would be a translation $\theta \to \theta + \theta_0$, and therefore it would lead to different starting values.

Since one component, each of the magnetic and velocity perturbations, is singular, a relevant factor was introduced to obtain a finite value and to make the plots in figures 7.4 and 7.6 visible over the whole range of values $0 < \theta < \pi$. The scale in figure 7.4 would be larger without this factor and could be reduced by an additional constant factor like 0.1. In all cases of figures 7.3 to 7.6, the objective was to plot the dependence of the wavefields visibly along the whole of the circular magnetic field lines of a dipole for several values of the dimensionless frequency.

The main feature of this chapter is to consider the Alfvén wave propagation along a closed magnetic field line, in fact, the most straightforward closed curve: the circle. In situations in which the closed magnetic field is not a circle, like the magnetic field of the Earth, Sun and other planets and stars, the local curvature would replace the radius of the circle; this approximation is valid if the wavelength λ is much smaller (or the wavenumber κ is much greater) than the length scale of the change of curvature

$$\lambda = \frac{2\pi}{\kappa} \leq \frac{R(\theta)}{R'(\theta)} = \frac{\mathrm{d}}{\mathrm{d}\theta}\{\log[R(\theta)]\} \tag{7.102}$$

where and $R(\theta)$ is the radius of curvature at the angular position θ of the closed magnetic field line.

The present model considers a constant Alfvén speed (7.27) with the direction varying along a circle. The case of an Alfvén wave propagating with constant direction and changing Alfvén speed has been studied in detail in the case of atmospheres like the Sun and radial flows like the solar wind (see references in the third paragraph of the introduction of this chapter [128, 171–175, 177–197]). An Alfvén speed increasing with distance leads to a waveform stretching with an increasing spacing of the nodes, smaller waveform slope and less dissipation; the reverse occurs for Alfvén speed decreasing with distance.

8 | On the generation of harmonics by the non-linear buckling of an elastic beam

"Logic is the foundation of the certainty of all the knowledge we acquire."

— Leonhard Euler

Contents

The Bernoulli [75] and Euler [76] theory of beams is a standard introductory subject in textbooks on elasticity [77–81] and leads to the phenomenon of buckling, which has been considered in several conditions: (i) geometric and material non-linearities [83]; (ii) in combination with shear [84, 85] that is more significant for short stubby beams [86–90]; (iii) constraints [91–93], such as hyper or non-local elasticity [94, 95]; (iv) vibrations [96, 97], that can be excited by unsteady applied forces [98–101], leading to control problems [102]; (v) steady mechanical [103] or thermal [104–106] effects; and (vi) vibrations of tapered beams [107–116], with multiple applications like airplane wings and flexible aircraft and helicopters [117–121]. Among this wide range of topics related to the buckling of elastic beams, the present chapter focuses on geometric non-linearities associated with a large slope of the elastica.

The equation of the elastica of a beam is usually written in one of the two forms: (i) in Cartesian coordinates, $y = \zeta(x)$, with the x-axis along the undeformed beam; or (ii) in curvilinear coordinates, $s = \xi(\theta)$, with the arc length s as a function of the angle of inclination. The linear theory assumes for $y = \zeta(x)$ a small slope,

$$(\zeta')^2 \equiv \left(\frac{\mathrm{d}\zeta}{\mathrm{d}x}\right)^2 \ll 1, \tag{8.1}$$

where the prime in this chapter denotes the derivative with x, and implies that the maximum deflection is small, compared with the length, $(\zeta_{\max})^2 \ll L^2$, as explained in the figure 8.1. However, the latter condition of small maximum deflection relative to length does not imply [130] linearity (8.1) in the case of "ripples" with a large slope (figure 8.2). The condition of linearity can be expressed in terms of a small angle of inclination, $\theta^2 \ll 1$, that is equivalent to $\cos\theta \sim 1$ and $\sin\theta \sim \theta \sim \tan\theta = \zeta'$.

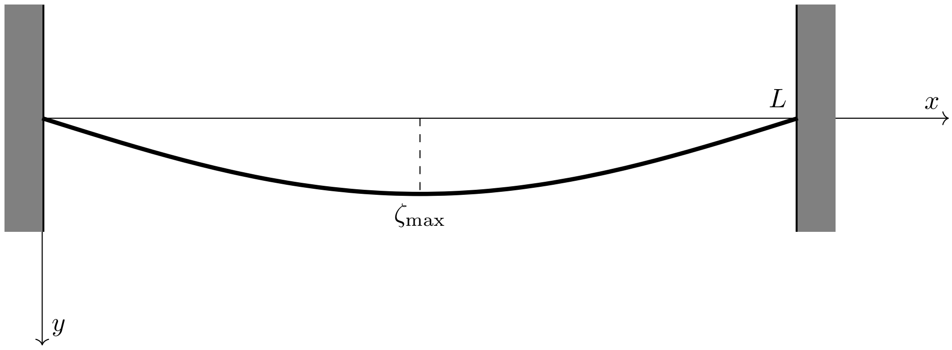

Figure 8.1: A linear deflection is defined by a small slope and implies that the maximum deflection is small compared with the distance between the supports.

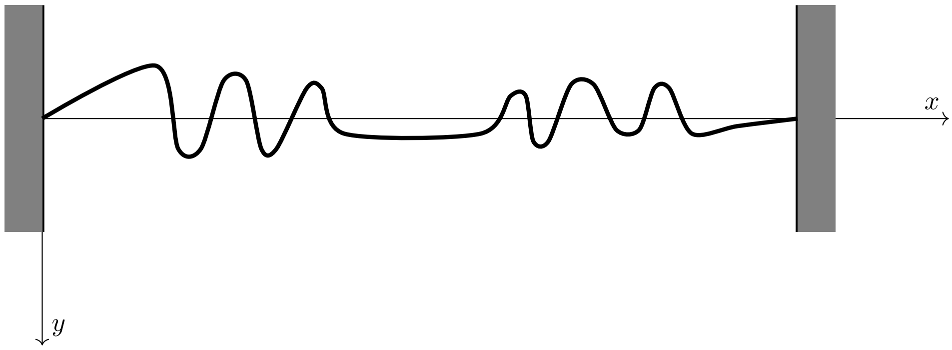

Figure 8.2: The converse to the figure 8.1 may not be true; for example, if the maximum deflection is small, but the slope is large due to the presence of steep "ripples", the deflection of the beam is non-linear.

The Euler–Bernoulli theory of beams states that the bending moment M is proportional to the curvature k,

$$M(x) = -EIk(x), \tag{8.2}$$

that is the product of the Young modulus E of the material by the moment of inertia I of the cross-section. For a beam of constant cross-sections made of a homogeneous material, the bending stiffness EI is constant. In the case of a uniform beam [219], that is, with constant bending stiffness, geometric non-linearities can arise from the curvature, $k \equiv \mathrm{d}\theta/\mathrm{d}s$, that is, the rate of change of the angle of inclination with the arc length

$$\mathrm{d}s = \left[(\mathrm{d}x)^2 + (\mathrm{d}\zeta)^2\right]^{1/2} = \mathrm{d}x\left(1 + \zeta'^2\right)^{1/2}. \tag{8.3}$$

The curvature is given by

$$k(x) = \frac{\mathrm{d}x}{\mathrm{d}s}\frac{\mathrm{d}}{\mathrm{d}x}(\arctan\zeta'), \tag{8.4}$$

thus, it is only in the case of a small slope (8.1) that the equation of the elastica is linear:

$$M(x) = -EI\zeta''(x). \tag{8.5}$$

If the slope of the elastica is not small, its shape is specified by non-linear ordinary differential equations [127, 132, 220, 221].

The linear theory shows that if a critical buckling load T_c is reached, a beam in the compression deforms and gains a buckled shape. Applying higher critical loads $T_{c,n}$, with $n = 1, 2, \ldots, \infty$, leads to a succession of harmonics $y = \zeta_n(x)$. In the present chapter, it is shown that geometric non-linearities associated with a large slope,

$$M(x) = -EI\zeta''\left[1 + (\zeta')^2\right]^{-3/2}, \tag{8.6a}$$

do not affect the critical buckling load, but change the shape of the elastica that becomes a superposition of harmonics of the linear case:

$$\zeta(x) = \sum_{m=1}^{\infty} A_m \zeta_m(x). \tag{8.6b}$$

The coefficients A_m are determined in this chapter for the three cases of (i) cantilever, (ii) clamped, and (iii) pinned beams, and the shape of the elastica is illustrated taking into account non-linear geometric effects associated with a large slope. Before proceeding to discuss non-linear geometric effects in the Euler–Bernoulli theory [75–81], the preceding classification of the references [83–121] is complemented by a brief discussion of some additional references. The method of the elastica for non-linear beams, schematised in figure 8.3, involves the solution of ordinary differential equations [127, 132, 219–221]. The exact analytical solutions can be obtained using elliptic functions [39, 222, 223] for simpler loading cases.

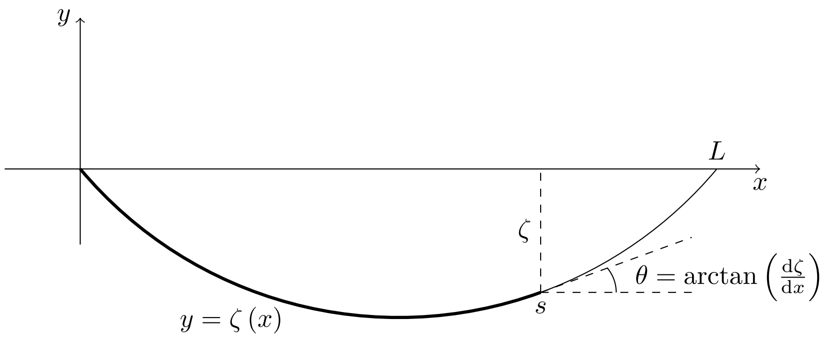

Figure 8.3: The Euler–Bernoulli theory of the elastica $y = \zeta(x)$ of beams is usually presented (i) in the linear case of a small slope, $\zeta'^2 \ll 1$, with $\zeta' \equiv d\zeta/dx$ using Cartesian coordinates with x along and y normal to the undeflected position; (ii) in the non-linear case of an unrestricted slope, $\zeta' \sim O(1)$, using curvilinear coordinates along the deflected position, namely, the arc length s and angle of deflection $\theta = \arctan(\zeta')$. In the present chapter, the Cartesian coordinates (x, y) are used as in (i), but without the restriction on slope, that is with $d\zeta/dx \sim O(1)$ as in (ii), corresponding to the non-linear bending of an Euler–Bernoulli beam with unrestricted slope.

The articles [224, 225] show that a combination of incomplete and complete elliptic integrals specifies large deflections. The results of these two articles are given with limited accuracy because, at that time, the calculations were performed with something other than digital computers. More accurate results of elliptic integrals are presented, for instance, in [226, 227]. Furthermore, to obtain highly precise numerical results, these problems may also be solved using the shooting-optimisation technique. The aforementioned two methods for solving large deflections of beams are presented in [228], where an inextensible elastic beam is hinged at one end, while the other end is assumed to be a frictionless support where the beam can slide freely. Additionally, the beam is under a moment gradient, and the moment at each end of the beam can be varied from zero to a full moment by a scaling parameter. In [228], the elastica theory serves to formulate the elliptic-integral method, and an iterative process obtains the results. At the same time, the governing set of differential equations is needed for the shooting-optimisation technique and is numerically integrated using the fourth-order Runge–Kutta method. The results obtained from both methods are in close agreement with each other. The paper [229] continues in this line of research, but considers the double curvature bending of the elastica under two applied moments in the same direction applied at the supports and complements earlier studies that confined bending to one of the single curvature-type bendings. The two aforementioned methods are used. The elliptic integral technique provides analytical solutions to the governing non-linear differential equation for elasticas, while the shooting optimisation method numerically integrates the equation using the fifth-order Cash–Karp Runge–Kutta method. Both methods provide almost the same stable and unstable equilibrium solutions and, for some cases of the unstable equilibrium configuration, the elastica can form a single loop or snap-back bending.

Continuing in this line of investigation, the paper [230] considers the large deflection problem of variable deformed arc-length beams, also with a uniform flexural rigidity, but under a point load. In [230], the ends are partially elastically supported against rotation (it covers both the cases of hinged or clamped ends). Both previously mentioned methods are also used, and the results obtained are in close agreement. This kind of problem highlights the possibility of two equilibrium states for a given load, implying the possibility of a snap-through phenomenon, the existence of a critical load, and a maximum arc length for equilibrium. The analytic elastica solution of slightly curved cantilever beams, fixed at one end while being deflected under couples and forces of various directions, is evaluated in [231] using elliptic integrals. It has been shown that in some cases, the solution is very sensitive to small errors in calculating elliptic integrals. An analytic elliptic solution for the post-buckling response of a linear-elastic and hygrothermal beam, subjected to an increase in temperature and moisture content, is presented in [232]. In [232], the beam is pinned at both ends, and therefore the extensibility of the beam cannot be ignored. Additionally, it shows that the critical load is a maximum and, in the post-buckling regime, the magnitude of the load decreases. The beam theory can be extended to more complex structures [233].

Other methods using the elastica approximation are helpful for more complex loadings. The paper [234] determines a parametric solution to the elastic pole-vaulting problem, where the pole is taken to be a thin uniform elastic column with the upper end being subjected to lateral and transverse forces and a bending moment at the same time as the bottom end is free to pivot during the vaulting. The parametric solution is given in terms of tabulated elliptic integrals. The investigation [235] provides a closed-form solution for the problem of a non-linear elastica and buckling analysis of a straight bar, due to concentrated and uniformly distributed loads, while the flexural rigidity varies along the bar. It achieves an integral closed-form solution of the equation governing the equilibrium of the bar by applying successive functional transformations. The paper [236] presents the buckling analysis of a continuous elastic bar on several rigid supports subjected to end-compressive forces and assumes that the compressive forces and flexural rigidities vary from one span to the next. The closed-form solution expressed by elliptic integrals is derived for each span. The same authors presented an analytic solution for the problem of non-linear elastic buckling of a straight bar subjected to bending compression due to forces and couples at the ends superimposed to a uniformly applied transverse load along its length in [237], by using functional transformations. The same authors also analysed the problem of non-linear buckling for a straight uniform bar, fixed at its base and free at its upper end, due to the bar's weight in [238]. It yields reliable results in agreement with the physical problem. The same procedure was used in [239] to study the problem of non-linear buckling for a straight bar of uniform cross-sections and flexural rigidity, lying on a continuous elastic medium, and subjected to terminal point-loads and bending moments. In all the works described above, the effects of transverse deformation due to axial, lateral, and transverse forces are negligible.

The paper [240] constructs an exact parametric analytic solution for the full non-linear differential equations of the cantilever elastica due to end loads, end couples, and also including the effects of transverse deformation, completing, for instance, the work [234]. Translational or torsional springs may be used [82] to brace a beam increasing its critical buckling load, or to have the opposite effect of decreasing the critical buckling load to facilitate demolition. The buckling can also be facilitated or opposed by supporting the beam on a continuous bed of springs [219]. A beam of variable cross-sections can taper in two directions [122], for example, in the case of a pyramidal beam representing an aeroplane wing with chords much larger than the thickness affecting the natural frequencies of bending modes.

Following this introduction to the Euler–Bernoulli theory of beams, the chapter's core focuses on geometric non-linearities associated with a significant slope of the elastica. The equation of the elastica of a uniform beam (section 8.1) is obtained without restriction on the slope of the elastica (section 8.1.1). The well-known solutions for the linear case of a small slope are briefly recalled (section 8.1.2) because they supply the harmonics for non-linear corrections (section 8.1.3). The linear and non-linear cases are also compared, as concerns the boundary condition with small and large slopes, respectively, at the free end of a cantilever beam (section 8.1.4). The cantilever beam is considered first (section 8.2) to obtain the non-linear shape of the elastica (section 8.2.1) and to compare the linear approximation with non-linear corrections of all orders (section 8.2.2). The non-linear effects on the shape of the elastica are illustrated using the representation as a superposition of linear harmonics, by truncating the series in an analytic approximation (section 8.2.3) and adding a more significant number of terms in a numerical computation (section 8.2.4). The non-linear buckling is also considered for clamped and pinned beams (section 8.3), starting with the non-linear effects of a large slope (section 8.3.1), that do not affect the critical buckling load (section 8.3.2), but do change the shape of the elastica by the generation of harmonics (section 8.3.3), illustrated by numerical calculations (section 8.3.4). The conclusion (section 8.4) highlights the use of linear buckling harmonics to specify the shape of the elastica for non-linear buckling with a large slope.

8.1 Non-linear bending of a beam with large slope

The non-linear bending of a beam with a large slope is considered to specify the relation between the axial tension, bending moment, and transverse force or shear stress (section 8.1.1). The resulting equation of the elastica is solved readily in the linear case of a small slope (section 8.1.2), specifying the harmonics to be used in the non-linear case (section 8.1.3). The linear and non-linear cases of small and large slopes, respectively, are also compared, as concerns the boundary condition at the free end of a cantilever beam (section 8.1.4).

8.1.1 Bending moment, transverse force and shear stress

The transversal distributed and point forces F at the end sections, with the longitudinal tension T, cause a bending moment M (denoted in the figure 8.4). The variation of the bending moment $-\mathrm{d}M$ along the arc length $\mathrm{d}s$ of the elastica is balanced by the transverse force F, plus the vertical component T_{y} of the tangential tension T:

$$-\mathrm{d}M = (F + T_{\mathrm{y}})\,\mathrm{d}s. \tag{8.7a}$$

The tangential tension and its vertical component are related (figure 8.5) by

$$T_{\mathrm{y}} = T \sin\theta = T\frac{\mathrm{d}\zeta}{\mathrm{d}s}, \tag{8.7b}$$

where $\mathrm{d}\zeta = \mathrm{d}y$ is the vertical displacement. Substitution of the last equation in (8.7a) yields the balance of bending moment, transverse force and tangential tension:

$$F + T\frac{\mathrm{d}\zeta}{\mathrm{d}s} = -\frac{\mathrm{d}M}{\mathrm{d}s}. \tag{8.7c}$$

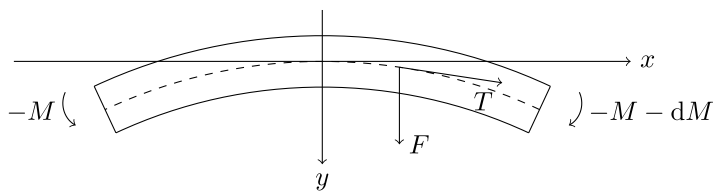

Figure 8.4: The bending moment M of a beam is associated with the axial tension T and transverse force F. Buckling can occur only for compression.

Using (8.2), which has the minus sign because the y axis points downwards, leads to: (i) the transverse force equal to

$$F = \frac{\mathrm{d}}{\mathrm{d}s}(EIk) - T\frac{\mathrm{d}\zeta}{\mathrm{d}s}; \tag{8.8}$$

(ii) the shear stress defined by the transverse force per unit length, explicitly

$$f = \frac{\mathrm{d}}{\mathrm{d}x}\frac{\mathrm{d}}{\mathrm{d}s}(EIk) - \frac{\mathrm{d}}{\mathrm{d}x}\left(T\frac{\mathrm{d}\zeta}{\mathrm{d}s}\right). \tag{8.9}$$

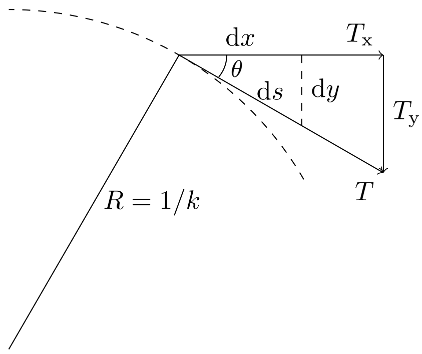

Figure 8.5: Sketch of the tangential force and its components with respect to the (x, y) reference frame of the undeflected beam. The dotted line represents the elastica of the beam.

After substituting (8.3) and (8.6a) in (8.7c), it follows that the transverse force is related to the shape of the elastica by

$$F = \left|1 + \zeta'^2\right|^{-1/2} \left(EI\zeta'' \left|1 + \zeta'^2\right|^{-3/2}\right)' - T\zeta' \left|1 + \zeta'^2\right|^{-1/2}, \tag{8.10}$$

while (8.9) leads to the relation between the shear stress and the shape of the elastica by

$$f = \left[\left|1 + \zeta'^2\right|^{-1/2} \left(EI\zeta'' \left|1 + \zeta'^2\right|^{-3/2}\right)'\right]' - \left(T\zeta' \left|1 + \zeta'^2\right|^{-1/2}\right)'. \tag{8.11}$$

The case considered in this chapter is of uniform axial tension,

$$T(x) \sim \mathrm{const}, \tag{8.12a}$$

and constant bending stiffness

$$E(x)\, I(x) \sim \mathrm{const}. \tag{8.12b}$$

A constant bending stiffness (8.12b) applies: (ii-a) to a homogeneous beam, $E \sim$ const, with uniform cross-section, $I \sim$ const; or (ii-b) to an inhomogeneous beam whose Young modulus varies along the length inversely to the moment of inertia of the cross-section. Since buckling occurs only for axial compression, $T < 0$, the buckling parameter p is defined by

$$p^2 \equiv -\frac{T}{EI} \tag{8.12c}$$

and has the dimensions of inverse length. It is real for a compression when $T < 0$ because $p^2 > 0$; otherwise, it is imaginary for a traction with $T > 0$ because $p^2 < 0$. For a uniform beam, the buckling parameter p is constant because EI and T are also constants for that case.

Simplifying the equation (8.10) for a uniform beam, the buckling parameter appears in the transverse force, specifically in the form

$$\frac{F}{EI} = \left|1+\zeta'^2\right|^{-1/2} \left(\zeta'' \left|1+\zeta'^2\right|^{-3/2}\right)' + p^2\zeta' \left|1+\zeta'^2\right|^{-1/2} \tag{8.13a}$$

$$= \left|1+\zeta'^2\right|^{-1/2} k' + p^2\eta \tag{8.13b}$$

$$= \left|1+\zeta'^2\right|^{-1/2} \eta'' + p^2\eta. \tag{8.13c}$$

It is the first fundamental equilibrium equation for a uniform beam. Simplifying the equation (8.11) for the same type of beams, the buckling parameter also appears in the shear stress expression, in the form

$$\frac{f}{EI} = \left[\left|1+\zeta'^2\right|^{-1/2} \left(\zeta'' \left|1+\zeta'^2\right|^{-3/2}\right)'\right]' + p^2 \left(\zeta' \left|1+\zeta'^2\right|^{-1/2}\right)' \tag{8.14a}$$

$$= \left(\left|1+\zeta'^2\right|^{-1/2} k'\right)' + p^2\eta' \tag{8.14b}$$

$$= \left(\left|1+\zeta'^2\right|^{-1/2} \eta''\right)' + p^2\eta'. \tag{8.14c}$$

It is the second fundamental equilibrium equation for a uniform beam. In both equations, there are two different types of linearity: (i) all terms are non-linear with respect to the slope of the elastica ζ', given by (8.1); (ii) one term is linear if the sine of the angle of inclination θ is used as a variable,

$$\sin\theta = \frac{\mathrm{d}y}{\mathrm{d}s} = \zeta' \left|1+\zeta'^2\right|^{-1/2} \equiv \eta. \tag{8.15a}$$

The curvature (8.4) is related to (8.15a) by

$$k = \left(\zeta' \left|1+\zeta'^2\right|^{-1/2}\right)' = \eta', \tag{8.15b}$$

that is a non-linear function of the slope of the elastica. Thus, the equation of the elastica for the transverse force F is: (i) of the third order in terms of the shape of the elastica ζ and has all non-linear terms in (8.13a); (ii) of the second order involving some terms linear with an auxiliary variable η in (8.13c), namely, the sine of the angle of inclination θ whose derivative is exactly the curvature k, as indicated in (8.15b). Furthermore, the equation of the elastica for the shear stress f is: (i) of the fourth order in terms of the shape of the elastica ζ and has all non-linear terms in (8.14a); (ii) of the third order involving some linear terms with the sine of the angle of inclination θ in (8.14c). Thus, the non-linearity does not lie entirely in the auxiliary variable η, and is preferred to solve the non-linear differential equation in terms of η, since the degree of the equation is reduced by one.

The third fundamental equation (8.6a) is

$$M(x) = -EIk = -EI\zeta'' \left|1+\zeta'^2\right|^{-3/2} = -EI\left(\zeta' \left|1+\zeta'^2\right|^{-1/2}\right)' = -EI\eta'. \tag{8.16}$$

The bending moment can be evaluated, again, as a function of ζ or as a function of η. The linear case of a small slope is reviewed briefly, in section 8.1.2, for comparison with the non-linear case of a large slope, that is the main focus of this chapter and occupies its remainder.

8.1.2 Linear buckling for small slope

The linear bending corresponds to the small slope (8.1) and leads to the following consequences: (i) the angle of inclination of the elastica in (8.15a) simplifies to

$$\eta = \zeta' = \theta, \tag{8.17}$$

where the inclination is equal to the derivative of deflection of the beam; (ii) the curvature k of the elastica, from (8.15b), simplifies to

$$k = \zeta''; \tag{8.18}$$

(iii) the simplification of the curvature leads to the bending moment

$$M = -EI\zeta''; \tag{8.19a}$$

(iv) the transverse force (8.10) and shear stress (8.11) simplify, respectively, to

$$F = \left(EI\zeta''\right)' - T\zeta', \tag{8.19b}$$

$$f = \left(EI\zeta''\right)'' - \left(T\zeta'\right)'. \tag{8.19c}$$

To deduce the last three equations (the constitutive and equilibrium equations), the only simplification regarded was to consider linear bending, and thence they can be applied to any type of beam (for instance, it is not necessary to be uniform).

In the case of linear deflection, when (8.1) is taken into account, and simultaneously of a uniform beam, when the equations (8.12a) and (8.12b) are considered (again, when it is valid the assumptions $EI \sim$ const and $T \sim$ const), the transverse force and shear stress simplify further, respectively, to

$$F = EI\zeta''' - T\zeta', \tag{8.20a}$$

$$f = EI\zeta'''' - T\zeta''. \tag{8.20b}$$

The beam is elastically stable if, and only if there is no deflection in the absence of shear stress. Otherwise, the beam is elastically unstable if, and only if there is deflection in the absence of shear stress. For a uniform beam, considering again the assumptions that T and EI are both constants, in the absence of shear stress, $f = 0$, instability is possible only if the buckling parameter is positive, $p^2 > 0$, in (8.14c), that is, under compression $T < 0$, corresponding to

$$T = -\left|T\right| \Rightarrow p^2 = \frac{|T|}{EI}, \tag{8.21a}$$

and leading to the linear differential equation of fourth order with constant coefficients

$$\zeta'''' + p^2\zeta'' = 0 \tag{8.21b}$$

for the shape of the elastica, whose solution is

$$\zeta(x) = \overline{A} + \overline{B}x + \overline{C}\cos(px) + \overline{D}\sin(px), \tag{8.21c}$$

where $\overline{A}$, $\overline{B}$, $\overline{C}$ and $\overline{D}$ are four arbitrary real constants. However, there is also a fifth indeterminate constant, namely, the buckling parameter p, that is intrinsically related to the critical axial tension.

For subsequent comparison with the non-linear theory, two sets of well-known results are quoted from the literature [77–79, 219] on linear buckling of beams: (i) firstly, the critical buckling load, that is, the magnitude of the compressive axial load at the onset of buckling, is highest for a clamped beam,

$$-T_1 = \frac{4\pi^2 EI}{L^2}, \tag{8.22a}$$

lowest for a cantilever beam,

$$-T_3 = \frac{\pi^2 EI}{4L^2}, \tag{8.22b}$$

and for a pinned beam, the value is in between, because

$$-T_1 > -T_2 = \frac{\pi^2 EI}{L^2} > -T_3; \tag{8.22c}$$

(ii) secondly, the shape of the buckled elastica in the linear approximation is, respectively, ζ_1 for the clamped, ζ_2 for the pinned, and ζ_3 for the cantilever cases, given, respectively, by

$$\zeta_1(x) = b\left[1 - \cos\left(\frac{2\pi x}{L}\right)\right], \tag{8.23a}$$

$$\zeta_2(x) = b\left[\sin\left(\frac{\pi x}{L}\right)\right], \tag{8.23b}$$

$$\zeta_3(x) = b\left[1 - \cos\left(\frac{\pi x}{2L}\right)\right], \tag{8.23c}$$

where the arbitrary real constant b is an amplitude and L is the length of the beam. The last results are deduced for the fundamental mode of buckling, that is, for the lowest possible value of T that buckles the beam. The linear results will be compared in the sequel with the lowest-order non-linear theory in the next subsection. The fundamental mode shapes of the buckled elastica using the linear approximation are plotted in the figure 8.6.

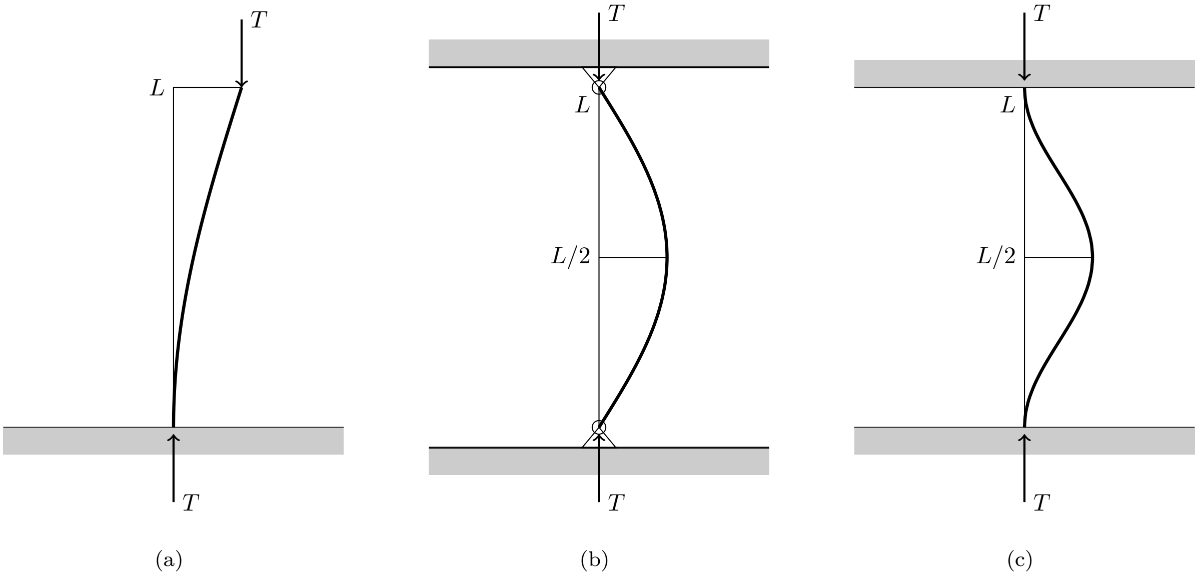

Figure 8.6: The critical buckling load for a beam under compression (figure 8.2) is the same in the linear and non-linear cases of small and large slope, respectively, and depends on the type of support. It is largest for clamping at both ends (right beam), intermediate if both ends are pinned (middle beam), and smallest for a cantilever beam clamped at one end and free at the other (left beam).

8.1.3 Lowest-order non-linear buckling for large slope

In the linear case of a small slope without forcing, the elastica satisfies a linear differential equation with constant coefficients of fourth order for the transverse displacement, as stated in the equation (8.21b). However, in the non-linear case of a large slope without forcing, regarding the definition (8.15a) that is equivalent to

$$\zeta' = \eta \left|1 - \eta^2\right|^{-1/2} \tag{8.24a}$$

used to derive the non-linear variable ζ as a function of η, the elastica satisfies a non-linear differential equation with constant coefficients of order three, using the equation (8.14c) with $f = 0$,

$$\left(\left|1 - \eta^2\right|^{1/2} \eta''\right)' + p^2 \eta' = 0, \tag{8.24b}$$

using the sine of the angle of inclination as a dependent variable that is non-linear. The last two expressions are valid for small or large deflections and can be linearised for small deflection, as in the section 8.1.2. However, although the relation (8.24a) is valid for any type of beam because it is a definition, the equation (8.24b) is only correct for uniform beams, in the absence of shear stress (to study the buckling phenomenon). Indeed, only uniform beams will be studied in the remainder of this chapter, and therefore, the comparison between different theories will be made only for that type of beams.

The differential equation (8.24b), for $p^2 \sim$ const because the beam is uniform, has a first integral

$$\left(\frac{A}{2} - p^2 \eta\right) \left|1 - \eta^2\right|^{-1/2} = \eta'' = \eta' \frac{\mathrm{d}\eta'}{\mathrm{d}\eta}, \tag{8.25a}$$

where A is an arbitrary constant. After rearranging the last expression in the form

$$2\eta' \mathrm{d}\eta' = A \left|1-\eta^2\right|^{-1/2} \mathrm{d}\eta - 2p^2 \left|1-\eta\right|^{-1/2} \eta \mathrm{d}\eta, \tag{8.25b}$$

it can be integrated [133] as

$$\eta'^2 = B + A \arcsin \eta + 2p^2 \left|1-\eta^2\right|^{1/2}, \tag{8.25c}$$

where B is another arbitrary constant. The last equation is still exact for a uniform beam without shear stress. Henceforth, there are two distinct approximations that can be done. The linear approximation of a small slope (8.1) implies $\eta^2 \leq \zeta'^2 \ll 1$ in (8.15a). Otherwise, the lowest-order non-linear approximation implies

$$\zeta'^4 \sim \eta^4 \ll 1, \tag{8.26a}$$

and if it is applied to (8.25c), then it results in

$$\eta'^2 = B + 2p^2 - p^2\eta^2 + A\eta, \tag{8.26b}$$

using only the leading terms of the power series for the square root or binominal [130] and for the arc of circular sine [39]. The integration of (8.26b) introduces another arbitrary constant C in

$$x + C = \int \left|B + 2p^2 + A\eta - p^2\eta^2\right|^{-1/2} \mathrm{d}\eta, \tag{8.26c}$$

which relates to the sine of the angle of inclination with the longitudinal coordinate of the beam, and is valid only for the lowest-order non-linear approximation (8.26a) and for the uniform beam, being valid (8.12a) and (8.12b).

The shape of the elastica, derived without any simplification, is given by the definition (8.24a) involving another constant of integration D in

$$\zeta(x) = D + \int^x \eta(\xi) \left|1 - [\eta(\xi)]^2\right|^{-1/2} \mathrm{d}\xi. \tag{8.27}$$

Thus, in the linear case of a small slope (8.1) and for a uniform beam, the shape of the elastica is given by (8.21c), while otherwise, in the lowest-order non-linear approximation (8.26a) also for a uniform beam, the shape of the elastica is given by (8.26c) and (8.27), in both cases involving four arbitrary constants plus the indeterminate value p. The four boundary conditions, two at each end of the beam: (i) specify three constants in terms of one, that is an arbitrary amplitude; and (ii) determine the eigenvalues p, of which the smallest specifies the critical buckling load, according to the definition (8.12c). It will be investigated in the sequel whether (i) the critical buckling load and (ii) the shape of the elastica are equal or different in the linear and non-linear cases of small (8.1) and moderate (8.26a) slopes, respectively. This will be ascertained by considering three classical cases of support by order of increasing critical buckling load in the linear case, namely: (i) cantilever beam in the section 8.2; (ii) pinned and clamped beams, both in section 8.3. In the case (i) of the cantilever beam, there is a boundary condition at the free end that is compared next (section 8.1.4) between the linear and non-linear cases of small and large slopes respectively.

8.1.4 Linear and non-linear boundary conditions at a free end

A cantilever beam, represented in the left scheme of the figure 8.6, is clamped at one end and free at the other end. Four boundary conditions must be known to evaluate the critical buckling load and the shape of the elastica. For a cantilever beam, the bending moment at the end of the beam is zero, $M(L) = 0$, and the transverse force must also vanish at that point, $F(L) = 0$. To obtain the force boundary condition at the free end, the equations (8.13a) to (8.13c) are used. The two aforementioned boundary conditions, regarding (8.13c) and (8.16) respectively, lead to the non-linear boundary conditions in terms of η, explicitly

$$\eta'(L) = 0, \tag{8.28a}$$

$$\left|1 - [\eta(L)]^2\right|^{1/2} \eta''(L) + p^2\eta(L) = 0. \tag{8.28b}$$

In the linear case of a small slope (8.1), the boundary conditions become

$$\zeta''(L) = 0, \tag{8.29a}$$

$$\zeta'''(L) + p^2\zeta'(L) = 0. \tag{8.29b}$$

On the other hand, in the non-linear case of an unrestricted slope, the free-end boundary condition of a zero-bending moment (8.16) is, in terms of the sine of the inclination of the elastica, equal to

$$\eta'(L) = 0 \tag{8.30a}$$

or, regarding (8.15a), in terms of the displacement of the elastica,

$$\zeta''(L)\left|1 + [\zeta'(L)]^2\right|^{-3/2} = 0. \tag{8.30b}$$

The free-end boundary condition of transverse force, again (8.13c) with (8.24a) for the case of an unrestricted slope, is

$$\eta''(L) + p^2\left|1 - [\eta(L)]^2\right|^{-1/2}\eta(L) = 0, \tag{8.31a}$$

or in terms (8.13a) of the displacement of the elastica

$$p^2\zeta'(L) + \left|1 + [\zeta'(L)]^2\right|^{-5/2}\left\{\zeta'''(L)\left|1 + [\zeta'(L)]^2\right| - 3\zeta'(L)\left[\zeta''(L)\right]^2\right\} = 0. \tag{8.31b}$$

The passage from (8.30a) to (8.30b) uses the equation (8.15a), while the passage from (8.31a) to

(8.31b) uses the next relation:

$$\eta'' = \left(\zeta'' \left|1+\zeta'^2\right|^{-3/2}\right)' = \left|1+\zeta'^2\right|^{-5/2} \left[\zeta''' \left(1+\zeta'^2\right) - 3\zeta'\zeta''^2\right]. \tag{8.32}$$

The boundary conditions for the displacement at the free end in the linear and non-linear cases of small and unrestricted slopes, respectively, of a uniform beam (when the equations (8.12a) to (8.12c) are valid): (i) coincide for the vanishing of the bending moment because (8.29a) is equivalent to (8.30b); (ii) however, do not coincide for the transverse force because (8.29b) is different from (8.31b), since the second term in (8.31b) differs from the first term in (8.29b).

8.2 Non-linear buckling of a cantilever beam

The non-linear equation of the elastica is integrated first for a cantilever beam (section 8.2.1) specifying the linear approximation (in agreement with section 8.2.2). The non-linear corrections are considered analytically for lowest-orders (section 8.2.3) and numerically for higher orders (section 8.2.4).

8.2.1 Non-linear elastica of a cantilever beam

The first integral of the differential equation for the elastica is (8.25a), arising from the integration of (8.24b), that is valid only for a uniform beam (and therefore the parameter p is constant because T and EI are also constants); however, it can be applied not only for linear, but also for the non-linear case. It involves a constant A and is rearranged in the next form:

$$\left|1-\eta^2\right|^{1/2} \eta'' + p^2\eta = A/2. \tag{8.33}$$

In the case of a cantilever beam, the transverse force must vanish at the free end, leading to the boundary condition (8.28b). Comparing to the last expression, then $A/2 = 0$, or $A = 0$. Consequently, the last condition simplifies the second integral (8.25c). Henceforth, in this section, the results are deduced with the lowest-order non-linear approximation (8.26a). With this approximation, the equation (8.26c) with $A = 0$ simplifies to

$$(x+C)\sqrt{B+2p^2} = \int \left|1-q^2\eta^2\right|^{-1/2} \mathrm{d}\eta = \frac{1}{q}\arcsin(q\eta), \tag{8.34a}$$

involving the constant

$$q = \frac{p}{\sqrt{B+2p^2}}. \tag{8.34b}$$

The primitive (8.34a) can be written in the form

$$\eta(x) = \frac{1}{q}\sin\left[q(x+C)\sqrt{B+2p^2}\right] = \sqrt{2+\frac{B}{p^2}}\sin\left[p(x+C)\right]. \tag{8.34c}$$

Up to this point, two assumptions were used: uniform beam and lowest-order non-linear approximation. The clamping boundary condition at the fixed end, $\zeta'(0) = 0$ (the slope of the elastica at that point must be zero), from (8.15a) which is an exact relation, implies $\eta(0) = 0$, and hence

$$0 = \eta(0) = \sqrt{2 + \frac{B}{p^2}} \sin(pC) \tag{8.35}$$

leading to the second result from the boundary conditions, $C = 0$. One could set $2 + Bp^{-2} = 0$ to verify the last boundary condition, but in that case, η would be equal to zero along the beam, and we are interested only in non-zero solutions of η and ζ. Substituting $C = 0$ in (8.34c) and introducing another non-zero arbitrary constant,

$$G \equiv \sqrt{2 + \frac{B}{p^2}}, \tag{8.36a}$$

lead to

$$\eta(x) = G \sin(px). \tag{8.36b}$$

In spite of $C = 0$ being valid, the more general solution of the last boundary condition would be $\sin(pC) = 0$ and consequently $\eta = G \sin(px) \cos(pC)$. However, in that case, the successive buckling loads and the shape of the elastica are the same as setting $C = 0$, which is simpler. The boundary condition stating that the bending moment vanishes at the free end, $M(L) = 0$, repeated here for convenience, is $\eta'(L) = 0$ in the non-linear case, and applied to (8.36b), considering that $\eta'(x) = pG\cos(px)$, it arrives at the condition $\cos(pL) = 0$. Thus, the successively buckling loads that make the beam unstable are

$$p_{3,n} L = \left(n - \frac{1}{2}\right)\pi, \tag{8.37}$$

where the first subscript 3 stands for the cantilever case, and the second subscript n stands for the n-th mode of the buckling.

Consequently, the critical buckling load is evaluated with the lowest possible value of the buckling parameter and it is equal to

$$p_{3,1} = \frac{\pi}{2L} \Rightarrow -T_3 = \frac{\pi^2 EI}{4L^2}, \tag{8.38}$$

which is the same in the linear (8.22b) and lowest-order non-linear (8.38) cases for a cantilever beam that is free to move at the free end. Knowing the sine of the slope of the elastica η, the non-linear slope ζ_3' is obtained substituting (8.36b) in the exact kinematic relation (8.24a):

$$\zeta_3'(x) = G\sin(px) \left|1 - G^2 \sin^2(px)\right|^{-1/2}. \tag{8.39}$$

To compare with the linear case, a relation between the constant G and another constant from the linear results is needed. In the linear case, $(\zeta_3')^2 \ll 1$ and the factor with the square root can be omitted. Then, the equation (8.39) in the linear case concerning the first mode of buckling (the results for this mode are shown in the section 8.1.3) leads to

$$\zeta_3'(x) = G\sin\left(p_{3,1}x\right) = G\sin\left(\frac{\pi x}{2L}\right). \tag{8.40a}$$

In agreement with the linear result (8.23c), the arbitrary constants G and b are related by

$$G = \frac{\pi b}{2L}, \tag{8.40b}$$

but generally, the relation must be $G = pb$.

In the non-linear case, the square root in (8.39) cannot be omitted. The assumption that the slope does not exceed unity, $|\zeta_3'| < 1$, leads, considering the exact relation (8.15a), to

$$G = |\eta_3(x)|_{\max} = |\zeta_3'| \left|1 + {\zeta_3'}^2\right|^{-1/2} < |\zeta_3'| < 1, \tag{8.41}$$

and thus the inverse square root in (8.39) can be expanded [39] in a binomial series,

$$\left|1 - G^2\sin^2\left(px\right)\right|^{-1/2} = \sum_{m=0}^{\infty} a_m G^{2m}\sin^{2m}\left(px\right), \tag{8.42}$$

with coefficients

$$\begin{aligned} a_m \equiv (-1)^m \binom{-1/2}{m} &= \frac{(-1)^m}{m!}\left(-\frac{1}{2}\right)\left(-\frac{1}{2}-1\right)\ldots\left(-\frac{1}{2}-m+1\right) \\ &= \frac{1}{m!}\frac{1}{2}\frac{3}{2}\ldots\frac{2m-1}{2} = \frac{(2m-1)!!}{m!2^m} = \frac{(2m-1)!!}{(2m)!!} = \frac{(2m)!}{[(2m)!!]^2} = \frac{(2m)!}{(m!)^2 2^{2m}}. \end{aligned} \tag{8.43}$$

The double factorial is used in the coefficients, whose its definition with some properties are reviewed in the next equations [39]:

$$\begin{aligned} (2m-1)!! &\equiv (2m-1)(2m-3)\ldots 5\cdot 3, \\ (2m)!! &\equiv 2m(2m-2)\ldots 4\cdot 2 = m!2^m, \\ (2m-1)!! = \frac{2m(2m-1)\ldots 3\cdot 2\cdot 1}{2m(2m-2)\ldots 4\cdot 2} &= \frac{(2m)!}{(2m)!!} = \frac{(2m)!}{m!2^m}. \end{aligned} \tag{8.44}$$

The first seven coefficients are indicated in table 8.1.

Coefficient	a_0	a_1	a_2	a_3	a_4	a_5	a_6
Numerical value	1	$\frac{1}{2}$	$\frac{3}{8}$	$\frac{5}{16}$	$\frac{35}{128}$	$\frac{63}{256}$	$\frac{231}{1024}$

Table 8.1: Numerical values for the first seven coefficients of the equation (8.43).

The coefficients (8.43) are valid for $m = 0, 1, \ldots$. The table 8.1 highlights the numerical results of the first seven coefficients. Thus, the slope of a uniform cantilever beam under axial compression is given by substituting the equation (8.42) in (8.39) that is equivalent to

$$\zeta_3'(x) = \sum_{m=0}^{\infty} a_m G^{2m+1} \sin^{2m+1}(px) = \sum_{m=0}^{\infty} \zeta_{3,m}'(x)\,. \tag{8.45}$$

The leading term, corresponding to $m = 0$ in the previous series, is the linear slope (deduced from the linear approximation) by comparing the last result with the equation (8.40a). The following terms are non-linear corrections of increasing order. Furthermore, the displacement can be obtained by integration of (8.45), and thus consists of the lowest-order linear approximation plus non-linear corrections of all orders that are evaluated next. At this point, in spite of having four boundary conditions for a cantilever beam, only three of them were used: the bending moment vanishing at $x = L$, the transverse force also vanishing at the same position, and the derivative of the elastica (its slope) at the beginning of the beam being zero.

8.2.2 Linear approximation and non-linear corrections of all orders

There is one last boundary condition that was not used yet: the beam is fixed at its beginning, and hence, the transversal displacement at that point is zero, $\zeta(0) = 0$. Integrating the equation (8.45), the displacement is given by a sum,

$$\zeta_3(x) = \sum_{m=0}^{\infty} \zeta_{3,m+1}(x), \tag{8.46a}$$

of terms

$$\zeta_{3,m+1}(x) \equiv a_m G^{2m+1} \int_0^x \sin^{2m+1}(p\xi)\,\mathrm{d}\xi. \tag{8.46b}$$

Note that in the equation (8.46a), there is no arbitrary constant of integration that is equal to zero, because of the boundary condition $\zeta(0) = 0$. Therefore, at this point, all four boundary conditions were used. The zero-order term is the linear approximation

$$\begin{aligned}\zeta_{3,1}(x) &= a_0 G \int_0^x \sin(p\xi)\,\mathrm{d}\xi = \frac{G}{p}\left[1 - \cos(px)\right] = \frac{2GL}{\pi}\left[1 - \cos(px)\right] \\ &= b\left[1 - \cos(px)\right] = 2b\sin^2\left(\frac{px}{2}\right),\end{aligned} \tag{8.47}$$

where (8.38) and (8.40b) were used to prove the third and fourth equalities successively in agreement with (8.23c). The lowest-order non-linear correction is

$$\begin{aligned}\zeta_{3,2}(x) &= a_1 G^3 \int_0^x \sin^3(p\xi)\,\mathrm{d}\xi = \frac{G^3}{2}\int_0^x \sin(p\xi)\left[1 - \cos^2(p\xi)\right]\,\mathrm{d}\xi \\ &= \frac{G^3}{2p}\left\{1 - \cos(px) + \frac{1}{3}\left[\cos^3(px) - 1\right]\right\} = \frac{G^3}{6p}\left\{2 - \cos(px)\left[3 - \cos^2(px)\right]\right\} \\ &= \frac{G^3}{24p}\left[8 - 9\cos(px) + \cos(3px)\right] = \frac{G^3}{12p}\left[9\sin^2\left(\frac{px}{2}\right) - \sin^2\left(\frac{3px}{2}\right)\right]\end{aligned} \tag{8.48}$$

where the value of a_1, indicated in table 8.1, and some elementary trigonometric relations [133] were used in the determination of $\zeta_{3,2}$.

The two lowest-order terms in (8.46a) have been evaluated explicitly in (8.47) corresponding to the first term, and (8.48) corresponding to the second term, in the case of a lowest-order non-linear approximation $(\zeta')^4 \ll 1$. To estimate the error of the truncation of the series (8.46a), the higher-order terms in (8.46b) may be considered. In order to explicitly evaluate the m-th order, the expansion of the odd power of sine [133] is used as a sum of sines of multiple angles:

$$\sin^{2m+1}(p\xi) = (-1)^m 2^{-2m} \sum_{j=0}^{m} \left\{ (-1)^j \binom{2m+1}{j} \sin[(2m-2j+1)p\xi] \right\}. \tag{8.49}$$

Substituting the last expression in the m-th order, the non-linear correction (8.46b) becomes

$$\begin{aligned} \zeta_{3,m+1}(x) &= a_m G^{2m+1} \int_0^x \sin^{2m+1}(p\xi)\,\mathrm{d}\xi \\ &= \frac{a_m}{p} G^{2m+1} (-1)^m 2^{-2m} \sum_{j=0}^{m} \left\{ (-1)^j \binom{2m+1}{j} \frac{1-\cos[(2m-2j+1)px]}{2m-2j+1} \right\} \\ &= \frac{a_m}{p} G^{2m+1} (-1)^m 2^{1-2m} \sum_{j=0}^{m} \left\{ \frac{(-1)^j}{2m-2j+1} \binom{2m+1}{j} \sin^2\left[\left(m - j + \frac{1}{2} \right) px \right] \right\}; \end{aligned} \tag{8.50}$$

it can be confirmed that substituting $m = 0$ and $m = 1$ in the last expression leads, respectively, to (8.47) and (8.48). The maximum deflection at the tip, considering the fundamental mode of buckling and regarding (8.38), is given by

$$\zeta_3(L) = \frac{2L}{\pi} \sum_{m=0}^{\infty} \left\{ a_m G^{2m+1} (-1)^m 2^{-2m} \sum_{j=0}^{m} \frac{(-1)^j}{2m-2j+1} \binom{2m+1}{j} \right\} \tag{8.51}$$

that relates the constant G to the maximum deflection.

8.2.3 Truncation of the series in the shape of the elastica

The exact shape of the buckled cantilever beam is given by the sum of the series (8.46a), having infinite terms. The series converges when $G < 1$ and diverges when $G > 1$. Therefore, $G < 1$ is a necessary condition to evaluate the series (8.46a). To obtain accurate results, only the first terms $\zeta_{3,m}$ need to be evaluated, and m can be small. The table 8.2 shows the number of iterations (the number of terms of the series) needed to calculate the sum (8.46a) with absolute and relative errors smaller than 10^{-15}; that is, the iterations stop when the difference between two consecutive terms, $\zeta_{3,m}$ and $\zeta_{3,m+1}$, is smaller than 10^{-15}, and when the ratio between that difference and the last term evaluated $\zeta_{3,m+1}$ is also smaller than 10^{-15}. To have an error with such a small order of magnitude, few terms are needed, for instance, with respect to the fundamental mode of buckling (with $n = 0$, for a beam with length $L = 0.8$, only the first 10 terms are needed). Furthermore, one can conclude that the number of iterations is intrinsically related to the value G for each case. When G becomes closer to 1, which is the boundary of convergence of the series, more iterations are needed to converge with the same error. For instance, looking at the data of table 8.2, the case when more iterations are needed is when $n = 2$ and $L = 0.8$, because it is the case when G is closest to 1. The parameter G is equal to $pb = (n - 1/2)\,\pi b/L$. Consequently, for the same parameter b, more iterations are necessary to obtain accurate results for shorter beams and for higher modes of buckling, corresponding to larger slope and stronger non-linearity, as highlighted in table 8.2.

	Number of Terms | Parameter G							
Order n	**Length L**							
	0.8	**1**	**2**	**3**	**4**	**5**	**6**	**7**
1	10 | 0.196	9 | 0.157	7 | 0.079	6 | 0.052	5 | 0.039	5 | 0.031	5 | 0.026	5 | 0.022
2	30 | 0.589	21 | 0.471	11 | 0.236	9 | 0.157	8 | 0.118	7 | 0.094	7 | 0.079	6 | 0.067

Table 8.2: Number of non-linear terms necessary to evaluate the sum in (8.46a) with absolute and relative errors smaller than 10^{-15}, for each length L of the beam and for the first two orders of the buckling load. It also shows the constant G for each case. The parameter b is equal to 0.1.

One specific example of the non-linear theory of buckling is illustrated next in the case of a cantilever beam, for which the linear approximation to the shape of the elastica (8.46a) is just the first term of the sum, substituting $m = 0$ in (8.50), or equivalently, the result (8.47). However, the exact shape using the lowest-order non-linear approximation is given by the infinite sum in (8.46a), and the table 8.2 highlights that when G is close to 1, the number of necessary terms increases very rapidly, possibly requiring a larger computational effort to obtain accurate results. Therefore, in the case of an arbitrary amplitude, the value $G = 0.8$, that satisfies (8.41) being close to the limit, is chosen to understand if the shape can be deduced with very few terms. The linear approximation ($m = 0$) of the shape of the elastica is

$$p\zeta_{3,1}(x) = 0.8[1 - \cos(px)] = 1.6\sin^2\left(\frac{px}{2}\right). \tag{8.52}$$

The dimensionless variables $p\zeta$ and px are used for plotting the successive iterations of the sum (8.46a) in the figure 8.7, to make the results not dependent on the explicit values of the order of buckling n and the length L. Considering now the non-linear terms, the corresponding lowest-order non-linear correction ($m = 1$) is

$$p\zeta_{3,2} \approx 0.02133[8 - 9\cos(px) + \cos(3px)] \approx 0.04266\left[9\sin^2\left(\frac{px}{2}\right) - \sin^2\left(\frac{3px}{2}\right)\right], \tag{8.53}$$

that is also plotted in the figure 8.7.

The total non-linear deflection of the buckled cantilever beam, using the lowest-order non-linear approximation (also plotted in the figure 8.7), shows that the maximum deflection of the fundamental mode of buckling, that occurs at $pL = \pi/2$, is $p\zeta_{3,1} = 0.8$ in the linear approximation, to which the first non-linear correction adds $p\zeta_{3,2} \approx 0.1707$, leading to the total value $p\,(\zeta_{3,1} + \zeta_{3,2}) \approx 0.9707$. The linear approximation (8.52), over its whole length, $0 \leq px \leq \pi/2$, leads to a monotonic shape of the elastica because

$$\frac{\mathrm{d}p\zeta_{3,1}}{\mathrm{d}x} = 0.8\sin(px) > 0. \tag{8.54}$$

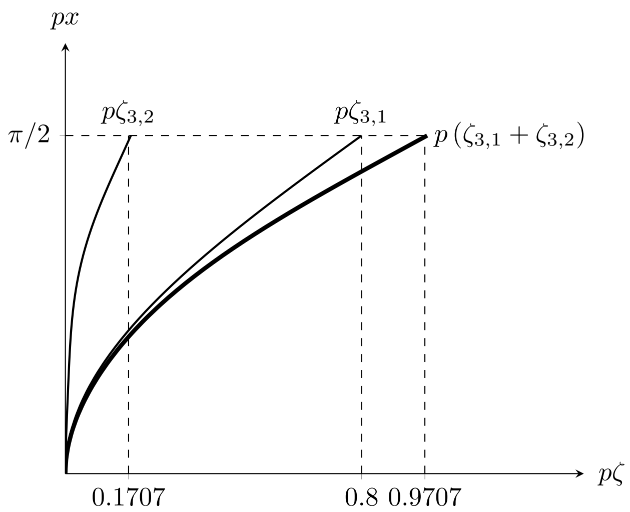

Figure 8.7: Different mode shapes of the buckled elastic cantilever beam for the fundamental mode of buckling.

The lowest-order non-linear correction (8.53) is also monotonic, since

$$\frac{\mathrm{d}p\zeta_{3,2}}{\mathrm{d}x} \approx 0.064[3\sin(px) - \sin(3px)] > 0, \tag{8.55}$$

thus increasing the deflection everywhere, and consequently, the maximum deflection is at the end of the beam. It is at that point where the difference between the linear approximation and the lowest-order non-linear correction is at its maximum.

The non-linear corrections of all higher orders (8.46a) are specified by (8.50), including the maximum deflection at the tip (8.51), and since they go beyond the hypothesis $(\zeta')^4 \ll 1$, they serve only as order-of-magnitude estimates of the error caused by truncating the non-linear series after the first non-linear term. The second-order non-linear correction, setting $m = 2$ in (8.50), would introduce the factor $a_2 = 3/8$ multiplied by a term, giving the result of order $3G^5/64 \approx 0.015$, that is a correction of approximately 6.3% compared with $p(\zeta_{3,1} + \zeta_{3,2})$. This would be hardly visible in the plot of the figure 8.7 that is limited to the sum of the linear approximation (8.52) plus the lowest-order non-linear correction (8.53). Thus, the buckled shape of a cantilever beam, for $0 \leq px \leq \pi/2$, is given exactly by (8.50) to all orders in the amplitude G, with the lowest-order non-linear approximation consisting of the linear approximation (8.47) and lowest-order non-linear correction (8.48). The higher-order terms go beyond the approximation $(\zeta')^4 \ll 1$ and apply only as an indication of the order of magnitude of the error due to stopping at the lowest-order non-linear correction; for example, the order of magnitude of the lowest-order non-linear approximation is sufficient, summing (8.52) with (8.53) in the case $G = 0.8$ to obtain the shape of the elastica using only the first two iterations (figure 8.7) with less than 7% in the accuracy error.

The non-linear shape of the buckled elastica in the post-buckling regime can be represented as a superposition of harmonics of the elastica in the linear approximation. In the case illustrated of a cantilever beam with moderate non-linearity, the buckled shape is approximated by a superposition of the fundamental and second harmonics with a suitable ratio of the amplitudes of the two terms, calculated using the method detailed in this chapter.

8.2.4 Numerical results for the buckling of a cantilever beam

The figures 8.8 to 8.10 are obtained using many more iterations of the series (8.46a) than the first two terms; they are obtained with 30 terms, that is, calculating the first 30 terms of the series, to obtain more accurate results, although the difference is not as significant as using only the first two terms. The figures show a solution for each case of the differential equation that specifies the shape of the elastica of a cantilever beam. To obtain the solution, it was assumed that $C = 0$; however, a more general condition would be $\sin(pC) = 0$, leading to $\eta = G\sin(px)\cos(pC)$ with $\cos(pC) = \pm 1$. The plots of the figures are obtained with $\cos(pC) = 1$, but one can assume $\cos(pC) = -1$, meaning that $-\eta$ is also a valid solution, and consequently, $-\zeta$. Therefore, ζ and $-\zeta$ are the two possible solutions for each case (in the plots, only one of them is sketched), meaning that the beam can buckle on one side or on the opposite side with equal probability.

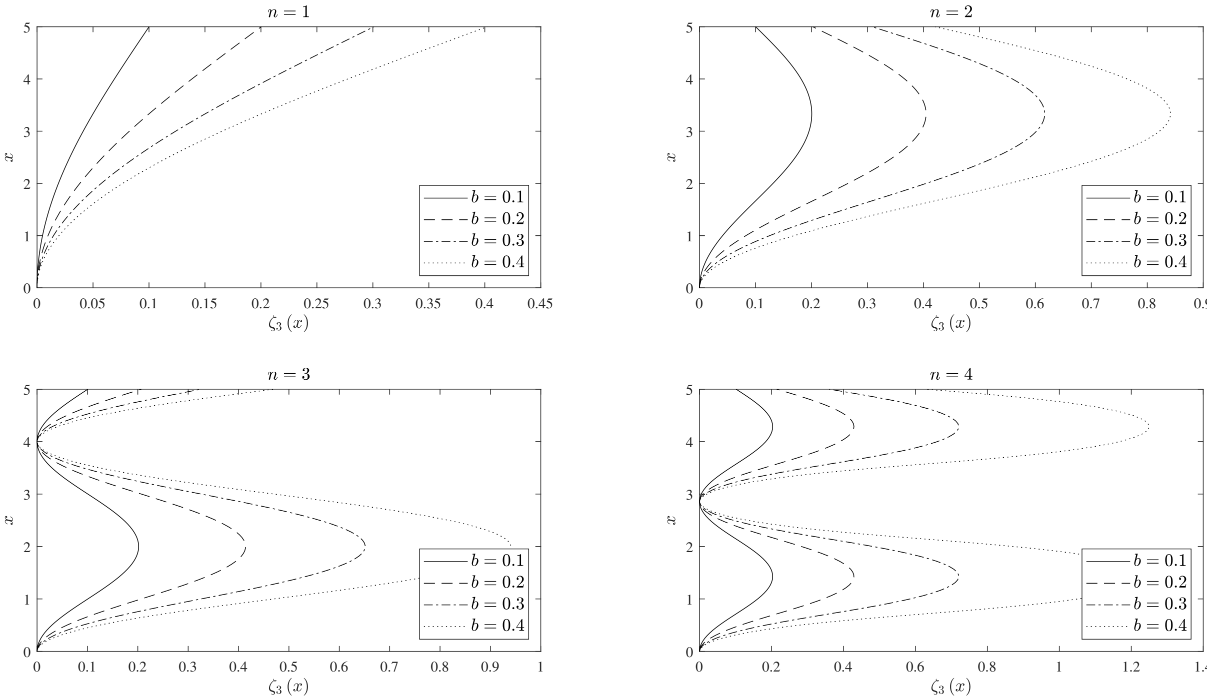

Figure 8.8: Different mode shapes of the buckled elastic cantilever beam for the four lowest buckling forces, $n = 1, \dots, 4$, as functions of the indeterminate constant b. The length of the beam is $L = 5$.

The figure 8.8 shows the effect of varying the indeterminate real constant b on the several mode shapes of the buckled elastic cantilever beam for the first four orders of buckling. The constant b only serves to obtain numerical results of ζ and does not influence the shape of the elastica. The effect of b is only on the magnitude of the elastica, not altering the positions of maximum and minimum deflection of the beam. These observations are valid independently of the order n and length of the beam L. For the fundamental mode of buckling, the shape of the beam increases monotonically, leading to a maximum amplitude at the tip, and for higher modes of buckling, the shape oscillates along the beam, leading to alternate peaks and nulls of the oscillation. Increasing the order n leads to more peaks and nulls because the period of the trigonometric functions is shorter.

The effect of length L on the shapes of the buckled elastic cantilever beam for the first four orders

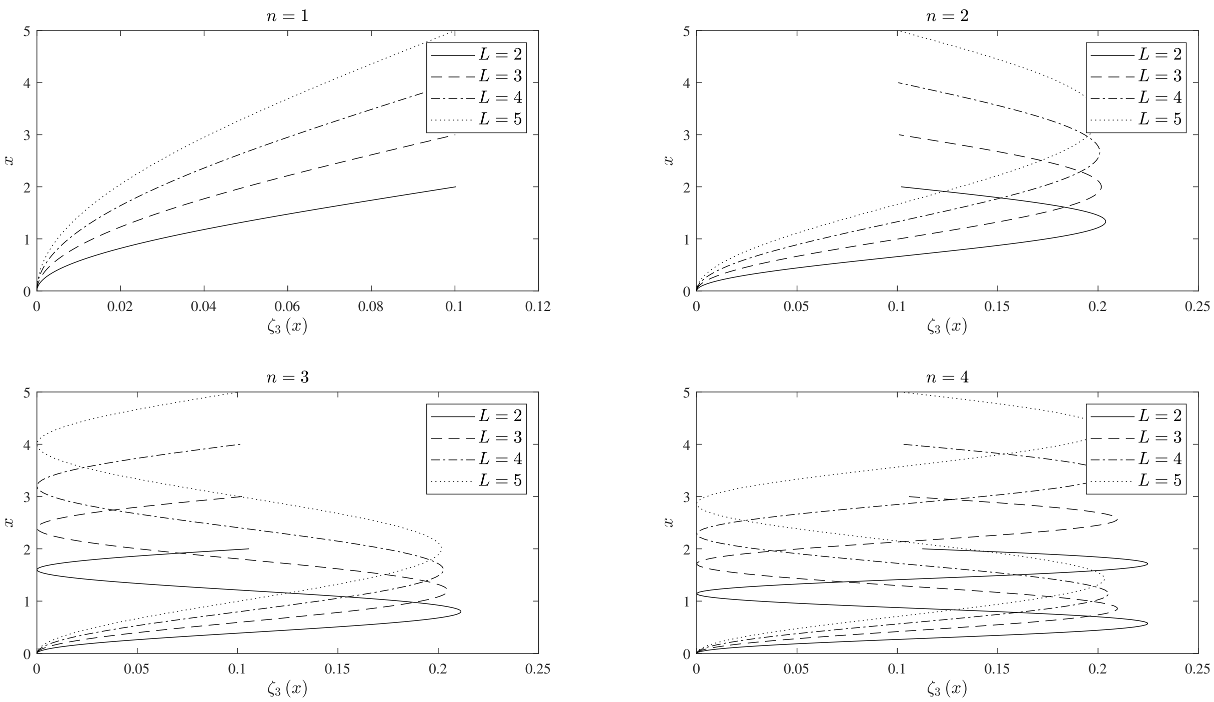

Figure 8.9: Different mode shapes of the buckled elastic cantilever beam for the four lowest buckling forces, $n = 1, \ldots, 4$, as functions of the length L of the beam. The indeterminate constant is set as $b = 0.1$.

of buckling is shown in the figure 8.9. Changing the length L does not significantly influence the values of maximum deflection, although this effect is more significant for higher modes of buckling. For longer beams, the maximum deflection of the buckled beam is lower. The reason is because, according to the equation (8.50), each term of the series (8.46a) is proportional to $G^{2m} = (pb)^{2m}$, and consequently, is proportional to L^{-2m}. The length L has a more significant effect in the positions of maximum deflection of the beam. While L is increasing, the period of the sine functions also becomes longer, and therefore, looking at the plots of figure 8.9 in a down-top approach, one can conclude that the first maximum occurs for the shorter beam, while the last maximum occurs for the longer beam.

In the figure 8.10, the difference between the linear approximation ($m = 0$) and the higher-order terms of the non-linear approximation ($m \geq 1$) is shown for several lengths and for the first four orders of buckling. The linear approximation is less accurate for shorter beams and for higher orders of buckling. The conclusion is the same as in the table 8.2. According to the table 8.2, more iterations are needed for shorter beams and for higher values of n, and therefore, the difference induced by the non-linear terms of the series (8.46a) is higher for these cases. A shorter beam and higher-order modes lead to “ripples” with a large slope (see figure 8.2), and thus larger non-linear effects. Furthermore, the maximum difference between the two levels of approximation occurs at the extreme amplitudes of the deformation of the beam, independently of the parameters n and L. The maximum difference therefore occurs when the derivative of ζ is zero, and is again more noticeable for shorter beams and higher values of n. For the fundamental mode of buckling ($n = 1$), the difference is negligible, and therefore, one can use the linear approximation to obtain accurate results. Moreover, comparing the two approximations, the beam buckles more when the lowest-order non-linear approximation is used than the linear approximation;

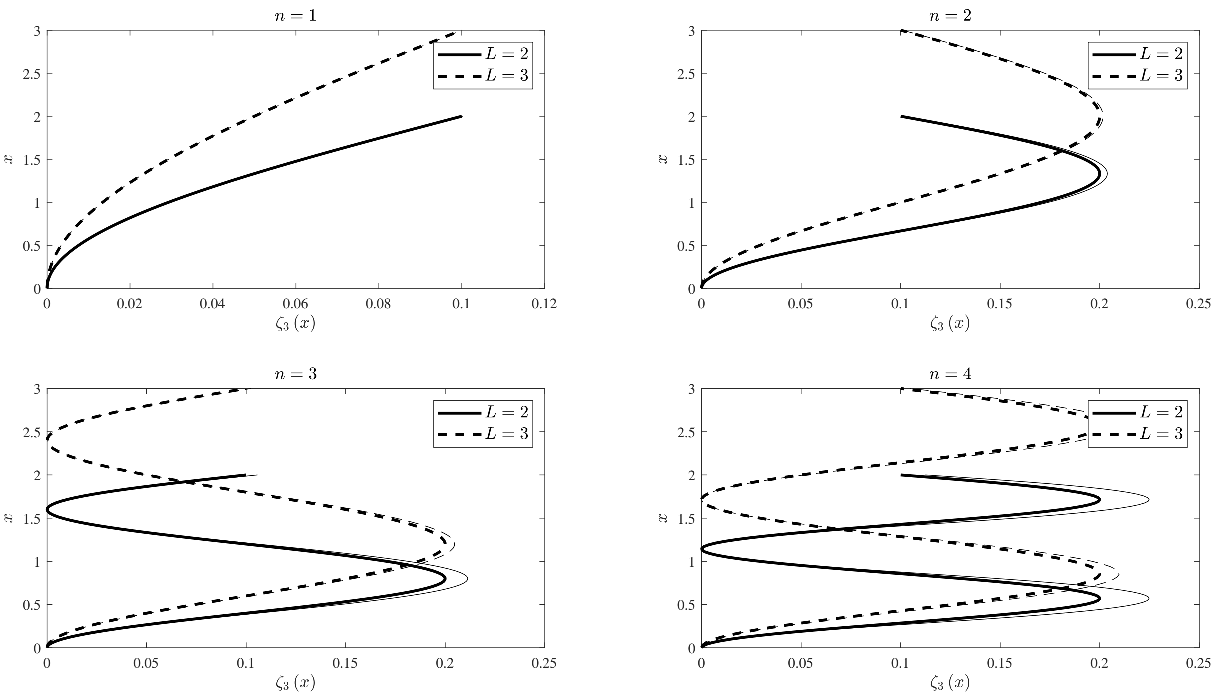

Figure 8.10: Comparison of the mode shapes of the buckled elastic cantilever beam assuming a small slope (thick lines), $(\zeta')^2 \ll 1$, or assuming the lowest-order non-linear slope (thin lines), $(\zeta')^4 \ll 1$, for the four lowest buckling forces, $n = 1, \ldots, 4$. The indeterminate constant is set as $b = 0.1$, and the length of the beam is $L = 2$ or $L = 3$.

that is, for the same axial tension and parameters of the beam, the value of the deflection obtained with the linear approximation is lower than with the non-linear approximation. Consequently, the linear approximation underestimates the strength of the buckling loads, and the rigidity of the beam appears to be higher in the linear case.

The lowest-order non-linear theory of the elastica of a buckled beam (section 8.1) is extended next from the cantilever beam (section 8.2) to pinned and clamped beams (section 8.3).

8.3 Non-linear buckling of clamped and pinned beams

The lowest-order non-linear theory of buckling (section 8.3.1) applies not only to a cantilever beam (section 8.2), but also to clamped and pinned beams (section 8.3.2), showing that, in all cases, the critical buckling load is the same as in the linear case (section 8.3.3), but the shape of the buckled elastica is due to the generation of linear harmonics, that is illustrated numerically (section 8.3.4).

8.3.1 Non-linear effects of large slope

The critical buckling load for a cantilever beam was shown to coincide in the linear (8.22b) and lowest-order non-linear (8.38) cases. Two possible explanations are that: (i) a cantilever beam can move at the free end; or (ii) the buckling is a linear phenomenon, and thus its onset is not affected by non-linear effects. The first explanation (i) can be tested by determining the critical buckling load of non-cantilever beams using the lowest-order non-linear theory. For a non-cantilever beam, the simplification $A = 0$ does not hold, because $F(L) = 0$ is not a boundary condition for pinned nor clamped beams. In the equation (8.26c), valid for uniform beams and simultaneously using the lowest-order non-linear approximation, the argument of the square root is written as

$$2p^2 + B + A\eta - p^2\eta^2 = 2p^2 + B + \frac{A^2}{4p^2} - \left(p\eta - \frac{A}{2p}\right)^2. \tag{8.56}$$

The constant G is now defined by

$$G^2 \equiv 2 + \frac{B}{p^2} + \left(\frac{A}{2p^2}\right)^2, \tag{8.57a}$$

so that in the case of a cantilever beam, $A = 0$ and then G coincides with the earlier definition (8.36a), and in (8.56) appears the square of a new dependent variable

$$z = \eta - \frac{A}{2p^2}. \tag{8.57b}$$

Substitution of (8.57a) and (8.57b) in (8.26c) leads to the integration [39]:

$$p(x + C) = \int \frac{\mathrm{d}\eta}{\sqrt{G^2 - z^2}} = \frac{1}{G}\int \frac{\mathrm{d}z}{\sqrt{1 - z^2/G^2}} = \arcsin\left(\frac{z}{G}\right). \tag{8.58}$$

Inverting (8.58), while using the new variables (8.57a) and (8.57b), specifies the sine of the slope, given by

$$\eta = H + G\sin\left[p(x + C)\right], \tag{8.59a}$$

hence it specifies the respective curvature and the bending moment, using (8.15b), given by

$$M = -EIGp\cos\left[p(x + C)\right] \tag{8.59b}$$

with amplitudes

$$H = \frac{A}{2p^2}, \tag{8.59c}$$

$$G^2 = 2 + \frac{B}{p^2} + H^2. \tag{8.59d}$$

The three arbitrary constants (A, B, C) may be replaced by (H, G, C), and the equations from (8.59a) to (8.59d) are valid for uniform clamped and pinned beams, considering the lowest-order non-linear approximation. Although H and G can simultaneously be zero, η would also be equal to zero and be a valid solution, but we are interested in only non-zero solutions of η and ζ.

8.3.2 Coincidence of linear and non-linear critical buckling loads

In the case of a beam clamped at both ends (right beam of the figure 8.6), from (8.15a) follow the boundary conditions $\eta(0) = 0$ and $\eta(L) = 0$, stating that the slope is zero at the start and end of the beam, and the two boundary conditions imply by (8.59a) that

$$H + G\sin(pC) = 0, \tag{8.60a}$$

$$H + G\sin(pC + pL) = 0. \tag{8.60b}$$

The compatibility of (8.60a) and (8.60b) requires

$$\sin(pC) = \sin(pC + pL), \tag{8.61a}$$

that leads to the next buckling forces:

$$p_{1,n}L = 2n\pi, \tag{8.61b}$$

where the subscript 1 stands for a clamped beam; thus, the critical buckling load for a clamped beam is determined by substituting the lowest possible value, $n = 1$, in the last expression,

$$p_{1,1} = \frac{2\pi}{L}. \tag{8.61c}$$

By comparing the results (8.22a) and (8.61c), the critical buckling load for the uniform clamped beam is the same in the linear theory and in the lowest-order non-linear theory.

From (8.59a), the curvature of the elastica (8.15b) is given by

$$k(x) = pG\cos[p(x + C)]. \tag{8.62}$$

In the case of a beam pinned at both ends (middle beam of the figure 8.6), the vanishing of the curvature at the start and end of the beam, respectively $k(0) = 0$ and $k(L) = 0$, leads to

$$\cos(pC) = 0 \tag{8.63a}$$

and

$$\cos(pC + pL) = 0 \tag{8.63b}$$

that are compatible for

$$p_{2,n}L = n\pi, \tag{8.63c}$$

where the subscript 2 stands for a pinned beam; thus, the critical buckling load for a pinned beam is obtained by substituting the lowest possible value $n = 1$ in the last expression, and is the same in the linear (8.22c) and lowest-order non-linear theories, repeated here for convenience

$$p_{2,1} = \frac{\pi}{L}. \tag{8.63d}$$

This dismisses the conjecture (i) and supports the conjecture (ii) at the beginning of this section, showing that the critical buckling load coincides in the linear and lowest-order non-linear theories because buckling is an instability triggered at linear level. The results for the linear theory are indicated in (8.22a) to (8.22c). The coincidence of the critical buckling loads does not extend to the shape of the buckled elastica (section 8.3.3) because the square of the slope appears in the curvature in the equation (8.6a).

8.3.3 Non-linear effects of the harmonics in the shape of the buckled elastica

The lowest-order non-linear approximation for the slope suggests (8.26a) and includes one order beyond the linear approximation for the shape (8.27) of the elastica,

$$\zeta(x) = \int_0^x \eta(\xi)\left\{1 + \frac{1}{2}[\eta(\xi)]^2\right\} \mathrm{d}\xi. \tag{8.64}$$

The constant D can be omitted either for clamped or pinned beams, because the transversal displacement is zero at the start of both beams, $\zeta(0) = 0$. The substitution of (8.59a) leads to

$$\begin{aligned}\zeta(x) = \int_0^x \Bigg[& H\left(1 + \frac{H^2}{2}\right) + G\left(1 + \frac{3H^2}{2}\right)\sin(p\xi + pC) \\ & + \frac{3HG^2}{2}\sin^2(p\xi + pC) + \frac{G^3}{2}\sin^3(p\xi + pC)\Bigg] \mathrm{d}\xi.\end{aligned} \tag{8.65}$$

The change of variable

$$\Psi = p\xi + pC \tag{8.66a}$$

leads to

$$\begin{aligned}p\zeta(x) = \int_{pC}^{px+pC} \Bigg[& H\left(1 + \frac{H^2}{2} + \frac{3G^2}{4}\right) + G\left(1 + \frac{3H^2}{2} + \frac{G^2}{2}\right)\sin\Psi \\ & - \frac{3HG^2}{4}\cos(2\Psi) - \frac{G^3}{2}\sin\Psi\cos^2\Psi\Bigg] \mathrm{d}\Psi.\end{aligned} \tag{8.66b}$$

Some trigonometric relations [133] are used to allow immediate integration:

$$\begin{aligned}\zeta(x) = {} & H\left(1 + \frac{H^2}{2} + \frac{3G^2}{4}\right)x + \frac{G}{p}\left(1 + \frac{3H^2}{2} + \frac{G^2}{2}\right)[\cos(pC) - \cos(px + pC)] \\ & + \frac{3HG^2}{8p}[\sin(2pC) - \sin(2px + 2pC)] + \frac{G^3}{6p}\left[\cos^3(px + pC) - \cos^3(pC)\right].\end{aligned} \tag{8.66c}$$

To deduce the last equation, valid for uniform clamped or pinned beams and using the lowest-order non-linear approximation, only one boundary condition was used, $\zeta(0) = 0$, when there was a total of four boundary conditions to be used. The shape of the elastica (8.66c) involves not only the buckling parameter or eigenvalue p, but also the constants G, H and C, adding up to four values to be determined, while there are three boundary conditions to be applied. Consequently, with four unknowns and three boundary conditions, there is always an arbitrary constant in the final results of the elastica, and thus it is only possible to determine its shape, but not explicit values.

In the case of the clamped beam, the possible buckling loads are given by the equation (8.61b), and using those values on the equation (8.66c), two boundary conditions have implicitly been used because the value of p is deduced from two boundary conditions, as demonstrated in the section 8.3.2. The fourth and last boundary condition to be used for the clamped beam is $\zeta(L) = 0$. For the successive values of p in the case of a clamped beam, $\sin(pL) = 0$ and $\cos(pL) = 1$. Consequently, for the clamped beam, $\cos(pL + pC) = \cos(pC)$ and $\sin(2pL + 2pC) = \sin(2pC)$. These two results are important to apply the last boundary condition. Substituting it in (8.66c) and knowing the last two results, the first relation between constants is

$$H\left(1 + \frac{H^2}{2} + \frac{3G^2}{4}\right) = 0; \tag{8.67a}$$

the second relation is one of (8.60a) or (8.60b), for example, the first one which is simpler and is repeated here,

$$H + G\sin(pC) = 0. \tag{8.67b}$$

The two previous relations express two constants in terms of the third constant. The pair of equations has two solutions other than the trivial case $G = 0 = H$, namely: (i) choosing $H = 0$, then, from (8.67b) follows $\sin(pC) = 0$; (ii) otherwise, from (8.67a), one can set $G^2 = -4/3 - 2H^2/3$, and consequently, the equation (8.67b) implies $\csc(pC) = -G/H$. However, in the case (ii), independently of the value H, the real constant G^2 is negative, which is an impossible condition. Therefore, only the case (i) is possible, setting $H = 0$, and consequently, $\sin(pC) = 0$ with $\cos(pC) = \pm 1$. Regarding these last conditions in the equation (8.66c), the shape of the elastica for a clamped beam, assuming $\cos(pC) = 1$, is

$$\zeta_1(x) = \frac{G}{p}\left(1 + \frac{G^2}{2}\right)[1 - \cos(px)] + \frac{G^3}{6p}\left[\cos^3(px) - 1\right]. \tag{8.68}$$

Assuming $\cos(pC) = -1$ would lead to the solution $-\zeta_1$, that is also a valid shape of the elastica.

In the case of a pinned beam, the successive valid buckling loads (8.63c) were inferred from two boundary conditions, as explained in the section 8.3.2. The fourth and last boundary condition to be used is again $\zeta(L) = 0$. Knowing that the buckling parameter is $p = n\pi/L$, then $\sin(pL) = 0$ and $\cos(pL) = 1$; consequently, $\sin(2pL + 2pC) = \sin(2pC)$, and therefore the last boundary condition leads to

$$\begin{aligned}0 = {} & H\left(1 + \frac{H^2}{2} + \frac{3G^2}{4}\right) + \frac{G}{p}\left(1 + \frac{3H^2}{2} + \frac{G^2}{2}\right)[\cos(pC) - \cos(pL + pC)] \\ & + \frac{G^3}{6p}\left[\cos^3(pL + pC) - \cos^3(pC)\right];\end{aligned} \tag{8.69}$$

the other boundary conditions indicated in the subsection 8.3.2 for pinned beams, (8.63a) and (8.63b), simplify (8.69) to (8.67a), and for the same reason as in the clamped beam, H is also zero for the pinned beam. Hence, the shape of the elastica for this case is (8.66c) with $H = 0$ and $\cos(pC) = 0$, and then simplifies to

$$\zeta_2\left(x\right) = \frac{G}{p}\left(1 + \frac{G^2}{2}\right)\sin\left(px\right) - \frac{G^3}{6p}\sin^3\left(px\right). \tag{8.70}$$

To deduce the above expression, it was assumed that $\sin\left(pC\right) = 1$, but it is also possible to assume $\sin\left(pC\right) = -1$, meaning that not only ζ_2, but also $-\zeta_2$ are valid solutions of the differential equation.

Thus, the shape of the buckled elastica in the lowest-order non-linear theory, therefore assuming (8.26a), is given by (8.66c) for a uniform beam clamped or pinned at the two ends, and then the sine of the slope (8.15a) of the buckled elastica in both beams is given by (8.59a). The critical buckling load is the same in linear and lowest-order non-linear theories, and is equal to (8.22a) or (8.22c) for a beam clamped or pinned, respectively. With respect to the shape of the elastica, the three constants (G, H and C), for a clamped beam, satisfy $H = 0$ and $\sin\left(pC\right) = 0$; for a pinned beam, they satisfy $H = 0$ and $\cos\left(pC\right) = 0$. In all the cases, there is one undetermined constant, namely G, and in both situations the parameter can be related to the parameter of linear approximation, b. The absence of non-linear effects on the critical buckling load and the presence of non-linear effects on the shape of the elastica can be explained in terms of the non-linear generation of harmonics, as shown next.

In the simplest case of a cantilever beam (8.37), the fundamental mode (8.23a) is the particular case $n = 1$ of the succession (8.37) of buckling harmonics,

$$\zeta_{3,n}(x) = Q\left\{1 - \cos\left[\frac{\pi x}{L}\left(n - \frac{1}{2}\right)\right]\right\}, \tag{8.71a}$$

using the linear approximation in the last equation and with increasing loads of buckling,

$$-T_{3,n} = \frac{\pi^2 EI}{L^2}\left(n - \frac{1}{2}\right)^2 = -4T_{3,1}\left(n - \frac{1}{2}\right)^2. \tag{8.71b}$$

The critical buckling load (8.22b) is the lowest load that corresponds to the fundamental buckling mode (8.23c). The non-linear theory (8.46a) leads to the generation of harmonics (8.50), changing the shape of the buckled elastica, but not the lowest critical buckling load.

In the case of clamped beams, where the equation (8.61b) can be used, and considering the linear approximation, there is also a succession of buckling harmonics,

$$\zeta_{1,n}(x) = Q\left[1 - \cos\left(\frac{2\pi n x}{L}\right)\right], \tag{8.72a}$$

with increasing loads,

$$-T_{1,n} = \frac{4\pi^2 EIn^2}{L^2} = -n^2 T_{1,1}, \tag{8.72b}$$

defining again the critical buckling load being the lowest load, which is equal to (8.22a) and corresponds to the fundamental buckling mode (8.23a).

In the case of pinned beams, using in this case the equation (8.63c) and again the linear approximation, a succession of buckling harmonics also exists,

$$\zeta_{2,n}(x) = Q\sin\left(\frac{n\pi x}{L}\right), \tag{8.73a}$$

with increasing loads,

$$-T_{2,n} = \frac{\pi^2 EIn^2}{L^2} = -n^2 T_{2,1}, \tag{8.73b}$$

and the critical buckling load in this type of beam is equal to (8.22c) that corresponds to the fundamental buckling mode (8.23b).

Otherwise, although the critical buckling loads are the same, the shape of the elastica changes if the linear approximation is not used. Considering the lowest-order non-linear approximation, for the clamped beam, the shape of the elastica (8.68), for instance when assuming $n = 1$ to deduce the fundamental mode of buckling, is given by

$$\zeta_1(x) = \frac{GL}{2\pi}\left(1+\frac{G^2}{2}\right)\left[1-\cos\left(\frac{2\pi x}{L}\right)\right] - \frac{G^3 L}{12\pi}\left[1-\cos^3\left(\frac{2\pi x}{L}\right)\right]. \tag{8.74a}$$

For the pinned beam, the shape of the elastica (8.70), assuming again the fundamental mode, therefore using in this case the equations (8.63d), is given by

$$\zeta_2(x) = \frac{GL}{\pi}\left(1+\frac{G^2}{2}\right)\sin\left(\frac{\pi x}{L}\right) - \frac{G^3 L}{6\pi}\sin^3\left(\frac{\pi x}{L}\right). \tag{8.74b}$$

For the cantilever beam, and assuming again the fundamental mode, the lowest-order non-linear approximation is the sum of (8.47) and (8.48), $\zeta_3(x) = \zeta_{3,1}(x) + \zeta_{3,2}(x)$, leading to

$$\begin{aligned}\zeta_3(x) &= \frac{2GL}{\pi}\left[1-\cos\left(\frac{\pi x}{2L}\right)\right] + \frac{G^3 L}{\pi}\left[1-\cos\left(\frac{\pi x}{2L}\right)+\frac{\cos^3\left(\frac{\pi x}{2L}\right)-1}{3}\right] \\ &= \frac{2GL}{\pi}\left(1+\frac{G^2}{2}\right)\left[1-\cos\left(\frac{\pi x}{2L}\right)\right] - \frac{G^3 L}{3\pi}\left[1-\cos^3\left(\frac{\pi x}{2L}\right)\right],\end{aligned} \tag{8.75}$$

that coincides with the case equivalent to (8.72a) of clamping at $x = 0$ with the free end at $x = L$ implying $A = 0$ and $H = 0$, hence following the conditions $A/2 = 0$ and $H = A/\left(2p^2\right)$.

8.3.4 Numerical results for the buckling of a clamped and pinned beams

The figures 8.11 to 8.13 are obtained using the lowest-order non-linear expression (8.68) and show the shape of the elastica using the lowest-order non-linear approximation for the clamped beams. To obtain the solution, it was assumed that $\cos(pC) = 1$; however, a more general condition would be $\cos(pC) = \pm 1$, leading to $\zeta = \pm\zeta_1$ with ζ_1 given by the expression (8.68). The plots of the figures are obtained with $\cos(pC) = 1$, but $\cos(pC) = -1$ can also be assumed, meaning that $-\zeta_1$ is also a valid solution. Therefore, ζ_1 and $-\zeta_1$ are the two possible solutions for each case (in the plots, only one of them is sketched), meaning that the beam can buckle on both sides with equal probability.

The figure 8.11 shows the effect of varying the indeterminate real constant b on the several mode shapes of the buckled elastic clamped beam for the four first orders of buckling. The constant b, as in the case of a cantilever beam, only serves to specify the amplitude of ζ_1 and does not influence the shape of the elastica. The effect of b is only on the magnitude of the elastica, not altering the positions of maximum and minimum deflection of the beam. These observations are valid independently of the order

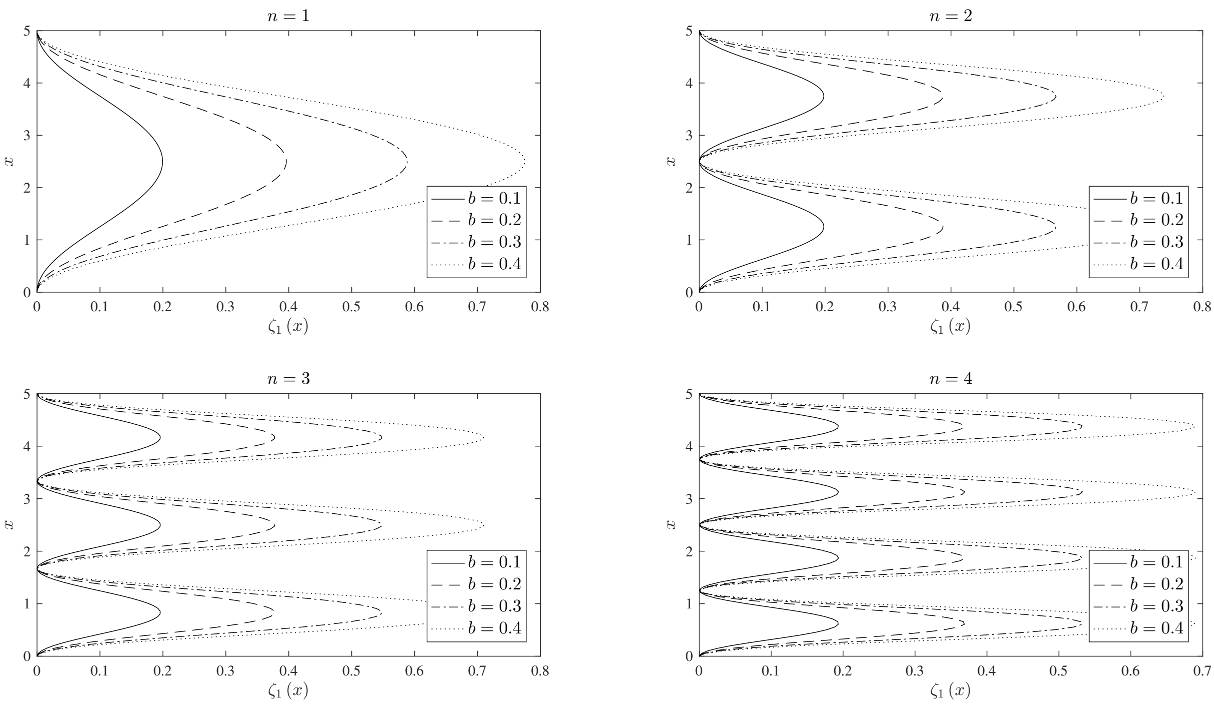

Figure 8.11: Different mode shapes of the buckled elastic clamped beam for the four lowest buckling forces, $n = 1, \ldots, 4$, as functions of the indeterminate constant b. The length of the beam is $L = 5$.

n and length of the beam L. However, for the fundamental mode of buckling, the shape of the beam does not increase monotonically, and the maximum amplitude is not at the tip, but is at the middle span of the beam. Not only for the fundamental mode, but also for higher modes of buckling, the shape oscillates along the beam, leading to alternate peaks and nulls of the oscillation. Increasing the order n leads to more peaks and nulls because the period of the trigonometric functions is shorter. The number of peaks and nulls (with nulls meaning points where there is no deflection) are, respectively, n and $n+1$, where n is the order of the mode (two nulls are at the beginning and end of the beam due to the imposed boundary conditions on the displacement).

The effect of length L on the shapes of the buckled elastic clamped beam for the first four orders of buckling is shown in the figure 8.12. As in the case of the cantilever beam, changing the length L does not significantly influence the maximum values of deflection, although this effect is more significant for higher modes of buckling. For longer beams, the maximum deflection of the buckled beam is higher. According to the equation (8.68), and in agreement to the linear approximation, the relation between the constants G and p is given by the relation

$$G\left(1+\frac{G^2}{2}\right)=pb \tag{8.76a}$$

and therefore the equation (8.68) can be simplified to

$$\zeta_1 = b\left[1-\cos\left(px\right)\right]+\frac{G^3}{6p}\left[\cos^3\left(px\right)-1\right]. \tag{8.76b}$$

Keeping constant the variables n and b, from (8.76a) for $G^2 < 1$, then $G \sim pb$, and thus $G^3/p \sim p^2 b \sim$

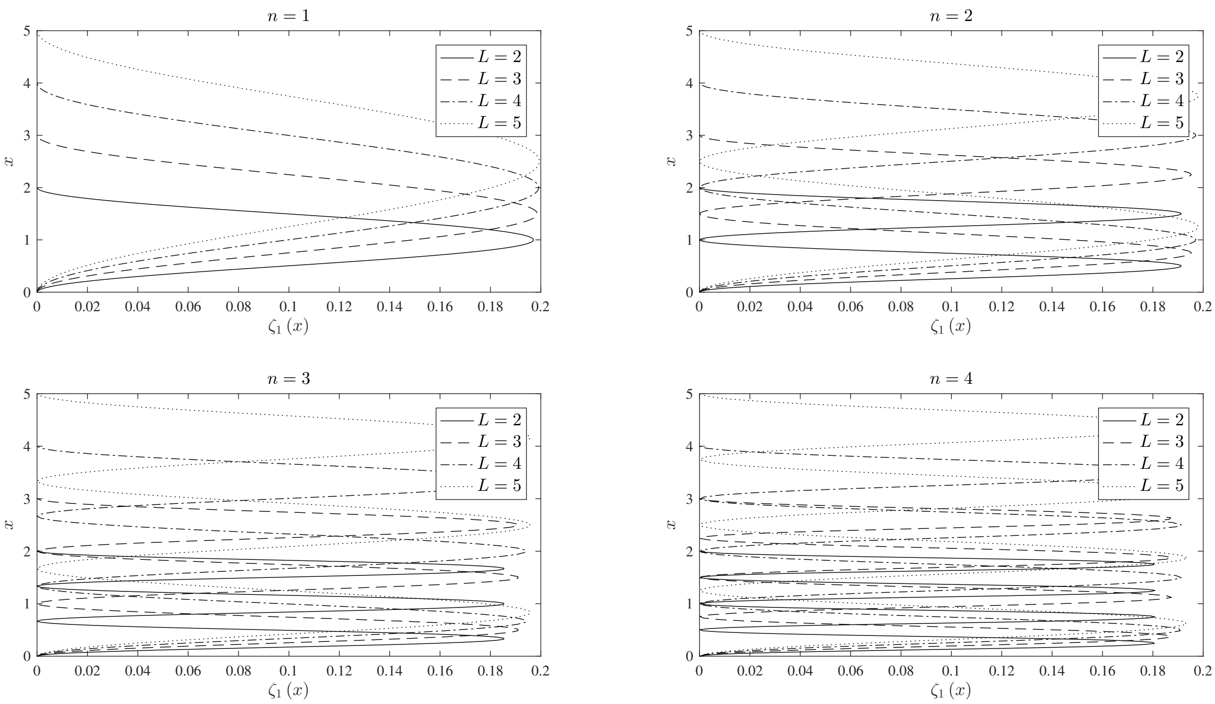

Figure 8.12: Different mode shapes of the buckled elastic clamped beam for the four lowest buckling forces, $n = 1, \ldots, 4$, as functions of the length L of the beam. The indeterminate constant is set as $b = 0.1$.

$n^2\pi^2 b/L^2$ decreases with increasing the length of the beam. Thus, the coefficient in the second term on the right-hand side of (8.76b) decreases for increasing L, and since the term in square brackets is negative, the value of ζ_1 increases. Therefore, the non-linear correction in the second term on the right-hand side of (8.76b) leads to a larger maximum deflection for the increasing length of the beam, as seen in figure 8.12. The length L has a more significant effect in the positions of maximum deflection of the beam. As in the case of a cantilever beam, while L is increasing, the period of the cosine functions also becomes longer, and therefore, looking at the plots of figure 8.12 from a down-top approach, one can conclude that the first maximum occurs for the shorter beam, while the last maximum occurs for the longer beam.

In the figure 8.13, the difference between the linear approximation and the lowest-order non-linear approximation is shown for several lengths and for the first four orders of buckling. The linear approximation is less accurate for shorter beams and for higher orders of buckling. It is the same conclusion as in the case of a cantilever beam. Furthermore, the maximum difference between the two levels of approximation occurs at the extreme amplitudes of the deformation of the beam, independently of the parameters n and L. The maximum difference therefore occurs when the derivative of ζ is zero, and again is more noticeable for shorter beams and higher values of n. For the fundamental mode of buckling ($n = 1$), the difference is negligible, and therefore, one can use the linear approximation to obtain accurate results. Moreover, comparing the two approximations, the beam buckles less when the lowest-order non-linear approximation is used than the linear approximation; that is, for the same axial tension and parameters of the beam, the value of the deflection obtained with the linear approximation is higher than with the non-linear approximation (it is opposite to the cases of cantilever and clamped beams). Consequently, the linear approximation overestimates the strength of the buckling loads, and the rigidity of the beam

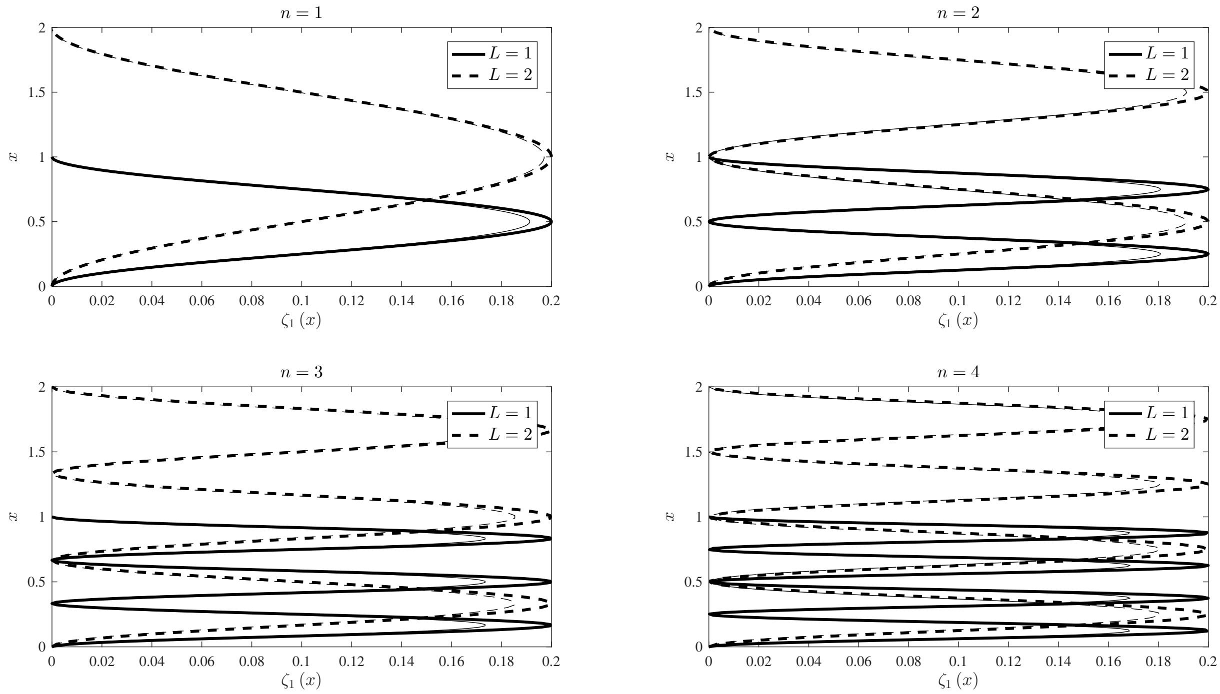

Figure 8.13: Comparison of the mode shapes of the buckled elastic clamped beam assuming small slope (thick lines), $(\zeta')^2 \ll 1$ or assuming a lowest-order non-linear slope (thin lines), $(\zeta')^4 \ll 1$, for the four lowest buckling forces, $n = 1, \ldots, 4$. The indeterminate constant is set as $b = 0.1$, and the length of the beam is $L = 1$ or $L = 2$.

appears to be lower in this case.

The figures 8.14 to 8.16 were obtained using exactly the expression (8.70), and show the shape of the elastica using the lowest-order non-linear approximation for the pinned beams. To obtain the solution, it was assumed that $\sin(pC) = 1$; however, a more general condition would be $\sin(pC) = \pm 1$, leading to $\zeta = \pm\zeta_2$ with ζ_2 given by the expression (8.70). The plots of the figures are obtained with $\sin(pC) = 1$, and assuming instead $\sin(pC) = -1$ means that $-\zeta_2$ is also a valid solution. Therefore, ζ_2 and $-\zeta_2$ are the two possible solutions for each case (in the plots, only one of them is sketched), meaning that the beam can buckle on the one side or in a symmetric way with equal probability.

The figure 8.14 shows the effect of varying the indeterminate real constant b on the several mode shapes of the buckled elastic clamped beam for the four first orders of buckling. The conclusions about the effect of varying b are the same as in the case of clamped beams. The number of peaks is equal to n, and the number of nulls (points where there is no deflection) is equal to $n + 1$, where n is the order of the mode.

The effect of length L on the shapes of the buckled elastic pinned beam for the first four orders of buckling is shown in figure 8.15. In this case, changing the length L does not significantly influence the values of maximum deflection, even for higher modes of buckling. By increasing the length of the beam, the maximum deflection of the buckled beam remains almost constant. As in the case of a cantilever and clamped beams, while L is increasing, the period of the sine functions also becomes longer, and therefore, looking at the plots of figure 8.15 from a down-top approach, one can conclude that the first maximum occurs for the shorter beam, while the last maximum occurs for the longer beam.

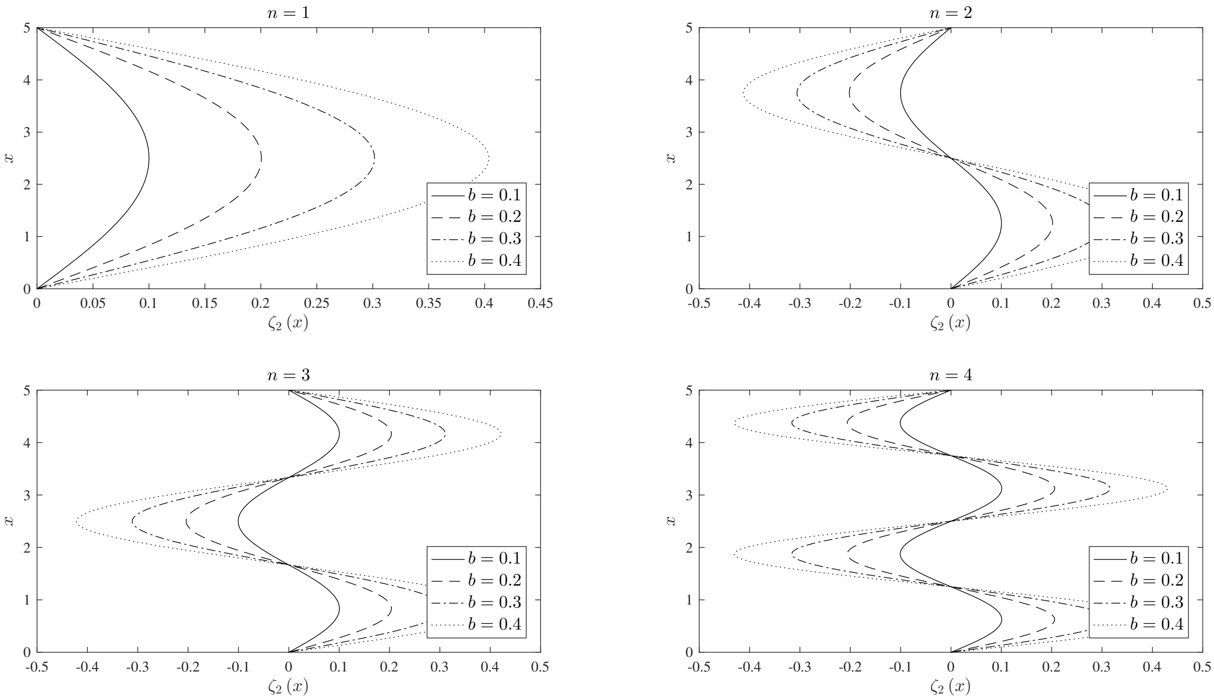

Figure 8.14: Different mode shapes of the buckled elastic pinned beam for the four lowest buckling forces, $n = 1, \ldots, 4$, as functions of the indeterminate constant b. The length of the beam is $L = 5$.

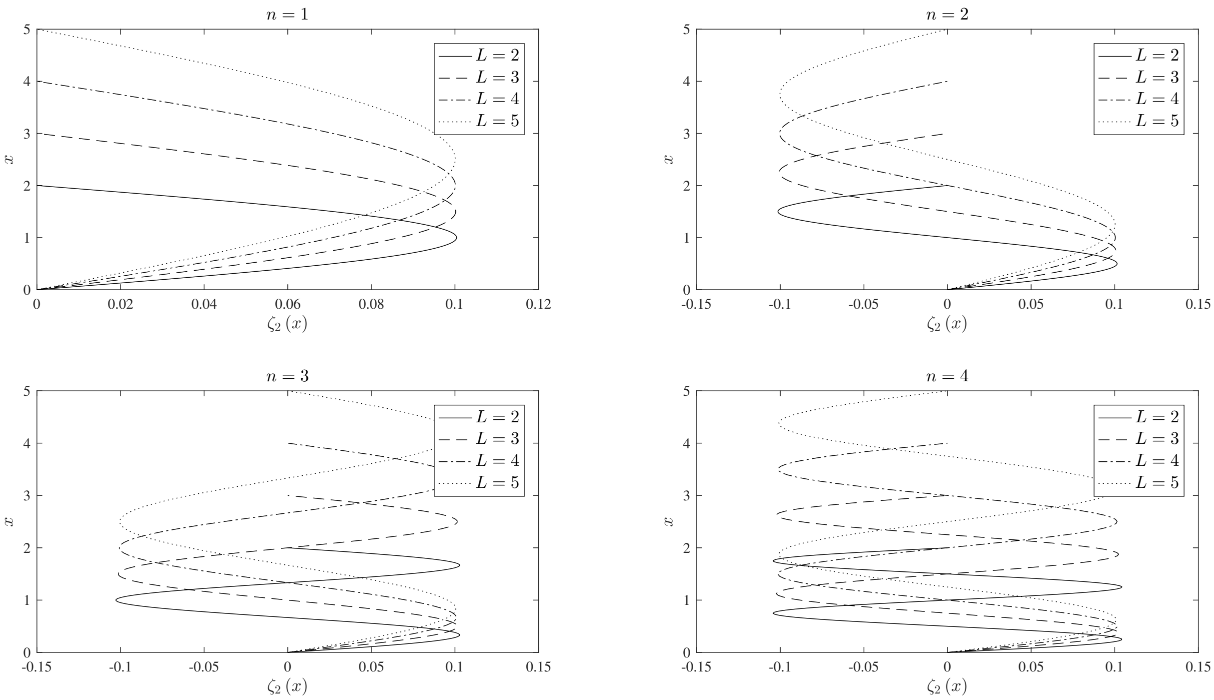

Figure 8.15: Different mode shapes of the buckled elastic pinned beam for the four lowest buckling forces, $n = 1, \ldots, 4$, as functions of the length L of the beam. The indeterminate constant is set as $b = 0.1$.

In the figure 8.16, the difference between the linear approximation and the lowest-order non-linear approximation is shown for several lengths and for the first four orders of buckling. The linear approximation is less accurate for shorter beams and for higher orders of buckling. Moreover, comparing the two approximations, the beam buckles more when the lowest-order non-linear approximation is used than the

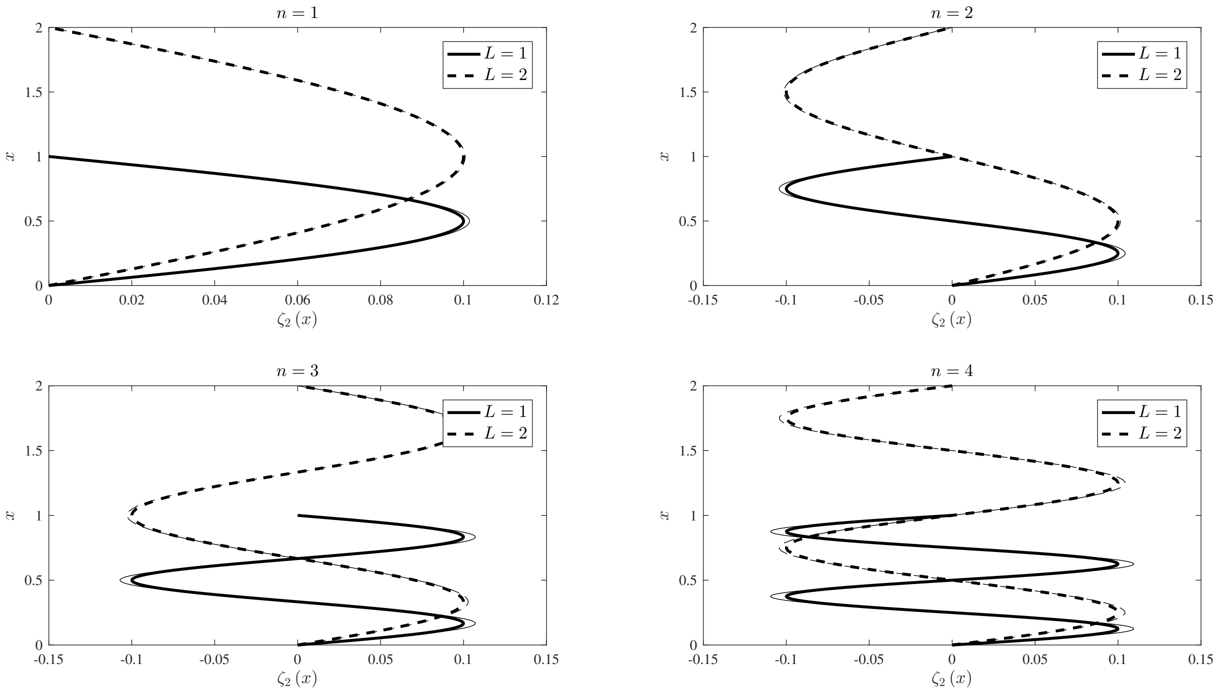

Figure 8.16: Comparison of the mode shapes of the buckled elastic pinned beam assuming a small slope (thick lines), $(\zeta')^2 \ll 1$ or assuming a lowest-order non-linear slope (thin lines), $(\zeta')^4 \ll 1$, for the four lowest buckling forces, $n = 1, \ldots, 4$. The indeterminate constant is set as $b = 0.1$, and the length of the beam is $L = 1$ or $L = 2$.

linear approximation; that is, for the same axial tension and parameters of the beam, the value of the deflection obtained with the linear approximation is lower than with the non-linear approximation (it is similar to the case of the cantilever beam and opposite to the case of a pinned beam). Consequently, the linear approximation underestimates the strength of the buckling loads, and the rigidity of the beam appears to be higher in this case. These conclusions are the same as in the cantilever beam and opposite to the pinned beams.

Shorter beams and higher-order modes lead to "ripples" with larger slope (figure 8.2) and stronger non-linear effects for all cases of support (cantilever, pinned or clamped).

8.4 Main conclusions of the chapter 8

For a cantilever or pinned or clamped beam, the linear buckling (using the linear approximation) corresponds to a succession of increasing axial loads, given respectively by (8.71b), (8.72b), and (8.73b), and corresponding harmonics, given respectively by (8.71a), (8.72a), and (8.73a) for the buckled shape of the elastica. Buckling first occurs for the smallest axial load corresponding to the fundamental buckled shape. The non-linear effect is to add harmonics to the fundamental mode; therefore, the first consequence is: (i) not changing the critical buckling load, which remains the lowest; (ii) changing the buckled shape of the elastica by superimposing on the fundamental linear mode its harmonics with specified amplitudes. The non-linear shape of the buckled elastica has been illustrated (a) for cantilever, pinned and clamped beams, respectively, in the figures 8.8–8.16; (b) each figure consists of four panels, one each for the fundamental mode $n = 1$, and for the following three modes $n = \{2, 3, 4\}$; (c) the first of each set of the three figures, namely, the figures 8.8, 8.11 and 8.14, shows the effect of changing amplitudes among four values; (d) the second of each set of the three figures, namely, the figures 8.9, 8.12 and 8.15, shows the effect of changing the length of the beam among four values; (e) the last of each set of three figures, namely, the figures 8.10, 8.13 and 8.16, indicates the magnitude of non-linear effects relative to the linear approximations. In all cases, the non-linear effects are more significant for higher-order modes of shorter beams, leading to "ripples" with a large slope (figure 8.2) compared with the smoother or less undulated fundamental mode (figure 8.1).

The table 8.3 compares the values of the successive loads (the first five orders) that can buckle the beam for the three cases studied between the linear and lowest-order non-linear approximations. Because the expressions to deduce the buckling loads are precisely the same in the two approximations, the table 8.3 shows that the critical values obtained in this chapter are exactly the same as that in the literature [77–79, 219] which considers linearisation of the equations.

		Buckling orders $\left(\times EI/L^2\right)$				
Beam	**Reference**	**1st**	**2nd**	**3rd**	**4th**	**5th**
Clamped	Present method	39.478	157.914	355.306	631.655	986.960
	Literature [77–79]	39.478	157.914	355.306	631.655	986.960
Pinned	Present method	9.870	39.478	88.826	157.914	246.740
	Literature [77–79]	9.870	39.478	88.826	157.914	246.740
Cantilever	Present method	2.467	22.207	61.685	120.903	199.859
	Literature [77–79]	2.467	22.207	61.685	120.903	199.859

Table 8.3: Successive buckling orders for clamped, pinned and cantilever beams, and comparison of numerical values between the method proposed on this chapter and the cited literature [77–79].

The critical buckling load can be changed by using translational or rotational springs that favour or oppose buckling [82], and the shape of the buckled elastica is further modified by transverse concentrated or distributed forces [130]. The two aspects of (i) the critical buckling load and (ii) the shape of the buckled elastica are implicit in the vast literature on the non-linear buckling of beams and have been made explicit using the theory of Euler–Bernoulli beams in its simplest form. The tables 8.4, 8.5 and 8.6 show the maximum numerical absolute errors between the linear approximation, used in the vast literature, and the lowest-order non-linear approximation, used in this chapter, for several lengths L of the beam, for the first four orders of buckling n and for each type of beam. For all three types of beams, the difference is more significant for shorter beams and for higher orders of buckling.

The solution of (8.6a) shows that the exact non-linear shape of the elastica is a superposition of harmonics of the linear problem (8.6b) where: (i) the fundamental buckling mode is determined from the linear approximation $(\zeta')^2 \ll 1$; and (ii) the generation of harmonics is a non-linear effect. The current approach to the non-linear theory of bending with a large scale of Euler–Bernoulli beams uses therefore a method that is different from the classical and more recent research, in that it represents non-linear effects as a generation of harmonics.

The representation of the non-linear buckled elastica by a series of linear harmonics is an alternative

Order n	Length L						
	1	**2**	**3**	**4**	**5**	**6**	**7**
1	0.866	0.288	0.137	0.079	0.051	0.036	0.027
2	1.909	0.866	0.469	0.288	0.193	0.137	0.102
3	2.612	1.423	0.861	0.563	0.392	0.286	0.217
4	3.131	1.909	1.252	0.866	0.626	0.469	0.363

Table 8.4: Maximum difference between the linear and lowest-order non-linear approximations of the deformation of the buckled clamped beam for several lengths of the beam and for the first four orders of the buckling load. The parameter b is equal to 0.1. The results are multiplied by 100.

Order n	Length L						
	1	**2**	**3**	**4**	**5**	**6**	**7**
1	0.144	0.040	0.018	0.010	0.007	0.005	0.003
2	0.433	0.144	0.069	0.040	0.026	0.018	0.013
3	0.0714	0.283	0.144	0.085	0.056	0.040	0.029
4	0.955	0.433	0.235	0.144	0.096	0.069	0.051

Table 8.5: Maximum difference between the linear and lowest-order non-linear approximations of the deformation of the buckled pinned beam for several lengths of the beam and for the first four orders of the buckling load. The parameter b is equal to 0.1. The results are multiplied by 100.

Order n	Length L						
	1	**2**	**3**	**4**	**5**	**6**	**7**
1	0.083	0.021	0.009	0.005	0.003	0.002	0.002
2	1.716	0.383	0.167	0.093	0.059	0.041	0.030
3	6.975	1.135	0.477	0.263	0.167	0.085	0.079
4	–	2.484	0.976	0.528	0.332	0.229	0.167

Table 8.6: Maximum difference between the linear and lowest-order non-linear approximations of the deformation of the buckled cantilever beam for several lengths of the beam and for the first four orders of the buckling load. The parameter b is equal to 0.1. The results are multiplied by 100.

to the classical solutions in terms of elliptic functions. This is an example of the fact that the answer to the same problem can have quite different representations. Two equivalent representations can be quite different in terms of the information they highlight, and this is the case here. There are three main differences: (i) the use of a series of elementary functions is more straightforward than the use of special functions; (ii) the elliptic functions are difficult to visualise, whereas the linear harmonics are more intuitive; (iii) the decomposition into linear harmonics shows, through their amplitudes, which are excited most, and give a more significant contribution to the final shape of the elastica. The latter information (iii) is totally missing from the solution in terms of elliptic functions. Among the different solutions to the same problem, it is often the simplest one that is most illuminating.

9 | On twin perturbation expansions for non-linear bending of plates

"If you would be a real seeker after truth, it is necessary that at least once in your life you doubt, as far as possible, all things."

— René Descartes

Contents

THE weak bending of a plate [129, 152, 241] is described by the transverse displacement and causes negligible in-plane stresses. The in-plane stresses [77, 133, 153, 242] are described by a stress function and, in the linear approximation, are decoupled from bending. The non-linear bending [79, 243, 244] corresponds to a large slope of the directrix that may be associated with large displacements and non-uniform in-plane stresses. The mathematical model used is based on the Föppl-von Kármán equations that assume (i) a linear or elastic stress-strain relation and (ii) small cross-terms of the displacement. The solution of a non-linear problem may be reduced to a sequence of linear problems employing perturbation expansions [245–247] that are widely used, including in the context of the theory of elasticity [248]. Thus, the strong non-linear bending is described by two variables (section 9.1), namely the transverse displacement and stress function, and they satisfy two differential equations that must be: (i) non-linear due to the large displacements, strains and stresses; (ii) coupled because a large bending displacement is associated with non-uniform in-plane stresses and vice-versa. The particular case of strong bending of a circular plate has received the most attention [249] by several methods, including analytical [250] or asymptotic [251] solutions and wavelet [252] or perturbation [253, 254] methods. A variational principle

[255] can obtain the fundamental equations and a uniqueness theorem has been proved [256]. The non-linear bending has been extended from homogeneous to functionally graded thin plates [257].

The first non-linear differential equation is the stress balance for the transverse displacement in the weak bending of a plate, which also applies to strong bending with non-constant in-plane stresses specified by the stress function (subsection 9.1.1). A second coupled equation relating the stress function and transverse displacement is obtained (subsection 9.1.3) from the exact strain tensor. The strain tensor has contributions from the transverse displacement, in-plane linear displacements and in-plane non-linear displacements (subsection 9.1.2). Neglecting the latter, the elastic energy (section 9.2) has contributions from the transverse displacement, in-plane displacements and their non-linear coupling (subsection 9.2.1): equating the variation of the total elastic energy to the work of transverse and in-plane forces leads to the balance equations (subsection 9.2.2) and boundary conditions (subsection 9.2.3). The boundary conditions involve: (i) the stress couples; (ii) the augmented turning moment, including the effect of in-plane stresses. The augmented turning moment adds, to the usual turning moment for the linear bending of elastic plates, an additional term involving the gradient of the normal displacement.

The solution of the balance equations together with the boundary conditions can be obtained (section 9.3) using twin perturbation expansions for the transverse displacement and in-plane stress function. In most applications of perturbation expansions [245–247], only the second or third order can be obtained explicitly. Exceptionally in the present case, the perturbation expansions for the Föppl-von Kármán equations can be obtained exactly and explicitly to all orders (subsection 9.3.1). The perturbation equations form a linear causal chain of ordinary differential equations, with biharmonic operators and forcing specified by the lower orders. In the axisymmetric case (subsection 9.3.2), the infinite system of double recurrent equations is simplified (subsection 9.3.3).

The non-linear coupling of bending and in-plane stresses can be calculated precisely to all orders (section 9.4) if the transverse force is a polynomial of the radius or an analytic function of the radius specified by a power series; the solution is set in finite terms in the case of a polynomial transverse force and by a convergent power series in the case when the transverse force is an analytic function of the radius (subsection 9.4.1). It is proved that if the perturbation parameter is less than unity, the perturbation expansion is bounded and the perturbation series is convergent. A simple particular example is a heavy circular plate (subsection 9.4.2) under axial compression (subsection 9.4.3). The method determines (section 9.5) the coupled transverse displacement and stress function (subsection 9.5.1), leading to all strain and stress components (subsection 9.5.2) and checking compliance with the boundary conditions (subsection 9.5.3).

The perturbation expansion provides a family of solutions. A unique choice to the perturbation parameter is made (section 9.6) such that the work of the external forces equals the elastic energy of deformation (subsection 9.6.1). The value of the perturbation parameter is (subsection 9.6.2) a real root of a polynomial of degree $M = 2N - 1$ in the case of a perturbation expansion to order N. A single root, with $M = 1$, is obtained for a first-order perturbation expansion, $N = 1$. The value of the perturbation parameter increases for thicker plates relative to the radius and stiffer plates relative to the weight (subsection 9.6.3). This completes the illustration of the general theory (section 9.7) of strong bending of elastic plates taking into account the non-linear coupling with in-plane stresses. The fundamental coupled non-linear equations for an elastic isotropic plate [151, 158, 258] can be extended to a pseudo-isotropic orthotropic plate (appendix E).

9.1 Coupling of the stress function and transverse displacement

The Föppl-von Kármán equations [79] for the coupling of the transverse displacement and in-plane stresses (subsection 9.1.1) in the strong bending of an elastic plate are derived (subsection 9.1.2) by a direct method (subsection 9.1.3) that is consistent with an alternative energy method (section 9.2). The direct method indicates the conditions of validity of the balance equations; these are confirmed by the variational method that also provides the boundary conditions. The boundary conditions add a cross-term to the separate boundary conditions for bending and in-plane stresses of plates.

9.1.1 Transverse displacement with non-uniform in-plane stresses

The balance equation [79, 129, 243, 244] specifying the transverse displacement for the weak bending of a plate under in-plane stresses also applies to the strong bending of the plate allowing for non-uniform in-plane stresses,

$$f = \nabla^2 \left(D\nabla^2\zeta\right) - hT_{\alpha\beta}\partial_{\alpha\beta}\zeta - h\left(\partial_\alpha\zeta\right)\left(\partial_\beta T_{\alpha\beta}\right), \tag{9.1}$$

where the indices α and β can assume the values 1 and 2 representing, for instance, the in-plane coordinates r_α or the in-plane velocity components v_α, ζ is the transverse displacement, h is the thickness of the plate, $T_{\alpha\beta}$ are the in-plane stresses represented by the second-order Cauchy stress tensor, D is the flexural rigidity, f is the transverse force per unit area and the vector $\nabla \equiv (\partial/\partial r_1, \partial/\partial r_2)$ is the in-plane gradient operator. The variable $\partial_\alpha \equiv \partial/\partial r_\alpha$ denotes the derivative with respect to r_α while $\partial_{\alpha\beta} \equiv \partial^2/\left(\partial r_\alpha \partial r_\beta\right)$ is the second derivative with respect to r_α and r_β. Repeated indices in a single term represent a summation over them, using the Einstein summation convention. The balance of the moments induced by forces implies that the Cauchy stress tensor is symmetric, that is, $T_{\alpha\beta} = T_{\beta\alpha}$ [79].

In the absence of inertia and in-plane volume forces,

$$f_\alpha = 0 = \frac{\partial}{\partial t}\left(\rho v_\alpha\right), \tag{9.2a}$$

the momentum equation states that the divergence of the stress tensor is zero [79],

$$\partial_\beta T_{\alpha\beta} = 0, \tag{9.2b}$$

implying that: (i) the last term on the right-hand side of (9.1) is zero; (ii) the in-plane stresses derive from a stress function,

$$T_{\mathrm{xx}} = \partial_{\mathrm{yy}}\Theta, \quad T_{\mathrm{yy}} = \partial_{\mathrm{xx}}\Theta, \quad T_{\mathrm{xy}} = -\partial_{\mathrm{xy}}\Theta. \tag{9.2c}$$

Assuming a constant flexural rigidity for an isotropic elastic plate [79, 129],

$$D \equiv \frac{Eh^3}{12\left(1-\sigma^2\right)}, \tag{9.3a}$$

the balance equation (9.1) becomes

$$\frac{f}{h} = \frac{Eh^2}{12\left(1-\sigma^2\right)}\boldsymbol{\nabla}^4\zeta - \left(\partial_{\mathrm{yy}}\Theta\right)\left(\partial_{\mathrm{xx}}\zeta\right) - \left(\partial_{\mathrm{xx}}\Theta\right)\left(\partial_{\mathrm{yy}}\zeta\right) + 2\left(\partial_{\mathrm{xy}}\Theta\right)\left(\partial_{\mathrm{xy}}\zeta\right). \tag{9.3b}$$

In the balance equation (9.3b), the first bending term on the right-hand side is linear for a transverse displacement with small slope, $\left|\partial_\alpha\zeta\right|^2 \ll 1$, and the other terms on the right-hand side are non-linear couplings to the in-plane stresses.

In order to close the system, a second relation between the transverse displacement and stress function is needed,

$$E\left[\left(\partial_{\mathrm{xy}}\zeta\right)^2 - \left(\partial_{\mathrm{xx}}\zeta\right)\left(\partial_{\mathrm{yy}}\zeta\right)\right] = \boldsymbol{\nabla}^4\Theta = \partial_{\mathrm{xxxx}}\Theta + \partial_{\mathrm{yyyy}}\Theta + 2\partial_{\mathrm{xxyy}}\Theta, \tag{9.4}$$

that will be obtained in the sequel (in subsections 9.1.2 and 9.1.3). Thus, the strong non-linear bending of a plate is specified by the biharmonic equation for the transverse displacement (9.3b) and stress function (9.4) with non-linear coupling through cross-terms. The coefficients involve the Young modulus E and Poisson ratio σ for an isotropic plate of thickness h, while the transverse force per unit area f appears as a forcing term. If the curvatures are small and the cross product with the stresses also,

$$\left(\partial_{\alpha\beta}\zeta\right)^2 \sim 0 \sim T_{\alpha\beta}\partial_{\alpha\beta}\zeta, \tag{9.5a}$$

the transverse displacement and stress function both satisfy decoupled biharmonic equations,

$$D\boldsymbol{\nabla}^4\zeta - f = 0 = \boldsymbol{\nabla}^4\Theta, \tag{9.5b}$$

respectively with forcing by the external transverse force per unit area f and without forcing. The strains and stresses are considered in the next subsection to prove (9.4) including the non-linear terms coupling to (9.3b). The extension of the coupled equations (9.3b) and (9.4) from isotropic to pseudo-isotropic orthotropic elastic plate is considered in the appendix E.

9.1.2 Linear and non-linear terms in the strain tensor

The total displacement $\mathbf{U}$ in the strong non-linear bending of a plate consists of a transverse displacement $\zeta\mathbf{e}_{\mathrm{z}}$ plus an in-plane displacement vector $\mathbf{u}$:

$$\mathbf{U} - \mathbf{e}_{\mathrm{z}}\zeta\left(x,y\right) = \mathbf{u}\left(x,y\right) = \mathbf{e}_{\mathrm{x}}u_{\mathrm{x}}\left(x,y\right) + \mathbf{e}_{\mathrm{y}}u_{\mathrm{y}}\left(x,y\right). \tag{9.6}$$

The arc length in the undeflected plane,

$$\left(\mathrm{d}l\right)^2 = \left(\mathrm{d}x\right)^2 + \left(\mathrm{d}y\right)^2, \tag{9.7a}$$

is increased in a bent plate by the in-plane displacement vector d$\mathbf{u}$ and transverse displacement dζ leading to

$$(\mathrm{d}L)^2 = (\mathrm{d}x + \mathrm{d}u_\mathrm{x})^2 + (\mathrm{d}y + \mathrm{d}u_\mathrm{y})^2 + (\mathrm{d}\zeta)^2 . \tag{9.7b}$$

The difference of square arc lengths is a quadratic form whose coefficients specify the Cartesian components of the exact strain tensor [3]:

$$\frac{(\mathrm{d}L)^2 - (\mathrm{d}l)^2}{2} = S_\mathrm{xx}\,(\mathrm{d}x)^2 + S_\mathrm{yy}\,(\mathrm{d}y)^2 + 2S_\mathrm{xy}\,\mathrm{d}x\,\mathrm{d}y. \tag{9.8a}$$

From (9.7a) and (9.7b) follows

$$\begin{aligned}(\mathrm{d}L)^2 - (\mathrm{d}l)^2 = {} & [(1+\partial_\mathrm{x}u_\mathrm{x})\,\mathrm{d}x + (\partial_\mathrm{y}u_\mathrm{x})\,\mathrm{d}y]^2 - (\mathrm{d}x)^2 - (\mathrm{d}y)^2 \\ & + [(\partial_\mathrm{x}u_\mathrm{y})\,\mathrm{d}x + (1+\partial_\mathrm{y}u_\mathrm{y})\,\mathrm{d}y]^2 + [(\partial_\mathrm{x}\zeta)\,\mathrm{d}x + (\partial_\mathrm{y}\zeta)\,\mathrm{d}y]^2 .\end{aligned} \tag{9.8b}$$

Thus, equating the coefficients of $(\mathrm{d}x)^2$, $(\mathrm{d}y)^2$ and $\mathrm{d}x\mathrm{d}y$ in (9.8a) and (9.8b) leads respectively to

$$2S_\mathrm{xx} = (\partial_\mathrm{x}\zeta)^2 + 2\partial_\mathrm{x}u_\mathrm{x} + (\partial_\mathrm{x}u_\mathrm{x})^2 + (\partial_\mathrm{x}u_\mathrm{y})^2 , \tag{9.9a}$$

$$2S_\mathrm{yy} = (\partial_\mathrm{y}\zeta)^2 + 2\partial_\mathrm{y}u_\mathrm{y} + (\partial_\mathrm{y}u_\mathrm{x})^2 + (\partial_\mathrm{y}u_\mathrm{y})^2 , \tag{9.9b}$$

$$2S_\mathrm{xy} = (\partial_\mathrm{x}\zeta)\,(\partial_\mathrm{y}\zeta) + (\partial_\mathrm{x}u_\mathrm{y} + \partial_\mathrm{y}u_\mathrm{x}) + [(\partial_\mathrm{x}u_\mathrm{x})\,(\partial_\mathrm{y}u_\mathrm{x}) + (\partial_\mathrm{x}u_\mathrm{y})\,(\partial_\mathrm{y}u_\mathrm{y})] . \tag{9.9c}$$

Hence, the exact non-linear in-plane strains (9.6) due to strong non-linear bending of plate with in-plane stresses are given by

$$2S_{\alpha\beta} = (\partial_\alpha\zeta)\,(\partial_\beta\zeta) + \partial_\alpha u_\beta + \partial_\beta u_\alpha + (\partial_\alpha u_\gamma)\,(\partial_\beta u_\gamma) \tag{9.10}$$

where the repeated index γ in the last term on the right-hand side of (9.10) is summed over the two Cartesian coordinates x and y. The exact non-linear strains (9.10) consist of three terms: (i) the product of the gradients of the transverse displacement that is non-linear as for a membrane; (ii) the symmetrised partial derivatives of the in-plane displacement, that correspond to the infinitesimal strain tensor or symmetric part of the displacement tensor; (iii) the cross-products of the displacement tensor that are non-linear, and are neglected in the sequel (subsection 9.1.3) compared with (ii).

9.1.3 Relation between the stresses and in-plane and transverse displacements

The theory of strong non-linear bending of a plate considers in the exact strain tensor (9.10) only the lowest-order terms, that is: (i) the linear in-plane strains omitting the non-linear part, with

$$(\partial_\alpha u_\gamma)\,(\partial_\beta u_\gamma) \ll 1; \tag{9.11a}$$

(ii) the gradients of the transverse displacement appear quadratically to lowest order and are retained in

$$2S_{\alpha\beta} = (\partial_\alpha \zeta)(\partial_\beta \zeta) + \partial_\alpha u_\beta + \partial_\beta u_\alpha. \tag{9.11b}$$

Thus, neglecting the non-linear in-plane strains (9.11a), the strain tensor (9.11b) has the in-plane components,

$$\partial_{\mathrm{x}} u_{\mathrm{x}} + \frac{1}{2}(\partial_{\mathrm{x}}\zeta)^2 = S_{\mathrm{xx}} = \frac{T_{\mathrm{xx}} - \sigma T_{\mathrm{yy}}}{E} = \frac{1}{E}(\partial_{\mathrm{yy}}\Theta - \sigma\partial_{\mathrm{xx}}\Theta), \tag{9.12a}$$

$$\partial_{\mathrm{y}} u_{\mathrm{y}} + \frac{1}{2}(\partial_{\mathrm{y}}\zeta)^2 = S_{\mathrm{yy}} = \frac{T_{\mathrm{yy}} - \sigma T_{\mathrm{xx}}}{E} = \frac{1}{E}(\partial_{\mathrm{xx}}\Theta - \sigma\partial_{\mathrm{yy}}\Theta), \tag{9.12b}$$

$$\partial_{\mathrm{x}} u_{\mathrm{y}} + \partial_{\mathrm{y}} u_{\mathrm{x}} + (\partial_{\mathrm{x}}\zeta)(\partial_{\mathrm{y}}\zeta) = 2S_{\mathrm{xy}} = 2\frac{1+\sigma}{E}T_{\mathrm{xy}} = -2\frac{1+\sigma}{E}\partial_{\mathrm{xy}}\Theta, \tag{9.12c}$$

where were used in succession [79, 133]: (i) the inverse Hooke law with zero out-of-plane normal stresses; (ii) the in-plane components of the stress tensor in terms of the stress function (9.2c).

Eliminating the in-plane displacements from (9.12a) to (9.12c), with

$$\begin{aligned}
0 &= E\left[\partial_{\mathrm{yy}}(\partial_{\mathrm{x}} u_{\mathrm{x}}) + \partial_{\mathrm{xx}}(\partial_{\mathrm{y}} u_{\mathrm{y}}) - \partial_{\mathrm{xy}}(\partial_{\mathrm{x}} u_{\mathrm{y}} + \partial_{\mathrm{y}} u_{\mathrm{x}})\right] \\
&= -\frac{E}{2}\left\{\partial_{\mathrm{yy}}(\partial_{\mathrm{x}}\zeta)^2 + \partial_{\mathrm{xx}}(\partial_{\mathrm{y}}\zeta)^2 - 2\partial_{\mathrm{xy}}\left[(\partial_{\mathrm{x}}\zeta)(\partial_{\mathrm{y}}\zeta)\right]\right\} \\
&\quad + \partial_{\mathrm{yy}}(\partial_{\mathrm{yy}}\Theta - \sigma\partial_{\mathrm{xx}}\Theta) + \partial_{\mathrm{xx}}(\partial_{\mathrm{xx}}\Theta - \sigma\partial_{\mathrm{yy}}\Theta) + 2(1+\sigma)\partial_{\mathrm{xyxy}}\Theta,
\end{aligned} \tag{9.13a}$$

leads to the relation between the transverse displacement and the stress function,

$$\begin{aligned}
E^{-1}(\partial_{\mathrm{xxxx}}\Theta + \partial_{\mathrm{yyyy}}\Theta + 2\partial_{\mathrm{xxyy}}\Theta) = E^{-1}\boldsymbol{\nabla}^4\Theta &= \partial_{\mathrm{y}}\left[(\partial_{\mathrm{x}}\zeta)(\partial_{\mathrm{xy}}\zeta)\right] \\
&\quad + \partial_{\mathrm{x}}\left[(\partial_{\mathrm{y}}\zeta)(\partial_{\mathrm{xy}}\zeta)\right] - \partial_{\mathrm{x}}\left[(\partial_{\mathrm{xy}}\zeta)(\partial_{\mathrm{y}}\zeta) + (\partial_{\mathrm{x}}\zeta)(\partial_{\mathrm{yy}}\zeta)\right] \\
&= (\partial_{\mathrm{xy}}\zeta)^2 - (\partial_{\mathrm{xx}}\zeta)(\partial_{\mathrm{yy}}\zeta),
\end{aligned} \tag{9.13b}$$

proving (9.13b) from (9.13a). Thus, the transverse ζ along with in-plane displacements u_{x} and u_{y} for the non-linear strong bending of a plate (9.6) specify the strains and stresses given by (9.12a) to (9.12c), using the lowest-order terms (9.11a) in the exact strains (9.10). Thus, the derivation of the Föppl-von Kármán equations (9.3b) and (9.4) has involved two assumptions: (i) linear stress-strain relations specified by the Hooke's law of elasticity in (9.12a) to (9.12c); (ii) small in-plane cross-strains (9.11a) in the total strain tensor (9.10) leading to (9.11b). The transverse displacement alone specifies the stress function (9.4) in the coupled system (9.3b), involving the existence of the elastic energies of deflection, bending and in-plane tension.

9.2 Energy method for the balance equations and boundary conditions

The energy method (subsection 9.2.1) can be applied to the strong bending of an elastic plate including coupling to the in-plane stresses leading to: (i) the same pair of non-linearly coupled balance equations for the stress function and transverse displacement (subsection 9.2.2) as had been obtained before by the direct method (section 9.1); (ii) in addition, the boundary conditions for the in-plane displacement vector and for the transverse displacement (subsection 9.2.3), with the latter involving the normal stress couple and augmented turning moment. The designation augmented turning moment is used because in addition to the usual turning moment due to bending there is an extra term involving the gradient of the transverse displacement.

9.2.1 Elastic energies of deflection, bending and in-plane deformation

The non-linear strong bending of a plate with in-plane stresses involves the total elastic energy per unit area,

$$E_{\mathrm{T}} \equiv E_1 + E_2 + E_3, \tag{9.14a}$$

consisting of three terms [129] due to: (i) bending, as for an isotropic plate,

$$2E_1 = D\left(\boldsymbol{\nabla}^2\zeta\right)^2 + 2D\left(1-\sigma\right)\left[\left(\partial_{\mathrm{xy}}\zeta\right)^2 - \left(\partial_{\mathrm{xx}}\zeta\right)\left(\partial_{\mathrm{yy}}\zeta\right)\right]; \tag{9.14b}$$

(ii-iii) the work of the in-plane elastic stresses on the total strains (9.11b) derived from the transverse and in-plane displacements,

$$2\left(E_2+E_3\right) = hT_{\alpha\beta}S_{\alpha\beta} = \frac{h}{2}\left[T_{\alpha\beta}\left(\partial_\alpha\zeta\right)\left(\partial_\beta\zeta\right) + T_{\alpha\beta}\partial_\alpha u_\beta + T_{\alpha\beta}\partial_\beta u_\alpha\right], \tag{9.14c}$$

corresponding respectively to transverse deflection and in-plane deformation. In (9.14c), the elastic energy per unit volume in square brackets on the right-hand side must be multiplied by the thickness h of the plate to specify the elastic energy per unit area that appears on the left-hand side. The principle of virtual work equates the variation of each contribution of the elastic energy with the corresponding form of work: (i-ii) the variation of the elastic energies of bending E_1 (9.14b) and transverse deflection E_2 (9.14c) equals the work in a transverse displacement due to the contribution of the total transverse force per unit area, that leads to

$$\int_{\mathcal{C}}\left(f_1+f_2\right)\delta\zeta\,\mathrm{d}S \equiv \int_{\mathcal{C}} f\delta\zeta\,\mathrm{d}S \equiv \delta W_1 + \delta W_2 = \int_{\mathcal{C}}\delta E_1\,\mathrm{d}S + \int_{\mathcal{C}}\delta E_2\,\mathrm{d}S \tag{9.15}$$

for the sum of the corresponding elastic energies; (iii) the elastic energy per unit volume of the in-plane deformation E_3 is associated to the work of the in-plane forces in a plane displacement,

$$\int_{\mathcal{C}} f_\alpha\delta u_\alpha\,\mathrm{d}S \equiv \delta W_3 = \int_{\mathcal{C}}\delta E_3\,\mathrm{d}S = \frac{h}{4}\int_{\mathcal{C}}\delta\left(T_{\alpha\beta}\partial_\alpha u_\beta + T_{\alpha\beta}\partial_\beta u_\alpha\right)\,\mathrm{d}S, \tag{9.16}$$

multiplied by the thickness h of the plate to convert to the elastic energy per unit area. The symmetric property of the stress tensor can be used to write the expression between curved parentheses in the last integral as $2T_{\alpha\beta}\partial_\beta u_\alpha$.

The variation of the elastic energy corresponding to in-plane deformation (9.16) is evaluated by

$$\begin{aligned} h^{-1}\int_{\mathcal{C}} \delta E_3 \, \mathrm{d}S &= \int_{\mathcal{C}} T_{\alpha\beta}\partial_\beta \left(\delta u_\alpha\right) \, \mathrm{d}S = \int_{\mathcal{C}} \left[\partial_\beta \left(T_{\alpha\beta}\delta u_\alpha\right) - \delta u_\alpha \left(\partial_\beta T_{\alpha\beta}\right)\right] \, \mathrm{d}S \\ &= \int_{\partial\mathcal{C}} T_{\alpha\beta}\delta u_\alpha n_\beta \, \mathrm{d}s - \int_{\mathcal{C}} \left(\partial_\beta T_{\alpha\beta}\right)\delta u_\alpha \, \mathrm{d}S \end{aligned} \tag{9.17a}$$

where: (i) the variation δ applies only to the displacement tensor, not to the stress tensor due to their linearity for an elastic material; (ii) the variation δ commutes with the differential ∂ in the first equality; (iii) an integration by parts is performed in the second equality; (iv) the divergence theorem is used in the last equality to transform the integral over the surface into one over its boundary. Substituting (9.17a) in (9.16) leads to the equality

$$\int_{\mathcal{C}} \left(f_\alpha + h\partial_\beta T_{\alpha\beta}\right)\delta u_\alpha \, \mathrm{d}S = h\int_{\partial\mathcal{C}} T_{\alpha\beta} n_\beta \delta u_\alpha \, \mathrm{d}s = 0 \tag{9.17b}$$

between surface and boundary integrals, implying that both must vanish. In the absence of inertia force,

$$\frac{\partial}{\partial t}\left(\rho\frac{\partial u_\alpha}{\partial t}\right) = 0, \tag{9.18a}$$

the vanishing of the integrand on the left-hand side of (9.17b) leads to the force balance equation in the plane,

$$h^{-1} f_\alpha + \partial_\beta T_{\alpha\beta} = 0, \tag{9.18b}$$

involving the force per unit area f_α converted to unit volume by dividing it by the thickness h of the plate.

The vanishing of the integrand in the right-hand side of (9.17b) leads to

$$0 = T_{\alpha\beta} n_\beta \delta u_\alpha = T_\alpha \delta u_\alpha = \mathbf{T}\cdot\delta\mathbf{u}, \tag{9.19a}$$

that is, to the boundary condition stating that the projection of the in-plane stress vector [129],

$$T_\alpha = T_{\alpha\beta} n_\beta, \tag{9.19b}$$

on the in-plane displacement is zero. This condition can be satisfied by

$$0 = T_\alpha \delta u_\alpha = \mathbf{T}\cdot\delta\mathbf{u} \Rightarrow \begin{cases} \mathbf{T} \perp \delta\mathbf{u} & \text{orthogonal stress}, \quad (9.20\text{a}) \\ \delta\mathbf{u} = 0 & \text{fixed}, \quad (9.20\text{b}) \\ \mathbf{T} = 0 & \text{free}, \quad (9.20\text{c}) \end{cases}$$

corresponding to: (i) orthogonal in-plane displacement and stress vector for (9.20a) the plate; (ii) zero in-plane displacement if (9.20b) the plate is fixed at the boundary; (iii) zero stress vector if (9.20c) the plate is free at the boundary.

The principle of virtual work may also be applied to the sum of elastic energies of bending, transverse deflection and in-plane deformation leading to the balance equations (subsection 9.2.2) and boundary conditions (subsection 9.2.3) for the strong bending of a thin plate.

9.2.2 Balance equations for the strong bending of a stressed plate

The total work in the non-linear strong bending of a plate is done by the transverse f and in-plane f_α forces respectively on the transverse $\delta\zeta$ and in-plane δu_α displacements,

$$\delta W = \delta W_1 + \delta W_2 + \delta W_3 = \int_{\mathcal{C}} (f\delta\zeta + f_\alpha \delta u_\alpha)\, \mathrm{d}S = \int_{\mathcal{C}} (\delta E_1 + \delta E_2 + \delta E_3)\, \mathrm{d}S, \tag{9.21a}$$

and equals the variation of the elastic energies of bending (9.14b) plus deflection stretching (9.14c). The variation of the elastic energy is given: (i-ii) for bending and deflection, as respectively for a plate and a membrane with the transverse force per unit area corresponding to the f_1 and f_2 contributions to the total force f, by (9.15); (iii) for in-plane deformation by (9.17a). These substitutions in (9.21a) lead to

$$\begin{aligned} 0 &= \int_{\mathcal{C}} \left\{ f - \boldsymbol{\nabla}^2 \left(D \boldsymbol{\nabla}^2 \zeta \right) + h\partial_\beta \left[T_{\alpha\beta} \left(\partial_\alpha \zeta \right) \right] \right\} \delta\zeta \, \mathrm{d}S + \int_{\mathcal{C}} \left(f_\alpha + h\partial_\beta T_{\alpha\beta} \right) \delta u_\alpha \, \mathrm{d}S \\ &= h \int_{\partial\mathcal{C}} T_{\alpha\beta} n_\beta \delta u_\alpha \, \mathrm{d}s + h \int_{\partial\mathcal{C}} T_{\alpha\beta} n_\beta \left(\partial_\alpha \zeta \right) \delta\zeta \, \mathrm{d}s + \int_{\partial\mathcal{C}} \left[N_\mathrm{n} \delta\zeta - M_\mathrm{n} \delta \left(\partial_\mathrm{n} \zeta \right) \right] \, \mathrm{d}s, \end{aligned} \tag{9.21b}$$

introducing the normal stress couple M_n and turning moment N_n in the third and last terms on the right-hand side of (9.21b). The surface and boundary integrals respectively on the right-hand side and left-hand side of (9.21b) can be equal only if both vanish. Also, both in the right-hand side and left-hand side of (9.21b) the variations of the transverse $\delta\zeta$ and in-plane δu_β displacements are independent, so the coefficient of each must vanish separately. These remarks applied to both sides of (9.21b) lead respectively to the balance equations and boundary conditions for the strong bending of a thin plate.

From (9.21b) follows that the non-linear strong bending of a plate involves three terms in the total elastic energy (9.14a) due to bending of a plate (9.14b) and the work of the in-plane stresses on the transverse and in-plane displacements (9.14c) corresponding respectively to deflection and extension, contraction and/or shear. The variation of the elastic energy of bending and deflection plus in-plane deformation is balanced by the work of respectively the transverse f and in-plane f_α forces per unit area, respectively (9.15) and (9.16), on the transverse $\delta\zeta$ and in-plane δu_α displacements, leading to the identity (9.21b) where: (i) the surface and boundary integrals respectively on the left-hand side and right-hand side must vanish leading to the balance equations and boundary conditions; (ii) the transverse $\delta\zeta$ and in-plane δu_α displacements are independent leading to two balance equations and two sets of boundary conditions. The vanishing of the integrand of the surface integral,

$$\left\{ f - \boldsymbol{\nabla}^2 \left(D \boldsymbol{\nabla}^2 \zeta \right) + h\partial_\beta \left[T_{\alpha\beta} \left(\partial_\alpha \zeta \right) \right] \right\} \delta\zeta + \left(f_\alpha + h\partial_\beta T_{\alpha\beta} \right) \delta u_\alpha = 0, \tag{9.22}$$

originates the transverse (9.3b) and in-plane (9.18b) balance equations. The vanishing of the boundary integral,

$$hT_{\alpha\beta}n_\beta\delta u_\alpha + N_\mathrm{n}\delta\zeta - M_\mathrm{n}\delta\left(\partial_\mathrm{n}\zeta\right) + hT_{\alpha\beta}n_\beta\left(\partial_\alpha\zeta\right)\delta\zeta = 0, \tag{9.23a}$$

implies that the first and last three terms vanish leading respectively to the boundary conditions for the in-plane displacements,

$$T_{\alpha\beta}n_\beta\delta u_\alpha = T_\alpha\delta u_\alpha = \mathbf{T}\cdot\delta\mathbf{u} = 0, \tag{9.23b}$$

and transverse displacement,

$$h^{-1}\left[N_\mathrm{n}\delta\zeta - M_\mathrm{n}\delta\left(\partial_\mathrm{n}\zeta\right)\right] = -T_{\alpha\beta}n_\beta\left(\partial_\alpha\zeta\right)\delta\zeta = -T_\alpha\left(\partial_\alpha\zeta\right)\delta\zeta = -\left(\mathbf{T}\cdot\boldsymbol{\nabla}\zeta\right)\delta\zeta, \tag{9.23c}$$

where was introduced the in-plane stress vector (9.19b).

9.2.3 Normal stress couple and augmented turning moment

The first boundary condition (9.23b) for the in-plane displacements leads to the same cases, stated in (9.20a) to (9.20c), as for in-plane stresses. The second set of boundary conditions (9.23c) involves [79, 129] the normal components of the stress couple,

$$M_\mathrm{n} \equiv -D\left\{\boldsymbol{\nabla}^2\zeta + (1-\sigma)\left[\sin(2\theta)\,\partial_\mathrm{xy}\zeta - \sin^2\theta\,\partial_\mathrm{xx}\zeta - \cos^2\theta\,\partial_\mathrm{yy}\zeta\right]\right\}, \tag{9.24}$$

and turning moment,

$$N_\mathrm{n} \equiv -D\left\{\partial_\mathrm{n}\left(\boldsymbol{\nabla}^2\zeta\right) - (1-\sigma)\,\partial_\mathrm{s}\left[\sin\theta\cos\theta\left(\partial_\mathrm{xx}\zeta - \partial_\mathrm{yy}\zeta\right) - \cos(2\theta)\,\partial_\mathrm{xy}\zeta\right]\right\}, \tag{9.25}$$

where ∂_n and ∂_s are the derivatives respectively along the normal and tangent to the boundary, and θ is the angle of the outward normal to the boundary with the x-axis, as in the figure 9.1. The boundary condition (9.23c) can be written in the form

$$-M_\mathrm{n}\delta\left(\partial_\mathrm{n}\zeta\right) + \overline{N}_\mathrm{n}\delta\zeta = 0 \tag{9.26}$$

where: (i) the normal stress couple (9.24) is the same for weak or strong bending; (ii) the normal turning moment for weak bending (9.25) is replaced for strong bending by the augmented normal turning moment,

$$\overline{N}_\mathrm{n} \equiv N_\mathrm{n} + hT_{\alpha\beta}n_\beta\left(\partial_\alpha\zeta\right) = N_\mathrm{n} + hT_\alpha\partial_\alpha\zeta = N_\mathrm{n} + h\mathbf{T}\cdot\boldsymbol{\nabla}\zeta, \tag{9.27}$$

that adds to the normal component of the turning moment (9.25) the projection of the in-plane stress vector (9.19b) on the gradient of the transverse displacement. The second set of boundary conditions,

$$0 = \overline{N}_\mathrm{n}\delta\zeta - M_\mathrm{n}\delta\left(\partial_\mathrm{n}\zeta\right) \Rightarrow \begin{cases} \zeta = \partial_\mathrm{n}\zeta = 0 & \text{clamped}, & (9.28\text{a}) \\ \zeta = M_\mathrm{n} = 0 & \text{pinned or supported}, & (9.28\text{b}) \\ M_\mathrm{n} = \overline{N}_\mathrm{n} = 0 & \text{free}, & (9.28\text{c}) \end{cases}$$

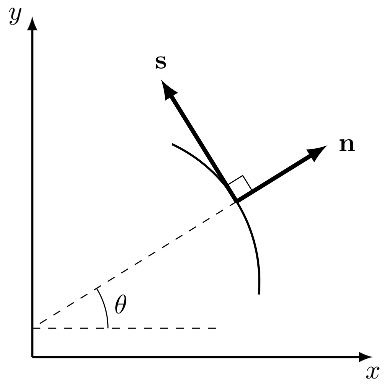

Figure 9.1: The unit vectors **n** and **s** are respectively normal and tangential to the boundary of a plate, while θ is the angle of the vector **n** with the x-axis.

includes the cases of clamped (9.28a), pinned or supported (9.28b), and free (9.28c) boundaries.

Having established by the two methods, namely the direct (section 9.1) and energy (section 9.2) methods, the balance equations and boundary conditions for the strong bending of an elastic plate including in-plane stresses, a general method of solution is presented next. The Föppl-von Kármán equations are considered in classical textbooks on elasticity [5, 6, 79, 152] and mathematically more rigorous derivations starting with three-dimensional elasticity [259] including asymptotic methods [260]. In the sequel expansion methods are used as perturbation methods, not to derive the Föppl-von Kármán equations, but rather to obtain solutions that: (i) are exact to all orders (section 9.3); (ii) are explicit in the axisymmetric case (section 9.4); (iii) are shown to converge as series for perturbation parameter less than unity; (iv) are calculated in detail in an example to lowest order of non-linearity (section 9.5); (v) include the specification of the asymptotic parameter in terms of geometric and material properties of the plate (section 9.6).

9.3 Solution via perturbation expansions explicit to all orders

A general method of solution of the coupled non-linear equations for the strong bending of an elastic plate including in-plane stresses is to use perturbation expansions for the transverse displacement and stress function (subsection 9.3.1). The perturbation equations are obtained explicitly for all orders, and simplify in the axisymmetric case (subsection 9.3.2).

9.3.1 Perturbation expansions for the transverse displacement and stress function

The perturbation expansions for the transverse displacement,

$$\zeta = \varepsilon\zeta_1 + \varepsilon^2\zeta_2 + \ldots + \varepsilon^n\zeta_n, \tag{9.29a}$$

and stress function,

$$\Theta = \varepsilon\Theta_1 + \varepsilon^2\Theta_2 + \ldots + \varepsilon^n\Theta_n, \tag{9.29b}$$

omit order zero assuming $\zeta_0 = 0 = \Theta_0$ and assume for small perturbation parameter ε either (i) a convergence as a series or (ii) a reasonably accurate approximation by truncation to some order $n \geq 2$. Substitution of the perturbation expansions (9.29a) and (9.29b) in the coupled equations (9.3b) and (9.4) for the strong bending of a plate leads at: (i) order one to decoupled stress function,

$$\boldsymbol{\nabla}^4 \Theta_1 = 0, \tag{9.30a}$$

and transverse displacement,

$$D \boldsymbol{\nabla}^4 \zeta_1 = f, \tag{9.30b}$$

satisfying respectively unforced and forced biharmonic equations, where the forcing in (9.30b) is due to the transverse force force per unit area that is assumed to be of the first order $f \sim O(\varepsilon)$; (ii) order two to the first non-linear coupling with biharmonic operators forced by order one terms,

$$\frac{1}{E} \boldsymbol{\nabla}^4 \Theta_2 = \left(\partial_{\mathrm{xy}} \zeta_1\right)^2 - \left(\partial_{\mathrm{xx}} \zeta_1\right)\left(\partial_{\mathrm{yy}} \zeta_1\right), \tag{9.31a}$$

$$\frac{D}{h} \boldsymbol{\nabla}^4 \zeta_2 = \left(\partial_{\mathrm{yy}} \Theta_1\right)\left(\partial_{\mathrm{xx}} \zeta_1\right) + \left(\partial_{\mathrm{xx}} \Theta_1\right)\left(\partial_{\mathrm{yy}} \zeta_1\right) - 2\left(\partial_{\mathrm{xy}} \Theta_1\right)\left(\partial_{\mathrm{xy}} \zeta_1\right); \tag{9.31b}$$

order $n \geq 2$ to biharmonic equations forced by all lower orders up to $n-1$,

$$\frac{1}{E} \boldsymbol{\nabla}^4 \Theta_n = \sum_{m=1}^{n-1} \left[\left(\partial_{\mathrm{xy}} \zeta_m\right)\left(\partial_{\mathrm{xy}} \zeta_{n-m}\right) - \left(\partial_{\mathrm{xx}} \zeta_m\right)\left(\partial_{\mathrm{yy}} \zeta_{n-m}\right)\right], \tag{9.32a}$$

$$\frac{D}{h} \boldsymbol{\nabla}^4 \zeta_n = \sum_{m=1}^{n-1} \left[\left(\partial_{\mathrm{yy}} \Theta_m\right)\left(\partial_{\mathrm{xx}} \zeta_{n-m}\right) + \left(\partial_{\mathrm{xx}} \Theta_m\right)\left(\partial_{\mathrm{yy}} \zeta_{n-m}\right) - 2\left(\partial_{\mathrm{xy}} \Theta_m\right)\left(\partial_{\mathrm{xy}} \zeta_{n-m}\right)\right], \tag{9.32b}$$

where the sums end at $m = n-1$ because $\zeta_0 = 0$.

The first-order equations (9.30a) and (9.30b) are linear in (Θ_1, ζ_1) with constant coefficient D and forcing f. The second order equations (9.31a) and (9.31b) are linear in (Θ_2, ζ_2) with forcing by the derivatives of first-order (Θ_1, ζ_1). The n-th order equations (9.32a) and (9.32b) are linear in (Θ_n, ζ_n) with forcing by all lower orders $(\Theta_{n-1}, \zeta_{n-1})$ down to (Θ_1, ζ_1). This is a typical causal chain of linear differential equations where each order n depends only on the preceding $n-1, n-2, \ldots, 2, 1$. This can be confirmed writing the system (9.32a) and (9.32b) in decoupled matrix form,

$$\begin{bmatrix} \frac{1}{E} \boldsymbol{\nabla}^4 & 0 \\ 0 & \frac{D}{h} \boldsymbol{\nabla}^4 \end{bmatrix} \begin{bmatrix} \Theta_n \\ \zeta_n \end{bmatrix} = \begin{bmatrix} F_n \\ G_n \end{bmatrix}, \tag{9.33a}$$

where the n-th order equation is linear on the dependent variables (Θ_n, ζ_n) because: (i) the matrix differential operator applies only to (Θ_n, ζ_n) that are decoupled since the matrix is diagonal; (ii) in the forcing terms,

$$F_n \equiv \sum_{m=1}^{n-1} \left[(\partial_{\mathrm{xy}}\zeta_m)(\partial_{\mathrm{xy}}\zeta_{n-m}) - (\partial_{\mathrm{xx}}\zeta_m)(\partial_{\mathrm{yy}}\zeta_{n-m}) \right], \tag{9.33b}$$

$$G_n \equiv \sum_{m=1}^{n-1} \left[(\partial_{\mathrm{yy}}\Theta_m)(\partial_{\mathrm{xx}}\zeta_{n-m}) + (\partial_{\mathrm{xx}}\Theta_m)(\partial_{\mathrm{yy}}\zeta_{n-m}) - 2(\partial_{\mathrm{xy}}\Theta_m)(\partial_{\mathrm{xy}}\zeta_{n-m}) \right], \tag{9.33c}$$

appear derivatives of all lower orders (ζ_1, Θ_1) up to $(\zeta_{n-1}, \Theta_{n-1})$, but not (ζ_n, Θ_n). Thus, the perturbation expansions (9.29a) and (9.29b) substituted in a system of non-linear coupled differential equations lead to a sequence of linear differential equations that: (i) are decoupled at the lowest order; (ii) become coupled first at next order; (iii) at order n are coupled by all lower orders as in a causal chain, that is a sequence of problems in which each iteration depends only on the preceding or "past" and not on the following or "future". To be more specific, the term "causal chain" is used as a short-hand to mean a sequence of deterministic ordinary differential equations in which the solution of each equation depends only on the solutions of preceding equations, in contrast with a fully coupled system. The perturbation expansions are applied next to the strong bending of a circular plate with axial symmetry.

9.3.2 Non-linear coupling of bending and in-plane deformation with axial symmetry

The relation between the Laplacian [130] in the plane in Cartesian coordinates and in polar coordinates with axial symmetry,

$$\partial_{\mathrm{xx}} + \partial_{\mathrm{yy}} = \nabla^2 = r^{-1}\partial_{\mathrm{r}}(r\partial_{\mathrm{r}}) = \partial_{\mathrm{rr}} + r^{-1}\partial_{\mathrm{r}}, \tag{9.34a}$$

suggests the transformation [129] from Cartesian coordinates in the plane to axisymmetric polar coordinates for the first and second order derivatives:

$$\{\partial_{\mathrm{x}}, \partial_{\mathrm{y}}\} \leftrightarrow \{\mathrm{d_r}, 0\}, \quad \{\partial_{\mathrm{xx}}, \partial_{\mathrm{yy}}, \partial_{\mathrm{xy}}\} \leftrightarrow \left\{\mathrm{d_{rr}}, r^{-1}\mathrm{d_r}, 0\right\}. \tag{9.34b}$$

Substituting (9.34b) in the non-linear bending equations (9.3b) and (9.4) leads to

$$\frac{1}{E}\nabla^4\Theta = -\zeta''\frac{\zeta'}{r} = -\frac{\left(\zeta'^2\right)'}{2r}, \tag{9.35a}$$

$$D\nabla^4\zeta - f = \frac{h}{r}\left(\Theta'\zeta'' + \Theta''\zeta'\right) = \frac{h}{r}\left(\Theta'\zeta'\right)'. \tag{9.35b}$$

In the case of axial symmetry, the stress function specifies the stresses [79, 133] by

$$T_{\mathrm{rr}} = \frac{\Theta'}{r}, \quad T_{\mathrm{tt}} = \Theta'', \quad T_{\mathrm{rt}} = 0. \tag{9.36a}$$

The inverse Hooke law [79, 133] specifies the strains

$$ES_{\mathrm{rr}} = T_{\mathrm{rr}} - \sigma T_{\mathrm{tt}}, \quad ES_{\mathrm{tt}} = T_{\mathrm{tt}} - \sigma T_{\mathrm{rr}},$$
$$ES_{\mathrm{rt}} = (1+\sigma)\, T_{\mathrm{rt}}, \quad ES_{\mathrm{zz}} = -\sigma\,(T_{\mathrm{rr}} + T_{\mathrm{tt}}) \tag{9.36b}$$

leading to

$$ES_{\mathrm{rr}} = \frac{\Theta'}{r} - \sigma\Theta'', \quad ES_{\mathrm{tt}} = \Theta'' - \frac{\sigma}{r}\Theta', \quad S_{\mathrm{rt}} = 0, \quad ES_{\mathrm{zz}} = -\sigma\left(\Theta'' + \frac{\Theta'}{r}\right) \tag{9.36c}$$

by (9.36a). The strains are given by (9.11b) with axial symmetry (9.34a) leading to

$$S_{\mathrm{rr}} = u'_{\mathrm{r}} + \frac{\zeta'^2}{2}, \quad S_{\mathrm{tt}} = \frac{u_{\mathrm{r}}}{r}, \quad S_{\mathrm{rt}} = 0, \quad S_{\mathrm{zz}} = -\frac{\sigma}{1-\sigma}\left(u'_{\mathrm{r}} + \frac{u_{\mathrm{r}}}{r} + \frac{\zeta'^2}{2}\right), \tag{9.36d}$$

for plane stresses [129]. The radial component of the stress couple is unaffected by in-plane stresses,

$$M_{\mathrm{r}} = -D\left(\zeta'' + \frac{\sigma}{r}\zeta'\right). \tag{9.37a}$$

The radial component of the augmented turning moment,

$$\overline{N}_{\mathrm{r}} = -D\left(\nabla^2\zeta\right)' + hT_{\mathrm{rr}}\zeta' = -D\left[\frac{(\zeta' r)'}{r}\right]' + \frac{h}{r}\Theta'\zeta', \tag{9.37b}$$

consists of two terms, namely: (i) the turning moment (9.25) with axial symmetry due to bending; (ii) augmented turning moment by the in-plane stresses (9.27). Thus, the axial symmetry, that is the dependence only on the distance from the axis, leads to: (i-ii) the stresses (9.36a) and strains (9.36d); (iii-iv) the radial stress couple (9.37a) and augmented turning moment (9.37b). All four relations (i-iv) depend on the stress function and transverse displacement that satisfy the system (9.35a) and (9.35b) of coupled non-linear differential equations specifying the strong bending of a thin isotropic plate.

The solution (subsection 9.4.1) for a clamped (subsection 9.4.3) heavy circular plate under axial compression (subsection 9.4.2) is obtained as an example of the use of perturbation expansion (subsection 9.3.1) with axial symmetry (subsection 9.3.3).

9.3.3 Strong bending of a circular plate by transverse loads

Consider a circular plate, sketched in the figure 9.2, under strong bending by a transverse force per unit area, $f(r)$, with axial symmetry (9.34b), leading to

$$\nabla^4\Theta = -\frac{E}{2r}\left(\zeta'^2\right)', \quad f = D\nabla^4\zeta - \frac{h}{r}\left(\Theta'\zeta'\right)'. \tag{9.38}$$

The perturbation expansions (9.29a) and (9.29b) substituted in the coupled non-linear strong bending equations (9.38) lead to the causal chain of differential equations that: (i) are decoupled at lowest order,

$$O(\varepsilon), \quad \nabla^4\Theta_1 = 0, \quad D\nabla^4\zeta_1 = f, \tag{9.39a}$$

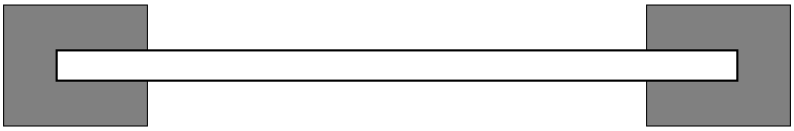

Figure 9.2: The method of perturbation expansions for the strong bending in an elastic plate, including in-plane stresses, simplifies in the axisymmetric case.

assuming that f is of the order ε; (ii) are first coupled at order two,

$$O\left(\varepsilon^2\right), \quad \boldsymbol{\nabla}^4\Theta_2 = -\frac{E}{2r}\left(\zeta_1'^2\right)', \quad \boldsymbol{\nabla}^4\zeta_2 = \frac{h}{Dr}\left(\Theta_1'\zeta_1'\right)'; \tag{9.39b}$$

(iii) are coupled at order n by all lower orders,

$$O\left(\varepsilon^n\right), \quad \boldsymbol{\nabla}^4\Theta_n = -\frac{E}{2r}\left[\sum_{m=1}^{n-1}\left(\zeta_m'\zeta_{n-m}'\right)\right]', \quad \boldsymbol{\nabla}^4\zeta_n = \frac{h}{Dr}\left[\sum_{m=1}^{n-1}\left(\Theta_m'\zeta_{n-m}'\right)\right]', \tag{9.39c}$$

where the sums end at $m = n-1$ because, due to the perturbation expansions, $\zeta_0' = 0$. Thus, the non-linear strong bending of a circular plate with axial symmetry is specified by the perturbation expansion (9.29a) and (9.29b) whose terms are the solutions of the causal chain of differential equations decoupled at lowest order (9.39a), first coupled at next order (9.39b) and increasingly coupled at higher orders (9.39c). This system is readily solved in the case of forcing by powers, polynomial or series of the radius in the next section.

9.4 Exact solution to all orders for arbitrary loading

Assuming that the transverse force per unit area is an analytic function of the radius, that is an axisymmetric power series or polynomial, the perturbation equations can be solved exactly for all orders, using the closed form solution of the axisymmetric biharmonic equation forced by a power (subsection 9.4.1). This is illustrated by the parametric expansions to the lowest non-linear order (subsection 9.4.3) for a heavy circular plate under axial compression (subsection 9.4.2).

9.4.1 Radially symmetric biharmonic equation forced by a power

The bending of the plate and associated in-plane stresses are caused by the transverse force per unit area that appears as the forcing terms of the coupled system of equations (9.3b) and (9.4). In the axisymmetric case, the transverse force per unit area (and in-plane stresses) is a function of the radius only, and if it is analytic, $f \in \mathcal{A}(\mathbb{R})$, it has a Taylor series [130],

$$f(r) = \sum_{k=0}^{\infty}\frac{r^k}{k!}f^{(k)}(0), \tag{9.40}$$

that is a linear combination of powers, and terminates in the case of a polynomial. In this case, the whole sequence of perturbation equations, from (9.39a) to (9.39c), to all orders consists of biharmonic equations forced by powers. The biharmonic operator with axial symmetry (9.34a) is given by [130]

$$\nabla^4\zeta = \frac{1}{r}\frac{\mathrm{d}}{\mathrm{d}r}\left\{r\frac{\mathrm{d}}{\mathrm{d}r}\left[\frac{1}{r}\frac{\mathrm{d}}{\mathrm{d}r}\left(r\frac{\mathrm{d}\zeta}{\mathrm{d}r}\right)\right]\right\} = \zeta'''' + \frac{2}{r}\zeta''' - \frac{1}{r^2}\zeta'' + \frac{1}{r^3}\zeta'. \tag{9.41a}$$

In the case of an axially symmetric biharmonic equation forced by a power,

$$C_k r^k = \nabla^4\zeta = \zeta'''' + \frac{2}{r}\zeta''' - \frac{1}{r^2}\zeta'' + \frac{1}{r^3}\zeta', \tag{9.41b}$$

a particular integral may be sought in the form

$$\zeta = J r^{k+4}, \tag{9.42a}$$

leading to

$$C r^k = \nabla^4\left(J r^{k+4}\right) = J r^k p_4(k) \tag{9.42b}$$

and involving the quartic polynomial

$$\begin{aligned} p_4(k) &= (k+4)(k+3)(k+2)(k+1) + 2(k+4)(k+3)(k+2) - (k+4)(k+3) + k + 4 \\ &= (k+4)(k+2)\left[(k+3)(k+1) + 2(k+3) - 1\right] \\ &= (k+4)(k+2)\left[(k+3)^2 - 1\right] = (k+4)^2(k+2)^2. \end{aligned} \tag{9.42c}$$

Thus, an axially symmetric equation forced by a power (9.41b) has the particular integral

$$\zeta(r) = \frac{C r^{k+4}}{(k+4)^2(k+2)^2}. \tag{9.42d}$$

This result can be used to obtain by superposition the particular integrals,

$$\tilde{\zeta}(r) = \sum_{k=0}^{K}\frac{C_k r^{k+4}}{(k+4)^2(k+2)^2}, \tag{9.43a}$$

of the axially symmetric biharmonic equation forced by an analytic function [39] of the radius that can be approximated by a polynomial:

$$\nabla^4\tilde{\zeta} = \sum_{k=0}^{K} C_k r^k. \tag{9.43b}$$

If the transverse force is a polynomial of degree K in (9.43b), the transverse displacement is given in finite terms by (9.43a) as a polynomial of degree $K+4$. A transverse force which is an analytic function (9.40) corresponds to a series $K=\infty$ in (9.43b) with $C_k \equiv f^{(k)}(0)/k!$, in this case the transverse displacement is given by the series (9.43a) with $K=\infty$; the series for the transverse force (9.40) converges for an analytic function, and hence the series for the transverse displacement $\tilde{\zeta}$ also converges, because its coefficients are of order C_k/k^4 and thus decay faster with a factor $k^{-4} \to 0$ as $k \to \infty$. Next is proved the convergence of the perturbation expansions (9.29a) and (9.29b) when the loads are analytic functions of the radius (9.40). The series (9.43a) with K finite or infinite converge at all orders and thus each n term of the series representing the transversal displacement, designated ζ_n as in the perturbation expansion, is bounded:

$$|\zeta_n(r)| \leq B \leq \infty. \tag{9.44a}$$

Thus, the perturbation expansion for finite order is bounded [39] by

$$|\zeta(r)| = \left|\sum_{n=1}^{N} \varepsilon^n \zeta_n(r)\right| \leq \sum_{n=1}^{N} \varepsilon^n |\zeta_n(r)| \leq \sum_{n=1}^{N} \varepsilon^n B = \varepsilon \frac{1-\varepsilon^N}{1-\varepsilon} B. \tag{9.44b}$$

For perturbation parameter less than unity, the limit $N \to \infty$ in (9.44b) shows that the perturbation series converges with upper bound:

$$\varepsilon < 1, \quad |\zeta(r)| = \left|\sum_{n=1}^{\infty} \varepsilon^n \zeta_n(r)\right| \leq \frac{B\varepsilon}{1-\varepsilon}. \tag{9.44c}$$

In both cases of finite (9.44b) or series (9.44c) perturbation expansion, the error of truncation R_N at the N-th term (or the remainder of the series) does not exceed:

$$R_N \equiv \left|\sum_{n=N+1}^{\infty} \varepsilon^n \zeta_n(r)\right| \leq \sum_{n=N+1}^{\infty} \varepsilon^n B = \frac{\varepsilon^{N+1}}{1-\varepsilon} B. \tag{9.44d}$$

It has been shown that in the case of forcing by a polynomial (9.43b) or analytic function (9.40) of the radius, the asymptotic expansion (9.29a) for the transverse displacement becomes a convergent series with the upper bound (9.44c) or with the remainder (9.44d) if the series is truncated after N terms as in (9.44b). The distinction between "asymptotic expansion" and "asymptotic series" can be made as follows. An "asymptotic expansion" is considered with a finite number of terms N, and is more accurate for smaller parameter ε; if the number of terms tends to infinity, the asymptotic expansion will diverge, so the best accuracy is limited and is obtained for an optimum number of terms. The asymptotic series is a stronger case than an asymptotic expansion, since it can be summed with any number of terms, and becomes exact as the number of terms tends to infinity, for any value of the parameter ε within its domain of convergence. Both the asymptotic expansion and series have a remainder R_N after N terms, and the distinction is that as the number of terms N tends to infinity, $N \to \infty$, the remainder diverges for an asymptotic expansion, $R_N \to \infty$, whereas it tends to zero for an asymptotic series, $R_N \to 0$. It can be confirmed that within the domain of convergence $\varepsilon < 1$ of the parameter ε in (9.44c), as $N \to \infty$, the remainder after N terms tends to zero in (9.44d), $R_N \to 0$; therefore the solution (9.44b) is an asymptotic series, that is a stronger result than an asymptotic expansion; for an asymptotic expansion, $R_N \to 0$ only for $\varepsilon \to 0$. An asymptotic series can be seen as particular stronger case of an asymptotic expansion: (i) the asymptotic expansion is exact only for $\varepsilon \to 0$, whereas the asymptotic series is exact for all $\varepsilon < 1$; (ii) for $\varepsilon \neq 0$ the asymptotic expansion can be summed with limited accuracy using a finite number of terms because it diverges for $N \to \infty$, whereas the asymptotic series can be summed exactly with an infinite number of terms because it converges as $N \to \infty$. For that reason there is no limit to the accuracy of an asymptotic series in contrast with an asymptotic expansion; a truncated asymptotic series is also an asymptotic expansion, but that is not using fully its properties.

Since the solution is an asymptotic series convergent for $0 < \varepsilon < 1$, it can be summed with any desired accuracy R_d by adding more terms to the convergent series (9.44b) to make the remainder (9.44d) smaller. To be more precise, an accuracy better than R_d corresponds to $R_N < R_\mathrm{d}$ in (9.44d),

$$\frac{\varepsilon^{N+1}}{1-\varepsilon} B = R_N < R_\mathrm{d}, \tag{9.44e}$$

and is obtained after N terms:

$$N + 1 > \left| \frac{\log\left[(1-\varepsilon) R_\mathrm{d}/B\right]}{\log \varepsilon} \right|. \tag{9.44f}$$

The proof of (9.44f) can be made as follows: (i) taking logarithms on both sides of (9.44e) leads to

$$(N+1) \log \varepsilon < \log \left[\frac{R_\mathrm{d}}{B} (1-\varepsilon) \right]; \tag{9.44g}$$

(ii) since $\varepsilon < 1$ in (9.44c), the left-hand side of (9.44g) is negative, so $\log \varepsilon < 0$; (iii) for small error R_d less than the n-th term B, $R_\mathrm{d} < B$, then $(R_\mathrm{d}/B)(1-\varepsilon) < 1$ because also $1 - \varepsilon < 1$, and hence the term in square brackets on the right-hand side of (9.44g) is less than unity, therefore its logarithm is negative; (iv) since both sides of the inequality $<$ in (9.44g) are negative, the sign is reversed to $>$ when taking the modulus,

$$(N+1) \left|\log \varepsilon\right| > \left| \log \left[\frac{R_\mathrm{d}}{B} (1-\varepsilon) \right] \right|, \tag{9.44h}$$

proving the relation (9.44f) that is equivalent to the last equation.

Thus, this method of solution applies to any order, and has minimum algebra when illustrated by the application to a heavy circular plate under axial compression.

9.4.2 Heavy circular plate under axial compression

At lowest order, there is a decoupling of: (i) the transverse deflection,

$$\zeta_1(r) = H \left(r^2 - a^2\right)^2 \tag{9.45a}$$

of a circular plate of radius a under its own weight,

$$f = \rho g h, \tag{9.45b}$$

where g is the gravitational acceleration, that is the solution [79] of

$$D \boldsymbol{\nabla}^4 \zeta_1 = \rho g h, \tag{9.45c}$$

with coefficient

$$H \equiv \frac{\rho g h}{64 D} = \frac{3 \rho g h \left(1 - \sigma^2\right)}{16 E h^3}; \tag{9.45d}$$

(ii) a uniform axial compression,

$$T_{\mathrm{rr}} = -p \tag{9.46a}$$

with pressure p, for which the biharmonic equation for the stress function,

$$\boldsymbol{\nabla}^4 \Theta_1 = 0, \tag{9.46b}$$

has solution [133]

$$\Theta_1 = -\frac{1}{2} p r^2. \tag{9.46c}$$

With the substitution of (9.45a) and (9.46c), the perturbation equations (9.39b) and (9.39c) are biharmonic with forcing (9.43b) by polynomials, so the particular integral (9.43a) can be applied to all orders. For the purpose of illustrating the method, it is sufficient to consider the second order, that is the lowest for which non-linear coupling of bending and in-plane deformation occurs.

9.4.3 Non-linear coupling of bending and compression

The lowest order stress function (9.46c) and transverse displacement (9.45a) have zero order radial derivatives, respectively

$$\Theta_1' (r) = -pr \tag{9.47a}$$

and

$$\zeta_1' (r) = 4Hr \left(r^2 - a^2\right), \tag{9.47b}$$

that appear in the next order forced biharmonic equations:

$$\boldsymbol{\nabla}^4 \Theta_2 = -\frac{8EH^2}{r} \left[r^2 \left(r^2 - a^2\right)^2\right]' = -16EH^2 \left(3r^4 - 4a^2r^2 + a^4\right) \tag{9.48a}$$

and

$$\boldsymbol{\nabla}^4 \zeta_2 = -\frac{4pHh}{Dr} \left[r^2 \left(r^2 - a^2\right)\right]' = -\frac{8pHh}{D} \left(2r^2 - a^2\right). \tag{9.48b}$$

The biharmonic equations (9.48a) and (9.48b) are forced by a polynomial (9.43b) and its particular integral (9.43a) specifies respectively the second-order stress function,

$$\begin{aligned}\Theta_2 (r) &= -16EH^2 \left(\frac{3r^8}{8^2 6^2} - \frac{4a^2r^6}{6^2 4^2} + \frac{a^4 r^4}{4^2 2^2}\right) = -\frac{16EH^2 r^4}{8^2 6^2} \left(3r^4 - 4 \cdot 2^2 a^2 r^2 + 6^2 a^4\right) \\ &= -\frac{EH^2 r^4}{144} \left(3r^4 - 16a^2r^2 + 36a^4\right),\end{aligned} \tag{9.49a}$$

and transverse displacement,

$$\zeta_2 (r) = -\frac{8pHh}{D} \left(\frac{2r^6}{6^2 4^2} - \frac{a^2 r^4}{4^2 2^2}\right) = -\frac{8pHhr^4}{6^2 4^2 D} \left(2r^2 - 3^2 a^2\right) = -\frac{pHhr^4}{72D} \left(2r^2 - 9a^2\right). \tag{9.49b}$$

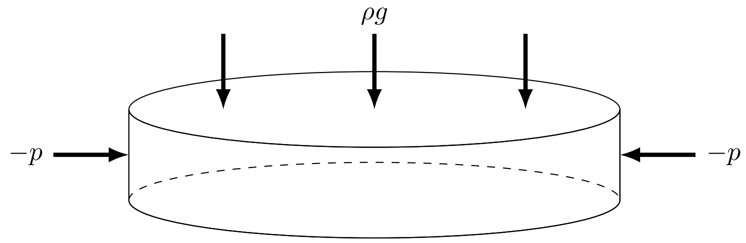

Figure 9.3: An example of the axisymmetric case is a heavy circular plate under axial compression at the rim.

The total stress function,

$$\Theta\left(r\right)=B_4r^2\log r+B_3r^2+B_2\log r+B_1-\frac{1}{2}pr^2-\frac{EH^2r^4}{144}\left(3r^4-16a^2r^2+36a^4\right), \tag{9.50a}$$

and transverse displacement,

$$\zeta\left(r\right)=C_4r^2\log r+C_3r^2+C_2\log r+C_1+H\left(r^2-a^2\right)^2-\frac{pHhr^4}{72D}\left(2r^2-9a^2\right), \tag{9.50b}$$

for the non-linear strong bending of a heavy circular plate under compression, as indicated in the figure 9.3, are given by the sum of: (i) the general integral,

$$\phi\left(r\right)=A_4r^2\log r+A_3r^2+A_2\log r+A_1, \tag{9.51a}$$

of the unforced biharmonic equation

$$\boldsymbol{\nabla}^4\phi=0, \tag{9.51b}$$

involving four arbitrary constants of integration, A_1 to A_4, that are distinct from the four constants of the stress function, B_1 to B_4, and from the four constants of transverse displacement, C_1 to C_4; (ii) the lowest decoupled, (9.46c) and (9.45a), and next coupled order, (9.49a) and (9.49b), that introduces coupling to the lowest order two in the particular integral. The complete integral is the sum of (i) and (ii). The two sets of four arbitrary constants of integration, B_1 to B_4 and C_1 to C_4, are determined from boundary conditions, for example, for a clamped plate under axial compression at the boundary.

9.5 Strong bending of heavy circular plate under compression

The boundary conditions for a clamped circular plate are used to determine the arbitrary constants in the stress function and transverse displacement (subsection 9.5.1). These specify all other dependent variables in the problem such as the radial displacement vector and all components of the stress and strain tensors (subsection 9.5.2). As a final check, the final compliance with the boundary conditions is verified by computation of all the terms involved (subsection 9.5.3).

9.5.1 Transverse displacement and stress function with clamping

The stress function (9.50a) leads by (9.36a) to the tangential stress

$$T_{\mathrm{tt}}(r) = B_4(2\log r + 3) + 2B_3 - \frac{B_2}{r^2} - p - \frac{EH^2r^2}{6}\left(7r^4 - 20a^2r^2 + 18a^4\right). \tag{9.52}$$

A finite stress at the centre, $T_{\mathrm{tt}}(0) < \infty$, implies $B_2 = B_4 = 0$ in (9.52), leading in (9.50a) to the stress function

$$\Theta(r) = B_3r^2 - \frac{1}{2}pr^2 - \frac{EH^2r^4}{144}\left(3r^4 - 16a^2r^2 + 36a^4\right), \tag{9.53}$$

where the constant $B_1 = 0$ can be omitted because it does not affect the stresses (9.36a), either tangential (9.52) or radial,

$$T_{\mathrm{rr}}(r) = 2B_3 - p - \frac{EH^2r^2}{6}\left(r^4 - 4a^2r^2 + 6a^4\right). \tag{9.54}$$

The boundary condition specifying the compression, $-p = T_{\mathrm{rr}}(a)$, determines the remaining constant of integration,

$$B_3 = \frac{EH^2a^6}{4}, \tag{9.55a}$$

that substituted in (9.53) determines the stress function:

$$\Theta(r) = -\frac{1}{2}pr^2 - \frac{EH^2r^2}{144}\left(3r^6 - 16a^2r^4 + 36a^4r^2 - 36a^6\right). \tag{9.55b}$$

In the transverse displacement (9.50b), two constants are zero, $C_2 = C_4 = 0$, because the transverse displacement must be finite and there is no concentrated force at the centre, leading to

$$\zeta(r) = C_3r^2 + C_1 + H\left(r^2 - a^2\right)^2 - \frac{pHhr^4}{72D}\left(2r^2 - 9a^2\right). \tag{9.56a}$$

The slope and displacement vanish on the boundary,

$$0 = \zeta'(a) = 2C_3a + \frac{pHha^5}{3D}, \tag{9.56b}$$

$$0 = \zeta(a) = C_1 + C_3a^2 + \frac{7pHha^6}{72D} \tag{9.56c}$$

determining respectively the two remaining constants of integration:

$$C_1 = \frac{5pHha^6}{72D}, \quad C_3 = -\frac{pHha^4}{6D}. \tag{9.56d}$$

Substituting the two constants in (9.56a) specifies the transverse displacement:

$$\zeta(r) = H\left(r^2 - a^2\right)^2 - \frac{pHh}{72D}\left(2r^6 - 9a^2r^4 + 12a^4r^2 - 5a^6\right). \tag{9.56e}$$

A clamped heavy circular plate under axial compression at the boundary, as sketched in the figure 9.4, has the stress function (9.55b) and transverse displacement (9.56e) to the second or lowest non-linear

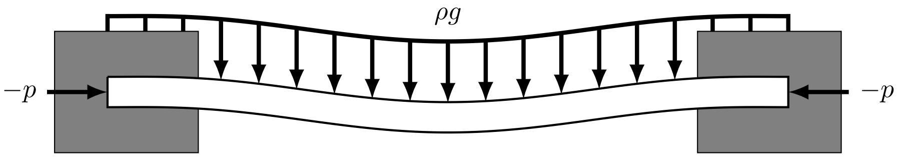

Figure 9.4: One of the possible boundary conditions is clamping.

approximation of transverse bending and in-plane deformation leading to the stresses, strains and in-plane displacements, obtained next in subsection 9.5.2. The slope, stress couple and augmented turning moment are obtained in subsection 9.5.3.

The figure 9.5 is an illustrative example of the application of strong bending of a circular plate under compression, showing the first two contributions ζ_1 (top plot) and ζ_2 (middle plots) in the perturbation expansion up to second order of vertical displacement ζ (bottom plots). The results apply to a steel plate[1] with Young's modulus $E = 200\,\text{GPa}$, Poisson's ratio $\nu = 0.265$ and mass density $\rho = 7850\,\text{kg/m}^3$. To get the results, the thickness of the plate is $h = 10\,\text{mm}$ while its radius is $a = 500\,\text{mm}$. Note that the first contribution ζ_1 does not depend explicitly on the value of the pressure p. In this particular case, the contribution of ζ_2 is much smaller than the contribution of ζ_1. The reason is due to the factor $H/D \sim 1/D^2$ in the expression of ζ_2 which has the order of magnitude equal to 10^{-8}, in opposition with the expression of ζ_1 which is proportional to $H \sim 1/D$ with order of magnitude equal to 10^{-4}. The figure 9.5 also depicts the influence of the pressure p in the contribution ζ_2 and consequently in the total normal displacement (in the bottom plots that show the displacement ζ, the solid line overlaps the dotted and dashed lines); it shows that when the pressure p has greater values, the normal displacement is also greater. The total displacement ζ follows the boundary conditions of no displacement and no angle of inclination at the boundary of the plate. Moreover, the displacement and its contributions are symmetric with respect to the axis $r = 0$ of the plate and reaches the maximum value at the centre of the plate $r = 0$.

9.5.2 Stresses, strains and radial displacement

The stress function (9.55b) specifies, by (9.36a), the non-zero stresses, namely radial,

$$T_{\text{rr}}(r) = -p - \frac{EH^2}{6}\left(r^6 - 4a^2r^4 + 6a^4r^2 - 3a^6\right), \tag{9.57a}$$

and tangential,

$$T_{\text{tt}}(r) = -p - \frac{EH^2}{6}\left(7r^6 - 20a^2r^4 + 18a^4r^2 - 3a^6\right). \tag{9.57b}$$

The radial and tangential stresses: (i) differ at the boundary where they respectively equal and are less than the compression,

$$T_{\text{rr}}(a) = -p > -p - \frac{EH^2a^6}{3} = T_{\text{tt}}(a); \tag{9.58a}$$

[1]The data associated to a steel plate, needed for the figures 9.5 to 9.7, is obtained from the site *The Engineering ToolBox*.

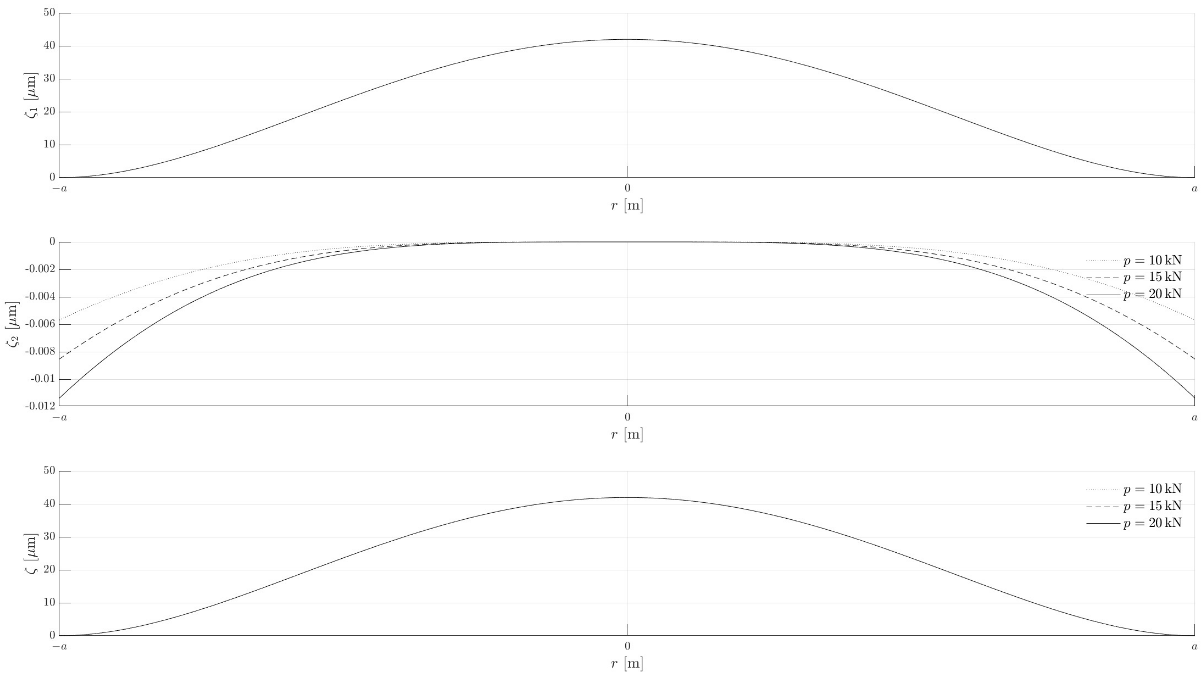

Figure 9.5: Vertical displacement ζ up to the second order (in the z-direction) of the steel plate with the next characteristics: Young's modulus $E = 200\,\mathrm{GPa}$, Poisson's ratio $\nu = 0.265$, mass density $\rho = 7850\,\mathrm{kg/m^3}$, thickness $h = 0.01\,\mathrm{m}$ and radius $a = 0.5\,\mathrm{m}$. The dotted, dashed and solid lines result from an applied pressure p of 10, 15 and 20 kN respectively.

(ii) coincide and are higher than the compression at the centre,

$$T_{\mathrm{rr}}(0) = -p + \frac{EH^2a^6}{2} = T_{\mathrm{tt}}(0)\,. \tag{9.58b}$$

The non-zero stresses (9.57a) and (9.57b) specify, by (9.36b), the non-zero strains, for example, the tangential strain,

$$S_{\mathrm{tt}}(r) = -\frac{1-\sigma}{E}p - \frac{H^2}{6}\left[(7-\sigma)\,r^6 - 4\,(5-\sigma)\,a^2r^4 + 6\,(3-\sigma)\,a^4r^2 - 3\,(1-\sigma)\,a^6\right] \tag{9.59a}$$

specifies the radial displacement,

$$\frac{u_{\mathrm{r}}(r)}{r} = S_{\mathrm{tt}}(r)\,, \tag{9.59b}$$

where on the right-hand side of (9.59a) the first term is the linear approximation and the second term is the lowest order non-linear correction. The tangential strain (9.59a) and radial displacement (9.59b) are respectively: (i) non-zero and zero at the centre,

$$S_{\mathrm{tt}}(0) = (1-\sigma)\left(-\frac{p}{E} + \frac{H^2a^6}{2}\right), \quad u_{\mathrm{r}}(0) = 0; \tag{9.60a}$$

(ii) both non-zero at the boundary,

$$S_{\mathrm{tt}}\left(a\right) = \frac{u_{\mathrm{r}}\left(a\right)}{a} = -\frac{1-\sigma}{E}p - \frac{H^2a^6}{3}, \tag{9.60b}$$

with the non-linear effect decreasing the strain and displacement in all non-zero cases.

The remaining non-zero strains are radial,

$$S_{\mathrm{rr}}\left(r\right) = -\frac{1-\sigma}{E}p - \frac{H^2}{6}\left[\left(1-7\sigma\right)r^6 - 4\left(1-5\sigma\right)a^2r^4 + 6\left(1-3\sigma\right)a^4r^2 - 3\left(1-\sigma\right)a^6\right], \tag{9.61a}$$

and out-of-plane with the latter specifying the normal displacement,

$$\frac{u_{\mathrm{z}}\left(r\right)}{z} = S_{\mathrm{zz}}\left(r\right) = \sigma\left[\frac{2p}{E} + \frac{H^2}{3}\left(4r^6 - 12a^2r^4 + 12a^4r^2 - 3a^6\right)\right], \tag{9.61b}$$

where on the right-hand side of (9.61a) and (9.61b) the first term is the linear approximation and the second term is the lowest order non-linear correction. The radial strain (9.61a) equals the tangential strain at the centre where it is larger than at the boundary only for $\sigma < 3/5$:

$$S_{\mathrm{rr}}\left(0\right) = \left(1-\sigma\right)\left(-\frac{p}{E} + \frac{H^2a^6}{2}\right) = S_{\mathrm{tt}}\left(0\right) > S_{\mathrm{rr}}\left(a\right) = -\frac{1-\sigma}{E}p + \frac{H^2a^6}{3}\sigma. \tag{9.62}$$

The transverse displacement is zero on the axis, $u_{\mathrm{z}}\left(0\right) = 0$, and the out-of-plane strain (9.61b) is lower at the centre than at the boundary:

$$S_{\mathrm{zz}}\left(0\right) = \sigma\left(\frac{2p}{E} - H^2a^6\right) < \sigma\left(\frac{2p}{E} + \frac{H^2a^6}{3}\right) = S_{\mathrm{zz}}\left(a\right). \tag{9.63}$$

The area and volume changes [3],

$$D_2\left(r\right) \equiv S_{\mathrm{rr}}\left(r\right) + S_{\mathrm{tt}}\left(r\right) = \frac{\left(1-\sigma\right)\left(T_{\mathrm{rr}} + T_{\mathrm{tt}}\right)}{E} = -\frac{\left(1-\sigma\right)}{\sigma}S_{\mathrm{zz}}\left(r\right), \tag{9.64a}$$

$$D_3\left(r\right) \equiv D_2\left(r\right) + S_{\mathrm{zz}}\left(r\right) = -\frac{1-\sigma}{\sigma}S_{\mathrm{zz}}\left(r\right) + S_{\mathrm{zz}}\left(r\right) = \frac{2\sigma-1}{\sigma}S_{\mathrm{zz}}\left(r\right) \tag{9.64b}$$

follow from (9.59a) and (9.62). The compliance with the boundary conditions is checked next.

The figure 9.6 shows the two non-zero and independent components of stress tensor (top plots) and the three independent components of strain tensor (bottom plots) due to the pressure applied at the rim of the plate and to the gravitational force. The results correspond to the same steel plate as in the figure 9.5. The dotted, dashed and solid lines are associated to the pressure p of 10 kN, 15 kN and 20 kN respectively, as in the last figure 9.5. The plots confirm several observations previously mentioned. The radial stress T_{rr} (red lines) is equal to the compressive pressure $-p$ at the boundary of the plate, specifically at the positions $r = -a$ and $r = a$. Increasing the value of the pressure increases also the values in modulus of the stress components. The radial stress is radially symmetric and reaches the maximum value at the centre of the plate $r = 0$. This observation also applies to the tangential stress T_{tt} (blue lines). Furthermore, the tangential stress is lower than the radial stress at all positions, except at

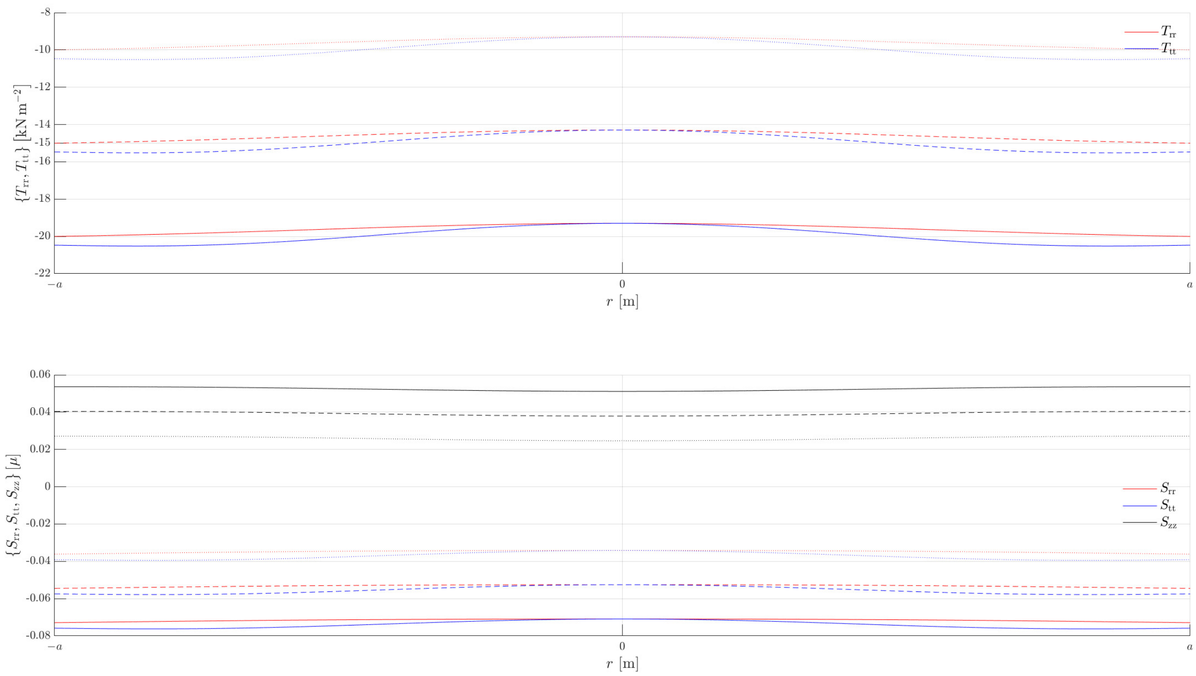

Figure 9.6: Stresses T_{ij} and strains S_{ij} in the steel plate with the next characteristics: Young's modulus $E = 200\,\text{GPa}$, Poisson's ratio $\nu = 0.265$, mass density $\rho = 7850\,\text{kg/m}^3$, thickness $h = 0.01\,\text{m}$ and radius $a = 0.5\,\text{m}$. The dotted, dashed and solid lines result from an applied pressure p of 10, 15 and 20 kN respectively.

the centre of the plate where they coincide. The bottom plots show the values of the strain components. As in the case of stress tensor, the tangential strain S_{tt} (blue lines) is lower than the radial strain S_{rr} (red lines) at all positions, except at the centre of the plate, $r = 0$, where both strain components coincide and reach the minimum value (in modulus) in this particular case. The axial strain S_{zz} (black lines) is also minimum at the centre of the plate. The absolute values of the three strain components increase for a greater value of the pressure p.

9.5.3 Slope, stress couple and augmented turning moment

From transverse displacement (9.56e), follows the slope

$$\zeta'(r) = 4Hr\left(r^2 - a^2\right) - \frac{pHhr}{6D}\left(r^4 - 3a^2r^2 + 2a^4\right) \tag{9.65}$$

that vanishes both at the boundary and centre, $\zeta'(a) = \zeta'(0) = 0$. The radial and tangential curvatures are given respectively by [4]

$$k_{\text{r}}(r) \equiv \zeta''(r) = 4H\left(3r^2 - a^2\right) - \frac{pHh}{6D}\left(5r^4 - 9a^2r^2 + 2a^4\right), \tag{9.66a}$$

$$k_{\text{t}} \equiv \frac{\zeta'(r)}{r} = 4H\left(r^2 - a^2\right) - \frac{pHh}{6D}\left(r^4 - 3a^2r^2 + 2a^4\right). \tag{9.66b}$$

They respectively do not and do vanish on the boundary,

$$k_{\mathrm{t}}(a) = 0 \neq k_{\mathrm{r}}(a) = Ha^2\left(8 + \frac{pa^2h}{3D}\right), \tag{9.67a}$$

and coincide at the centre,

$$k_{\mathrm{t}}(0) = Ha^2\left(-\frac{pha^2}{3D} - 4\right) = k_{\mathrm{r}}(0). \tag{9.67b}$$

The radial stress couple (9.37a) is given by

$$\begin{aligned} M_{\mathrm{r}}(r) = -D\left[k_{\mathrm{r}}(r) + \sigma k_{\mathrm{t}}(r)\right] &= -4HD\left[(3+\sigma)\,r^2 + (1+\sigma)\,a^2\right] \\ &+ \frac{pHh}{6}\left[(5+\sigma)\,r^4 - 3\,(3+\sigma)\,a^2r^2 + 2\,(1+\sigma)\,a^4\right]. \end{aligned} \tag{9.68}$$

It is non-zero at the centre,

$$M_{\mathrm{r}}(0) = (1+\sigma)\,Ha^2\left(4D + \frac{pha^2}{3}\right), \tag{9.69a}$$

while on the boundary it is also non-zero,

$$M_{\mathrm{r}}(a) = Ha^2\left(-\frac{pha^2}{3} - 8D\right), \tag{9.69b}$$

because the plate is clamped. It has a lowest-order non-linear correction in both cases.

The Laplacian of the transverse displacement (9.34a) is the sum of the radial (9.66a) and tangential (9.66b) curvatures and is given by

$$\boldsymbol{\nabla}^2\zeta = \zeta'' + \frac{\zeta'}{r} = k_{\mathrm{r}}(r) + k_{\mathrm{t}}(r) = 8H\left(2r^2 - a^2\right) - \frac{pHh}{3D}\left(3r^4 - 6a^2r^2 + 2a^4\right). \tag{9.70}$$

The turning moment is specified by the first term on the right-hand side of (9.37b) that equals the radial derivative of the bending stiffness multiplied by the Laplacian,

$$N_{\mathrm{r}}(r) = \left(D\boldsymbol{\nabla}^2\zeta\right)', \tag{9.71a}$$

and in the case of constant bending stiffness is specified by

$$N_{\mathrm{r}}(r) = D\left(\zeta''' + \frac{\zeta''}{r} - \frac{\zeta'}{r^2}\right) = 32HDr - 4pHhr\left(r^2 - a^2\right). \tag{9.71b}$$

The augmented turning moment (9.37b) adds to the turning moment (9.71b) a term involving the derivatives of the transverse displacement (9.56e) and stress function (9.55b) leading to

$$\overline{N}_{\mathrm{r}}(r) - N_{\mathrm{r}}(r) = \frac{h}{r}\Theta'\zeta' = hT_{\mathrm{rr}}\zeta', \tag{9.72}$$

where may be substituted (9.65) and (9.57a). At the centre, the turning moment (9.71b) vanishes, $N_{\mathrm{r}}(0) = 0$, and also the augmented turning moment, $\overline{N}_{\mathrm{r}}(0) = 0$. On the boundary, the turning moment and augmented turning moment (9.72) coincide and so do not vanish, $\overline{N}_{\mathrm{r}}(a) = N_{\mathrm{r}}(a) = 32HDa$, because the plate is clamped. The strong bending of a heavy clamped circular plate to the lowest order of non-linearity is an example of the method of perturbation expansions that, in the axisymmetric case, with transverse force and in-plane stresses, polynomial functions apply exactly to all orders of non-linearity.

The figure 9.7 shows not only the two components of the curvature (top plots), but also the radial stress couple, the turning moment and the augmented turning moment (bottom plots) due to the pressure applied at the boundary of the plate and to the gravitational force. The results correspond to the same steel plate as in the figures 9.5 and 9.6. The dotted, dashed and solid lines correspond to the pressure p of 10 kN, 15 kN and 20 kN respectively, as in the last figures 9.5 and 9.6. Both the curvatures are symmetric with respect to the axis of the circular plate. The radial curvature k_r (red lines of top plots) is greater than the tangential curvature k_t (blue lines of top plots), except at the centre of the plate, $r = 0$, where both curvatures coincide. Furthermore, the tangential curvature vanishes at the extreme radial positions of the plate, $r = -a$ and $r = a$. The radial stress couple N_r (black lines of bottom plots) has radial symmetry and has a maximum value at the centre of the plate, $r = 0$. Otherwise, the turning moment M_r (black lines of bottom plots) and augmented turning moment $\overline{M}_\mathrm{r}$ (black lines of bottom plots) do not have radial symmetry and they both vanish at $r = 0$. Moreover, they have symmetric extreme values at the boundary of the plate and at that positions, the turning moments coincide. Although they are not visible, the dotted and dashed lines exist in the figure 9.7, but the solid lines overlap them. It means that with this set of values in the pressure p, there is not such a large influence on the final values of the stress couple and turning moment.

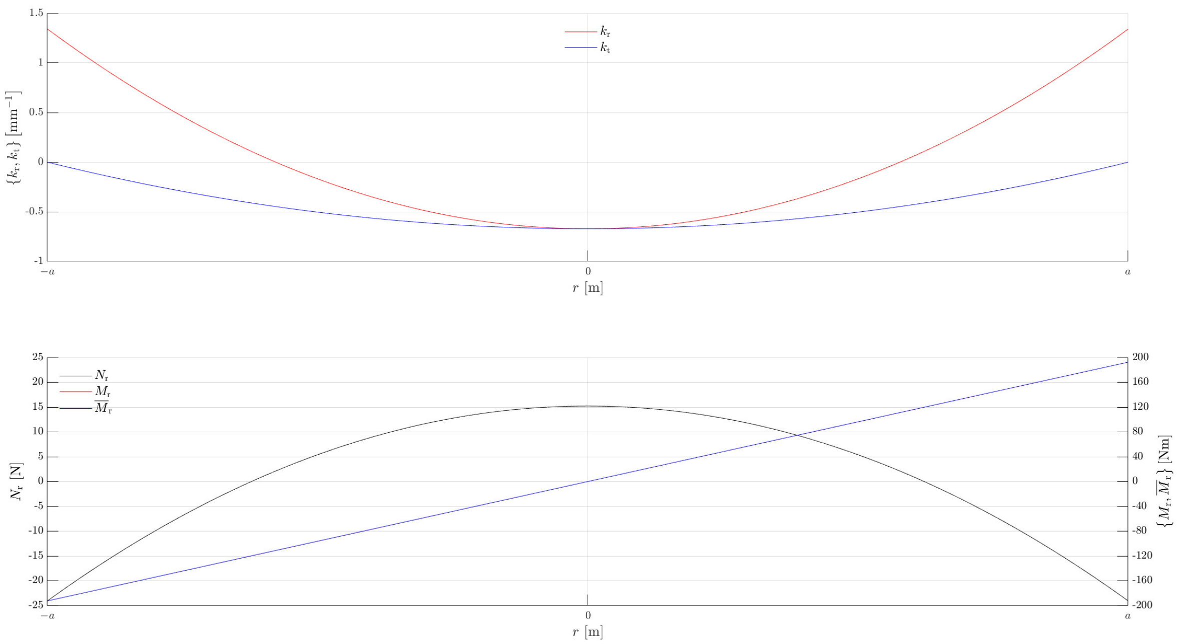

Figure 9.7: Radial curvature k_r, tangential curvature k_t, radial stress couple N_r, turning moment M_r and augmented turning moment $\overline{M}_\mathrm{r}$ of the steel plate with the next characteristics: Young's modulus $E = 200\,\mathrm{GPa}$, Poisson's ratio $\nu = 0.265$, mass density $\rho = 7850\,\mathrm{kg/m^3}$, thickness $h = 0.01\,\mathrm{m}$ and radius $a = 0.5\,\mathrm{m}$. The dotted, dashed and solid lines associate respectively to the pressure p of 10, 15 and 20 kN.

9.6 Determination of parameter in perturbation expansion

The parameter in the perturbation expansions (9.29a) and (9.29b) can be determined equating the elastic energy to the work of external forces (subsection 9.6.1). If the perturbation expansion is taken to order N, the perturbation parameter is the root of a polynomial of degree $M = 2N - 1$, implying that it is unique $M = 1$ for the lowest order $N = 1$ of perturbation (subsection 9.6.2). This specifies the perturbation parameter as a function of loads, stiffness and geometry of the plate (subsection 9.6.3).

9.6.1 Balance of work versus gravity and elastic energy

The work of the pressure in a radial displacement is

$$\mathrm{d}W \equiv -p\,\mathrm{d}u_\mathrm{r} \tag{9.73a}$$

and for a displacement from zero to u_r is given by

$$W = -p \int_0^{u_\mathrm{r}} \mathrm{d}u_\mathrm{r} = -pu_\mathrm{r}. \tag{9.73b}$$

The total work is its integral over all directions, $0 \le \theta \le 2\pi$, and radius, $0 \le r \le a$, leading to

$$\overline{W} \equiv -ph \int_0^{2\pi} \mathrm{d}\theta \int_0^a u_\mathrm{r}\left(r\right)\,\mathrm{d}r = -2\pi hp \int_0^a u_\mathrm{r}\left(r\right)\,\mathrm{d}r, \tag{9.73c}$$

multiplied by the thickness h of the plate.

Besides the work of the pressure in a radial displacement (9.73a), there is work of the weight in a transverse displacement:

$$\mathrm{d}\Phi \equiv \rho g h\,\mathrm{d}\zeta; \tag{9.74a}$$

for a given displacement from 0 to ζ, this leads to the gravity potential energy

$$\Phi = \rho g h \int_0^{\zeta} \mathrm{d}\zeta = \rho g \zeta. \tag{9.74b}$$

The total gravity potential energy integrated over the circular plate of radius a is

$$\overline{\Phi} \equiv h \int_0^{2\pi} \mathrm{d}\theta \int_0^a \Phi\left(r\right) r\,\mathrm{d}r = 2\pi\rho g h \int_0^a \zeta\left(r\right) r\,\mathrm{d}r. \tag{9.74c}$$

The deformation energy per unit volume related to the work of the in-plane elastic stresses on the total strains, regarding (9.14c), and in the case of linear elastic stress-strain relation, is given by

$$2E_\mathrm{d} \equiv 2\frac{E_2 + E_3}{h} = T_{\alpha\beta}S_{\alpha\beta} = T_\mathrm{rr}S_\mathrm{rr} + T_\mathrm{tt}S_\mathrm{tt}, \tag{9.75a}$$

involving the non-zero stresses in (9.36a). Multiplying by the thickness h of the plate and integrating over the area specify the total energy of deformation:

$$2\overline{E} \equiv h \int_0^{2\pi} \mathrm{d}\theta \int_0^a 2E_{\mathrm{d}}(r)\, r\, \mathrm{d}r = 2\pi h \int_0^a \left[T_{\mathrm{rr}}(r)\, S_{\mathrm{rr}}(r) + T_{\mathrm{tt}}(r)\, S_{\mathrm{tt}}(r)\right] r\, \mathrm{d}r. \tag{9.75b}$$

The sum of the work of the pressure (9.73c) and gravity potential energy (9.74c) must equal the total deformation energy (9.75b),

$$\overline{W} + \overline{\Phi} = \overline{E}, \tag{9.76}$$

and this relation is used to determine the parameter ε in the asymptotic expansions (9.29a) and (9.29b).

9.6.2 Perturbation expansions to lowest and highest orders

The perturbation expansions (9.29a) and (9.29b) apply to the transverse ζ and radial u_{r} displacements, and strain and stress tensors:

$$\left\{\zeta(r), u_{\mathrm{r}}(r), S_{\alpha\beta}(r), T_{\alpha\beta}(r)\right\} = \sum_{n=0}^{N} \varepsilon^n \left\{\zeta_{n+1}(r), u_{\mathrm{r},n+1}(r), S_{\alpha\beta,n+1}(r), T_{\alpha\beta,n+1}(r)\right\}, \tag{9.77}$$

using $n = 0$ for the lowest order and perturbations up to order N. The choice $\varepsilon^0 = 1$ for the lowest order and $\varepsilon^1 = \varepsilon$ for the next order is made because: (i) the work of the pressure forces (9.73c) and gravity potential energy (9.74c) is linear and starts at lowest order $\varepsilon^0 = 1$ with next order $\varepsilon^1 = \varepsilon$; (ii) the energy of deformation (9.76) is quadratic, hence with lowest order $\varepsilon^0 = 1$, and next orders ε and ε^2; (iii) starting the sum in (9.77) at $n = 0$ allows the lowest orders of work of the pressure and energy of deformation to be matched since $\varepsilon^0 = 1$ does not appear; (iv) this also ensures that higher order matchings are consistent. The perturbation expansions (9.29a) and (9.29b) corresponding to (9.77) can be taken to any order $N = \infty$ since the corresponding series (9.44a) and (9.44c) converge. Using (9.77), the work of the pressure is given by a single perturbation expansion,

$$\overline{W} = \sum_{n=0}^{N} \varepsilon^n \overline{W}_n, \tag{9.78a}$$

with terms

$$\overline{W}_n \equiv -2\pi p h \int_0^a u_{\mathrm{r},n+1}(r)\, \mathrm{d}r, \tag{9.78b}$$

and the gravity potential energy is also specified by the single perturbation expansion,

$$\overline{\Phi} = \sum_{n=0}^{\infty} \varepsilon^n \overline{\Phi}_n, \tag{9.79a}$$

with terms

$$\overline{\Phi}_n \equiv 2\pi \rho g h \int_0^a \zeta_{n+1}(r)\, r\, \mathrm{d}r, \tag{9.79b}$$

whereas the deformation energy (9.75b) is given by a double perturbation expansion,

$$\overline{E} = \sum_{n=0}^{N} \sum_{m=0}^{n} \varepsilon^{n+m} \overline{E}_{n,m}, \tag{9.80a}$$

with diagonal $n = m$ and cross $n \neq m$ terms:

$$\overline{E}_{n,n} \equiv \pi h \int_0^a T_{\alpha\beta,n+1}(r)\, S_{\alpha\beta,n+1}(r)\, r\, \mathrm{d}r, \tag{9.80b}$$

$$\overline{E}_{n,m} \equiv \pi h \int_0^a \left[T_{\alpha\beta,n+1}(r)\, S_{\alpha\beta,m+1}(r) + T_{\alpha\beta,m+1}(r)\, S_{\alpha\beta,n+1}(r)\right] r\, \mathrm{d}r. \tag{9.80c}$$

Equating, as in (9.76), the work of the pressure (9.78a) plus the gravity potential energy (9.79a) to the elastic energy of deformation (9.80a) leads to

$$\sum_{n=0}^{N} \varepsilon^{n} \left(\overline{W}_n + \overline{\Phi}_n\right) = \sum_{n=0}^{N} \sum_{m=0}^{n} \varepsilon^{n+m} \overline{E}_{n,m}, \tag{9.81}$$

so that the left-hand side is a polynomial of degree N and the right-hand side is a polynomial of degree $2N$, and the perturbation parameter ε is a real root. Using the identity (9.76) at lowest order,

$$\overline{W}_0 + \overline{\Phi}_0 = \overline{E}_{0,0}, \tag{9.82}$$

cancels the leading terms on both sides of (9.81) and allows a division by ε in

$$\sum_{n=1}^{N} \varepsilon^{n-1} \left(\overline{W}_n + \overline{\Phi}_n\right) = \sum_{n=1}^{N} \sum_{m=0}^{n} \varepsilon^{n+m-1} \overline{E}_{n,m}, \tag{9.83}$$

so that the left-hand side is a polynomial of degree $N - 1$ and the right-hand side is a polynomial of degree $2N - 1$. For the lowest order perturbation $N = 1$, there is a single root $2N - 1 = 1$ and unique value of the asymptotic parameter ε. This can be confirmed using the lowest order $N = 1$ in the work of the pressure (9.78a),

$$\overline{W} = \overline{W}_0 + \varepsilon \overline{W}_1, \tag{9.84a}$$

in the gravity potential energy (9.79a),

$$\overline{\Phi} = \overline{\Phi}_0 + \varepsilon \overline{\Phi}_1, \tag{9.84b}$$

and in the elastic energy of deformation (9.80a),

$$\overline{E} = \overline{E}_{0,0} + \varepsilon \overline{E}_{1,0} + \varepsilon^2 \overline{E}_{1,1}. \tag{9.84c}$$

The equality (9.81) with $N = 1$ for (9.84a), (9.84b) and (9.84c) becomes

$$\overline{W}_0 + \overline{\Phi}_0 + \varepsilon \left(\overline{W}_1 + \overline{\Phi}_1\right) = \overline{E}_{0,0} + \varepsilon \overline{E}_{1,0} + \varepsilon^2 \overline{E}_{1,1} \tag{9.85a}$$

and using (9.82) simplifies to

$$\overline{W}_1 + \overline{\Phi}_1 = \overline{E}_{1,0} + \varepsilon \overline{E}_{1,1}, \tag{9.85b}$$

that is equivalent to

$$\varepsilon = \frac{\overline{W}_1 + \overline{\Phi}_1 - \overline{E}_{1,0}}{\overline{E}_{1,1}}. \tag{9.85c}$$

This specifies uniquely the expansion parameter, that is given by a ratio with: (i) numerator equal to the first-order work of the pressure $\overline{W}_1$ plus the first-order gravity potential $\overline{\Phi}_1$ minus the deformation energy $\overline{E}_{1,0}$ of cross-orders zero and one; (ii) denominator equal to the deformation energy $\overline{E}_{1,1}$ of order one. From (9.85c) follows the dependence of the perturbation expansion parameter on external loads, material properties and geometric properties.

9.6.3 Dependence on loads, material and geometry

The radial displacement is given by (9.59a) and (9.59b) with the first term on the right-hand side for the lowest order,

$$u_{\mathrm{r},1}(r) = -\frac{1-\sigma}{E} pr, \tag{9.86a}$$

and remaining terms for the lowest order perturbation,

$$u_{\mathrm{r},2}(r) = -\frac{H^2 r}{6}\left[(7-\sigma) r^6 - 4(5-\sigma) a^2 r^4 + 6(3-\sigma) a^4 r^2 - 3(1-\sigma) a^6\right]. \tag{9.86b}$$

Likewise, the transverse displacement is given at the lowest order by (9.45a), equivalent to

$$\zeta_1(r) = H\left(r^2 - a^2\right)^2, \tag{9.87a}$$

and the second order perturbation is equal to

$$\zeta_2(r) = \frac{pHh}{72D}\left(2r^6 - 9a^2r^4 + 12a^4r^2 - 5a^6\right), \tag{9.87b}$$

by the remaining terms on the right-hand side of (9.56e). Also, the radial (9.57a) and azimuthal (9.57b) stresses are constant at lowest order,

$$T_{\mathrm{rr},1} = -p = T_{\mathrm{tt},1}, \tag{9.88a}$$

and at the second order are given by:

$$\{T_{\mathrm{rr},2}(r), T_{\mathrm{tt},2}(r)\} = -\frac{EH^2}{6}\left\{r^6 - 4a^2r^4 + 6a^4r^2 - 3a^6, 7r^6 - 20a^2r^4 + 18a^4r^2 - 3a^6\right\}. \tag{9.88b}$$

The radial (9.61a) and azimuthal (9.59a) strains are constant at lowest order,

$$S_{\mathrm{rr},1} = -\frac{1-\sigma}{E} p = S_{\mathrm{tt},1}, \tag{9.89a}$$

and given by

$$\{S_{\mathrm{rr},2}(r), S_{\mathrm{tt},2}(r)\} = -\frac{H^2}{6}\left\{(1-7\sigma)r^6 - 4(1-5\sigma)a^2r^4 + 6(1-3\sigma)a^4r^2 - 3(1-\sigma)a^6,\right.$$
$$\left.(7-\sigma)r^6 - 4(5-\sigma)a^2r^4 + 6(3-\sigma)a^4r^2 - 3(1-\sigma)a^6\right\}. \tag{9.89b}$$

for the second order perturbation.

At lowest order: (i) the work of the pressure in a radial displacement (9.78b), using (9.86a), is given by

$$\overline{W}_0 = -2\pi ph\int_0^a u_{\mathrm{r},1}(r)\,\mathrm{d}r = 2\pi h\frac{1-\sigma}{E}p^2\int_0^a r\,\mathrm{d}r = \pi h\frac{1-\sigma}{E}p^2a^2; \tag{9.90}$$

(ii) the elastic energy (9.82) associated with the stresses (9.88a) and strains (9.89a) due to the pressure at zero order,

$$\overline{E}_{0,0} = \pi h\int_0^a (T_{\mathrm{rr},1}S_{\mathrm{rr},1} + T_{\mathrm{tt},1}S_{\mathrm{tt},1})\,r\,\mathrm{d}r = 2\pi h\frac{1-\sigma}{E}p^2\int_0^a r\,\mathrm{d}r = \pi h\frac{1-\sigma}{E}p^2a^2 = \overline{W}_0, \tag{9.91}$$

balances the work of the pressure (9.90); (iii) the gravity potential energy (9.79b) is given to zero order by

$$\overline{\Phi}_0 = 2\pi\rho ghH\int_0^a \left(r^4 - 2a^2r^2 + a^4\right)r\,\mathrm{d}r = \frac{\pi}{3}\rho ghHa^6; \tag{9.92}$$

it corresponds to the cross-strains S_{rz}, whose square is neglected in (9.11a), so that the corresponding energy does not appear in the zero-order energy balance (9.82). This does not affect the first and second-order energy terms in (9.85b), that specify the perturbation parameter (9.85c).

The perturbation parameter (9.85c) involves four quantities: (i) the first order work (9.78b) involving (9.86b) given by

$$\overline{W}_1 = -2\pi ph\int_0^a u_{\mathrm{r},2}(r)\,\mathrm{d}r = \frac{\pi phH^2a^8}{3}X_1, \tag{9.93a}$$

with a numerical factor equal to

$$X_1 \equiv a^{-8}\int_0^a \left[(7-\sigma)r^7 - 4(5-\sigma)a^2r^5 + 6(3-\sigma)a^4r^3 - 3(1-\sigma)a^6r\right]\mathrm{d}r$$
$$= \frac{7-\sigma}{8} - \frac{10-2\sigma}{3} + \frac{9-3\sigma}{2} - \frac{3-3\sigma}{2} = \frac{13}{24}(1+\sigma); \tag{9.93b}$$

(ii) the first order gravity potential (9.79b) involving (9.87b) given by

$$\overline{\Phi}_1 = \frac{\pi\rho gpHh^2}{36D}\int_0^a \left(2r^6 - 9a^2r^4 + 12a^4r^2 - 5a^6\right)r\,\mathrm{d}r$$
$$= \frac{\pi\rho gpHh^2}{36D}a^8\left(\frac{1}{4} - \frac{3}{2} + 3 - \frac{5}{2}\right) = -\frac{\pi\rho gpHh^2}{48D}a^8 = -\frac{3}{64}\frac{\pi p\rho^2g^2\left(1-\sigma^2\right)^2a^8}{E^2h^3}; \tag{9.94}$$

(iii) the zero-first order cross energy (9.80c),

$$\overline{E}_{1,0} = \pi h\int_0^a (T_{\mathrm{rr},1}S_{\mathrm{rr},2} + T_{\mathrm{rr},2}S_{\mathrm{rr},1} + T_{\mathrm{tt},1}S_{\mathrm{tt},2} + T_{\mathrm{tt},2}S_{\mathrm{tt},1})\,r\,\mathrm{d}r, \tag{9.95a}$$

involving all the relations from (9.88a) to (9.89b) and leading to

$$\overline{E}_{1,0} = \frac{\pi phH^2}{3} a^8 (1-\sigma) X_2 \tag{9.95b}$$

with numerical factor

$$X_2 \equiv a^{-8} \int_0^a \left(8r^6 - 24a^2r^4 + 24a^4r^2 - 6a^6\right) r \, \mathrm{d}r = 1 - 4 + 6 - 3 = 0, \tag{9.95c}$$

showing that the cross deformation energy between the two lowest orders is zero; (iv) the first-order energy (9.80b),

$$\overline{E}_{1,1} = \pi h \int_0^a \left(T_{\mathrm{rr},2} S_{\mathrm{rr},2} + T_{\mathrm{tt},2} S_{\mathrm{tt},2}\right) r \, \mathrm{d}r, \tag{9.96a}$$

involving (9.88b) and (9.89b) in

$$\overline{E}_{1,1} = \frac{\pi phH^4}{36} a^{14} X_3, \tag{9.96b}$$

with numerical factor calculated by

$$\begin{aligned}
X_3 \equiv a^{-14} \int_0^a & \left\{\left(r^6 - 4a^2r^4 + 6a^4r^2 - 3a^6\right)\right. \\
& \times \left[(1-7\sigma) r^6 - 4(1-5\sigma) a^2r^4 + 6(1-3\sigma) a^4r^2 - 3(1-\sigma) a^6\right] \\
& + \left(7r^6 - 20a^2r^4 + 18a^4r^2 - 3a^6\right) \\
& \times \left.\left[(7-\sigma) r^6 - 4(5-\sigma) a^2r^4 + 6(3-\sigma) a^4r^2 - 3(1-\sigma) a^6\right]\right\} r \, \mathrm{d}r \\
& = \frac{50-14\sigma}{14} - \frac{288-96\sigma}{12} + \frac{680-280\sigma}{10} - \frac{816-432\sigma}{8} + \frac{504-360\sigma}{6} - 144\frac{1-\sigma}{4} + \frac{18}{2} \\
& = \frac{18}{7},
\end{aligned} \tag{9.96c}$$

as the integral of $2 \times 4 \times 4 = 32$ products, corresponding to powers of r^{13}, r^{11}, r^9, r^7, r^5, r^3 and r^1, leading to a sum of seven terms, that does not depend on σ.

At zero order, the ratio of the total gravity potential energy (9.92) to the total work of the pressure in a radial displacement (9.90) is

$$\frac{\overline{\Phi}_0}{\overline{W}_0} = \frac{E}{3} \frac{\rho gH}{1-\sigma} \frac{a^4}{p^2} = \frac{1+\sigma}{16} \left(\frac{\rho gh}{p}\right)^2 \left(\frac{a}{h}\right)^4, \tag{9.97}$$

using (9.45d). Likewise the ratio of first-order perturbations (9.94) and (9.93a) is

$$\frac{\overline{\Phi}_1}{\overline{W}_1} = -\frac{3}{26} \frac{1}{1+\sigma} \frac{\rho gh}{DH} = -\frac{96}{13} \frac{1}{1+\sigma}. \tag{9.98}$$

Since the ratio (9.98) is neither too large nor too small, both terms should be included in the evaluation of asymptotic perturbation parameter (9.85c) using (9.93a), (9.94), (9.95b) and (9.96b), leading to

$$\varepsilon = \frac{X_4}{a^6 H^2}, \tag{9.99a}$$

with the coefficients

$$X_3^{-1} X_4 \equiv 12X_1 - \frac{3}{4}\frac{\rho g h}{DH} - 12\left(1-\sigma\right) X_2 = \frac{13}{2}\left(1+\sigma\right) - 48. \tag{9.99b}$$

Substitution of (9.45d) and (9.99b) in (9.99a) shows that the perturbation parameter,

$$\varepsilon = -\frac{256}{7}\frac{83-13\sigma}{\left(1-\sigma^2\right)^2}\left(\frac{E}{\rho g h}\right)^2\left(\frac{h}{a}\right)^6, \tag{9.99c}$$

indicates when coupling of bending and in-plane stresses is stronger, that is for larger: (i) ratio of thickness to diameter to the sixth power, that is thick plates; (ii) ratio of Young modulus to weight per unit area to the square, that is stiff light plates. The negative sign of the asymptotic expansion parameter implies that the first-order coupling reduces the zero-order decoupled values. The assumption (9.11a) of neglecting the square of cross-strains implies that at zero order the work of the pressure (9.90) balances the elastic energy (9.91), so that in (9.82) the gravity potential energy must be negligible, implying

$$\overline{\Phi}_0 \ll \overline{W}_0 \Rightarrow \wedge \equiv \left(\frac{\rho g h}{E}\right)^2\left(\frac{a}{h}\right)^4 \ll \frac{16}{1+\sigma}, \tag{9.100}$$

from (9.97). Substituting (9.100) in (9.99c) sets a lower bound for the modulus of the perturbation parameter:

$$|\varepsilon| = \frac{256}{7}\frac{83-13\sigma}{\left(1-\sigma^2\right)^2}\left(\frac{h}{a}\right)^2\frac{1}{\wedge} \gg \frac{16}{7}\frac{83-13\sigma}{\left(1-\sigma^2\right)\left(1-\sigma\right)}\left(\frac{h}{a}\right)^2. \tag{9.101}$$

The restriction (9.101) arises from the zero order energy balance, that must be satisfied regardless of higher-order terms specifying the perturbation parameter (9.99c). The restriction (9.101) for thin plates may be consistent with small perturbation parameter $\varepsilon < 0.3$, whose square is negligible, $\varepsilon^2 = 0.09 \ll 1$, so that the second-order approximation applies in the perturbation expansions (9.77). For larger $\varepsilon > 0.3$, more terms are needed in the perturbation expansion (9.77) with truncation error (9.44d) and the perturbation parameter is a real root of (9.83). The full perturbation expansion as a series with $N = \infty$ converges, as stated in (9.44c), with remainder (9.44d) for real roots smaller than unity of the series equality (9.83). These remarks are not a full discussion of the conditions of validity of the Föppl-von Kármán equations, that can be found in the literature [259, 260], and concern only the present application.

9.7 Main conclusions of the chapter 9

The present chapter contributes to the theory of non-linear elasticity [248] with a focus on the strong bending of plates [243, 244] coupling to in-plane stresses. The Föppl-von Kármán equations are obtained by two distinct methods, non-variational (section 9.1) and variational (section 9.2). They assume linear stress-strain relations for elasticity and neglect cross-strains. The variational method also specifies the boundary conditions involving the stress couples and augmented turning moment. The augmented turning moment adds a term involving the in-plane stresses to the turning moment for the bending of a plate. The solution method is a perturbation expansion that is obtained explicitly to all orders (section 9.3).

In the axisymmetric case, all orders can be solved exactly for any loading that is an analytic function of the radius. It is shown that the perturbation series converges for perturbation parameter less than unity (section 9.4). The method is illustrated for a heavy circular plate under axial compression, including the lowest-order non-linear coupling between transverse and in-plane displacements, strains and stresses (section 9.5). The perturbation parameter is shown to scale (section 9.6) on (i) the sixth power cube of the ratio of the thickness to the radius of the plate and on (ii) the square of the Young modulus divided by the weight per unit area, indicating when coupling of bending with in-plane stresses is stronger.

The general method of perturbation expansions for the strong bending of an elastic plate, including in-plane stresses, is summarised next, starting with the axisymmetric case and proceeding to the general case. It has been shown that the strong bending, under the equations (9.3b) and (9.4), with axial symmetry (9.34b), of a heavy plate under uniform axial compression (9.58a) at its circular clamped boundary with radius a, is specified to first order, that is the lowest order of non-linearity, by the stress function (9.55b) and transverse displacement (9.56e) that lead in the interior of the plate, respectively: (i) at the centre, to the stresses (9.58b), strains (9.62) and (9.63) and radial stress couple (9.69a); (ii) at the boundary, to the stress (9.58a), strains (9.60b), (9.62) and (9.63) and radial stress couple (9.69b). The unaugmented (9.71b) and augmented (9.72) radial turning moments do not generally coincide except at the centre where they vanish and at the boundary where they are non-zero.

This case is an example of the general method of solution of the non-linear equations (9.3b) and (9.4) for the strong bending of plates via perturbation expansions (9.29a) and (9.29b), leading to the causal chain of linear differential equations in which each depends on all the preceding. In the case of axial symmetry (9.34b), the equations for non-linear bending (9.38) lead to the perturbation sequence (9.39a), (9.39b) and (9.39c). If the transverse force per unit area and in-plane stresses at the lowest linear order are polynomials of the radius, the solutions (9.43b) and (9.43a) apply to all higher orders, specifying the stress function (9.29b) and transverse displacement (9.29a) to any order of accuracy. From them, it can be calculated the stresses (9.36a), strains (9.36b), in-plane and out-of-plane displacements, the radial stress couple (9.37a) and the augmented turning moment (9.37b). The boundary conditions can be applied, such as (9.28a) to (9.28c) and (9.20a) to (9.20c) respectively for the transverse and in-plane displacements. The preceding theory for isotropic elastic plates can be extended to pseudo-isotropic orthotropic plates (appendix E)

Among the many applications of perturbation expansions [79, 133, 243–248], the present case of non-linear bending of elastic plates coupled to in-plane stresses is exceptional, in that explicit perturbation equations for the transverse displacement and in-plane stress function are obtained to all orders. A second notable feature is that an explicit analytical solution can be obtained for all orders in the axisymmetric case with shear stress represented by a polynomial or analytic function of the radius. A third feature is the proof of convergence of the perturbation expansion to infinite order as a series for perturbation parameter less than unity. A fourth feature is the extension of the Föppl-von Kármán equations from isotropic plates to a more general subclass of orthotropic plates, designated pseudo-isotropic orthotropic plates [249–253].

References

[1] Y. C. Fung. *A first course in continuum mechanics for physical and biological engineers and scientists.* Prentice-Hall, Englewood Cliffs, NJ, 3rd edition, 1994. ISBN 978-0130615244.

[2] M. E. Gurtin. *An Introduction to Continuum Mechanics*, volume 158 of *Mathematics in science and engineering.* Academic Press, New York, NY, 1981. ISBN 0123097509.

[3] G. T. Mase and G. E. Mase. *Continuum mechanics for engineers.* CRC Press, Boca Raton, FL, 2nd edition, 1999. ISBN 0849318556.

[4] P. L. Gould. *Introduction to Linear Elasticity.* Springer-Verlag New York, New York, NY, 2nd edition, 1994. ISBN 978-1461287285. doi: 10.1007/978-1-4612-4296-3.

[5] A. C. Ugural and S. K. Fenster. *Advanced Strength and Applied Elasticity.* Prentice Hall Professional Technical Reference, Upper Saddle River, NJ, 4th edition, 2003. ISBN 0130473928.

[6] R. Szilard. *Theories and Applications of Plate Analysis: Classical, Numerical and Engineering Methods.* John Wiley & Sons, Hoboken, NJ, 2004. ISBN 0471429899.

[7] S. P. Timoshenko and J. N. Goodier. *Theory of elasticity.* Engineering societies monographs. McGraw-Hill Book Company, New York, NY, 2nd edition, 1951.

[8] O. Zaporozhets, V. Tokarev, and K. Attenborough. *Aircraft Noise: Assessment, prediction and control.* Spon Press, Abingdon, 1st edition, 2011. ISBN 978-0415240666.

[9] ICAO. *Doc 9829, Guidance on the Balanced Approach to Aircraft Noise Management.* International Civil Aviation Organization, 2nd edition, 2008. ISBN 978-9292310370.

[10] ICAO. *Doc 9911, Recommended Method for Computing Noise Contours Around Airports.* International Civil Aviation Organization, 1st edition, 2008. ISBN 978-9292312251.

[11] ISO. *20906, Acoustics — Unattended monitoring of aircraft sound in the vicinity of airports.* International Organization for Standardization, 1st edition, 2009.

[12] ISO. *1996-2, Acoustics — Description, measurement and assessment of environmental noise — Part 2: Determination of sound pressure levels.* International Organization for Standardization, 3rd edition, 2017.

[13] B. Wang and J. Kang. Effects of urban morphology on the traffic noise distribution through noise mapping: A comparative study between UK and China. *Applied Acoustics*, 72(8):556–568, 2011. ISSN 0003-682X. doi: 10.1016/j.apacoust.2011.01.011.

[14] Y. Hao and J. Kang. Influence of mesoscale urban morphology on the spatial noise attenuation of flyover aircrafts. *Applied Acoustics*, 84:73–82, 2014. ISSN 0003-682X. doi: 10.1016/j.apacoust.2013.12.001.

[15] R. Flores, P. Gagliardi, C. Asensio, and G. Licitra. A Case Study of the Influence of Urban Morphology on Aircraft Noise. *Acoustics Australia*, 45:389–401, 2017. ISSN 1839-2571. doi: 10.1007/s40857-017-0102-y.

[16] L. M. B. C. Campos and P. G. T. Á. Serrão. On the effect of atmospheric temperature gradients and ground impedance on sound. *International Journal of Aeroacoustics*, 13(5-6):427–448, 2014. ISSN 2048-4003. doi: 10.1260/1475-472X.13.5-6.427.

[17] L. M. B. C. Campos and F. S. R. P. Cunha. On the power spectra of sound transmitted through turbulence. *International Journal of Aeroacoustics*, 11(3-4):475–520, sep 2012. ISSN 2048-4003. doi: 10.1260/1475-472X.11.3-4.475.

[18] D. G. Albert and L. Liu. The effect of buildings on acoustic pulse propagation in an urban environment. *The Journal of the Acoustical Society of America*, 127(3):1335–1346, mar 2010. ISSN 0001-4966. doi: 10.1121/1.3277245.

[19] P. M. Morse and H. Feshbach. *Methods of Theoretical Physics*, volume 1-2 of *International series in pure and applied physics*. McGraw-Hill, New York, NY, 1953.

[20] L. D. Landau and E. M. Lifshitz. *Fluid mechanics*, volume 6 of *Course of Theoretical Physics*. Pergamon Press, Oxford, 2nd edition, 1987. ISBN 0080339328.

[21] M. J. Lighthill. *Waves in Fluids*. Cambridge University Press, Cambridge, 1st edition, 1978. ISBN 978-0521216890.

[22] A. D. Pierce. *Acoustics: An Introduction to Its Physical Principles and Applications*. Springer International Publishing, Cham, 3rd edition, 2019. ISBN 978-3030112134. doi: 10.1007/978-3-030-11214-1.

[23] M. S. Howe. *Acoustics of Fluid-Structure Interactions*. Cambridge monographs on mechanics. Cambridge University Press, Cambridge, 1998. ISBN 0521633206.

[24] J. A. Stratton. *Electromagnetic theory*. International series in pure and applied physics. McGraw-Hill book company, New York, NY, 1941.

[25] L. D. Landau and E. M. Lifshitz. *The Classical Theory of Fields*, volume 2 of *Course of Theoretical Physics*. Butterworth-Heinemann, Oxford, 4th edition, 1987. ISBN 978-0750627689.

[26] D. S. Jones. *The theory of electromagnetism*. Pergamon Press, Oxford, 1964.

[27] A. P. Dowling and J. E. F. Williams. *Sound and sources of sound*. Ellis Horwood series in engineering science. Ellis Horwood, Chichester, 1983. ISBN 978-0853125273.

[28] K. Attenborough. Review of Ground Effects on Outdoor Sound Propagation from Continuous Broadband Sources. *Applied Acoustics*, 24(4):289–319, 1988. ISSN 0003-682X. doi: 10.1016/0003-682X(88)90086-2.

[29] A. Sommerfeld. Über die Ausbreitung der Wellen in der drahtlosen Telegraphie. *Annalen der Physik*, 333(4):665–736, 1909. ISSN 0003-3804. doi: 10.1002/andp.19093330402.

[30] I. Rudnick. The Propagation of an Acoustic Wave along a Boundary. *The Journal of the Acoustical Society of America*, 19(2):348–356, 1947. ISSN 0001-4966. doi: 10.1121/1.1916490.

[31] U. Ingard. On the Reflection of a Spherical Sound Wave from an Infinite Plane. *The Journal of the Acoustical Society of America*, 23(3):329–335, may 1951. ISSN 0001-4966. doi: 10.1121/1.1906767.

[32] G. Taraldsen. A note on reflection of spherical waves. *The Journal of the Acoustical Society of America*, 117(6):3389–3392, 2005. ISSN 0001-4966. doi: 10.1121/1.1904303.

[33] M. J. T. Smith. *Aircraft Noise*. Cambridge Aerospace Series. Cambridge University Press, Cambridge, aug 1989. ISBN 978-0521331869. doi: 10.1017/CBO9780511584527.

[34] O. Zaporozhets, V. Tokarev, and K. Attenborough. *Aircraft Noise: Assessment, Prediction and Control*. CRC Press, London, 1st edition, may 2011. ISBN 978-1138073029. doi: 10.1201/b12545.

[35] M. E. Delany. Sound propagation in the atmosphere: a historical review. *Acta Acustica united with Acustica*, 38(4):201–223, oct 1977. ISSN 1610-1928.

[36] L. C. Sutherland and G. A. Daigle. Atmospheric sound propagation. In M. J. Crocker, editor, *Encylclopedia of Acoustics*, chapter 28, pages 305–329. Wiley, New York, NY, 1998. ISBN 978-0471252931.

[37] L. M. B. C. Campos. The spectral broadening of sound by turbulent shear layers. Part 1. The transmission of sound through turbulent shear layers. *Journal of Fluid Mechanics*, 89(4):723–749, dec 1978. doi: 10.1017/S0022112078002827.

[38] R. Raspet, S. W. Lee, E. Kuester, D. C. Chang, W. F. Richards, R. Gilbert, and N. Bong. A fast-field program for sound propagation in a layered atmosphere above an impedance ground. *The Journal of the Acoustical Society of America*, 77(2):345–352, feb 1985. ISSN 0001-496. doi: 10.1121/1.391906.

[39] L. M. B. C. Campos. *Complex Analysis with Applications to Flows and Fields*, volume 1 of *Mathematics and Physics for Science and Technology*. CRC Press, Boca Raton, FL, 1st edition, sep 2011. ISBN 978-1420071184. doi: 10.1201/b13580.

[40] S. P. Pao, A. R. Wenzel, and P. B. Oncley. NASA Technical Paper 1104, Prediction of Ground Effects on Aircraft Noise. Technical report, NASA, 1978.

[41] ICAO. *Doc 9911, Recommended Method for Computing Noise Contours Around Airports*. International Civil Aviation Organization, Montréal, 2nd edition, 2018. ISBN 978-9292583606.

[42] A. R. Wenzel. Propagation of waves along an impedance boundary. *The Journal of the Acoustical Society of America*, 55(5):956–963, may 1974. ISSN 0001-4966. doi: 10.1121/1.1914669.

[43] M. E. Delany and E. N. Bazley. Monopole radiation in the presence of an absorbing plane. *Journal of Sound and Vibration*, 13(3):269–279, nov 1970. ISSN 0022-460X. doi: 10.1016/S0022-460X(70)80019-0.

[44] M. E. Delany and E. N. Bazley. A note on the effect of ground absorption in the measurement of aircraft noise. *Journal of Sound and Vibration*, 16(3):315–322, jun 1971. ISSN 0022-460X. doi: 10.1016/0022-460X(71)90589-X.

[45] P. M. Morse and K. U. Ingard. *Theoretical acoustics*. International series in pure and applied physics. McGraw-Hill Book Company, New York, NY, 1968.

[46] J. W. Strutt. The Problem of the Whispering Gallery. *The London, Edinburgh, and Dublin Philosophical Magazine and Journal of Science*, 20(120):1001–1004, dec 1910. ISSN 1941-5982. doi: 10.1080/14786441008636993.

[47] L. M. B. C. Campos. On waves in gases. Part I: Acoustics of jets, turbulence, and ducts. *Reviews of Modern Physics*, 58(1):117–182, jan 1986. ISSN 0034-6861. doi: 10.1103/RevModPhys.58.117.

[48] L. M. B. C. Campos. On 36 Forms of the Acoustic Wave Equation in Potential Flows and Inhomogeneous Media. *Applied Mechanics Reviews*, 60(4):149–171, jul 2007. ISSN 0003-6900. doi: 10.1115/1.2750670.

[49] P. A. Nelson and S. J. Elliott. *Active Control of Sound*. Academic Press, London, 1st edition, 1992. ISBN 978-0125154253.

[50] L. M. B. C. Campos and F. J. P. Lau. On Active Noise Reduction in a Cylindrical Duct with Flow. *The International Journal of Acoustics and Vibration*, 14(3):150–162, 2009. ISSN 2415-1408. doi: 10.20855/ijav.2009.14.3246.

[51] J. W. Strutt. On the Propagation of Sound in narrow Tubes of variable section. *The London, Edinburgh, and Dublin Philosophical Magazine and Journal of Science*, 31(182):89–96, feb 1916. ISSN 1941-5982. doi: 10.1080/14786440208635477.

[52] N. W. McLachlan. *Loud Speakers: Theory, Performance, Testing and Design*. Oxford Engineering Science Series. Clarendon Press, Oxford, jul 1934.

[53] A. G. Webster. Acoustical Impedance, and the Theory of Horns and of the Phonograph. *Proceedings of the National Academy of Sciences of the United States of America*, 5(7):275–282, may 1919. ISSN 0027-8424.

[54] V. Salmon. A New Family of Horns. *The Journal of the Acoustical Society of America*, 17(3): 212–218, jan 1946. ISSN 0001-4966. doi: 10.1121/1.1916317.

[55] E. S. Weibel. On Webster's Horn Equation. *The Journal of the Acoustical Society of America*, 27 (4):726–727, jul 1955. ISSN 0001-4966. doi: 10.1121/1.1908007.

[56] E. Eisner. Complete Solutions of the "Webster" Horn Equation. *The Journal of the Acoustical Society of America*, 41(4B):1126–1146, apr 1967. ISSN 0001-4966. doi: 10.1121/1.1910444.

[57] R. W. Pyle Jr. Solid Torsional Horns. *The Journal of the Acoustical Society of America*, 41(4B): 1147–1156, apr 1967. ISSN 0001-4966. doi: 10.1121/1.1910445.

[58] B. N. Nagarkar and R. D. Finch. Sinusoidal Horns. *The Journal of the Acoustical Society of America*, 50(1A):23–31, jul 1971. ISSN 0001-4966. doi: 10.1121/1.1912609.

[59] C. Molloy. N-parameter ducts. *The Journal of the Acoustical Society of America*, 57(5):1030–1035, may 1975. ISSN 0001-4966. doi: 10.1121/1.380569.

[60] L. M. B. C. Campos. Some general properties of the exact acoustic fields in horns and baffles. *Journal of Sound and Vibration*, 95(2):177–201, jul 1984. ISSN 0022-460X. doi: 10.1016/0022-460X(84)90541-8.

[61] N. A. Eisenberg and T. W. Kao. Propagation of Sound through a Variable-Area Duct with a Steady Compressible Flow. *The Journal of the Acoustical Society of America*, 49(1B):169–175, 1971. ISSN 0001-4966. doi: 10.1121/1.1912314.

[62] E. Lumsdaine and S. Ragab. Effect of flow on quasi-one-dimensional acoustic wave propagation in a variable area duct of finite length. *Journal of Sound and Vibration*, 53(1):47–61, 1977. ISSN 0022-460X. doi: 10.1016/0022-460X(77)90093-1.

[63] L. M. B. C. Campos. On the fundamental acoustic mode in variable area, low Mach number nozzles. *Progress in Aerospace Sciences*, 22(1):1–27, jan 1985. ISSN 0376-0421. doi: 10.1016/0376-0421(85)90003-X.

[64] L. M. B. C. Campos and F. J. P. Lau. On the convection of sound in inverse catenoidal nozzles. *Journal of Sound and Vibration*, 244(2):195–209, jul 2001. ISSN 0022-460X. doi: 10.1006/jsvi.2000.3470.

[65] A. Cummings. Sound Transmission in Curved Duct Bends. *Journal of Sound and Vibration*, 35(4): 451–477, 1974. ISSN 0022-460X.

[66] M. K. Meyerand and P. Mungur. Sound propagation in curved ducts. *Progress in Astronautics and Aeronautics*, 44:347–362, 1976.

[67] W. C. Osborne. Higher mode propagation of sound in short curved bends of rectangular cross-section. *Journal of Sound and Vibration*, 45(1):39–52, mar 1976. ISSN 0022-460X. doi: 10.1016/0022-460X(76)90666-0.

[68] S. H. Ko and L. T. Ho. Sound attenuation in acoustically lined curved ducts in the absence of fluid flow. *Journal of Sound and Vibration*, 53(2):189–201, jul 1977. ISSN 0022-460X. doi: 10.1016/0022-460X(77)90465-5.

[69] D. H. Keefe and A. H. Benade. Wave propagation in strongly curved ducts. *The Journal of the Acoustical Society of America*, 74(1):320–332, jul 1983. ISSN 0001-4966. doi: 10.1121/1.389681.

[70] D. Firth and F. J. Fahy. Acoustic characteristics of circular bends in pipes. *Journal of Sound and Vibration*, 97(2):287–303, nov 1984. ISSN 0022-460X. doi: 10.1016/0022-460X(84)90323-7.

[71] S. Félix and V. Pagneux. Ray-wave correspondence in bent waveguides. *Wave Motion*, 41(4): 339–355, apr 2005. ISSN 0165-2125. doi: 10.1016/j.wavemoti.2004.08.003.

[72] S. Félix, J.-P. Dalmont, and C. J. Nederveen. Effects of bending portions of the air column on the acoustical resonances of a wind instrument. *The Journal of the Acoustical Society of America*, 131 (5):4164–4172, may 2012. ISSN 0001-4966. doi: 10.1121/1.3699267.

[73] C. Yang. Acoustic attenuation of a curved duct containing a curved axial microperforated panel. *The Journal of the Acoustical Society of America*, 145(1):501–511, jan 2019. ISSN 0001-4966. doi: 10.1121/1.5087823.

[74] L. M. B. C. Campos and P. G. T. Á. Serrão. On helicoidal rectangular coordinates for the acoustics of bent and twisted tubes. *Wave Motion*, 38(1):53–66, jun 2003. ISSN 0165-2125. doi: 10.1016/S0165-2125(03)00011-8.

[75] J. Bernoulli. Véritable hypothèse de la résistance des solides, avec la démonstration de la courbure de corps qui font resort. In *Mémoires de Mathématique et de Physique de l'Académie Royale des Sciences*, pages 176–186. Académie royale des sciences, Paris, mar 1705.

[76] L. Euler. *Methodus inveniendi líneas curvas maximi minimive proprietate gaudantes, sive solutio problematis isoperimetrici latíssimo sensu accepti.* Apud Marcum-Michaelem Bousquet & Socios, Laussane, Geneva, 1744.

[77] A. E. H. Love. *A treatise on the mathematical theory of elasticity.* Dover Books on Engineering. Dover Publications, New York, NY, 4th edition, 1944.

[78] S. P. Timoshenko and J. G. Monroe. *Theory of elastic stability.* McGraw-Hill Book Company, New York, NY, 2nd edition, 1961.

[79] L. D. Landau and E. M. Lifshitz. *Theory of Elasticity*, volume 7 of *Course of Theoretical Physics.* Pergamon Press, Oxford, 2nd edition, 1970.

[80] V. G. Rekach. *Manual of the Theory of Elasticity.* Mir Publishers, Moscow, 1st edition, 1979.

[81] S. S. Antman. *Nonlinear Problems of Elasticity*, volume 107 of *Applied Mathematical Sciences.* Springer Science+Business Media, New York, NY, 1st edition, 1995. ISBN 978-1475741490. doi: 10.1007/978-1-4757-4147-6.

[82] L. M. B. C. Campos and A. C. Marta. On the prevention or facilitation of buckling of beams. *International Journal of Mechanical Sciences*, 79:95–104, feb 2014. ISSN 0020-7403. doi: 10.1016/j.ijmecsci.2013.12.003.

[83] S. L. Chan. Geometric and material non-linear analysis of beam-columns and frames using the minimum residual displacement method. *International Journal for Numerical Methods in Engineering*, 26(12):2657–2669, dec 1988. ISSN 0029-5981. doi: 10.1002/nme.1620261206.

[84] R. K. Kapania and S. Raciti. Recent Advances in Analysis of Laminated Beams and Plates, Part I: Shear Effects and Buckling. *AIAA Journal*, 27(7):923–935, jul 1989. ISSN 0001-1452. doi: 10.2514/3.10202.

[85] H. Huang and G. A. Kardomateas. Buckling and Initial Postbuckling Behavior of Sandwich Beams Including Transverse Shear. *AIAA Journal*, 40(11):2331–2335, nov 2002. ISSN 0001-1452. doi: 10.2514/2.1571.

[86] N. Silvestre. Generalised beam theory to analyse the buckling behaviour of circular cylindrical shells and tubes. *Thin-Walled Structures*, 45(2):185–198, feb 2007. ISSN 0263-8231. doi: 10.1016/j.tws.2007.02.001.

[87] S. P. Machado. Non-linear buckling and postbuckling behavior of thin-walled beams considering shear deformation. *International Journal of Non-Linear Mechanics*, 43(5):345–365, jun 2008. ISSN 0020-7462. doi: 10.1016/j.ijnonlinmec.2007.12.019.

[88] G. C. Ruta, V. Varano, M. Pignataro, and N. L. Rizzi. A beam model for the flexural–torsional buckling of thin-walled members with some applications. *Thin-Walled Structures*, 46(7-9):816–822, jul 2008. ISSN 0263-8231. doi: 10.1016/j.tws.2008.01.020.

[89] G. Mancusi and L. Feo. Non-linear pre-buckling behavior of shear deformable thin-walled composite beams with open cross-section. *Composites Part B: Engineering*, 47:379–390, apr 2013. ISSN 1359-8368. doi: 10.1016/j.compositesb.2012.11.003.

[90] D. Lanc, G. Turkalj, T. P. Vo, and J. Brnić. Nonlinear buckling behaviours of thin-walled functionally graded open section beams. *Composite Structures*, 152:829–839, sep 2016. ISSN 0263-8223. doi: 10.1016/j.compstruct.2016.06.023.

[91] J. W. Hutchinson and B. Budiansky. Dynamic Buckling Estimates. *AIAA Journal*, 4(3):525–530, mar 1966. ISSN 0001-1452. doi: 10.2514/3.3468.

[92] J. Zhao, J. Jia, X. He, and H. Wang. Post-buckling and Snap-Through Behavior of Inclined Slender Beams. *Journal of Applied Mechanics*, 75(4), 2008. ISSN 0021-8936. doi: 10.1115/1.2870953.

[93] C. Vega-Posada, M. Areiza-Hurtado, and J. D. Aristizabal-Ochoa. Large-deflection and post-buckling behavior of slender beam-columns with non-linear end-restraints. *International Journal of Non-Linear Mechanics*, 46(1):79–95, jan 2011. ISSN 0020-7462. doi: 10.1016/j.ijnonlinmec.2010.07.006.

[94] A. Goriely, R. Vandiver, and M. Destrade. Nonlinear Euler buckling. *Proceedings of the Royal Society A: Mathematical, Physical and Engineering Sciences*, 464(2099):3003–3019, nov 2008. ISSN 1364-5021. doi: 10.1098/rspa.2008.0184.

[95] L. Li and Y. Hu. Buckling analysis of size-dependent nonlinear beams based on a nonlocal strain gradient theory. *International Journal of Engineering Science*, 97:84–94, dec 2015. ISSN 0020-7225. doi: 10.1016/S0020-7683(00)00300-0.

[96] A. H. Nayfeh, W. Kreider, and T. J. Anderson. Investigation of natural frequencies and mode shapes of buckled beams. *AIAA Journal*, 33(6):1121–1126, jun 1995. ISSN 0001-1452. doi: 10.2514/3.12669.

[97] W. Lestari and S. Hanagud. Nonlinear vibration of buckled beams: some exact solutions. *International Journal of Solids and Structures*, 38(26-27):4741–4757, jun 2001. ISSN 0020-7683. doi: 10.1016/S0020-7683(00)00300-0.

[98] A. M. Abou-Rayan, A. H. Nayfeh, D. T. Mook, and M. A. Nayfeh. Nonlinear Response of a Parametrically Excited Buckled Beam. *Nonlinear Dynamics*, 4(5):499–525, oct 1993. ISSN 0924-090X. doi: 10.1007/BF00053693.

[99] A. H. Nayfeh, W. Lacarbonara, and C.-M. Chin. Nonlinear Normal Modes of Buckled Beams: Three-to-One and One-to-One Internal Resonances. *Nonlinear Dynamics*, 18(3):253–273, 1999. ISSN 0924-090X. doi: 10.1023/A:1008389024738.

[100] J. S. Jensen. Buckling of an elastic beam with added high-frequency excitation. *International Journal of Non-Linear Mechanics*, 35(2):217–227, mar 2000. ISSN 0020-7462. doi: 10.1016/S0020-7462(99)00010-4.

[101] S. A. Emam and A. H. Nayfeh. Non-linear response of buckled beams to 1:1 and 3:1 internal resonances. *International Journal of Non-Linear Mechanics*, 52:12–25, jun 2013. ISSN 0020-7462. doi: 10.1016/j.ijnonlinmec.2013.01.018.

[102] O. C. Pinto and P. B. Gonçalves. Non-linear control of buckled beams under step loading. *Mechanical Systems and Signal Processing*, 14(6):967–985, nov 2000. ISSN 0888-3270. doi: 10.1006/mssp.2000.1300.

[103] S. Li and Y. Zhou. Post-buckling of a hinged-fixed beam under uniformly distributed follower forces. *Mechanics Research Communications*, 32(4):359–367, jul 2005. ISSN 0093-6413. doi: 10.1016/j.mechrescom.2004.10.019.

[104] S.-r. Li, J.-h. Zhang, and Y.-g. Zhao. Thermal post-buckling of Functionally Graded Material Timoshenko beams. *Applied Mathematics and Mechanics*, 27(6):803–810, jun 2006. ISSN 0253-4827. doi: 10.1007/s10483-006-0611-y.

[105] S.-R. Li and R. C. Batra. Thermal Buckling and Postbuckling of Euler-Bernoulli Beams Supported on Nonlinear Elastic Foundations. *AIAA Journal*, 45(3):712–720, mar 2007. ISSN 0001-1452. doi: 10.2514/1.24720.

[106] X. Song and S.-R. Li. Thermal buckling and post-buckling of pinned–fixed Euler–Bernoulli beams on an elastic foundation. *Mechanics Research Communications*, 34(2):164–171, mar 2007. ISSN 0093-6413. doi: 10.1016/j.mechrescom.2006.06.006.

[107] A. Ono. Lateral vibrations of tapered bars. *Journal of the Society of Mechanical Engineers*, 28(99): 429–441, jul 1925. ISSN 2433-1546. doi: 10.1299/jsmemagazine.28.99_429.

[108] H. D. Conway, E. C. H. Becker, and J. F. Dubil. Vibration Frequencies of Tapered Bars and Circular Plates. *Journal of Applied Mechanics*, 31(2):329–331, jun 1964. ISSN 0021-8936. doi: 10.1115/1.3629606.

[109] J. H. Gaines and E. Volterra. Transverse Vibrations of Cantilever Bars of Variable Cross Section. *The Journal of the Acoustical Society of America*, 39(4):674–679, apr 1966. ISSN 0001-4966. doi: 10.1121/1.1909940.

[110] H.-C. Wang. Generalized Hypergeometric Function Solutions on the Transverse Vibration of a Class of Nonuniform Beams. *Journal of Applied Mechanics*, 34(3):702–708, sep 1967. ISSN 0021-8936. doi: 10.1115/1.3607764.

[111] S. Naguleswaran. Vibration of an Euler-Bernoulli beam of constant depth and with linearly varying breadth. *Journal of Sound and Vibration*, 153(3):509–522, mar 1992. ISSN 0022-460X. doi: 10.1016/0022-460X(92)90379-C.

[112] B. Downs. Transverse Vibrations of Cantilever Beams Having Unequal Breadth and Depth Tapers. *Journal of Applied Mechanics*, 44(4):737–742, dec 1977. ISSN 0021-8936. doi: 10.1115/1.3424165.

[113] M. Amabili and R. Garziera. A technique for the systematic choice of admissible functions in the Rayleigh-Ritz method. *Journal of Sound and Vibration*, 224(3):519–539, jul 1999. ISSN 0022-460X. doi: 10.1006/jsvi.1999.2198.

[114] D. Zhou and Y. K. Cheung. The free vibration of a type of tapered beams. *Computer Methods in Applied Mechanics and Engineering*, 188(1-3):203–216, jul 2000. ISSN 0045-7825. doi: 10.1016/S0045-7825(99)00148-6.

[115] M. Bayat, I. Pakar, and M. Bayat. Analytical study on the vibration frequencies of tapered beams. *Latin American Journal of Solids and Structures*, 8(2):149–162, jun 2011. ISSN 1679-7825. doi: 10.1590/S1679-78252011000200003.

[116] C. Y. Wang. Vibration of a tapered cantilever of constant thickness and linearly tapered width. *Archive of Applied Mechanics*, 83(1):171–176, jan 2013. ISSN 0939-1533. doi: 10.1007/s00419-012-0637-1.

[117] A. V. Balakrishnan and K. W. Iliff. Continuum Aeroelastic Model for Inviscid Subsonic Bending-Torsion Wing Flutter. *Journal of Aerospace Engineering*, 20(3):152–164, jul 2007. ISSN 0893-1321. doi: 10.1061/(ASCE)0893-1321(2007)20:3(152).

[118] C.-S. Chang and D. H. Hodges. Parametric Studies on Ground Vibration Test Modeling for Highly Flexible Aircraft. *Journal of Aircraft*, 44(6):2049–2059, nov 2007. ISSN 0021-8669. doi: 10.2514/1.30733.

[119] W. Su and C. E. S. Cesnik. Dynamic Response of Highly Flexible Flying Wings. *AIAA Journal*, 49(2):324–339, feb 2011. ISSN 0001-1452. doi: 10.2514/1.J050496.

[120] X. Changchuan, Y. Lan, L. Yi, and Y. Chao. Stability of Very Flexible Aircraft with Coupled Nonlinear Aeroelasticity and Flight Dynamics. *Journal of Aircraft*, 55(2):862–874, mar 2018. ISSN 0021-8669. doi: 10.2514/1.C034162.

[121] X. Rui, L. K. Abbas, F. Yang, G. Wang, H. Yu, and Y. Wang. Flapwise Vibration Computations of Coupled Helicopter Rotor/Fuselage: Application of Multibody System Dynamics. *AIAA Journal*, 56(2):818–835, feb 2018. ISSN 0001-1452. doi: 10.2514/1.J056591.

[122] L. M. B. C. Campos and A. C. Marta. On The Vibrations of Pyramidal Beams With Rectangular Cross-Section and Application to Unswept Wings. *The Quarterly Journal of Mechanics and Applied Mathematics*, 74(1):1–31, feb 2021. ISSN 0033-5614. doi: 10.1093/qjmam/hbaa017.

[123] L. Pernod, B. Lossouarn, J.-A. Astolfi, and J.-F. Deü. Vibration damping of marine lifting surfaces with resonant piezoelectric shunts. *Journal of Sound and Vibration*, 496, mar 2021. ISSN 0022-460X. doi: 10.1016/j.jsv.2020.115921.

[124] P. R. Saffari, M. Fakhraie, and M. A. Roudbari. Size-Dependent Vibration Problem of Two Vertically-Aligned Single-Walled Boron Nitride Nanotubes Conveying Fluid in Thermal Environment Via Nonlocal Strain Gradient Shell Model. *Journal of Solid Mechanics*, 13(2):164–185, 2021. ISSN 2008-3505. doi: 10.22034/jsm.2020.1895313.1561.

[125] C. Thongchom, P. R. Saffari, P. R. Saffari, N. Refahati, S. Sirimontree, S. Keawsawasvong, and S. Titotto. Dynamic response of fluid-conveying hybrid smart carbon nanotubes considering slip boundary conditions under a moving nanoparticle. *Mechanics of Advanced Materials and Structures*, mar 2022. ISSN 1537-6494. doi: 10.1080/15376494.2022.2051101.

[126] L. M. B. C. Campos. Note on a generalization of Gauss least squares method applied to active noise reduction systems. *Journal of Sound and Vibration*, 219(5):925–926, feb 1999. ISSN 0022-460X. doi: 10.1006/jsvi.1998.1894.

[127] L. M. B. C. Campos. *Linear Differential Equations and Oscillators*, volume 4 of *Mathematics and Physics for Science and Technology*. CRC Press, Boca Raton, FL, 1st edition, nov 2019. ISBN 978-0367137182. doi: 10.1201/9780429028984.

[128] L. M. B. C. Campos. On waves in gases. Part II: Interaction of sound with magnetic and internal modes. *Reviews of Modern Physics*, 59(2):363–463, apr 1987. doi: 10.1103/RevModPhys.59.363.

[129] L. M. B. C. Campos. *Higher-Order Differential Equations and Elasticity*, volume 4 of *Mathematics and Physics for Science and Technology*. CRC Press, Boca Raton, FL, 1st edition, nov 2019. ISBN 978-0367137205. doi: 10.1201/9780429029691.

[130] L. M. B. C. Campos. *Generalized Calculus with Applications to Matter and Forces*, volume 3 of *Mathematics and Physics for Science and Technology*. CRC Press, Boca Raton, FL, 1st edition, oct 2014. ISBN 978-0367378721. doi: 10.1201/b17019.

[131] M. J. Lighthill. *Introduction to Fourier analysis and generalised functions*. Cambridge monographs on mechanics and applied mathematics. Cambridge University Press, Cambridge, 1958.

[132] A. R. Forsyth. *A treatise on differential equations*. Macmillan, London, 6th edition, 1956.

[133] L. M. B. C. Campos. *Transcendental Representations with Applications to Solids and Fluids*, volume 2 of *Mathematics and Physics for Science and Technology*. CRC Press, Boca Raton, FL, 1st edition, apr 2012. ISBN 978-1439834312. doi: 10.1201/b11862.

[134] L. M. B. C. Campos. *Simultaneous Differential Equations and Multi-Dimensional Vibrations*, volume 4 of *Mathematics and Physics for Science and Technology*. CRC Press, Boca Raton, FL, 1st edition, nov 2019. ISBN 978-0367137212. doi: 10.1201/9780429030253.

[135] S. Ballantine. On the propagation of sound in the general Bessel horn of infinite length. *Journal of the Franklin Institute*, 203(1):85–102, jan 1927. ISSN 0016-0032. doi: 10.1016/S0016-0032(27)90099-4.

[136] H. F. Olson. A Horn Consisting of Manifold Exponential Sections. *Journal of the Society of Motion Picture Engineers*, 30(5):511–518, may 1938. ISSN 0097-5834. doi: 10.5594/J16575.

[137] D. A. Bies. Tapering a Bar for Uniform Stress in Longitudinal Oscillation. *The Journal of the Acoustical Society of America*, 34(10):1567–1569, oct 1962. ISSN 0001-4966. doi: 10.1121/1.1909049.

[138] L. M. B. C. Campos and A. J. P. Santos. On the propagation and damping of longitudinal oscillations in tapered visco-elastic bars. *Journal of Sound and Vibration*, 126(1):109–125, oct 1988. ISSN 0022-460X. doi: 10.1016/0022-460X(88)90402-6.

[139] L. M. B. C. Campos. On the propagation of sound in nozzles of variable cross-section containing low Mach number mean flows. *Zeitschrift für Flugwissenschaften und Weltraumforschung*, 8:97–109, 1984.

[140] L. M. B. C. Campos and F. J. P. Lau. On sound in an inverse sinusoidal nozzle with low Mach number mean flow. *The Journal of the Acoustical Society of America*, 100(1):355–363, jul 1996. ISSN 0001-4966. doi: 10.1121/1.415852.

[141] L. M. B. C. Campos and F. J. P. Lau. On the acoustics of low Mach number bulged, throated and baffled nozzles. *Journal of Sound and Vibration*, 196(5):611–633, oct 1996. ISSN 0022-460X. doi: 10.1006/jsvi.1996.0505.

[142] W. Rostafinski. Analysis of propagation of waves of acoustic frequencies in curved ducts. *The Journal of the Acoustical Society of America*, 56(1):11–15, jul 1974. ISSN 0001-4966. doi: 10.1121/1.1903225.

[143] C. K. W. Tam. A study of sound transmission in curved duct bends by the Galerkin method. *Journal of Sound and Vibration*, 45(1):91–104, mar 1976. ISSN 0022460X. doi: 10.1016/0022-460X(76)90669-6.

[144] M. El-Raheb and P. Wagner. Acoustic propagation in a rigid torus. *The Journal of the Acoustical Society of America*, 71(6):1335–1346, jun 1982. ISSN 0001-4966. doi: 10.1121/1.387853.

[145] C. J. Nederveen. Influence of a toroidal bend on wind instrument tuning. *The Journal of the Acoustical Society of America*, 104(3):1616–1626, sep 1998. ISSN 0001-4966. doi: 10.1121/1.424374.

[146] S. Félix and V. Pagneux. Sound propagation in rigid bends: A multimodal approach. *The Journal of the Acoustical Society of America*, 110(3):1329–1337, sep 2001. ISSN 0001-4966. doi: 10.1121/1.1391249.

[147] S. Félix and V. Pagneux. Multimodal analysis of acoustic propagation in three-dimensional bends. *Wave Motion*, 36(2):157–168, aug 2002. ISSN 0165-2125. doi: 10.1016/S0165-2125(02)00009-4.

[148] S. Félix and V. Pagneux. Sound attenuation in lined bends. *The Journal of the Acoustical Society of America*, 116(4):1921–1931, oct 2004. ISSN 0001-4966. doi: 10.1121/1.1788733.

[149] H. D. Conway. The large deflection of simply supported beams. *The London, Edinburgh, and Dublin Philosophical Magazine and Journal of Science*, 38(287):905–911, dec 1947. ISSN 1941-5982. doi: 10.1080/14786444708561149.

[150] F. Saltari, C. Riso, G. D. Matteis, and F. Mastroddi. Finite-Element-Based Modeling for Flight Dynamics and Aeroelasticity of Flexible Aircraft. *Journal of Aircraft*, 54(6):2350–2366, nov 2017. ISSN 0021-8669. doi: 10.2514/1.C034159.

[151] G. Lamé. *Leçons sur la théorie mathématique de l'élasticité des corps solides.* Gauthier-Villars, Paris, 2nd edition, 1866.

[152] S. Timoshenko and S. Woinowsky-Krieger. *Theory of plates and shells.* Engineering societies monographs. McGraw-Hill Book Company, New York, NY, 2nd edition, 1959.

[153] I. S. Sokolnikoff. *Mathematical Theory of Elasticity.* McGraw-Hill Book Company, 2nd edition, 1956.

[154] J. N. Goodier and P. G. Hodge. *Elasticity and Plasticity*, volume 1 of *Surveys in Applied Mathematics.* John Wiley & Sons, New York, NY, 1958.

[155] F. R. Eirich. *Rheology Theory and Applications*, volume 1-5. Academic Press, New York, NY, 1956-1969.

[156] G. B. Warburton. *The Dynamical Behaviour of Structures.* Structures and Solid Body Mechanics Series. Pergamon Press, Oxford, 2nd edition, 1976. ISBN 0080203647.

[157] E. H. Mansfield. *The bending and stretching of plates.* Cambridge University Press, Cambridge, 2nd edition, 1989.

[158] W. Prager. *Introduction to Mechanics of Continua.* Dover Publications, Mineola, NY, 1973. ISBN 978-0486605845.

[159] W. Flügge. *Tensor Analysis and Continuum Mechanics.* Springer-Verlag Berlin Heidelberg, Berlin, 1st edition, 1972. ISBN 978-3642883842. doi: 10.1007/978-3-642-88382-8.

[160] W. C. Young and R. G. Budynas. *Roark's Formulas for Stress and Strain.* McGraw-Hill, New York, NY, 7th edition, 2002. ISBN 007072542X.

[161] J. B. Wilbur, C. H. Norris, and S. Utku. *Elementary structural analysis.* McGraw-Hill book company, New York, NY, 3rd edition, 1976. ISBN 978-0070472563.

[162] Y. N. Rabotnov. *Elements of hereditary solid mechanics.* Mir Publishers, Moscow, 1980.

[163] R. W. Clough and J. Penzien. *Dynamics of structures.* Computers & Structures, Berkeley, CA, 3rd edition, 2003. ISBN 978-0070850989.

[164] D. S. Chandrasekharaiah and L. Debnath. *Continuum mechanics.* Academic Press, San Diego, CA, 1994. ISBN 978-0121678807.

[165] L. A. Segel and G. H. Handelman. *Mathematics applied to continuum mechanics.* Dover Publications, New York, NY, 1987. ISBN 978-0486653693.

[166] A. N. Palazotto and S. T. Dennis. *Nonlinear Analysis of Shell Structures.* AIAA Education Series. American Institute of Aeronautics & Astronautics, Washington, DC, 1992.

[167] T. J. Chung. *Applied Continuum Mechanics.* Cambridge University Press, Cambridge, 1996. ISBN 978-0521482974.

[168] P. L. Gatti. *Applied structural and mechanical vibrations: theory and methods.* CRC Press, Boca Raton, FL, 2nd edition, 2014. ISBN 978-0415565783.

[169] O. D. Kellogg. *Foundations of Potential Theory.* Dover Publications, New York, NY, 1953. ISBN 0486601447.

[170] W. D. MacMillan. *The Theory of the Potential.* Dover Publications, New York, NY, 1958.

[171] H. Alfvén. Granulation, Magneto-Hydrodynamic Waves, and the Heating of the Solar Corona. *Monthly Notices of the Royal Astronomical Society*, 107(2):211–219, jul 1947. doi: 10.1093/mnras/107.2.211.

[172] H. Alfvén. *Cosmical Electrodynamics*. The International Series of Monographs on Physics. Clarendon Press - Oxford University Press, Oxford, 1950.

[173] H. Alfvén and C.-G. Fälthammar. *Cosmical Electrodynamics: Fundamental Principles*. The International Series of Monographs on Physics. Clarendon Press - Oxford University Press, Oxford, 2nd edition, 1963.

[174] L. M. B. C. Campos. On the generation and radiation of magneto-acoustic waves. *Journal of Fluid Mechanics*, 81(3):529–549, jul 1977. ISSN 0022-1120. doi: 10.1017/S0022112077002213.

[175] L. M. B. C. Campos. On hydromagnetic waves in atmospheres with application to the Sun. *Theoretical and Computational Fluid Dynamics*, 10(1-4):37–70, 1998. ISSN 0935-4964. doi: 10.1007/s001620050050.

[176] L. M. B. C. Campos and P. J. S. Gil. On spiral coordinates with application to wave propagation. *Journal of Fluid Mechanics*, 301:153–173, oct 1995. ISSN 1469-7645. doi: 10.1017/S0022112095003843.

[177] M. J. Lighthill. Studies on Magneto-Hydrodynamic Waves and other Anisotropic Wave Motions. *Philosophical Transactions of the Royal Society A: Mathematical, Physical and Engineering Sciences*, 252(1014):397–430, 1960. ISSN 0080-4614. doi: 10.1098/rsta.1960.0010.

[178] H. Cabannes. *Theoretical Magnetofluidddynamics*, volume 13 of *Applied Mathematics and Mechanics*. Academic Press, New York, 1970. ISBN 978-0121537500.

[179] H. K. Moffatt. *Magnetic Field Generation in Electrically Conducting Fluids*. Cambridge Monographs on Mechanics. Cambridge University Press, 1st edition, feb 1978. ISBN 978-0521216401.

[180] V. C. A. Ferraro and C. Plumpton. *An Introduction to Magneto-Fluid Mechanics*. Oxford University Press, London, 2nd edition, 1966.

[181] B. Leroy. Propagation of Waves in an Atmosphere in the Presence of a Magnetic Field. *Astronomy & Astrophysics*, 91:136–146, nov 1980.

[182] S. J. Schwartz, P. S. Cally, and N. Bel. Chromospheric and coronal Alfvénic oscillations in non-vertical magnetic fields. *Solar Physics*, 92(1-2):81–98, may 1984. ISSN 0038-0938. doi: 10.1007/BF00157237.

[183] B. Leroy. Propagation of Alfvén waves in an isothermal atmosphere when the displacement current is not neglected. *Astronomy & Astrophysics*, 125:371–374, sep 1983. ISSN 0004-6361.

[184] L. M. B. C. Campos. On the Hall effect on vertical Alfvén waves in an isothermal atmosphere. *Physics of Fluids B: Plasma Physics*, 4(9):2975–2982, sep 1992. ISSN 0899-8221. doi: 10.1063/1.860136.

[185] Y. D. Zhugzhda. Low-frequency oscillatory convection in the strong magnetic field. *Cosmic Electrodynamics*, 2:267–279, 1971.

[186] L. M. B. C. Campos. An exact solution for spherical Alfvén waves. *European Journal of Mechanics – B/Fluids*, 13(5):613–628, 1994.

[187] L. M. B. C. Campos and N. L. Isaeva. On vertical spinning Alfvén waves in a magnetic flux tube. *Journal of Plasma Physics*, 48(3):415–434, 1992. ISSN 1469-7807. doi: 10.1017/S0022377800016664.

[188] L. M. B. C. Campos. On oblique Alfvén waves in a viscous and resistive atmosphere. *Journal of Physics A: Mathematical and General*, 21(13):2911–2930, 1988. ISSN 1361-6447. doi: 10.1088/0305-4470/21/13/015.

[189] L. M. B. C. Campos. On the dissipation of atmospheric Alfvén waves in uniform and non-uniform magnetic fields. *Geophysical & Astrophysical Fluid Dynamics*, 48(4):193–215, nov 1989. ISSN 0309-1929. doi: 10.1080/03091928908218529.

[190] L. M. B. C. Campos. Exact and approximate methods for Alfvén waves in dissipative atmospheres. *Wave Motion*, 17(2):101–112, mar 1993. ISSN 0165-2125. doi: 10.1016/0165-2125(93)90019-C.

[191] Y.-Q. Lou. Alfvénic disturbances in the equatorial solar wind with a spiral magnetic field. *Journal of Geophysical Research: Space Physics*, 99(A8):14747–14760, aug 1994. ISSN 0148-0227. doi: 10.1029/94JA00928.

[192] R. Oliver, J. L. Ballester, A. W. Hood, and E. R. Priest. Magnetohydrodynamic waves in a potential coronal arcade. *Astronomy & Astrophysics*, 273:647–658, jun 1993.

[193] J. F. McKenzie, W.-H. IP, and W. I. Axford. The acceleration of minor ion species in the solar wind. *Astrophysics and Space Science*, 64(1):183–211, aug 1979. ISSN 0004-640X. doi: 10.1007/BF00640041.

[194] M. Velli. On the propagation of ideal, linear Alfvén waves in radially stratified stellar atmospheres and winds. *Astronomy & Astrophysics*, 270:304–314, mar 1993. ISSN 0004-6361.

[195] J. F. McKenzie. Interaction between Alfvén waves and a multicomponent plasma with differential ion streaming. *Journal of Geophysical Research: Space Physics*, 99(A3):4193–4200, mar 1994. ISSN 0148-0227. doi: 10.1029/93JA02928.

[196] L. Nocera, B. Leroy, and E. R. Priest. Phase mixing of propagating Alfvén waves. *Astronomy & Astrophysics*, 133:387–394, apr 1984. ISSN 0004-6361.

[197] L. Nocera, E. R. Priest, and J. V. Hollweg. Nonlinear Development of Phase-Mixed Alfvén Waves. *Geophysical & Astrophysical Fluid Dynamics*, 35(1-4):111–129, 1986. ISSN 1029-0419. doi: 10.1080/03091928608245889.

[198] R. Bruno and V. Carbone. The Solar Wind as a Turbulence Laboratory. *Living Reviews in Solar Physics*, 2(1), 2005. ISSN 2367-3648. doi: 10.12942/lrsp-2013-2.

[199] N. K. Dwivedi, S. Kumar, P. Kovacs, E. Yordanova, M. Echim, R. P. Sharma, M. L. Khodachenko, and Y. Sasunov. Implication of kinetic Alfvén waves to magnetic field turbulence spectra:

Earth's magnetosheath. *Astrophysics and Space Science*, 364(6), jun 2019. ISSN 0004-640X. doi: 10.1007/s10509-019-3592-2.

[200] A. Balogh, C. M. Carr, M. H. Acuña, M. W. Dunlop, T. J. Beek, P. Brown, K.-H. Fornacon, E. Georgescu, K.-H. Glassmeier, J. Harris, G. Musmann, T. Oddy, and K. Schwingenschuh. The Cluster Magnetic Field Investigation: overview of in-flight performance and initial results. *Annales Geophysicae*, 19(10/12):1207–1217, 2001. doi: 10.5194/angeo-19-1207-2001.

[201] H. Rème, C. Aoustin, J. M. Bosqued, I. Dandouras, B. Lavraud, J. A. Sauvaud, A. Barthe, J. Bouyssou, T. Camus, O. Coeur-Joly, A. Cros, J. Cuvilo, F. Ducay, Y. Garbarowitz, J. L. Medale, E. Penou, H. Perrier, D. Romefort, J. Rouzaud, C. Vallat, D. Alcaydé, C. Jacquey, C. Mazelle, C. d'Uston, E. Möbius, L. M. Kistler, K. Crocker, M. Granoff, C. Mouikis, M. Popecki, M. Vosbury, B. Klecker, D. Hovestadt, H. Kucharek, E. Kuenneth, G. Paschmann, M. Scholer, N. Sckopke, E. Seidenschwang, C. W. Carlson, D. W. Curtis, C. Ingraham, R. P. Lin, J. P. McFadden, G. K. Parks, T. Phan, V. Formisano, E. Amata, M. B. Bavassano-Cattaneo, P. Baldetti, R. Bruno, G. Chionchio, A. Di Lellis, M. F. Marcucci, G. Pallocchia, A. Korth, P. W. Daly, B. Graeve, H. Rosenbauer, V. Vasyliunas, M. McCarthy, M. Wilber, L. Eliasson, R. Lundin, S. Olsen, E. G. Shelley, S. Fuselier, A. G. Ghielmetti, W. Lennartsson, C. P. Escoubet, H. Balsiger, R. Friedel, J.-B. Cao, R. A. Kovrazhkin, I. Papamastorakis, R. Pellat, J. Scudder, and B. Sonnerup. First multispacecraft ion measurements in and near the Earth's magnetosphere with the identical Cluster ion spectrometry (CIS) experiment. *Annales Geophysicae*, 19(10–12):1303–1354, 2001. doi: 10.5194/angeo-19-1303-2001.

[202] M. A. Lee. Coupled hydromagnetic wave excitation and ion acceleration upstream of the Earth's bow shock. *Journal of Geophysical Research: Space Physics*, 87(A7):5063–5080, jul 1982. ISSN 0148-0227. doi: 10.1029/JA087iA07p05063.

[203] M. Scholer, H. Kucharek, and K.-H. Trattner. Injection and acceleration of H^+ and He^{2+} at Earth's bow shock. *Annales Geophysicae*, 17(5):583–594, 1999. ISSN 1432-0576. doi: 10.1007/s00585-999-0583-6.

[204] D. C. Ellison, E. Möbius, and G. Paschmann. Particle injection and acceleration at earth's bow shock: Comparison of upstream and downstream events. *The Astrophysical Journal*, 352:376–394, mar 1990. ISSN 0004-637X. doi: 10.1086/168544.

[205] E. G. Berezhko and S. N. Taneev. Ion acceleration and Alfvén wave generation at the Earth's bow shock. *Astronomy Letters*, 33(5):346–353, may 2007. ISSN 1063-7737. doi: 10.1134/S1063773707050088.

[206] B. E. Gordon, M. A. Lee, E. Möbius, and K. J. Trattner. Coupled hydromagnetic wave excitation and ion acceleration at interplanetary traveling shocks and Earth's bow shock revisited. *Journal of Geophysical Research: Space Physics*, 104(A12):28263–28277, dec 1999. ISSN 0148-0227. doi: 10.1029/1999JA900356.

[207] P. P. Belyaev, S. V. Polyakov, V. O. Rapoport, and V. Y. Trakhtengerts. The ionospheric Alfvén resonator. *Journal of Atmospheric and Terrestrial Physics*, 52(9):781–788, sep 1990. ISSN 0021-9169. doi: 10.1016/0021-9169(90)90010-K.

[208] A. S. Leonovich and V. A. Mazur. An electromagnetic field, induced in the ionosphere and atmosphere and on the earth's surface by low-frequency Alfvén oscillations of the magnetosphere: General theory. *Planetary and Space Science*, 39(4):529–546, apr 1991. ISSN 0032-0633. doi: 10.1016/0032-0633(91)90048-F.

[209] A. S. Leonovich and V. A. Mazur. Penetration to the Earth's surface of standing Alfvén waves excited by external currents in the ionosphere. *Annales Geophysicae*, 14(5):545–556, 1996. ISSN 0992-7689. doi: 10.1007/s00585-996-0545-1.

[210] E. Fedorov, N. Mazur, V. Pilipenko, and M. Engebretson. Interaction of magnetospheric Alfvén waves with the ionosphere in the Pc1 frequency band. *Journal of Geophysical Research: Space Physics*, 121(1):321–337, jan 2016. ISSN 2169-9380. doi: 10.1002/2015JA021020.

[211] J. D. Jackson. *Classical Electrodynamics.* John Wiley & Sons, New York, NY, 2nd edition, 1975. ISBN 978-0471431329.

[212] R. L. Lysak. Propagation of Alfvén waves through the ionosphere. *Physics and Chemistry of the Earth*, 22(7-8):757–766, jan 1997. ISSN 0079-1946. doi: 10.1016/S0079-1946(97)00208-5.

[213] P. V. Foukal. *Solar Astrophysics.* Wiley-VCH, Weinheim, 1st edition, 1990. ISBN 978-0471839354.

[214] T. J. I. Bromwich. *An Introduction to the Theory of Infinite Series.* Macmillan, London, 2nd edition, 1926.

[215] K. Knopp. *Theory and Application of Infinite Series.* Dover Publications, New York, NY, 1990. ISBN 0486661652.

[216] M. Abramowitz and I. Stegun, editors. *Handbook of mathematical functions with formulas, graphs, and mathematical tables.* Dover Books on Mathematics. Dover Publications, New York, NY, 1965. ISBN 978-0486612720.

[217] E. T. Whittaker and G. N. Watson. *A Course of Modern Analysis.* Cambridge Mathematical Library. Cambridge University Press, Cambridge, 4th edition, 1996. ISBN 978-0511608759. doi: 10.1017/CBO9780511608759.

[218] E. T. Copson. *An introduction to the theory of functions of a complex variable.* Clarendon Press - Oxford University Press, Oxford, 1935.

[219] L. M. B. C. Campos. *Higher-Order Differential Equations and Elasticity*, volume 4 of *Mathematics and Physics for Science and Technology.* CRC Press, Boca Raton, FL, 1st edition, nov 2019. ISBN 978-0367137205. doi: 10.1201/9780429029691.

[220] F. G. Tricomi. *Equazioni differenziali.* Paolo Boringhieri, Rome, 3rd edition, 1961.

[221] M. Braun. *Differential Equations and Their Applications*, volume 15 of *Applied Mathematical Sciences*. Springer-Verlag, New York, NY, 3$^{\text{rd}}$ edition, 1983. ISBN 978-0387979380. doi: 10.1007/978-1-4684-9229-3.

[222] P. M. H. Laurent. *Théorie élémentaire des fonctions elliptiques.* Gauthier-Villars, Paris, 1880.

[223] A. G. Greenhill. *The applications of elliptic functions.* Macmillan and Company, London, 1892.

[224] H. J. Barten. On the deflection of a cantilever beam. *Quarterly of Applied Mathematics*, 2(2): 168–171, jul 1944. ISSN 0033-569X. doi: 10.1090/qam/10879.

[225] K. E. Bisshopp and D. C. Drucker. Large deflection of cantilever beams. *Quarterly of Applied Mathematics*, 3(3):272–275, oct 1945. ISSN 0033-569X. doi: 10.1090/qam/13360.

[226] K. Mattiasson. Numerical results from large deflection beam and frame problems analysed by means of elliptic integrals. *International Journal for Numerical Methods in Engineering*, 17(1):145–153, jan 1981. ISSN 0029-5981. doi: 10.1002/nme.1620170113.

[227] J. H. Lau. Large deflection of beams with combined loads. *ASCE Journal of Engineering Mechanics*, 108(1):180–185, 1982.

[228] S. Chucheepsakul, S. Buncharoen, and C. M. Wang. Large Deflection of Beams under Moment Gradient. *ASCE Journal of Engineering Mechanics*, 120(9):1848–1860, sep 1994. ISSN 0733-9399. doi: 10.1061/(ASCE)0733-9399(1994)120:9(1848).

[229] S. Chucheepsakul, C. M. Wang, X. Q. He, and T. Monprapussorn. Double Curvature Bending of Variable-Arc-Length Elasticas. *Journal of Applied Mechanics*, 66(1):87–94, mar 1999. ISSN 0021-8936. doi: 10.1115/1.2789173.

[230] C. M. Wang, K. Y. Lam, X. Q. He, and S. Chucheepsakul. Large deflections of an end supported beam subjected to a point load. *International Journal of Non-Linear Mechanics*, 32(1):63–72, jan 1997. ISSN 0020-7462. doi: 10.1016/S0020-7462(96)00017-0.

[231] F. De Bona and S. Zelenika. A generalized elastica-type approach to the analysis of large displacements of spring-strips. *Proceedings of the Institution of Mechanical Engineers, Part C: Journal of Mechanical Engineering Science*, 211(7):509–517, jul 1997. ISSN 0954-4062. doi: 10.1243/0954406971521890.

[232] D. W. Coffin and F. Bloom. Elastica solution for the hygrothermal buckling of a beam. *International Journal of Non-Linear Mechanics*, 34(5):935–947, sep 1999. ISSN 0020-7462. doi: 10.1016/S0020-7462(98)00067-5.

[233] M. Rezaiee-Pajand and A. R. Masoodi. Stability Analysis of Frame Having FG Tapered Beam–Column. *International Journal of Steel Structures*, 19(2):446–468, apr 2019. ISSN 1598-2351. doi: 10.1007/s13296-018-0133-8.

[234] G. M. Griner. A Parametric Solution to the Elastic Pole-Vaulting Pole Problem. *Journal of Applied Mechanics*, 51(2):409–414, jun 1984. ISSN 0021-8936. doi: 10.1115/1.3167633.

[235] D. E. Panayotounakos and P. S. Theocaris. Nonlinear and buckling analysis of continuous bars lying on rigid supports. *AIAA Journal*, 24(3):479–484, mar 1986. ISSN 0001-1452. doi: 10.2514/3.9293.

[236] D. E. Panayotounakos and P. S. Theocaris. Exact solution for an approximate differential equation of a straight bar under conditions of a non-linear equilibrium. *International Journal of Non-Linear Mechanics*, 21(5):421–429, jan 1986. ISSN 0020-7462. doi: 10.1016/0020-7462(86)90024-7.

[237] D. E. Panayotounakos and P. S. Theocaris. Analytic Solutions for Nonlinear Differential Equations Describing the Elastica of Straight Bars: Theory. *Journal of the Franklin Institute*, 325(5):621–633, jan 1988. ISSN 0016-0032. doi: 10.1016/0016-0032(88)90037-3.

[238] D. E. Panayotounakos and P. S. Theocaris. Large deflections of buckled bars under distributed axial load. *International Journal of Solids and Structures*, 24(12):1179–1192, 1988. ISSN 0020-7683. doi: 10.1016/0020-7683(88)90084-4.

[239] D. E. Panayotounakos. Non-linear and buckling analysis of bars lying on an elastic foundation. *International Journal of Non-Linear Mechanics*, 24(4):295–307, jan 1989. ISSN 0020-7462. doi: 10.1016/0020-7462(89)90047-4.

[240] A. B. Sotiropoulou and D. E. Panayotounakos. Exact parametric analytic solutions of the elastica ODEs for bars including effects of the transverse deformation. *International Journal of Non-Linear Mechanics*, 39(10):1555–1570, dec 2004. ISSN 0020-7462. doi: 10.1016/j.ijnonlinmec.2003.09.004.

[241] A. F. Bower. *Applied Mechanics of Solids*. CRC Press, Boca Raton, FL, 1st edition, 2010. ISBN 978-1439802472.

[242] R. B. Hetnarski and J. Ignaczak. *The Mathematical Theory of Elasticity*. CRC Press, Boca Raton, FL, 2nd edition, 2011. ISBN 978-1138374355.

[243] A. Föppl. *Vorlesungen über technische Mechanik*, volume 3. BG Teubner, Leipzig, 1897.

[244] T. von Kármán. Festigkeitsprobleme im Maschinenbau, 1910.

[245] J. Kevorkian and J. D. Cole. *Perturbation Methods in Applied Mathematics*, volume 34 of *Applied Mathematical Sciences*. Springer-Verlag Berlin Heidelberg, New York, NY, 1st edition, 1981. ISBN 978-1441928122. doi: 10.1007/978-1-4757-4213-8.

[246] E. J. Hinch. *Perturbation Methods*. Cambridge texts in applied mathematics. Cambridge University Press, Cambridge, 1991. ISBN 978-0521373104. doi: 10.1017/CBO9781139172189.

[247] A. W. Bush. *Perturbation Methods for Engineers and Scientists*. CRC Press Library of Engineering Mathematics. CRC Press, Boca Raton, FL, 1st edition, 1992. ISBN 978-0367402846.

[248] W. T. Koiter. *Elastic Stability of Solids and Structures*. Cambridge University Press, New York, NY, 1st edition, 2009. ISBN 978-0521515283.

[249] J. J. Vincent. The bending of a Thin Circular Plate. *The London, Edinburgh, and Dublin Philosophical Magazine and Journal of Science*, 12(75):185–196, 1931. ISSN 1941-5982. doi: 10.1080/14786443109461792.

[250] R. A. Van Gorder. Analytical method for the construction of solutions to the Föppl-von Kármán equations governing deflections of a thin flat plate. *International Journal of Non-Linear Mechanics*, 47(3):1–6, 2012. ISSN 0020-7462. doi: 10.1016/j.ijnonlinmec.2012.01.004.

[251] J. P. Frakes and J. G. Simmonds. Asymptotic Solutions of the Von Karman Equations for a Circular Plate Under a Concentrated Load. *Journal of Applied Mechanics*, 52(2):326–330, 1985. ISSN 1528-9036. doi: 10.1115/1.3169048.

[252] Q. Yu, H. Xu, and S. Liao. Coiflets solutions for Föppl-von Kármán equations governing large deflection of a thin flat plate by a novel wavelet-homotopy approach. *Numerical Algorithms*, 79(4): 993–1020, 2018. ISSN 1017-1398. doi: 10.1007/s11075-018-0470-x.

[253] J. Cao. Computer-extended perturbation solution for the large deflection of a circular plate. Part I: Uniform loading with clamped edge. *The Quarterly Journal of Mechanics and Applied Mathematics*, 49(2):163–178, 1996. ISSN 0033-5614. doi: 10.1093/qjmam/49.2.163.

[254] X.-T. He, L. Cao, Y.-Z. Wang, J.-Y. Sun, and Z.-L. Zheng. A biparametric perturbation method for the Föppl–von Kármán equations of bimodular thin plates. *Journal of Mathematical Analysis and Applications*, 455(2):1688–1705, 2017. ISSN 0022-247X. doi: 10.1016/j.jmaa.2017.06.046.

[255] M. Brunetti, A. Favata, A. Paolone, and S. Vidoli. A mixed variational principle for the Föppl–von Kármán equations. *Applied Mathematical Modelling*, 79:381–391, 2020. ISSN 0307-904X. doi: 10.1016/j.apm.2019.10.041.

[256] E. L. Reiss. A Uniqueness Theorem for the Nonlinear Axisymmetric Bending of Circular Plates. *AIAA Journal*, 1(11):2650–2652, 1963. ISSN 0001-1452. doi: 10.2514/3.2142.

[257] X.-T. He, Y.-H. Li, G.-H. Liu, Z.-X. Yang, and J.-Y. Sun. Non-linear Bending of Functionally Graded Thin Plates with Different Moduli in Tension and Compression and its General Perturbation Solution. *Applied Sciences*, 8(5):1–19, 2018. ISSN 2076-3417. doi: 10.3390/app8050731.

[258] A. P. Boresi, K. P. Chong, and J. D. Lee. *Elasticity in Engineering Mechanics*. John Wiley & Sons, Hoboken, NJ, 3rd edition, 2011. ISBN 978-0470402559. doi: 10.1002/9780470950005.

[259] P. Podio-Guidugli. A New Quasilinear Model for Plate Buckling. *Journal of Elasticity*, 71(1-3): 157–182, 2003. ISSN 0374-3535. doi: 10.1023/B:ELAS.0000005554.76200.9e.

[260] P. G. Ciarlet. *Mathematical Elasticity: Theory of Plates*, volume 2 of *Classics in Applied Mathematics*. Society for Industrial and Applied Mathematics, Philadelphia, PA, jan 2021. ISBN 978-1611976793. doi: 10.1137/1.9781611976809.

A | Further research on multipath effects due to a corner

Contents

A.1 Effect of relative elevation angles of observer and source

The relative elevation angles of observer α and source β lead to three cases: (i) observer above (figures 2.1 and 2.2), already considered in subsection 2.1.4; (ii) source above (figure A.1), treated next in appendix A.1.1; (iii) observer and source on the same elevation angle (figure A.2) which is the intermediate case between the preceding two, that will be considered in appendix A.1.2. The far field approximation (in subsection 2.2.3) for source elevation above the observer is also considered in appendix A.1.3. In the intermediate case of observer and source on the same elevation angle, the exact directivity takes a simple form at arbitrary distance, that will be treated in appendix A.1.4.

A.1.1 Case of observer elevation angle lower than the source elevation angle

The direct signal, using the equations (2.1a) to (2.2), the signal reflected at the ground, using the equations (2.5a) to (2.6b), and the signal reflected at the wall, using the equations (2.7a) to (2.8b), apply to any relative position of observer and source. The fourth signal is given by the equations (2.9a) to (2.10c) when the first reflection is on the ground and the second on the wall, that is, for source at elevation below than the observer elevation, $\beta \leq \alpha$ (figure 2.2). In the opposite case of source elevation above than the observer elevation (figure A.1), the first reflection is on the wall at $(0, y_{31})$ and the second on the ground at $(x_{32}, 0)$, where the height y_{31} and horizontal distance x_{32} are determined by the coupled equations

$$\frac{y_{\mathrm{S}} - y_{31}}{x_{\mathrm{S}}} = \frac{y_{31}}{x_{32}}, \tag{A.1a}$$

$$\frac{x_{32}}{y_{31}} = \frac{x_{\mathrm{O}} - x_{32}}{y_{\mathrm{O}}}. \tag{A.1b}$$

Solving the equations above for y_{31} gives the equalities

$$\frac{x_{32} y_{\mathrm{S}}}{x_{\mathrm{S}} + x_{32}} = y_{31} = \frac{x_{32} y_{\mathrm{O}}}{x_{\mathrm{O}} - x_{32}} \tag{A.2}$$

from which follows

$$y_{\mathrm{O}} \left(x_{\mathrm{S}} + x_{32}\right) = y_{\mathrm{S}} \left(x_{\mathrm{O}} - x_{32}\right), \tag{A.3a}$$

which specifies the second reflection point x_{32} on the ground,

$$x_{32} = \frac{x_{\mathrm{O}} y_{\mathrm{S}} - y_{\mathrm{O}} x_{\mathrm{S}}}{y_{\mathrm{S}} + y_{\mathrm{O}}} = -x_{31}; \tag{A.4a}$$

the first reflection point, on the wall, is obtained substituting (A.3a) in one of the relations (A.2), leading to

$$y_{31} = \frac{x_{\mathrm{O}} y_{\mathrm{S}} - y_{\mathrm{O}} x_{\mathrm{S}}}{x_{\mathrm{S}} + x_{\mathrm{O}}} = -y_{32}. \tag{A.4b}$$

Note that the two last relations coincide with (2.9e) and (2.9f) respectively with reversed sign. From the last two relations, the three distances are determined: (i) from the source to the first reflection on the wall,

$$r_{31} = \left[x_{\mathrm{S}}^2 + \left(y_{\mathrm{S}} - y_{31}\right)^2\right]^{1/2} = |x_{\mathrm{S}}| \left[1 + \frac{\left(y_{\mathrm{S}} + y_{\mathrm{O}}\right)^2}{\left(x_{\mathrm{S}} + x_{\mathrm{O}}\right)^2}\right]^{1/2}; \tag{A.5a}$$

(ii) between reflection points on the wall and on the ground,

$$r_{32} = \left[\left(x_{32}\right)^2 + \left(y_{31}\right)^2\right]^{1/2} = |x_{\mathrm{O}} y_{\mathrm{S}} - y_{\mathrm{O}} x_{\mathrm{S}}| \left[\frac{1}{\left(x_{\mathrm{S}} + x_{\mathrm{O}}\right)^2} + \frac{1}{\left(y_{\mathrm{S}} + y_{\mathrm{O}}\right)^2}\right]^{1/2}; \tag{A.5b}$$

(iii) from the reflection point on the ground to the observer,

$$r_{33} = \left[\left(x_{\mathrm{O}} - x_{32}\right)^2 + y_{\mathrm{O}}^2\right]^{1/2} = |y_{\mathrm{O}}| \left[1 + \frac{\left(x_{\mathrm{S}} + x_{\mathrm{O}}\right)^2}{\left(y_{\mathrm{S}} + y_{\mathrm{O}}\right)^2}\right]^{1/2}. \tag{A.5c}$$

The last three equations are valid if $\beta \geq \alpha$. Comparing the cases of observer at higher elevation angle than the source, that is, the equations (2.10a) to (2.10c), with the reverse case, that is, the equations (A.5a) to (A.5c), it is clear that: (i) only the distance between the reflection points r_{32} coincide; (ii) the distance from the reflection point on the ground exchanges y_{S} if it is measured the distance r_{31} from the source in (2.10a) by y_{O} if it is measured the distance r_{33} from the observer in (A.5c); (iii) the distance from the reflection point on the wall exchanges x_{O} if it is measured the distance r_{33} from the observer in (2.10c) by x_{S} if it is measured the distance r_{31} from the source in (A.5a). In both cases, the last term of

(2.3) holds, with distinct expressions for the distances r_{3i} with $i = \{1, 2, 3\}$. The remaining terms of the total signal (2.3) are unchanged.

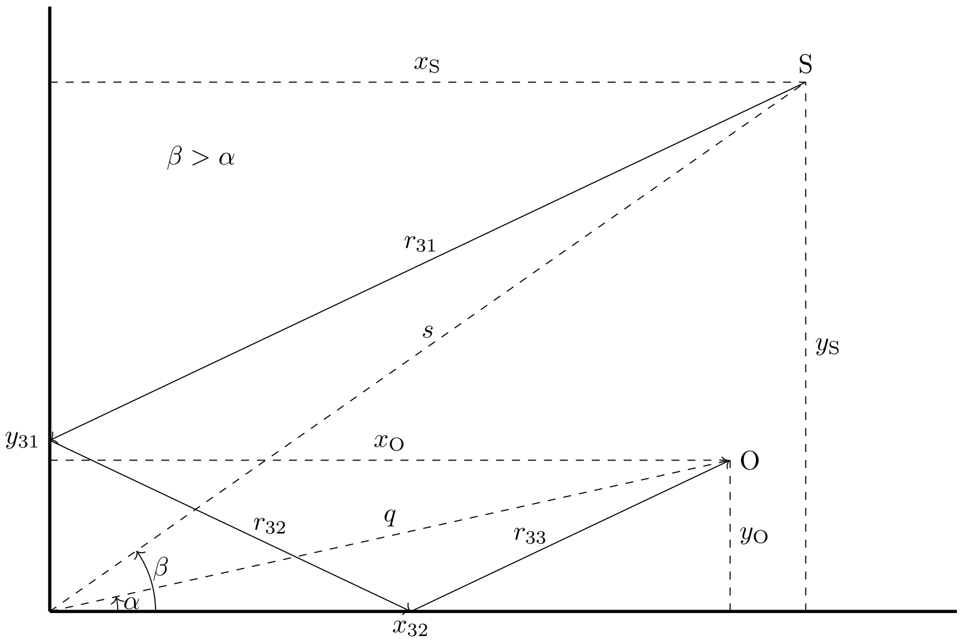

Figure A.1: The same as the figure 2.2, but with the difference that the elevation angle β for the source is larger than for the observer α, that is, $\alpha < \beta$, showing again the double reflection path as the figure 2.2, where in this case the first reflection is on the wall and the second reflection is on the ground.

A.1.2 Case of observer and source on the same azimuth

The case when the observer is on the same elevation angle than the source (figure A.2) can be treated as intermediate case between observer above (figures 2.1 and 2.2) and observer below (figure A.1). In this case, both formulas, (2.9a) to (2.10c) for $\beta \leq \alpha$, and (A.1a) to (A.5c) for $\beta \geq \alpha$, must hold. From (A.2), it follows that the reflection point is the origin, at the corner,

$$x_{31} = x_{32} = 0 = y_{31} = y_{32}, \tag{A.6a}$$

when the condition

$$\frac{y_S}{x_S} = \tan\beta = \tan\alpha = \frac{y_O}{x_O} \tag{A.6b}$$

of source and observer on the same azimuth angle is met. The distance between the "two" coincident reflection points is zero, therefore

$$r_{32} = 0 \tag{A.7a}$$

in (2.10b) or (A.5b); the distance from the source to the origin is, regarding (2.10a) or (A.5a),

$$r_{31} = \left(x_S^2 + y_S^2\right)^{1/2} = s, \tag{A.7b}$$

and from the observer to the origin is, regarding (2.10c) or (A.5c),

$$r_{33} = \left(x_{\mathrm{O}}^2 + y_{\mathrm{O}}^2\right)^{1/2} = q, \tag{A.7c}$$

where comparison with (2.1a) and (2.1b) was made. These values simplify the last term of (2.3), which remains valid as an expression for the total signal.

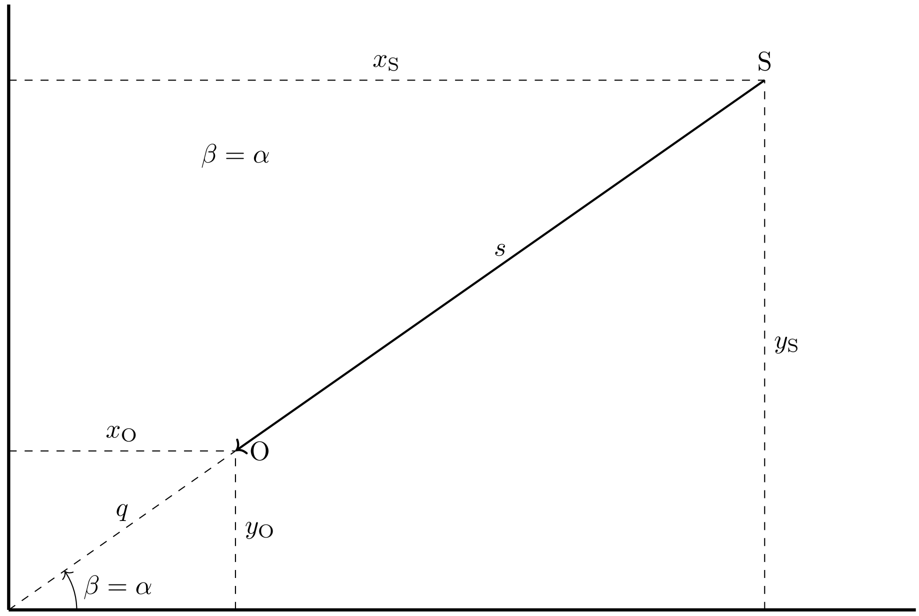

Figure A.2: The intermediate case between the figures 2.2 and A.1 is that of the observer and source with the same elevation angle, that is, $\alpha = \beta$ and "double reflection" at the origin.

A.1.3 Far field approximation for all elevation angles

The far field approximations for the direct signal (2.14), reflected signal on the ground, (2.15a) and (2.15b), and reflected signal on the wall, (2.16a) and (2.16b), hold regardless of the relative positions of observer and source. For the fourth signal, involving double reflection, the far field approximation, (2.17a) to (2.17c), for the observer elevation above than the source elevation, is replaced in the opposite case by the equations (A.5a) to (A.5c), leading to

$$r_{31} = s - q \tan\beta \sin(\beta - \alpha), \tag{A.8a}$$

$$r_{32} = q \sec\beta \csc\beta \sin(\beta - \alpha), \tag{A.8b}$$

$$r_{33} = q \sin\alpha \csc\beta. \tag{A.8c}$$

The last three expressions are valid if $\alpha \leq \beta$ and considering that the distance from the corner to the source is much larger than the distance from the corner to the observer, that is, $q^2 \ll s^2$. These expressions affect only the last term of (2.3), so (2.18a) remains valid with (2.18b) and (2.18c) unchanged whilst (2.18d) is replaced by

$$C(\alpha, \beta) = \cos(\alpha - \beta) + \sin\alpha \csc\beta + \sin(\beta - \alpha) \sec\beta (\csc\beta - \sin\beta); \tag{A.9}$$

thus, (A.9) is similar to (2.18d) with the exchanges $\cos\alpha \leftrightarrow \sin\alpha$ and $\sec\beta \leftrightarrow \csc\beta$, plus some sign changes as the elevation of source and observer are reversed. This result is valid for a source in the far field and an observer in the near field, and can be replaced by the exact formula (2.3) using (2.1a) and (2.1b) in the formulas for the distances in the multipath factor (2.12b). In the case (A.6b) of equal source and observer elevation angles, $\beta = \alpha$, not only the relations (2.18b) and (2.18c) are simplified, but also (2.18d) and (A.9) coincide,

$$A(\alpha, \alpha) = 2\sin^2\alpha, \tag{A.10a}$$

$$B(\alpha, \alpha) = 2\cos^2\alpha, \tag{A.10b}$$

$$C(\alpha, \alpha) = 2, \tag{A.10c}$$

then the multipath factor (2.18a), for $\beta = \alpha$ and $q^2 \ll s^2$, simplifies to

$$\begin{aligned} F = 1 &+ R_\mathrm{h}\left(1 - \frac{2q}{s}\sin^2\alpha\right)\exp\left(\mathrm{i}2kq\sin^2\alpha\right) + R_\mathrm{v}\left(1 - \frac{2q}{s}\cos^2\alpha\right)\exp\left(\mathrm{i}2kq\cos^2\alpha\right) \\ &+ R_\mathrm{h}R_\mathrm{v}\left(1 - \frac{2q}{s}\right)\exp\left(\mathrm{i}2kq\right). \end{aligned} \tag{A.11}$$

The correction factor (A.11) will be next written exactly, to all orders in q/s.

A.1.4 Exact directivity for equal elevations of observer and source

The exact multipath factor is calculated next, for the observer and source at arbitrary distances with the same elevation angle, using: (i) the distance (2.14), for $\alpha = \beta$, from the source to the observer

$$r = \left|s^2 + q^2 - 2sq\right|^{1/2} = s - q; \tag{A.12}$$

(ii) the distances from the source (2.6a) and observer (2.6b) to the reflection point on the ground, for $\alpha = \beta$, in the case of single reflection,

$$r_{11} = \left[\sin^2\alpha + \left(\frac{s-q}{s+q}\right)^2\cos^2\alpha\right]^{1/2} s, \tag{A.13a}$$

$$r_{12} = \left[\sin^2\alpha + \left(\frac{s-q}{s+q}\right)^2\cos^2\alpha\right]^{1/2} q; \tag{A.13b}$$

(iii) the distances from the source (2.8a) and observer (2.8b) to the reflection point on the wall, for $\alpha = \beta$, in the case of single reflection,

$$r_{21} = \left[\cos^2\alpha + \left(\frac{s-q}{s+q}\right)^2\sin^2\alpha\right]^{1/2} s, \tag{A.14a}$$

$$r_{22} = \left[\cos^2\alpha + \left(\frac{s-q}{s+q}\right)^2\sin^2\alpha\right]^{1/2} q; \tag{A.14b}$$

(iv) in the case of double reflection, the distances from the source to the reflection point, given by (2.10a) or (A.5a), from the observer to the same reflection point, given by (2.10c) or (A.5c), and between the two reflection points, given by (2.10b) or (A.5b), noting that both reflection points are at the corner, and therefore these distances simplify to

$$r_{31} = s, \tag{A.15a}$$

$$r_{32} = 0, \tag{A.15b}$$

$$r_{33} = q. \tag{A.15c}$$

Substituting the equations (A.13a) to (A.15c) in (2.12b), for $\alpha = \beta$, specifies the exact multipath factor

$$\begin{aligned} F = {} & 1 + R_\mathrm{h} R_\mathrm{v} \frac{s-q}{s+q} \exp\left(\mathrm{i}2kq\right) + \exp\left[\mathrm{i}k\left(q-s\right)\right] \\ & \times \left\{ R_\mathrm{h} \left[\cos^2\alpha + \left(\frac{s+q}{s-q}\right)^2 \sin^2\alpha\right]^{-1/2} \exp\left(\mathrm{i}k\sqrt{\left(s+q\right)^2 \sin^2\alpha + \left(s-q\right)^2 \cos^2\alpha}\right) \right. \\ & \left. + R_\mathrm{v} \left[\sin^2\alpha + \left(\frac{s+q}{s-q}\right)^2 \cos^2\alpha\right]^{-1/2} \exp\left(\mathrm{i}k\sqrt{\left(s+q\right)^2 \cos^2\alpha + \left(s-q\right)^2 \sin^2\alpha}\right) \right\}. \end{aligned} \tag{A.16}$$

The approximation of (A.16) to $O\left(q^2/s^2\right)$ coincides with (A.11).

A.2 Multipath factor as a function of frequency

The exact expression (2.12b) and far field approximation (2.18a) of the multipath factor are shown to be quite consistent in the figure 2.9, for fixed observer location in the near field with $x_\mathrm{O} = 3$ and $y_\mathrm{O} = 2$ meters, rigid walls, $R_\mathrm{h} = R_\mathrm{v} = 1$, large source distance, $s = 700\,\mathrm{m}$, and fixed frequency, $f = 1\,\mathrm{kHz}$, over all source directions, $0 \leq \beta \leq 90°$. In the figures A.3 to A.6, the modulus (top) and phase (bottom) of the multipath factor are shown over the full audible frequency range, $20 \leq f \leq 20000\,\mathrm{Hz}$, for four fixed angles of the source, respectively $\beta = 2.45°$, $\beta = 30°$, $\beta = 45°$ and $\beta = 60°$. The exact expression (2.12b) and far field approximation (2.18a) are indistinguishable in all figures, because the thin and solid lines are very close, and the graphs are very dense. The shape of the envelopes of amplitude and phase is strongly affected by the angle of the source: (i) for a small angle, $\beta = 2.45°$, corresponding to grazing incidence (figure A.3), the amplitude envelope is a rectified sinusoid (top) and the phase envelope is a sequence of parallelograms (bottom); (ii) for a low angle, $\beta = 30°$, below the diagonal, both the amplitude and phase (figure A.4) have a jagged appearance like random noise; (iii) for the intermediate angle, $\beta = 45°$, bisecting the corner (figure A.5), the amplitude (top) and phase (bottom) have a solid core with many protruding peaks; (iv) for a high angle, $\beta = 60°$, above the diagonal (figure A.6), the solid core has modulation and the peaks are broadened into sinusoids. As an overall conclusion for a single monochromatic source of waves (sound, light or electromagnetic) the reflection in a corner can lead to complex interference patterns both for amplitude and phase.

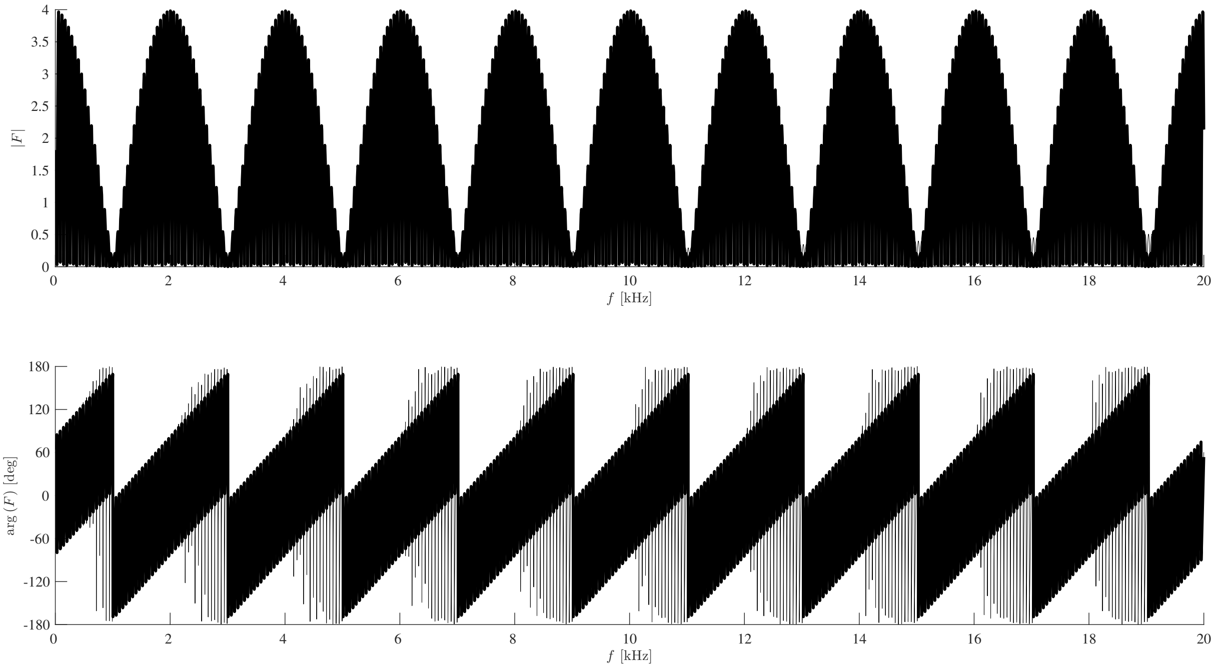

Figure A.3: The same as figure 2.9 with fixed grazing source direction, $\beta = 2.45°$, showing the amplitude (top) and phase (bottom) of the multipath factor as a function of frequency over the audible range, $20 \leq f \leq 20000\,\text{Hz}$.

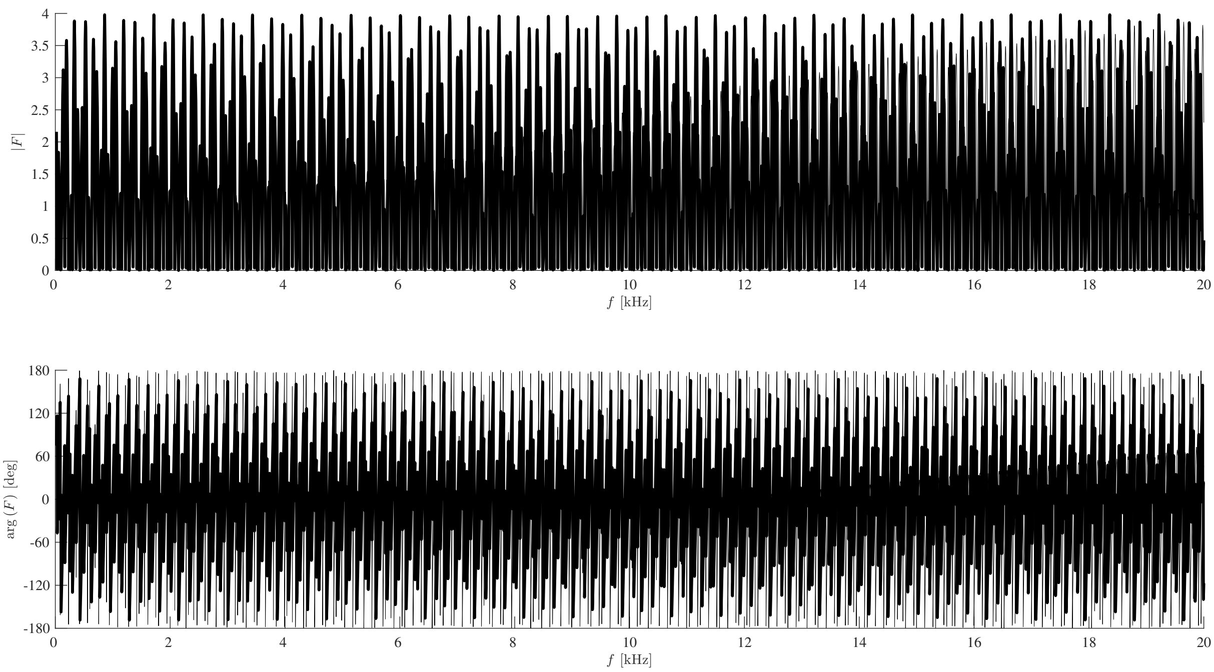

Figure A.4: The same as figure A.3 for low source direction, $\beta = 30°$, below the diagonal.

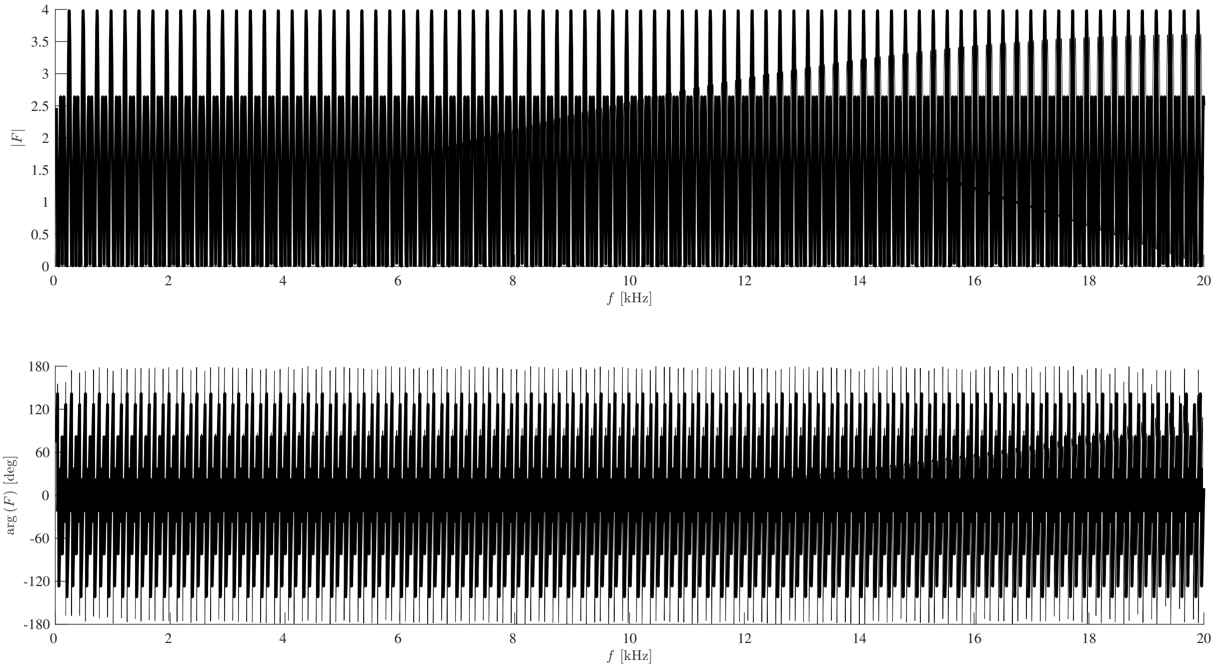

Figure A.5: The same as figure A.3 for intermediate source direction, $\beta = 45°$, along the diagonal of the two walls.

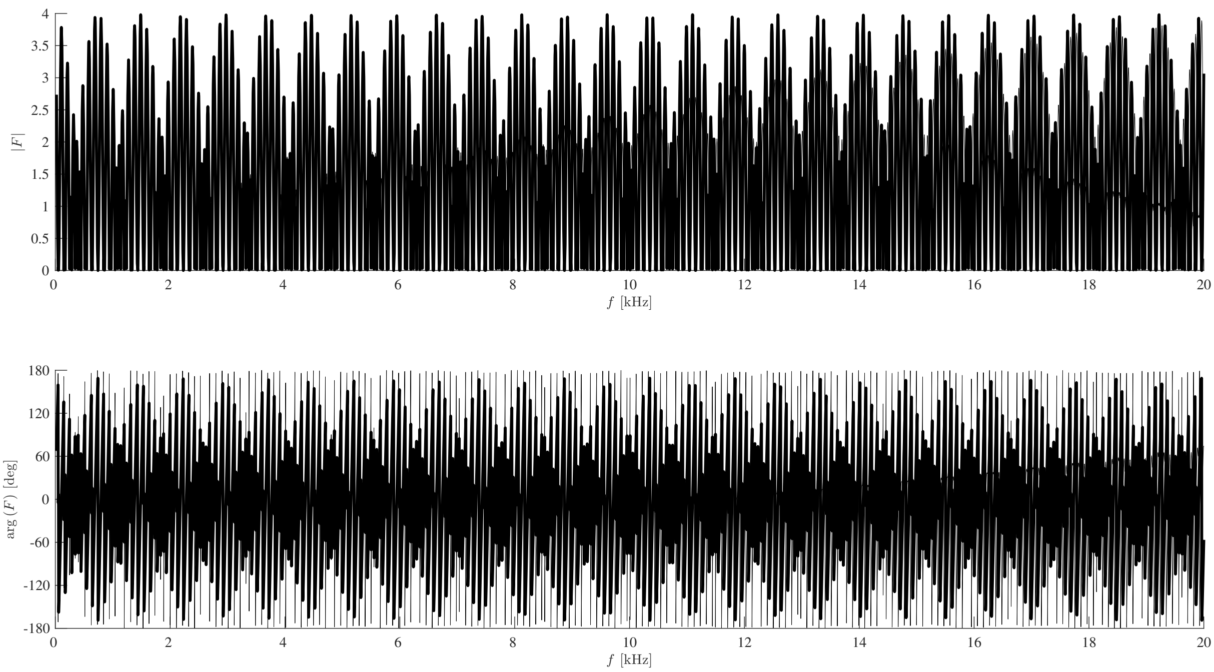

Figure A.6: The same as figure A.3 for high source direction, $\beta = 60°$, above the diagonal.

A.3 Reflection factors from a variety of surfaces

When an incident sound wave of pressure I crosses an interface between two different media, for instance, when a wave impinges on the ground, making an angle θ with the normal to the surface, only a transmitted wave of pressure T escapes through the interface and travels through the second medium while the wave may also be reflected from the interface to propagate in the same medium than the incident wave with the value of the pressure being R. At all times and at all points on the plane discontinuity, the pressures of the two sides of the boundary must be equal and the particle displacements, normal to the interface, must also be identical. Setting these boundary conditions, the reflection coefficient, or equivalently, the ratio between the pressures of the reflected and incident waves depends on the specific acoustic impedances of both media and the inclination of the incident wave, leading to the expression

$$\frac{R}{I} = \frac{\rho_1 c_1 / \cos\phi - \rho_0 c_0 / \cos\theta}{\rho_1 c_1 / \cos\phi + \rho_0 c_0 / \cos\theta} \equiv R_\mathrm{p} \tag{A.17}$$

where ρ is the density, c is the sound speed and for a harmonic wave is equal to ω/k (k is the wavenumber and ω is the angular frequency), and ϕ is the angle the transmitted wave makes with the normal of the interface, specified by the Snell's law [27]. The reflection coefficient (A.17) depends on the plane wave impedances $\rho_1 c_1$ and $\rho_0 c_0$ on the two sides of the interface, modified to take into account the angle with the normal for the incident θ and transmitted ϕ waves, that affect the normal velocities in the impedances $p_1/u_1 = \rho_1 c_1/\cos\phi$ and $p_0/u_0 = \rho_0 c_0/\cos\theta$. In the case of a sound incident on a plane material layer dividing a fluid with uniform acoustics properties, ρ and c, for instance, a wall of the building, and making an angle θ with the normal of the layer, some sound will be reflected and some will be transmitted through the wall. Setting the continuity of the normal displacement of the waves at the wall and equating the pressure difference across the wall with the inertia of the surface material of mass m per unit area, the ratio between the pressures of the reflected and incident waves is

$$\frac{R}{I} = \frac{\mathrm{i}\omega m \cos\theta}{2\rho c + \mathrm{i}\omega m \cos\theta}. \tag{A.18}$$

The high-frequency waves are mostly reflected, whereas the low-frequency waves are mainly transmitted and get through all, but the most massive walls with very little attenuation [27]. In both cases, the acoustic pressure is obtained by adding the pressure of a direct wave from the source with the pressure of a reflected wave from the surface, the latter being the pressure of the incident wave multiplied by the reflection coefficient, determined in one of the last two equations. The equations (A.17) and (A.18) are derived for plane waves. In the case of a point source emitting a spherical wave, the plane wave approximation is inadequate since the boundary conditions at the surface can be met only in the presence of a lateral wave that significantly changes the sound field for grazing incidences.

The reflection of a spherical wave by a plane wall was first considered by Sommerfeld [29], using a method of virtual sources that is relevant to outdoor sound propagation. Rudnick [30] wrote the velocity potential of sound waves as the sum of the potentials of the direct wave function due to the point source with the secondary wave function due to the reflection on the ground. Knowing that elementary cylindrical waves can represent a sound wave in a homogeneous medium, Rudnick [30] applied the same previously mentioned boundary conditions to evaluate the velocity potentials and obtained the reflection coefficient for spherical waves, leading to the expression

$$\frac{R}{I} = R_\mathrm{p} + (1 - R_\mathrm{p}) \left(1 + 2\mathrm{i}\sqrt{w}\mathrm{e}^{-w} \int_{-\mathrm{i}\sqrt{w}}^{\infty} \mathrm{e}^{-u^2} \,\mathrm{d}u \right) \tag{A.19}$$

where the term in parentheses is usually called the boundary loss factor and w is given by

$$w = \mathrm{i}\frac{4k_1 R_2}{\left(1-R_\mathrm{p}\right)^2}\left(\frac{\rho_1 c_1}{\rho_2 c_2}\right)^2\left[1-\left(\frac{k_1}{k_2}\cos\theta\right)^2\right] \tag{A.20}$$

with R_2 being the distance travelled by the reflected wave. As pointed out by Rudnick [30], when the receiver is very far from the source compared to the wavelength in air, w becomes very large and consequently the term in curved parentheses approaches 0, approximating the reflection coefficient to R_p that is the solution of a plane incident wave. Rudnick used a boundary between two semi-infinite homogeneous media and the conditions of continuity of pressure and normal displacement. The final result was to express the last two equations explicitly in terms of the propagation constants of the media. Ingard [31] studied the same problem, but the boundary conditions at the wall were expressed in terms of a normal impedance independent of the angle of incidence and arrived at a very similar expression to the reflected wave to the one obtained by Rudnick. Furthermore, in both cases, the spherical wave reflection coefficient depends on the plane wave reflection coefficient and the boundary loss factor. This factor is a function of the normal impedance and the position of the field point (in the former case, it is a function of the acoustic impedance of both media and the position of the field point). The difference lies in the expression for that parameter. If the normal impedance of the wall is ρc, the reflection coefficient is

$$\frac{R}{I} = R_\mathrm{p} + \left(1-R_\mathrm{p}\right)\left[1+\rho_1 \mathrm{e}^{\rho_1}\mathrm{Ei}\left(-\rho_1\right)\right] \tag{A.21}$$

with ρ_1 given by

$$\rho_1 = \mathrm{i}kR_2\left(1+\cos\theta\right) \tag{A.22}$$

in which R_2 and θ are again the distance travelled by the reflected wave and the angle of incidence, respectively, whereas Ei is an “exponential integral” function [31]. This means that the reflection coefficient depends on several parameters and it is not only the frequency that influences the reflection, having a minor role in this characteristic. Taraldsen [32] rewrote the exact solution given by Ingard and proved that the boundary loss factor, a term in the reflection coefficient, is a function of only two complex dimensionless quantities and it is sufficient to have the general solution where the source and receiver are on the ground. Because the frequency alone is not the main parameter that predicts sound waves' reflection, the spectral dependence of reflection effects is not considered. Although the study of acoustic waves is made for a wide range of frequencies, the reflection coefficient is considered to be a constant for each surface, independent of the frequency, to simplify the problem.

Despite that, several experimental studies were performed to understand the outdoor acoustic propagation. Parkin and Scholes measured the pressure level of acoustic waves originated from a jet engine (at 1.82 m above the ground) and propagating at nearly grazing incidence above different grounds, at two distances from the source [28]. The measurements were taken when the temperature difference between monitoring points at 1.2 m and 12.2 m heights was less than 0.3 °C and with wind speeds less than 1.52 ms^{-1}. The experiments show that acoustic waves, when propagating near grassland, snow, or cultivated land, have much stronger attenuation (they are mostly transmitted to the ground), usually between 250 Hz and 800 Hz than either at frequencies below 250 Hz or frequencies in the range of 800 Hz to 2000 Hz. Thus, the sound pressure level far away from the source is much lower than at a point near the source due only to ground effects, making a ground effect dip in the plot of sound pressure level versus frequency. Moreover, waves with frequencies below 250 Hz are enhanced compared with the same waves if the ground surface does not exist (mainly due to the reflection on the ground). Attenborough [28] reviewed the theory of the sound interaction with the ground and developed theoretical models for the prediction of sound propagation near the ground surface, applied to the Parkin and Scholes data. The interaction has been shown to depend upon the positions of the source and receiver and upon the acoustical properties of the ground. Attenborough pointed out that at frequencies less than 300 Hz and for ranges greater than 50 m over grassland, the reflection coefficient gives rise to surface waves decaying principally as the inverse square root of horizontal range and exponentially with height above the ground, and concluded that they are the major carriers of acoustic noise over long distances because they fit well to the experimental data for low frequencies [28].

B | Time averages over a period

Contents

SEVERAL averages over a period, for instance in the equations (4.22a) to (4.22b), were used in the chapters 4 and 5. In all cases, the period τ of the function to be integrated must be determined.

(i) To evaluate the relation (4.25), the period of the function $\sin(\omega_n t - \alpha_n)\sin(\omega_r t - \alpha_r)$ has to be determined. The period of the trigonometric function $\sin(\omega_n t - \alpha_n)$ is $2\pi/\omega_n = 2L/(nc)$ while the period of $\sin(\omega_r t - \alpha_r)$ is $2L/(rc)$. Generally, the product of the two functions does not result in a periodic function. In this case, $2L/c$ is a period of both functions and therefore $2L/c$ is also a period of the multiplication of both (however, this does not imply that $2L/c$ is the lowest period; in some cases, the lowest period is L/c). For that reason, the value of τ in (4.22a) is $2L/c$ for any combination of the values of n and r. The integrals in (4.25) are then given by

$$\begin{aligned}\langle\sin(\omega_n t - \alpha_n)\sin(\omega_r t - \alpha_r)\rangle &= \frac{1}{2}\langle\cos[(\omega_n - \omega_r)t + \alpha_r - \alpha_n]\rangle \\ &\quad + \frac{1}{2}\langle\cos[(\omega_n + \omega_r)t - \alpha_r - \alpha_n]\rangle = \frac{1}{2}\delta_{nr}, \qquad \text{(B.1)}\\ \langle\cos(\omega_n t - \alpha_n)\cos(\omega_r t - \alpha_r)\rangle &= \frac{1}{2}\langle\cos[(\omega_n + \omega_r)t - \alpha_n - \alpha_r]\rangle \\ &\quad + \frac{1}{2}\langle\cos[(\omega_n - \omega_r)t + \alpha_r - \alpha_n]\rangle = \frac{1}{2}\delta_{nr} \qquad \text{(B.2)}\end{aligned}$$

where δ_{nr} is the identity matrix. This result follows from the fact that when $\omega_n \neq \omega_r$, the time average is zero, otherwise it is $\cos(\alpha_r - \alpha_n)/2$. But in this last case, when $\omega_r = \omega_n$, meaning the same mode of oscillation, then $\alpha_r = \alpha_n$, and so the result is simplified to $1/2$.

(ii) In (4.32), the time averages are

$$\langle\cos(\omega t + \beta)\cos(\omega_n t - \alpha_n)\rangle = \frac{1}{2}\langle\cos[(\omega + \omega_n)t + \beta - \alpha_n]\rangle + \frac{1}{2}\langle\cos[(\omega - \omega_n)t - \beta - \alpha_n]\rangle = 0, \quad \text{(B.3)}$$

$$\langle\sin(\omega t + \beta)\sin(\omega_n t - \alpha_n)\rangle = \frac{1}{2}\langle\cos[(\omega - \omega_n)t + \beta + \alpha_n]\rangle - \frac{1}{2}\langle\cos[(\omega + \omega_n)t + \beta - \alpha_n]\rangle = 0, \quad \text{(B.4)}$$

assuming that $\omega/\omega_n = p/q$ is a rational number so that $\cos[(\omega \mp \omega_n)\, t]$ is a periodic function with period

$$\tau = \frac{2\pi}{\omega \mp \omega_n} = \frac{2\pi}{\omega_n} \frac{1}{p/q \pm 1} = \frac{\tau_n q}{p \pm q}. \tag{B.5}$$

Generally, let τ_1 be a period of $f(t)$ and let τ_2 be a period of $g(t)$. Suppose that there are two positive integers c_1 and c_2 such that $c_1\tau_1 = c_2\tau_2 = \tau$. Then, the product of the two functions is also a periodic function. The period is τ. On the other hand, if it is not possible to get the positive integers c_1 and c_2, maybe the function $f(t)\, g(t)$ is not periodic. For example, if $f(t)$ is $\sin(\omega_n t - \alpha_n)$ and has $\tau_1 = 2\pi/\omega_n = n\pi c/L$ as a period, and $g(t)$ is $\sin(\omega t + \beta)$ and has $\tau_2 = 2\pi/\omega$ as a period, then $f(t)\, g(t)$ is a periodic function if $c_1 2\pi/\omega = c_2 2\pi/\omega_n$ (meaning that ω/ω_n must be equal to a rational number) or equivalently if $\omega = (nc_2/c_1)(\pi c/L)$. In this case, if the period of ω_n is $2L/(nc)$, then $2L/c$ is also a period of the same function, regardless of the value of n. Consequently, $\sin(\omega t)\sin(\omega_n t)$ is a periodic function if $\omega = (c_2/c_1)(\pi c/L)$ or if $\omega L/(\pi c) = c_2/c_1$. The period of the product of both functions is $\tau = c_1\tau_1 = c_1\pi c/L = c_2\tau_2 = c_2 2\pi/\omega$.

(iii) The time averages evaluated in (i) can be simplified when $\omega_n = \omega_r \equiv \omega$ and $\alpha_n = \alpha_r \equiv \alpha$, leading to the time averages (4.37a) given by

$$\left\langle \sin^2(\omega t - \alpha)\right\rangle = \frac{1}{2}, \tag{B.6}$$

$$\left\langle \cos^2(\omega t - \alpha)\right\rangle = \frac{1}{2} \tag{B.7}$$

where (B.6) and (B.7) follow from (B.1) and (B.2) respectively with $n = r$;

(iv) The function in (4.37b) is not periodic due to the term ωt. In this case, it is assumed that $\tau = 2\pi/\omega$. With this assumption, this last result depends on which "period" the integration is evaluated. For instance, if the limits of the integral are 2π and 4π, the result of the integration would not be the same. Using a trigonometric identity and the integration by parts, the time average for the first "period" is equal to

$$\begin{aligned} \langle \omega t \cos(\omega t - \alpha)\sin(\omega t + \beta)\rangle &= \frac{1}{2\pi}\int_0^{2\pi} \theta\cos(\theta - \alpha)\sin(\theta + \beta)\ \mathrm{d}\theta \\ &= \frac{1}{4\pi}\int_0^{2\pi} \theta\left[\sin(\alpha + \beta) - \sin(\alpha - \beta - 2\theta)\right]\ \mathrm{d}\theta \\ &= \frac{\pi}{2}\sin(\alpha + \beta) - \frac{1}{4}\cos(\beta - \alpha). \end{aligned} \tag{B.8}$$

(v) In (4.37c), the integration for the first period is given by

$$\left\langle (\omega t)^2 \sin^2(\omega t + \beta)\right\rangle = \frac{1}{4\pi}\int_0^{2\pi} \theta^2\left[1 - \cos(2\theta + 2\beta)\right]\ \mathrm{d}\theta = \frac{2\pi^2}{3} - I, \tag{B.9a}$$

with

$$I \equiv \frac{1}{4\pi}\int_0^{2\pi} \theta^2 \cos(2\theta + 2\beta)\ \mathrm{d}\theta = \frac{\pi}{2}\sin(2\beta) + \frac{1}{4}\cos(2\beta). \tag{B.9b}$$

To evaluate the integral I, it was performed another integration by parts. Substituting (B.9b) in (B.9a) gives

$$\left\langle (\omega t)^2 \sin^2(\omega t + \beta) \right\rangle = \frac{2\pi^2}{3} - \frac{\pi}{2}\sin(2\beta) - \frac{1}{4}\cos(2\beta)\,. \tag{B.9c}$$

(vi) The time average (4.37d), from $t = 0$ to $t = 2\pi/\omega$ (the function is not periodic), is given by

$$\begin{aligned} \left\langle [\sin(\omega t + \beta) + \omega t \cos(\omega t + \beta)]^2 \right\rangle &= \left\langle \sin^2(\omega t + \beta) \right\rangle + \left\langle (\omega t)^2 \cos^2(\omega t + \beta) \right\rangle \\ &\quad + 2\left\langle \omega t \sin(\omega t + \beta)\cos(\omega t + \beta) \right\rangle \\ &= \frac{1}{2} + \frac{2\pi^2}{3} + \frac{\pi}{2}\sin(2\beta) - \frac{1}{4}\cos(2\beta)\,, \end{aligned} \tag{B.10}$$

using (B.6) for the first time average and (B.8) for the third time average, both with $\alpha = -\beta$. The second time average is obtained similarly to (B.9a), knowing that $\cos^2(\theta + \beta) = 1 + \cos(2\theta + 2\beta)$, so the time average of $(\omega t)^2 \cos^2(\omega t + \beta)$ is equal to $2\pi^2/3 + I$.

(vii) In (4.37e), knowing that

$$\langle \sin(\omega t - \alpha)\sin(\omega t + \beta) \rangle = \frac{1}{2}\cos(\alpha + \beta) - \frac{1}{2}\langle \cos(\beta - \alpha + 2\omega t) \rangle = \frac{1}{2}\cos(\alpha + \beta)\,, \tag{B.11a}$$

the time average is equal to

$$\langle \sin(\omega t - \alpha)[\sin(\omega t + \beta) + \omega t \cos(\omega t + \beta)] \rangle = \frac{1}{2}\cos(\alpha + \beta) - \frac{\pi}{2}\sin(\alpha + \beta) - \frac{1}{4}\cos(\beta - \alpha)\,, \tag{B.11b}$$

where were used the results (B.11a) and (B.8) with the transformation $\alpha \to \beta$ and $\beta \to -\alpha$.

B.1 Further averages over a period for damped oscillations

In the equations (5.84a) to (5.84e), written in the chapter 5, that explains how to counter damped oscillations by forcing, are used several averages over a period. The following results were deduced from the usual integration rules and following the same reasoning than at the beginning of this appendix. The first one is

$$\langle \{\sin(2\theta), \cos(2\theta)\} \rangle = \frac{1}{2\pi}\int_0^{2\pi} \{\sin(2\theta), \cos(2\theta)\}\, \mathrm{d}\theta = \frac{1}{4\pi}\left[-\cos(2\theta), \sin(2\theta)\right]_0^{2\pi} = 0 \tag{B.12}$$

that follows from an immediate integration. Consequently, using trigonometric relations and knowing the last result, the following integration can be performed immediately:

$$\left\langle \left\{\cos^2\theta, \sin^2\theta\right\} \right\rangle = \left\langle \frac{1}{2} \pm \frac{1}{2}\cos(2\theta) \right\rangle = \frac{1}{2}. \tag{B.13}$$

The next integration is done by parts, and with the result (B.12), one can obtain the following result:

$$\begin{aligned}\langle\theta\sin(2\theta)\rangle &= \frac{1}{2\pi}\int_0^{2\pi}\theta\sin(2\theta)\ \mathrm{d}\theta\\ &= -\frac{1}{4\pi}\left[\theta\cos(2\theta)\right]_0^{2\pi}+\frac{1}{4\pi}\int_0^{2\pi}\cos(2\theta)\ \mathrm{d}\theta=-\frac{1}{2}.\end{aligned}\tag{B.14}$$

Doing again an integration by parts, and using not only trigonometric relations, but also the previous results, the following time average can be done:

$$\begin{aligned}\left\langle\theta\left\{\sin^2\theta,\cos^2\theta\right\}\right\rangle &= \frac{1}{2\pi}\int_0^{2\pi}\theta\left\{\sin^2\theta,\cos^2\theta\right\}\ \mathrm{d}\theta=\frac{1}{4\pi}\int_0^{2\pi}\left[\theta\mp\theta\cos(2\theta)\right]\ \mathrm{d}\theta\\ &= \frac{(2\pi)^2}{8\pi}\mp\frac{1}{8\pi}\left[\theta\sin(2\theta)\right]_0^{2\pi}\pm\int_0^{2\pi}\sin(2\theta)\ \mathrm{d}\theta=\frac{\pi}{2}.\end{aligned}\tag{B.15}$$

The last time average can be done integrating by parts twice and knowing the result (B.12):

$$\begin{aligned}\left\langle\theta^2\sin(2\theta)\right\rangle &= \frac{1}{2\pi}\int_0^{2\pi}\theta^2\sin(2\theta)\ \mathrm{d}\theta=-\frac{1}{4\pi}\left[\theta^2\cos(2\theta)\right]_0^{2\pi}+\frac{1}{2\pi}\int_0^{2\pi}\theta\cos(2\theta)\ \mathrm{d}\theta\\ &= -\frac{(2\pi)^2}{4\pi}+\frac{1}{4\pi}\left[\theta\sin(2\theta)\right]_0^{2\pi}-\frac{1}{4\pi}\int_0^{2\pi}\sin(2\theta)\ \mathrm{d}\theta=-\pi.\end{aligned}\tag{B.16}$$

C | Multipolar expansion for steady magnetic fields

THE Maxwell equations for a steady magnetic field (assuming $\partial/\partial t = 0$), particularly the Gauss's law for magnetism and Ampère-Maxwell equation [24–26], are

$$\nabla \cdot \boldsymbol{B} = 0, \tag{C.1a}$$

$$\nabla \times \boldsymbol{H} = \boldsymbol{J} \tag{C.1b}$$

where $\boldsymbol{H}$ is the magnetic field, $\boldsymbol{B}$ is the magnetic induction and $\boldsymbol{J}$ is the electric current density per unit volume. For an isotropic medium with constant magnetic permeability ($\mu = \text{const}$), the constitutive relation [24–26]

$$\boldsymbol{B} = \mu \boldsymbol{H} \tag{C.2a}$$

leads to

$$\nabla \cdot \boldsymbol{H} = 0. \tag{C.2b}$$

Using the vector identity [24–26]

$$\nabla^2 \boldsymbol{H} = \nabla \left(\nabla \cdot \boldsymbol{H} \right) - \nabla \times \left(\nabla \times \boldsymbol{H} \right), \tag{C.3}$$

the curl of (C.1b) is given by

$$\nabla \times \boldsymbol{J} = \nabla \times \left(\nabla \times \boldsymbol{H} \right) \tag{C.4a}$$

leading to

$$\nabla \times \boldsymbol{J} = -\nabla^2 \boldsymbol{H} \tag{C.4b}$$

by use of the equations (C.3) and (C.2b). Thus, the steady magnetic field satisfies a vector Poisson equation

$$\nabla^2 \boldsymbol{H} = \boldsymbol{Q} \tag{C.5a}$$

forced by the curl of the electric current

$$\boldsymbol{Q} = -\nabla \times \boldsymbol{J}. \tag{C.5b}$$

For a distribution of electric currents over a domain $\mathcal{D}$ with source coordinates $\boldsymbol{y}$, the magnetic field at an observer position $\boldsymbol{x}$ is given by the Poisson integral [169, 170]

$$\boldsymbol{H}(\boldsymbol{x}) = \frac{1}{4\pi} \int_{\mathcal{D}} \frac{\boldsymbol{Q}(\boldsymbol{y})}{|\boldsymbol{x} - \boldsymbol{y}|} \, \mathrm{d}^3\boldsymbol{y}. \tag{C.6}$$

If the observer $\boldsymbol{x}$ lies outside the source $\boldsymbol{y}$ region, the distance $|\boldsymbol{x} - \boldsymbol{y}|$ is not zero and its inverse may be expanded in a Maclaurin series of powers of $\boldsymbol{y}$ around $\boldsymbol{y} = \boldsymbol{0}$

$$\frac{1}{|\boldsymbol{x} - \boldsymbol{y}|} = \frac{1}{|\boldsymbol{x}|} + \sum_{n=1}^{\infty} \frac{M_n}{|\boldsymbol{x}|^n} \tag{C.7}$$

with coefficients

$$M_n(\boldsymbol{x}, \boldsymbol{y}) = \sum_{i_1, \ldots, i_n = 1}^{3} y_{i_1} \ldots y_{i_n} \lim_{\boldsymbol{y} \to \boldsymbol{0}} \frac{\partial^n}{\partial y_{i_1} \ldots \partial y_{i_n}} \left(\frac{1}{|\boldsymbol{x} - \boldsymbol{y}|} \right). \tag{C.8}$$

Substitution of (C.8) in (C.6) leads to the multipolar expansion

$$\boldsymbol{H}(\boldsymbol{x}) = \frac{\boldsymbol{N}_0}{|\boldsymbol{x}|} + \sum_{n=1}^{\infty} \frac{\boldsymbol{N}_n}{|\boldsymbol{x}|^n} \tag{C.9}$$

showing that the magnetic field is the sum of a series of inverse powers of the distance with: (i) lowest-order vector coefficient

$$\boldsymbol{N}_0 = \int_{\mathcal{D}} \boldsymbol{Q}(\boldsymbol{y}) \, \mathrm{d}^3\boldsymbol{y} \tag{C.10a}$$

specified by the integral of the "source" term (C.5b) in (C.5a) over the domain $\mathcal{D}$, corresponding to a dipole; (ii) the remaining terms in (C.9) that are higher-order multipoles with moments given by

$$\boldsymbol{N}_n = \int_{\partial\mathcal{D}} \boldsymbol{Q}(\boldsymbol{y}) \, M_n(\boldsymbol{x}, \boldsymbol{y}) \, \mathrm{d}^3\boldsymbol{y} \tag{C.10b}$$

involving the source term (C.5b) and the relative positions of source and observer (C.8). In the near field for small $|\boldsymbol{x}|$, all terms in the multipolar expansion (C.9) have to be considered. In the far field for large $|\boldsymbol{x}|$, the multipolar expansion (C.9) is dominated by the lowest-order dipole term (C.10a).

D | Cylindrical and spherical dipolar coordinates

The plane dipolar coordinates can be extended to three dimensions as cylindrical dipolar coordinates $(\alpha,\, \beta,\, z)$ by adding an orthogonal Cartesian coordinate z with unit scale factor, $h_{\mathrm{z}} = 1$. Thus, the cylindrical dipolar coordinates where z is a Cartesian axis orthogonal to the $(\alpha,\, \beta)$ plane,

$$\mathrm{d}l^2 = s^2 \left[(\mathrm{d}\alpha)^2 + (\mathrm{d}\beta)^2 \right] + (h_{\mathrm{z}})^2 (\mathrm{d}z)^2 \,, \tag{D.1}$$

have the arclength equal to

$$\mathrm{d}l^2 = \frac{1}{\alpha^2 + \beta^2} \left[(\mathrm{d}\alpha)^2 + (\mathrm{d}\beta)^2 \right] + (\mathrm{d}z)^2 \,. \tag{D.2}$$

The coordinate surfaces (figure D.1) are: (i) $\alpha = \mathrm{const}$ as a cylinder, with axis parallel to the Oz-axis, passing through the Ox-axis at $(1/(2\alpha), 0, 0)$, with radius $1/(2\alpha)$, so that the Oz-axis is a generator; (ii) $\beta = \mathrm{const}$ that is also a cylinder, with axis parallel to the Oz-axis, passing through the Ox-axis at $(0, 1/(2\beta), 0)$, with radius $1/(2\beta)$, so that the Oz-axis is a generator; (iii) a plane $z = \mathrm{const}$, orthogonal to the α and β cylinders. The coordinate curves are: (i) $\{\alpha, z\} = \mathrm{const}$ as a circle, on the plane $z = \mathrm{const}$, with centre at $(1/(2\alpha), 0, z)$, and radius $1/(2\alpha)$, touching the Oz-axis at $(0, 0, z)$; (ii) $\beta, z = \mathrm{const}$ as a circle, on the plane $z = \mathrm{const}$, with centre at $(0, 1/(2\beta), z)$, and radius $1/(2\beta)$, touching the Oz-axis at $(0, 0, z)$; (iii) and $\{\alpha, \beta\} = \mathrm{const}$ as a straight line parallel to the Oz-axis, passing through the point $(\alpha, \beta, 0)$, which is the common generator of the two cylinders $\{\alpha, \beta\} = \mathrm{const}$.

Spherical dipolar coordinates $(\alpha,\, \beta,\, \phi)$ are obtained by rotating plane dipolar coordinates $(\alpha,\, \beta)$ around the Ox-axis, thus adding as third coordinate the azimuthal angle ϕ whose corresponding scale factor is

$$h_\phi = r \sin\theta = \frac{\beta}{(\alpha^2 + \beta^2)} = \beta s \tag{D.3}$$

where (7.14b) and (7.17b) were used. The arclength

$$(\mathrm{d}l)^2 = s^2 \left[(\mathrm{d}\alpha)^2 + (\mathrm{d}\beta)^2 \right] + (h_\phi)^2 (\mathrm{d}\phi)^2 = s^2 \left[(\mathrm{d}\alpha)^2 + (\mathrm{d}\beta)^2 + \beta^2 (\mathrm{d}\phi)^2 \right] \tag{D.4}$$

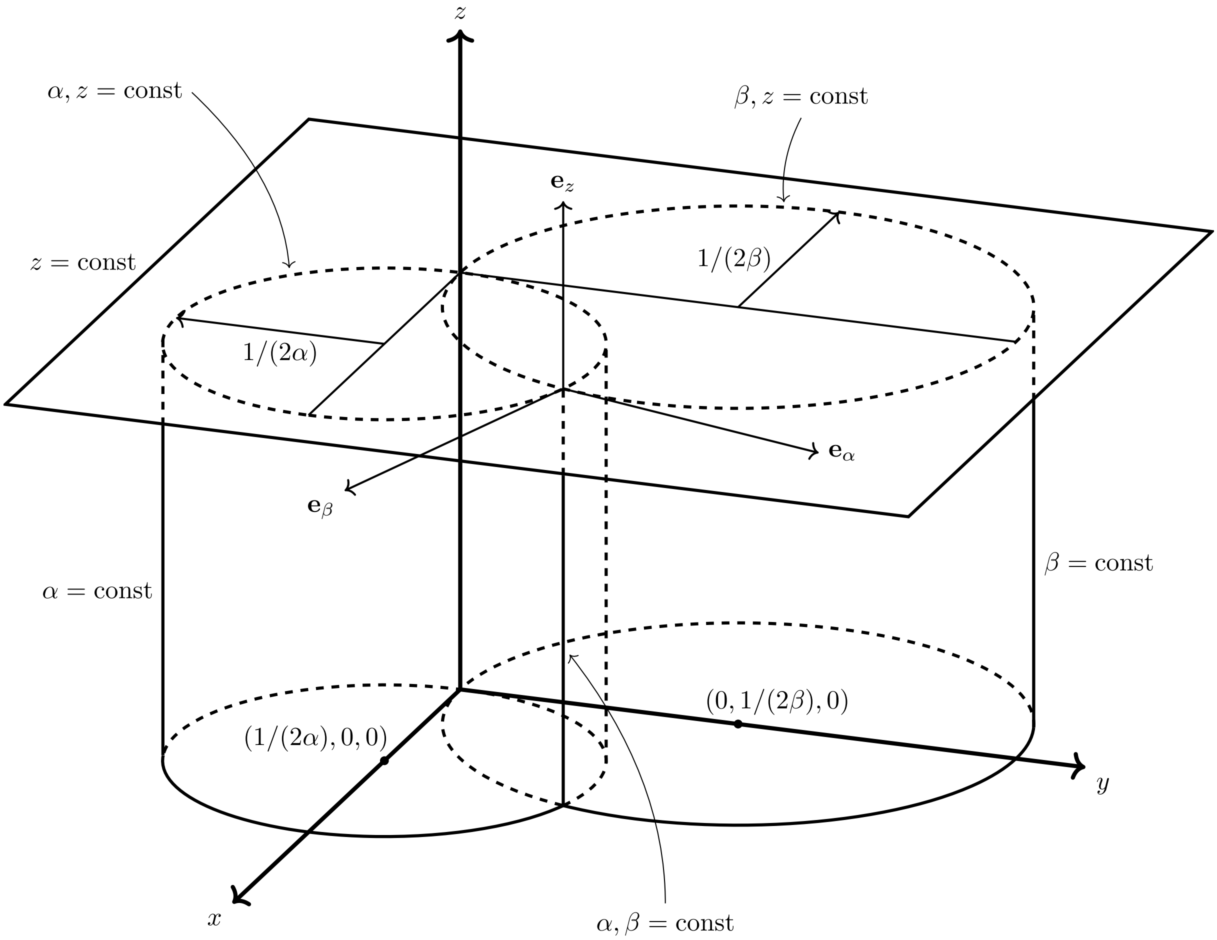

Figure D.1: The translation of plane dipolar coordinates (figure 7.1) along the normal to their plane leads to cylindrical dipolar coordinates whose coordinate surfaces are: (i) a cylinder with vertical axis passing through the x coordinate axis and a generator along the z axis; (ii) another cylinder with vertical axis passing through the y coordinate axis and a generator along the z axis; (iii) horizontal plane that is orthogonal to both families of cylinders that are also orthogonal to each other.

is given by

$$(\mathrm{d}l)^2 = \frac{1}{(\alpha^2 + \beta^2)^2} \left[(\mathrm{d}\alpha)^2 + (\mathrm{d}\beta)^2 + \beta^2 (\mathrm{d}\phi)^2 \right]. \tag{D.5}$$

The coordinate surfaces (figure D.2) are: (i) $\alpha = \mathrm{const}$ as a sphere, with centre on the Ox-axis at $(1/(2\alpha), 0, 0)$ and radius $1/(2\alpha)$, so that it is tangent to the yOz plane at the origin; (ii) $\beta = \mathrm{const}$ as a torus, with cross-section a circle of radius $1/(2\beta)$, along the Ox-axis, and line of centres a circle in the yOz-plane, of radius $1/(2\beta)$ and centre at the origin, so the torus touches itself at the origin; (iii) $\phi = \mathrm{const}$ as a semi-plane, passing through the Ox-axis, and making an angle ϕ with the Oz-axis. The coordinate curves are: (i) $\{\alpha, \phi\} = \mathrm{const}$ as a circle of radius $1/(2\alpha)$ with centre on the plane $\phi = \mathrm{const}$ at a distance $1/(2\alpha)$ from the Oy-axis, to which it is tangent; (ii) $\{\beta, \phi\} = \mathrm{const}$ as a circle of radius $1/(2\beta)$ with centre on the plane $\phi = \mathrm{const}$ at a distance $1/(2\beta)$ from the Ox-axis, to which it is tangent; (iii) $\{\alpha, \beta\} = \mathrm{const}$ as a circle on a plane perpendicular to the Ox-axis, at a distance r from the origin, with centre on the Ox-axis at $(x, 0, 0)$ and radius y given by

$$x = r\cos\theta = r^2\alpha = \frac{\alpha}{\alpha^2+\beta^2}, \tag{D.6a}$$

$$y = r\sin\theta = r^2\beta = \frac{\beta}{\alpha^2+\beta^2}, \tag{D.6b}$$

where both equations of (7.14) and equation (7.16a) were used.

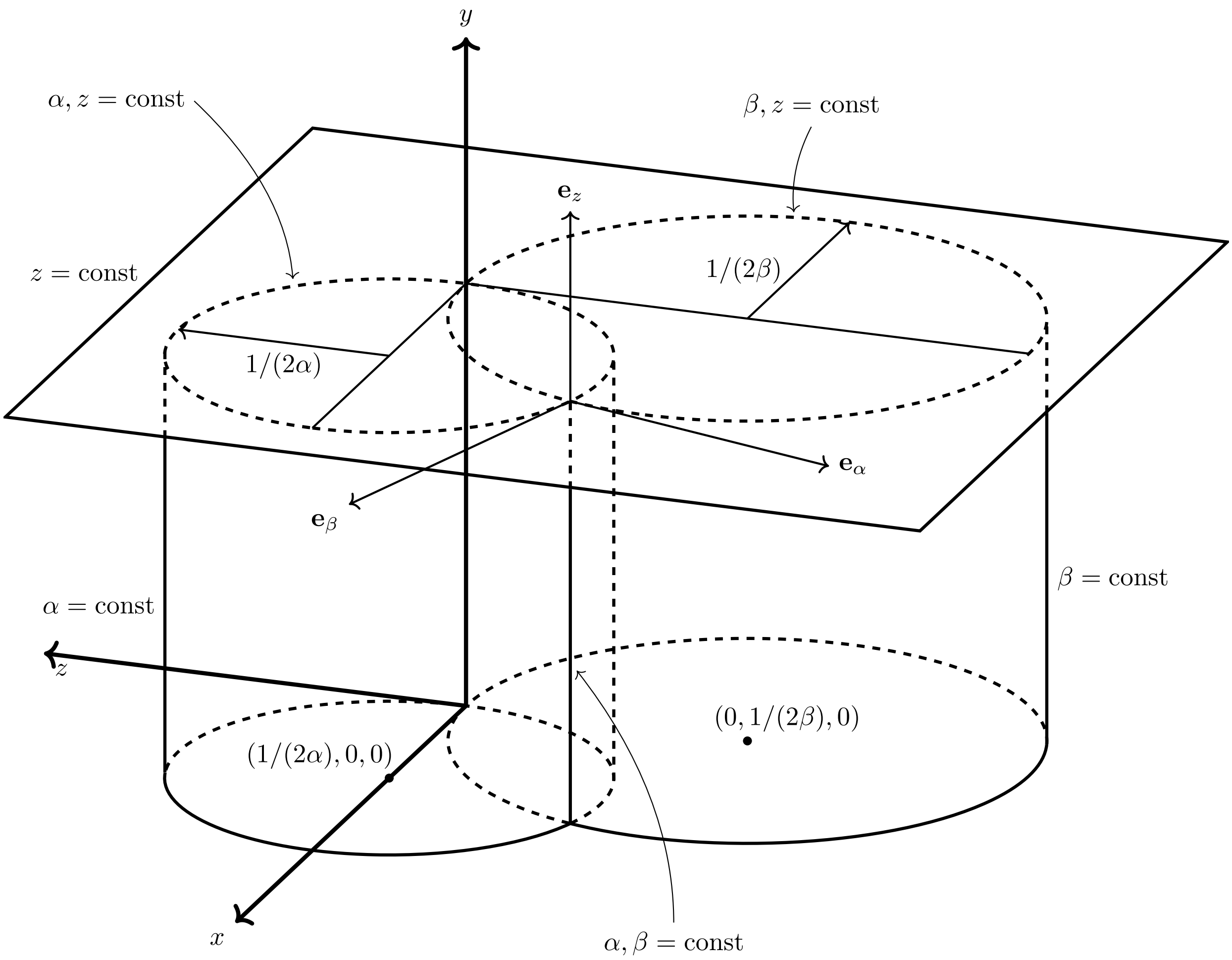

Figure D.2: Rotating the plane dipolar coordinates (figure 7.1) around the x axis leads to spherical dipolar coordinates whose coordinate surfaces are: (i) a sphere $\alpha = \text{const}$ with centre on the x axis passing through the origin; (ii) a torus $\beta = \text{const}$ with the origin as the interior point where touch all circular cross-sections through planes passing through the x axis; (iii) any plane $\phi = \text{const}$ that pass through the x axis is orthogonal both to the sphere (i) and torus (ii).

E | Strong bending of an orthotropic or pseudo isotropic plate

THE stress-strain relation for an orthotropic elastic material [129] is specified by the stiffness matrix

$$\begin{bmatrix} T_{\mathrm{xx}} \\ T_{\mathrm{yy}} \\ T_{\mathrm{zz}} \\ T_{\mathrm{xy}} \\ T_{\mathrm{xz}} \\ T_{\mathrm{yz}} \end{bmatrix} = \begin{bmatrix} C_{11} & C_{12} & C_{13} & 0 & 0 & 0 \\ C_{12} & C_{22} & C_{23} & 0 & 0 & 0 \\ C_{13} & C_{23} & C_{33} & 0 & 0 & 0 \\ 0 & 0 & 0 & C_{44} & 0 & 0 \\ 0 & 0 & 0 & 0 & C_{55} & 0 \\ 0 & 0 & 0 & 0 & 0 & C_{66} \end{bmatrix} \begin{bmatrix} S_{\mathrm{xx}} \\ S_{\mathrm{yy}} \\ S_{\mathrm{zz}} \\ S_{\mathrm{xy}} \\ S_{\mathrm{xz}} \\ S_{\mathrm{yz}} \end{bmatrix}. \tag{E.1}$$

The case of a pseudo-isotropic orthotropic material imposes two additional relations [129],

$$C_{33}\left(C_{22} - C_{11}\right) = \left(C_{23}\right)^2 - \left(C_{13}\right)^2, \tag{E.2a}$$

$$C_{44}C_{33} = C_{33}\left(C_{11} - C_{12}\right) + C_{13}\left(C_{23} - C_{13}\right), \tag{E.2b}$$

and as a consequence of the preceding, the both relations leads to

$$C_{44}C_{33} = C_{33}\left(C_{22} - C_{12}\right) - C_{23}\left(C_{23} - C_{13}\right). \tag{E.2c}$$

The notable property of a pseudo-isotropic orthotropic elastic material is that it generalises the isotropic elastic material while satisfying the same bending balance equation (9.1) with the generalised bending stiffness:

$$D = \frac{h^3}{12}\left(C_{11} - C_{13}\frac{C_{13}}{C_{33}}\right). \tag{E.3}$$

In the case of an isotropic elastic material, the generalised bending stiffness simplifies to (9.3a). Thus, the balance equation (9.3b) remains valid, with

$$\frac{f}{h} = \frac{D}{h}\boldsymbol{\nabla}^4\zeta - \left(\partial_{\mathrm{yy}}\Theta\right)\left(\partial_{\mathrm{xx}}\zeta\right) - \left(\partial_{\mathrm{xx}}\Theta\right)\left(\partial_{\mathrm{yy}}\zeta\right) + 2\left(\partial_{\mathrm{xy}}\Theta\right)\left(\partial_{\mathrm{xy}}\zeta\right), \tag{E.4}$$

replacing the first bending stiffness for an isotropic plate (9.3a) by that for a pseudo-isotropic orthotropic plate (E.3),

$$\frac{Eh^3}{12\left(1-\sigma^2\right)} \leftarrow D \rightarrow \frac{h^3}{12}\left(C_{11} - C_{13}\frac{C_{13}}{C_{33}}\right). \tag{E.5}$$

Concerning the second complementary equation (9.4) of the pair: (i) the derivation from (9.6) to the first equalities in (9.12a) to (9.12c) is independent of the type of material; (ii) the elimination of the in-plane displacement is made as in (9.13a) retaining the strains from the first equalities in (9.12a) to (9.12c), leading to

$$\frac{1}{2}\left[\partial_{\mathrm{yy}}\left(\partial_{\mathrm{x}}\zeta\right)^2 + \partial_{\mathrm{xx}}\left(\partial_{\mathrm{y}}\zeta\right)^2 - 2\partial_{\mathrm{xy}}\left(\partial_{\mathrm{x}}\zeta\right)\left(\partial_{\mathrm{y}}\zeta\right)\right] = \partial_{\mathrm{yy}}S_{\mathrm{xx}} + \partial_{\mathrm{xx}}S_{\mathrm{yy}} - 2\partial_{\mathrm{xy}}S_{\mathrm{xy}}; \tag{E.6}$$

(iii) the left-hand side of (E.6) is simplified as in (9.13b), leading to

$$\left(\partial_{\mathrm{xy}}\zeta\right)^2 - \left(\partial_{\mathrm{xx}}\zeta\right)\left(\partial_{\mathrm{yy}}\zeta\right) = \partial_{\mathrm{yy}}\left(A_{11}T_{\mathrm{xx}} + A_{12}T_{\mathrm{yy}}\right) + \partial_{\mathrm{xx}}\left(A_{12}T_{\mathrm{xx}} + A_{22}T_{\mathrm{yy}}\right) - 2\partial_{\mathrm{xy}}\left(A_{44}T_{\mathrm{xy}}\right), \tag{E.7}$$

and on the right-hand side is used the compliance matrix, with the relation between strains and stresses given by [129]

$$\begin{bmatrix} S_{\mathrm{xx}} \\ S_{\mathrm{yy}} \\ S_{\mathrm{zz}} \\ S_{\mathrm{xy}} \\ S_{\mathrm{xz}} \\ S_{\mathrm{yz}} \end{bmatrix} = \begin{bmatrix} A_{11} & A_{12} & A_{13} & 0 & 0 & 0 \\ A_{12} & A_{22} & A_{23} & 0 & 0 & 0 \\ A_{13} & A_{23} & A_{33} & 0 & 0 & 0 \\ 0 & 0 & 0 & A_{44} & 0 & 0 \\ 0 & 0 & 0 & 0 & A_{55} & 0 \\ 0 & 0 & 0 & 0 & 0 & A_{66} \end{bmatrix} \begin{bmatrix} T_{\mathrm{xx}} \\ T_{\mathrm{yy}} \\ T_{\mathrm{zz}} \\ T_{\mathrm{xy}} \\ T_{\mathrm{xz}} \\ T_{\mathrm{yz}} \end{bmatrix}, \tag{E.8}$$

that is the inverse of the stiffness matrix in (E.1) for an orthotropic material bearing in mind that for a plate there are only in-plane stresses $T_{\mathrm{zz}} = T_{\mathrm{xz}} = T_{\mathrm{yz}} = 0$; (iv) substituting (9.2c) in (E.7), it follows that the complementary equation relating the transverse displacement to the stress function for the strong bending of an orthotropic plate is

$$\left(\partial_{\mathrm{xy}}\zeta\right)^2 - \left(\partial_{\mathrm{xx}}\zeta\right)\left(\partial_{\mathrm{yy}}\zeta\right) = A_{22}\partial_{\mathrm{xxxx}}\Theta + A_{11}\partial_{\mathrm{yyyy}}\Theta + 2\left(A_{12} + A_{44}\right)\partial_{\mathrm{xxyy}}\Theta, \tag{E.9}$$

assuming that the components of the compliance matrix are constant, $A_{ab} = \mathrm{const}$. The first (E.4) and second (E.9) equations of the coupled pair are valid respectively for a pseudo-isotropic and general orthotropic plate.

Writing the compliance matrix present in (E.8) in the form

$$\begin{bmatrix} S_{\mathrm{xx}} \\ S_{\mathrm{yy}} \\ S_{\mathrm{zz}} \\ S_{\mathrm{xy}} \\ S_{\mathrm{xz}} \\ S_{\mathrm{yz}} \end{bmatrix} = \begin{bmatrix} \frac{1}{E_{\mathrm{x}}} & -\frac{\sigma_{\mathrm{yx}}}{E_{\mathrm{y}}} & -\frac{\sigma_{\mathrm{zx}}}{E_{\mathrm{z}}} & 0 & 0 & 0 \\ -\frac{\sigma_{\mathrm{xy}}}{E_{\mathrm{x}}} & \frac{1}{E_{\mathrm{y}}} & -\frac{\sigma_{\mathrm{zy}}}{E_{\mathrm{y}}} & 0 & 0 & 0 \\ -\frac{\sigma_{\mathrm{xz}}}{E_{\mathrm{x}}} & -\frac{\sigma_{\mathrm{yz}}}{E_{\mathrm{y}}} & \frac{1}{E_{\mathrm{z}}} & 0 & 0 & 0 \\ 0 & 0 & 0 & \frac{1}{2G_{\mathrm{xy}}} & 0 & 0 \\ 0 & 0 & 0 & 0 & \frac{1}{2G_{\mathrm{xz}}} & 0 \\ 0 & 0 & 0 & 0 & 0 & \frac{1}{2G_{\mathrm{yz}}} \end{bmatrix} \begin{bmatrix} T_{\mathrm{xx}} \\ T_{\mathrm{yy}} \\ T_{\mathrm{zz}} \\ T_{\mathrm{xy}} \\ T_{\mathrm{xz}} \\ T_{\mathrm{yz}} \end{bmatrix}, \tag{E.10}$$

in terms of the generalised Young moduli and Poison ratios [129], leads to (E.1), equivalent to the next equation, for its inverse, that is the stiffness matrix given by

$$\begin{bmatrix} T_{\mathrm{xx}} \\ T_{\mathrm{yy}} \\ T_{\mathrm{zz}} \\ T_{\mathrm{xy}} \\ T_{\mathrm{xz}} \\ T_{\mathrm{yz}} \end{bmatrix} = \begin{bmatrix} \frac{1-\sigma_{\mathrm{yz}}\sigma_{\mathrm{zy}}}{C_0 E_{\mathrm{y}} E_{\mathrm{z}}} & \frac{\sigma_{\mathrm{yx}}+\sigma_{\mathrm{yz}}\sigma_{\mathrm{zx}}}{C_0 E_{\mathrm{y}} E_{\mathrm{z}}} & \frac{\sigma_{\mathrm{zx}}+\sigma_{\mathrm{zy}}\sigma_{\mathrm{yx}}}{C_0 E_{\mathrm{y}} E_{\mathrm{z}}} & 0 & 0 & 0 \\ \frac{\sigma_{\mathrm{xy}}+\sigma_{\mathrm{xz}}\sigma_{\mathrm{zy}}}{C_0 E_{\mathrm{x}} E_{\mathrm{z}}} & \frac{1-\sigma_{\mathrm{xz}}\sigma_{\mathrm{zx}}}{C_0 E_{\mathrm{x}} E_{\mathrm{z}}} & \frac{\sigma_{\mathrm{zy}}+\sigma_{\mathrm{zx}}\sigma_{\mathrm{xy}}}{C_0 E_{\mathrm{x}} E_{\mathrm{z}}} & 0 & 0 & 0 \\ \frac{\sigma_{\mathrm{xz}}+\sigma_{\mathrm{xy}}\sigma_{\mathrm{yz}}}{C_0 E_{\mathrm{x}} E_{\mathrm{y}}} & \frac{\sigma_{\mathrm{yz}}+\sigma_{\mathrm{yx}}\sigma_{\mathrm{xz}}}{C_0 E_{\mathrm{x}} E_{\mathrm{y}}} & \frac{1-\sigma_{\mathrm{xy}}\sigma_{\mathrm{yx}}}{C_0 E_{\mathrm{x}} E_{\mathrm{y}}} & 0 & 0 & 0 \\ 0 & 0 & 0 & 2G_{\mathrm{xy}} & 0 & 0 \\ 0 & 0 & 0 & 0 & 2G_{\mathrm{xz}} & 0 \\ 0 & 0 & 0 & 0 & 0 & 2G_{\mathrm{yz}} \end{bmatrix} \begin{bmatrix} S_{\mathrm{xx}} \\ S_{\mathrm{yy}} \\ S_{\mathrm{zz}} \\ S_{\mathrm{xy}} \\ S_{\mathrm{xz}} \\ S_{\mathrm{yz}} \end{bmatrix} \tag{E.11}$$

where $C_0 = \mathrm{Det}\,(C_{ij})$ for $i, j = \{1, 2, 3\}$ and $E_{\mathrm{x}} E_{\mathrm{y}} E_{\mathrm{z}} C_0 = 1 - \sigma_{\mathrm{xy}}\sigma_{\mathrm{yx}} - \sigma_{\mathrm{xz}}\sigma_{\mathrm{zx}} - \sigma_{\mathrm{yz}}\sigma_{\mathrm{zy}} - 2\sigma_{\mathrm{xy}}\sigma_{\mathrm{yz}}\sigma_{\mathrm{zx}}$.

In the complementary equation (E.9) there are three coefficients specified by the compliance matrix (E.10),

$$A_{11} = 1/E_{\mathrm{x}} \tag{E.12a}$$

$$A_{22} = 1/E_{\mathrm{y}} \tag{E.12b}$$

$$2\,(A_{12} + A_{44}) = -2\sigma_{\mathrm{xy}}/E_{\mathrm{x}} + 1/G_{\mathrm{xy}}. \tag{E.12c}$$

Several coefficients of the stiffness matrix in (E.11) are needed,

$$C_{11} = \frac{1 - \sigma_{\mathrm{yz}}\sigma_{\mathrm{zy}}}{C_0 E_{\mathrm{y}} E_{\mathrm{z}}}, \tag{E.13a}$$

$$C_{22} = \frac{1 - \sigma_{\mathrm{xz}}\sigma_{\mathrm{zx}}}{C_0 E_{\mathrm{x}} E_{\mathrm{z}}}, \tag{E.13b}$$

$$C_{33} = \frac{1 - \sigma_{\mathrm{xy}}\sigma_{\mathrm{yx}}}{C_0 E_{\mathrm{x}} E_{\mathrm{y}}}, \tag{E.13c}$$

$$C_{44} = 2G_{\mathrm{xy}}, \tag{E.13d}$$

$$C_{12} = \frac{\sigma_{\mathrm{yx}} + \sigma_{\mathrm{yz}}\sigma_{\mathrm{zx}}}{C_0 E_{\mathrm{y}} E_{\mathrm{z}}}, \tag{E.13e}$$

$$C_{13} = \frac{\sigma_{\mathrm{zx}} + \sigma_{\mathrm{zy}}\sigma_{\mathrm{yx}}}{C_0 E_{\mathrm{y}} E_{\mathrm{z}}}, \tag{E.13f}$$

$$C_{23} = \frac{\sigma_{\mathrm{zy}} + \sigma_{\mathrm{zx}}\sigma_{\mathrm{xy}}}{C_0 E_{\mathrm{x}} E_{\mathrm{z}}}, \tag{E.13g}$$

namely: (i) three in the first bending stiffness (E.5),

$$D = \frac{h^3}{12 C_0 E_{\mathrm{y}} E_{\mathrm{z}}} \left[1 - \sigma_{\mathrm{yz}}\sigma_{\mathrm{zy}} - \frac{E_{\mathrm{x}}}{E_{\mathrm{z}}} \frac{\left(\sigma_{\mathrm{zx}} + \sigma_{\mathrm{zy}}\sigma_{\mathrm{yx}}\right)^2}{1 - \sigma_{\mathrm{xy}}\sigma_{\mathrm{yx}}} \right]; \tag{E.14a}$$

(ii) one in the second bending stiffness,

$$\overline{C}_{44} \equiv \frac{h^3}{12} C_{44} = \frac{h^3 G_{\mathrm{xy}}}{6}; \tag{E.14b}$$

(iii) five in the first condition (E.2a) condition for a pseudo-isotropic orthotropic material,

$$\begin{aligned} &E_{\mathrm{z}} \left(1 - \sigma_{\mathrm{xy}}\sigma_{\mathrm{yx}}\right) \left[E_{\mathrm{y}} \left(1 - \sigma_{\mathrm{xz}}\sigma_{\mathrm{zx}}\right) - E_{\mathrm{x}} \left(1 - \sigma_{\mathrm{yz}}\sigma_{\mathrm{zy}}\right) \right] \\ &\quad = \left[E_{\mathrm{y}} \left(\sigma_{\mathrm{zy}} + \sigma_{\mathrm{zx}}\sigma_{\mathrm{xy}}\right) \right]^2 - \left[E_{\mathrm{x}} \left(\sigma_{\mathrm{zx}} + \sigma_{\mathrm{zy}}\sigma_{\mathrm{yx}}\right) \right]^2; \end{aligned} \tag{E.15a}$$

(iv) six in the second condition (E.2b) for a pseudo-isotropic orthotropic material,

$$\begin{aligned} &E_{\mathrm{z}} \left(1 - \sigma_{\mathrm{xy}}\sigma_{\mathrm{yx}}\right) \left\{ 2 C_0 E_{\mathrm{x}} E_{\mathrm{y}} E_{\mathrm{z}} G_{\mathrm{xy}} - E_{\mathrm{x}} \left[1 - \sigma_{\mathrm{yx}} - \sigma_{\mathrm{yz}} \left(\sigma_{\mathrm{zx}} + \sigma_{\mathrm{zy}}\right) \right] \right\} \\ &\quad = E_{\mathrm{x}} \left(\sigma_{\mathrm{zx}} + \sigma_{\mathrm{zy}}\sigma_{\mathrm{yx}}\right) \left[E_{\mathrm{y}} \left(\sigma_{\mathrm{zy}} + \sigma_{\mathrm{zx}}\sigma_{\mathrm{xy}}\right) - E_{\mathrm{x}} \left(\sigma_{\mathrm{zx}} + \sigma_{\mathrm{zy}}\sigma_{\mathrm{yx}}\right) \right]. \end{aligned} \tag{E.15b}$$

In conclusion, the transverse displacement and stress function in the strong non-linear deflection of an elastic plate made of a pseudo-isotropic orthotropic material satisfy the coupled non-linear fourth-order partial differential equations (E.4) and (E.9) where: (i) the first bending stiffness (E.5) is given by (E.14a); (ii) the second bending stiffness is given by (E.14b). Four and seven terms of the compliance (E.10) and stiffness (E.11) matrices appear respectively in the balance equations (i-ii) and boundary conditions (iii-iv). The three Young moduli E_i, six Poison ratios σ_{ij} and the three shear moduli G_{ij} satisfy the symmetry relations in the compliance matrix (E.10) implying

$$\sigma_{ij} E_j = \sigma_{ji} E_i, \tag{E.16a}$$

while the symmetry of the stiffness matrix (E.11) implies

$$\left(\sigma_{ij} + \sigma_{ik}\sigma_{kj}\right) E_j = E_i \left(\sigma_{ji} + \sigma_{jk}\sigma_{ki}\right). \tag{E.16b}$$

In the two previous relations, the repeated indices do not mean summation. They are valid when each index – i, j and k – takes a value between 1 and 3, meaning one of the Cartesian directions, and when none of the three indices have the same value. In addition, a pseudo-isotropic orthotropic material satisfies two additional relations (E.2a) and (E.2b), equivalent to (E.15a) and (E.15b).